Time-Resolved Single-Frequency Infrared Spectroscopy Provides Atomistic Insight into the Functioning of the Two Photosystems of Oxygenic Photosynthesis

Dissertation
zur Erlangung des Grades eines
Doktors der Naturwissenschaften
(Dr. rer. nat.)

am Fachbereich Physik
der Freien Universität Berlin

vorgelegt von
Sarah Maya Mäusle

Berlin 2024

Selbstständigkeitserklärung

Name: Mäusle
Vorname: Sarah Maya

Ich erkläre gegenüber der Freien Universität Berlin, dass ich die vorliegende Dissertation selbstständig und ohne Benutzung anderer als der angegebenen Quellen und Hilfsmittel angefertigt habe. Die vorliegende Arbeit ist frei von Plagiaten. Alle Ausführungen, die wörtlich oder inhaltlich aus anderen Schriften entnommen sind, habe ich als solche kenntlich gemacht. Diese Dissertation wurde in gleicher oder ähnlicher Form noch in keinem früheren Promotionsverfahren eingereicht.

Mit einer Prüfung meiner Arbeit durch ein Plagiatsprüfungsprogramm erkläre ich mich einverstanden.

Datum: _____   Unterschrift: _____

Abstract

Photosystems I and II (PSI, PSII) are two large protein complexes that are part of the electron transport chain of oxygenic photosynthesis in plants, algae, and cyanobacteria. The activity of these photosystems is indispensable in oxygenic photosynthesis, the process that powers life on Earth by converting solar energy into chemical energy. PSII harbors the light-driven water splitting process, which results in the removal of four protons and four electrons from two water molecules. This process is coupled to the release of molecular oxygen (O_2) and is thus also referred to as *photosynthetic oxygen evolution* or *oxygen evolution reaction* (OER); it is responsible for creating the oxygen in the Earth's atmosphere. The OER cycle of PSII (S-state cycle) involves four successive photon absorption events, which lead to the stepwise accumulation of four oxidation equivalents at the catalytic site, a protein-bound Mn_4CaO_x cluster, prior to O_2 formation. In contrast, the PSI reactions can be discussed as a one-photon process: upon absorption, charge separation takes place and the electron is transported down one of two paths (the A- or B-branch), finally reducing the mobile electron carrier ferredoxin. In both photosystems, the light-induced processes are still insufficiently understood regarding the temporal sequence of atomistic events.

The focus of this thesis is the investigation of the S-state transitions in PSII by means of time-resolved single-frequency infrared (TRSF-IR) spectroscopy in the wavenumber range from 1800 cm^{-1} to 1300 cm^{-1}. Measurements on spinach PSII membrane particles in H_2O, D_2O and at several different pH values allowed for the characterization of the kinetics of three S-state transitions ($S_1{\rightarrow}S_2$, $S_2{\rightarrow}S_3$ and $S_3{\rightarrow}S_0$). Global analysis of time-resolved spectral data sets resulted in decay-associated spectra (DAS), which are essentially spectral fingerprints of individual kinetic phases. The DAS of the proton transfer (PT) and electron transfer (ET) phases of the O_2-producing $S_3{\rightarrow}S_0$ transition mostly reproduced the results of a previous step-scan Fourier-transform infrared (FTIR) study (Greife et al., 2023), but also managed to resolve a crucial deuteration-induced band shift, which was left undetected by the FTIR study.

Global analysis of a data set on a spinach PSII sample depleted of its Mn_4CaO_x cluster resulted in DAS that showed great similarity to previously reported FTIR spectra of two PSII co-factors (Q_A and P680). Double difference spectra of intact minus Mn depleted PSII revealed that certain spectral regions are likely to be more strongly affected by a high fraction of broken PSII centers than others.

The comparative analysis of spinach PSII membranes to PSII core particles from *Thermosynechococcus vestitus* BP-1 (*T. vestitus*) and *Synechocystis* sp. PCC 6803 revealed that while at some wavenumbers the IR difference transients are very similar to each other, they differ drastically at others. It was found that the likely source of this observation is a differing amount of broken PSII centers in the different samples. Measurements of *T. vestitus* in D_2O revealed similar kinetic isotope effects as observed for spinach PSII.

PSII from *Synechocystis* carrying either the D1-N298A or the D1-D61A mutation was investigated and compared to wild-type PSII. While the monophasic O_2-producing ET step of the $S_3{\rightarrow}S_0$ transition was found to be drastically slowed in D1-D61A, it was found to be biphasic in D1-N298A. We assign the two observed kinetic phases to (i) O_2-evolution occurring at a similar rate as in wild-type PSII and (ii) strongly decelerated substrate water insertion into the Mn_4CaO_x cluster, which in wild-type PSII occurs faster than the rate-limiting step and is therefore usually not spectroscopically detectable.

Measurements on three PSI wild-type variants allowed for the first ever IR spectroscopic observation of ET down the A- and B-branch at room temperature. Global analysis of the nanosecond kinetics resulted in DAS of forward ET down the A-branch.

All in all, TRSF-IR measurements allowed for the kinetic and spectral characterization of various PSII and PSI samples, resulting in a small contribution toward a full understanding of the molecular mechanisms of oxygenic photosynthesis.

Zusammenfassung

Die Photosysteme I und II (PSI, PSII) sind zwei große Proteinkomplexe, die Teil der Elektronentransportkette der oxygenen Photosynthese in Pflanzen, Algen und Cyanobakterien sind. Die Aktivität dieser Photosysteme ist unabdingbar für die oxygene Photosynthese, die das Leben auf der Erde durch die Umwandlung von Solarenergie in chemische Energie antreibt. PSII katalysiert den lichtgetriebenen Wasserspaltungsprozess, bei dem vier Protonen und vier Elektronen aus zwei Wassermolekülen entfernt werden. Dieser Prozess, der die Atmosphäre unserer Erde mit Sauerstoff angereichert hat, ist an die Freisetzung von molekularem Sauerstoff (O_2) gekoppelt, weswegen er auch als photosynthetische Sauerstoffentwicklung oder Sauerstoffentwicklungsreaktion (OER) bezeichnet wird. Der OER-Zyklus von PSII (S-Zustandszyklus) umfasst vier aufeinanderfolgende Photonenabsorptionsereignisse, die zur schrittweisen Ansammlung von vier Oxidationsäquivalenten am katalytischen Zentrum, einem proteingebundenen Mn_4CaO_x-Cluster, führen, bevor schließlich O_2 gebildet wird. Im Gegensatz dazu können die PSI-Reaktionen als ein Ein-Photonen-Prozess beschrieben werden: Nach der Absorption wird eine Ladungstrennung initiiert und das Elektron folgt einem von zwei Pfaden (A- oder B-Zweig), bevor es schließlich den mobilen Elektronenträger Ferredoxin reduziert. In beiden Photosystemen sind die lichtinduzierten Prozesse hinsichtlich der zeitlichen Abfolge der atomistischen Ereignisse noch unzureichend verstanden.

Der Fokus dieser Dissertation liegt auf der Untersuchung der S-Zustandsübergänge in PSII mittels zeitaufgelöster Einzelfrequenz-Infrarotspektroskopie (TRSF-IR) im Wellenzahlbereich von $1800\ cm^{-1}$ bis $1300\ cm^{-1}$. Messungen an Spinat-PSII-Membranpartikeln in H_2O, D_2O und bei mehreren verschiedenen pH-Werten ermöglichten die Charakterisierung der Kinetiken von drei S-Zustandsübergängen ($S_1{\rightarrow}S_2$, $S_2{\rightarrow}S_3$ und $S_3{\rightarrow}S_0$). Die globale Analyse zeitaufgelöster spektraler Datensätze ergab Zerfallsspektren (DAS), die als spektrale Fingerabdrücke der kinetischen Phasen interpretiert werden können. Die DAS der Protonentransfer- (PT) und Elektronentransfer- (ET) Phasen des O_2-produzierenden $S_3{\rightarrow}S_0$ Übergangs konnten größtenteils die Ergebnisse einer vorherigen Step-Scan Fourier-Transform Infrarot (FTIR) Studie reproduzieren (Greife et al., 2023), konnten darüber hinaus jedoch auch eine entscheidende deuterierungsinduzierte Bandenverschiebung auflösen, die in der FTIR-Studie nicht detektiert wurde.

Die globale Analyse eines Datensatzes zu einer Mn_4CaO_x-Cluster-losen Spinat-PSII-Probe ergab DAS, die große Ähnlichkeit mit zuvor veröffentlichten FTIR-Spektren zweier PSII-Kofaktoren (Q_A und P680) aufwiesen. Die Doppeldifferenzspektren von intaktem minus Mn_4CaO_x-Cluster-losen PSII zeigten, dass gewisse spektrale Bereiche wahrscheinlich stärker von einem hohen Anteil kaputter PSII-Zentren betroffen sind als andere.

Die vergleichende Analyse von Spinat-PSII-Membranen sowie PSII-Kernpartikeln aus *Thermosynechococcus vestitus* BP-1 (*T. vestitus*) und *Synechocystis* sp. PCC 6803 ergab, dass die IR-Differenztransienten bei einigen Wellenzahlen sehr ähnlich sind, sich jedoch bei anderen drastisch unterscheiden. Es wurde festgestellt, dass die Ursache dieser Beobachtung wahrscheinlich auf einen variierenden Anteil kaputter PSII-Zentren in den verschiedenen Proben zurückzuführen ist. Messungen an *T. vestitus* in D_2O wiesen ähnliche kinetische Isotopeneffekte auf wie die, die für Spinat-PSII beobachtet wurden.

Punktmutiertes PSII aus *Synechocystis*, das entweder die D1-N298A- oder D1-D61A-Mutation trägt, wurde untersucht und mit Wildtyp-PSII verglichen. Während der monophasische O_2-produzierende ET-Schritt des $S_3{\rightarrow}S_0$ Übergangs in D1-D61A drastisch verlangsamt erschien, zeigte er sich in D1-N298A biphasisch. Wir ordnen die beiden beobachteten kinetischen Phasen folgenden Ereignissen zu: (i) der O_2-Produktion, die mit einer ähnlichen Geschwindigkeit wie im Wildtyp auftritt, und (ii) der stark verlangsamten Substratwasser-Einfügung in den Mn_4CaO_x-Cluster. Die zweite Phase erfolgt im Wildtyp-PSII schneller als der ratenlimitierende Schritt, weshalb sie normalerweise nicht spektroskopisch nachweisbar ist.

Messungen an drei PSI-Wildtypvarianten ermöglichten erstmals die IR-spektroskopische Beobachtung des ET entlang der A- und B-Zweige bei Raumtemperatur. Die globale Analyse der Kinetiken im Nanosekundenbereich ergab DAS des Vorwärts-ET entlang des A-Zweigs.

Insgesamt ermöglichten die im Rahmen dieser Arbeit durchgeführten TRSF-IR-Messungen die kinetische und spektrale Charakterisierung verschiedener PSII- und PSI-Proben. Dies leistete einen kleinen Beitrag zum vollständigen Verständnis der molekularen Mechanismen der oxygenen Photosynthese.

Brief Overview

Table of Contents

List of Abbreviations

A$_{-1A}$, A$_{0A}$, A$_{1A}$ primary acceptors along the A-branch of PSI
A$_{-1B}$, A$_{0B}$, A$_{1B}$ primary acceptors along the B-branch of PSI
A/D analog-to-digital
ADP adenosine diphosphate
ATP adenosine triphosphate
β–DM n-dodecyl-β-D-maltoside
BSA bovine serum albumin
Chl chlorophyll
C. thermalis *Chroococcidiopsis thermalis*
cw continuous wave
cyt b_6f cytochrome b_6f
DAS decay associated spectrum
DFT density functional theory
DMSO dimethyl sulfoxide
EPR electron paramagnetic resonance
ET electron transfer
EXAFS extended X-ray absorption fine structure
FaRLiP far-red light photoacclimation
Fd ferredoxin
FNR ferredoxin-NADP$^+$ reductase
FRET Förster resonance energy transfer
FRL far-red light
FTIR Fourier-transform infrared spectroscopy
FWHM full width at half maximum
HEPPS 4-(2-Hydroxyethyl)-piperazine-1-propane sulphonic acid
IR infrared
IRF instrument response function
KIE kinetic isotope effect
MCT mercury cadmium telluride
MD molecular dynamics
MES 2-(N-morpholino)-ethane sulfonic acid
Milli-Q water ultra-purified water (from a Millipore system)
MOPS 3-(N-morpholino)-propane sulfonic acid
NADP$^+$ nicotinamide adenine dinucleotide phosphate (oxidized)
NADPH nicotinamide adenine dinucleotide phosphate (reduced)
Nd:YAG neodymium-doped yttrium aluminium garnet
OD optical density
OEC oxygen-evolving complex
P680 pigment 680 (primary donor chlorophyll of PSII)
P700 pigment 700 (primary donor chlorophyll of PSI)
PC plastocyanin
PCET proton-coupled electron transfer
Pheo pheophytin
PhQ phylloquinone

pL general term for pH and pD, i.e. the negative decadic logarithm of the proton or deuteron concentration

PM power meter

PMS phenazine methosulfate

PPBQ phenyl-*p*-benzoquinone

PQ plastoquinone

PQH$_2$ plastoquinol

PSI photosystem I

PSII photosystem II

PT proton transfer

PTFE polytetrafluoroethylene

Q$_A$ primary quinone acceptor of PSII

Q$_B$ secondary quinone acceptor of PSII

QCL quantum cascade laser

QM/MM quantum mechanics/molecular mechanics

RT room temperature

SFX Serial femtosecond crystallography

S/N signal-to-noise

T. elongatus *Thermosynechococcus elongatus* (has been renamed to *T. vestitus*)

TEMED tetramethylethylenediamine

TRIS tris(hydroxymethyl)aminomethane

TRSF-IR time-resolved single-frequency infrared spectroscopy

T. vestitus *Thermosynechococcus vestitus*

T. vulcanus *Thermosynechococcus vulcanus*

UV-Vis ultraviolet-visible

VE-water de-ionized water (German: *vollentsalztes Wasser*)

WL white light

WT wild-type

Y$_Z$ tyrosine Z (tyrosine-161 of the D1 subunit of PSII)

List of Publications

2024 **Three rate-controlling protein roles in photosynthetic O_2-evolution suggested by time-resolved experiments on genetically modified photosystems**
Sarah M. Mäusle, Ricardo Assunção, Gianluca Parisse, Philipp S. Simon, Daniele Narzi, Leonardo Guidoni, Richard J. Debus, and Holger Dau
(*manuscript submitted*)

2024 **Nanosecond Time-Resolved Infrared Spectroscopy for the Study of Electron Transfer in Photosystem I**
Sarah M. Mäusle, Neva Agarwala, Victor G. Eichmann, Holger Dau, Dennis J. Nürnberg, and Gary Hastings
Photosynth. Res. 159:229–239   https://doi.org/10.1007/s11120-023-01035-9

2023 **Tracking the first electron transfer step at the donor side of oxygen-evolving photosystem II by time-resolved infrared spectroscopy**
M. Yahia Dekmak, **Sarah M. Mäusle**, Janosch Brandhorst, Philipp S. Simon, and Holger Dau
Photosynth. Res.   https://doi.org/10.1007/s11120-023-01057-3

2020 **Activation energies for two steps in the $S_2 \rightarrow S_3$ transition of photosynthetic water oxidation from time-resolved single-frequency infrared spectroscopy**
Sarah M. Mäusle, Aiganym Abzaliyeva, Paul Greife, Philipp S. Simon, Rebeca Perez, Yvonne Zilliges, and Holger Dau
J. Chem. Phys. 153(21):215101   https://doi.org/10.1063/5.0027995

1 | Introduction and Background

About 2.4 billion years ago planet Earth was devastated by a catastrophe that wiped out most life that had so carefully developed until then: the great oxygenation event. While photosynthesis was a brilliant way of securing energy, the life forms at the time were in no way prepared to deal with large amounts of oxygen that were consequently found in the atmosphere. Oxygen is a strong oxidizing agent, meaning it readily reacts with many molecules, easily causing damage to proteins and DNA. As life forms on Earth continued to evolve, they adapted to these newly found high levels of atmospheric oxygen. Today, the metabolism of most multicellular organisms is highly dependent on oxygen.

Photosynthetic organisms not only produce the oxygen we breathe, but they also convert carbon dioxide from the atmosphere to carbohydrates that we eat. Requiring only water and light for the generation of high-energy electrons, photosynthesis is an entirely clean and renewable source of energy. Scientists have been studying it—macroscopically— for hundreds of years. In the 1950s a new wave of photosynthesis research emerged, beginning to shed light on its molecular mechanisms (Junge, 2019).

In view of the energy crisis of our time, photosynthesis research is more relevant than ever, with hopes of learning from nature to develop new and sustainable ways of gathering energy, e.g. by means of artificial photosynthesis (Dau et al., 2019). With a rising global population, feeding all of humanity will become increasingly difficult[1]; improving crop yields by improving the plants' light absorption—or also their protection against excess light—is another direction of applied photosynthesis research (Long et al., 2015).

On a more fundamental level, the structure, function and molecular mechanisms of individual proteins of the photosynthetic chain are being studied to improve our basic understanding of this crucial process (Stirbet et al., 2020). In this thesis, the protein complexes photosystem II (PSII) and photosystem I (PSI) are studied on a molecular level. This is done not only with the motivation to gain insight into photosynthetic processes, but simultaneously the proteins also serve as model systems to investigate the role of protonation dynamics in protein function—which plays an exceptionally important part in the reaction cycle of PSII.

---

[1]This might seem like a cynical statement in light of the fact that every day people are starving all over the world. The amount of food currently available *theoretically* suffices to feed the world, but it is not distributed as needed.

In recent years, there have been great advancements in X-ray crystallographic methods, and three-dimensional structural information on PSII is available at several distinct time points during its reaction cycle (Müh and Zouni, 2020). A weakness of crystallographic studies, however, is their inability to detect protons—which is in contrast a strong-suit of infrared (IR) spectroscopy. In this thesis, time-resolved IR spectroscopy is applied to spinach PSII (Chapter 5), to investigate the kinetics of its reaction cycle. In Chapter 6, PSII samples from different organisms are investigated and compared. By introducing two different single point mutations into PSII, we slow down certain steps in the reaction cycle (Chapter 7), making it possible to investigate a previously "invisible" step. In Chapter 8 we observe electron transfer down the two paths of PSI.

This chapter here will provide the required background knowledge to understand and discuss the results throughout the thesis. It will begin with a general introduction to photosynthesis, PSII and PSI, followed by an introduction to infrared spectroscopy and a brief look into reaction dynamics. Once the basics have been established, a deeper look will be taken at past and ongoing research on PSI and PSII. In Chapter 2, the IR spectroscopy setup will be discussed in detail, along with the analysis procedures applied to the acquired data. Chapter 3 will briefly describe all other employed methods. In Chapter 4, foundational IR spectroscopic results on PSII will be established and discussed, supporting the discussion of the main results in the subsequent chapters.

1.1 Photosynthesis

Photosynthesis is the process by which plants, algae and some bacteria such as cyanobacteria harvest light energy and convert it into chemical energy. The term photosynthesis encompasses many different steps and has traditionally been divided into two main processes: (i) The light reactions, which start with light harvesting leading ultimately to the reduction of $NADP^+$ and ADP to NADPH and ATP, respectively, and (ii) the dark reactions, in which NADPH and ATP are used for the metabolism of more complex energy carriers (Nelson and Ben-Shem, 2004). In plants the photosynthetic reactions take place mainly inside chloroplasts, which are organelles compartmentalized by a lipid-bilayer. Within the chloroplasts there are further membranous structures called thylakoids, which are the site of the light reactions. The dark reactions take place in the stroma of the chloroplasts, i.e. the aqueous region within the chloroplasts, as well as the cytoplasm. Chloroplasts originally evolved through an endosymbiotic process (Hohmann-Marriott and Blankenship, 2011), during which plants likely took up ancestral cyanobacteria and incorporated them into their cells. In cyanobacteria the thylakoids are separate structures from the cell membrane (unlike in some other photosynthetic bacteria), and they are located directly in the cytoplasm (in contrast to plant cells). Thus, the chloroplast stroma in plant cells corresponds to the cytoplasm in cyanobacteria. The following description will focus on the situation in plant cells, but some major differences to cyanobacteria will be pointed out. The fundamental principles of photosynthesis laid out here are based on descriptions found in the books *Molecular Mechanisms of Photosynthesis* by Blankenship (2021) and *Photosynthesis* by Lawlor (2001); more in depth knowledge will be cited accordingly. Note that details may deviate between different photosynthetic species and the following should just be read as a rough overview.
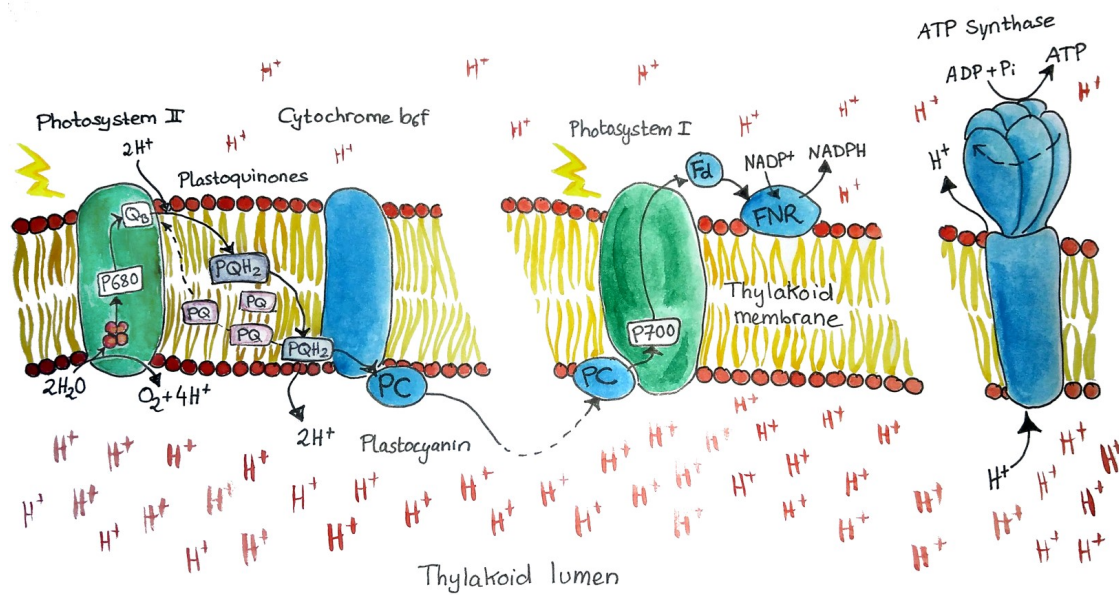
Figure 1.1: Cartoon of the Electron Transport Chain in Oxygenic Photosynthesis. Following the absorption of a photon, the electron transport chain commences in PSII, leading to the reduction of plastoquinone Q_B and the oxidation of the Mn_4CaO_x cluster (which, after four such events, leads to the oxidation of water and production of O_2). Doubly reduced Q_B is released into the plastoquinone pool and the two electrons are carried to cyt b_6f, which catalyzes the reduction of plastocyanin (PC). In PSI the electron transport chain is again triggered by the absorption of a photon, leading to the reduction of ferredoxin (Fd), which allows NADPH reduction at the ferredoxin-NADP$^+$ reductase (FNR). The electron hole in PSI is refilled by PC. The ATP synthase, powered by the proton motive force, produces and releases ATP into the stroma.

1.1.1 Photosynthetic Electron Transfer Chain (Light Reactions)

Photosynthesis begins with the absorption of light by Photosystem II (Shevela et al., 2021), one of two major pigment-protein complexes (see Fig. 1.1). The harvested light energy fuels the process of water oxidation, producing molecular oxygen as a byproduct on the luminal side (a more detailed description of PSII will follow in Section 1.1.3). The generated free electrons leave the protein on the stromal side by reducing plastoquinones (PQ), which act as mobile electron carriers. In their doubly reduced anionic state, plastoquinones readily take up two protons from the stroma before diffusing through the thylakoid membrane in their plastoquinol form (PQH$_2$). Once PQH$_2$ reaches the luminal side of a cytochrome b_6f (cyt b_6f) protein complex, it is oxidized again, thereby releasing its two protons into the lumen and thus contributing to establishing a proton gradient across the membrane. Each of the two electrons is individually taken up by an iron-sulfur cluster of cyt b_6f, which in turn reduces a plastocyanin (PC) protein, whereby each PC takes up only one electron. In some cyanobacteria, PC is replaced by cytochrome c_6 (cyt c_6). Both PC and cyt c_6 act as mobile electron carriers, responsible for delivering electrons to Photosystem I (PSI), the second major pigment-protein complex (Nelson and Junge, 2015).

In plant cells PSI and PSII are not evenly distributed in the thylakoid membrane. PSII is found mostly in regions where the thylakoids form so-called grana stacks, while PSI is found mostly in the non-stacked regions. Cytochrome b_6f is found in both regions; thus

the distances that PQH_2 and PC/cyt c_6 need to travel are quite versatile ranging from just a few to hundreds of nanometers.

The absorption of a photon triggers the electron transport chain across PSI (see Section 1.1.4 for details), leading ultimately to the reduction of the iron-sulfur cluster of the small, soluble protein ferredoxin (Fd). Fd donates an electron to the ferredoxin-$NADP^+$ reductase (FNR), a protein which—as its name states—catalyzes the reduction $NADP^+$ to NADPH. The reduction of $NADP^+$ requires two electrons, and therefore two Fd proteins are needed as donors. FNR has a flavin adenine dinucleotide cofactor, which allows for the storage of a first electron; upon donation of a second electron, NADPH is produced and released into the stroma.

Instead of the above-described linear electron flow, PSI and cyt b_6f can instead also partake in cyclic electron flow, during which the electrons do not proceed to FNR, but are instead cycled back to cyt b_6f. This ultimately leads to the accumulation of ATP without generating NADPH. Details can be found in a review by Yamori and Shikanai (2016).

The unstacked region of the thylakoid membrane hosts another important protein complex: the ATP synthase, which catalyzes the conversion of adenosine diphosphate (ADP) and phosphate to adenosine triphosphate (ATP), a universal energy carrier needed for countless functions within cells. The generation of ATP is powered by the proton motive force, which is the sum of the chemical potential (difference in pH) and the electrical potential (difference in charge) across the membrane (Junge and Nelson, 2015).

1.1.2 Metabolism of Secondary Photosynthetic Products (Dark Reactions)

While ATP and NADPH are important energy carriers and needed for the catalysis of many reactions, they do not function as long-term energy storage. Other, more stable molecules such as carbohydrates, proteins and fats are more suitable for energy storage within cells. The Calvin-Benson cycle describes the series of reactions in the chloroplast stroma during which carbon is fixed by reducing CO_2 and synthesizing triose phosphate, a process which consumes ATP and NADPH. Triose phosphate is a building block for the synthesis of e.g. starch and sucrose. Non-photosynthetic organisms consume these carbohydrates, which can be used for generating ATP and NADPH in mitochondria. As these metabolic reactions are not the focus of this thesis, a more detailed description will be omitted here, but can e.g. be found in Chapter 9 of *Molecular Mechanisms of Photosynthesis* by Blankenship (2021).

1.1.3 Photosystem II

Photosystem II is a large membrane protein complex of roughly 350 kDA per monomer, consisting of about 20 protein subunits (depending on the organism). A cartoon of the crystal structure can be seen in Fig. 1.2a. The central proteins D1 (PsbA) and D2 (PsbD) form a hetero-dimer and are highly conserved across different species, as are the two additional core proteins CP43 and CP47 (Enami et al., 2008). PsbO stands out by its beta-barrel structure and is known as the Mn-stabilizing protein. In its absence, the oxygen evolution efficiency of PSII has been observed to be reduced. Some of the more peripheral subunits vary significantly between species; the extrinsic subunits PsbV and PsbU in cyanobacteria are replaced by PsbP and PsbQ in higher plants (Shen, 2015). PSII is usually found in dimeric form and forms super-complexes with light-harvesting systems (light-harvesting complex II (LHCII) in plants and phycobilisomes in cyanobacteria).
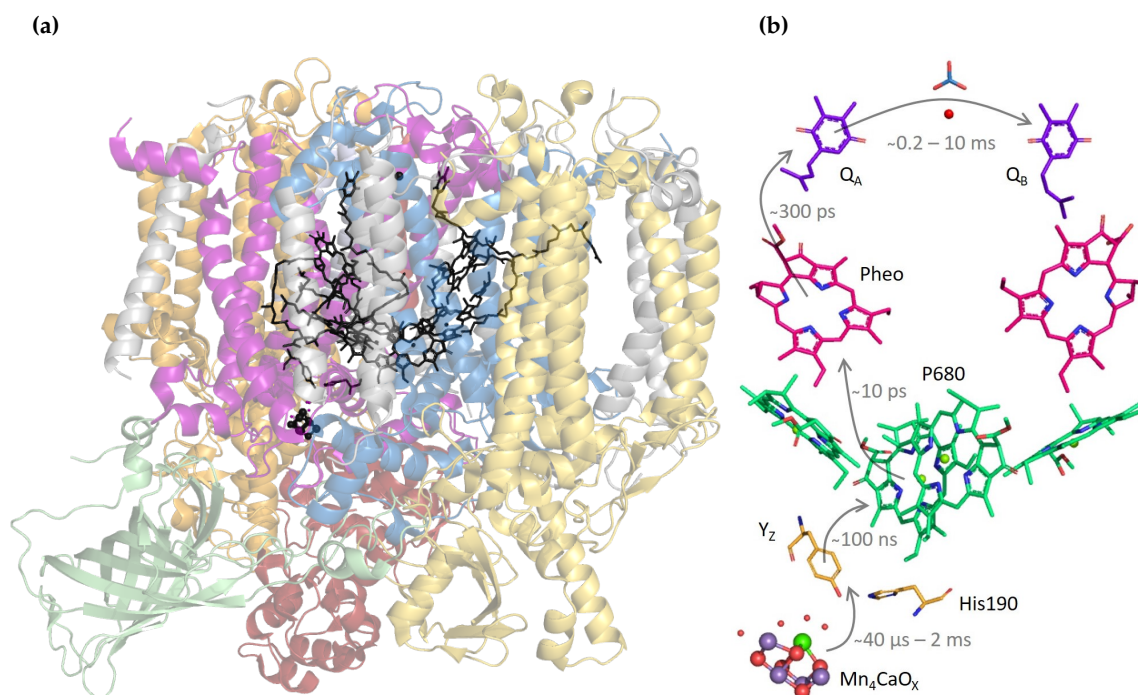
Figure 1.2: Crystal structure of a PSII monomer from *T. vulcanus*. (a) A cartoon depiction of the protein chains, with the following color code: D1: *purple*, D2: *blue*, CP43: *yellow*, CP47: *orange*, PsbV and PsbU: *red*, PsbO: *green*, all other 12 subunits: *grey*. The most important cofactors are shown as sticks (*black*). **(b)** A detailed view of the most important cofactors, including the electron transport pathway. Starting at the special chlorophyll unit P680 (*green*), the electron moves via a pheophytin (*pink*) to plastoquinone Q_A and then on to Q_B (*purple*). The two plastoquinones are bridged by a non-heme iron (*red dot*) and a bicarbonate. The hole at P680 is filled by an electron donation of tyrosine Y_Z (*yellow*), which in turn gets reduced by the Mn_4CaO_x cluster. The hydrocarbon tails of the chlorophylls, pheophytins and plastoquinones have been truncated in (b) for visual simplicity. PDB ID: 3WU2, published by Umena et al. (2011). Image rendered in PyMOL.

Its function as a water-plastoquinone oxidoreductase produces molecular oxygen as a side-product, making it the most important source of O_2 in our atmosphere (Lubitz et al., 2019). The catalytic process is triggered and driven by light energy and can be summarized as follows:

$$2\,H_2O + 2\,PQ + 4\,H_s^+ \rightarrow O_2 + 2\,PQH_2 + 4\,H_l^+ \quad , \tag{1.1}$$

where H_s^+ and H_l^+ denote protons on the stromal and luminal side, respectively.

The luminal side of PSII is often referred to as the electron donor side, as water oxidation takes place there, while the stromal side is referred to as the electron acceptor side. The reactions at donor and acceptor side can be looked at individually, revealing a four-electron chemistry for the former and a two-electron chemistry for the latter:

$$\begin{aligned} 2\,H_2O &\rightarrow O_2 + 4\,H_l^+ + 4\,e^- \quad \text{(donor side)} \\ 2\,PQ + 4\,e^- + 4\,H_s^+ &\rightarrow 2\,PQH_2 \quad \text{(acceptor side)} \quad . \end{aligned} \tag{1.2}$$
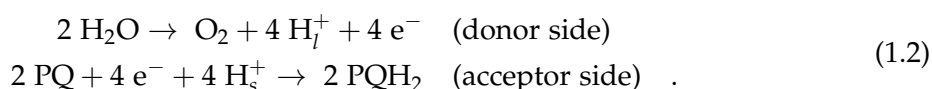
In both cases, multi-electron chemistry needs to be reconciled with a one-photon absorption event. For the acceptor side this merely means that an electron needs to be temporarily

stored. For the donor side, however, four oxidative equivalents need to be gathered one by one and stored safely, without causing oxidative damage to the protein, until water oxidation can finally take place. The way nature solved this issue is—from the perspective of a scientist—both elegant and impressive, and will be discussed in the following.

The process starts with the absorption of a photon by a chlorophyll (or other pigment) associated with PSII. Förster resonance energy transfer (FRET) allows for the transfer of the harvested energy to other nearby pigments (Şener et al., 2011). FRET is a non-radiative process, based on dipole-dipole coupling between a donor and an acceptor pigment. The fluorescence emission spectrum of the donor must overlap with the absorption spectrum of the acceptor and the energy transfer efficiency is strongly dependent on the distance between the pigment-pair. After a series of energy transfer events, the energy arrives at the special chlorophyll unit P680 (named after its absorption peak in the visible spectrum), where charge separation takes place (see Fig.1.2b). The excited electron is quickly taken up (within about 10 ps) by a neighboring pheophytin molecule, preventing recombination. Plastoquinone Q_A oxidizes the pheophytin within about 300 ps and subsequently reduces the plastoquinone Q_B in about 0.5–10 ms. Q_B, unlike Q_A, is only loosely bound to the protein. The intrinsically unstable, radical semiquinone form of Q_B is stabilized by its binding pocket, until the entire ET chain is repeated and a second electron is delivered to Q_B. After being doubly reduced, Q_B leaves its binding pocket in its stable plastoquinol form and takes up two protons from the stroma. Meanwhile, the electron hole at P680 is filled by an electron donation from its neighboring redox-active tyrosine unit Y_Z, occurring within about 20 ns–25μs (see Section 1.5.2 on P680$^+$ reduction kinetics). Tyrosine Y_Z oxidizes one of the Mn ions of the Mn_4CaO_x cluster in about 40 μs–2 ms, changing its redox state from Mn^{III} to Mn^{IV} (see review by Cox et al. (2020)).

This electron transport chain, effectively carrying an electron from one side of the protein to the other, is enabled by the differing midpoint redox potentials of the involved molecules, which strongly favor ET in the above-described direction. This phenomenon can be nicely visualized by depicting the ET chain as a function of redox potential, also called *Z-Scheme* (see e.g. Govindjee et al. (2017)).

The Mn_4CaO_x cluster is the heart of the protein and responsible for reconciling the fast single-photon absorption event (leading to a single-electron charge separation) with the slow four-electron redox chemistry. Together with its immediate protein environment, the Mn_4CaO_x cluster is often referred to as the oxygen-evolving complex (OEC).

The fact that four absorption events are needed for oxygen evolution was already observed by Joliot et al. (1969) and the connection to the Mn cluster (of which details were not known yet), was made soon after by Kok et al. (1970). The latter paper also first introduced the S-state nomenclature S_0 to S_4, describing the redox state of the Mn_4CaO_x cluster with S_0 being the most reduced state and S_4 the most oxidized state. The cycle of four photon absorption events, leading to the accumulation of four oxidative equivalents needed to drive water oxidation, is often named the Kok cycle, Kok-Joliot cycle, water oxidation cycle or S-state cycle (Fig. 1.3a). The states S_0 through S_3 are semi-stable for several seconds, while the S_4 state is transient. In the $S_3{\rightarrow}S_0$ transition, the oxidation of a Mn ion has *not* been observed experimentally and it is now widely accepted that the final oxidation event directly involves the substrate water, rather than a Mn ion (see reviews by Shevela et al. (2023) and Cox et al. (2020)). Fig. 1.3b shows exemplary flash-number dependent signals, demonstrating the typical period-of-four and period-of-two patterns of the donor and acceptor side, respectively.
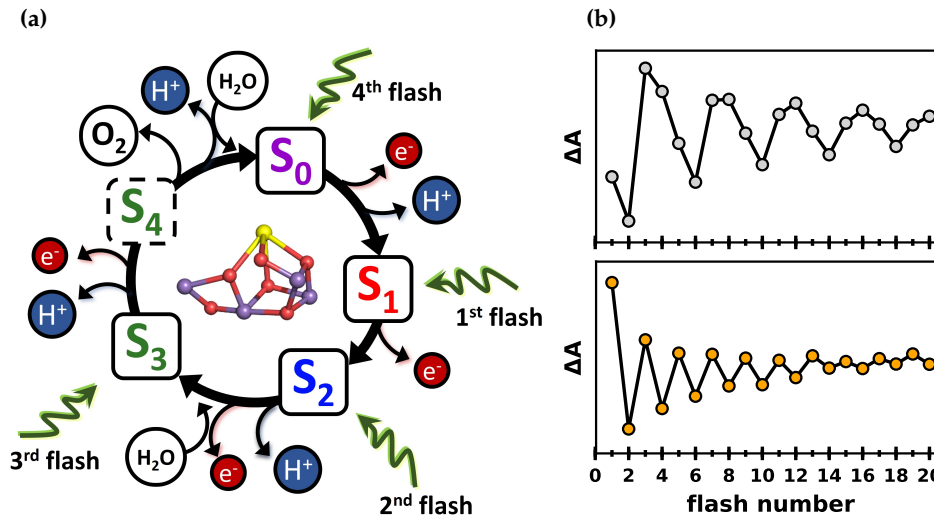
Figure 1.3: The S-state cycle of PSII. (a) The S-states S_0 to S_4 denote the accumulated oxidative equivalents at the Mn_4CaO_x cluster, as first described by Kok et al. (1970). The first excitation flash applied to dark-adapted PSII triggers mostly the $S_1 \rightarrow S_2$ transition, the second the $S_2 \rightarrow S_3$ transition, the third the $S_3 \rightarrow S_0$ transition and fourth flash the $S_0 \rightarrow S_1$ transition. The S_4 state is transient and, unlike the other S-states, not a semi-stable intermediate. Between the electron (e^-) removal steps protons (H^+) are also removed from the Mn_4CaO_x cluster, compensating for the change in overall charge. The insertion of the two substrate water molecules, as well as O_2 evolution is also indicated. A cartoon of the Mn_4CaO_x cluster is shown in the center; it was rendered in PyMOL (PDB ID: 8F4D) using the X-ray crystallographic data by Bhowmick et al. (2023). **(b)** Examples of flash-number dependent (infrared) signals, showing the dampened period-of-four behavior of the S-state cycle (top, *grey*) and the period-of-two behavior of the quinones (bottom, *orange*). The data was recorded on spinach PSII membrane particles at 1395 cm^{-1} and 1478 cm^{-1}, respectively.

Already the first experiments by Kok and Joliot in the 60s and 70s showed that that the maximum yield of O_2 (after giving the sample time to dark-adapt) is measured after three excitation flashes, rather than four, indicating that the S_1 state is the predominantly dark-stable state. More recent studies have established that intermittently between the electron removal steps, also protons are removed from the OEC (Klauss et al., 2012a). This allows for the redox potential of the Mn_4CaO_x cluster to stay relatively constant throughout the cycle, a prerequisite for efficient cycling through all S-states.

Nevertheless, the S-state transitions never show 100% efficiency. The percentage of failed transition to the next S-state, usually termed *miss factor*, is at least 5–10% per transition and can easily be higher e.g. in damaged photosystems or in the trivial case of too low light intensity. For simplicity it is often assumed that the miss factor is universal for the entire cycle, but in recent years it has been shown that the miss factor is in fact S-state dependent (Han et al., 2012).

A more detailed look at ongoing research and open questions can be found in Chapter 1.5, including the currently proposed mechanism for water oxidation and state of research with emphasis on infrared spectroscopic studies.
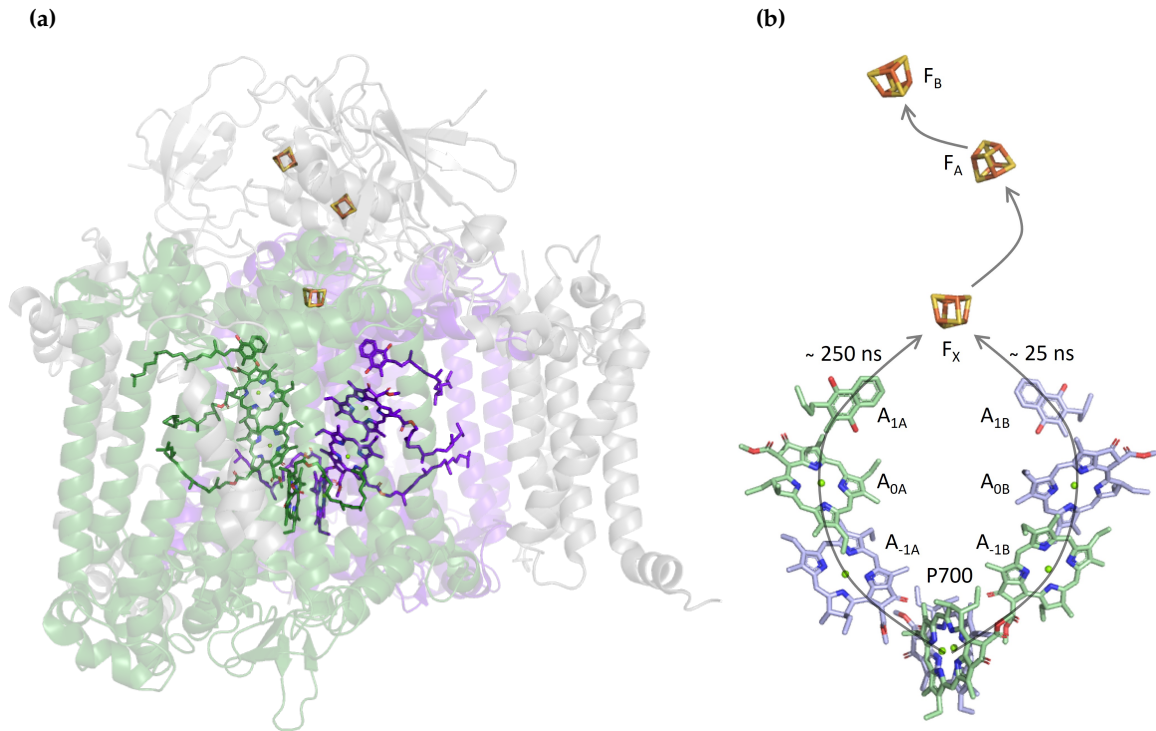
Figure 1.4: Crystal structure of a PSI monomer from *T. vestitus* BP-1. The PsaA subunit is shown in *green*, PsaB in *purple* and all other subunits in *grey*. **(a)** All protein subunits are shown in cartoon style, depicting their secondary structures. The most important co-factors are shown in their stick representation. **(b)** A detailed view of the co-factors involved in electron transport. P700, A_{0A} and A_{0B}, as well as A_{-1A} and A_{-1B}, are chlorophylls; A_{1A} and A_{1B} are phylloquinones; F_X, F_A and F_B are iron-sulfur clusters. The hydrocarbon tails of the chlorophylls and phylloquinones have been truncated in (b) for visual simplicity. PDB ID: 1JB0, published by Jordan et al. (2001). The images were rendered in PyMOL.

1.1.4 Photosystem I

Photosystem I is large protein-pigment complex of roughly 250 kDa per monomer in cyanobacteria (Çoruh et al., 2021) and 650 kDa in plants (Nelson and Junge, 2015). It is most commonly found in monomeric form in plants and algae, but in trimeric—and in some cases tetrameric—form in cyanobacteria (Li et al., 2019). Each monomer consists of about 12–18 subunits. Fig. 1.4a shows the crystal structure of a PSI monomer from *T. vestitus* in cartoon style, with the main co-factors shown in stick form. The central core proteins of PSI, PsaA and PsaB, are by far the largest subunits of about 80 kDa each. They host the ET pathway across the protein. As in PSII, PSI also forms super-complexes with light-harvesting systems (light-harvesting complex I (LHCI) in plants and phycobilisomes in cyanobacteria).

In its function as plastocyanin/cytochrome c_6-ferredoxin oxidoreductase, PSI shuttles electrons from the luminal side of the thylakoid membrane to the stromal side. As in PSI, the ET chain begins with the absorption of a photon by any pigment that is part of the light-harvesting system. The energy is transferred to the special chlorophyll unit P700 via FRET. Within less than a picosecond, the free electron is taken up by either the chlorophyll in the A_{0A} or in the A_{0B} binding site (Fig. 1.4b). The two different paths the electron can

take are termed the A- and B-branch, after the protein subunit that the respective branch is mostly associated with (A-branch: PsaA, B-branch: PsaB). From the A_{0A}/A_{0B} chlorophyll the electron moves to the phylloquinone (PhQ) in the A_{1A} or A_{1B} binding site within about 20 ps. Phylloquinone A_{1B} reduces the iron-sulfur cluster F_x within about 25 ns, while F_x reduction by A_{1A} is about ten-fold slower. At F_x the two branches merge; ET from F_x on to F_a/F_b takes place within about 180 ns (Byrdin et al., 2006). F_b finally reduces ferredoxin, which carries the electron to the FNR (see Chapter 1.1.1).

It has been shown that both branches are used by the protein—but to varying extent depending on the organism (Makita and Hastings, 2016) and the measurement temperature (Mula et al., 2012; Makita and Hastings, 2015; Agalarov and Brettel, 2003). However, there are still many open questions concerning the functional details of the branches. Both the A- and B-branch have a similar protein environment and the reason for their different forward ET kinetics is not obvious.

A more detailed look at the on-going research on the kinetics down the two branches, as well as other open questions in PSI research will be outlined in Chapter 1.4, with an emphasis on (IR) spectroscopic studies.

1.2 Infrared Spectroscopy

Optical spectroscopy is the study of light, i.e. electromagnetic radiation, interacting with matter. In absorption spectroscopic methods, light is directed through a sample and the transmitted light is detected. By comparing the intensity of light that reaches the detector to a reference (e.g., the intensity of light that reaches the detector in absence of a sample), the absorption by the sample can be estimated (Lambert-Beer law, see also Chapter 2.3.1). Displaying absorption as a function of energy (often expressed in terms of wavelength) results in absorption spectra. This, of course, requires determining the absorption at individual wavelengths. When dealing with a broadband light source, this can e.g. be done by using a monochromator to select individual wavelengths either before the light hits the sample or before the light hits the detector.

Infrared light is the frequency range of the electromagnetic spectrum spanning between roughly 300 GHz to 400 THz, which corresponds to wavelengths of about 1 mm to 750 nm. Infrared spectroscopy usually exploits the part of the IR range that corresponds to the frequencies of molecular vibrations, as will be discussed in more detail below, and thus belongs in the category of *vibrational spectroscopy*. In the following sections we will look at some general background to (infrared) absorption, before moving on to different methods of IR spectroscopy. Finally, IR spectroscopy applied to research on proteins will be discussed.

1.2.1 Theoretical Background

This section is (unless cited otherwise) based mostly on textbook knowledge: see Chapter 1 of *Modern Vibrational Spectroscopy and Micro-Spectroscopy* by Max Diem (2015) for theory on absorption and vibrational modes.

A single atom has several electronic levels: the ground state is the energetically lowest level and by absorbing a photon a higher excited state can be reached. In the simplest model, the photon needs to have the exact amount of energy as the energy gap between the two levels.
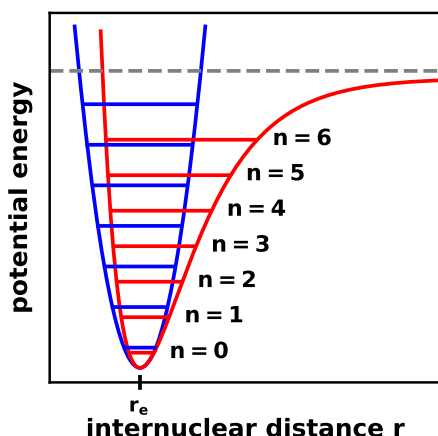
Figure 1.5: Energy levels of a harmonic (*blue*) and an anharmonic (*red*) oscillator. The equilibrium bond length (r_e) and the dissociation energy required for bond breakage (*dashed line*) are indicated.

Electronic excitation is achieved by photons with frequencies in the ultraviolet-visible (UV-Vis) range. Molecules additionally have vibrational levels, arising from vibrational modes of the molecular bonds. A molecule with N atoms has 3N degrees of freedom (corresponding to the movement in x-, y- and z-direction of each atom). Considering all linear combinations of possible atom movements, only three of them will result in a translational movement of the molecule (e.g. if all atoms move in x-direction). Another three will lead to a rotational movement. All other combinations of atom movements will rather result in changes to inter-atomic distances and/or angles, and thus lead to atomic vibrations. Most molecules thus have 3N−6 normal vibrational modes, with the exception of linear molecules, which only have two degrees of rotational freedom and thus have 3N−5 vibrational modes.

In the simple case of a diatomic molecule, only one vibrational mode exists and its frequency is given by

$$\nu = \frac{1}{2\pi} \cdot \sqrt{\frac{k}{\mu}} \qquad , \tag{1.3}$$

where k is the bond force constant and μ is the reduced mass of the two atoms. The wavenumber $\tilde{\nu}$ (inverse of the wavelength, typically given in cm^{-1}) relates to the frequency ν as follows: $\tilde{\nu} = \nu/c$ (where c is the speed of light). A stronger bond strength thus leads to a vibrational mode with a larger wavenumber, while a larger reduced mass of the atoms leads to a smaller wavenumber. For molecules with three or more atoms, a simple solution, as such presented in equation 1.3, does not exist (three-body-problem). Predicting an IR spectrum of a large protein complex such as PSII or PSI is thus not trivial and requires expensive simulations at an—at least partially—quantum mechanical level.

Each vibrational mode has a ground state and higher vibrational states, that, when approximated by a harmonic oscillator (Fig. 1.5), are defined by

$$E_n = (n + \frac{1}{2})h\nu \qquad , \tag{1.4}$$

where h is Planck's constant and n is the energy level (the ground state being $n = 0$). A more correct description of the energy levels usually however requires a description by an anharmonic oscillator, where the gaps between the energy levels are not uniform but rather decrease with increasing energy level. The vibrational ground state always has an energy larger than zero, as can be seen in equation 1.4, which is referred to as the zero-point energy. This implies that molecules always undergo vibrational motion.
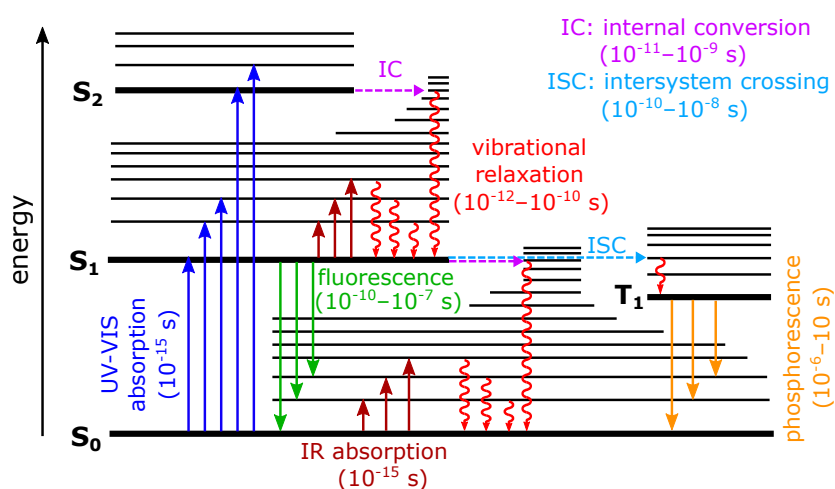
Figure 1.6: Jablonski Diagram. Three electronic states are indicated by thick horizontal lines (the ground state S_0 and two higher states); the thinner horizontal lines indicate higher vibrational levels. The absorption of a UV-Vis photon leads to the excitation into a higher electronic state and usually also a higher vibrational level. Vibrational relaxation into the vibrational ground state (indicated by red squiggly arrows) occurs within 1–100 ps. A non-radiative transition from a higher electronic state to a higher vibrational level of a lower electronic state is called internal conversion (IC). The non-radiative transition from an excited electronic singlet state to a triplet state is called intersystem crossing (ISC). Fluorescence or phosphorescence occurs if the excess energy is emitted as photon from a higher singlet or triplet state, respectively. The absorption of an infrared photon can also lead to the occupation of higher vibrational states; the selection rules for this event are discussed in the text. Each vibrational level is additionally split into rotational levels (not shown). This diagram is named after the physicist Aleksander Jabłoński.

The electronic and vibrational energy levels are shown in form of a Jablonski diagram in Fig. 1.6. As stated above, the absorption of a UV-Vis photon leads to the occupation of a higher electronic level (e.g. S_1), but mostly also to a higher vibrational level. Relaxation back into the vibrational ground state occurs within about 1–100 ps, whereby the energy is dissipated to the molecule's surroundings, essentially heating the sample. Relaxation back into the electronic ground state may occur in several different ways:

(i) fluorescence, where the excess energy is emitted as a photon;

(ii) internal conversion, where a transition occurs from a higher electronic state to a higher vibrational state of a lower electronic one, followed by vibrational relaxation;

(iii) intersystem crossing, where a transition occurs from an electronic singlet state to a triplet state. After vibrational relaxation to the triplet vibrational ground state, this may lead to phosphorescence (if the energy is emitted as a photon) or (after another intersystem crossing event) to vibrational relaxation.

These processes are exploited in many different spectroscopic methods. In infrared spectroscopy, higher vibrational levels are reached by directly absorbing IR light. The vibrational modes of a molecule—and the frequencies at which they absorb—are to varying extents dependent on the molecule's structure, conformation and environment. IR absorption spectra thus contain a lot of information on the sample: Some molecular vibrations are very specific to a functional group while not much affected by their environment; bands of such vibrations are thus useful to identify chemical components of a sample. Other vibrational modes are strongly dependent on their chemical environment and are thus

characteristic of a specific molecule, which is why they are called *fingerprint bands*. Some schematic examples of vibrational modes are shown in Fig. 1.7.

There are, however, some selection rules as to when IR absorption can take place. Next to the rule that the energy of the photon must match the energy gap of the vibrational levels ($\Delta E = h\nu$), and the amplitude of the incoming light must be greater than zero, the dipole transition moment μ must also be non-zero. An often mentioned example for a vibrational mode with a dipole transition moment of zero is the symmetrical stretching vibration of CO_2 (Fig 1.7d). As this motion does not cause a change in the molecule's dipole, it will not absorb IR light of the frequency associated with that vibrational mode and is thus IR-inactive.

For harmonic oscillators another selection rule applies, which states that the vibrational level cannot change by more than one ($\Delta n = \pm 1$). For anharmonic oscillators, such transitions (e.g. from ground state to the second vibrational level) are weakly allowed; thus overtones of the main absorption peak may appear at roughly double (and multiples) of the wavenumber.

At room temperature the Boltzmann distribution predicts that mostly the vibrational ground state will be inhabited[2]. Thus, absorption of a photon will usually take place from the vibrational ground state. However, if a sample is excited with IR light with a very high photon flux, two subsequent photons may cause excitation into a higher vibrational mode. As the energy gaps become smaller between higher vibrational levels (for anharmonic oscillators), small side peaks may theoretically appear in absorption spectra. However, with a single-frequency IR source with a wavenumber precision of <1 cm^{-1}, as used in this thesis, this would not be observable.

Figure 1.7: Schematic examples of vibrational modes shown for a tri-atomic group of a molecule. (a) Symmetrical stretching mode. **(b)** Asymmetrical stretching mode. **(c)** Bending mode. **(d)** Symmetrical stretching mode of a symmetrical, linear tri-atomic molecule, such as CO_2.

1.2.2 Methods of Infrared Spectroscopy

There are many different ways of conducting infrared spectroscopic experiments. In the following, we will take a brief look at the ones most relevant to this thesis. A more complete overview can be found in reviews by Mezzetti et al. (2022) and Lorenz-Fonfria (2020).

Fourier Transform Infrared Spectroscopy
A widespread method for obtaining IR spectra is Fourier Transform Infrared Spectroscopy (FTIR). An FTIR setup usually contains a globar, which provides a broadband thermal light source. A Michelson interferometer splits the incoming IR beam, directing half to a fixed mirror and half to a movable mirror. The two beams are reflected and are rejoined before going through the sample, causing the two beams to interfere. Their interference depends, of course, on the wavenumber as well as on the displacement of the movable mirror (a path difference of $\Delta x = n\lambda$, e.g., causes positive interference). The transmitted signal, obtained

---

[2]This is true for the wavenumber range of interest in this thesis (above 1300 cm^{-1}). For much smaller wavenumbers this is not necessarily the case, e.g. a vibrational mode with a wavenumber of 320 cm^{-1} has a ~20% to be in an excited vibrational state.

as a function of the mirror position, is called an interferogram. By later Fourier transforming the data, an absorption spectrum can be calculated. Thus, instead of employing a way of measuring the absorption at individual wavenumbers, the entire transmitted broadband light is detected simultaneously at one detector. For many (biophysical) applications, a laser is used as an excitation source to trigger some sort of a reaction, which can then be monitored via changes in the IR signal (as will be discussed in more detail in Section 1.2.3).

There are two main modes in which FTIR spectroscopy can be performed: rapid-scan and step-scan. In rapid-scan FTIR, the mirror moves continuously, and the time resolution is limited by the time it takes for the mirror to move the entire path back and forth. This mode is often used for obtaining steady-state spectra or also for time-resolved spectra, if studying a system where a time resolution of several milliseconds is sufficient.

In step-scan mode, the mirror is moved in small increments, and at every mirror position the time-resolved signal is acquired. When monitoring e.g. a biochemical reaction, this requires a sample that can be triggered multiple times, i.e. the reaction needs to be cyclic or reversible (with relatively short recovery times). The signal at the individual mirror positions is later stitched together to form an interferogram for each time point. This allows for obtaining time-resolved spectra with a temporal resolution down to tens to hundreds of nanoseconds Mezzetti et al. (2022); for biological systems, however a time resolution of microseconds is more realistically achievable (due to noise constraints).

In FTIR spectroscopy, data pre-processing is of critical importance. Various algorithmic approaches exist to tackle issues such as phase-correction; different approaches may lead to differences in the final spectra.

Single-Frequency Infrared Spectroscopy

For studies that require a sub-microsecond to microsecond time resolution single-frequency methods are usually the preferred choice. There are several different approaches; they can be grouped into the following:

(i) dispersive methods, that use a broadband IR source and a monochromator to detect the signal at individual wavenumbers;

(ii) methods based on continuous wave (cw) IR lasers, such as quantum cascade lasers (QCL), that provide a (tunable) monochromatic infrared source;

(iii) ultra-fast pump-probe (dispersive) methods, which employ a pulsed excitation beam (pump) and a broad-band pulsed IR beam (probe). Here, the time resolution is limited by possible delay times between pump and probe.

The third category is typically employed for the investigation of ultra-fast processes, which are not within the scope of this thesis. The setup in the here presented work falls into the second category; detailed information on the instrumentation, experimental procedure and data processing can be found in Chapter 2.

An advantage of IR laser-based systems over dispersive systems is that the transmitted signal is typically much higher, resulting in an improved signal-to-noise (S/N) ratio. In the past years, QCLs have been continuously improved. By providing cw monochromatic light with a very narrow linewidth ($\ll 0.1$ cm^{-1}), a broad frequency coverage (in our system 1890–1310 cm^{-1}) and very high brilliance, QCL-based systems allow for the acquisition of high S/N data even with a low number of repeated measurements.
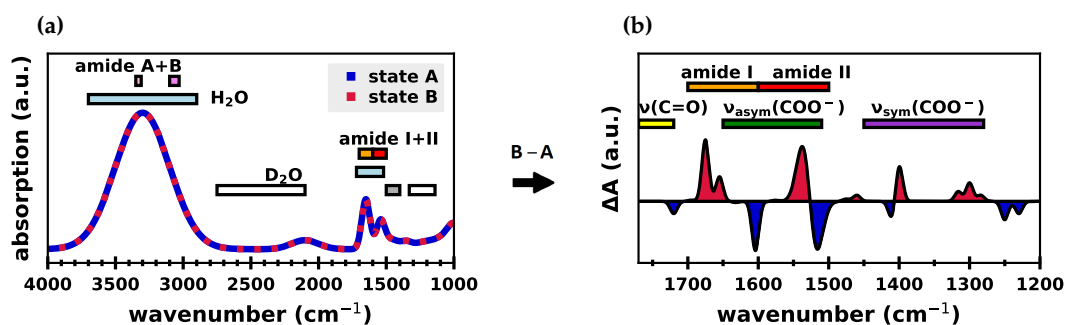
Figure 1.8: Exemplary IR spectra of proteins in water. (a) Absolute IR spectrum (4000–1000 cm^{-1}) of a (fictional) protein in H_2O in a starting state A (*blue*) and in a second state B (*red*), e.g. after a reaction was triggered by a laser flash. The rough spectral region of some groups of vibrational modes are indicated by horizontal bars: Amide A and B modes (*pink*), amide I and II (*orange* and *red*) and two strong water bands (*light blue*). The white bars indicate where the position of the water bands would be in deuterated water (D_2O); the grey bar indicates an HDO band which would also appear. **(b)** Difference spectrum (1770–1200 cm^{-1}) of state B minus state A, revealing bands that differ between the two states. Bands associated with state B will appear positive, while bands associated with state A will appear negative. The amide I and II (*orange* and *red*), the symmetrical and asymmetrical carboxylate stretching region (*purple* and *green*) and the C=O stretching region (*yellow*) are indicated with horizontal bars. Difference bands are around three orders of magnitude smaller than the absolute bands. The shown difference bands are purely fictional and serve only to demonstrate the general principles of difference absorption spectroscopy.

1.2.3 Difference Infrared Spectroscopy on Proteins

Proteins typically consist of about a thousand to tens of thousands of atoms. With $3N-6$ degrees of vibrational freedom, this may result in over a hundred thousand vibrational modes for large protein complexes such as PSII. It may, therefore, be unsurprising that IR spectra of proteins do not show distinct narrow bands, but rather very broad features, as demonstrated in Fig. 1.8a. In liquid samples water contributes with very pronounced, broad bands, and needs to be accounted for by e.g. subtracting a measurement of only the solvent. Absolute IR spectra in themselves can provide some insight, such as information on the secondary structures of the protein (Barth and Zscherp, 2002). A very commonly used approach to declutter the spectra, however, is to trigger a reaction or conformational change in the protein and to subtract the spectra before and after from each other (Fig. 1.8b). Such a difference spectrum will show only bands that differ between the two states, greatly reducing the amount of vibrational modes contributing to the spectrum.

There are many different ways to trigger a change within a protein, e.g. electrochemically or by mixing two compounds; an extensive overview can be found in the section on *Perturbation Methods* in the review by Lorenz-Fonfria (2020). The possibly most commonly used trigger, however, is *light*. In the simplest case, the protein of interest is itself light-activated, as is the case for PSI and PSII. However, light can also be used as a trigger to e.g. release caged compounds and thus initiate mixing. By using short laser pulses for excitation, the thus triggered reaction can also be observed in a time-resolved manner.

Vibrational modes of proteins can be put into the two general categories of *backbone* and *side chain* vibrations, which are discussed in detail in a series of reviews by Andreas Barth (Barth, 2000; Barth and Zscherp, 2002; Barth, 2007). The amide (or more specifically:

peptide) character of the protein backbone (Fig. 1.9) gives rise to several characteristic vibrational modes, which are hence called *amide bands*. The—for this work—most important amide bands are (i) the amide I band (centered around 1650 cm^{-1}) which is dominated by the C=O stretching mode of the peptide bonds, and (ii) the amide II band (centered around 1550 cm^{-1}), which is dominated by the out-of-phase NH-bending and CN-stretching vibration.

Various different side chain vibrational modes contribute to the spectral region of ∼1750–1000 cm^{-1}; tabular overviews can be found in the aforementioned reviews by A. Barth. Of special significance are vibrational modes of aspartate and glutamate residues. In their deprotonated form, they exhibit COO$^-$ symmetrical and asymmetrical stretching vibrations, while in their protonated form they contribute in form of C=O stretching vibrations; the approximate spectral region of these vibrations is indicated in Fig. 1.8b.

Figure 1.9: Protein backbone at the example of a di-peptide. Two amino acids with side chains R$_1$ and R$_2$ are connected via a peptide bond (*red*), forming a di-peptide.

The assignment of peaks in difference spectra to individual chemical groups is, in principle, possible, but becomes harder the larger the molecule. For a large protein complex such as PSII, band assignment is far from trivial. Several strategies to single out bands exist, such as isotope labeling, site-directed mutagenesis or introduction of unnatural amino acids (see review by Lorenz-Fonfria (2020) for a detailed overview). Introducing a small change into the protein mostly does not merely affect just one vibrational mode. Often *in silico* approaches, where IR spectra of proteins are simulated by e.g. density functional theory (DFT) or by a combination of quantum mechanics and molecular mechanics (QM/MM), are needed to complement and interpret the experimental data; and even then, definitive band assignment is not always achieved.

1.3 Reaction Dynamics

In the following a few points regarding chemical reactions and their dynamics will be outlined, which are important for the understanding of this thesis. A comprehensive coverage of the subject can be found in the textbook *Physical Chemistry* by Atkins et al. (2018).

1.3.1 Arrhenius Equation

The observation that the rates k of chemical reactions are often strictly temperature dependent led to the formation of the Arrhenius equation:

$$k = A \cdot e^{-E_a/k_B T} \qquad , \qquad (1.5)$$

where A is the pre-exponential factor, E_a is the activation energy and k_B is Boltzmann's constant. The pre-exponential factor is also called the frequency factor, as it can be interpreted as to how likely it is that the reactants meet in a way that makes the reaction possible. The activation energy is the minimal energy needed to drive the reaction once the reactants have met. Thus, the higher the activation energy, the less likely it is (according to the Boltzmann's distribution) that the reactants will have the required energy, effectively lowering the reaction rate.

When writing the Arrhenius equation as

$$\ln(k) = \ln(A) - E_a/k_B T \qquad , \tag{1.6}$$

it is apparent that the reaction rate is linearly dependent on the inverse temperature. Plotting the natural logarithm of experimentally determined rate constants as a function of inverse temperature thus results in a line with an intercept at $\ln(A)$ and a slope of $-E_a/k_B T$.

1.3.2 Transition State Theory

Transition state theory (Eyring, 1935; Evans and Polanyi, 1935; Mortimer and Eyring, 1980) describes how during a chemical reaction the potential energy of the reactants increase until they form a so-called activated complex. At this energetically highest point the reactants have reached the transition state, from which the products can be formed. This process is shown schematically in Fig. 1.10.

An exergonic reaction, i.e. a reaction which can take place "spontaneously", is generally associated with a negative change in the Gibbs free energy $(-\Delta G)$. The total change in Gibbs free energy can be described as

$$\Delta G = \Delta H - T\Delta S \qquad , \tag{1.7}$$

where ΔH is the change in enthalpy and ΔS is the change in entropy of the system.

The change in Gibbs free energy needed to reach the transition state is called Gibbs energy of activation $(\Delta G^{\ddagger})$. The rate constant associated with the reaction can be written as

$$k = \frac{\kappa k_B T}{h} \cdot e^{-\Delta G^{\ddagger}/k_B T} \qquad , \tag{1.8}$$

where κ is the transmission coefficient (which is often assumed to be unity), h is Planck's constant, T is the temperature of the system and k_B is Boltzmann's constant. With $\kappa = 1$ and insertion of equation 1.7 follows:

$$k = \frac{k_B T}{h} \cdot e^{\Delta S^{\ddagger}/k_B} \cdot e^{-\Delta H^{\ddagger}/k_B T} \qquad , \tag{1.9}$$

which is one form of the Eyring equation. The entropic term in equation 1.9 is directly related to the pre-exponential factor A of the Arrhenius equation while the enthalpic term is related to the activation energy E_a as follows:

$$\begin{aligned} \Delta H^{\ddagger} &= E_a - k_B T \\ \Delta S^{\ddagger} &= k_B \cdot \ln\left(\frac{h * A}{k_B T}\right) - k_B \qquad . \end{aligned} \tag{1.10}$$
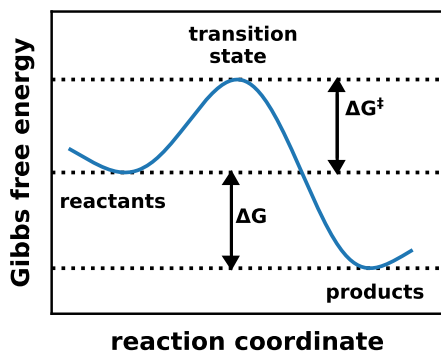
Figure 1.10: Change in Gibbs free energy during a reaction. The energy of the reactants increases until the transition state is reached, allowing the formation of the products. The activation Gibbs free energy $\Delta G^{\ddagger}$, as well as the overall change in Gibbs free energy ΔG, are indicated by arrows. The final Gibbs energy of the products is lower than that of the reactants (negative ΔG), thus the reaction is exergonic.

While the Arrhenius equation is an empirical formulation, the Eyring equation draws a connection to the enthalpy and entropy of the system, allowing a deeper interpretation of the observed reactions. As the Eyring parameters are temperature dependent, they are often calculated for a value in the middle of the temperature range of interest, $T = T_O$.

The applicability of transition state theory to the final proton-coupled ET step during the $S_3 \rightarrow S_0$ transition has been discussed by Dau and Greife (2023).

1.3.3 Kinetic Isotope Effect

The rates of chemical reactions are affected by the chemical isotopes of the reactants. Heavier isotopes generally have a lower zero-point vibrational energy, which leads to a lower starting point in the energy profile of Fig. 1.10. Simply speaking, this results in a higher activation energy and thus in a lower rate constant.

This effect is called a kinetic isotope effect (KIE) and can be quantified by dividing the rate constant of the lighter isotope by the rate constant of the heavier isotope. The deuterium isotope effect can e.g. be observed by replacing water with heavy (deuterated) water:

$$\mathrm{KIE} = \frac{k_\mathrm{H}}{k_\mathrm{D}} = \frac{\tau_\mathrm{D}}{\tau_\mathrm{H}} \qquad . \tag{1.11}$$

Kinetic isotope effects are considered to be a primary effect if bonds directly to the isotopic atom are broken or made, otherwise the effect is considered to be a secondary effect. Kinetic isotope effects can either be normal (KIE > 0) or inverse (KIE < 0). For more detailed insight the review by Scheiner (2000) may be considered.

1.4 Diving Deeper: Past and Present Research on Photosystem I

In the following, a closer look will be taken at past and present research on PSI. We will begin with a brief look at early spectroscopic studies from the 70s and 80s, moving gradually toward more recent studies and open questions. Detailed historic perspectives and reviews of PSI research up to the mid 2000s can be found in the book *Photosystem I: The Light-Driven Plastocyanin: Ferredoxin Oxidoreductase* by Golbeck (2006).

1.4.1 Spectroscopic Studies

In the early seventies, spectroscopic studies established the basics of the electron transport chain in PSI. Malkin and Bearden (1971) observed a ferredoxin-like electron paramagnetic resonance (EPR) signal on a sample that was devoid of soluble ferredoxin, which indicated the presence of a bound electron acceptor within chloroplasts. In a follow-up paper they determined this "primary electron acceptor" to more specifically be part of PSI (Bearden and Malkin, 1972). Flash-induced visible spectroscopy identified a unit termed P430 (named for its absorption maximum), that was believed to be associated with the primary electron acceptor, allowing for a first kinetic characterization (Hiyama and Ke, 1971).

By performing EPR experiments as well as redox-titrations, Ke et al. (1973) discovered that most likely more than one iron-sulfur species was involved. McIntosh et al. (1975) found that there was another electron acceptor preceding the two iron-sulfur species in the electron transport chain. It soon was found by Sauer et al. (1978) that there was a fourth even earlier electron acceptor, which they termed A_1 and P430 was assigned to the two

iron-sulfur species termed A and B. Shuvalov et al. (1979) were able to assign A_2 to a third iron-sulfur unit.

In the late 1980s the iron-sulfur species were finally associated with [4Fe-4S] clusters (Wynn and Malkin, 1988), which was later confirmed by structural studies (Schubert et al., 1997; Jordan et al., 2001). Using EPR spectroscopy, Snyder et al. (1991) were able to definitively assign A_1 to vitamin K_1, also known as phylloquinone.

In the 1990s, the first evidence for two branches in the electron transfer chain emerged. Sétif and Brettel (1993) observed biphasic nanosecond kinetics, but it remained unclear whether this was artefactual due to damaged PSI centers. Joliot and Joliot (1999) were finally able to confirm the biphasic kinetics in whole cells, thereby eliminating the possibility of introducing artefacts due to damaged centers. Guergova-Kuras et al. (2001) performed a series of experiments on PSI with strategical site-mutations, showing that the fast and slow kinetic component can be slowed down individually without affecting the other kinetic component, thereby indicating that both branches are active. Another EPR study confirmed that the fast phase is associated with phylloquinone B and the slow phase with phylloquinone A (Purton et al., 2001).

Several models were proposed that could explain ET down the two branches; they can be grouped in two main ideas: (a) PSI switches between two (conformational) states, allowing unidirectional ET down either the A- or the B-branch, or (b) ET down PSI occurs intrinsically bidirectional and the A- and B-branch have a certain probability to be selected after each charge separation event. These models are extensively discussed in a review by Redding and van der Est (2006), along with other models dealing with the possibility of ET occurring down only one branch.

By performing experiments on mutants in which the reduction potentials of the chlorophylls in the A_0 binding pockets were reduced, Li et al. (2006) provided further evidence that ET occurs down both branches. Their results were backed with DFT calculations that identified the bidirectional "branch competition model" as the model that best explains the experimental data. Recent ultrafast spectroscopic studies also favor that model, as summarized in a review by Cherepanov et al. (2022).

There utilization ratio between the two branches has been reported to be around 1:1 in eukaryotic systems and ranging between 1:4 and 1:9 (favoring the A-branch) in prokaryotes (see article by Santabarbara et al. (2010) and references therein).

1.4.2 FTIR Spectroscopy on PSI

In the 1980s the first FTIR difference spectra on bacterial reaction centers were published by Mäntele et al. (1985), soon followed by the first difference spectra on both photosystem I and II by the same group (Tavitian et al., 1986). By the late 1990s the experimental conditions had been significantly improved and evidence emerged that P700 is a dimer of chlorophyll a molecules: the broad mid-IR band generally found for in the $\sim$4000–2000 cm^{-1} region was assigned to an electronic transition of P700$^+$(Breton et al., 1999) arising from an unpaired electron distributed among two or more chlorophyll molecules.

The same group had previously investigated this broad mid-IR band in bacterial reaction centers (Breton et al., 1992), which proved to be unaffected by H_2O/D_2O exchange, thus arguing against the assignment of a broad water band. They instead showed that the band is in agreement with an electronic transition arising from the interaction of the two P700$^+$ chlorophylls.
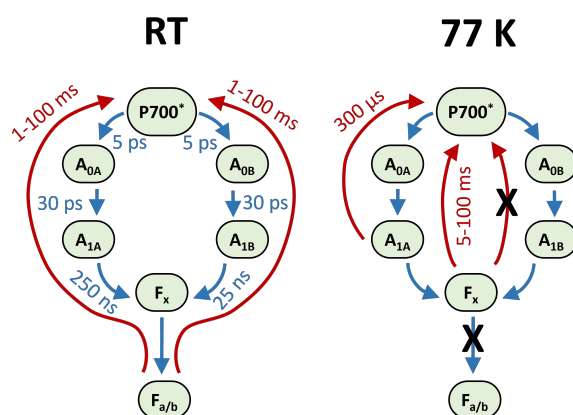
Figure 1.11: Electron transfer pathways in PSI at room temperature and at low temperature.
Schematic view of the co-factors involved in ET at room temperature (*left*) and at 77 K (*right*). The blue arrows indicate forward ET, while the red arrows denote backward ET leading to $P700^+$ recombination. Approximate time constants of the individual ET steps are indicated. At 77 K, a permanent $P700^+/F_x^-$ species is formed in some of the centers (believed to be associated with the B-branch), and thus backward ET is partially blocked. Furthermore, ET from F_x to $F_{a/b}$ is also blocked at 77 K. Both blocked pathways are indicated by an "X" on the respective arrow.

Band assignments to C=O groups of the primary chlorophyll groups were attempted by comparing difference spectra of excited singlet and triplet states, i.e. $P700^+/P700$ and $^3P700/P700$ (Breton et al., 1999). Some of the assignments were challenged by Hastings et al. (2001), who investigated $(P700^+-P700)$ spectra of two different species, as well as a H(A676)S mutant[3] of *C. reinhardtii* (the histidine was chosen for being an axial ligand to P700). Further studies of point mutations affecting ligation to P700 soon followed (Breton et al., 2002; Witt et al., 2002; Wang et al., 2003).

While P700 difference spectra can be acquired by photoaccumulation and thus using rapid-scan FTIR, the investigation of co-factors further down the electron transfer chain is slightly less straightforward. Instrumental advancements opened up the option of using step-scan FTIR at low temperatures to study the A_1 co-factor. A summary of early work on this can be found in a book chapter (Hastings, 2006) as well as a review (Hastings, 2015). At the heart of those studies is the fact that ET in PSI is partially blocked at 77 K: in a large fraction of the PSI centers the $P700^+/A_{1A}^-$ state recombines in about 300 µs. A smaller fraction advances to $P700^+/F_x^-$ before recombining in 5–100 ms; a third fraction forms an irreversible $P700^+/F_x^-$ state (Schlodder et al., 1998; Hastings, 2015). It has been suggested that the first two fractions are associated with ET on the A-branch and the third fraction with ET on the B-branch (Srinivasan and Golbeck, 2009); the different ET pathways are schematically summarized in Fig. 1.11.

From the observations above follows that the first ~100 µs of flash-induced step-scan FTIR spectra of PSI at 77 K are predominantly $P700^+/A_{1A}^-$ spectra, while photoaccumulated spectra at 77 K are associated mainly with $P700^+/F_x^-$. Contributions of the iron-sulfur cluster to the mid-IR spectra are mostly negligible (Breton et al., 1999; Hastings and Sivakumar, 2001), thus by subtracting the photoaccumulated spectra from the first 54 µs of the time-resolved spectra, $(A_{1A}^--A_{1A})$ double difference spectra can be produced.

---

[3] H676S mutation of PsaA

19

To gain more insight into the A_1 cofactor, a series of studies were performed in which the natural PhQ (2-methyl-3-phytyl-1,4-naphthoquinone) was replaced by different quinones. These experiments were done on PSI isolated from *menB* knockout mutants. As *menB* codes for the phytyl-transferase, which is essential for producing PhQ, the A_1 binding site of *menB*⁻ mutants is instead filled with plastoquinone-9 (which is the quinone found in the Q_A and Q_B binding sites of PSII) (Zybailov et al., 2000). Other quinones can easily be incorporated into the A_1 binding site by incubating the *menB*⁻ PSI mutants with a large amount of the desired quinone (Bandaranayake et al., 2006). FTIR spectra at 77 K of wild-type PSI and *menB*⁻ PSI into which PhQ was reintegrated look very similar. Employing isotope exchange experiments as well as the incorporation of PhQ analogues has led to several assignments of quinone bands (Hastings, 2015; Agarwala et al., 2023).

1.4.3   Far-Red Light Absorbing PSI Variants

The most commonly found chlorophyll in both photosystems is chlorophyll *a*. However, some species additionally synthesize and utilize other chlorophylls with absorption spectra reaching further into the far-red region. *Acaryochloris marina* (*A. marina*) is an extreme example, as >90% of its chlorophyll molecules are chlorophyll *d*, a pigment that can absorb about 40 nm further into the red than chlorophyll *a* (Loughlin et al., 2013). A further species of chlorophyll, termed chlorophyll *f* was discovered relatively recently (Chen et al., 2010), which pushes the absorption limit even further into the far-red region (>760 nm). Chlorophyll *a*, *b*, *d* and *f* all have very similar structures (Fig. 1.12); chlorophyll *c* (not shown) is somewhat more different (most notably it lacks the phytol tail).

While *A. marina* always predominantly utilizes Chl *d*, other cyanobacteria (which use mostly Chl *a*) have been observed to additionally synthesize Chl *d* and Chl *f* when grown under far-red light (FRL) (Chen et al., 2010). Gan et al. (2014) observed an even more ex-
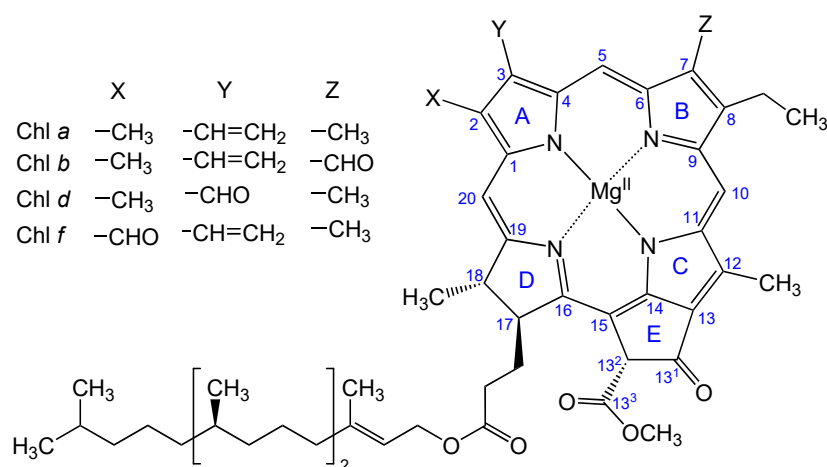
Figure 1.12: Chemical structures of chlorophylls *a*, *b*, *d* and *f*. Chlorophylls are Mg²⁺ containing tetrapyrrole rings with an extra ring attached to ring C. The types of chlorophylls shown here always contain a phytol tail (bottom left), a 13²-carbomethoxy group, a 13¹-carbonyl group, two methyl groups (at C-18 and C-12) and an 8-ethyl group. Additionally they have some variable side chains as indicated in the figure. Pheophytins are identical to chlorophylls, merely lacking the chelated magnesium. Chlorophyll *a'* (not shown) is an epimer of Chlorophyll *a*, differing only in the stereochemistry at C-13².

tensive response when culturing *Leptolyngbya* sp. strain JSC-1 under FRL: They found that most of the core proteins of both PSI and PSII were replaced and that the phycobilisomes had an altered structure; they termed this phenomenon *far-red light photoacclimation* (FaR-LiP). They identified a FarLiP gene cluster and found 12 other species of cyanobacteria that carry a similar one. One of them, *Chroococcidiopsis thermalis* PCC 7203, was further studied by Nürnberg et al. (2018), who showed that Chl *f* in that species does not merely have a light-harvesting role, but is directly involved in photochemistry in both PSI and PSII. Another group challenged this conclusion (Cherepanov et al., 2020), suggesting that in *Fischerella thermalis* PCC 7521 Chl *f* functions merely as an antenna pigment. To date, the location of the Chl *f* molecules in far-red light acclimated PSI still remains under debate.

1.5   Diving Deeper: Past and Present Research on Photosystem II

In the 1960s Boardman and Anderson (1964) succeeded in isolating PSI and PSII spinach membrane fragments from each other—a protocol which was later refined by Berthold et al. (1981)—and in the 1980s, protocols for extracting O_2-evolving core complexes from cyanobacteria were established (Tang and Satoh, 1985), paving the way for many subsequent studies.

In the following, an overview of several different aspects of PSII research will be given; the last section will look specifically at IR spectroscopic studies. This summary is, however, by no means complete. Excellent reviews are available for many sub-topics and will be referenced when appropriate.

A topic that will not be covered in depth is the role of Y_D and the history of research on the two redox active tyrosines, but the reviews by Rutherford et al. (2004) and Styring et al. (2012) are recommended for further reading in this direction.

A modified version of the section on $P680^+$ reduction kinetics has also been used as part of the introductory section of a manuscript (Dekmak et al., 2023).

1.5.1   Unravelling the Events of the S-State Cycle

Over the past decades, the events at the OEC have been investigated by countless studies, which in their entirety have drawn a detailed picture of the reaction cycle of PSII. Many excellent and in-depth reviews have been recently published (Vinyard and Brudvig, 2017; Lubitz et al., 2019; Junge, 2019; Cox et al., 2020; Shevela et al., 2023), which served as the foundation to writing this section.

As described in Chapter 1.1.3, protons and electrons are released intermittently from the OEC (Fig. 1.13). Every S-state transition, induced by the absorption of a photon and the following charge separation at P680, leads to a more oxidized OEC. Only the transition from S_4 back to S_0, which restores the OEC to its most reduced state, happens spontaneously: while S_0 through S_3 are semi-stable states, S_4 is short-lived and transient. The proton release pattern of 1:0:1:2 for the $S_0 \rightarrow S_1 \rightarrow S_2 \rightarrow S_3 \rightarrow S_0$ transitions has been demonstrated by many spectroscopic studies (Schlodder and Witt, 1999; Suzuki et al., 2009; Klauss et al., 2012a, 2015).

The first high resolution crystallographic structure of PSII was published by Umena et al. (2011). This structure was ground-breaking, but was affected by radiation damage: it was shown that intense X-ray beams can cause the reduction of Mn atoms, effectively
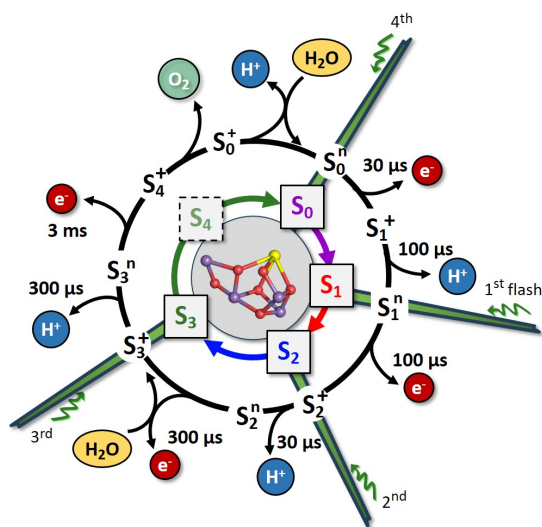
Figure 1.13: Extended S-state cycle. The inner circle shows the traditional S-state cycle as described by Kok et al. (1970), while the outer circle shows the extended version, also denoting the net charge of the cluster (Klauss et al., 2012a). The given time constants are approximate values. See text for detailed description of the S-state transitions. The Mn_4CaO_x cluster in the middle was rendered in PyMOL (PDB ID: 8F4D). A modified version of this figure is part of a manuscript (Mäusle et al. (*in preparation*)).

altering the OEC (Yano et al., 2005). Studies applying serial femtosecond X-ray crystallography (SFX) with X-ray free-electron lasers (XFELs) have since managed to minimize this problem via the "diffract before destroy" principle. This new technique also has allowed several groups to obtain high resolution structures of PSII at room temperature in all semi-stable S-states and also at certain time-points *during* S-state transitions (Kern et al., 2018; Suga et al., 2019; Ibrahim et al., 2020; Bhowmick et al., 2023).

$S_0 \rightarrow S_1$ Transition

Even though the $S_0 \rightarrow S_1$ transition is technically the first in the S-state cycle, experimentally it is the last and thus in some ways the most difficult to study: assuming a miss factor of 10% and a 100% dark-adapted S_1 population, only 66% percent of the PSII centers will undergo a successful $S_0 \rightarrow S_1$ transition upon the fourth excitation flash and about 25% will undergo the $S_3 \rightarrow S_0$ transition (see Chapter 2.3.3 for the mathematics behind this).

The $S_0 \rightarrow S_1$ transition is characterized by an electron and a proton transfer event; the total charge of the Mn_4CaO_x cluster thus remains neutral. The ET takes place with a time constant of $\sim$40–70 µs (Dekker et al., 1984; Haumann et al., 1997; Zaharieva et al., 2016), although some studies question this having observed slower rates (Noguchi et al., 2012). The ET was found to exhibit an activation energy of $\sim$50 meV (Renger and Hanssum, 1992) and an H/D kinetic isotope effect of 1.3 (Haumann et al., 1997). For the PT event a time constant of 100 µs, an activation energy of 340 meV and a KIE of 3.0 were observed (Klauss et al., 2012a). The S_0 structure of the Mn_4CaO_x cluster is shown in Fig. 1.14 (*top left*).

$S_1 \rightarrow S_2$ Transition

The $S_1 \rightarrow S_2$ transition is initiated by the first excitation flash applied to dark adapted samples. Exhibiting only a single electron transfer, the overall charge of the Mn_4CaO_x cluster changes from neutral to positive. The ET step exhibits an activation energy of 120–160 meV (Renger and Hanssum, 1992; Haumann et al., 1997; Klauss et al., 2012a) and a time constant of about 100 µs at room temperature (RT) (Dekker et al., 1984; Haumann et al., 1997; Gerencsér and Dau, 2010; Haumann et al., 2005); however a slightly faster time constant of about 70–80 µs at 10 °C was measured with time-resolved IR (Sakamoto et al., 2017; Takemoto et al., 2019). Several studies found a small KIE of 1.2–1.3 (Haumann et al., 1997; Klauss et al., 2012a; Gerencsér and Dau, 2010; Sakamoto et al., 2017). The S_1 structure of the Mn_4CaO_x cluster is shown in Fig. 1.14 (*top right*).
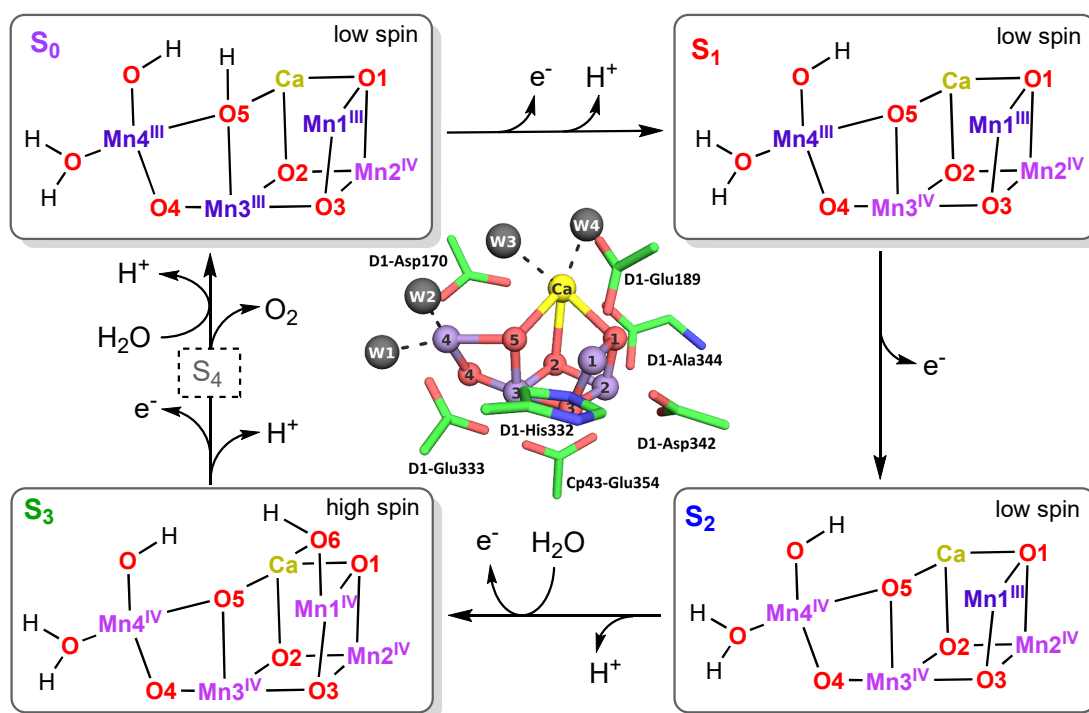
Figure 1.14: Structure of the Mn_4CaO_x cluster during the different S-state transitions. Manganese atoms are shown in purple, oxygen in red and calcium in yellow. The oxidation state of the Mn atoms is indicated in roman numerals; Mn^{III} ions are shown in a darker shade of purple than Mn^{IV} ions. *Top left*: The S_0 state, which is the most reduced state of the Mn_4CaO_x cluster. Mn2 has a +IV oxidation state; all other Mn atoms are +III. This structure gives a low spin EPR signal. *Top right*: Deprotonation of O5 and oxidation of Mn3 lead to the S_1 state, which also gives a low spin EPR signal. *Bottom right*: After oxidation of Mn4, the S_2 state is reached. The shown structure gives a low spin EPR signal and is often referred to as the *open cubane* structure in contrast to the *closed cubane*, which gives a high spin EPR signal. The structure of the latter has been omitted here as it has not been observed at room temperature (Ibrahim et al., 2020). *Bottom left*: Following the removal of a proton, oxidation of Mn1 and insertion of a water molecule, the S_3 state is formed. Mn1 is now ligated to a new oxygen, O6. Removal of another electron and proton leads to the formation of the transient S_4 state, after which O_2 is released. Another water molecule is inserted and a proton is removed, reverting the Mn_4CaO_x cluster back to the S_0 state. *Center*: Crystallographic structure of the OEC. The four water molecules ligated to the Mn_4CaO_x cluster are indicated in grey (W1 to W4); the directly ligated amino acids are shown in a truncated form. The structure in the center was rendered in PyMOL using a PSII structure gathered by Ibrahim et al. (2020) 150 µs after the second excitation flash (PDB ID: 6w1r); all other structures were drawn with ChemDraw, based on a similar scheme in Cox et al. (2020) and refined with information from Greife et al. (2023).

$S_2 \rightarrow S_3$ Transition

The second sequential excitation flash applied to dark adapted PSII samples results in predominantly the $S_2 \rightarrow S_3$ transition, which involves a proton and an electron removal, as well as a water insertion event. The overall charge of the Mn_4CaO_x cluster thus remains positive.

The PT event has been characterized with an unusually large KIE of 4–6 (Klauss et al., 2012a, 2015; Zaharieva et al., 2016); a significantly smaller KIE of 1.2 was found by

Sakamoto et al. (2017). (The latter study does not assign this phase to a proton release event, but rather a rearrangement of H-bonds around Y_Z^{ox}). A time constant of about 30 µs was found at room temperature (Klauss et al., 2012a; Zaharieva et al., 2016) and 100 µs at 10 °C (Sakamoto et al., 2017; Takemoto et al., 2019). The activation energy of the PT (470 meV) was found to be high (Klauss et al., 2012a), even higher than the ∼360 meV determined for the ET step (Haumann et al., 1997; Renger and Hanssum, 1992). A time constant of about 300–350 µs for the ET (at RT) was observed by various studies (Renger and Hanssum, 1992; Haumann et al., 1997, 2005; Gerencsér and Dau, 2010; Zaharieva et al., 2016), together with a KIE of 1.7–1.9 (Gerencsér and Dau, 2010; Sakamoto et al., 2017; Zaharieva et al., 2016). Time-resolved IR studies by Takumi Noguchi's group also observed a time constant of about 350 µs, but at 10 °C (Sakamoto et al., 2017; Takemoto et al., 2019).

EPR experiments on the S_2 state result in two distinct signals: a multiline signal around $g = 2$ (Dismukes and Siderer, 1981), associated with a low spin state, and a signal around $g = 4.1$ (Casey and Sauer, 1984), associated with a high spin state. The low and high spin states have been associated with an *open cubane* (S_2^A) and a *closed cubane* (S_2^B) structure of the Mn_4CaO_x cluster, respectively, as reviewed by Lubitz et al. (2023). Recent results from crystallographic studies found no evidence for the closed cubane structure at RT (Ibrahim et al., 2020); it is possible, however, that the two structures interchange very quickly. If the closed cubane structure does play a role at physiological temperatures, O5 and O6 may be swapped in the S_3 structure (Fig. 1.14, *bottom left*).

SFX experiments have in recent years provided snapshots of PSII at several time points during the $S_2 \rightarrow S_3$ transition: Ibrahim et al. (2020) observed an elongation of the Mn1-Mn4 distance at around 150 µs, which they hypothesize could be triggered by the deprotonation of Y_Z. They observe appearance of O6 between 150–400 µs concomitantly with the oxidation of Mn1. They favor W3 as the water that is inserted as O6, in line with several other studies (Kim and Debus, 2019; Ugur et al., 2016), but cannot exclude other options.

Very recently, Li et al. (2024) have presented further SFX results which claim that W3 is unlikely to be the source of O6, as they do not observe any density changes around it. They instead favor W26, which is part of the so-called water wheel (a cluster of five hydrogen-bonded waters).

$S_3 \rightarrow S_0$ Transition

The $S_3 \rightarrow S_0$ transition is the most complex, comprising a PT and ET, upon which the transient S_4 state is reached, which has often been described as *elusive*. Water insertion and a second proton removal finally revert the Mn_4CaO_x cluster back to the S_0 state. The net charge of the cluster changes from positive in the S_3 to neutral in the S_0 state.

It is well known that oxygen evolution occurs after a "lag phase", which is assumed to be a preceding deprotonation event. This PT step has been characterized with a time constant of 150–250 µs (at RT) (Haumann et al., 2005; Gerencsér and Dau, 2010; Zaharieva et al., 2016) and 550 µs at 10 °C (Noguchi et al., 2012), with a KIE of 2.4–2.5 (Gerencsér and Dau, 2010; Zaharieva et al., 2016). The activation energy of this step was observed to be 145–175 meV (Rappaport et al., 2011; Zaharieva, I., Grabolle, M., Chernev, P., Dau, 2013). The ET step, which happens on the same time scale as O_2 evolution, takes place with a time constant of 1.3–1.8 ms (RT) (Gerencsér and Dau, 2010; Haumann et al., 2005; Renger and Hanssum, 1992; Buchta et al., 2007; Dekker et al., 1984; Zaharieva et al., 2016). Haumann et al. (1997) found that the time constants of PSII from pea seedlings were generally slowed

down slightly in core particles compared to thylakoids, but this was especially pronounced in this ET step (1.9 ms vs. 6.6 ms). So far it has not been achieved to spectroscopically observe the second proton transfer and water insertion event.

Recently, Bhowmick et al. (2023) published SFX structures at several time points during the $S_3 \rightarrow S_0$ transition. They observed structural changes indicating a first deprotonation event at around 200–500 µs via D1-D61/D1-E65/D2-E312. Changes indicative of Y_Z reduction—and thus S_4 state formation—are seen around 500–730 µs; O_2 release, indicated by the shortening of the Mn1-Mn4 distance is observed around 1.2 ms. The delay between these two steps is interpreted as evidence for an intermediate state, possibly a peroxide species. While they observe the disappearance of O6 after 1.2 ms, all other members of the Mn_4CaO_x cluster (including O5) remain visible at all times, which is taken as an indication that water insertion takes place immediately after O_2 release.

Structure of the Oxygen-Evolving Complex

A combination of X-ray crystallographic studies, EPR and extended X-ray absorption fine structure (EXAFS) has continuously elucidated the structure of the OEC more and more. Today, we know that the manganese cluster consists of four manganese, one calcium and five or six oxygen atoms (Mn_4CaO_x), the latter depending on the S-state. Four water molecules are ligated to the cluster, two to Mn4 and two to the calcium atom. The cluster is furthermore ligated by the carboxylate groups of five amino acid side chains (D1-Asp170, D1-Glu189, D1-Glu333, D1-Asp342, CP43-Glu354), as well as the carboxylate group of the C-terminal alanine D1-Ala344 (see Fig. 1.14, *center*). A histidine (D1-His332) is the only non-negatively charged first sphere amino acid ligand. While not direct ligands, Y_Z and its hydrogen bonding partner D1-His190 are also in relatively close proximity, which is essential as Y_Z serves as a direct redox partner of the Mn cluster.

Water and Proton Channels

There are several H-bond network channels that allow substrate water access to and/or proton egress from the OEC: the Cl1 ("broad") channel, the O4 ("narrow") channel and the O1 ("large") channel. The Cl1 channel is thought to allow proton egress in the $S_2 \rightarrow S_3$ and $S_3 \rightarrow S_0$ transition (Service et al., 2010; Hussein et al., 2021), while in the $S_0 \rightarrow S_1$ transition the O4 channel might have that function (Saito et al., 2015; Kern et al., 2018). The O1 channel could be an entry pathway for substrate water (Sirohiwal and Pantazis, 2022; Ibrahim et al., 2020; Hussein et al., 2021; Bhowmick et al., 2023), but the O4 and Cl1 channels have not been ruled out for that function either; see review by Shevela et al. (2023). This topic is overall still being investigated and debated.

Mechanism of Water Oxidation

The molecular mechanism of oxygen formation during the $S_3 \rightarrow S_0$ transition has been a subject of debate for many years. While there is still no definite proof for a specific mechanism that unambiguously rules out any other pathways, evidence from both experimental and computational approaches favor certain ideas over others. Mechanisms that involve Mn^V formation are disfavored, as there is a lack of any experimental evidence of such a manganese species in PSII (Haumann et al., 2005). The currently most popular mechanism suggests the formation of an oxo-oxyl intermediate, which was first suggested by calculations of Per Siegbahn (Siegbahn, 2006, 2009, 2013) and has since been favored also by others (Allgöwer et al., 2022; Greife et al., 2023), including crystallographic studies (Suga et al., 2019; Bhowmick et al., 2023).

The reaction could take place as laid out in the following (where $-$ and $=$ denote single and double bonds, respectively): Beginning with the S_3 structure shown in Fig. 1.14, Y_Z reduction by O6 and concomitant deprotonation of O6 leads to the formation of an oxyl radical:

$$Y_Z^{ox} \quad H - \overset{-II}{O}6 - \overset{IV}{Mn}1 \rightarrow Y_Z \quad \overset{-I}{O}6^{\bullet} - \overset{IV}{Mn}1 \tag{1.12}$$
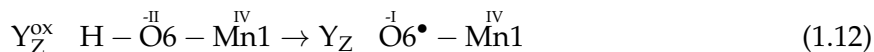
As the Mn cluster is now in its most oxidized state, this can be seen as the S_4 state (Greife et al., 2023). The O6-oxyl and the O5-oxo react and form a peroxide, thereby reducing one manganese atom (Mn4):

$$(\overset{IV}{Mn}4, \overset{IV}{Mn}3) - \overset{-II}{O}5 \quad \overset{-I}{O}6^{\bullet} - \overset{IV}{Mn}1 \rightarrow \overset{III}{Mn}4 \quad \overset{IV}{Mn}3 - \overset{-I}{O}5 - \overset{-I}{O}6 - \overset{IV}{Mn}1 \tag{1.13}$$
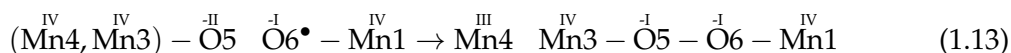
Finally, two more Mn atoms are reduced, O_2 is released and the OEC reverts back to the S_0 state:

$$\overset{IV}{Mn}3 - \overset{-I}{O}5 - \overset{-I}{O}6 - \overset{IV}{Mn}1 \rightarrow \overset{III}{Mn}3 \quad \overset{0}{O}5 = \overset{0}{O}6 \quad \overset{III}{Mn}1 \tag{1.14}$$

The above reaction scheme was written based on Extended Data Fig. 8 of Greife et al. (2023).

Some other mechanistic proposals include a nucleophilic attack of a Ca-bound water on an oxygen bound to the dangling Mn4 or early-onset O_2 formation during in the S_3 state; see reviews by Pantazis (2018), Cox et al. (2020) and Lubitz et al. (2023) for more details.

1.5.2 Acceptor-Side and P680$^+$ Reduction Kinetics

The events at the OEC are preceded by several pivotal electron transfer steps. On the electron acceptor side of PSII, Pheo$^-$ reduces the plastoquinone in the Q_A binding site within roughly 300 ps (Nuijs et al., 1986), making the recombination of the electron and hole less likely. Q_A and Q_B are bridged by a non-heme iron, which is ligated to a bicarbonate (see review by Müh et al., 2012). It was found that the ET from Q_A^- to Fe^{3+} happens with a half-time of 15–25 μs ($\tau = 20$–35 μs) (Petrouleas and Diner, 1987; Chernev et al., 2011). de Wijn and Van Gorkom (2001) found that ET from Q_A^- to Q_B takes place with a time constant of 0.2–0.4 ms and 0.6–0.8 ms if Q_B is a semiquinone. If the Q_B site is empty and has to be refilled first, they observed a time constant of 2–3 ms or even 100 ms if QBH$_2$ is bound and needs be exchanged for an oxidized plastoquinone. In the presence of Fe^{2+}, Chernev et al. (2011) observed that Q_A^- to Q_B does not result in an oxidation state change of the iron, but in a coordination change to the bicarbonate (bidentate to monodentate).

When PPBQ is used as an exogenous (artificial) electron acceptor in PSII preparations, the kinetics are altered. Unlike the naturally occurring plastoquinone, PPBQ does not remain as a semiquinone upon the first reduction. Instead, it takes a second electron from the non-heme iron, oxidizing it from Fe^{2+} to Fe^{3+}. Upon the next flash, instead of generating a Q_B semiquinone, the iron is reduced from Fe^{3+} back to Fe^{2+} (Zimmermann and Rutherford, 1986).

On the electron donor side of PSII, the redox-active tyrosine Y_Z has the important task of bridging the gap between the special chlorophyll unit P680 and the Mn_4CaO_x cluster. It was already observed nearly 50 years ago that P680$^+$ reduction kinetics are multiphasic and S-state dependent (Gläser et al., 1976). Subsequent spectroscopic studies confirmed this, revealing P680$^+$ reduction kinetics spanning over four decades from tens of nanoseconds to hundreds of microseconds (Brettel et al., 1984; Schlodder et al., 1985). A slow S-state independent 200 μs phase was attributed to P680$^+$/Q_A^- recombination (Schlodder et al., 1985;

Christen et al., 1998), resulting in an unsuccessful S-state transition. A fast nanosecond phase of about 20-60 ns was found to be more pronounced in the $S_0{\to}S_1$ and $S_1{\to}S_2$ transitions than in the $S_2{\to}S_3$ and $S_3{\to}S_0$ transitions, and some studies furthermore reported slightly slower time constants for the latter two (Brettel et al., 1984; Meyer et al., 1989; Haumann et al., 1997; Ahlbrink et al., 1998; Jeans et al., 2002). It was found that this phase showed a relatively low activation energy of about 100 meV (Eckert and Renger, 1988) and virtually no H_2O/D_2O kinetic isotope effect (Haumann et al., 1997; Ahlbrink et al., 1998; Schilstra et al., 1998). It was proposed (Eckert and Renger, 1988) and later discussed in more detail (Christen and Renger, 1999; Renger, 2004) that this fast nanosecond phase could be linked to the fast movement of a proton between His190 and Y_Z, but is kinetically limited by an electron transfer (hence the lack of H/D kinetic isotope effect).

A slower nanosecond phase of about 100–800 ns was observed to be clearly more pronounced (Eckert and Renger, 1988; Meyer et al., 1989; Lukins et al., 1996; Ahlbrink et al., 1998; Schilstra et al., 1998; Jeans et al., 2002) or even exclusively found (Brettel et al., 1984; Klauss et al., 2012b) in the S_2 and S_3 states. Experiments in deuterated water again showed no KIE (Haumann et al., 1997; Ahlbrink et al., 1998; Schilstra et al., 1998), but the activation energy ($\sim$250–300 meV) was found to be higher than for the fast nanosecond phase (Jeans et al., 2002; Kühn et al., 2004; Klauss et al., 2012b). This slow nanosecond phase was interpreted as a local "dielectric" relaxation process (Renger, 2004) and later also as nuclear rearrangements resulting in a contraction of about 50 Å^3 (Klauss et al., 2012b).

Besides the S-state independent 200 μs phase, two further microsecond phases of about 1–8 and 20–40 μs were reported, which showed a KIE upon H_2O/D_2O exchange and mostly exhibited strongest contributions in the $S_2{\to}S_3$ and $S_3{\to}S_0$ transitions (Schlodder et al., 1985; Eckert and Renger, 1988; Lukins et al., 1996; Christen et al., 1998; Schilstra et al., 1998; Christen and Renger, 1999; Christen et al., 1999). The microsecond kinetics have been interpreted as "large scale proton relaxation" events (Renger, 2004). In Mn depleted PSII samples the nanosecond kinetics are mostly absent and the $P680^+$ reduction kinetics are dominated by multiphasic microsecond phases (Haumann et al., 1997; Hays et al., 1999).

1.5.3 IR Spectroscopy on PSII

FTIR Studies of Inactive PSII

Many co-factors of PSII were studied by FTIR spectroscopy in the 90s and 2000s, as reviewed by Noguchi and Berthomieu (2005) and Berthomieu and Hienerwadel (2005). The samples for these studies were mostly Mn-depleted and sometimes also depleted of Q_A. Triplet minus singlet excited P680 difference spectra showed two pairs of bands (one with very high intensity, one much less pronounced) that were attributed to keto C=O vibrations (see Fig. 1.12 for the structure of chlorophylls) (Noguchi et al., 1993). $P680^+/P680$ spectra revealed a differential-shaped pair of bands (Noguchi et al., 1998; Breton et al., 1997) that agreed with the more weakly pronounced $P680^3/P680$ bands. The stronger C=O keto band of the triplet state did not show a counterpart in the $P680^+/P680$ spectra, which led to the conclusion that most of the triplet population was located on a non-P680 chlorophyll.

The $P680^+/P680$ difference spectra show a very broad spectral feature ranging from about 1000 cm^{-1} up to as far as 6000 cm^{-1} (Noguchi et al., 1998; Breton, 2001; Okubo et al., 2007); analogously to a similar feature in bacterial reaction centers and PSI (see Section 1.4.2), this broad band was attributed to an electronic transition originating from the dimeric nature of $P680^+$. The $P680^+/P680$ difference spectra confirmed that the radical

cation charge of P680$^+$ is mainly localized on one chlorophyll (Okubo et al., 2007; Nagao et al., 2017b), which is of significance as the charge localization impacts the redox potential (Takahashi et al., 2008).

By altering the illumination protocol as well as the measurement temperature, difference spectra of Y_Z^{ox}/Y_Z (Zhang et al., 1997; Berthomieu et al., 1998), Y_D^{ox}/Y_D (Hienerwadel et al., 1996, 1997; Berthomieu et al., 1998) and Q_A^-/Q_A (Hienerwadel et al., 1996; Noguchi et al., 1999) were obtained by several groups in the 90s. Q_B and the role of bicarbonate and the non-heme iron were also investigated (Berthomieu and Hienerwadel, 2001). While some band assignments were possible, a complete and definite assignment of all the features in these spectra has never been achieved.

More recently, FTIR has also been applied to investigate what happens to the proton of the redox active tyrosines after their oxidation, finding that Y_D mostly releases it to the bulk (Nakamura and Noguchi, 2015), while Y_Z shifts it to its neighboring histidine, His190, (Nakamura et al., 2014).

Infrared Studies of O_2-Evolving PSII
Since the 1990s and 2000s, FTIR has also been widely applied to study the individual S-state transitions of oxygen-evolving PSII. Noguchi (2007) reviewed the early studies, summarizing attempts of assigning bands: By observing band shift behavior upon ^{13}C and/or ^{15}N labeling, many prominent bands in the 1800–1200 cm^{-1} region were grouped to amide I, amide II or COO$^-$ modes (Noguchi and Sugiura, 2003). As prominent COOH bands were mostly not observed, it was concluded that the COO$^-$ bands did not primarily reflect (de)-protonation events. Instead, these bands were interpreted as arising from the carboxylate ligands of the Mn_4CaO_x cluster, which are sensitive to the events of the S-state cycle.

More specific assignments, i.e. the assignment of bands to individual amino acid residues has also been attempted, as reviewed by Debus (2015). By employing a combination of point mutations and isotope labeling, a band around 1355 cm^{-1} was assigned to the COO$^-$ group of the C-terminal D1-Ala344 residue (Chu et al., 2004). Mutating CP43-E354 perturbed the spectra at several wavenumbers, but did not allow the unambiguous assignment to a specific band (Debus, 2015, and citations therein).

Mutating four other Mn_4CaO_x cluster-ligating D1-residues (Asp170, Glu189, Glu333 and Asp342) unexpectedly had virtually no effect on the FTIR spectra (see Debus, 2015, and citations therein). It was concluded that most of the COO$^-$ bands must be associated not with the first coordination sphere ligands of the Mn_4CaO_x cluster, but with residues further away. Recently, however, Shimada et al. (2022b) found that some specific mutations in vicinity of the Mn_4CaO_x cluster can undergo a post-translational conversion back to carboxylate residues, effectively undoing the mutation (Asn→Asp, Gln→Glu, His→Asp), offering an explanation as to why the FTIR spectra of the first sphere mutants resembled wild-type spectra.

Besides FTIR studies, Takumi Noguchi's group has also published time-resolved single-frequency data on all S-state transitions (Noguchi et al., 2012). They investigated the effect of pH and H/D exchange on the $S_1{\rightarrow}S_2$ and $S_2{\rightarrow}S_3$ transitions (Sakamoto et al., 2017; Takemoto et al., 2019). Furthermore, they investigated several point-mutants, including D1-Asn298Ala (Shimada et al., 2020; Okamoto et al., 2021; Shimada et al., 2022a).

Only one step-scan FTIR study has been published to date (Greife et al., 2023), where especially the kinetics of the $S_3{\rightarrow}S_0$ transition are observed and discussed in detail; all other published FTIR studies on PSII were done without notable time resolution.

2 | Time-Resolved Single-Frequency Infrared Spectroscopy

QUANTUM Cascade Lasers (QCL) present a powerful new tool in the field of infrared spectroscopy. Our time-resolved single-frequency (TRSF) IR setup, often simply referred to as the QCL setup, is custom built and one of a kind. It was first established by Philipp Simon, as reported in his doctoral thesis (Simon, 2019) This Chapter will describe the setup as it is as of now, outline modifications made to it since Philipp's thesis, discuss data processing/analysis in Python and finally look at some major issues that were discovered.

2.1 The Setup

In the center of the setup is an x-y-movable sample holder, in which several CaF_2 plates (25 mm diameter) can be placed (see Fig. 2.1). The sample holder is in an air-tight compartment, flooded with dry air; CaF_2 windows allow the laser beams to enter and exit. The compartment is temperature controlled with two water-cooled Peltier elements[4] that can be controlled via software. An additional temperature and humidity sensor[5] allows the readout of the temperature directly at the sample holder.

A quantum cascade laser[6] with previously two—and since mid-2022 three—cavities serves as continuous wave (cw) infrared source. The QCL is tunable to single frequencies between 1890–1310 cm^{-1} (5.3–7.6 μm). A 90° off-axis parabolic gold-coated mirror is used to focus the QCL beam before hitting the sample and a second identical mirror parallelizes the beam again (see Fig. 2.2 for a detailed scheme of the beam path). The sample holder is positioned such that the sample is slightly outside the focal point, ensuring that only a small sample spot is probed, without causing unnecessarily much heating. The transmitted IR beam is detected by a thermoelectrically cooled 10 MHz pre-amplified[7] mercury cadmium telluride (MCT) detector[8]. Before going through the sample, the IR beam is split by a wedged CaF_2 plate and the reflected portion is directed onto a second MCT detector. The

---

[4]Quick-Cool QC-71-1.4-6.0, Quick-Ohm Küpper & Co. GmbH
[5]TSP01, Thorlabs, Inc.
[6]MIRcat-1000, Daylight Solutions, Inc.
[7]MIPDC-10, Vigo Photonics
[8]PVI-4TE-8, Vigo Photonics
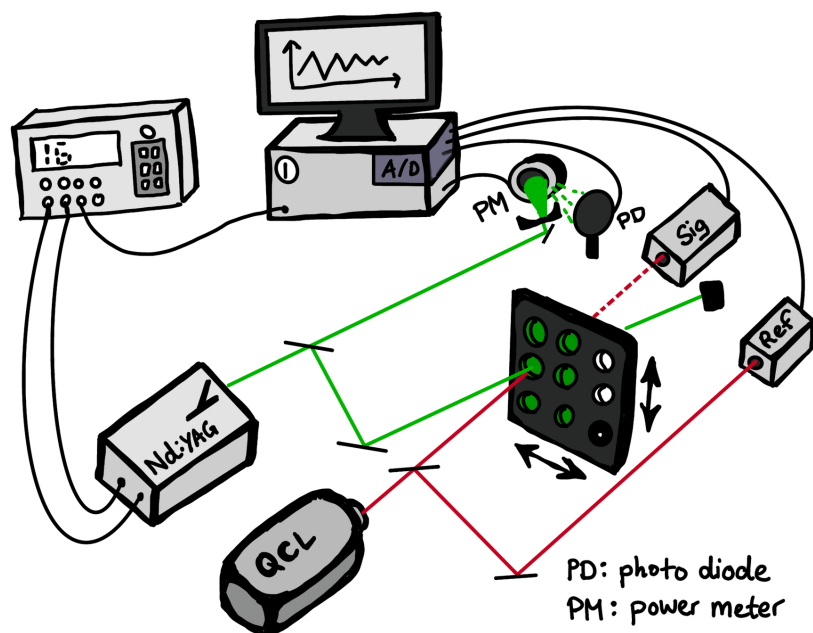
Figure 2.1: General scheme of the single-frequency IR setup. Samples sandwiched between two CaF$_2$ plates are mounted on a sample holder attached to an x-y-movable stage. An Nd:YAG laser (532 nm) is used as a excitation source. A QCL serves as the probe IR source. An MCT detector (Sig) measures the transmitted IR signal; a second MCT detector (Ref) serves as reference. A power meter (PM) measures the energy of each excitation flash; a photo diode (PD) records the timing of each flash. An A/D converter records the IR data, as well as the photo diode data. A pulse generator (*top left*) orchestrates the triggering of laser and data acquisition.

two detectors are paired and the combination of signal and reference detector is used to account for internal QCL-induced noise.

A frequency-doubled (532 nm) Q-switched Nd:YAG laser[9] with a pulse width of 5±2 ns is used as an excitation source. The intensity of the laser is regulated by a motorized attenuator. The beam size is set to 1 mm diameter with an iris. Half of the beam is directed onto a power meter, which records the energy of every flash. A photodiode placed nearby records a time trace of the excitation flash by measuring a portion of the laser light that is scattered off the power meter. The second half of the green laser beam is directed onto the sample. The IR beam and excitation beam are aligned such that they overlap, whereby the green beam is larger than the IR, ensuring the entire probed sample spot is excited.

A pulse generator is used to trigger the flash lamps and the Q-switch of the green laser. The latter is triggered with a delay of 160 μs, resulting in the emission of a nanosecond laser pulse. Data acquisition with an analog-to-digital (A/D) converter[10] (16-bit, 2 GSample, 130 MS/s) is triggered 20 ms before the laser (see Tab. A1.1 in the appendix for the detailed pulse generator settings).

Stage movement and data acquisition are controlled by two separate C++ programs (MultiScan and Stage Control), originally adapted for the setup by Petko Chernev and Philipp Simon (Simon, 2019). Fig. 2.3 shows a flow chart of the entire procedure. In a

---

[9]Minilite II, Amplitude Laser, Inc.
[10]M4i.4411-x8, Spectrum Instrumentation GmbH
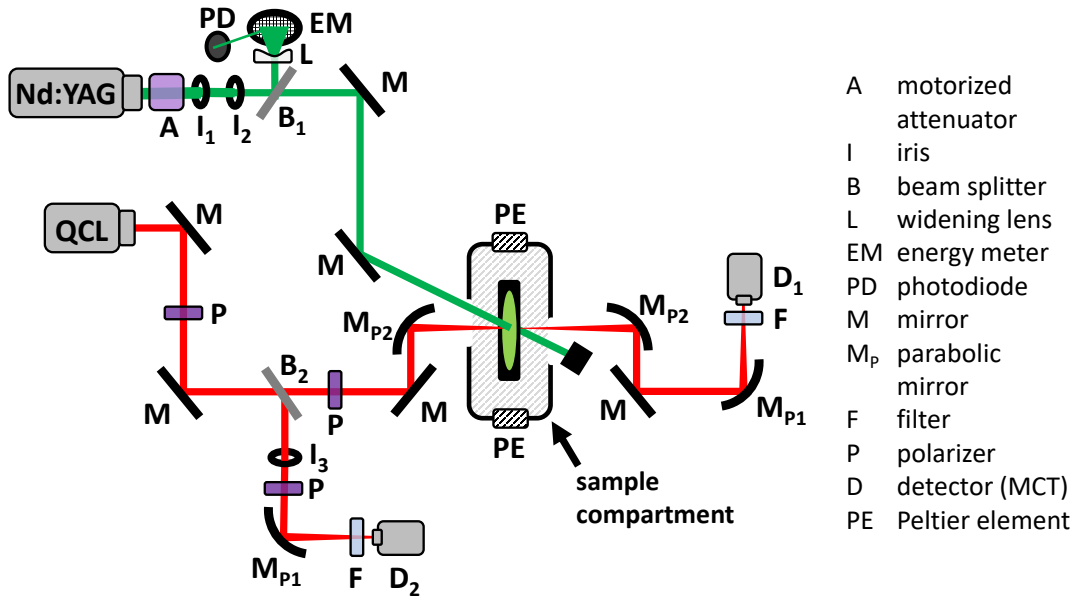
Figure 2.2: Detailed scheme of the beam paths. The beam path of the frequency-doubled (532 nm) Nd:YAG laser is depicted in green. The beam is directed into a motorized attenuator (A). It passes through two irises[11](I_1 set to 2.0 mm and I_2 set to 1.0 mm). A 50:50 beamsplitter (B_1) is used to direct half of the beam onto an energy meter (EM), after being widened by a lens (L) to prevent damage. Some of the light scattered of the energy meter is detected by a photo diode (PD) and recorded by an A/D converter (not shown). The transmitted half of the beam is directed onto the sample and finally hits a beam block. The infrared beam path of the QCL is shown in red. The IR beam is attenuated by a polarizer (P), which is set to either 180° (during measurements) or 192° (for calibration). The beam is split by a wedged CaF_2 plate (B_2), which transmits a large portion of the beam and reflects roughly 4–9%. The reflected portion of the beam (reference pathway) goes through an iris (I_3) to cut away higher order reflections. The beam goes through another polarizer (P) for further variable attenuation, before hitting a 90° off-axis parabolic mirror (M_{P1}) with a reflective focal length of 101.6 mm, which focuses the beam onto an MCT detector (D_2). The distance between the parabolic mirror and the detector is about 70–80 mm. A longpass filter (F) protects the detector by only transmitting light above 4.5 µm). The IR beam transmitted by B_2 (signal pathway) also passes through another polarizer (P) for variable attenuation and is adjusted according to sample thickness and wavenumber. The beam is focused by an off-axis parabolic mirror (M_{P2}) with a reflective focal length of 203.2 mm, passes through the sample (which is located slightly outside the focus point) and is then parallelized by another parabolic mirror of the same focal length. The beam is focused and filtered in the same way as for the reference pathway. The sample compartment has a CaF_2 window on either side to allow the beams to enter and exit. It is temperature controlled by two Peltier elements (PE). This scheme depicts the setup as until August 2022. Some mirrors, which serve merely to change the direction of the beams in order to accommodate the geometry of the setup, have been omitted. The mirrors in the green path are optimized for 532 nm; the mirrors in the IR path are gold-coated.

---

[11]The first iris is technically no longer necessary. However, by keeping the two irises, the laser path can be easily readjusted after e.g. moving the laser.
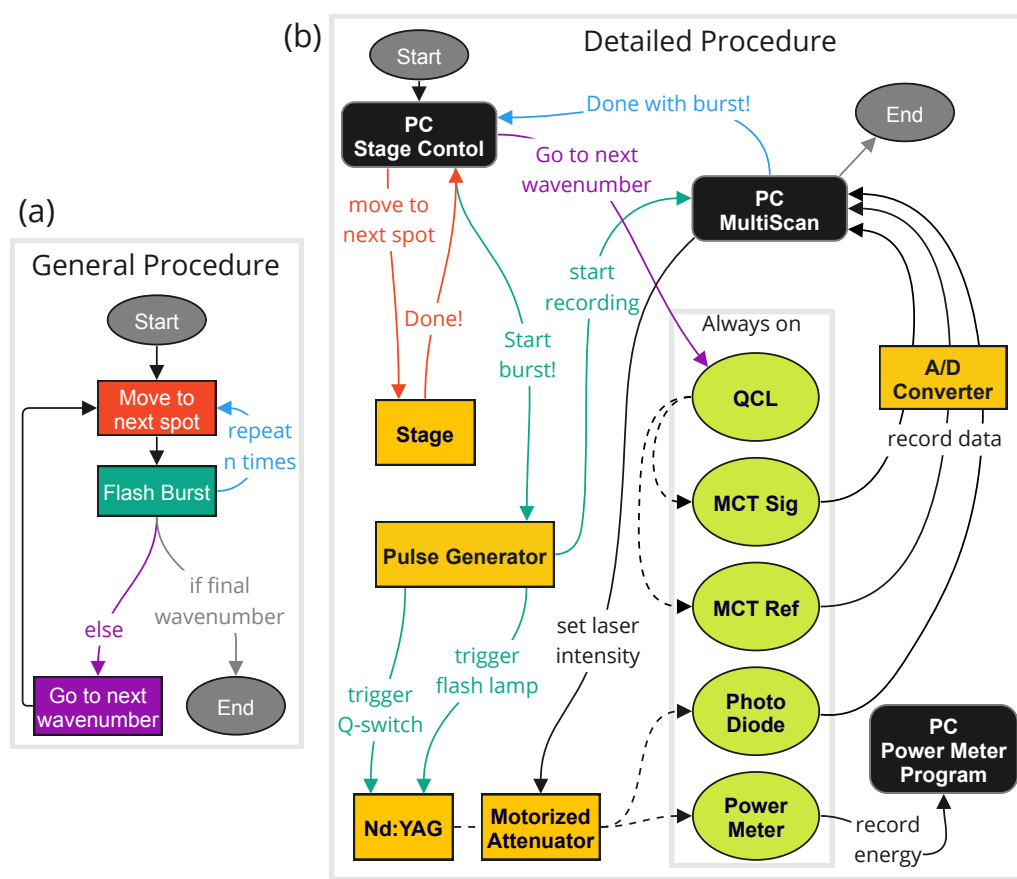
Figure 2.3: Overview of the automated data acquisition procedure. (a) A general scheme of the procedure. Upon starting the measurement, the stage is signaled to move to the first spot. The stage program signals the pulse generator to start a burst. After the flash burst, the MultiScan program signals the Stage program to move to the next spot. After all spots have been measured, MultiScan signals the QCL to change to the next wavenumber. All of this is repeated until the final wavenumber has been measured. **(b)** A detailed scheme of the procedure; the colors are chosen to match those of the scheme in (a). After the Stage program signals the pulse generator to start a burst, the pulse generator triggers the flash lamp and Q-switch of the Nd:YAG laser. It also triggers the MultiScan program to start recording the data, making it receive data from the A/D converter. The A/D converter digitizes the signal detected by the MCT detectors and the photo diode. Prior to starting a measurement, the user has to set the number of flashes per burst in the pulse generator (typically 6 'dark flashes', where Q-switch and flash lamp triggers are disabled plus 10 'real' flashes). The total number of flashes (typically 16) is also input into the MultiScan program. The number n of repeats is determined by the number of sample spots (determined by the user). If one wavenumber is to be measured repeatedly, the user may input the desired number of repeats into the MultiScan and Stage programs. The QCL may then simply be operated in the continuous mode.

typical measurement[12], six sample plates are mounted onto the sample holder and 33 spots are measured individually per plate, resulting in a total of 198 measurement spots. Upon starting the measurement, the stage drives to the first sample spot and sends a signal to the pulse generator, which starts a burst of 16 triggers at 1 Hz. The first six trigger only

---

[12]The numbers are exemplary and can easily be changed in the user interface of the C++ programs.
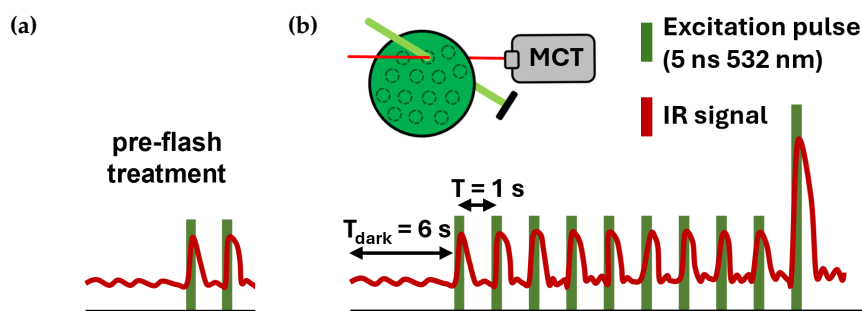
Figure 2.4: Standard flash protocol for PSII samples. (a) Prior to the first measurement, a pre-flash treatment of two saturating excitation flashes is applied to each sample spot. **(b)** Upon reaching a new sample spot, the IR signal is measured for six seconds ("dark signal"), before a 1 Hz flash sequence of 10 saturating excitation flashes is applied to the sample. For each excitation flash, the IR absorption changes are recorded starting 20 ms prior to the flash up to 800 ms after the flash. The 10th flash has approximately three times the intensity of the first nine, which later allows for a heat artefact correction (see Chapter 2.4). After each distinct sample spot has been measured, the next measurement round will begin again at the first spot (which thus had time to dark-adapt). Note that the pre-flash treatment is not repeated.

the data acquisition (and the flash lamp of the excitation laser), but not the Q-switch of the laser, thus 6 s of IR transmission in the dark are recorded. The next 10 trigger also the Q-switch, thus 10 sets of flash-induced IR absorption changes are recorded. Before the last flash, the motorized attenuator is triggered to decrease attenuation, resulting in a tenth excitation flash with higher intensity (see Fig. 2.4 for the standard flash protocol for PSII samples).

The triggers are delayed relative to each other in such a way that the data acquisition is triggered 20 ms before the excitation flash (with a total measurement time of 820 ms). The data from the A/D converter is transferred to the measurement PC in first-in-first-out mode and is then binned in a quasi-logarithmic manner before saving the data as tab-separated values (TSV) to a .dat file. The stage is then signaled to move to the next sample spot and the procedure is repeated, until all the sample spots have been measured. Measuring all 198 spots takes about one hour, which gives a PSII sample enough time to dark-adapt before remeasuring the same spots.

The programs can be set to repeat such measurement rounds as often as required. The wavenumber of the QCL may be switched automatically after any specified number of measured spots.

Next to the .dat files, also a laser log file is saved, where each reading (in J) of the power meter is recorded together with a time stamp. A file containing the temperature and humidity readings in 1 s intervals is also generated.

2.2 Modifications Done to the Setup

Over the years, several modifications were made to the setup, which will be briefly described in the following.

Temperature Control
Previously, the only temperature readout (for direct feedback to the Peltier cooling system) was on the wall of the sample compartment. However, it was found that the temperature

on the wall does not very well represent the temperature at the sample. A new temperature probe was mounted onto the stage next to the sample holder, enabling the recording of the air temperature and humidity, as well as the temperature directly at the sample holder. After trying out different positions of the probes, it was found that the best results were obtained by keeping the feedback probe on the compartment wall and simply setting the setpoint of the temperature a couple of degrees below the target temperature. The Peltier temperature control unit was furthermore connected to the PC, to allow control by software. This enabled the possibility to adjust the temperature remotely.

These changes were already reported in Aiga Abzaliyeva's master thesis (Abzaliyeva, 2020), as they were crucial to her temperature-dependent measurements.

Improvements for Laser Safety

In the past, the excitation laser beam was out in the open, making it necessary to wear laser safety goggles at all times while a measurement was running. In combination with PSII work, which demands a dark lab, this made parallel work on the other setup in the lab impossible.

The excitation laser was moved onto the same table as the rest of the setup, which allowed for the possibility to have the entire beam path encased and therefore making safety goggles unnecessary while the encasement is closed.

New Excitation Laser

The previously used Inlite Nd:YAG laser was replaced by a Minilite model of the same company. This brought with it the advantage of no longer having to operate the flash lamps at 10 Hz. While the pulse generator settings were quite complicated before, they are now straightforward.

Laser Attenuation

The excitation laser intensity used to be switched between low and high intensity by changing the delay between triggering the flash-lamps and the Q-switch. However, this caused a lot of issues (as described in Chapter 2.7). The intensity is now controlled by a motorized attenuator (see Chapter 2.7.3 for details). This further simplified the pulse generator settings.

Setup Software Changes

Some small modifications were made to the C++ programs. Besides fixing a few minor bugs, the following changes were made:
  ▷ A "skip" button was added to MultiScan. Remotely logging in to the setup PC during a measurement usually causes the program to get stuck (probably because the CPU and/or memory is briefly completely occupied, making the program miss a trigger from the pulse generator). Previously, the program and thus the measurement had to then be restarted entirely (meaning the measurement would restart from the first sample spot, whether or not it had been given enough dark-adaptation time). Now, clicking the skip button will make the program stop waiting for the trigger and send out a signal to the Stage program to drive to the next spot, thus bypassing the issue.
  ▷ A so-called Quick-Spec option was added to the Stage program, allowing for the wavenumber to be changed after any desired number of flash bursts. This provides the option of measuring more than just one wavenumber per hour, thus enabling the acquisition of spectral data. (For spinach PSII ~30 bursts per wavenumber were found to yield good results; for PSI core complexes great results were obtained with just one burst per wavenumber.)

▷ The option to measure repeatedly on the same spot was added to the Stage program. This was necessary for measurements on PSI.

▷ An interface between MultiScan and the motorized attenuator was implemented. Currently, the MultiScan user interface takes two attenuator values: a setting for the first flashes (usually set to around 30% transmission) and a setting for the final flash (100%). A tick box allows for the artefact flash to be deactivated, in which case the final flash will have the same setting as the other flashes.

▷ A "saturation curve" tick box was added to MultiScan. When activated, the text box, which usually takes a list of wavenumbers, can instead be filled with numbers from 0 to 100, corresponding to the transmission setting of the motorized attenuator. It is thus possible to do a series of automated measurements at varying excitation energies.

IR Path Changes

The IR beams were previously focused onto gold-coated diffusive reflectors and only a portion of the reflected light was captured by the MCT detectors. This made it hard to control noise ($\sim$ 10 kHz) in the IR signal (see Chapter 2.5). Both the signal and reference beam paths were changed such that the IR beams are now focused onto the detectors. As a result, the IR beams had to be attenuated more strongly to avoid damage to the detectors. For this purpose, two additional polarizing filters were installed.

New Quantum Cascade Laser

The QCL was recently exchanged[13] for a newer model[14] with improved properties. Besides the larger wavenumber coverage, the most significant difference is the improved pointing stability of the new laser, which eliminated a big noise source (discussed in more detail in Chapter 2.5). Most—but not all—measurements presented in this thesis were done with the old QCL.

Laser Table

The laser table was not sufficiently supplied with pressure by the building's internal compressed air supply system. To enable a proper inflation of the table, a compressed air generator was acquired[15].

Air Conditioner

It was found that in summer high temperatures in the lab made it difficult or sometimes even impossible to cool down the sample compartment sufficiently. As a solution, an air conditioner was installed.

2.3   Data Processing and Analysis in Python

During data acquisition, the data is binned in a quasi-logarithmic way, i.e. the bin size is increased slightly every few bins (the smallest bin-size is about 15 ns). This is necessary in order to compress the data: a measurement with 16 flashes results in about 200 TSV files with roughly 1.4 MB size each. Without logarithmic binning each file would have roughly 50 million rows of data instead of 1500, resulting in files of nearly 50 GB size.

---

[13]M. Y. Dekmak exchanged the lasers. Some small additional changes were made to the beam path (e.g. another polarizer was added for additional beam attenuation), which are not shown in Fig. 2.2.

[14]MIRcat-QT-Z-2300, Daylight Solutions, Inc.

[15]Silver-Line L-S20, PLANET-AIR GmbH

All further data processing and analysis is done with self-written Python scripts. The rough procedure is based on Philipp Simon's approach, as used for his thesis. The implementation, however, was done from scratch and some of his ideas were also further built on and improved, with a strong emphasis on automation. The data processing procedure can now be applied in a nearly fully automated way, while still allowing for user interference and optimization. The scripts were continuously worked on and improved over the years. The final version was carefully revised and extensively commented on. In the following the scripts will be outlined mostly in a general manner; a few lines of Python code will be displayed to demonstrate how to use the scripts.

Note that all scripts were written in Python 3.7 and may not be compatible with newer (or older) Python versions.

2.3.1   From Raw Data to Final Transient

The data processing and analysis procedure can be performed by three lines of code:

```
1  data = AnalyzeQCLData(wavenumber=1400, info="BBY", dark_flashes=6,
       real_flashes=9, artefact_flash=1, data_directory=r"S:\Data\Measurement")
2  data.ReadInData()
3  data.analyse_data()
```

The first line initializes the procedure and returns an object which will eventually contain all the raw and processed data. The second line calls a function to read in the data stored in the given directory and then sorts the data into different arrays corresponding to the three channels: Ch0 (MCT signal), Ch1 (MCT reference signal) and Ch2 (diode signal). The third line prompts the actual data processing and analysis. If no parameters are given to the analyse_data function, default parameters will be used.

The following line of code will print out all parameters that can be given to the analyse_data function:

```
1  data.print_analysis_options()
```

The analyze_data function calls a number of other functions, which one by one process the data: These functions can be grouped into two main categories: filtering the data for various quality scores (see 2.3.2) and general data processing (see below).

Figure 2.5: Flowchart of the data processing procedure in python.

The main steps that are applied to the data (aside from filtering) are summarized as a flow chart in Figure 2.5 and will be explained in more detail in the following.

Time axis correction
Along with the IR signal, every excitation flash as detected by the photodiode is also recorded by the A/D converter. While the laser flash has a pulse width of about 5 ns, the measured signal looks a lot wider, due to a 15 ns rise time of the photodiode. The signal is fit to a Gaussian and then shifted such that the peak is at t = 15 ns (Fig. 2.6).

For data sets acquired before the motorized attenuator was integrated into the setup (instead using variation of the Q-switch delay for setting the excitation intensity), the low-
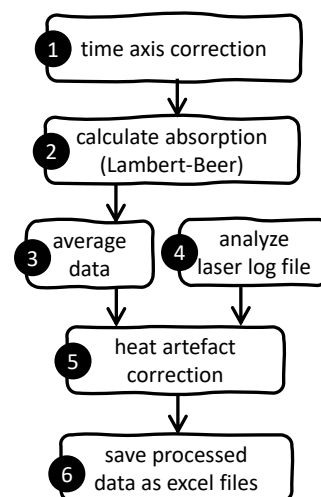
Figure 2.6: Photodiode data of the 532 nm laser flashes. The data points (*circles*) of low- and high-energy flashes (*orange* and *red*, respectively) are shown alongside Gaussian fit curves (*solid lines*). The excitation energy was set using **(a)** the Q-switch delay and **(b)** the motorized attenuator.

and high-energy flashes have different shapes (Fig. 2.6a) and different timings. For those data sets, the high-energy transient is additionally shifted in an attempt to optimize the timing with respect to the low-energy flashes. For this, two different approaches have been tested. The method yielding the best results was to determine the starting points where the photodiode data starts to rise and overlay those points.

Calculation of absorption signal

The difference absorption is calculated (in mOD) from the raw data using Lambert-Beer's law:

$$\Delta A(t) = -1000 \cdot \log_{10}\left(\frac{A(t)}{A_0}\right) \quad , \tag{2.1}$$

where $A(t)$ is the raw signal (in mV) and A_0 is the average signal before t=0. This is done for both the signal and the reference channel. By subtracting one from the other, QCL-induced noise is accounted for:

$$\Delta A(t) = \Delta A_{\text{sig}}(t) - \Delta A_{\text{ref}}(t) \quad . \tag{2.2}$$

Calculate mean signal

The average difference absorption signal is calculated from all data sets that passed the quality filters. If the high-energy flash has a different time axis, the data is shifted to match the time axis of the low-energy flashes. This requires some interpolation because of the non-linear binning of the data.

Analyze laser log file

The laser log file contains information on every excitation flash (energy and time stamp). The recorded flashes are matched to the IR data sets. The average energy of the flashes is needed for the heat artefact correction procedure.

Heat artefact correction

See Section 2.4.

Save processed data

As a final step of the automated data processing procedure, the averaged data is saved as an excel file, which contains the following data:

▷ heat artefact corrected flash-induced transients
▷ uncorrected flash-induced transients
▷ heat artefact transient and fit curve
▷ average energy values of high and low excitation transients

▷ averaged raw Ch0, Ch1 and Ch2 data
▷ dark data transients obtained without excitation flashes
▷ standard errors of all transients
▷ some additional information, such as wavenumber and total number of averaged data sets
▷ a list of all used files

Additionally to the excel file, a few figures are also generated and saved as jpeg files: a figure of the first four flash transients, a figure of the heat artefact transient, a figure of flash number dependent values at different time points and a figure of the filter results (see Fig. A1.1 in the Appendix). The latter is helpful for adjusting the data process procedure if e.g. too many data sets are filtered out.

2.3.2 Filtering Data

Prior to averaging the data to obtain a final transient, all data sets are submitted to several quality checks. In the following these "filters" will be briefly described (in the order as they are applied to the data in the script).

▷ Missing flash filter: checks the diode data for data sets where no excitation flash was recorded.
▷ Miss-trigger filter: checks diode data for data sets where the excitation flash is not at the expected temporal position. This filter is mostly relevant for old data sets acquired with the Inlite laser, which had flash lamps that had to be operated at 10 Hz. While the pulse generator was set to trigger the Q-switch at 1 Hz, it sometimes mistakenly triggered more often.
▷ Intensity filter: checks Ch0 and Ch1 for values above 1 mV (saturated signal) and below 0.2 mV (poor signal-to-noise).
▷ Manual filter: the user may define certain data sets to be sorted out (by their index).
▷ Jumps filter: checks data for extreme jumps in the signal (applied to difference absorption data).
▷ Dark data filter: checks data for strong fluctuations in the dark data (applied to difference absorption data).
▷ Steady-state filter: checks for data sets with strong fluctuations between ~ 400 and 800 ms (applied to difference absorption data).
▷ 100 μs/kHz noise filter: check for strong fluctuations around 100 μs (applied to difference absorption data).
▷ Laser log filter: checks whether per data set the expected number of flashes has been recorded. If more flashes were detected, the pulse generator may have triggered the laser too often; if fewer flashes were detected, either the laser was not triggered or the flash energy was too low to be detected by the power meter.

Some of the filters overlap in their functionality, e.g. the miss-trigger filter and the laser log filter. However, there are rare—but recurring—cases where only the one or the other filter can catch the problematic data set. Any changes to the data acquisition process may make new/adjusted filters necessary. All filters have several parameters that can be changed when calling analyse_data(). For most of the filters, the most important parameter to be adjusted by the user is *threshold*, which determines what value is the cut off between keeping and discarding the file.
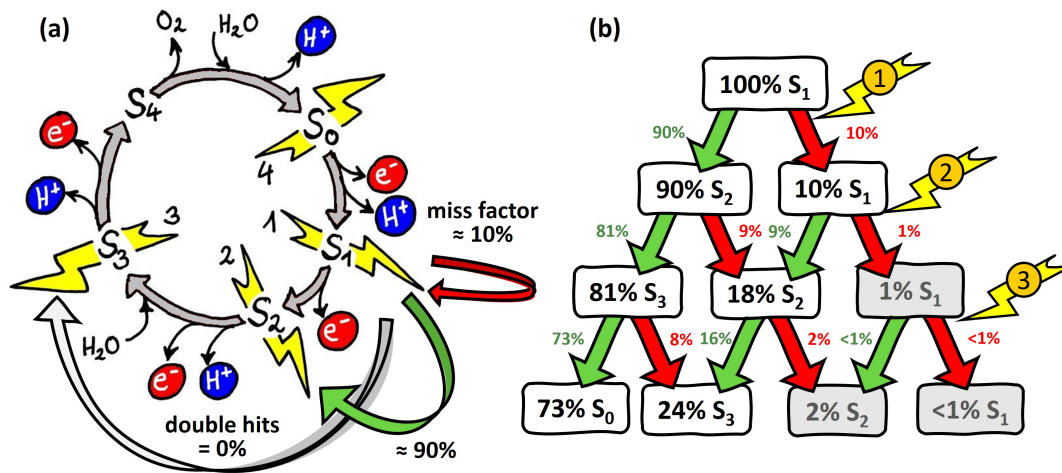
Figure 2.7: Mixing of S-states. (a) A scheme of the S-state cycle, showing the influence of the miss factor and double hit factor at the example of the $S_1 \rightarrow S_2$ transition: The green arrow shows that while most of the PSII centers undergo the transition, roughly 10% remain in the S_1 state (red arrow). Double hit events lead to a transition from the S_1 to the S_3 within one excitation flash (grey arrow). **(b)** Exemplary calculation of S-state mixing. The squares indicate the S-state populations between excitation flashes. The green arrows indicate the fraction of PSII centers advancing to the next respective S-state, while the red arrows indicate the fraction of misses. When starting with 100% in the S_1 state, a miss factor of 10% will already lead to significant mixing of the third flash transition (73% $S_3 \rightarrow S_0$ and 16% $S_2 \rightarrow S_3$). Note that the S_3 population after the third flash will be 24% rather than 16%, because 8% of the centers remain in the S_3 state without advancing.

2.3.3 Obtaining Pure S-State Transitions

As described in Section 1.1.3, the PSII reaction cycle requires four photon absorption events to complete, resulting in oxygen evolution. The individual S-state transitions, however, are not 100% efficient. The fraction of transitions that fail to complete upon the absorption of a photon is termed miss factor and is usually around 10%. When using an excitation laser with nanosecond pulses, the fraction of double hits, i.e. PSII centers advancing two S-states during one excitation pulse, is expected to be zero. A simplified S-state cycle is shown in Fig. 2.7(a), with a red arrow indicating the miss factor and the grey arrow indicating double hits. Experimentally, after given time to dark-adapt for 30–60 minutes, most of the PSII centers will be in the dark-stable S_1 state, thus the first flash transition corresponds predominantly to the $S_1 \rightarrow S_2$ transition. With every excitation flash the population will become more and more mixed. Fig. 2.7(b) shows an example of a 100% S_1 starting population and a miss factor of 10%. After the first flash, 90% of the PSII centers will be in the S_2 state, but after the third flash only 73% will be in the S_0 state and 24% will be in the S_3 state.

While the starting population can be 100% S_1 in some cases (Han et al., 2022), this depends on the PSII system as well as the measurement conditions (Isgandarova et al., 2003). If the starting population is instead, e.g., 90% S_1 and 10% S_0, the mixing of S-states will be even stronger pronounced. When analyzing data of the individual transitions, e.g. by multi-exponential fitting, mixed S-states will of course influence the results. It is thus common practice in PSII research to try to deconvolve the data into pure S-state transitions. To be able to do so, we acquire data not only on the first four flashes, but rather on 10

consecutive flashes. In the following a mathematical approach to S-state deconvolution will be laid out.

The starting population $\mathbf{P_0}$ of the different S-states can be denoted as follows:

$$\mathbf{P_0} = \begin{pmatrix} P_0(S_1) \\ P_0(S_2) \\ P_0(S_3) \\ P_0(S_0) \end{pmatrix} \text{, e.g. } \mathbf{P_0} = \begin{pmatrix} 100\% \\ 0\% \\ 0\% \\ 0\% \end{pmatrix} \text{ if all PSII units are in the } S_1 \text{ state at the start. We}$$

can apply a transition matrix $\mathbf{M_{trans}}$ to $\mathbf{P_0}$ to calculate the propagation of the S-states to $\mathbf{P_1}$, i.e. the population following a first excitation flash:

$$\mathbf{P_1} \qquad = \qquad\qquad\qquad \mathbf{M_{trans}} \qquad\qquad\qquad \cdot \qquad \mathbf{P_0}$$

$$\mathbf{P_1} = \begin{pmatrix} P_1(S_1) \\ P_1(S_2) \\ P_1(S_3) \\ P_1(S_0) \end{pmatrix} = \begin{pmatrix} m & 0 & dh & 1-m-dh \\ 1-m-dh & m & 0 & dh \\ dh & 1-m-dh & m & 0 \\ 0 & dh & 1-m-dh & m \end{pmatrix} \cdot \begin{pmatrix} P_0(S_1) \\ P_0(S_2) \\ P_0(S_3) \\ P_0(S_0) \end{pmatrix}, \tag{2.3}$$

where m is the miss factor and dh is the fraction of double-hits. So, if we break this down, the S_1 population after the first flash, e.g., can be calculated as follows:

$$P_1(S_1) = m \cdot P_0(S_1) + dh \cdot P_0(S_3) + (1-m-dh) \cdot P_0(S_0) \quad . \tag{2.4}$$

In more general terms, the population after the nth flash is: $\mathbf{P_n} = \mathbf{M_{trans}} \cdot \mathbf{P_{n-1}}$, which can also be written as $\mathbf{P_n} = (\mathbf{M_{trans}})^n \cdot \mathbf{P_0}$.

What we observe after the nth excitation flash, however, is not the same as the sum of all S-state populations after the nth flash. Rather we have to consider that PSII particles that do not transition into the next S-state will also not give an IR signal, while double hits will give a signal for both S-states they propagate through. The full truth is undoubtedly even more complex, considering that the reason for misses may not be that the PSII centers are not excited (indeed unlikely with saturating laser flashes), but rather that the excitation events are unproductive, e.g. due to recombination of the charge separated pair. This means that early parts of the transients likely contain some signal related to miss-events, while in the steady-state miss-events should be largely silent. In the following, we will assume for simplicity that all misses are entirely silent. The observation matrix is thus a slightly altered version of the transition matrix:

$$\mathbf{M_{obs}} = \begin{pmatrix} 0 & 0 & dh & 1-m \\ 1-m & 0 & 0 & dh \\ dh & 1-m & 0 & 0 \\ 0 & dh & 1-m & 0 \end{pmatrix} \tag{2.5}$$

The absorption signal after the nth flash $A(n)$ (corresponding to a mix of the S-state transitions) can thus be written as:

$$A(n) = \qquad\qquad \mathbf{M_{obs}} \qquad\qquad \cdot \qquad ((\mathbf{M_{trans}})^{n-1} \cdot \mathbf{P_0}) \quad \cdot \mathbf{S}$$

$$A(n) = \begin{pmatrix} 0 & 0 & dh & 1-m \\ 1-m & 0 & 0 & dh \\ dh & 1-m & 0 & 0 \\ 0 & dh & 1-m & 0 \end{pmatrix} \cdot \begin{pmatrix} P_{n-1}(S_1) \\ P_{n-1}(S_2) \\ P_{n-1}(S_3) \\ P_{n-1}(S_0) \end{pmatrix} \cdot \begin{pmatrix} S_1 \\ S_2 \\ S_3 \\ S_0 \end{pmatrix}, \tag{2.6}$$

where $\mathbf{S} = \begin{pmatrix} S_1 \\ S_2 \\ S_3 \\ S_0 \end{pmatrix} = \begin{pmatrix} S_1 \to S_2 \\ S_2 \to S_3 \\ S_3 \to S_0 \\ S_0 \to S_1 \end{pmatrix}$ are the signals of the pure S-state transitions.

Since the above equation cannot be solved for $\mathbf{S}$ by a simple matrix inversion, we instead need to approximate $\mathbf{S}$ for a given m, dh and P_0. The approximated $\mathbf{S}$ can then be inserted into Equation 2.6 to obtain $A_{sim}(n)$. By varying m and dh and minimizing the difference between the measured and simulated absorption changes ($\sum (A_{mes} - A_{sim})^2$) we can obtain an optimal estimate for the pure S-state transitions.

Varying $\mathbf{P_0}$ does not actually influence the simulated signal (because of the way that $\mathbf{P_0}$ influences the estimation of $\mathbf{S}$) and thus cannot be estimated by this minimization process. However, if we are observing a signal which is specific to only one S-state transition, e.g. O_2 evolution, then the $\mathbf{S}$-vector simplifies to $\mathbf{S} = \begin{pmatrix} 0 & 0 & S_3 & 0 \end{pmatrix}$, which leads to $\mathbf{P_0}$ having an influence of A_{sim} and thus on $\sum (A_{mes} - A_{sim})^2$ after all.

A Python script performing the above-described approach has been implemented. The double-hit parameter is set to zero by default, but can also be optimized by the script if deemed appropriate. The user can choose whether the entire transient is to be used in the minimization process or e.g. only the last few hundred milliseconds. The starting population is 100% $\mathbf{S_0}$ by default, but can be changed to any mix of S-states. The miss factor can also be fixed to a specific value if it was pre-determined in some other way.

As already hinted above, this approach is a simplification for various reasons. *Inter alia* the assumption that the miss factor is the same for all S-state transitions has been shown to be incorrect (Pham and Messinger, 2016): It has been suggested that the $S_0 \to S_1$ and $S_1 \to S_2$ transitions exhibit a very low fraction of misses, while the $S_2 \to S_3$ was shown to have the largest miss factor (Han et al., 2022). An option for S-state dependent miss factors was also implemented[16]; different approaches applied to the IR data in this thesis are discussed in Chapter 4.

2.3.4 Multi-Exponential Fitting

A simple and common approach to quantifying kinetics is to fit the time-resolved absorption changes to a sum of exponentials. Any measured process will occur distributed within a certain time window. Many chemical processes are well described by a simple exponential distribution and the time constant can be seen as an average time at which the process occurs.

In this thesis, two different versions of an exponential function are used:

$$y(t) = y_0 + \sum^i A_i \cdot (1 - e^{-t/\tau_i}) \quad , \tag{2.7}$$

where y_0 corresponds to the value at t=0 and a decay is described by a *negative* amplitude, and

$$y(t) = y_0 + \sum^i A_i \cdot e^{-t/\tau_i} \quad , \tag{2.8}$$

---

[16]Only the average miss factor is optimized, while the miss factor distribution over the S-state transitions is defined by the user. Optimization of the individual S-state dependent miss factors is not possible without signals that unambiguously distinguish between the different S-states (see e.g. Isgandarova et al., 2003).

where y_0 corresponds to the value at t → ∞ and a decay is described by a *positive* amplitude. The two equations are interchangeable, giving the same time constants as well as amplitudes of the same magnitude. They differ only in the definition of the offset y_0 and the sign of the amplitudes (Fig. 2.8). A time constant τ from an exponential function should not be confused with the half-time $t_{1/2}$, which is the time at which an exponential function has decayed to half its amplitude; these two values are related as follows: $t_{1/2} = \ln(2) \cdot \tau$.

The parameters of an exponential function best describing a measured transient can be determined with a least-squares optimization process. For this, the parameters are iteratively varied by small amounts. During each iteration the residuals, i.e. the difference between data and exponential function, are calculated. The sum of the squares of the residuals, i.e. $\sum(y_{\text{data}}(t) - y_{\text{sim}}(t))^2$, is the number that is minimized.

The starting guess for the parameters needs to be fairly good, otherwise such algorithms often get trapped in local minima and the optimization process fails.

A fitting procedure was implemented in Python 3.7, using the least_squares algorithm from the scipy.optimize package for the optimization step. The standard errors of a transient can be used as weights to improve the fit quality. The implemented script automatically calculates a good set of initial parameters, but also allows the user to change them if necessary. Time constants can be held to specific values. The fitting can be done either locally on one data set or globally on multiple data sets, where the amplitudes are then determined individually for each data set while the time constants are optimized globally for all data sets.
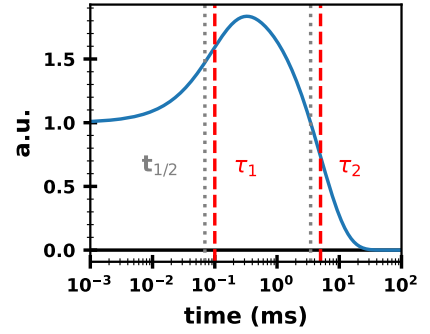
Figure 2.8: Example of a multi-exponential function. This curve is described by equation 2.7 with A_1=1, A_2=-2, τ_1=0.1, τ_2=5 and y_0=1. When using equation 2.8, the time constants are the same with A_1=-1, A_2=2 and y_0=0. The red vertical lines mark the time constants and the grey dotted line the associated half times.

Decay Associated Spectra

When globally fitting an entire time-resolved spectral data set, the resulting amplitudes can be plotted as a function of wavenumber. Such plots resemble spectra themselves and are associated with a certain time constant, hence the name *decay associated spectra* (DAS). For a global fitting procedure involving, e.g., 200 transients, the computing time easily becomes quite high (on a standard personal computer). The computing time can be decreased significantly (by 2–3 orders of magnitude) by not handling the amplitudes as parameters to be optimized, but by rather calculating them via a matrix inversion during each iteration.

For one data set, a multi-exponential equation can be written as:

$$y(t) = (A_1, ..., A_n, y_0) \cdot \begin{pmatrix} 1 - e^{-t/\tau_1} \\ \vdots \\ 1 - e^{-t/\tau_n} \\ 1 \end{pmatrix} , \qquad (2.9)$$

$$\mathbf{y} = \mathbf{a} \cdot \mathbf{M}$$

where $\mathbf{M}$ is a matrix with one column for each value of t. We cannot solve for $\mathbf{a}$ directly, but we can rewrite the equation:

$$\begin{aligned} \mathbf{y}.T &= (\mathbf{a} \cdot \mathbf{M}).T \\ \mathbf{y}.T &= \mathbf{M}.T \cdot \mathbf{a}.T \quad , \end{aligned}$$

(2.10)

the last row now being the format needed to use a least-squares approach of the Python scipy package (linalg.lstsq) to solve for transpose of $\mathbf{a}$. A variation of the fitting procedure that calculates the amplitudes in this manner rather than handling them as parameters has been implemented.

Accounting for the Instrumentation Response

The instrumentation response of an experiment can be described by an instrument response function (IRF). In an ideal experiment with an infinitesimally small IRF, the measured signal of a step function (Fig 2.9a, *dashed blue line*) would be zero until $t = 0$ and then reach the maximal signal instantaneously. However, due to e.g. the limited detector speed and sampling rate of the A/D converter, as well as the 5 ns pulse width of the excitation laser, the IRF is not negligibly small, resulting in an increase of the signal over a few tens of nanoseconds.

The IRF was first roughly estimated by fitting a Gaussian into the rise of a data set that shows no kinetics in the nanosecond to microsecond region (Fig 2.9a, *yellow*). The parameters were refined by convolving the Gaussian with a step function ($y(t < 0) = 0$ and $y(t \geq 0) = 1$) and comparing the convolved function with the data (Fig 2.9a, *yellow* and *red*). This led to the following approximation of the IRF:

$$\text{IRF}(t) = e^{\frac{-(t-t_0)^2}{2\sigma^2}} \quad , \quad \text{with } \sigma = 17 \text{ ns and } t_0 = 0 \quad .$$

(2.11)

Note that the time axis needs to be adjusted for this approach, such that the initial rise of the data is centered around the peak of the Gaussian (here it was chosen to center both around zero).
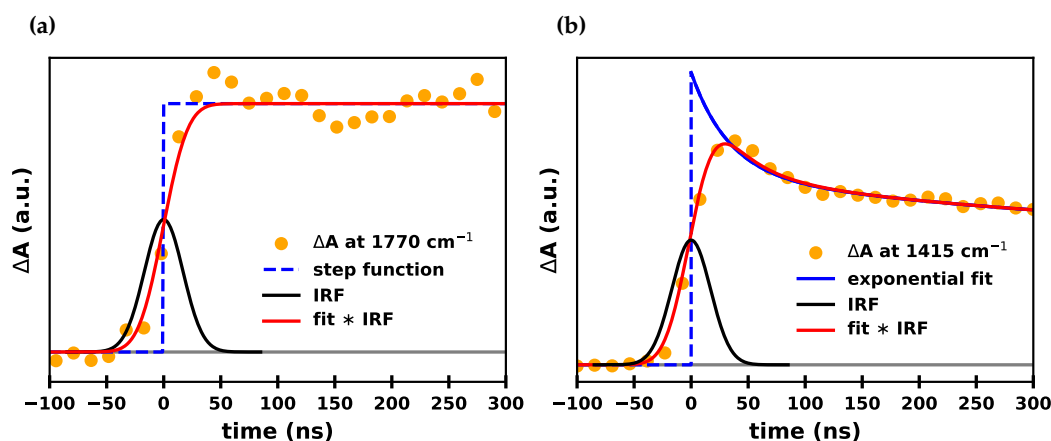
Figure 2.9: Accounting for the Instrument Response. (a) PSI core particles from *T. vestitus* at 1770 cm^{-1} (*yellow*), a step function that jumps from 0 to 1 at $t = 0$ (*blue*), a Gaussian IRF (*black*) and the convolution of step function and IRF (*red*). The convolved function simulates the data at 1770 cm^{-1} well. **(b)** PSI core particles from *T. vestitus* at 1415 cm^{-1} (*yellow*), and exponential function (*blue*), a Gaussian IRF (*black*) and the convolution of the exponential function and the IRF (*red*), which nicely simulates both the rise and decay of the data.

At 1415 cm^{-1} PSI core particles show fast nanosecond kinetics following excitation. Convolving the Gaussian IRF with an exponential function well describes the rise of the signal due to instrumentation response, as well as the subsequent biophysical decay kinetics (Fig 2.9b).

The IRF can be neglected when looking at kinetics slower than $\sim$200 ns. When trying to fit the very early section of the transient, however, it should not be ignored. For this, an alternate fitting procedure was implemented, which convolves the exponential function with the IRF in every iteration of the optimization process and uses the convolved function to calculate the residuals.

2.4 Excitation Laser Induced Heat Artefact

All time-resolved infrared difference absorption transients of PSI and PSII are affected by a excitation-induced heat artefact that builds up within the time resolution of the setup and decays until about 100 ms after the flash. As observed with FTIR measurements by Görlin (2012), heating up a PSII spectrum causes a frequency shift to lower frequencies. The difference spectrum of two PSII spectra measured at temperatures of 1 K difference greatly resembles the first derivative of an absolute spectrum.

The spectral signatures of the heat artefacts observed with the QCL setup (shown in Fig. 2.10 for PSI and PSII) also resemble the first derivative of an absolute spectrum (Fig. 2.10d). Deviations of the heat artefact spectrum from the derivative of the absolute spectrum around the amide I band might be caused due to strong water absorption in that region (Görlin, 2012). As shown by Simon (2019) and Schönborn (2017), buffer ingredients influence the heat artefact as well. Especially betaine was found to contribute significantly, due to some sharp absorption bands. Following Philipp Simon's assessment that measurements of spinach PSII membranes in buffer without betaine show no loss in activity (Simon, 2019), the measurements in this thesis were also performed without betaine.

Besides heating of the sample, some other effects may also contribute to the heat artefact. A photothermal beam deflection effect, e.g., could in theory be present, but was not observed so far (Simon, 2019).

In cyanobacterial core complex samples, the heat artefact is much less pronounced (Fig. 2.10b). This is presumably due to the fact that—compared to spinach PSII membrane particles—significantly fewer chlorophyll molecules per PSII unit are present in those samples, as was also observed by Okubo et al. (2007).

2.4.1 Correcting for the Heat Artefact

The heat artefact will be discussed at the example of PSII. For the most part, the heat artefact correction can be performed analogously for PSI; the steps that are specific to PSII will be pointed out as such.

The approach below for the correction of the heat artefact is based on the following assumption: When exciting the sample with saturating laser intensities, the signal due to PSII activity is maximal. When further increasing the excitation energy, the PSII signal remains the same, but the heat artefact signal increases linearly with the excitation energy.
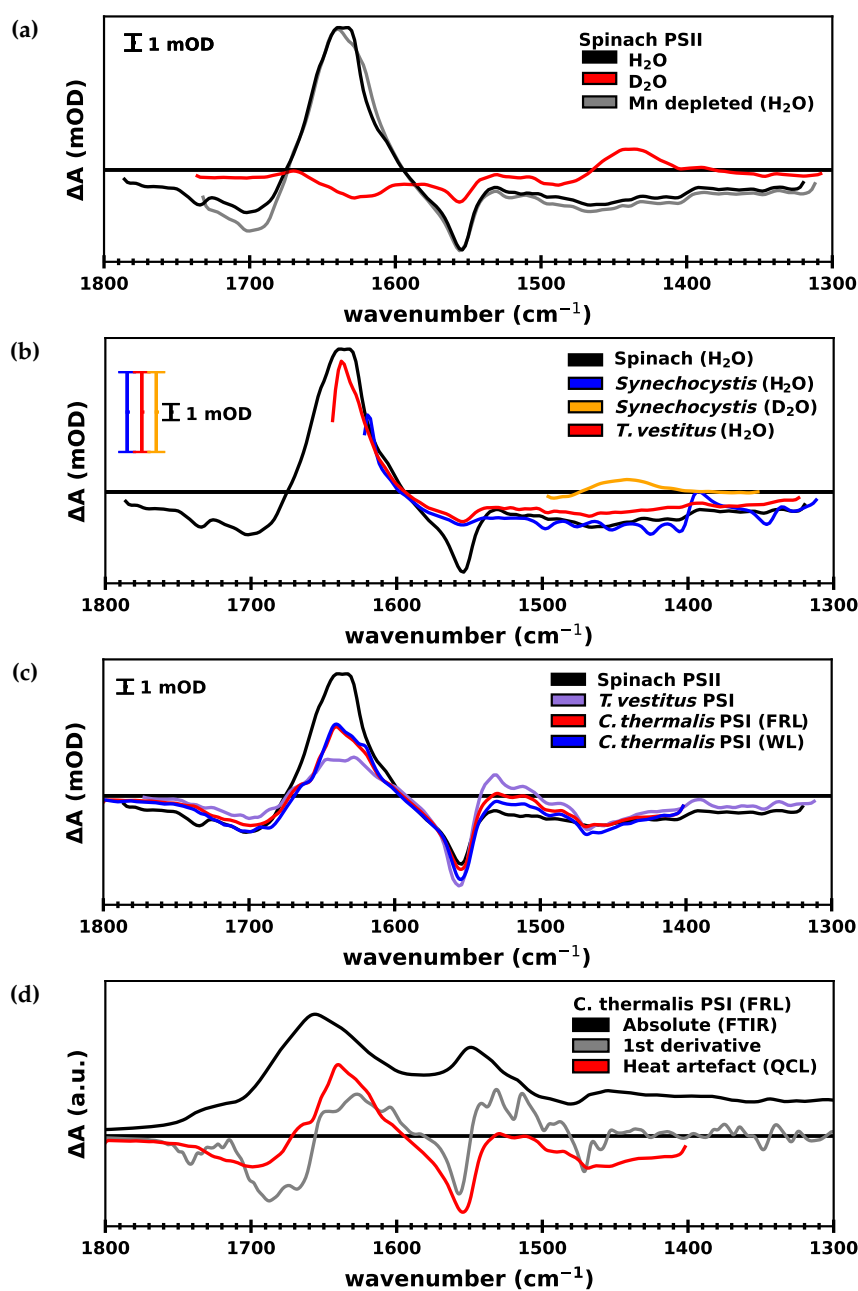
Figure 2.10: Heat artefact spectra of various PSI and PSII samples. All spectra show the values averaged between 0.1–1 µs. **(a)** Heat artefact spectra of intact spinach PSII membrane particles in H_2O (*black*) and D_2O buffer (*red*) at pL 6.2, as well as Mn depleted spinach PSII in H_2O (*grey*). **(b)** Heat artefact spectra of PSII core complexes from *Synechocystis* sp. PCC 6803 in H_2O (*blue*) and D_2O (*yellow*), as well as core complexes from *T. vestitus* in H_2O (*red*) at pL 6.0. A spinach PSII spectrum from panel a is shown for comparison (*black*). The cyanobacterial spectra were multiplied by five, as indicated by the scale bars. **(c)** Heat artefact spectra of PSI core complexes from *T. vestitus* (*purple*) and *C. thermalis* grown under far red light (FRL) (*red*) and white light (WL) conditions (*blue*). A spinach PSII spectrum from panel a is shown for comparison (*black*). **(d)** An absolute FTIR spectrum of FRL grown *C. thermalis* (*black*) and its first derivative (*grey*). A QCL heat artefact spectrum of the same sample type (*red*) is also shown. All QCL spectra were smoothed by convolving with a Gaussian with $\sigma = 2.5$, resulting in a spectral resolution of about 6 cm^{-1}.

45

Figure 2.11: Heat artefact correction procedure at the example of spinach PSII at 1395 cm^{-1} in D$_2$O buffer. (a) The averaged low-energy transient (*light blue*) is subtracted from the high-energy transient (*dark blue*); as both were excited with a saturating laser pulse, this results in a heat artefact (HA) transient (*dark grey*). The heat artefact transient is fit to a sum of exponentials (*black*). The dotted and dashed black lines show the HA scaled to match th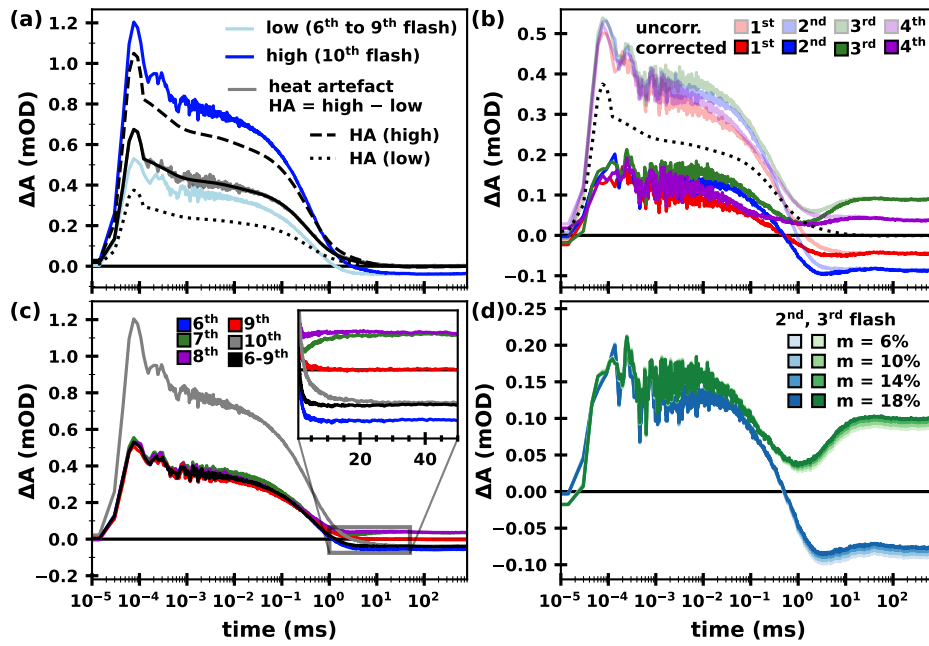e energy of the low- and high-energy transients, respectively. **(b)** The first four flash transients are shown before heat artefact correction (*transparent colors*). Subtracting the scaled heat artefact fit (*dotted grey line*) from each transient, results in their corrected counterpart (*opaque colors*). **(c)** Because of imperfect S-state cycling, the high-energy 10th flash (*grey*) contains a mixture of S-states. A weighted average of the preceding low-energy transients (*black*) is calculated, which mimics the S-state mixing of the high-energy 10th flash transient: Assuming a miss factor of 8% the respective weights of the 6th, 7th, 8th and 9th flash transient are 60%, 1%, 7% and 33%. Around 40 ms the heat artefact has decayed completely. The inset shows that, unlike the weighted average, none of the 6th to 9th flash transients decay to the same value as the 10th flash. **(d)** The effect of assuming different miss factors (6%, 10%, 14% or 18%) on the HA correction, shown at the example of corrected 2nd (*blues*) and 3rd (*greens*) flash transients.

This allows us to calculate the heat artefact transient in the following way (visualized in Fig. 2.11a):

$$\begin{aligned}
\Delta A_{\text{high}} &= \Delta A_{\text{PSII}} + \text{HA}_{\text{high}} \\
\Delta A_{\text{low}} &= \Delta A_{\text{PSII}} + \text{HA}_{\text{low}} \\
\Delta A_{\text{high}} - \Delta A_{\text{low}} &= \text{HA}_{\text{high}} - \text{HA}_{\text{low}} = \text{HA} \quad ,
\end{aligned}$$

(2.12)

where ΔA_{high} and ΔA_{low} are the difference IR signals measured at saturating laser intensities, ΔA_{PSII} is the portion of the signal due to PSII kinetics and HA is the portion of the signal due to heat artefact kinetics.
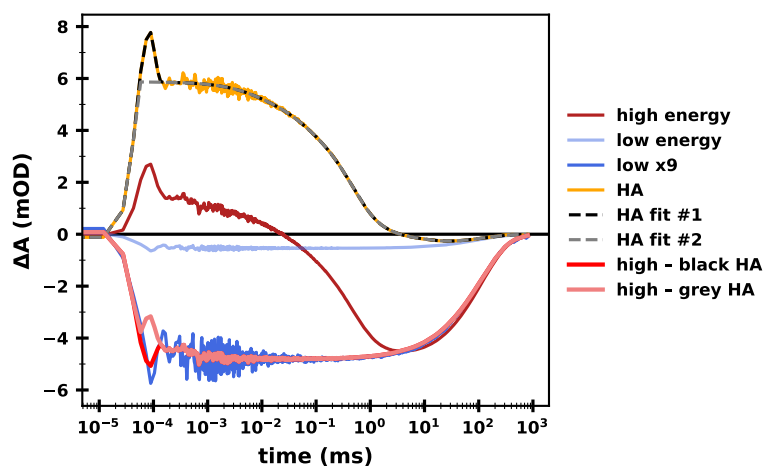
Figure 2.12: Effect of including or excluding the early 'bump' in the heat artefact transient. Difference absorption of PSI core particles from *T. vestitus* at 1637 cm⁻¹ at high excitation energy (*dark red*) and very low excitation energy (*blue*). The grey and black dashed lines show two different ways of fitting the heat artefact transient (*yellow*). The corrected high-energy transient is more similar to the low-energy transient (which has a negligible heat artefact contribution) if using the first fit approach (*black*).

The heat artefact is then scaled down to match the low excitation energy and finally subtracted from the measured signal:

$$
\begin{aligned}
\mathrm{HA_{low}} &= \mathrm{HA} \cdot \frac{E_{\mathrm{low}}}{E_{\mathrm{high}} - E_{\mathrm{low}}} \\
\Delta A_{\mathrm{PSII}} &= \Delta A_{\mathrm{low}} - \mathrm{HA_{low}} \quad .
\end{aligned}
\tag{2.13}
$$

The high-energy transient is corrected in an equivalent manner. To prevent introducing additional noise into the transient, the heat artefact transient is not directly subtracted from the data. The heat artefact transient is rather fit to a sum of exponentials and the resulting fit curve is subtracted from the data (Fig. 2.11b).

A complication specific to PSII is that the individual flash transients show an S-state dependent signal. The standard measurement protocol gives a series of ten excitation flashes: the first nine of low excitation energy and the tenth with high excitation energy. ΔA_{low} must thus be calculated from the low-energy transients in such a way that its PSII signal (ΔA_{PSII}) matches that of ΔA_{high} (Fig. 2.11c). By assuming a specific miss factor, it can be calculated in what way the 6th, 7th, 8th and 9th flash transient must be averaged (see also Section 2.3.3). Varying the miss factor estimation between 6 and 18% has a relatively small effect on the heat artefact correction (Fig. 2.11d).

For PSI measurements, each flash transient is expected to show the same signal, simplifying the procedure. The PSI measurement protocol was a series of five low-energy excitation flashes followed by a high-energy flash. A simple mean of the 2nd through 5th flashes was used to calculate ΔA_{low}. The first flash was omitted to account for the possibility that it might show some slightly altered behavior.

It is unclear what causes the bump around 100 ns in the heat artefact transient (grey curve in Fig. 2.11b). It seems unlikely to be of the same heating origin as the rest of the transient and might rather be an artefact of a different origin. Whatever its cause, it was found that including it in the heat artefact transient yields the best results. This is nicely

demonstrated with a PSI sample at 1637 cm^{-1} (Fig. 2.12): When including the bump in the heat artefact transient, the corrected flashes all show the same behavior around 0.1 μs (see also Fig A1.2 in the Appendix). If it is ignored, the corrected transients show inconsistent early behavior.

Thus, the procedure used for the data in this thesis was to fit the heat artefact transient to a sum of exponentials starting at about 0.2 μs. Leading up to 0.2 μs the data points of the calculated heat artefact transient are used as they are.
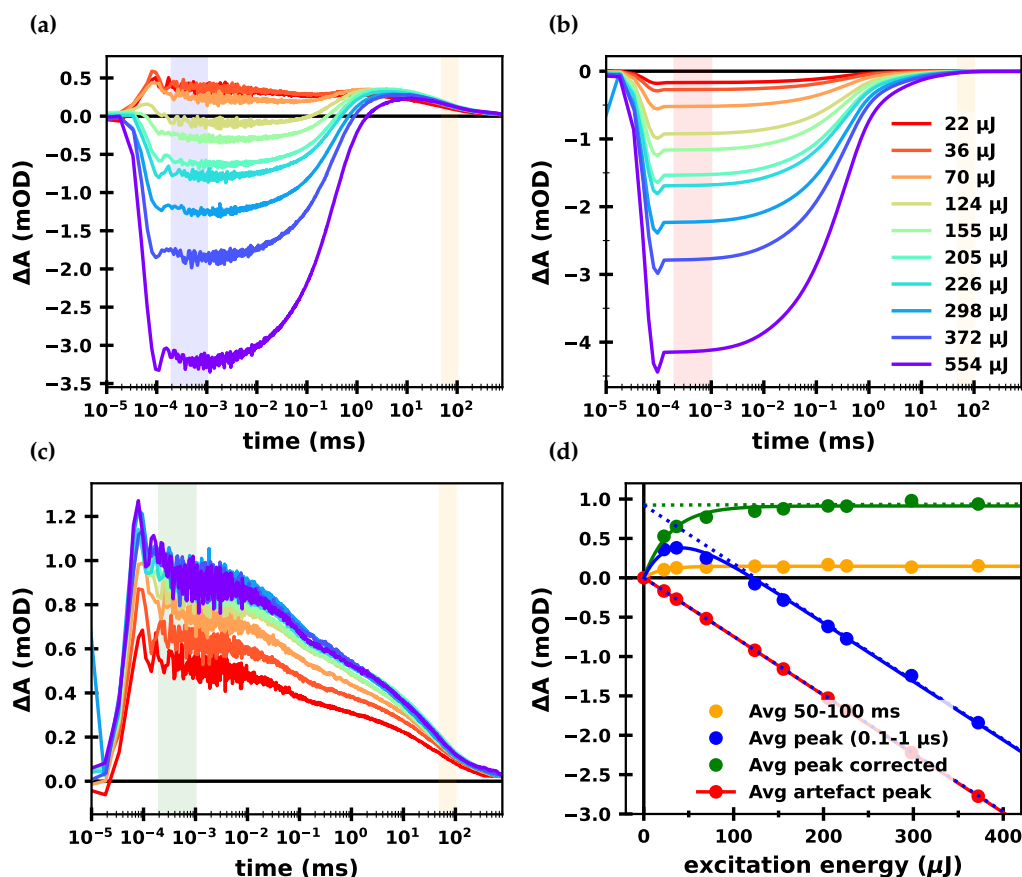
Figure 2.13: Saturation curve of spinach PSII membrane particles at 1478 cm^{-1}. (a) Ten transients averaged over the first nine excitation flashes at increasing excitation energy before heat artefact correction. **(b)** A fit of the heat artefact contribution of each transient. The heat artefact transient was calculated from a data set measured at $E_{\text{low}} = 200$ μJ and $E_{\text{high}} = 700$ μJ and fit to a sum of exponentials. The magnitude of the artefact fit was scaled according to the average excitation energy of each data set. **(c)** The ten transients after heat artefact correction. **(d)** Saturation curve obtained from the transients. The yellow dots show the averaged absorption of each transient between 50 and 100 ms (unaffected by the heat artefact); the yellow curve was obtained by fitting the data with one exponential. The blue data shows the averaged peak of each transient (average of 100 ns to 1 μs); the curve was obtained by fitting the data with one exponential plus a linear regression. The dotted line is the result of a linear regression of the last four points. The green data shows the averaged peak of each corrected transient, fitted with one exponential. The dotted green line is a linear regression of the last four points. The red dots show the averaged peak of the calculated artefact for each transient. The vertical colored strips in the first three plots show the areas of the transients that were averaged to obtain the data of the same color shown in (d).

2.4.2 Saturation Curves

In order to efficiently cycle PSII samples through their S-state cycle, they need to be excited with saturating excitation flashes, meaning that enough energy is provided to excite all PSII units in the sample. Acquiring data at several different excitation energies allows for the calculation of a saturating curve, from which the minimum excitation energy can be determined that is needed to fully excite the sample. Underlying this approach is the assumption that the heat artefact scales linearly with the excitation energy.

In the following, a saturation curve for spinach PSII membrane particles is derived. The data in Fig. 2.13 comprises eight transients at 1478 cm^{-1} at various excitation energies ranging from 16 µJ to 389 µJ. This wavenumber is sensitive only to the acceptor side of PSII, thus usually a period of two behavior can be seen. These transients, however, are the average of all nine subsequent excitation flashes, as an attempt to average out any flash-dependence (as not all the transients were obtained at saturating intensity).

Figure 2.13(a) shows the uncorrected transients with increasing excitation energy from red to purple, while (b) shows the heat artefact associated with each transient. Subtracting (b) from (a) results in corrected transients (c), which—judging by visual inspection—are identical for $\sim E_{exc} > 200$ µ. By plotting the average peak values of the corrected transients as a function of excitation energy, a saturation curve is obtained (d, *green*), which follows an exponential behavior with a time constant of $\sim \tau_E = 33$ µJ. From this it can be calculated that a minimum of 150 µJ needs to be applied to reach 99% saturation. The exact number will of course vary with the sample thickness, so a slightly higher excitation should be used. Saturation curves were measured after any major changes to the setup and for new sample types.

For PSII core complexes from *T. vestitus* and *Synechocystis* saturation curves at 1478 cm^{-1} (Fig 2.14) were performed in the same manner as described above. The procedure for core complexes from PSI is nearly identical. Since every flash induces the same reaction in PSI, data at any wavenumber is well suited for a saturation curve. Figure A1.2 in the Appendix shows the procedure at 1635 cm^{-1} for PSI core particles from *T. vestitus*.
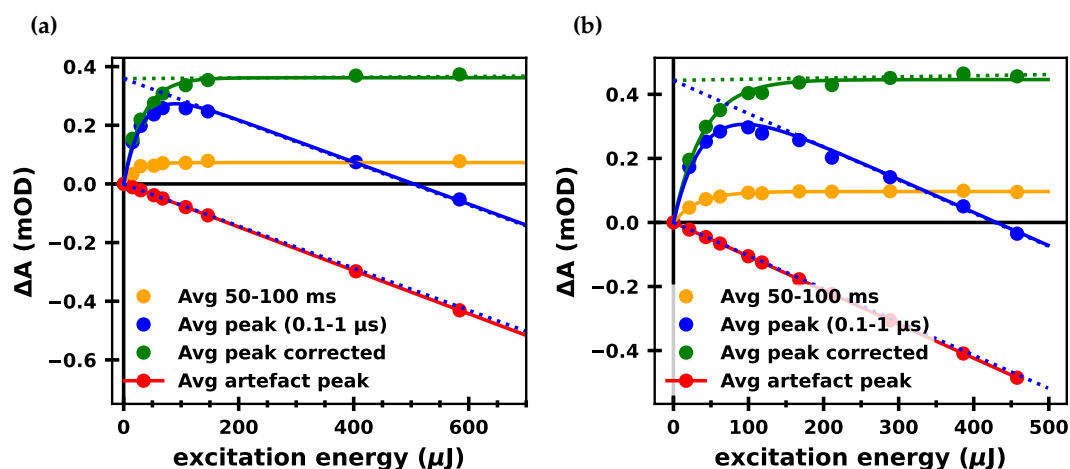

Figure 2.14: Saturation curve of PSII core particles at 1478 cm^{-1}. (a) PSII core complexes from *Synechocystis* sp. PCC 6803. **(b)** PSII core complexes from *T. vestitus*. The procedure was equivalent to that shown in Fig. 2.13.

2.5 Noise and other Artefacts

The transients obtained from the measurements on the setup are frequently affected by different types of noise and artefacts. In the following three major and recurring issues will be presented together with how these issues were generally handled.

Noise occurring with 50 Hz
From time to time the measurements are affected by a 50 Hz oscillation (Fig. 2.15a, *orange*). By carefully grounding various devices and using the same circuits, issues with 50 Hz noise now occur relatively seldom. Most of the time disconnecting and then reconnecting the BNC cables connecting the detectors with either the oscilloscope or the A/D converter can remove the noise. 50 Hz sometimes occurs not constantly throughout the measurement, but just in individual data sets. In such a case, they can be filtered out with the "steady-state filter" in the Python data processing script (see Section 2.3.2). Data sets that are strongly affected by 50 Hz are generally deemed unusable.

Noise occurring with $\sim$ 10 kHz
The biggest issue with the setup was, for a very long time, noise oscillating with 100 μs, i.e. about 10 kHz (Fig. 2.15b, *blue*). This noise very much perturbs the region of interest for PSII kinetics. This noise was found to be wavenumber-dependent, i.e. upon changing the wavenumber it often randomly either got worse or better, and furthermore it was found to be non-identical in the signal and reference channels. By calibrating the focusing mirror in front of the MCT detectors, it was possible to reduce or even eliminate it (by observing the signal on the oscilloscope in real-time while calibrating). By cutting away part of the IR beam with a piece of paper, this noise could also be induced.

This noise, however, was also dependent on the sample spot: it seems the local sample thickness influenced how strongly it occurred, often making it nearly impossible to find a calibration of the setup that was completely devoid of it. A filter was implemented into the Python data processing script to filter out data sets that are especially strongly affected.

The source of the 10 kHz noise was a mystery for a very long time. Only after replacing the QCL with a newer model—with an increased pointing stability—the situation began to clarify itself, as with the new QCL this noise is effectively non-existent. We speculate the following: The old QCL had a poor pointing stability between different wavenumber
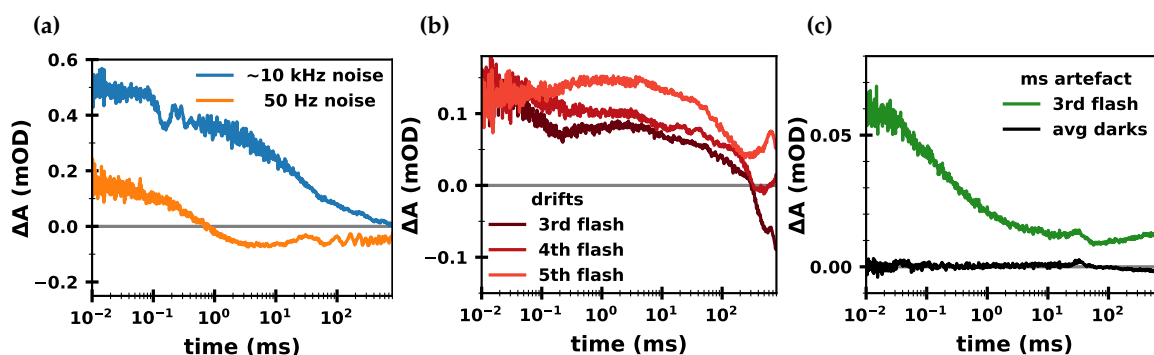

Figure 2.15: Examples of frequently occurring noise in the transients. (a) 50 Hz noise (*orange*) and 10 kHz (*blue*). **(b)** Drifts in the millisecond region, that are different after each excitation flash. **(c)** Millisecond artefact, which is visible only in transients with a very low difference signal.

settings, as well as over time, which was the reason that the beam had to be constantly recalibrated to hit the MCT detectors (which have a small detection surface). When only partially hitting the detectors, this noise—which is possibly an interference effect—would occur, just as when cutting away a portion of the beam with a piece of paper.

This noise issue used to strongly limit the usability of automated wavenumber scans with the setup. The new QCL thus drastically improved the setup, making the measurements of time-resolved spectral data sets a viable and powerful option.

Artefact in the millisecond-region

When averaging many low-signal transients, an artefact becomes visible in the millisecond region (Fig. 2.15c). Upon closer inspection it was found that this artefact appears in all channels of the A/D converter card. Subtracting 'dark data', i.e. data sets measured without laser excitation, does not lead to a good correction of the artefact, indicating that it has a flash-dependent component. Subtracting the artefact as recorded in the photodiode channel (Ch2) from the raw signal and reference channel data (after changing its magnitude with an empirical scaling factor) was found to give better results. Further analysis of this artefact— with the goal of eliminating it altogether—is recommended.

Drifts in the late millisecond-region

Sometimes the hundreds of milliseconds region of the transients is affected by drifts of the signal (Fig. 2.15b); the origin of these drifts is unknown. They have been observed most frequently in the amide II region. A filter to filter out strongly affected data sets is part of the Python data processing script. This issue also seems to have become less frequent with the new QCL.

2.6   Measuring Spectra

Time-resolved spectral data sets can be acquired with the setup. As described in Section 2.2 a 'quick-spec' option was added to the setup control software, allowing to measure at several wavenumbers in one hour. One complication, however, is that the absolute absorption varies greatly in some parts of the spectrum, e.g. in the amide I region. To avoid too low or too high signals in the detectors (both of which will result in unusable data), the QCL beam attenuation sometimes needs to be adjusted manually when switching wavenumber. The
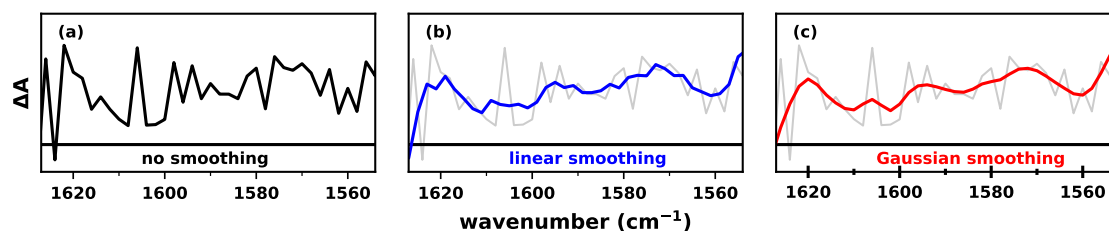
Figure 2.16: Effect of linear vs. Gaussian smoothing on spectral data. A spinach PSII spectrum averaged between 100 and 200 ns after the first excitation flash shown **(a)** non-smoothed, **(b)** smoothed linearly with a sliding average algorithm over four neighbouring data points and **(c)** smoothed by convolution with a Gaussian with a width of $\sigma = 2.5$ (which, depending on the FWHM of the starting spectrum, results in a resolution of about 6 to 8 cm^{-1} FWHM, see Equation 2.14). In (b) and (c) the non-smoothed data is shown in *grey* for direct comparison. An especially noisy data set was chosen with the purpose of visually exaggerating the effect of the two smoothing algorithms.
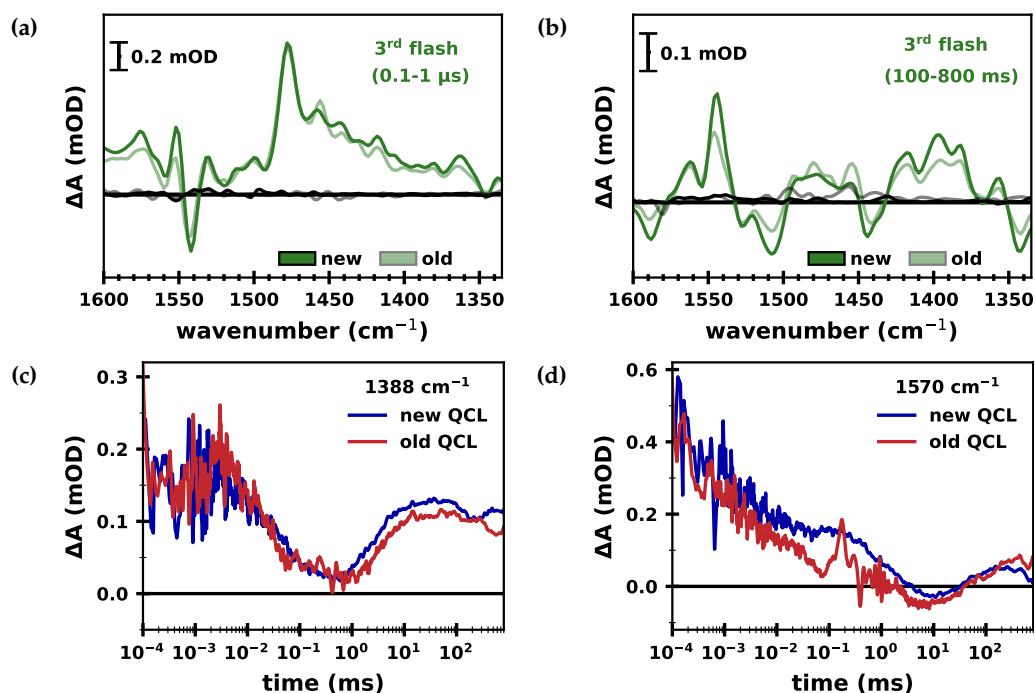
Figure 2.17: Comparison of spectral data sets (third flash) of spinach PSII obtained with the old vs. the new QCL. (a–b) Spectra averaged between 0.1–1µs and 100–800 ms, respectively, obtained by measuring a transient at every 2 cm^{-1}. The spectra were smoothed across the wavenumber axis by convolution with a Gaussian with a width of $\sigma = 2.5$. Spectra acquired with the new and old QCL is shown in *dark* and *light green*, respectively. The black and grey lines show spectra obtained without flash illumination and thus indicate the noise level. **(c–d)** Transient absorption changes at 1388 and 1570 cm^{-1}, respectively, smoothed across the time axis with a window size of 10. Data acquired with the new QCL is show in *blue*, while data of the old QCL is shown in *red*.

lower-frequency region up to about 1500 cm^{-1} can be measured in one go; in some extreme points of the spectrum the attenuation needs to be adapted for every few wavenumber steps.

Nevertheless, a data set covering the region from 1300 to 1750 cm^{-1} in 2 cm^{-1} steps can be acquired within a few days. This means, however, that more than 200 data sets need to be processed. A few small scripts were implemented to make this easier: one e.g. automatically sorts all files associated with one wavenumber into its own subfolder, so that they can then be automatically handled by the data processing script.

Once all data has been processed, it can be smoothed using a sliding average algorithm to improve the signal-to-noise (the S/N is generally relatively poor in these data sets, as each wavenumber is only given a short measurement time). Smoothing can be done both along the time axis, as well as the wavenumber axis. For smoothing along the wavenumber axis, Gaussian smoothing gives far better results than a simple unweighted sliding average approach: it significantly reduces the noise level without strongly impacting the spectral resolution or reducing the peak amplitudes (Fig. 2.16). It has previously been applied to spectral data obtained with QCLs by Schultz et al. (2018).

Gaussian smoothing is done by convolving the spectra with a Gaussian function; the standard deviation σ then determines the resulting spatial resolution. It can be shown that a convolution of two Gaussians ($g(x) = a \cdot e^{-x^2/2\sigma^2}$) with σ_1 and σ_2 results in a Gaussian

with $\sigma_{\text{conv}}^2 = \sigma_1^2 + \sigma_2^2$. If our spectrum has an initial resolution corresponding to σ_{ini} and we aim for a resolution of σ_{final}, we need to convolve the spectrum with a Gaussian with $\sigma_{\text{smooth}}^2 = \sigma_{\text{final}}^2 - \sigma_{\text{ini}}^2$. A more intuitive way to think of spectral resolution is the full-width half-maximum (FWHM) of peaks, which relates to σ as follows: FWHM $= 2\sqrt{2 \cdot \ln 2}\,\sigma \approx 2.355\,\sigma$. In conclusion, the Gaussian for smoothing can be chosen with the help of the following relation:

$$\sigma_{\text{smooth}} = \sqrt{\text{FWHM}_{\text{final}}^2 - \text{FWHM}_{\text{initial}}^2}/2.355 \quad , \tag{2.14}$$

where $\text{FWHM}_{\text{final}}$ is the desired final resolution. Most spectra shown throughout this thesis were smoothed with a Gaussian of $\sigma = 2.5$. Thus, if we estimate the starting resolution of a spectrum acquired in 2 cm^{-1} steps to be between 2–4 cm^{-1}, the final resolution lies between 6.2–7.1 cm^{-1}.

The first attempts at measuring spectra were made with the old QCL. Due to its poor pointing stability, the data were in parts extremely noisy. However, applying the smoothing algorithm greatly improved the data and resulted in usable spectra (Fig. 2.17a and b, *light green*). The S/N of individual transients of such 'scan data' was, however, highly wavenumber dependent (see Fig. 2.17c vs. d, *red*).

After replacing the old QCL with the newer version, the noise issues nearly completely disappeared, making the setup much more powerful. The S/N of the time-resolved spectral data sets has greatly improved (Fig. 2.17c and d, *blue*).

2.7 Issues Connected to Excitation Laser Intensity

After more than three years into the project, a major issue concerning the TRSF-IR data was discovered. It turned out that the excitation energy measured by the power meter was not in agreement with the energy actually delivered to the sample, resulting in a faulty heat artefact correction. The following section will depict how the issue was discovered and verified as well as discuss how it affects the data.

2.7.1 Identifying the Problem

A discrepancy was first noticed when comparing spinach PSII transients measured on samples from different preparations (see Fig. 2.18a): While the millisecond region of the transients appeared very similar, the nanosecond-to-microsecond region differed greatly in amplitude. While at first glance it seemed possible that the differences are solely due to inherently varying properties of the preparations (e.g. intactness of the sample), the fact that especially the sub-microsecond regions of the transients are highly affected by the heat artefact implied that the heat artefact correction could also be a source of the observed differences.

In order to determine whether the data were affected by a systematic error, a series of measurements of spinach PSII samples 388 and 414[17] was performed with varying experimental settings. To make sure both samples were measured at always exactly the same conditions, they were prepared in parallel using the same buffer. For each set of settings, a measurement was first performed on one sample for half an hour and immediately followed by a measurement on the other sample. Figure 2.18b shows the third flash transients

---

[17]All the spinach PSII membrane particle preparations performed in our lab are given a number as a unique identifier.
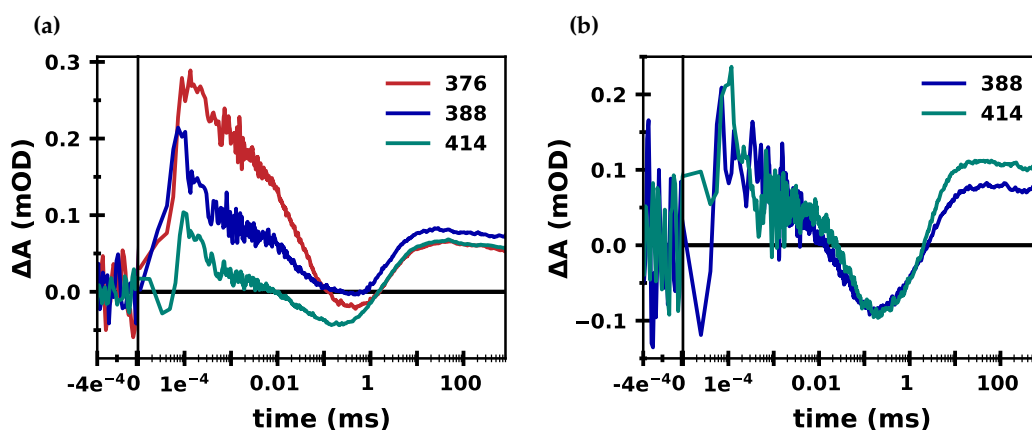
Figure 2.18: Third flash transients of different spinach PSII samples. (a) Transients of three samples (different PSII preparations, named 376, 388 and 414) measured at 1400 cm^{-1} on different days. While the millisecond-region of the transients are very similar, the pre-millisecond regions show great variation. **(b)** Transients of two different samples at 1395 cm^{-1} measured in parallel. Both transients show very similar behavior. All transients were smoothed with a sliding average algorithm (window size: 6) for easier visual comparison.

of the two samples measured at roughly 300 µJ and 900 µJ, which look much more similar than in the data shown in Fig. 2.18a. This was the first strong indication that the heat artefact correction might be faulty.

A set of measurements was done on spinach PSII sample 413, where the laser intensity of both the low- and high-energy flashes were increased by changing the laser internal attenuator (by moving the lever on the laser head). Figure 2.19a shows that with increasing excitation energy, the corrected third flash transient changes drastically. A look at the un-
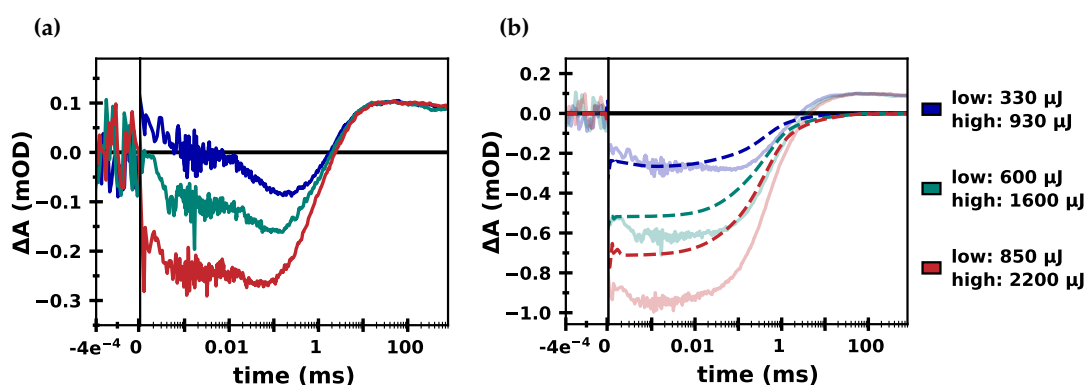
Figure 2.19: Third flash transients of the same spinach PSII membrane sample at 1395 cm^{-1} at varying excitation energy. (a) Heat artefact corrected transients measured at 330, 600 and 840 µJ. The high-energy 10th flash transients were obtained at 930, 1600 and 2200 µJ, respectively. The transients strongly differ in their amplitude in the pre-millisecond region. **(b)** The same transients prior to heat artefact correction (*transparent*) and their calculated heat artefacts (*dashed lines*). The amplitude of the transients and the heat artefacts do not increase with the same proportions, even though the excitation flashes are saturating in all cases.
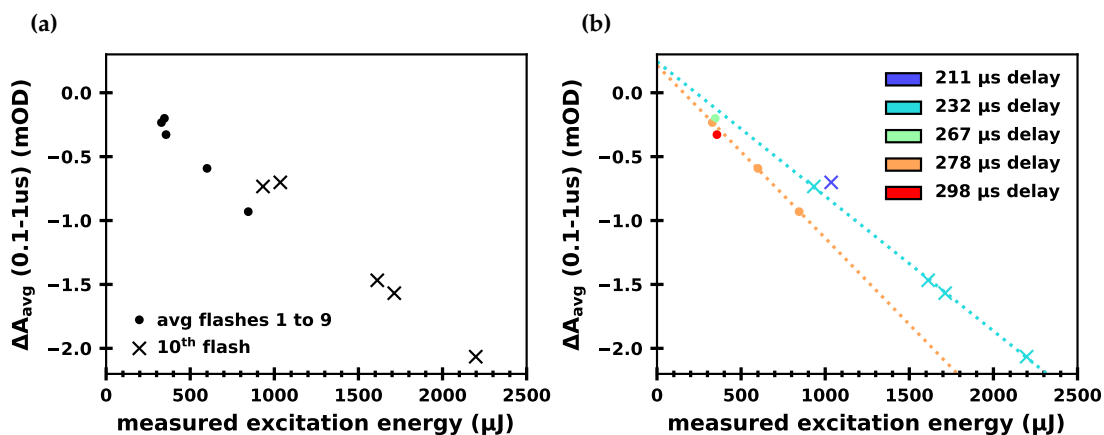
Figure 2.20: Averaged absorption signal (100 ns to 1 μs) of $S_3 \rightarrow S_0$ transients of spinach PSII membrane particles at 1395 cm^{-1}. The circles are averages of the first nine flash transients; the crosses were obtained by averaging the tenth flash transient. **(a)** There is no clear linear relation between excitation energy and averaged absorption signal, however, **(b)** when taking into account the Q-switch delay (*various colors*), a linear behavior of the data obtained at the same Q-switch delay becomes apparent.

corrected flashes and calculated heat artefacts (Fig. 2.19b) shows that with changing laser intensity, the relative sizes of uncorrected transient and calculated heat artefact changes. As we are applying saturating laser flashes, we expect the amplitude of the heat artefact contribution to increase linearly with increasing excitation energy. The corrected transients, however, should all look identical; these data sets thus confirm that the heat artefact correction is indeed faulty.

After carefully re-examining the data processing algorithm and excluding the possibility of introducing the error at that stage, a hunt for a systematic error—evidently present in the setup—began. From the observations described so far, it was clear that the excitation energy is somehow affecting the data in an unexpected way.

To pinpoint the root of the issue, measurements at varying laser intensity were performed, whereby the intensity was adjusted either by changing the internal attenuator or by changing the Q-switch delay. In Fig. 2.20 the averaged transient amplitude between 100 ns and 1 μs was plotted as a function of excitation energy as measured at the power meter. In Fig. 2.20a it becomes apparent that there is no clear linear correlation between averaged peak and measured excitation energy, even when looking just at the tenth flash transient (crosses) or the averaged transients of flashes 1 to 9 (dots). However, when taking the Q-switch delay into account, as shown in Fig. 2.20b, we see perfectly linear behavior for a given Q-switch delay.

2.7.2 Understanding the Problem

Having identified the Q-switch delay as the source of the issue, a series of test measurements were performed to see whether the Q-switch delay indeed influences how much energy is delivered to the sample versus how much is measured at the power meter.

For this, the sample holder was removed and a second power meter—in the following referred to as PM2—was placed in its stead (see Fig. 2.21). The test measurements were conducted by measuring the green laser intensity at the original power meter (PM1) and
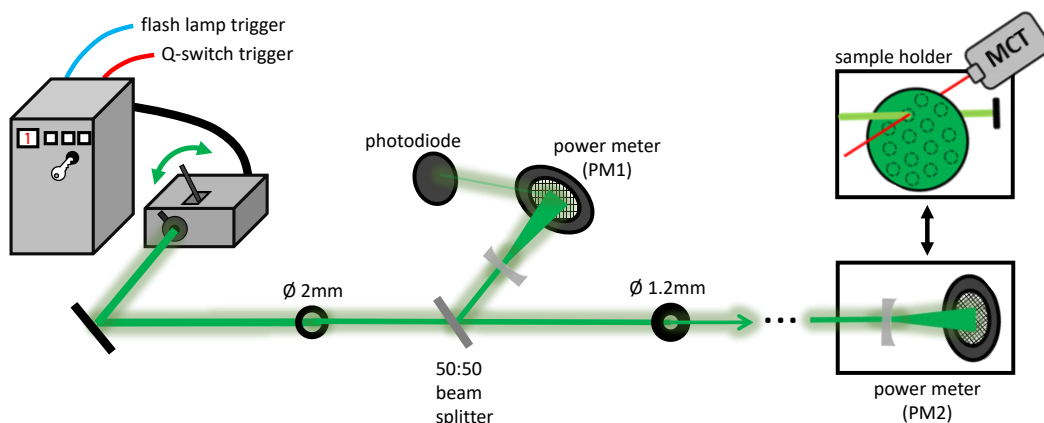
Figure 2.21: The setup as used for the test measurements using two power meters. The green laser path was mostly the same as for previous single-frequency IR experiments. The laser beam goes through a 2 mm iris, before hitting a polarization-independent 50:50 beam splitter. The deflected portion of the beam is broadened by a concave lens and hits the first power meter (PM1). The transmitted portion of the beam goes through a second iris set to 1.2 mm and hits a second power meter (PM2), positioned where usually the sample holder is. This scheme is simplified, i.e. a few mirrors were left out.

PM2 at the same time. For each setting, 20 laser flashes at 5 Hz were recorded and averaged. Figure 2.22a shows the recorded laser energy as a function of Q-switch delay, revealing a maximum at 160 µs, which is expected according to the Minilite II manual. It is apparent that the values of PM2 are significantly lower than PM1; unequal values are expected due to several reasons: By using the second iris to cut the beam from a 2 mm diameter to 1.2 mm, the area of the beam is reduced by a factor of roughly 3 (since the energy is not equally distributed across the beam area, however, the expected reduction of energy is of course not the same.) Differences in absolute intensity furthermore depend on the precision of the alignment of the beam onto the power meters, which may have been poorer for the improvised placement of PM2. PM2 additionally has some visible damage to its surface, further adding to an expected lower value. Finally, the 50:50 beam splitter is not 100% polarization independent: according to the manufacturer's specifications[18], roughly 40% of p-polarized and 55% s-polarized light is transmitted; the frequency-doubled Minilite II emits s-polarized light.

The absolute energy values, however, are of limited interest. In order to correctly calculate the heat artefact contribution it is essential that the energy measured at the power meter is always proportional to the energy delivered to the sample. Fig. 2.22b shows that the ratio of the two power meter readings (PM1/PM2) is *not* consistent. It varies between a factor of 4 to 6, depending on the Q-switch delay.

Figure 2.22c shows the power meter readings at different laser-internal attenuator settings (which can be changed my moving a little lever on the laser head) and (d) shows that the ratios follow the same Q-switch dependence for all lever positions. In Fig. 2.22e the influence of the second iris diameter was investigated: When gradually changing the iris from its standard setting of 1.2 mm to fully open, we can see in (f) that the influence of the Q-switch delay diminishes.

---

[18]UV fused silica broadband plate 50:50 beamsplitters, item number BSW10 (Thorlabs, Inc.)
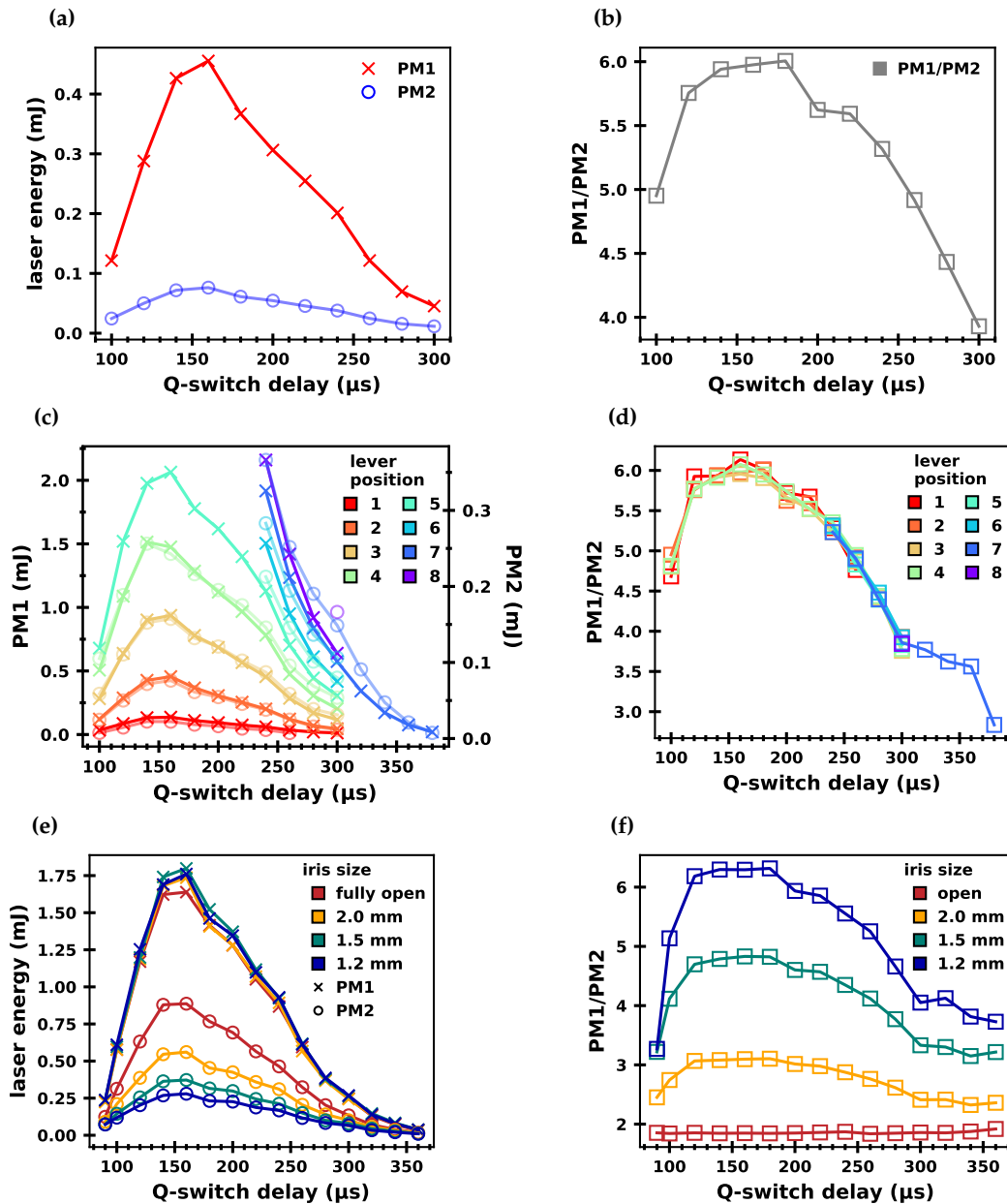
Figure 2.22: Comparison of parallel power meter measurements. (a) The measured laser energy at power meter 1 (PM1) (*red crosses*) and power meter 2 (PM2) (*blue circles*). PM1 is placed right behind the 50:50 beam splitter, while PM2 is placed where usually the sample holder is (see Fig. 2.21). **(b)** The ratio of the two power meter readings (PM1/PM2), which shows a dependence on the Q-switch delay with a maximum between 150 and 200 µs. **(c)** Measured laser energy of the two power meters PM1 and PM2 as a function of Q-switch delay at different attenuation settings (lever position) and **(d)** the ratio of PM1 and PM2. **(e)** PM1 and PM2 readings with the second iris set to 1.2 mm, 1.5 mm, 2.0 mm and fully open, as well as **(f)** the ratio of the PM1 and PM2 at those iris settings.

These test measurements finally led to the following conclusions: Changing the delay between flash-lamp and Q-switch triggering leads to tiny deflections of the beam, which leads to different portions of the beam being cut off by the 1.2 mm iris. As a result, the energy measured at the power meter is not proportional to the energy delivered to the sample. Since we typically used Q-switch delays around 260 μs for the low-energy flashes and around 230 μs for high-energy, this led to a *systematic underestimation* of the heat artefact.

A question that may be asked is why this issue remained undetected for so long. It was only discovered after the excitation laser was moved closer to the setup. In an attempt to not alter the beam path too much, some of the mirrors were not hit directly in the center, i.e. the overall alignment was poorer than before, which most likely enhanced the effect. Prior to moving the laser, the beam had to travel a longer path before hitting the beamsplitter and power meter, thus having more time to widen slightly. Cutting away portions of the wider beam with the iris may have had a less strong effect than it has now.

2.7.3 Fixing the Problem: Adapting the Setup

Properly fixing the issue required altering the green laser path as well as installing an alternate way to attenuate the laser, which does not involve the Q-switch delay. The latter was also motivated by the fact that employing the Q-switch delay this way was in fact sub-optimal for several reasons:

▷ The final, high-energy flash was generated by sending an additional Q-switch trigger to the laser, some microseconds before the one which would trigger the low-energy flash. Such two subsequent triggers can cause damage to the Marx bank in the laser over time; we had to replace it once already.

▷ A Q-switch delay around 160 μs results not only in the highest energy output, but also optimizes other properties of the laser, including pulse width.
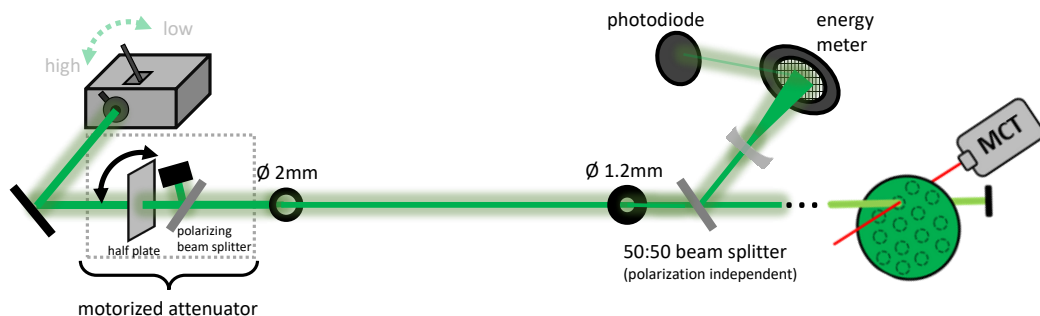
Figure 2.23: The green laser path of the setup with a new motorized attenuator and repositioned optical elements. The motorized attenuator now replaces the Q-switch delay for switching between high and low-energy excitation. The second iris is now placed before the 50:50 beam splitter. In order to prevent the second iris being very far from the sample holder, the beam splitter was moved as close to the sample holder as possible. This scheme is simplified, i.e. a few mirrors (used merely for changing the direction of the beam) were omitted.
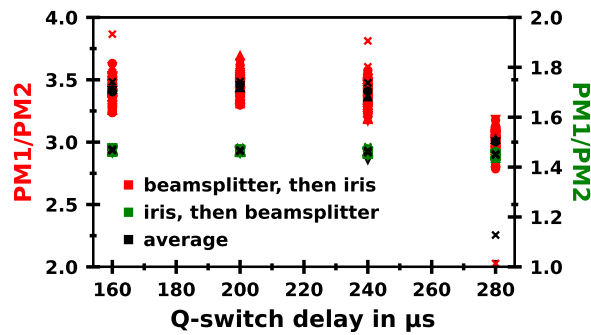
Figure 2.24: Power meter measurements after changing the setup. PM1/PM2 with the iris (1.2 mm) before the beam splitter (as shown in Fig. 2.23) is shown in green; PM1/PM2 with the iris after the beam splitter is shown in red. The individual markers show the shot to shot difference, with 20 shots acquired with the motorized attenuator set to 25, 50, 75 and 100% (denoted by the symbols X, O, ∧, V, respectively). The black markers are the averaged value of all data at a given Q-switch delay. The green data shows that the ratio of the power meters is stable in the new setup for different attenuator settings and Q-switch delays.

▷ As the Q-switch delay is controlled by a pulse generator, changing it remotely is not possible, which meant that adjusting the laser intensity was only possible when being physically present in the lab.

A motorized attenuator was implemented as a new mode of controlling the excitation energy. The attenuator consists of a lambda half plate and a Brewster type polarizer (see Fig. 2.23 on the left). The half plate can be turned by a motor in less than 0.2 s, thereby changing the polarization of the laser beam. The polarizer transmits p-polarized light but reflects s-polarized light; the polarization of the beam thus determines the energy output (0.1% to >98% of input energy).

The attenuator can be easily calibrated and controlled by software provided by the company. For the TRSF measurements, the attenuator is directly controlled within the setup control software (see also Section 2.2).

The 2 mm iris remains in its former position, while the 1.2 mm iris was moved slightly to make space for the beam splitter to be placed behind it.

To verify that the changes made to the setup do not reproduce the same problem as before, another test measurement with two power meters was done. Figure 2.24 shows the ratios of PM1 and PM2 with the 1.2 mm iris behind the beam splitter as it used to be (red) and in its new position in front of the beam splitter (green). While there are still quite some shot-to-shot fluctuations with the former, it is striking that the fluctuations are much less severe than before changing the setup. This may be due to a generally improved alignment as well as the fact that the path difference between the two power meters is now smaller. The green data shows that with all the new changes, including setting the iris in front of the beam splitter, the ratio of the two power meters is very stable with only a small Q-switch delay dependency. Using the motorized attenuator at the optimal Q-switch delay should thus deliver very reliable results.

2.7.4 Dealing with Affected Data

An automatic calculation of a correction factor for the magnitude of the heat artefact is not possible with data recorded at only two different Q-switch delays per data set. While the Q-
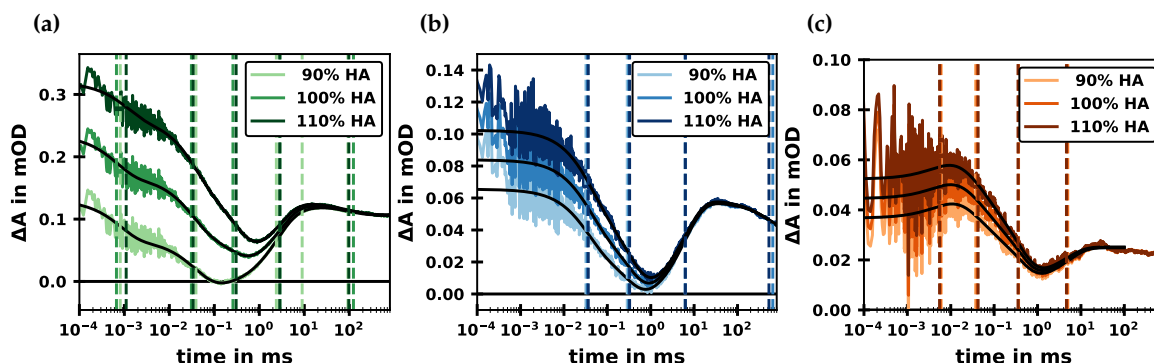
Figure 2.25: The effect of under- or overestimating the heat artefact by 10% at 1400cm⁻¹. Third flash transients of **(a)** spinach PSII membrane particles, **(b)** core complexes from *T. vestitus* and **(c)** core complexes from *Synechocystis* after subtracting the heat artefact with 90%, 100% or 110% of its calculated magnitude. All data sets were fit to a sum of exponentials; the resulting time constants are indicated with vertical lines. The spinach PSII sample is clearly most affected by varying the magnitude of the heat artefact.

switch delays used for individual measurements were recorded, the effect is also dependent on the calibration of the beam path, making it impossible to determine a globally valid correction factor.

An attempt to correct affected data would be to repeat the measurement at a chosen wavenumber for each sample and to derive an empirical correction factor by comparing the heat artefact corrected data. However, any differences in sample preparation etc. would introduce a bias.

The effect of the Q-switch delay on the data was extreme in Fig. 2.19. However, this was partly also due to poor beam path calibration, meaning most data sets are not affected as strongly. An attempt to estimate worst-case scenarios for measurements on PSII membrane particles as well as cyanobacterial core complexes is depicted in Fig. 2.25, which shows the effect of subtracting the heat artefact as calculated vs. subtracting a 10% larger and a 10% smaller heat artefact. It is striking that the effect on spinach PSII data is much stronger (Fig. 2.25a) than on PSII core complexes from *T. vestitus* (Fig. 2.25b) and *Synechocystis* (Fig. 2.25c). For the latter two samples the time constants (indicated by vertical lines) are also hardly affected when performing a multi-exponential fit. For the spinach PSII data, however, both the transient itself as well as the fit results are quite drastically affected.

It was finally concluded that core complex data, due to a generally smaller heat artefact, can be used without the need for a correction factor. It should be noted that old data—i.e. before moving the excitation laser—is almost certainly not as heavily affected as show here. For old data sets on spinach PSII membrane particles I nevertheless decided the best course of action was to repeat the measurements.

3 | Further Methods and Materials

ALL other methods besides IR spectroscopy are covered in this chapter. The procedure of isolating PSII and PSI core particles from cyanobacteria is not described in detail, as these samples were kindly provided by cooperation partners.

3.1 Isolation of PSII-enriched Thylakoid Membrane Particles from Spinach

In the early 80s, D. Berthold, G. Babcock and C. Yocum published a protocol for extracting functional, oxygen-evolving thylakoid membranes from spinach (Berthold et al., 1981), a modification and continuation of previous work of the same group (Robinson and Yocum, 1980). Based on their last names, samples obtained through their method are often termed *BBY particles*. The protocol was further refined by Schiller and Dau (2000) to yield especially high oxygen-evolution rates. Over the years, some more minor changes have been implemented in our lab; the complete procedure will be laid out in the following.

About 4 kg of fresh spinach leaves are kept in the dark (and preferably at 4°C) for several hours before beginning with the preparation. All devices, beakers, etc. are prepared ahead of time, as the first steps of the preparation are time-sensitive. The spinach leaves are placed into a tub with ice and water. Any damaged leaves are discarded; the stems of the intact leaves are removed.

Once enough spinach leaves have been selected, they are blended together with 1 l of a cell-breaking buffer (Table 3.1, buffer A). The resulting thick liquid is filtered through coarse cheesecloth, to get rid of the spinach pulp. In a second filtering step, the now more homogeneous liquid is poured through fine cheesecloth. The double-filtered solution is centrifuged in 1000 ml tubes for 10 minutes at 17,000 g in the 4 °C pre-cooled centrifuge[19].

After discarding the supernatant, the pellets are resuspended in a hypertonic buffer (Table 3.1, buffer B) with a coarse paint brush. The sample is diluted to a total of 250 ml and then centrifuged in 40 ml centrifugation tubes for 2 min at 1,100 g. The cell-debris containing pellet is discarded and the supernatant, containing the chloroplasts, is centrifuged once more for 12 min (5 min at 4,000 g and 7 min at 50,000 g) to extract the thlyakoids.

To isolate the PSII-rich grana-stacks of the thylakoid membrane, the thylakoids need to undergo a detergent-treatment with Triton X-100. This step is critical, as too much detergent will result in a low PSII yield, while too little detergent will result in contamination of the final sample with PSI and other protein complexes. To determine the correct amount

---

[19]Sorvall Lynx 6000 centrifuge, Thermo Scientific GmbH

Table 3.1: Buffers needed for the preparation of PSII membrane particles from spinach. Buffer A is a cell-breaking buffer, buffer B is a hypertonic buffer, buffer C and buffer T are needed for the extraction of grana stacks, and buffer D is the cryo-buffer used for storage.

buffer	content	pH
A	400 mM sucrose, 25 mM HEPES, 1 mM EDTA, 15 mM NaCl, 5 mM $MgCl_2$, 5 mM $CaCl_2$, 2 g/l BSA, 1 g/l ascorbate	7.5
B	25 mM MES, 150 mM NaCl, 5 mM $MgCl_2$	6.2
C	1 M betaine, 25 mM MES, 15 mM NaCl, 10 mM $MgCl_2$, 5 mM $CaCl_2$	6.2
D	1 M betaine, 25mM MES, 15 mM NaCl, 5 mM $MgCl_2$, 5 mM $CaCl_2$	6.2
T	20 ml Triton X-100 + 60 ml buffer C without betaine	6.2

of Triton X-100, first the chlorophyll concentration of the sample solution needs to be measured. This is done by pipetting 40 μl of the sample into 10 ml of 80% aqueous acetone, using a 10 ml volumetric flask for precision, and proceeding as described in section 3.2.

The amount of buffered Triton X-100 solution (Table 3.1, buffer T) is determined by the following equation:

$$V_T = \frac{C_{\text{Chl}} \cdot V_{\text{sample}}}{10 \text{ mg/ml}} \quad . \tag{3.1}$$

The sample is diluted with buffer C such that the final concentration after adding Triton X-100 will be 2 mg/ml. The Triton X-100 solution is now slowly added to the sample solution while stirring with a magnetic stirrer. Following a 1 min incubation time, the Triton X-100-sample suspension is centrifuged for 2 min at 1,100 g. The supernatant, which should now contain the extracted grana-stacks, is centrifuged at 12 min at 50,000 g.

The resulting pellet is carefully resuspended in a cryo-buffer (Table 3.1, buffer D), while avoiding to resuspend the white part of the pellet containing starch, and centrifuged once more for 12 min (the first 5 min at 4,000 g and then at 50,000 g for 7 min). This step is repeated three times. The final pellets are resuspended in a total of 50 ml buffer D and aliquoted into 1 ml reaction tubes. The final chlorophyll concentration is determined and the samples are flash-frozen in liquid nitrogen before storing them in a -80°C freezer.

3.2 Assessing the Chlorophyll Content in a PSII Sample

The content of chlorophyll *a* and *b* in a PSII sample can be assessed by measuring the absorption at 663.6 nm and 646.6 nm, as reported by Porra et al. (1989). For this, the sample is diluted in 80% aqueous acetone. The acetone-sample solution is centrifuged for 4 minutes at 1350 g to extract the chlorophylls. The supernatant, which contains the chlorophylls, is pipetted into a cuvette and the absorption at the aforementioned wavelengths is measured in a UV-vis spectrometer.

The amount of chlorophyll *a* (in μg/ml) can be calculated by the following equation:

$$f \cdot (12.25 \cdot A_{663.6nm} - 2.55 \cdot A_{646.6nm}) \quad , \tag{3.2}$$

where f is the dilution factor. If e.g. 40 µl of the sample was diluted in 10 ml aqueous acetone (as in section 3.1), then $f = 250$. For calculating the amount in mg/ml the prefactor is thus 0.25.

The amount of chlorophyll b (in µg/ml) can analogously be calculated by

$$f \cdot (20.31 \cdot A_{646.6nm} - 4.91 \cdot A_{663.6nm}) \quad . \tag{3.3}$$

Other solvents such as methanol can be used instead of acetone; however a slightly different equation must then be used.

3.3 Assessing the Oxygen Evolution Activity of PSII Samples

The standard procedure for evaluating the quality of PSII samples is to measure their oxygen evolution activity with a Clark-type electrode; see Fig. 3.1 for a photograph of the setup. The experimental protocol—as performed by myself for all spinach PSII membrane particles[20]—will be outlined in the following. The measured rates for the spinach and cyanobacterial samples used in this thesis can be found in Tables 3.2 and 3.3, respectively.

Before beginning a measurement, the silver electrode is polished with toothpaste, rinsed with water and dried. A few drops of KCl-saturated water are dripped on both the silver and platinum electrodes, before placing a square piece of (cigarette) filter paper on the latter. A piece of membrane is subsequently placed on top and both the filter paper and membrane are tucked into the well containing the silver electrode. While the filter paper created a connection between the two electrodes, the membrane isolated the electrodes and the KCl solution from the sample solution, which later will be placed on top. Two O-rings help to keep the filter paper and membrane in place and to avoid leaking. The sample chamber is mounted onto the electrode piece and connected to the water-in and water-out tubes for temperature control, which is set to 28 °C. A small magnetic stirrer is placed into the sample chamber.
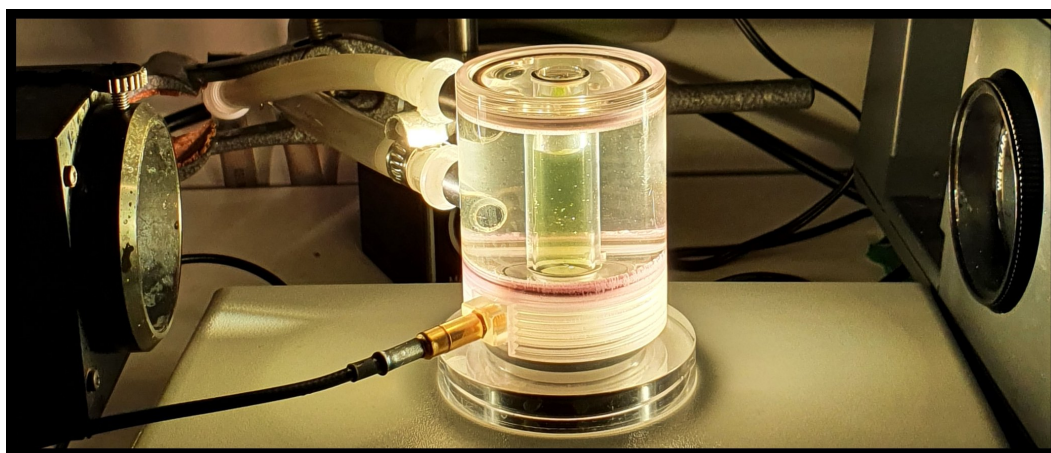
Figure 3.1: Photograph of the Clark-type Electrode Setup for Measuring Oxygen Evolution Activity. The sample chamber is filled with a green PSII solution and illuminated from both sides. The sample chamber is surrounded by a water chamber for temperature control. The electrodes (not visible) are below the sample chamber, separated from the sample by a membrane.

---

[20]The activity measurements for all other samples were done in a comparable manner by the cooperation partners who prepared the samples.

Table 3.2: Oxygen Evolution Rates of Spinach PSII Samples. All values were measured at 28 °C and are the average of three repeats. The amount of chlorophyll *a* and *b* is determined by measuring the absorption at 663.6 and 646.6 nm, as described in Section 3.3; the value given here is the sum of chlorophyll *a* and *b*.

sample	O$_2$ activity (μmol O$_2$/(mg Chl)/h)	[Chl] (mg/ml)	[Chl *a*]/[Chl *b*]
BBY 376	954	3.04	2.42
BBY 386	1032	1.70	2.68
BBY 388	1093	1.79	2.54
BBY 400	947	1.41	2.50
BBY 413	1024	4.47	2.43
BBY 414	1021	3.46	2.57
BBY 416	1125	4.70	2.43

Table 3.3: Oxygen evolution rates of cyanobacterial PSII core complex samples. All values were measured at 28 °C and are the average of three repeats. The amount of chlorophyll a and b is determined by measuring the absorption at 663.6 and 646.6 nm, as described in Section 3.3; the value given here is the sum of chlorophyll *a* and *b*. The *T. vestitus* sample has a his-tag at the C-terminal end of CP43 and was purified from a strain in which the psbD2 gene has been deleted.

core complex sample	O$_2$ activity (μmol O$_2$/(mg Chl)/h)	prepared/ provided by
Thermosynechococcus vestitus BP-1	$\sim$2500	R. Perez, Y. Zilliges
Synechocystis sp. PCC 6803	5010 $\pm$ 50	R. J. Debus, R. L. Burnap
Synechocystis D61A mutant	900 $\pm$ 270	R. J. Debus
Synechocystis N298A mutant	670 $\pm$ 170	R. J. Debus

The system is calibrated by comparing air-saturated deionized water (which is left out the day before) with O$_2$-free water. First, the sample chamber is filled with air-saturated water. Once the oxygen production rate has reached a maximum, an excess amount of sodium dithionite is added, which reacts strongly with oxygen and effectively removes all molecular O$_2$ from the solution. Once the oxygen rate has reached its minimum, the software calculates the calibration factor. The sample chamber is rinsed carefully several times to make sure no sodium dithionite is left behind.

The PSII sample is thawed on ice and subsequently changed into the measurement buffer (1 M trimethylgylcine, 25 mM MES, 15 mM NaCl, 5 mM CaCl$_2$). A sample stock solution is prepared containing 0.25 mg/Chl/ml. For every measurement, 2 ml buffer and 40 μl of the sample stock are pipetted into the sample chamber, followed by 40 μl ferricyanide (50 mM) and 10 μl DCBQ (50 mM). Adding the substances may briefly disrupt the rate measurement; once a plateau has been reached again, the two strong light sources are turned on simultaneously, illuminating the sample in a fully saturating manner. The software is used to find and record the maximal O$_2$ production rate. For every sample the measurement is performed at least three times and the averaged value is recorded.

3.4   Manganese Depletion of Spinach PSII Membrane Particles

The following protocol for Mn depletion is based on the paper by Allakhverdiev (1994) and was modified by Chernev et al. (2020).

After thawing spinach PSII membrane particles on ice, they are diluted into high-salt TEMED-buffer (20 mM MES, 500 mM $MgCl_2$, 20 mM TEMED, pH 6.5) to reach a concentration of 0.2 mg Chl/ml and incubated for 10 minutes in the dark, during which the manganese ions are reduced by TEMED and three PSII subunits (PsbQ, PsbP and PsbO) are removed. The sample is then centrifuged for 12 minutes at 4 °C at 50.000 g. The resulting pellet is carefully resuspended in high-pH buffer (35 mM NaCl, 20 mM TRIS, pH 9.0) and centrifuged again at the same settings. This washing step is repeated to a total of three times. After the final washing step, the pellet is resuspended in storage buffer (1 M betaine, 15 mM NaCl, 5 mM $CaCl_2$, 25 mM MES, pH 6.3) and diluted to a concentration of 1 mg Chl/ml. The sample is flash-frozen in liquid nitrogen and stored at -80°C until usage.

3.5   Preparation of Biological Samples for IR Spectroscopy

All PSII samples are always handled carefully under dim green light. PSI samples can be exposed to light without taking damage. Depending on the nature of the sample, it is prepared for an IR spectroscopic measurement by e.g. buffer exchange as described below (3.5.1 – 3.5.3). All samples are finally sandwiched between two calcium fluoride (CaF_2) plates[21] (see Fig. 3.2). For this several CaF_2 plate pairs are prepared beforehand by thoroughly cleaning them with isopropanol (removing any silicon grease stains), ethanol and dry air (removing any dust particles). Two small drops of silicon grease are placed on opposite sides of a CaF_2 plate. A second CaF_2 plate is placed on top and the two plates are turned against each other, until a thin layer of silicon grease forms a ring the edge of the plates. They are carefully taken apart again. One of the plates is placed into the sample holder, which is lying flat on the table, and (unless otherwise stated) a 15 μm PTFE spacer[22] is placed on top of the silicon grease ring. The PSII or PSI sample is added to the middle of the CaF_2 plate and then covered with a second greased CaF_2 plate. A thicker PTFE ring is
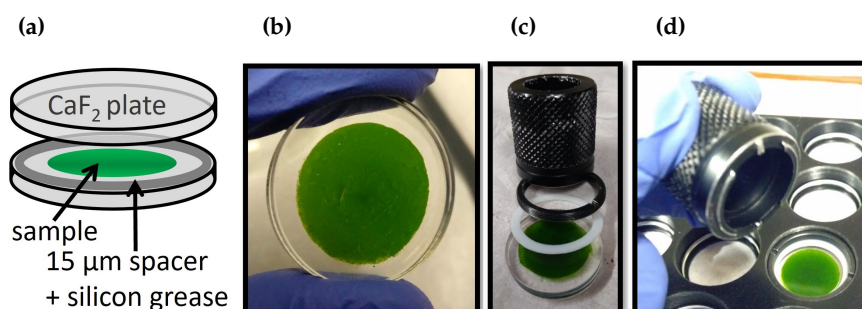
Figure 3.2: Preparation of the sample sandwiched between CaF$_2$ plates. (a) Schematic view of a sample-CaF$_2$-sandwich. **(b)** Photograph of a spinach PSII-CaF$_2$-sandwich. **(c)** Photograph of a spinach PSII-CaF$_2$-sandwich, the protective PTFE ring (*white*), the threaded metal ring (*black*) and the tool for screwing the metal ring into the sample holder. **(d)** A Photograph of the sample-sandwich mounted onto the sample holder.

---

[21]25 mm diameter, 2 mm thickness, optically polished on both sides (Crystal GmbH)
[22]BIOZOL Diagnostica Vertrieb GmbH

Table 3.4: Measurement buffers for IR experiments MilliQ or D_2O; pH 6.2, pH 6.0. Buffer 3 is the measurement buffer originally used for cyanobacterial core complex samples. To improve sample stability, however, a buffer exchange was avoided when possible and later cyanobacterial measurements were done in their storage buffers (buffer 4 for *Synechocystis* samples and buffer 5 for *T. vestitus* samples). The pD of D_2O buffers was adjusted using a pH meter, with $pD = pH_{readout} + 0.4$ (Glasoe and Long, 1960).

buffer	sample type	content
1	spinach PSII membrane particles	25 mM MES, 15 mM NaCl, 5 mM $MgCl_2$, 5 mM $CaCl_2$
2	spinach PSII membrane particles	25 mM MES, 25 mM MOPS, 25 mMH HEPPS, 10 mM NaCl, 5 mM $MgCl_2$, 5 mM $CaCl_2$
3	cyanobacterial PSII core complexes	10 mM MES, 5 mM $CaCl_2$, 5 mM NaCl 0.06% β-DM, 400 mM sucrose
4	PSII core complexes (*Synechocystis*)	50 mM MES, 1.2 M betaine, 20 mM $CaCl_2$, 5 mM $MgCl_2$, 50 mM histidine, 1 mM EDTA, 0.03% β-DM, 10% glycerol
5	PSII core complexes (*T. vestitus*)	40 mM MES, 10 mM $CaCl_2$, 10 mM $MgCl_2$, 100 mM betaine, 0.04%β-DM, 10% glycerol
6	cyanobacterial PSI core complexes	50 mM TRIS, 0.04% β-DM

placed on top of the second plate for protection. A metal ring is screwed in which presses the plates firmly together, thereby spreading the sample between the plates.

The sample holder is now mounted onto the x-y-movable stage and the sample compartment is closed. Before beginning a measurement, the sample compartment should be given some time to reach the desired measurement temperature. As the sample compartment is continuously flushed with dry air, the humidity will drop down to close to 0% in about 30–45 min.

3.5.1 PSII-enriched Thylakoid Membrane Particles from Spinach

PSII membrane particles from spinach corresponding to about 4 mg Chl are thawed on ice for two hours. The sample is then diluted into about 30 ml of measurement buffer. While earlier measurements were done in a MES buffer, later a buffer with three buffering agents (MES, MOPS and HEPPS) was used in order to expand the available pH range (Table 3.4: buffers 1 and 2, respectively). The sample is centrifuged at 50,000 g for 12 minutes at 4 °C. After decanting the supernatant, the pellet is carefully resuspended in a small amount of measurement buffer using a soft brush, before again filling up the tube to about 30 ml. A 30 μm filter[23] is prepared by washing with VE-water and making sure liquid is easily flowing through. The filter is then washed a few times with the measurement buffer. A 3D-printed adapter piece is placed on a fresh centrifugation tube and the filter is fitted on top. The liquid sample is then slowly poured through the filter. This step removes any sample aggregates or any other large-sized contaminations[24]. After repeating the centrifugation

---

[23]neoCulture cell strainer from neoLab Migge GmbH

[24]This filtering step was implemented by Paul Greife because of a bead contamination in the lab, which sometimes lead to damaged CaF_2 plates. The adapter piece was designed and 3D-printed by myself.

step, the supernatant is decanted and the tube with the pellet is placed on ice in a light-protected black box until used in the IR lab as described above.

The pellet is carefully scraped out of the centrifugation tube using a spatula and placed on the lid of a Petri dish. For standard spinach PSII measurements, PPBQ (in DMSO) is added as an artificial electron acceptor (for every mg of Chl 1 μl of 700 mM PPBQ is added). For this PPBQ is pipetted onto the sample on the Petri dish and is carefully mixed using two spatulas. A small amount of the final sample is then placed onto each prepared CaF_2 window, again using a spatula.

3.5.2 Cyanobacterial PSII Core Complexes

A sample amount equivalent to 200 μg of Chl (ideally around 200 μl) is taken out shortly before starting the protocol and left to thaw on ice. As core complex samples thaw quickly and are fragile, they do not need to (and should not) sit on ice for two hours prior to usage. A table-top centrifuge cooled to 4°C is used for all centrifugation steps. A concentrator[25] is washed with 0.3 ml Milli-Q water for 10 min at 14,000 g using a fixed-angle micro-reaction tube rotor and then stored on ice until needed. Shortly before further usage, the concentrator is centrifuged upside down for 3 min at 1,000 g to remove any residual water.

Figure 3.3: A photograph of a cyanobacterial PSII core complex sample between two CaF$_2$ plates. Core complex samples are typically of a lighter green and more transparent color.

The sample is loaded onto the concentrator and centrifuged at 14,000 g for 15 min. The concentrator is subsequently turned upside down into a fresh, pre-cooled collection tube. Another spin for 3 min at 1,000 g collects the sample into the tube. The volume of the final sample (V_f) can be estimated by carefully taking the sample into a 100 μl pipette and decreasing the pipette volume until the sample begins to extrude from the tip.

Freshly prepared 0.1 M potassium ferricyanide ($K_3[Fe(CN)_6]$), dissolved in H_2O (or D_2O) is added to the sample as artificial electron acceptor. The amount is determined by the final sample volume: $V_{ferricyanide} = V_f/10$. The final sample solution is pipetted onto several CaF_2 plates (10–15 μl per plate) and sandwiched as described above (see also Fig. 3.3).

Buffer exchange

If a buffer exchange is necessary, it is performed before the concentration step. Two buffer exchange columns[26] are prepared as follows: They are inverted several times to resuspend the gel, before snapping off the cap and taking off the lid. A 1 min centrifugation in the swing-out rotor at the lowest possible speed (37 g) removes the liquid of the storage buffer. To exchange all the buffer molecules trapped in the column, several centrifugal washing steps are needed (two times with 0.5 ml Milli-Q water, five times with 0.5 ml measurement buffer), all at 37 g. The final centrifugation step should be performed shortly before usage of the columns. If necessary, the columns are stored with 0.5 ml buffer and closed lid until needed.
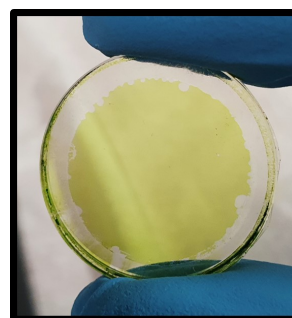
---

[25]Amicon ultra 0.5 ml centrifugal filter with a 100 kDa cutoff (Merck KGaA)
[26]Bio-Spin 6 column with a 6,000 kDA cutoff (BioRad Laboratories GmbH), stored in TRIS buffer

A sample amount corresponding to 100 μg of Chl is now loaded onto each of the columns before centrifuging for 1 min at 37 g; the flow-through is collected in a tube labeled *1*. The following is repeated four times (or until the flow-through is no longer green): About 70 μl of measurement buffer is loaded onto each column followed by centrifugation; the flow-through is collected in a separate tube for each spin step. The tubes containing dark green sample (usually tubes 2, 3 and 4) are combined and concentrated as described above.

The buffer exchange columns should not be loaded with more than 100 μl. If the starting concentration is much lower than 1 mg/ml the sample is pre-concentrated using the same type of concentrators before applying the sample to the buffer exchange columns.

3.5.3   Cyanobacterial PSI Core Complexes

The PSI sample is diluted in a total volume of 8 ml measurement buffer (buffer 6 in Table 3.4, pH 8), such that a concentration of about 0.2 mg/ml is reached. The sample is ultra-centrifuged[27] at 300,000 g for about 3 h, which results in a soft pellet. The supernatant is immediately but carefully discarded, to avoid resuspension of the pellet. 0.1 μl of each of the two electron donors PMS (20 μM, in Milli-Q water) and sodium ascorbate (20 mM, in buffer) are pipetted onto the center of a prepared CaF_2 plate. A small amount of the PSI pellet is scooped out of the centrifugation tube with a spatula and mixed into the electron donors on the plate. The second CaF_2 plate is swiftly placed on the sample to prevent the sample from drying out.

---

[27]Sorvall WX Ultra 80 ultracentrifuge, Thermo Scientific GmbH

4 | Supporting Data and Foundational Results

IN this chapter, we will take a look at different factors that influence time-resolved IR experiments on PSII. The following key questions will be addressed: How does an aging sample affect the IR results when measuring over several days? How are the kinetics altered by the addition of the artificial electron donor PPBQ? The vibrational IR spectrum of PSII is overlayed with a broad electronic P680$^+$ band—what does this mean for time-resolved experiments? Do experiments on PSII samples from different spinach membrane particle preparations give the same results? How is the IR data affected by depleting spinach PSII membranes of their Mn_4CaO_x cluster and how is this informative for experiments on intact PSII? In literature often an S-state independent miss factor is assumed for simplicity—how strongly are the IR transients affected by different deconvolution approaches?

Insight into these points will help to understand and interpret the results of the following chapters. They may also point out some shortcomings of these experiments and what to look out for when designing future experiments.

4.1 Assessing the Long-term Stability of Spinach PSII Samples

When handled carefully and kept in the dark, spinach PSII membrane particles can be pushed through many rounds of the S-state cycle. The addition of an excess amount of PPBQ ensures that the electron acceptor side of PSII is not the limiting factor. Even after several days of measuring on the same sample, clear S-state dependent behavior can still be observed. In the following a closer look will be taken at whether and how IR data measured over more than 50 hours is altered over time.

Experimental Details

To assess how strongly the time-resolved IR signal is affected by being repeatedly exposed to bursts of excitation flashes, a long-term experiment was performed, i.e. the IR signal was measured repeatedly at the same wavenumber (1400 cm^{-1}). 212 individual sample spots were targeted with a burst of 10 excitation flashes at 1 Hz; this gave each sample spot a dark adaptation time of about 70 min before being exposed to the next flash burst.

The data was analyzed in batches of two rounds of targeting all sample spots, i.e. 424 data sets per batch, resulting in a total of 23 data batches. After data filtering, 250–320 data
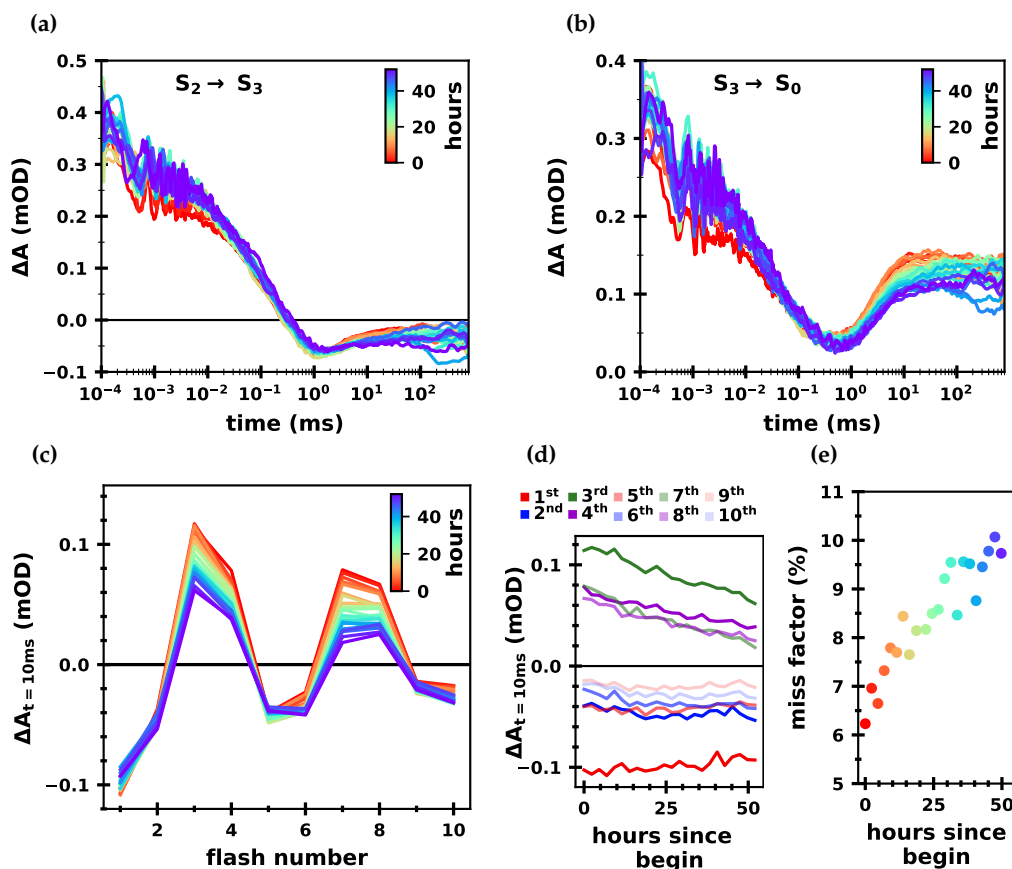
Figure 4.1: Long-term IR measurement of spinach PSII membrane particles at 1400 cm^{-1}. The IR difference absorption of **(a)** the $S_2{\to}S_3$ transition and **(b)** the $S_3{\to}S_0$ transition is show over the course of over 50 hours in batches of about 2.5 hours. The transients were smoothed with a sliding average algorithm with a window size of 10. **(c)** Flash-number dependent IR difference absorption averaged between 9.5–10.5 ms over the course of 50 hours. **(d)** The same data as in (c), but shown as a function of time for each flash. **(e)** The miss factor as a function of measurement time.

sets remained per batch, whereby less data sets were filtered out in earlier batches. This change in number of discarded data sets was mostly due to changes in signal intensity reaching the detector: over time, more signals fell below or above the threshold, i.e. the transmitted signal became too high or too low. This may have been due to the stage drifting slightly over time (an issue that became more pronounced in the following months until it became very apparent and was fixed). The sample was relatively inhomogeneous to start with, with varying sample thickness[28].

The measurements were performed in MES buffer at pH 6.2 (buffer 1 in Table 3.4) at 10°C (spinach PSII preparation 414). Prior to the first full-length flash burst, the sample was pre-flashed twice and given an hour to dark-adapt. The measurements were done with the older QCL model. The flash-induced data was deconvolved into transients directly related

---

[28]The level of (in)homogeneity of the sample appears to depend on a mixture of lab experience and sheer luck—sometimes sandwiching the sample between CaF$_2$ plates works out well and sometimes less so. Little imperfections in the CaF$_2$ plates—and other unknown factors—may also contribute to this.
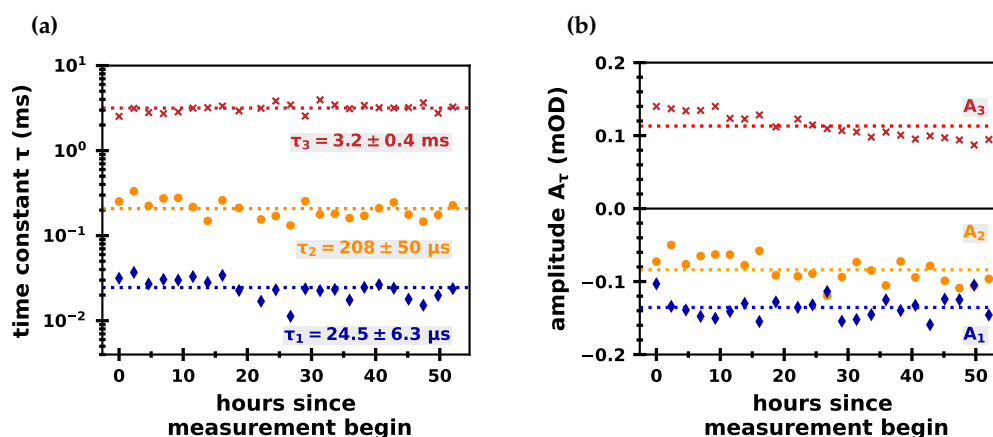
Figure 4.2: Fit results of the $S_3 \rightarrow S_0$ transition of a long-term IR measurement at 1400 cm^{-1} of spinach PSII membrane particles. (a) Time constants and **(b)** their respective amplitudes obtained from fitting the data shown in Fig. 4.1 to a sum of exponentials. The average values over all data batches are shown as dotted lines.

to the individual S-state transitions assuming a starting population of 100% S_1 and an S-state independent miss factor.

Results and Discussion

At first glance, the IR transients of the individual data batches look quite similar, as shown for the $S_2 \rightarrow S_3$ and $S_3 \rightarrow S_0$ transitions in Fig. 4.1a and b, respectively. To minimize the influence of the miss factor, which indeed increases clearly over time from about 6 to 10% (Fig. 4.1e), the data is shown after deconvolution. Both the $S_2 \rightarrow S_3$ and $S_3 \rightarrow S_0$ transients show some drifts in the late millisecond region, which can be assumed to be artefactual. The first batch (red line) shows a clearly lower starting amplitude than the later batches. However, in a second similar long-term experiment, this was not observed (*not shown*), so possibly this is also merely artefactual.

The millisecond region of the $S_3 \rightarrow S_0$ transients is more strongly affected: The amplitude of the millisecond rise becomes lower in later measurement batches. This trend is also visible in the flash-number dependent IR signal around 10 ms (Fig. 4.1c and d): While the overall period-of-four pattern remains strongly pronounced in all data batches, the amplitude of the flashes strongly related to the $S_3 \rightarrow S_0$ transition (especially the 3rd and 7th flash) are dampened in later batches.

To quantify this effect, the $S_3 \rightarrow S_0$ transient of each data batch was fit to a sum of three exponentials and an offset; the resulting time constants and their amplitudes are shown in Fig. 4.2. The time constants show some variation between batches but reveal no clear trend. The amplitude of the millisecond rising phase, however, shows a clear decrease in later measurements, which is in line with the observations described above.

The aforementioned second long-term measurement was overall more noisy and was performed before fixing the heat artefact issue (see Section 2.7); its key results (Fig. A2.1 in the Appendix) are nevertheless consistent with the observations described above.

Overall, these results lead to the conclusion that possibly specifically the electron transfer step of the $S_3 \rightarrow S_0$ transition becomes less efficient in later measurement batches. The unaltered time constant suggests that the process does not become slower but rather fails more often. This implies an S-state dependent contribution to the miss factor as a conse-

quence of an aging sample, but it does not give insight as to whether the miss factor at the start of the experiments is S-state dependent.

The fact that none of the obtained time constants are significantly altered, suggests that repeated measurements on the same sample can be done without having to fear strongly perturbed results. One should bear in mind, however, that the amplitudes might be affected and thus not over-interpret amplitude ratios. Specifically, also in spectral data sets, one should consider that, especially in the $S_3 \rightarrow S_0$ transition, parts of the spectra that were measured first might show larger amplitudes than other parts of the spectra.

4.2 Effect of the Artificial Electron Donor PPBQ on the IR Data

Under physiological conditions, a large plastoquinone pool is available to allow constant exchange (i.e. after every two charge separation events) of the quinone bound to the Q_B-binding site, thus providing an oxidized acceptor-side that is capable of taking up electrons. In spinach PSII membrane particles, however, this pool is greatly diminished during the sample preparation procedure and thus the acceptor side can only undergo a few cycles before its functionality becomes greatly impaired. For experiments that require many turnovers, such as IR experiments, it is therefore common practice to add an artificial electron acceptor (PPBQ in this work) that can bind to the Q_B binding site and replace the plastoquinones' functionality.

In the following, the effect of addition of PPBQ to spinach PSII samples—or its omission—on time-resolved IR data will be examined and discussed. The results of this Subchapter have in parts been made available in the Supporting Information of a manuscript (Dekmak et al., 2023).

Experimental Details
The measurements on spinach PSII membrane particles without addition of PPBQ were performed at 10°C and pH 6.2, same as the sample to which PPBQ was added. All data shown here was obtained on spinach PSII from preparation 416. Both samples were pre-flashed twice and subsequently given an hour to dark-adapt before applying the first burst of 10 flashes. For more details on the sample preparation see Chapter 3.5.

Results and Discussion
Acceptor-side kinetics were observed at 1478 cm^{-1}, which show a fast rise within the time resolution of the experimental setup and a subsequent multi-phasic decay in all ten sequential flash-induced transients for both PSII with and without PPBQ (the first four flash-induced transients are shown Fig. 4.3a and b). The band at 1478 cm^{-1} has been assigned to a C$=$O mode of Q_A^- (Hienerwadel and Berthomieu, 1995), while 1480 cm^{-1} is predominantly associated with Q_B (Suzuki et al., 2005a); thus the quinones in both binding pockets are expected to contribute to the kinetics at 1478 cm^{-1}. Q_BH_2 on the other hand likely does not absorb at 1478 cm^{-1}, as shown for ubiquinol in photosynthetic bacterial reaction centers (Mezzetti et al., 2023, 2003); to our knowledge no FTIR studies were done on plastoquinol in PSII.

The absorption changes observed without addition of PPBQ (Fig. 4.3b) do not decay to zero within the measurement time of 800 ms, but rather alternate between a positive and a negative difference absorption. This can also be seen in the dark orange line in Fig. 4.3c, showing the flash-number dependent IR signal averaged between 600–800 ms (albeit the pattern becomes slightly less clear at later flash numbers). A positive difference signal after
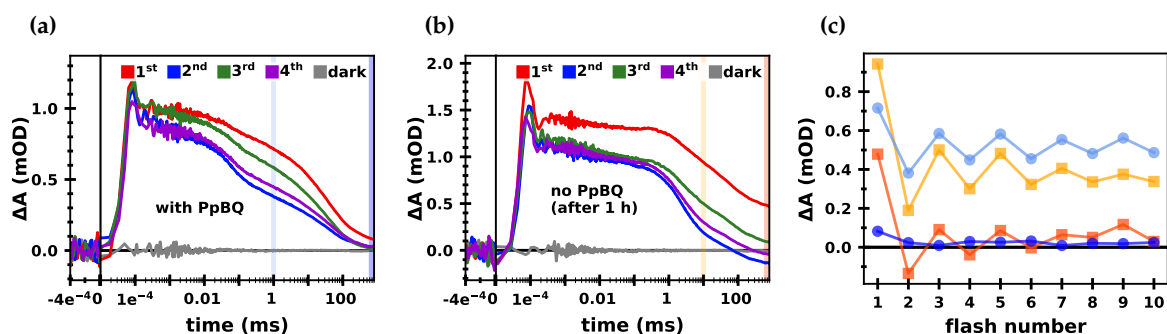
Figure 4.3: Acceptor side kinetics observed at 1478 cm^{-1} with and without PPBQ. IR difference absorption of spinach PSII membrane particles following the first four excitation flashes **(a)** with addition of PPBQ and **(b)** without any exogenous electron acceptor. **(c)** Flash-number dependent IR difference signals of PSII with PPBQ (*circles*) averaged between 0.1–1.1 ms (*light blue*) and between 600–800 ms (*dark blue*), as well as PSII without PPBQ (*squares*) averaged between 9–11 ms (*light orange*) and 600–800 ms (*dark orange*). The averaging time ranges are also indicated in panels (a) and (b) with vertical bars of the same colors.

an odd number of flashes can be explained by the reduction of Q_B to Q_B^- (see Fig. 4.4a), resulting in a long-lived absorption signal around 1478 cm^{-1}. Following an even number of flashes, Q_B^- is reduced once more and takes up two protons, forming the neutral Q_BH_2 which does not absorb at 1478 cm^{-1}; the difference absorption signal thus falls below the level of that prior to the excitation flash.

The absorption changes observed in presence of PPBQ (Fig. 4.3a) on the other hand decay back to zero within 800 ms following all excitation flashes except for the first one. This is in line with previous findings by Petrouleas and Diner (1987) who found that PPBQ does not form a stable semiquinone in the Q_B binding pocket. Instead, after an odd number of flashes, a second electron is extracted from the non-heme iron ($Fe^{2+} \rightarrow Fe^{3+}$), leading to a doubly reduced, neutral PPBQ molecule (Fig. 4.4b). After an even number of flashes, the quinone in the Q_B site is not reduced at all, but it is rather the non-heme iron that takes up the electron ($Fe^{3+} \rightarrow Fe^{2+}$). Thus, no long-lived semiquinones are formed in the presence of PPBQ, leading to the absence of long-lived absorption contributions at 1478 cm^{-1} (dark blue line in Fig. 4.3c).
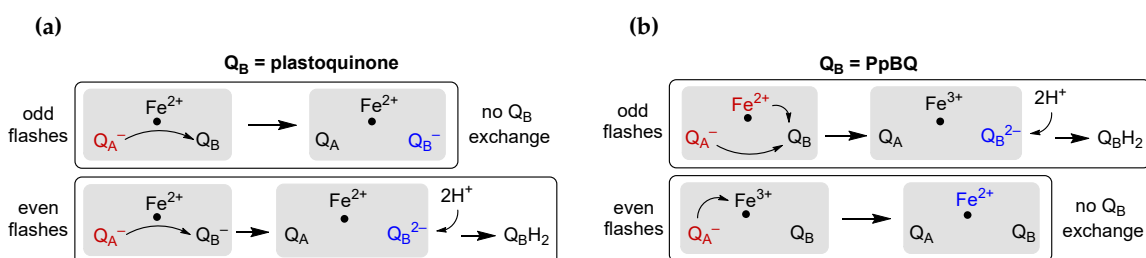
Figure 4.4: Scheme of the non-heme iron and quinone chemistry at the acceptor-side of PSII. The electron transfer chain from Q_A to Q_B is shown following an odd or even number of excitation flashes and **(a)** if the Q_B pocket is filled with a plastoquinone molecule or **(b)** with a PPBQ molecule. Particles that are about to donate an electron are highlighted in red and particles that have just accepted an electron are marked in blue.
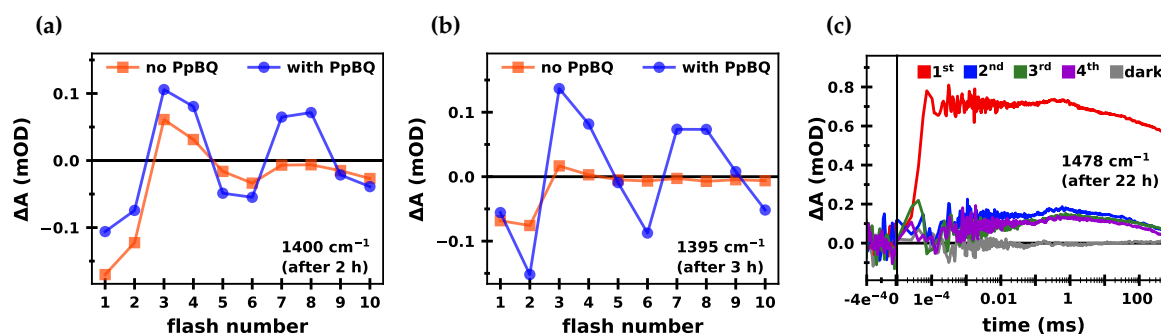
Figure 4.5: Fast aging of spinach PSII membrane particles without PPBQ. Steady-state flash-number dependent IR difference signals (averaged between 400–800 ms) at **(a)** 1400 cm^{-1} and **(b)** 1395 cm^{-1} of PSII samples with (*blue*) and without (*orange*) PPBQ. **(c)** IR difference absorption transients of PSII without PPBQ at 1478 cm^{-1} induced by the first four excitation flashes, obtained 22 h after the first measurement on the sample.

A fast-decaying component between 10–100 μs is present only in samples with PPBQ (and clearly more strongly pronounced after an even number of flashes), and can be assigned to electron transfer from Q_A^- to Fe^{3+}, as that is the expected time range for this event (Chernev et al., 2011). The very fast decay kinetics visible roughly between 0.1–10 μs can be assigned to $P680^+$ reduction kinetics (see also Chapter 4.3).

At 1400 cm^{-1}, the flash-number dependent steady-state values show a clear period-of-four oscillation for measurements both with and without PPBQ (Fig. 4.5a), although in the latter case the oscillation is strongly dampened. In a subsequent measurement at 1395 cm^{-1} (Fig. 4.5b), the oscillating pattern of PSII without PPBQ is already nearly completely absent. Figure 4.5c shows transients at 1478 cm^{-1} obtained on the sample without PPBQ roughly 22 h after begin of the measurement series. Following the first excitation flash, there is still a clear change in absorption, but nearly a factor two lower than in the transients of Fig. 4.3b (which was the first data set to be acquired following the pre-flashes). The subsequent excitation flashes induce only comparatively small absorption changes. These observations confirm that a spinach PSII membrane sample cannot be driven efficiently through the S-state cycle (at 1 s flash spacing) more than a few times without the addition of exogenous electron acceptor: Without a large oxidized quinone pool to replace the reduced quinones, the acceptor side cannot keep up with the electron donor side.

In core complex preparations, where PSII is stripped of its membrane and instead embedded in detergent, the plastoquinone pool has been removed completely; for such samples ferricyanide is commonly used as an exogenous electron acceptor. While ferricyanide has the advantage of not altering the non-heme iron chemistry as opposed to PPBQ, it does not work well in membrane particle preparations, presumably because it cannot efficiently access the Q_B binding site (Shevela and Messinger, 2012).

From these results we can confirm that the addition of exogenous electron acceptor is needed to conduct IR experiments efficiently. We can also conclude that our PSII membrane particles do not lose their non-heme iron during the preparation process, as the non-heme iron chemistry is very well visible in the data.

4.3 Time-Dependent P680$^+$ Background Signal

After the QCL in our laboratory was exchanged for a newer model, a larger spectral region became available to us. Measurements at wavenumbers above 1750 cm^{-1} somewhat unexpectedly exhibited quite pronounced flash-induced kinetics. In this section, experiments on intact as well as Mn depleted spinach PSII membranes are presented that clearly identify these signals as P680$^+$ reduction kinetics that arise due to a very broad electronic band previously observed by Noguchi et al. (1998) and others. Furthermore, the P680$^+$ kinetics for two different sample types (spinach PSII membrane particles and core complexes from *Synechocystis* sp. PCC 6803) are analyzed and compared, and the significance of this P680$^+$ background signal to time-resolved IR experiments on PSII is discussed.

A detailed analysis of the multiphasic P680$^+$ reduction kinetics and their discussion in the context of previous research on P680$^+$ will not be presented here, as this is in the focus of another doctoral project (see also Dekmak et al., 2023).

Experimental Details I—Proof of Concept Measurements
The spinach PSII samples were prepared in MES-MOPS-HEPPS buffer (buffer 2 in Table 3.4, pH 6.2) as described in Chapter 3.5. PPBQ was used as an artificial electron acceptor for intact (sample 416) as well as Mn depleted PSII (sample 403). For the intact sample, the typical number of six sample plates were prepared; for the Mn depleted sample only one plate was used. The dark-adaptation time before re-illumination of the latter sample was thus only about 15 minutes instead of the usual hour. A test measurement, in which the dark adaptation time was increased to an hour by pausing the measurement between bursts of flashes, showed that the lower dark-adaptation time did not alter the kinetics (*not shown*).

The two samples were both mounted into the sample holder at the same time and measured intermittently, to ensure they were measured under the same conditions. Only IR changes at 1780 cm^{-1} were measured.

Experimental Details II—Measurements for Background Correction
On three separate measurement days, data sets of spinach PSII (sample 416) in H$_2$O and D$_2$O buffer (pL 6.2) and of *Synechocystis* sp. PCC 6803 core complexes in H$_2$O buffer (pH 6.0) were acquired around 1780 cm^{-1}. For each sample, IR absorption changes at a selection of other wavenumbers was also acquired, to test background subtraction of data measured on the exact same sample. For the *Synechocystis* sample, no buffer exchange was done; the sample was rather measured in its storage buffer.

Results and Discussion
Absorption changes at 1780 cm^{-1} of intact and Mn depleted spinach PII samples following four consecutive excitation flashes are shown in Fig. 4.6a and b, respectively. Both samples show very clear flash-induced kinetics: a fast rise within the time resolution of the setup and a subsequent multiphasic decay back to (around) zero. While most of the wavenumber covered by our experimental setup (1890–1310 cm^{-1}) is rich in protein vibrations, the range from about 1750 up to 1890 cm^{-1} is not expected to exhibit vibrational difference bands. Indeed, sharp bands are not observed (Dekmak et al., 2023), but rather a very broad positive feature. Photoaccumulated P680$^+$/P680 spectra exhibit a very broad band stretching across roughly 6000–1000 cm^{-1} (Okubo et al., 2007), which has been attributed to P680$^+$, arising from asymmetric charge distribution across the radical primary donor (Breton et al., 1992).

The kinetics at 1780 cm^{-1} of intact PSII indeed show a period-of-four dependency on the flash-number (Fig. 4.6a and c, squares). Especially the pattern of low, high, high, low
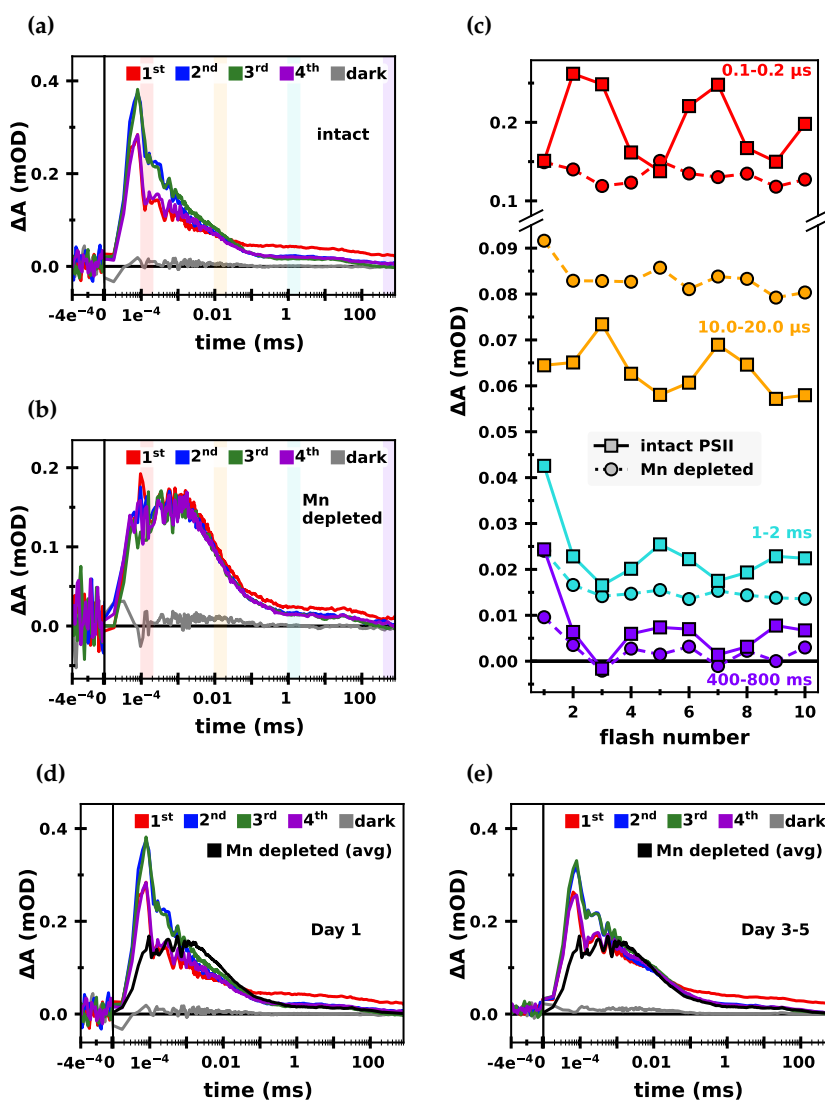
Figure 4.6: IR absorption changes at 1780 cm^{-1} of intact and Mn depleted spinach PSII membrane particles. IR transients of the first four excitation flashes of **(a)** intact PSII membrane particles (preparation 416) and **(b)** Mn depleted PSII, measured on the same day and under identical measurement conditions.[29] **(c)** Flash number dependent IR difference absorption at different time points of intact (*squares*) and Mn depleted PSII (*circles*). The colors of the lines correspond to the colors of the vertical bars in (a) and (b), which highlight the regions of the transients that were averaged. **(d)** IR transients of the first four excitation flashes of intact PSII on the first measurement day (*colored lines*), as well as the absorption changes of Mn depleted PSII, averaged over all flash-induced transients (*black*). **(f)** IR transients of intact PSII after 3–5 days of measuring the sample (*colored lines*). The same averaged Mn depleted transient as in (d) is again shown in black.

(1st to 4th flash) in the sub-microsecond region of the transient is perfectly in line with previous reports on P680$^+$ reduction kinetics (Renger, 2004); see also the introductory

---

[29]During that measurement day, the setup seems to have had an issue: The IR signal acquired in the dark (without excitation) showed a positive signal above noise level (grey lines in panels Fig. 4.6 (a), (b), (d) and (e)). The source of this artefact is unknown; this phenomenon occurred only for a few days (and was observed only once previously). As we only noticed it in the data once it was no longer occurring, it was not possible to investigate it more closely.
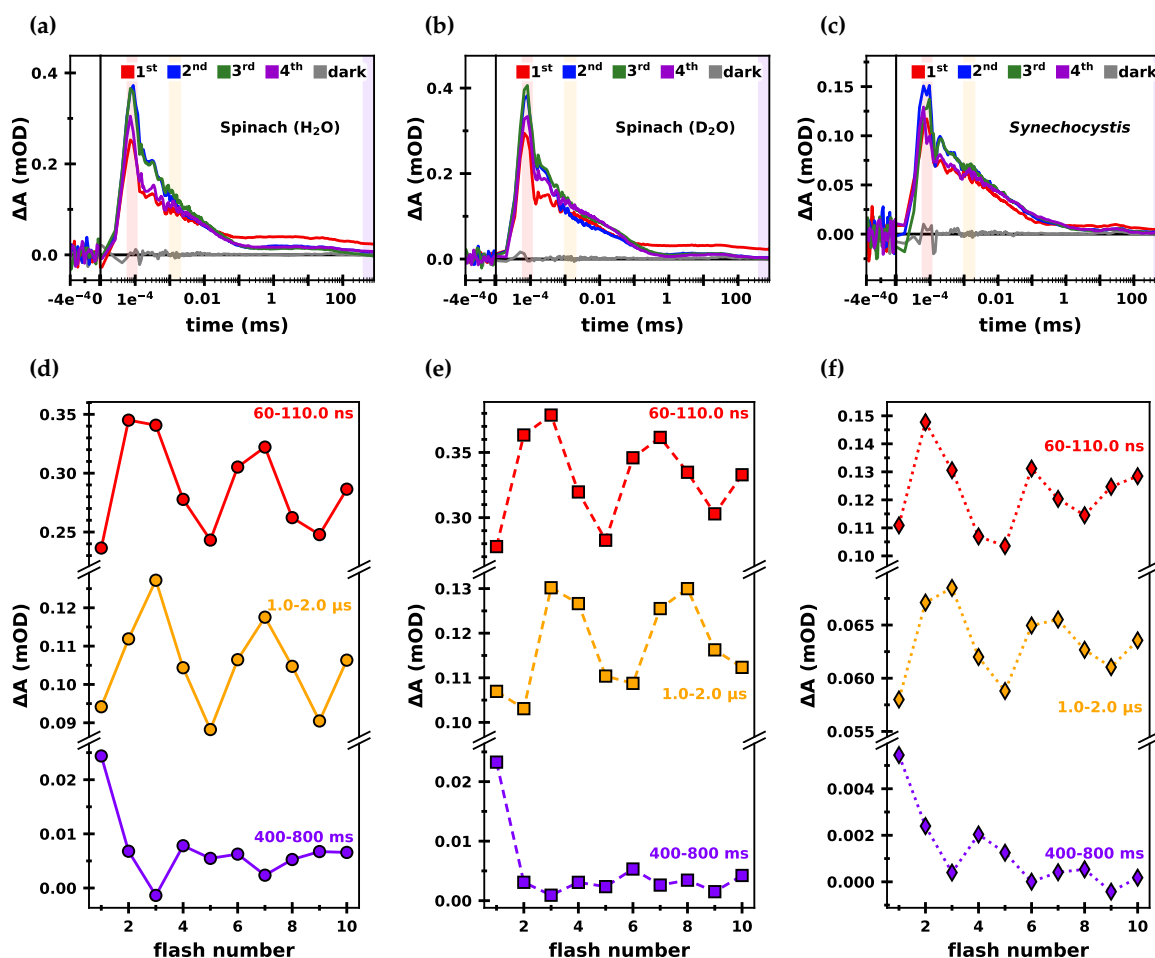
Figure 4.7: P680$^+$ background signal around 1780 cm^{-1} of spinach PSII membrane particles and core particles from *Synechocystis* sp. PCC 6803. IR absorption changes induced by four consecutive excitation flashes in **(a)** spinach PSII in H$_2$O (1780 cm^{-1}), **(b)** spinach PSII in D$_2$O (1790 cm^{-1}) and **(c)** PSII core particles from *Synechocystis* in H$_2$O (1780 cm^{-1}). **(d–f)** Flash-dependent IR difference signal at three different time points (60–110 ns, 1–2 µs and 400–800 ms) of the data sets shown in (a–c). The transients in panel (a) and (b) were smoothed with a sliding average algorithm with a window size of 10; a window size of 20 was applied to the data in panel (c).

Section 1.5.2 for a literature overview of P680$^+$ kinetics. The clearly slowed down decay kinetics observed in the Mn depleted sample is also in line with previous reports (Haumann et al., 1997). These observations clearly supported the assignment of the broad feature to P680$^+$; this broad band, effectively leading to an up-shift of the vibrational spectra of PSII, has since been investigated in more detail by Dekmak et al. (2023).

Measurements performed on the intact PSII sample at 1780 cm^{-1} over several days revealed that the signal changed over time (Fig.4.6d and e): After several days of measuring, the fast sub-microsecond kinetics became clearly less pronounced (and the initial amplitude of the signal was lower), while the slower microsecond kinetics became more dominant. The kinetics of the aged sample indeed showed more similarity to those of the Mn depleted sample (black line). A possible explanation of this observation is the accumulation of broken centers over the course of several measurement days: after 3–5 days of repeated

saturating excitation it can be expected that the PSII centers are not as functionally intact as in the beginning.

Having established that the signal above 1750 cm^{-1} can attributed to P680$^+$ kinetics and that thus most likely the entire region between 1900–1300 cm^{-1} is affected by a time-dependent background signal (Dekmak et al., 2023), high-quality transients of this signal were acquired for three different samples to allow for background correction (Fig. 4.7). As this background signal was noticed after nearly all the experiments for this thesis had been finished, it was not possible to obtain data of it for all samples presented in this work.

At first glance, the transients of spinach PSII membranes in H$_2$O (1780 cm^{-1}) and in D$_2$O (1790 cm^{-1}) look quite similar (Fig. 4.7a and b); however, as expected (Schilstra et al., 1998), the microsecond kinetics are slightly slowed down in D$_2$O. In *Synechocystis* core complexes in H$_2$O (Fig. 4.7c), the microsecond kinetics are clearly more strongly pronounced than in the spinach samples. In fact, the transients resemble more the 3–5 day old sample in Fig. 4.6e. This could be seen as an indication that the core complex sample has more non-functional PSII units than the spinach membrane particles. Indeed, lab experience shows that core complexes are much more fragile samples, thus this observation is relatively unsurprising.

Inspection of flash-number dependent IR values at 60–110 ns and 1–2 μs reveals clear period-of-four patterns for all three samples (Fig. 4.7 d–f); at around 400–800 ms on the other hand, the most striking observation is the high value in the first-flash transient and the lack of a clear oscillatory behavior thereafter. This positive offset in the millisecond region is unlikely to be arising from P680$^+$ reduction kinetics as it is too long-lived. More likely it could relate to broad-band quinone contributions, which have previously been observed between 3000–2500 cm^{-1} (Suzuki et al., 2005a) and could possibly extend to the lower wavenumber range studied here. The higher contribution in the first-flash transients
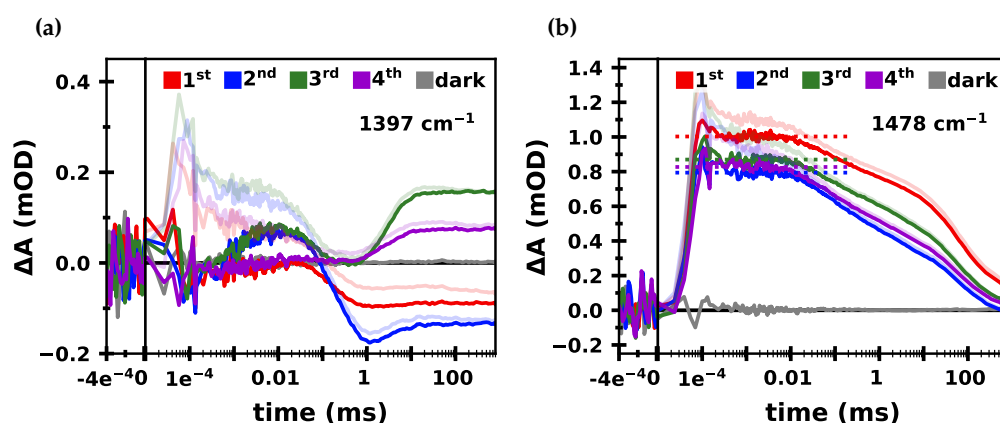
Figure 4.8: IR difference absorption at 1397 and 1478 cm^{-1} before and after P680$^+$ background subtraction. Flash-induced absorption changes of spinach PSII membrane particles after subtraction of the P680$^+$ signal obtained at 1780 cm^{-1} (Fig. 4.7a) at **(a)** 1397 cm^{-1} and **(b)** 1478 cm^{-1} (opaque lines). The first flash is shown in red (primarily S$_1$→S$_2$), the second in blue (S$_2$→S$_3$), the third in green (S$_3$→S$_0$) and the fourth in purple (S$_0$→S$_1$). The transients prior to P680$^+$ subtraction are shown in transparent colors. The data sets at 1397, 1478 and 1780 cm^{-1} were all measured on the same sample (same measurement day). All data was smoothed with a sliding average algorithm (window size of 10 data points).

are then likely to arise from non-Q_B-PSII units, which stably accumulate Q_A^- (see also the Supporting Information of Dekmak et al., 2023).

The transients in Fig. 4.7 will be used for $P680^+$ background correction in later chapters. In Fig. 4.8 examples of such background corrections are shown for spinach PSII in H_2O: At $1397\ cm^{-1}$ (Fig. 4.8a) subtracting the $P680^+$ background results in nearly complete removal of kinetics up to about 100 µs in the first- and fourth-flash transients. In the second- and third-flash transients, there is a fast microsecond rise. Prior to background subtraction, all transients showed a multiphasic decaying behavior.

At $1478\ cm^{-1}$ (Fig. 4.8b), the background subtraction removes nearly all kinetics above noise-level up to about 10 µs; the fast nano- and microsecond behavior is thus replaced by a plateau in all flash-transients.

These two examples already hint at the importance of correctly accounting for—or at least keeping in mind—the $P680^+$ background kinetics to avoid miss-interpretations of the time-resolved IR data. A more detailed analysis of the kinetics of the individual S-state transitions will follow in Chapters 5 and 6.

4.4 Spinach PSII Depleted of its Mn_4CaO_x Cluster

It is likely that during PSII preparations of all kinds, a certain fraction of PSII units will lose their Mn_4CaO_x cluster. While cells in living photosynthetic organisms might be able to re-activate centers that have lost their Mn_4CaO_x cluster, PSII membrane particles and core complexes lacking a Mn_4CaO_x cluster will simply be non-functional. The effect of such broken, Mn depleted centers on the IR data will be investigated in this subchapter.

Experimental Details
Spinach PSII membrane particles (preparation 413) were depleted of their Mn_4CaO_x cluster as described in Chapter 3.4. For the IR measurements, the sample was prepared in the same manner as intact PSII membrane particles, including the addition of exogenous electron acceptor PPBQ. A total of 198 individual sample spots were measured (on six CaF_2 plates). A series of 10 saturating excitation flashes were applied to each spot; roughly an hour of dark-adaptation time passed before the same spot was measured again. All measurements were done at 10 °C and in MES-MOPS-HEPPS buffer (buffer 2 in Table 3.4, pH 6.2).

A time-resolved spectral data set was acquired by tuning through the QCL range from low to high wavenumbers in $2\ cm^{-1}$ steps and acquiring 33 sets of flash-induced transients at each wavenumber. Subsequently high S/N transients (obtained by averaging of 500–1000 individual flash-induced transients) were acquired at six wavenumbers.

Unless stated otherwise, all decay associated spectra shown in this chapter were obtained by fitting with Equation 2.7, meaning a positive amplitude corresponds to a rising phase and negative amplitude corresponds to a decaying phase.

Results and Discussion
The high S/N data sets were deconvolved into transients corresponding to the S-state transitions (Fig. 4.9). While Mn depleted PSII is not expected to cycle through the S-state cycle, the acceptor-side may still be functional and thus this is strictly speaking rather a deconvolution into the period-of-two acceptor-side reactions—but for simplicity we will stick to the S-state notation. The data indeed shows a clearly pronounced period-of-two behavior, as is evident by the near identical transients of the $S_1 \rightarrow S_2$ and $S_3 \rightarrow S_0$, as well as the $S_0 \rightarrow S_1$ and $S_2 \rightarrow S_3$ transitions. Transient absorption changes at nine additional wavenumbers (taken
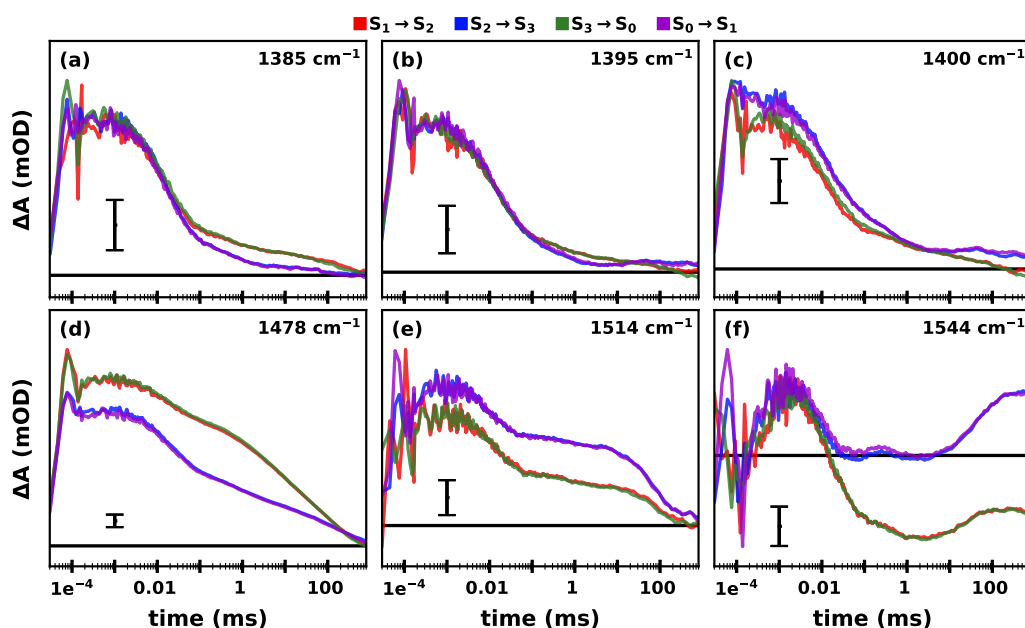
Figure 4.9: IR difference transients of Mn depleted PSII. Difference absorption at **(a)** 1385 cm^{-1}, **(b)** 1395 cm^{-1}, **(c)** 1400 cm^{-1}, **(d)** 1478 cm^{-1}, **(e)** 1514 cm^{-1} and **(g)** 1544 cm^{-1}. Each panel shows a transient corresponding to the $S_1 \rightarrow S_2$ (*red*), $S_2 \rightarrow S_3$ (*blue*), $S_3 \rightarrow S_0$ (*green*) and $S_0 \rightarrow S_1$ (*purple*) transition. All data sets (each consisting of a sequence of 10 consecutive flash-induced transients) were deconvolved assuming a starting population of 85% S_1 and 15% S_0 and a miss factor of 12%. The transients were smoothed with a sliding average algorithm with a window size of 10. The scale bar corresponds to 0.1 mOD.
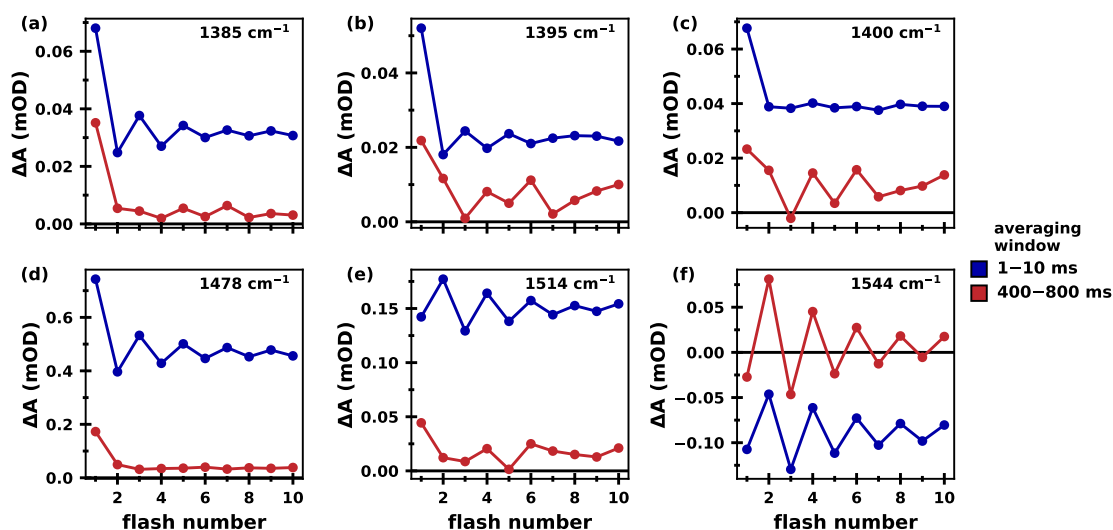
Figure 4.10: Flash-number dependent IR signal of Mn depleted spinach PSII. The steady-state IR values (averaged between 400–800 ms, *blue*) and the values averaged around 1–10 ms (*red*) are shown as a function of flash number at **(a)** 1385 cm^{-1}, **(b)** 1395 cm^{-1}, **(c)** 1400 cm^{-1}, **(d)** 1478 cm^{-1}, **(e)** 1514 cm^{-1} and **(f)** 1544 cm^{-1}.

from the time-resolved spectral data set) are shown in Fig. A2.3 in the Appendix, further supporting this observation.

Figure 4.11: Temporal evolution of the IR difference spectra of Mn depleted spinach PSII particles. The earliest spectra (*red*) show the IR difference absorption averaged between 100 to 215 ns after induction of the **(a)** $S_2 \rightarrow S_3$ and **(b)** $S_3 \rightarrow S_0$ transition; the latest spectra (*purple*) where averaged from 464 to 800 ms. Each decade, 10^n, is represented by three logari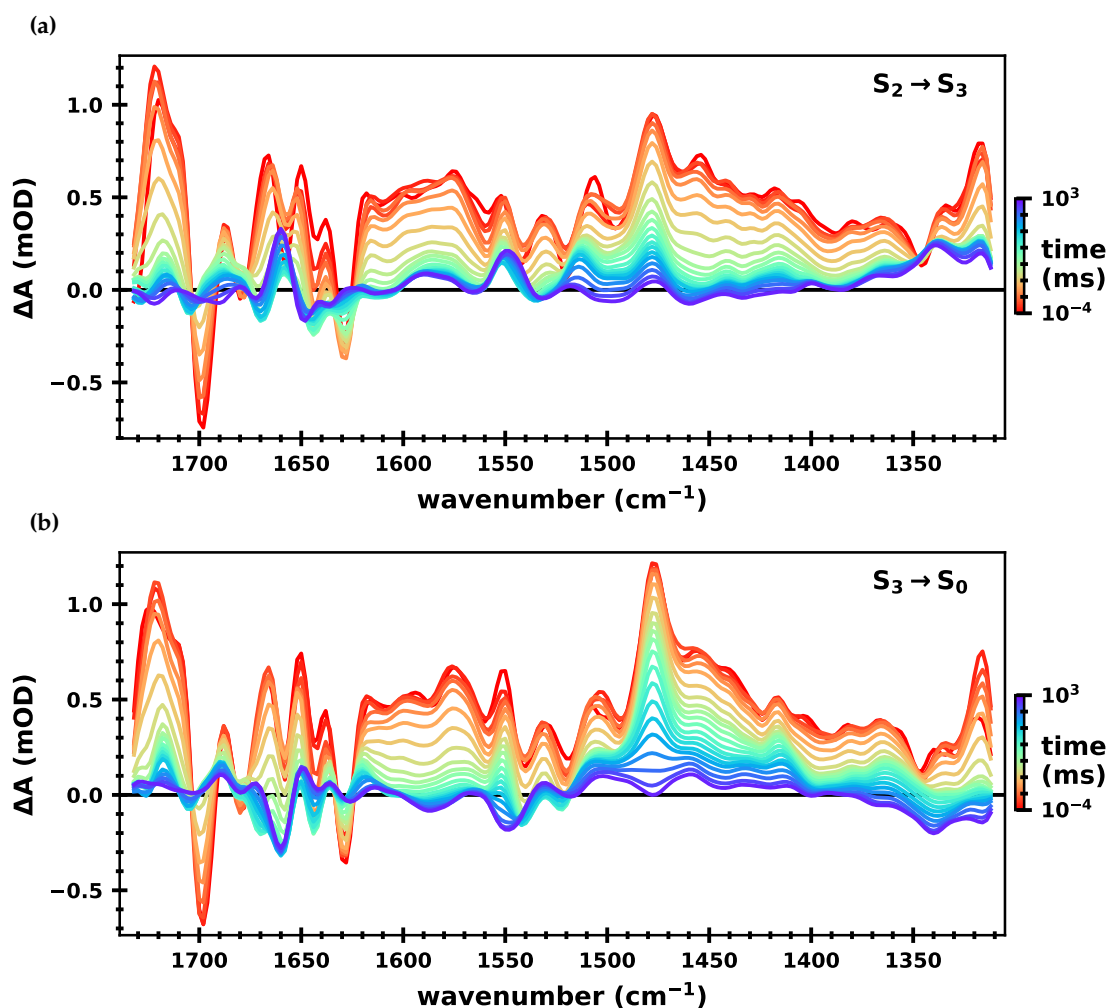thmically spaced intervals of $[1 \cdot 10^n, 2.15 \cdot 10^n]$, $[2.15 \cdot 10^n, 4.64 \cdot 10^n]$ and $[4.64 \cdot 10^n, 10 \cdot 10^n]$. The spectra of the $S_0 \rightarrow S_1$ and $S_1 \rightarrow S_2$ transitions look similar to those shown in (a) and (b), respectively (*not shown*). The spectra corresponding to the pure S-state transitions were deconvolved from 10 flash-induced spectra, assuming a starting population of 85% S_1 and 15% S_0 and a miss factor of 12%. Gaussian smoothing ($\sigma = 2.5$) was applied along the wavenumber axis and linear smoothing ($n = 10$) along the time axis.

Flash-number dependent IR difference values averaged between 1–10 ms and 400–800 ms (Fig. 4.10) also reveal a strong period-of-two oscillation in most cases, while clear period-of-four behavior is absent. From this we can draw the conclusion that donor-side of the PSII sample has indeed been deactivated, while the acceptor-side remains intact. Interestingly, some wavenumbers such as 1544 cm^{-1} show a very strong period-of-two behavior (Fig. 4.10), while measurements of intact PSII at the same wavenumber (at pH 6.2) show only a period-of-four pattern (see Chapter 5). The absence of a clear period-of-two pattern in the intact PSII measurements, may lead to the false conclusion that the wavenumber is

devoid of acceptor-side contribution, while in fact it is merely obscured by the strongly visible donor-side contributions.

The temporal evolution of the $S_2 \rightarrow S_3$ and $S_3 \rightarrow S_0$ transition of the time-resolved spectral data set is shown in Fig. 4.11. The initial spectra (red lines) resemble a mixture of $P680^+/P680$ and Q_A^-/Q_A spectra (Okubo et al., 2007; Berthomieu et al., 1990); the latter contribution is clearly strongly in the $S_3 \rightarrow S_0$ spectra. The steady-state spectra (purple) resemble non-heme iron spectra (Berthomieu and Hienerwadel, 2001), as will be discussed in more detail further down.

The $S_2 \rightarrow S_3$ as well as the $S_3 \rightarrow S_0$ transition of the high S/N data sets were fit globally to a sum of eight exponentials, resulting in a set of time constants for even- and a set of time constants for odd-numbered acceptor-side reactions. These time constants were fixed in a global fit of the time-resolved spectral data set; the resulting decay associated spectra of the $S_2 \rightarrow S_3$ and $S_3 \rightarrow S_0$ transition are shown in Fig. 4.12. The fit quality was overall good (see Fig. A2.5 in the Appendix); the residuals of the early millisecond-regime of the amide I region, however, show some imperfections. The amide I peaks in the DAS should thus not be overinterpreted.

Throughout large parts of the DAS, the $S_2 \rightarrow S_3$ and $S_3 \rightarrow S_0$ transition look very similar. One striking difference is that the $S_3 \rightarrow S_0$ spectra show clearly stronger contributions around 1478 cm^{-1}, especially in the DAS of the four millisecond-phases. In the following, the spectra of Fig. 4.12 will be discussed one by one and tentatively assigned to specific processes where possible:

(a) The DAS of the 890/800 ns phase shows a derivate-like feature around the amide I and amide II regions. Below 1500 cm^{-1} the DAS is mostly feature-less and does not show a downshift from zero, arguing against the involvement of $P680^+/P680$. The spectrum shows some similarity to the first derivative of the heat artefact spectrum (Fig. A2.6 in the Appendix), which might be merely coincidental. It is currently unclear which process this DAS is connected to; it could be related to a fast relaxation process following the initial excitation of the system.

(b) The DAS of the 11/9.4 μs phase strongly resembles previously reported FTIR spectra of $P680^+/P680$, obtained by photoaccumulation of $P680^+$ in Mn depleted PSII (Nagao et al., 2017b; Okubo et al., 2007). The DAS is inverted compared to the aforementioned FTIR spectra, meaning it reflects the decay of $P680^+$. A time constant of about 10 μs is also in agreement with previous reports for P680 reduction kinetics: Haumann et al. (1997) found that in Mn depleted samples, the P680 reduction occurs with half-times of 6 and 35 μs (which corresponds to time constants of about 9 and 50 μs).

(c) The DAS of the 49/39 μs phase again resembles $P680^+/P680$ spectra. In the $S_2 \rightarrow S_3$ spectrum a negative peak at 1478 cm^{-1} additionally hints at quinone contributions (Q_A^- decay), which could be explained by electron transfer from Q_A^- to Fe^{3+} occurring with a time constant of about 20 μs (Chernev et al., 2011). ET from Q_A^- to Fe^{3+} only occurs in even-numbered S-state transitions (for an overview of iron-quinone chemistry see Fig. 4.4).

(d) The shape of the DAS of the 570/560 μs phase does not allow for an obvious assignment. Around this time, the electron transfer from Q_A to Q_B is expected; possibly that event contributes to these spectra.

(e) The DAS of the 3.4 ms phase ($S_3 \rightarrow S_0$) strongly resembles an inverted Q_A^-/Q_A spectrum, indicating that it is associated with the disappearance of a Q_A^- population. This phase could be connected to ET from Q_A^- to Q_B, which—in the presence of PPBQ—
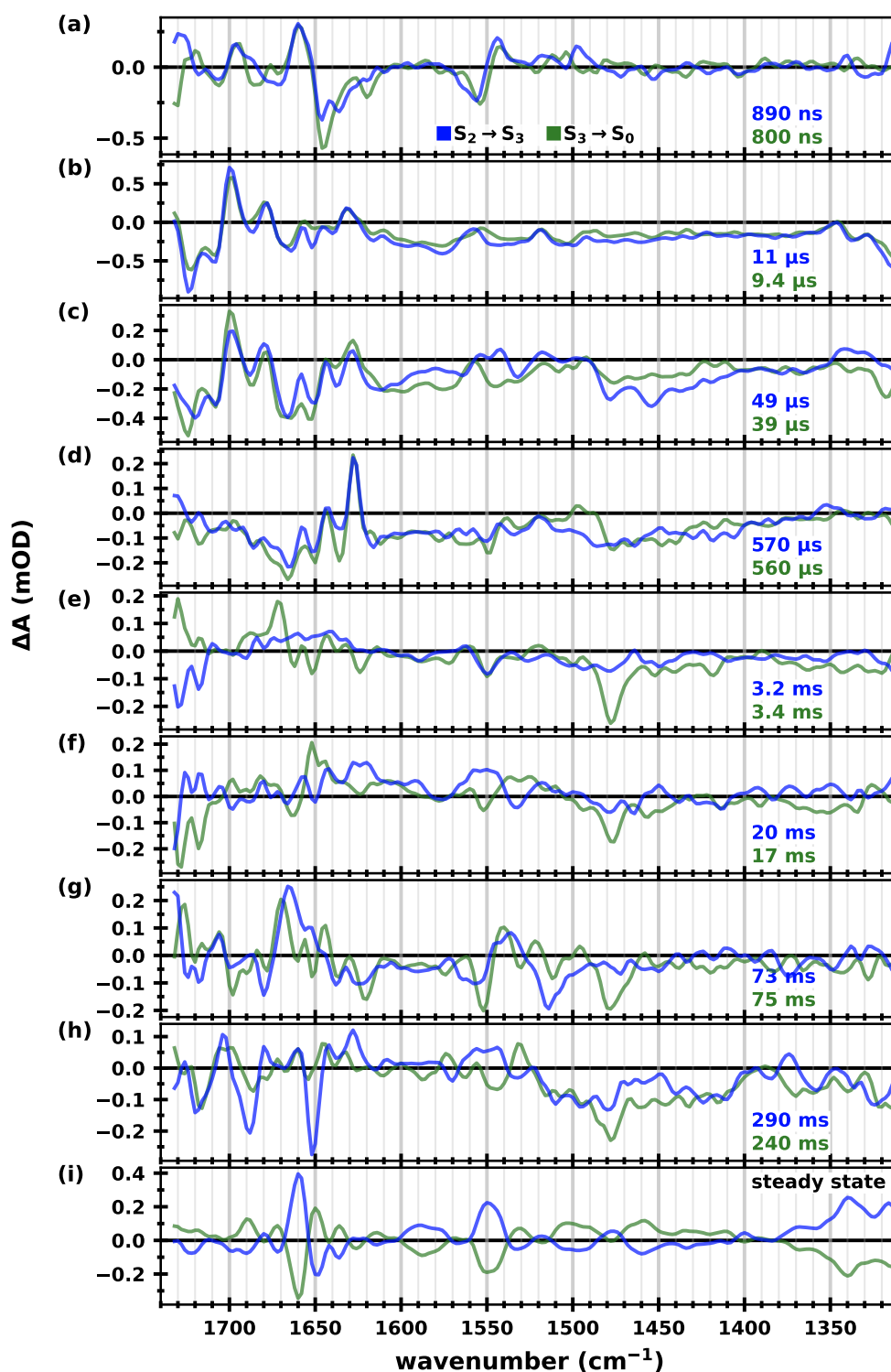
Figure 4.12: Decay associated spectra of Mn depleted spinach PSII. (a–h) DAS of the S$_2$→S$_3$ (*blue*) and S$_3$→S$_0$ (*green*) transition from fitting the spectral data shown in Fig. 4.11 to a sum of eight exponentials and an offset (Eq. 2.7) in the range from 100 ns to 800 ms. **(i)** Steady state spectra, obtained by averaging the IR signal between 400–800 ms. The time constants were pre-determined by globally fitting the small set of transients with high S/N shown in Fig. 4.9. The DAS of all four S-state transitions are shown in Fig. A2.4 in the Appendix.

extracts a second electron from Fe^{2+} and becomes a neutral, hydrated plastoquinol, which no longer absorbs around 1478 cm^{-1}.

(f) – (h) The DAS of the 20/17 ms, 73/75 ms and 290/240 ms phases all show contributions of quinone relaxation that are—especially in the slower phases—mixed with other contributions. The slowest phase could be dominated Y_Z^{ox}–Q_A^- recombination.

(i) The steady-state spectra of the $S_2{\rightarrow}S_3$ and $S_3{\rightarrow}S_0$ transition are nearly perfect reflections of each other across the x-axis. The $S_2{\rightarrow}S_3$ spectrum resembles previous FTIR spectra of Fe^{2+}/Fe^{3+} (Berthomieu and Hienerwadel, 2001; Takahashi et al., 2010), implying that the $S_3{\rightarrow}S_0$ transition thus resembles Fe^{3+}/Fe^{2+}. This is in perfect agreement with the expectation that—in presence of PPBQ—the non-heme iron is oxidized to Fe^{3+} during odd S-state transitions and reduced back to Fe^{2+} during even S-state transitions (Petrouleas and Diner, 1987).

For facilitated comparison with previously published spectra, some of the above discussed spectra are shown again in a slightly different way (and with labeled peaks) in Fig. 4.13, enabling direct comparison with $P680^+$/P680, Q_A^-/Q_A and Fe^{2+}/Fe^{3+} spectra. The $P680^+$/P680 spectrum (Fig. 4.13a) strongly resembles the FTIR spectrum on spinach PSII published by Okubo et al. (2007): while the amplitude ratios are not show some differences, all major peak positions are near identical. The absence of clear peaks between 1492 and 1346 cm^{-1} is also found in both spectra. The following small differences were noticed:

(i) A small, but clearly discernible peak at 1600 cm^{-1} (Okubo et al., 2007; Nagao et al., 2017b) appears rather as a shoulder of a broad peak in Fig. 4.13a.

(ii) A small side-peak was previously reported around 1540 cm^{-1}, which here appears as part of a broad peak around 1536 cm^{-1}.

The peaks of the here presented Q_A^-/Q_A spectrum (Fig. 4.13b) are for most parts also found in previously reported FTIR spectra (Berthomieu et al., 1990; Noguchi et al., 1999; Suzuki et al., 2005a; Remy et al., 2004), although their relative amplitudes vary strongly (even between the aforementioned FTIR spectra). Some notable differences were nevertheless detected:

(i) The small peaks at 1452 and 1500 cm^{-1} in Fig. 4.13b are upshifted to 1455–1458 cm^{-1} and 1503 cm^{-1}, respectively, in all FTIR spectra.

(ii) Most FTIR spectra show clear peaks at about 1614 and 1574 cm^{-1}, as does the here presented spectrum, but the region between those peaks varies strongly between all spectra.

(iii) The FTIR spectra show a peak around 1720 cm^{-1}, which significantly more pronounced than the peak at 1722 cm^{-1} in the here presented DAS. The region between 1698–1722 cm^{-1} does not agree well with the FTIR spectra (but also again shows some variability between the three FTIR publications).

Comparing the Fe^{2+}/Fe^{3+} spectrum (Fig. 4.13c) to FTIR spectra published by Berthomieu and Hienerwadel (2001) and Takahashi et al. (2010) again revealed strong similarities, i.e. including the characteristic broad peak around 1588 cm^{-1} and the strong peaks at 1550 cm^{-1} (found at 1552 cm^{-1} in the FTIR spectra), 1660 cm^{-1} and 1340 cm^{-1}. Careful comparison revealed the following differences:

(i) The broad minimum at 1498 cm^{-1} features a small peak (maximum) in the FTIR spectra.

(ii) At 1720 cm^{-1} the FTIR spectra show small maxima instead of a minimum.
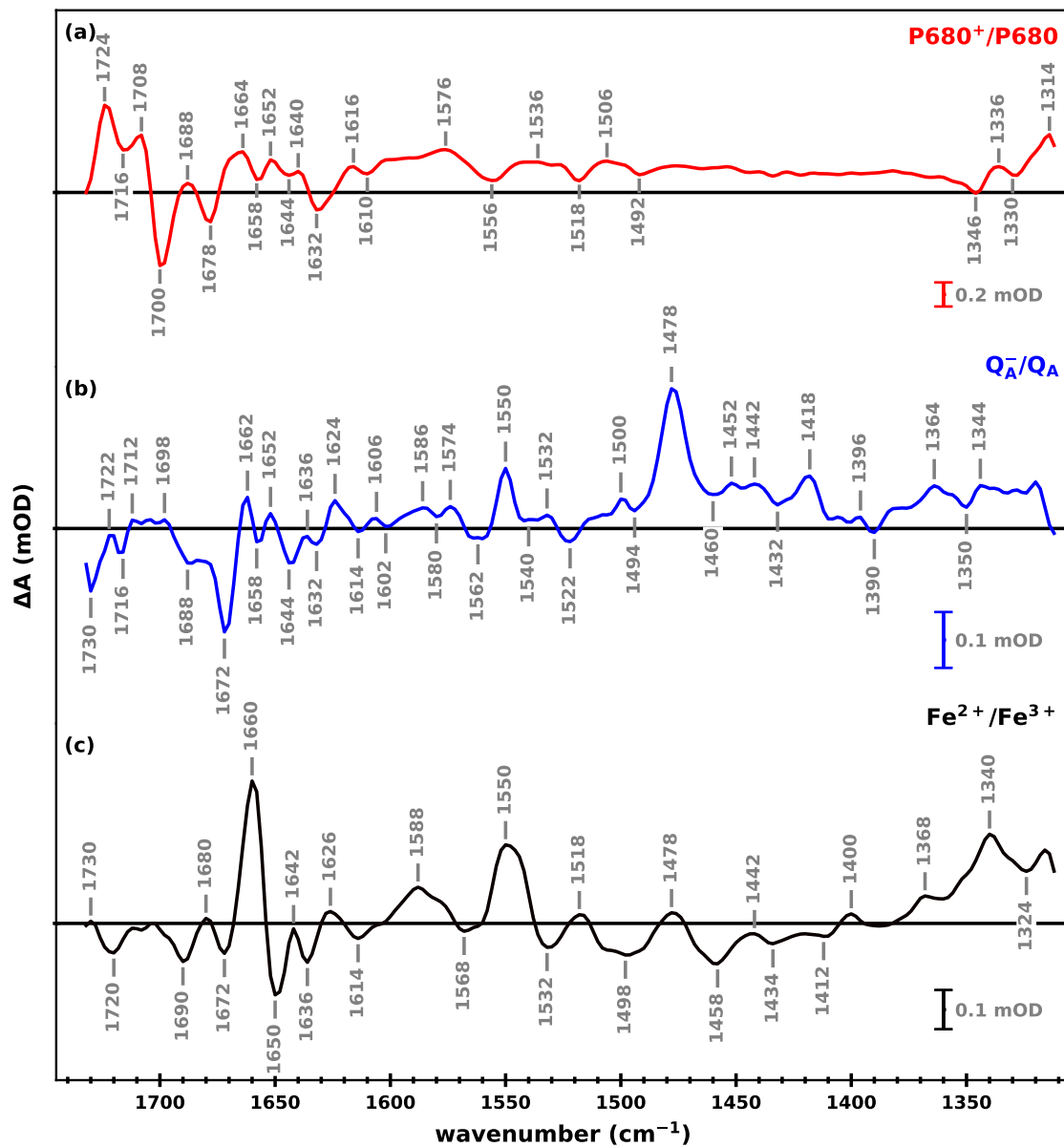
Figure 4.13: Spectra of Mn depleted spinach PSII related to P680$^+$/P680, Q$_A^-$/Q$_A$ and Fe^{2+}/Fe^{3+}. (a) Decay associated spectra of the ~10 μs component shown in Figs. 4.12 and A2.4, averaged over all four S-states and vertically inverted. This spectrum shows great similarity with previously reported P680$^+$/P680 FTIR spectra. **(b)** Averaged decay associated spectra of the 3.4 ms component of the S$_1$→S$_2$ and S$_3$→S$_0$ transition shown in Figs. 4.12 and A2.4, vertically inverted. This spectrum shows great similarity with previously reported Q$_A^-$/Q$_A$ FTIR spectra. **(c)** Steady-state spectra averaged over all four S-states; the spectra of the S$_1$→S$_2$ and S$_3$→S$_0$ transition were inverted before averaging. This spectrum shows great similarity with previously reported Fe^{2+}/Fe^{3+} FTIR spectra.

The FTIR spectrum by Berthomieu and Hienerwadel (2001) is somewhat noisy around the amide I region, but the here presented DAS matches quite well with the amide I region as published by Takahashi et al. (2010).

A direct comparison of transient absorption changes of Mn depleted and intact PSII at 1478 cm^{-1} (Fig. 4.14b) reveals that acceptor-side kinetics show a similar behavior in both
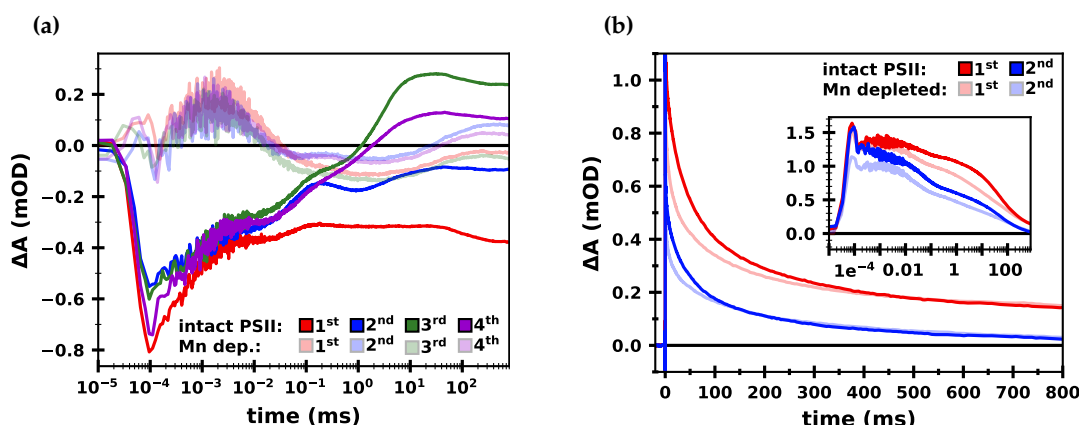
Figure 4.14: Comparison of flash-induced IR transients of intact and Mn depleted spinach PSII. (a) IR difference absorption at 1544 cm^{-1} of intact (*opaque colors*) and Mn depleted PSII (*transparent colors*) after the first (*red*), second (*blue*), third (*green*) and fourth (*purple*) excitation flash. **(b)** IR difference absorption at 1478 cm^{-1} following the first two excitation flashes. The inset shows the same data, but on a semi-logarithmic scale. The shown data is non-smoothed and not deconvolved.

samples. Differences likely origin from (a) altered P680 reduction kinetics, which are slowed in Mn depleted PSII (Haumann et al., 1997) and (b) from altered Q_A^-/Q_A recombination: It was found that the mid-point potential of Q_A^-/Q_A is increased in inactivated PSII (Krieger et al., 1995), limiting forward electron transfer and increasing the rate of recombination (this was however challenged by Kato and Noguchi (2022)).

Comparing the transient absorption changes at 1544 cm^{-1}, on the other hand, shows strong differences between intact and Mn depleted PSII: While intact PSII starts with an initial strongly negative signal, Mn depleted PSII shows a slightly positive initial difference absorbance. The final, steady-state values are completely different between the two sample types.

Clearly the differences between intact and Mn depleted PSII are much more pronounced at some wavenumbers than at others. Double difference spectra of intact minus Mn de-
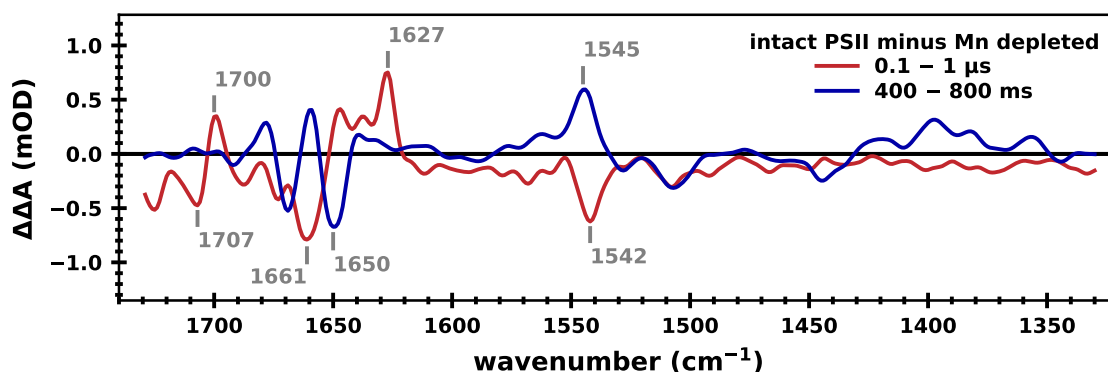

Figure 4.15: Double difference IR spectra of the $S_3 \rightarrow S_0$ transition of intact and Mn depleted spinach PSII. The spectrum of Mn depleted PSII averaged between 0.1–1 µs and 400–800 ms was subtracted from equivalent spectra of intact PSII, resulting in two double difference spectra (*red* and *blue*, respectively).

pleted PSII at two different time points are shown in Fig. 4.15, revealing that at 1544 cm^{-1} the differences are indeed especially large. The amide I region is also strongly affected by Mn depletion. The Mn depletion procedure not only removes the Mn_4CaO_x cluster, but also some of the extrinsic protein subunits (see also Chapter 3.4); as amide I modes are sensitive to secondary structure elements, this may contribute to the differences between intact and Mn depleted PSII around 1650 cm^{-1}.

Overall, the time-resolved spectral data set of Mn depleted spinach PSII exceeded expectations in its information content: From a single global fit across the available spectral range, two DAS were obtained that clearly reflect $P680^+/P680$ and Q_A^-/Q_A spectra, while the steady-state spectra clearly reflect Fe^{2+}/Fe^{3+} spectra. In contrast, spectra of these three cofactors have previously been measured with FTIR by applying three separate sophisticated measurement protocols.

Comparing transients as well as spectra between Mn depleted and intact PSII furthermore informs of possible changes in the IR signal that may occur when the donor-side is damaged, which will aid the interpretation of results in subsequent chapters.

4.5 Spinach PSII Membrane Particles: Does the Preparation Affect the Data?

Our spinach PSII membrane particles are prepared from store-bought fresh spinach leaves as described in Chapter 3.1. Different preparation batches are made from different plants, grown under different conditions depending on the time of the year and other factors outside of our control. In this chapter we will investigate whether samples from different preparation batches give the same results in time-resolved IR spectroscopy.

Experimental Details
Time-resolved IR experiments were performed on four different spinach PSII samples; all experiments were done in pH 6.2 (buffer 2 in Table 3.4) and at 10 °C. Samples from preparation batches 376 and 400 showed a O_2-activity of about 950 µmol O_2/(mg Chl)/h, while batches 388 and 416 showed an activity of about 1100 µmol O_2/(mg Chl)/h (Table 3.2). Exogenous electron acceptor PPBQ was added to all samples and every sample spot was pre-flashed twice before the first measurement. All data was deconvolved into pure S-state transitions (assuming a starting population of 85% S_1 and 15% S_0) to allow for better comparison despite possible miss factor differences.

Results and Discussion
Before comparing results from different PSII preparations, first the reproducibility of data of the *same* batch needs to be assessed. Figure 4.16 shows IR transients ($S_3{\rightarrow}S_0$) of spinach PSII 416 at several wavenumbers of six independent measurements. Visual inspection reveals that there is some variability between different measurements: The millisecond rise-phase that is likely connected to the ET event leading to O_2 evolution varies in its amplitude at 1384, 1395 and 1544 cm^{-1}; in one data set at 1384 cm^{-1} this phase is only half as strongly pronounced as in the other measurements.

At 1478 cm^{-1} there is also some variability and one transient (*red*) stands out from the others (also compared to the transients shown in Fig. 4.17). At the other wavenumbers the kinetics (if not their amplitudes) appear to be reproducible.

Figure 4.17 shows transients at the same four wavenumbers measured on PSII samples from different spinach preparations. The variability at 1384 and 1395 cm^{-1} is similar to that of independent measurements of the same sample batch; the variability at 1478 cm^{-1} is
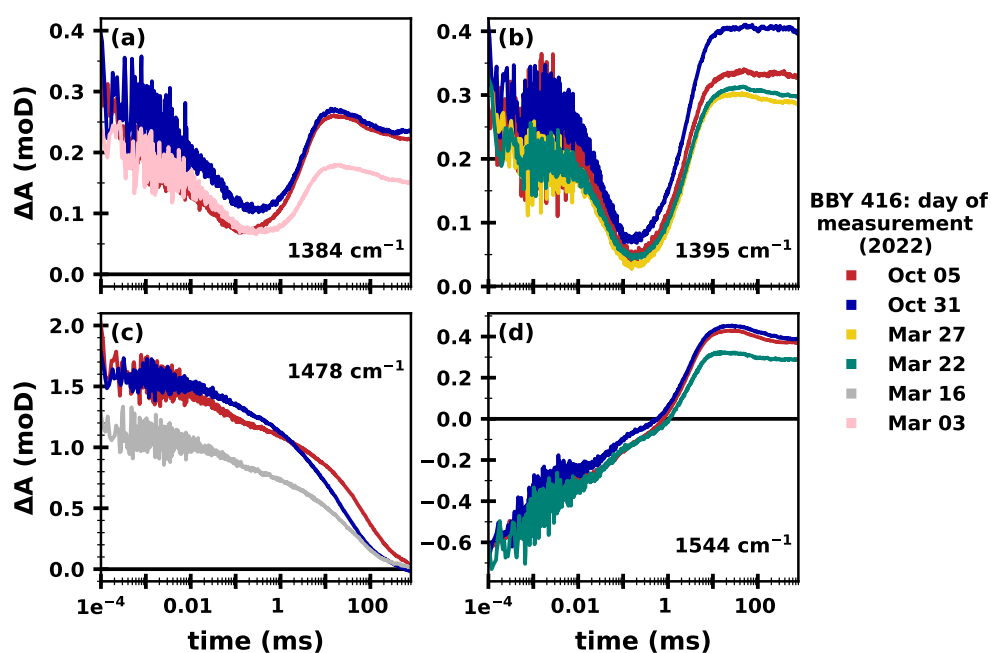
Figure 4.16: IR difference transients of repeated measurements of spinach PSII membranes of the same preparation. Transients showing the $S_3 \rightarrow S_0$ transition at 1384, 1395, 1478 and 1544 cm^{-1} measured on different days but on the same sample batch.
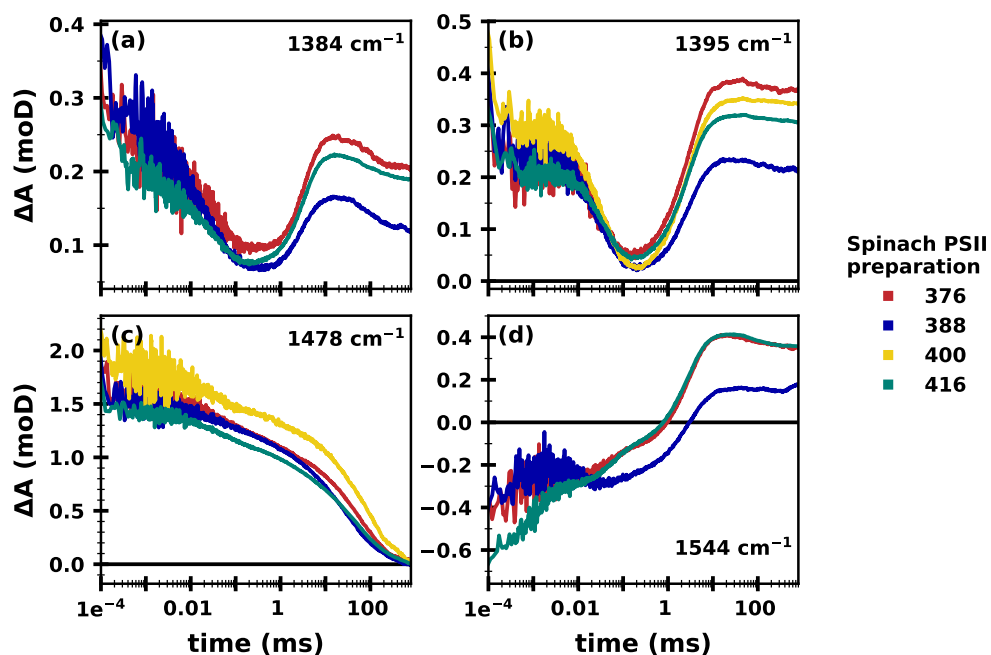
Figure 4.17: IR transients of the $S_3 \rightarrow S_0$ transition of spinach PSII membranes from different preparations. The IR difference absorption is shown at 1384, 1395, 1378 and 1544 cm^{-1} for PSII samples of four different preparations (numbered 376, 388, 400, 416). For each sample preparation, the data was averaged over all data acquired at a given wavenumber.

actually *smaller*. This leads to the conclusion that the red curve in Fig. 4.16c is an outlier, possibly due to an issue with the electron acceptor used that day.

Figure 4.18: IR difference spectra of the $S_3 \rightarrow S_0$ transition of spinach PSII membranes from different preparations. The spectral data sets are shown averaged between **(a)** 0.1–1µs and **(b)** 700–800 ms. Spectra of preparation 376, 388 and 416 are shown in red, blue and green, respectively. All spectral data sets were deconvolved assuming a miss factor of 8% and a starting population of 85% S_1 and 15% S_0.

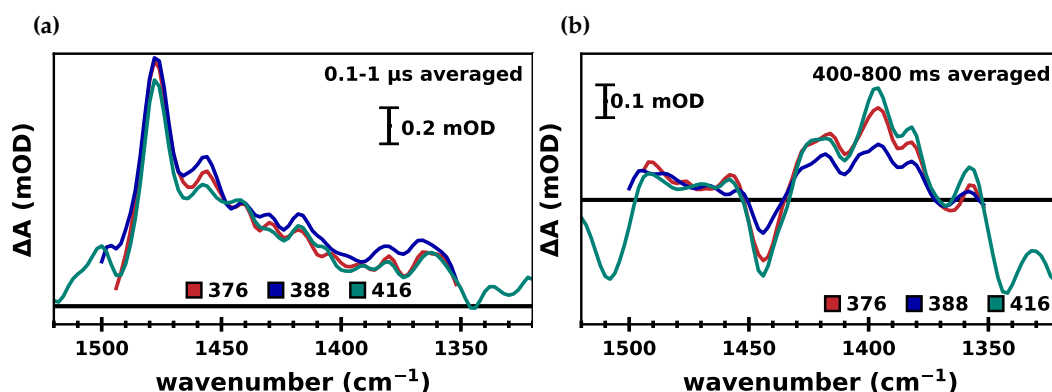The transients at 1544 cm^{-1} show not only variability in the amplitude, but also in the shape of the curves. Interestingly, samples 376 and 416 show the same amplitude of the millisecond-rise phase, and yet show distinctly different behavior between 0.1–1 µs. As we saw in the previous Subchapter, Mn depleted PSII units have a strong influence on the shape of the transient at 1544 cm^{-1}, thus it is well possible that the differences we see here are due to varying amounts of broken centers.

For three of the samples, time-resolved spectral data sets were acquired from 1350-1500 cm^{-1} (Fig. 4.18). The initial spectra (averaged between 0.1–1 µs) look very similar, both in peak position and amplitude. The steady-state spectra also exhibit mostly identical peak positions, but the amplitudes of sample 388 are mostly smaller than in the other two samples. Considering the variability of sample 416 (Fig. 4.16) this may simply have been due to poor sample handling or other experimental factors affecting the data that day.

All in all, the here presented data show that different spinach PSII membrane particles (importantly all with high O_2 evolution activity) result in comparable IR difference transients and spectra. The amplitudes of the kinetics may however be affected by the preparation or the day-to-day handling of the sample. At some wavenumbers (e.g. around 1544 cm^{-1}) the IR data may be more prone to exhibit variability than at others, which is possibly connected to the wavenumber-dependent influence of Mn depleted PSII units on the data (Fig. 4.15).

4.6 Deconvolving Transients into Pure S-State Transitions—Comparison of Different Approaches

As the S-state transitions are not 100% efficient, flash-induced data sets do not correspond to merely one transition but rather a mixture of several. Furthermore, while the S_1 state is the most dark-stable state, a 100% S_1 starting population is often not a realistic assumption (strongly depending on the experimental conditions). In photosynthesis research a commonly used solution is to attempt a deconvolution of the flash-data into data corre-

sponding to pure S-state transitions; the mathematical basis for such an approach is given in Chapter 2.3.3.

What determines the miss factor? It was found that it is the acceptor-side that is rate limiting at high flash frequencies Shevela and Messinger (2012): when using PPBQ as an exogenous electron acceptor, the O_2 production was not affected when varying the flash frequency between 1 and 30 Hz. PSII units with e.g. altered Q_B binding sites however still contribute to the miss factor by leading to $Q_A^-/P680^+$ recombination. In fully functioning PSII centers, in which acceptor-side limitations are ruled out, there is nevertheless still a miss factor, which was found to be S-state dependent (Han et al., 2022).

In this section we will look at some different options during the convolution approach and see how they affect the data.

Experimental Details
Spinach PSII membrane particles (batch 416) were prepared for IR experiments as described in Chapter 3.5.1. The measurements were done at 10 °C and in pH 6.2. As the first flash often induces some kinetics that are exclusive to the first flash transient and are thus not
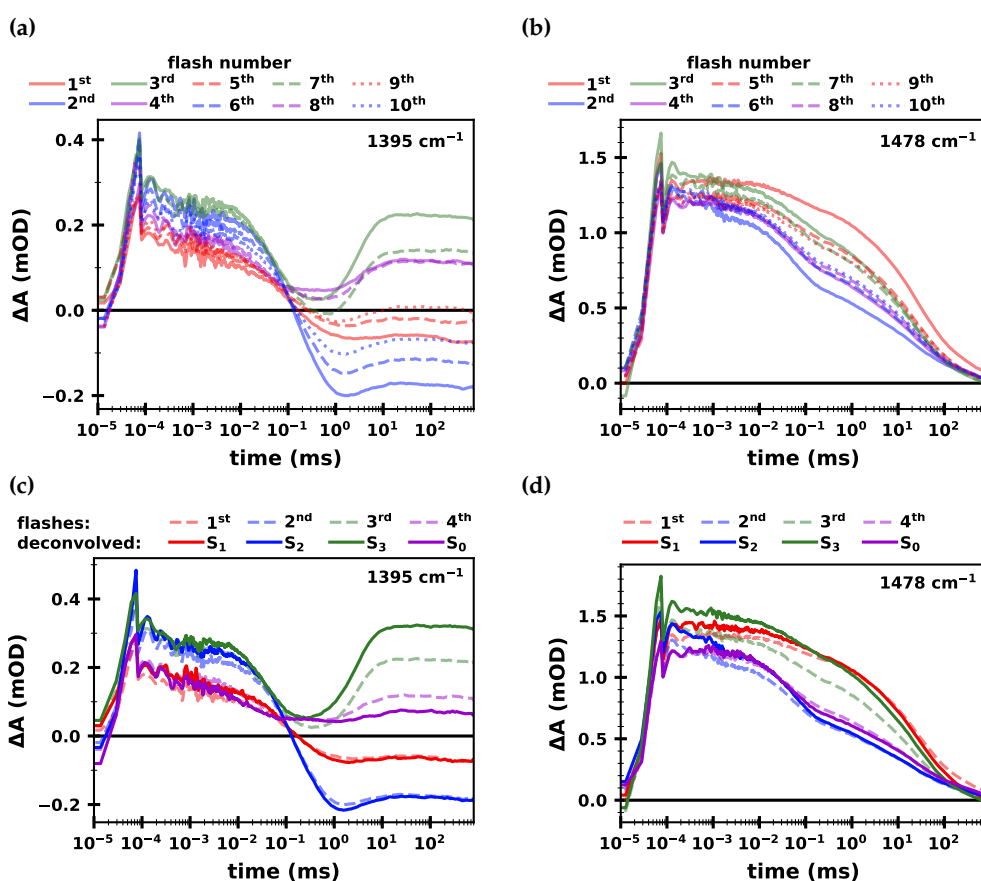
Figure 4.19: Comparison of the flash-transients prior to and after deconvolution. Transients following 10 consecutive excitation flashes at **(a)** 1395 cm^{-1} and **(b)** 1478 cm^{-1}. **(c–d)** Direct comparison of transients following the 1st (*red*), 2nd (*blue*), 3rd (*green*) and 4th (*purple*) excitation flash (*transparent dashed lines*) with transients corresponding to the deconvolved S-states (*solid opaque lines* of the same color). The deconvolution was done assuming an initial population of 100% S_1.

necessarily connected to a functional $S_1 \rightarrow S_2$ transition, the first flash data is not considered by the deconvolution algorithm in the here shown data. Whether or not omission of the 1st flash has a large effect is strongly dependent on the data set.

Results and Discussion

Two sets of 10 consecutive flash-induced transients (Fig. 4.19a and b) make up the data sets that will be deconvolved in different ways in the following. Figure 4.19c and d shows transients at 1395 and 1478 cm^{-1} before and after deconvolution when assuming a starting population of 100% S_1. While the first and second flash transients look quite similar to their deconvolved counterparts, the $S_3 \rightarrow S_0$ transients is strongly affected by the deconvolution; at 1395 cm^{-1} the amplitude of the millisecond rise phase is significantly larger after deconvolution.

Figure 4.20 shows different deconvolution approaches of the data at 1395 cm^{-1} (colored lines) together with the basic approach of assuming a starting population of 100% S_1 and

Figure 4.20: S-state transients resulting from different deconvolution approaches of a spinach PSII data set at 1395 cm^{-1}. **(a)** Deconvolution assuming an S-state independent miss factor of 8% with a 100% S_1 starting population (*black*) or a starting population of 90% S_1 and 10% S_0 (*colored lines*). **(b)** Deconvolution assuming a 100% S_1 starting population and S-state independent miss factor of 8% (*black*, same as in a) or a miss factor of 28% in the $S_2 \rightarrow S_3$ transition and a miss factor of 0% for all other transitions (*colored lines*). **(c)** Same as (b), but the misses are assumed to be observable. **(d)** Transients when assuming an S-state dependent miss factor of 7, 12, 3 and 8% for the S-state transitions $S_1 \rightarrow S_2$, $S_2 \rightarrow S_3$, $S_3 \rightarrow S_0$ and $S_0 \rightarrow S_1$, respectively, and a 100% S_1 starting population.

an S-state independent miss factor (black lines). When assuming a starting population of only 90% S_1 and 10% S_0, the amplitude of the millisecond rise phase of the $S_3 \rightarrow S_0$ transition becomes even more pronounced (colored lines in Fig. 4.20a). Instead assuming (again with a starting population of 100% S_1) that all transitions are 100% efficient except for the $S_2 \rightarrow S_3$ transition (Fig. 4.20b) also results in a larger millisecond rise phase in $S_3 \rightarrow S_0$, but additionally the amplitude of the $S_2 \rightarrow S_3$ transient becomes overall larger. (Note that the sum of the miss factors of all S-state transitions is always around 30%.) Assuming a miss factor only in the $S_1 \rightarrow S_2$ transition, the millisecond rise of the $S_3 \rightarrow S_0$ transition becomes even more pronounced (*not shown*)—but that assumption goes against all previously reported findings in literature. This observation may serve as words of caution against blindly using an arbitrary—aim such as to maximize the amplitude of a certain phase—as a score to determine the best deconvolution approach.

So far we have assumed that misses, i.e. unsuccessful S-state transitions, do not give an IR difference signal. If we assume the opposite together with a 28% miss factor of the $S_2 \rightarrow S_3$ transition (Fig. 4.20c) the amplitudes of the $S_2 \rightarrow S_3$ transition appear less enhanced. For this approach the definition of the observation matrix was altered to be identical to the transition matrix (see Equations 2.3 and 2.5).

Assuming completely visible or invisible misses are both simplifications: During a miss-event, initial charge separation will still take place in most cases, but then lead to recombination rather than forward electron transfer. So in reality, the IR difference signal of a miss will probably look similar to a successful transient in the early nanosecond to microsecond time range, but not at later times.

The data in Fig. 4.20d was deconvolved assuming S-state-dependent miss factors of $\alpha_1 = 10\%$, $\alpha_2 = 16\%$, $\alpha_3 = 4\%$ and $\alpha_0 = 11\%$, which corresponds to the distribution of miss factors as reported by Han et al. (2012) for their EPR data at 20 °C (they reported somewhat higher miss factors; the numbers used here were scaled down to a total miss factor of about 30%). The deconvolved transients obtained with this approach look nearly identical to the transients obtained when assuming a miss factor of 8% in all S-state transitions. The same is true when using the miss factors determined at 1 °C of the same study (*not shown*).

Figure 4.21a shows the S-state transients at 1478 cm^{-1} when assuming an S-state independent miss factor and invisible miss events, i.e. events that do not give an IR difference signal. The transients look nearly the same when instead assuming the misses are visible (Fig. 4.21b); merely the amplitudes are smaller in all transients, as there is now no need to compensate for an invisible contribution.

When assuming S-state dependent miss factors (Figure 4.21c and d), assuming invisible or visible miss events has a larger effect: The deconvolved transients obtained from assuming invisible misses (c) shows a less clear period-of-two behavior in the early region of the transients, while deconvolution assuming visible misses (d) produces transients with a slightly poorer period-of-two behavior in the millisecond region of the transients. This is in line with the notion that unsuccessful S-state transitions are likely to undergo charge separation as well as the first steps along the acceptor-side electron pathway, but then, at least in parts, lead to backward electron transfer and recombination and thus they are in part visible and in part invisible in the IR transients.

Estimation of S-State-Dependent Miss Factors?
The S-state-dependent miss factors used here were obtained either by fixing all but one to zero or by fixing them to values from literature. One may ask: why not try to estimate

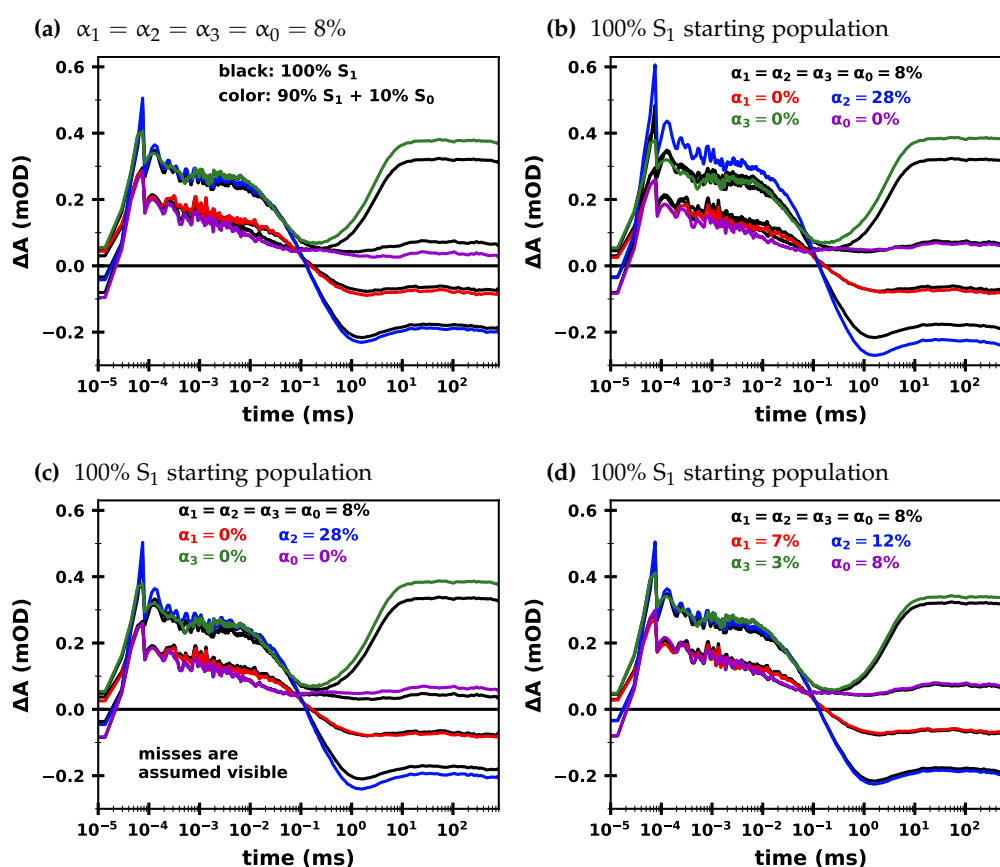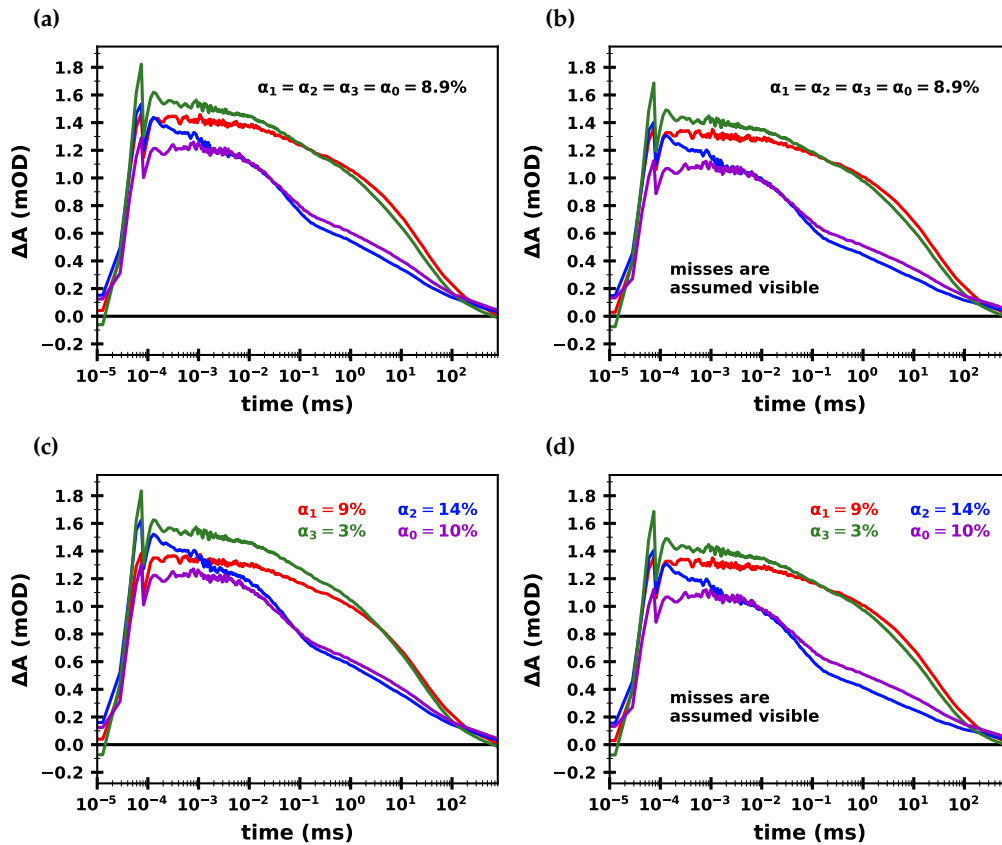**Figure 4.21: S-state transients resulting from different deconvolution approaches of a spinach PSII data set at 1478 cm^{-1}.** In all approaches a 100% S_1 starting population was assumed. **(a)** Transients when assuming an S-state independent miss factor of 8%. **(b)** Same as in (a), but the misses are assumed to be observable. **(c)** Transients when assuming an S-state dependent miss factor of 9, 14, 3 and 10% for the S-state transitions $S_1{\to}S_2$, $S_2{\to}S_3$, $S_3{\to}S_0$ and $S_0{\to}S_1$, respectively. **(d)** Same as in (c), but the misses are assumed to be observable.

the S-state dependent miss factors by a minimization approach? This unfortunately is not easily done, as the minimization score is the difference between the flash transients and the simulated flash transients. The simulated flash transients are obtained from applying the determined miss factor(s) to the deconvolved data, i.e. effectively reversing the deconvolution. What determines how well the simulated transients match the original data is the sum of all miss factors rather than the miss factors of the individual transitions and thus minimization will not find a unique solution. A mathematical discussion of this issue has been published by Lavorel (1976).

Estimation of the Starting Population?
Long-term dark-adapted PSII centers should be exclusively in the dark-stable S_1 and S_0 states, as the S_2 and S_3 states decay to S_1 on the seconds to minutes time scale due to reduction by Q_B^- (Robinson and Crofts, 1983) and/or reduction by Y_D (Vass and Styring, 1991; Styring and Rutherford, 1987). Our pre-flashing protocol of two flashes and subsequent dark adaptation of an hour should thus give us a 100% S_1 starting population. Our flash protocol of 16 consecutive flashes, assuming a miss factor of 8%, should lead to 13% S_0, 48% S_2 and 2.6% S_3, of which the latter two will decay back to $S_1{\to}S_2$ within minutes.

93

At pH 6.2, Y_D^{ox} reduction by S_0 has a half-life of about 12 min, i.e. a time constant of about 17 min (Vass and Styring, 1991), and thus $S_0 \rightarrow S_1$ should decay to 3% of its initial population within an hour. After one hour the overall S_0 population should thus be less than 0.5%. Hence our flash protocol should in theory allow for a nearly full dark adaption back to 100% S_1. This however requires Y_D to be available in its oxidized form. Furthermore, some scattered light from neighboring spot excitation may possibly also contribute to a persistent S_0 population. Carefully planned IR experiments with varied dark adaptation times could give further insight.

Can the starting population P_0 be estimated by a minimization approach? As described briefly in Chapter 2.3.3, P_0 influences the estimation of the pure S-state transients, but its influence is basically reversed when flash-transients are simulated from the S-state transients, and thus the minimization score $\sum (A_{mes} - A_{sim})^2$, determined by the flash-transients A_{mes} and the simulated flash-transients A_{sim}, is independent of P_0. In data from e.g. oxygen polarography experiments, which gives only a signal in the $S_3 \rightarrow S_0$ transition, the situation is different and P_0 has a direct influence on the minimization score (see Chapter 2.3.3). If we can identify a signal or kinetic phase in the IR data that is exclusive to one S-state transition and zero in all others, an estimation of P_0 can be attempted by minimizing the phase in all other S-state transitions. A possible candidate would be the millisecond-rise phase of the $S_3 \rightarrow S_0$ transition at wavenumbers around 1395 cm^{-1}. An attempt at minimizing the amplitude of this phase by varying P_0 was made, but the results varied greatly depending on the data set (between 75-95% S_1 and 25-5% S_0; *not shown*). This approach is, however, revisited in Chapter 5.

Differences between Different PSII Variants?

Isgandarova et al. (2003) found that $S_0 \rightarrow S_1$ oxidation by Y_D^{ox} was slowed about four times in *T. vestitus* compared to spinach thylakoids (at 20 °C). The situation in *Synechocystis* sp. PCC 6803 has—to our knowledge—not been studied and is thus unclear. As the miss factor has been observed to be higher in *Synechocystis* sp. PCC 6803 core particles than in spinach PSII membranes (14% vs. 8%, see Chapter 6), the S_0 population following a burst of 16 flashes will also be higher. An S_0 starting population thus seems likely in both *T. vestitus* and *Synechocystis* PSII core particles.

Conclusions

Isgandarova et al. (2003) found that fitting their O_2 patterns to S-state dependent misses (e.g. $\alpha_0 = \alpha_1 = \alpha_3 = 0$ and $\alpha_2 \gg 0$) gave similar (slightly better) results than fitting to a single (S-state independent) miss factor under the assumption of a non-100% S_1 starting population. Their discussion of many different fit approaches, also considering different Y_D oxidation states, makes it quite clear that the situation is complicated.

The analysis presented in this chapter also shows that it is not easy to determine which approach delivers the best results. It is not possible to estimate S-state dependent miss factors by a minimization approach (Lavorel, 1976), and an incorrectly assumed miss factor distribution may introduce artefactual changes in the relative amplitudes (see Figs. 4.20b and 4.21c and d). Thus, in this thesis an S-state independent miss factor will be assumed.

As discussed above, the starting population P_0 cannot be easily determined. Most of the results shown in later chapters of this work were done assuming a starting population of 85–90% S_1 and 15–10% S_0. All analysis was also performed for a 100% S_1 starting population, which always gave comparable results (*not shown*).

4.7   Summary and Conclusions

Some the data presented in this chapter could in itself be evaluated and discussed in much more detail, but such analysis is beyond the scope of this thesis. The main goal of this chapter was merely to support and facilitate the interpretation of the following chapters.

The following key results were discussed:

▷ Long-term stability of spinach PSII membrane particles: When measuring over the course of tens of hours, the miss factor increases over time and the amplitude of the ET event of the $S_3 \rightarrow S_0$ transition decreases. The time constants determined for the PT and ET events of the S-state transitions however are not impaired.

▷ Experiments with addition of PPBQ reveal iron-quinone chemistry; experiments without PPBQ can only undergo a few S-state cycle turnovers and age very quickly.

▷ $P680^+$ reduction kinetics are present in the time-resolved IR data of PSII, most likely throughout the entire wavenumber range covered by the QCL. These background kinetics are important to consider when looking at kinetics faster than $\sim$100 μs. $P680^+$ reduction transients were measured around 1780 cm^{-1} and will be used for background subtraction in some of the following chapters.

▷ IR difference absorption of Mn depleted spinach PSII show a strong period-of-two behavior at most wavenumbers. The transients give insight into possible IR contributions of broken PSII centers. Decay associated spectra of Mn depleted spinach PSII reproduce $P680^+/P680$ (Nagao et al., 2017b; Okubo et al., 2007) and Q_A^-/Q_A spectra (Berthomieu et al., 1990; Noguchi et al., 1999; Suzuki et al., 2005a; Remy et al., 2004); the steady-state spectra strongly resemble Fe^{2+}/Fe^{3+} spectra (Berthomieu and Hienerwadel, 2001; Takahashi et al., 2010).

▷ A comparison of IR transients of different spinach PSII preparations show that the transients are mostly reproducible between different samples. At 1544 cm^{-1}, however, differences were observed—possibly connected to the fact that Mn depleted PSII transients differ strongly from intact PSII transients at this wavenumber.

▷ Different deconvolution approaches for obtaining IR transients relating to pure S-state transitions were discussed. Throughout this thesis, an S-state independent miss factor will be assumed, as well as (mostly) a small S_0 starting population (15–10%) in addition to a predominant S_1 population.

5 | Characterizing the S-State Transitions of Spinach PSII

PSII-enriched spinach membrane particles have served as a model system for photosynthesis research since the 1970s. Compared to cyanobacterial PSII, which requires growing cells over an extended period of time, functional spinach PSII membrane particles are relatively easy and fast to prepare. They can be pushed through many rounds of the S-state cycle—in the presence of an artificial electron acceptor such as PPBQ—making them suitable also for time-costly measurements. (For a detailed overview over the events of the S-state cycle see Chapter 1.5.)

In this Chapter, the S-state transitions of spinach PSII membrane particles are characterized by measurements in H_2O and D_2O-based buffer, allowing for the observation of H_2O/D_2O (H/D) kinetic isotope effects (KIE), as well as measurements at different pH values. The transient absorption changes are fitted to multi-exponential functions to extract time constants. Time-resolved spectral data sets furthermore allow for spectral characterization via global fits resulting in decay associated spectra (DAS).

By applying time-resolved single-frequency IR spectroscopy to spinach PSII membrane particles, this work reproduces and builds upon previous spectroscopic studies.

Following the description of experimental details, we will first take a general look at the H/D KIE, at deuteration-induced band shifts of the steady-state spectra, and at the influence of pH on the flash-data, before looking at the $S_1{\rightarrow}S_2$, $S_2{\rightarrow}S_3$ and $S_3{\rightarrow}S_0$ transitions in detail. The $S_0{\rightarrow}S_1$ transition will not be discussed in detail, as extraction of pure $S_0{\rightarrow}S_1$ data is very difficult with our flash-protocol. To study this transition, other flash protocols are more suitable, e.g. as employed by Shimizu et al. (2018).

5.1 Experimental Details

The spinach PSII membrane particles were extracted from fresh spinach leaves as described in Chapter 3.1. Most of the data shown in this Chapter was measured on Preparation 416, which showed an O_2-activity of 1125 μmol O_2/(mg Chl)/h (Table 3.2). Prior to an IR experiment, the samples were thawed on ice and exchanged into a MES-MOPS-HEPPS measurement buffer (buffer 2 in Table 3.4; some older measurements at pH 6.2 were done in buffer 1, which contains only MES as a buffering agent). While betaine is present in the storage buffer (because of its well-known stabilizing effect on PSII), all measurements were

done in buffers *without* betaine, to avoid contributions from its strong IR absorption bands in the frequency range of interest.

For D_2O samples, the centrifugation temperature was set to 8 °C rather than 4 °C, to avoid freezing of the sample due to the higher freezing point of D_2O. For the same reason, the time the sample was left on ice after the buffer exchange was kept to a minimum. To avoid exchange of D_2O from the sample pellet with H_2O from the humidity in the air, the supernatant was not discarded after the second centrifugation step until shortly before placing the sample onto the CaF_2 plates (as described in Chapter 3.5).

The standard flash-protocol of measuring for 6 s without excitation ("dark signal") followed by 10 saturating excitation flashes per sample spot was employed for all measurements. A flash-induced heat artefact was accounted for as described in Chapter 2.4.1.

The shown transients are averages of at least around 150 and up to 4000 individual flash-induced transients. The time-resolved spectral data sets were obtained by measuring a transient at every 2 cm^{-1} with only about 30 individual transients averaged per wavenumber (thus of significantly lower S/N than most transients shown in the following). The spectral data sets were smoothed by applying a Gaussian smoothing algorithm along the wavenumber axis with $\sigma = 2.5$ and a sliding average algorithm along the time axis with a window size of 10 data points (smoothing was done before fitting the data).

Unless stated otherwise, the data shown in this Chapter was always obtained in H_2O-based buffer at pH 6.2 and at a measurement temperature of 10 °C. Deconvolution of the data into pure S-state transitions was done assuming a starting population of 74% S_1, 14% S_2 and 12% S_0 (see Section 5.1.1); the 1st flash data was omitted by the deconvolution algorithm.

Note that the buffering range of the buffer 2 is pH 5.5–8.7; the precision of the pH of the measurements at pH 4.6 is thus uncertain.

Strategy for Quantitative Data Analysis
When fitting the transients of the entire available spectral range ($\sim$1800–1300 cm^{-1}) globally to sums of exponentials, a large number of components is required, *inter alia* because acceptor-side, donor-side as well as $P680^+$ reduction processes contribute. Too many exponential components, however, easily lead to overfitting of the data and thus to meaningless time constants. As this work aims mostly at gaining insight into donor-side processes, the following strategy was applied: For each data set (i.e. each S-state transition in H_2O or D_2O etc.) several high S/N transients were selected that showed strongly pronounced kinetics around time points of expected ET and PT events related to the S-state cycle, while bands with very strong acceptor-side contributions (such as 1478 cm^{-1}) were mostly avoided. The selected transients were then globally fit to a sum of exponentials, i.e. the time constants were constrained to be the same at all wavenumbers. The wavenumber-dependent amplitudes were not treated as fit parameters, but rather determined by matrix inversion. The number of components was chosen such that the residuals indicated an acceptable fit quality, i.e. a mostly uniform distribution around zero. The obtained time constants were later fixed in global fits (of lower S/N spectral data sets) across the entire wavenumber range.

As the $S_1{\rightarrow}S_2$ and $S_3{\rightarrow}S_0$ data are expected to show the same acceptor-side kinetics, the slow $S_1{\rightarrow}S_2$ kinetics can be used for an acceptor-side correction of the $S_3{\rightarrow}S_0$ data. To facilitate this, the acceptor-side time constants were predetermined by fitting the 1st flash data in H_2O locally at 1478 cm^{-1} (see Figs. A3.5 and A3.6 and their accompanying text in

the Appendix) and then fixed in further (global) fits of $S_1 \rightarrow S_2$ data as well as in fits of $S_3 \rightarrow S_0$ data.

5.1.1 Determination of the Initial Dark-Adapted S-State Population

The data in this chapter was initially analyzed assuming a starting dark-adapted population of 85% S_1 and 15% S_0. It was only upon near completion of the chapter that it was recognized that the data clearly show a non-zero S_2 initial population—see Figs. A3.18 and A3.19 and accompanying text in the Appendix.

As the S_2 and S_3 states should readily decay to S_1 in the given one-hour dark-adaptation time window (Robinson and Crofts, 1983; Vass and Styring, 1991; Styring and Rutherford, 1987), this implies a systematic error in the experimental setup: The most plausible explanation is that the sample spots are partly illuminated by excitation flashes meant for other
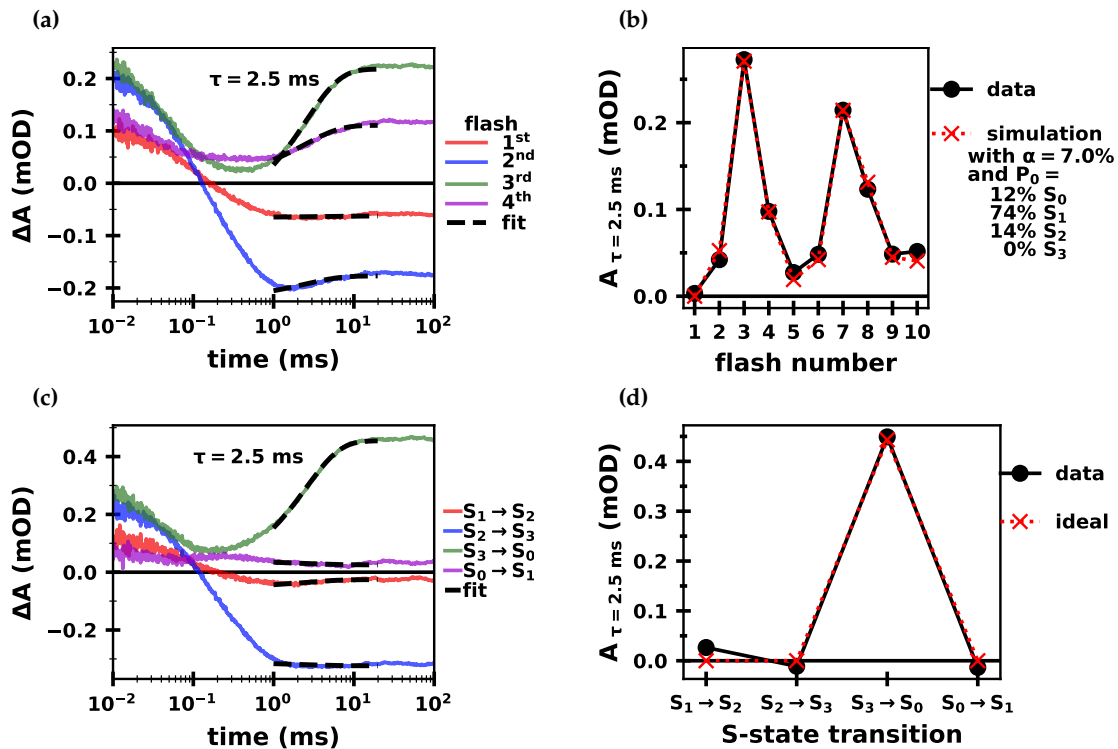

Figure 5.1: Estimation of the dark-adapted initial population P_0 at 1395 cm^{-1}. (a) The first four of the ten flash-induced transients (*colored lines*). Each transient was fit to a single exponential ($\tau = 2.5$ ms) and an offset (fit range 1–20 ms); the resulting fit curves are shown as *black dashed lines*. **(b)** The amplitudes $A(\tau)$ of the fit curves shown in (a) as a function of flash number. This amplitude pattern was deconvolved assuming only the $S_3 \rightarrow S_0$ transition results in a signal (see main text for details), resulting in an estimation of the initial population and the miss factor. By applying the estimated miss factor to the deconvolved amplitudes, the amplitude pattern was simulated (*red crosses*). **(c)** The S-state transients, deconvolved with the miss factor and initial population determined in (b). The four transients were again fit to a single exponential and an offset. **(d)** The S-state-dependent amplitudes (*black circles*) of the exponential fits shown in (c). In a perfect solution, the amplitudes would be zero in all transitions except for $S_3 \rightarrow S_0$ (indicated with *red crosses*).

nearby sample spots, thus significantly reducing their actual dark adaptation times. The measurement protocol thus needs to be revised and adapted for future experiments.

For the here presented data, the starting population P$_0$ was estimated as described in the following, utilizing a data set at 1395 cm^{-1} (pH 6.2). This wavenumber was chosen for its especially small acceptor-side contributions.[30] All ten flash-induced transients were fit between 1–20 ms to a single exponential ($\tau =2.5$ ms) and an offset; the first four transients and fit curves are shown in Fig. 5.1a. The resulting amplitudes A(τ) are shown in Fig. 5.1b and should represent exclusively the events occurring concomitant with oxygen-evolution (assuming acceptor-side contributions are indeed negligible). This amplitude pattern was then deconvolved assuming that only the S$_3\rightarrow$S$_0$ transition results in a signal (see Chapter 2.3.3 for details on the deconvolution procedure), resulting in an estimated miss factor of 7.0% and an initial population of 12% S$_0$, 74% S$_1$ and 14% S$_2$. The S$_3$ population was fixed to zero (otherwise a similar distribution including 2% S$_3$ was found; *not shown*). Note that unlike in all other deconvolution procedures used in this thesis, the 1st flash was *not* excluded in the deconvolution of the amplitude pattern.[31]

Deconvolution of the flash transients with the estimated miss factor and initial population resulted in the S-state transients shown in Fig. 5.1c. Unlike in panel a, the millisecond rising phase is now negligible in all transitions but S$_3\rightarrow$S$_0$. This is also reflected in panel d, which shows the amplitudes of the 2.5 ms phase of the four deconvolved transients.

The here estimated initial population distribution was used for the deconvolution of all data sets in this chapter. This is, of course, a simplified approach, as different data sets may differ from each other with regard to their initial S-state population, especially those measured at different pH values or in D$_2$O. However, the estimation of the initial population P$_0$ is also based on strong assumptions and assuming a different P$_0$ for each individual data set could introduce further bias. For future experiments it is crucial that an initial S$_2$ population is avoided rather than dealt with on the level of data processing/analysis.

5.2   General Effect of pH and H$_2$O/D$_2$O Exchange on the Flash-Data

5.2.1   Effect of pH on Single-Frequency Data

Figure 5.2a–g shows the transients at 1384 cm^{-1} following the first four excitation flashes at increasing pH value from top to bottom. Visual inspection shows that in the pH range between 5.4–7.0, the flash-transients show very clear distinct behavior, indicating (i) that at this wavenumber we see kinetics associated with events of the S-state cycle and (ii) that the cycling efficiency is relatively high (i.e. the miss factor is low). At pH 7.8 the first four flash transients look more similar to each other and at pH 4.6 and 8.6 nearly all S-state dependence is gone. These observations are also reflected in the flash-number dependent steady-state values (Fig. 5.3b): in the pH range of 5.4–7.0 there is a clear period-of-four behavior; at pH 4.6 this period-of-four oscillation is strongly dampened and at pH 8.6 is replaced with a period-of-two oscillation. At pH 7.8 contributions of both oscillations are clearly discernible. 1384 cm^{-1} is in the region of symmetric carboxylate stretching modes

---

[30]This is evident e.g. in Fig. 5.3c, which shows that even at high pH no (or hardly any) period-of-two pattern is discernible at 1395 cm^{-1}.

[31]The first flash is often excluded as it may contain signals exclusive to the first flash (rather than to S$_1\rightarrow$S$_2$), e.g. of non-functional PSII units, and including it in the deconvolution procedure may artificially introduce such signals into the other S-state transients.
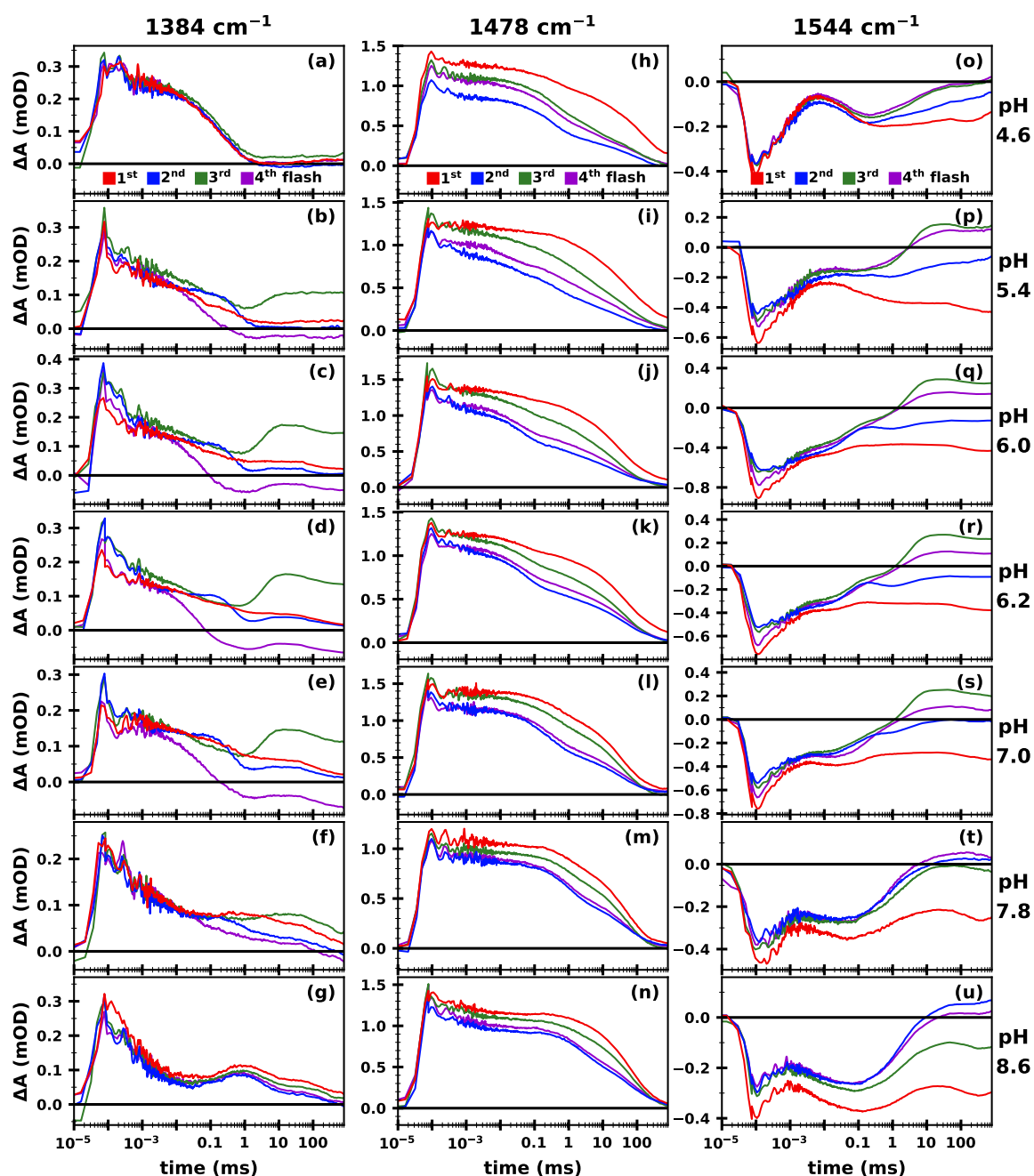
Figure 5.2: IR-difference absorption of four sequential flash-induced transients of spinach PSII at 1384, 1478 and 1544 cm^{-1} in H$_2$O buffer at various pH values. Transient absorption changes at **(a–g)** 1384 cm^{-1}, **(h–n)** 1478 cm^{-1} and **(o–u)** 1544 cm^{-1} following the 1st (*red*), 2nd (*blue*), 3rd (*green*) and 4th (*purple*) excitation flashes are shown from top to bottom at increasing pH values (4.6, 5.4, 6.0, 6.2, 7.0 and 8.6).

($\sim$1450–1350 cm^{-1}) (Larkin, 2018). As the Mn$_4$CaO$_x$ cluster is ligated by several proteinogenic carboxylate groups (see Fig. 1.14 *center*), this region has proven useful for monitoring changes in the OEC (Noguchi et al., 2012; Sakamoto et al., 2017).

Transients at 1478 cm^{-1} (Fig. 5.2h–n) show a clear period-of-two behavior at all measured pH values, although at pH 4.6 a very strong dampening is observed (Fig. 5.3e, f).
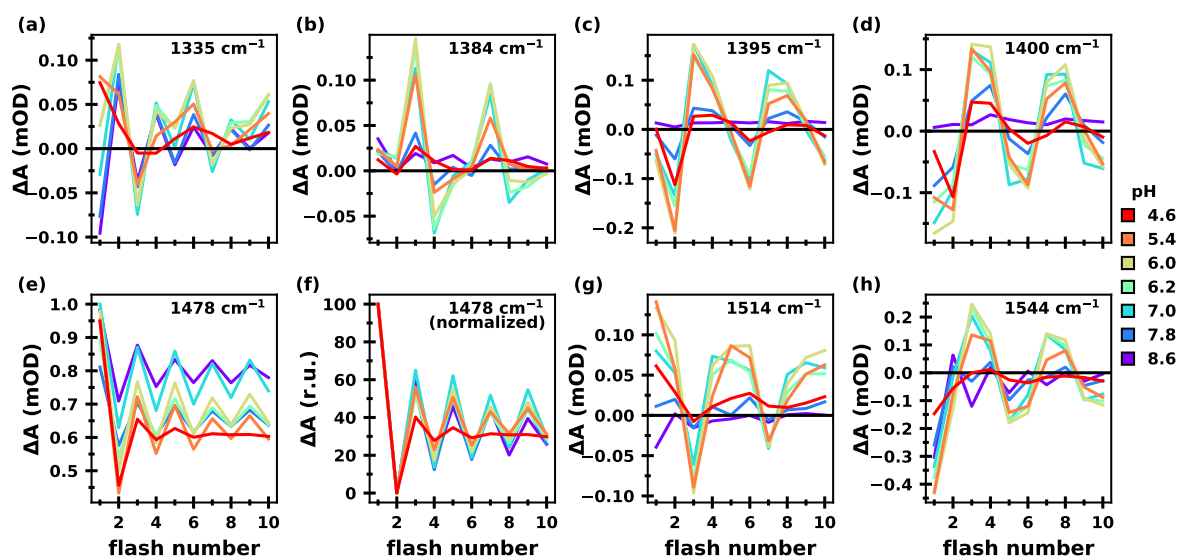
Figure 5.3: Flash-number dependent steady-state IR difference absorption in H₂O-based buffer at different pH values. The steady-state values (400–800 ms) are shown at **(a)** 1335 cm⁻¹, **(b)** 1384 cm⁻¹, **(c)** 1395 cm⁻¹, **(d)** 1400 cm⁻¹, **(g)** 1514 cm⁻¹ and **(h)** 1544 cm⁻¹ for data obtained at seven different pH values between pH 4.6–8.6. **(e)** Flash-number dependent IR difference values at 1478 cm⁻¹ averaged between 10 µs–100 ms. **(f)** The same data as in (e), but normalized and shifted for easier visual comparison.

This wavenumber has been previously assigned to the CO stretching mode of the Q_A^- semiquinone anion (Berthomieu et al., 1990), and the data shown here clearly supports the assignment to acceptor-side reactions. Faster kinetic contributions (<100 µs) contribute significantly to the time-resolved IR difference signal at lower pH values, while slow components dominate the transients at high pH. At pH 8.6. however, a fast component (~1 µs) seems to additionally emerge. An in-depth analysis of acceptor-side kinetics is beyond the scope of this thesis, but could be interesting to revisit in future.

At 1544 cm⁻¹ both the transients (Fig. 5.2o–u) as well as the flash-number dependent steady-state values (Fig. 5.3h) show a clear period-of-four behavior in the pH range of 5.4–7.0. Similarly to the data at 1384 cm⁻¹, this oscillation is strongly dampened at pH 4.6 and is replaced by a period-of-two pattern at pH 7.8 and 8.6. This wavenumber is in the amide II region of protein vibrations (Barth, 2007); H/D exchange measurements on ¹⁵N labeled as well as unlabeled samples confirmed its assignment to peptide backbone vibrations (NH bending coupled with CN stretching) (Noguchi et al., 1995b).

The sub-millisecond behavior of the transients at 1384 and 1544 cm⁻¹ at pH 4.6 (Fig. 5.2a, o) show some similarity to transients of Mn depleted PSII (see Fig. 4.9a, f), which might indicate that a significant portion of the PSII units is damaged at low pH.

The pH dependence of transients at three additional wavenumbers (1335, 1395 and 1514 cm⁻¹) is presented in Fig. A3.2 in the Appendix; the associated flash-number dependent steady-state values (Fig. 5.3a, c, g) resemble the behavior discussed for 1544 and 1384 cm⁻¹.
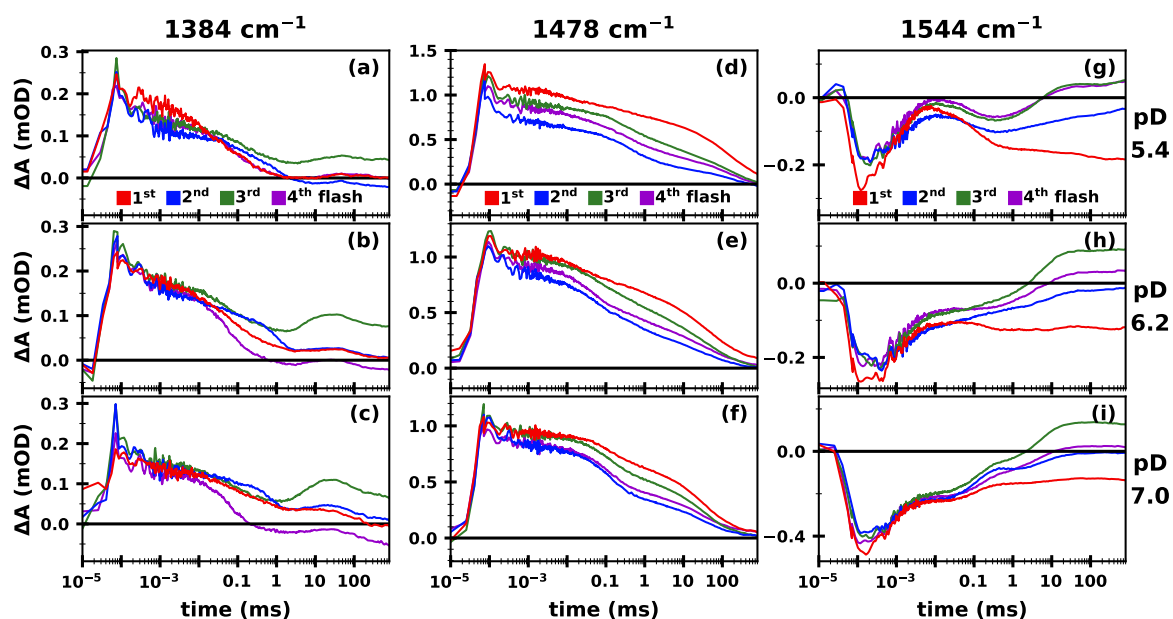
Figure 5.4: IR-difference absorption of four sequential flash-induced transients of spinach PSII at 1384, 1478 and 1544 cm^{-1} in D$_2$O buffer at various pD values. Transient absorption changes at **(a–c)** 1384 cm^{-1}, **(d-f)** 1478 cm^{-1} and **(g–i)** 1544 cm^{-1} following the 1st (*red*), 2nd (*blue*), 3rd (*green*) and 4th (*purple*) excitation flashes are shown from top to bottom at increasing pD values (5.4, 6.2 and 7.0).
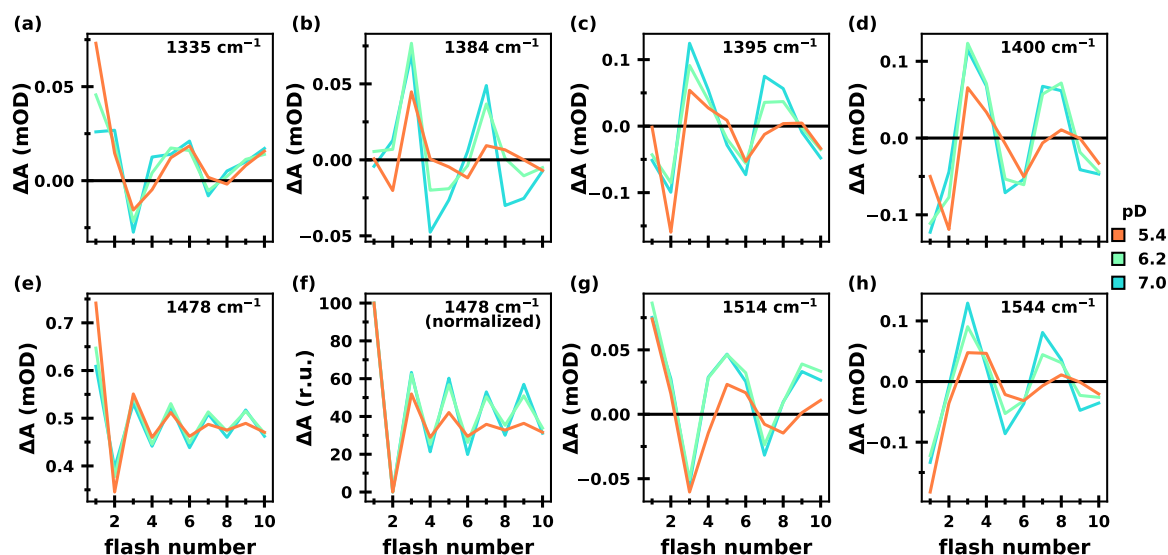
Figure 5.5: Flash-number dependent steady-state IR difference absorption in D$_2$O-based buffer at different pD values. The steady-state values (400–800 ms) are shown at **(a)** 1335 cm^{-1}, **(b)** 1384 cm^{-1}, **(c)** 1395 cm^{-1}, **(d)** 1400 cm^{-1}, **(g)** 1514 cm^{-1} and **(h)** 1544 cm^{-1} for data obtained at three different pD values (5.4, 6.2 and 7.0). **(e)** Flash-number dependent IR difference values at 1478 cm^{-1} averaged between 10 μs–100 ms. **(f)** The same data as in (e), but normalized and shifted for easier visual comparison.

5.2.2   Single-Frequency Data in D$_2$O

Figure 5.4 shows transient IR absorption changes at 1384, 1478 and 1544 cm^{-1} in D$_2$O-based buffer at three different pD values. One first glance, the transients resemble their H$_2$O counterparts. The data at pD 5.4, however, appears more perturbed than the data at pH 5.4; this is confirmed by their more strongly dampened oscillatory pattern of the flash-number-dependent IR difference signal (Fig. 5.5). Careful visual comparison of e.g. Fig. 5.2d to Fig. 5.4b also reveals slowing down of kinetics (e.g. the decay around 0.5 ms in the 2nd flash data slows to more than a millisecond in D$_2$O). This is expected and is termed a kinetic isotope effect (see also Chapter 1.3.3); a quantisation of the observed effect will follow in the subsequent sections.

5.2.3   Dependency of the Miss Factor on the pL

The flash-data obtained at seven different wavenumbers at various pL values[32] in H$_2$O as well as D$_2$O (most of which shown in the above figures) were all deconvolved into pure S-state transitions using the approach described in Chapter 2.3.3. The resulting estimated miss factor of each data set as well as the averaged miss factor at each pH and pD value is shown in Figs. 5.6a and b, respectively.

From the investigated pH range, pH 7.0 appears to result in the lowest miss factor, which is in agreement with a previous FTIR study on *T. vestitus* (Suzuki et al., 2005b). They, however, did not observe an overall strong alkaline inhibition; merely the efficiency of the S$_3$→S$_0$ transition was slightly lower at pH values above 8.0. Both an EPR study on spinach membrane particles (Bernát et al., 2002), as well as a flash-induced oxygen-yield study on spinach thylakoids (Christen et al., 1999), found that the optimal miss factor was around pH 6.5 and both more acidic as well as more alkaline pH values lead to an increased miss factor.

Messinger and Renger (1994) found that the miss factor was lowest at pH 7.0 or 6.5, depending on whether the thylakoids were synchronized to S$_1$Y$_D^{ox}$ or S$_1$Y$_D$. The pre-flash protocol applied to the here presented samples (2 flashes followed by an hour of dark adaptation) should result in a predominant Y$_D^{ox}$ population, which thus agrees with an optimal pH of 7.0. The fact that pH 7.0 is found to be the overall optimal pH (and not just for the measurement directly following the pre-flash treatment) indicates that our flash protocol (10 flashes followed by an hour of dark adaptation) keeps Y$_D$ mostly in its oxidized form.

From the investigated pD values, pD 7.0 also results in the lowest miss factor; however, since no measurements were done at higher pD values, no conclusion for an optimal miss factor can be drawn from this data. A generally higher miss factor in D$_2$O may in part be due to slowed P680$^+$ reduction kinetics, leading to a higher amount of P680$^+$/Q$_A^-$ recombination (Christen et al., 1998; Christen and Renger, 1999).

It is striking that the pL dependency seems much stronger pronounced in D$_2$O than in H$_2$O: while a pH of 5.4 results in a miss factor of only 11 %, a pD of 5.4 results in a miss factor of about 20 %. At pL 6.2 the difference in miss factor is less pronounced (8 vs. 11%) and at pD 7.0 the values are very similar. This is similar to findings by Christen et al. (1999), who found that the miss factor at pL 7.0 was only slightly smaller in H$_2$O than in

---

[32]The pL with L=(H, D) refers to the negative decadic logarithm of the proton (pH) or deuteron (pD) concentration.
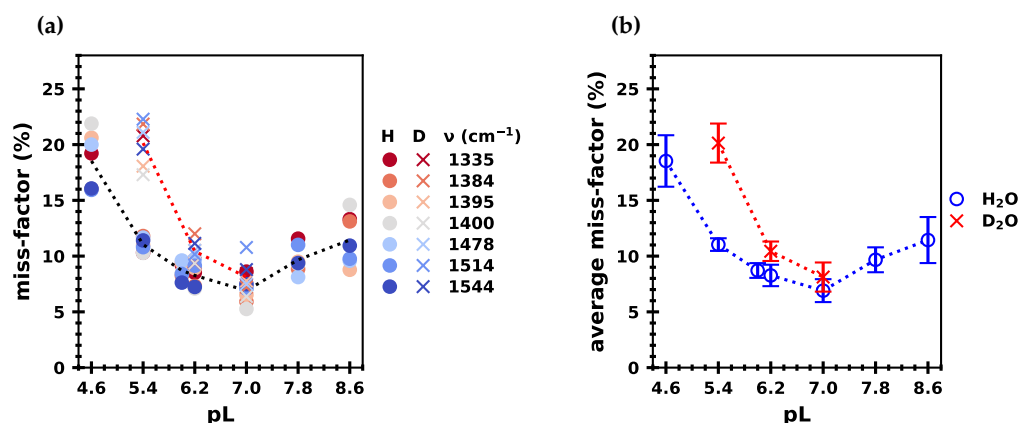
Figure 5.6: Dependency of the miss factor on the pL value. (a) The miss factors for various wavenumbers (indicated by different colors) in H_2O (*circles*) and D_2O (*crosses*) were determined individually by applying a deconvolution algorithm to the flash-induced IR transients. **(b)** The average miss factor and its standard deviation as a function of pL in H_2O (*blue circles*) and in D_2O (*red crosses*).

D_2O; furthermore, they found that the optimal miss factor in D_2O was at pL 7.5, where in fact it was *lower* than the miss factor in H_2O.

As discussed by Zaharieva et al. (2011), inhibition of oxygen evolution at acidic pH values is expected, as H^+ is one of the products of the water splitting reaction and thus at higher H^+ concentration the driving force of the reaction becomes lower. Acidic inhibition is indeed observed in the here presented data, as well as in several previous studies (Zaharieva et al., 2011; Suzuki et al., 2005b; Bernát et al., 2002; Christen et al., 1999). Concerning alkaline inhibition, there is less consensus:

In a delayed fluorescence study employing a pH-jump protocol (Zaharieva et al., 2011), the authors were able to distinguish between inactivation/damage of an S-state and inhibition of the individual S-state transitions. Unlike other studies (Suzuki et al., 2005b; Bernát et al., 2002; Christen et al., 1999), they did not, however, detect any inhibition in the alkaline regime. Thus, based on the results presented here (i.e. the clear period-of-two behavior at high pH values in Fig. 5.3f), as well as the unchanged fluorescence yield arising from $P680^+/Q_A^-$ recombination reported by Zaharieva et al. (2011), we can conclude that the acceptor-side is still fully functioning at high pH values.[33]

However, Fig. 5.3 also shows that e.g. at 1395 cm^{-1}, the flash-dependent steady-state IR pattern is strongly diminished at pH 7.8 and 8.6. In contrast, at 1544 cm^{-1}, the period-of-four behavior is replaced by a clear period-of-two behavior at high pH. Judging from measurements of Mn depleted spinach PSII, acceptor-side kinetics clearly contribute to the IR difference absorption at 1544, but hardly so at 1395 cm^{-1} (see Fig. 4.9 in Chapter 4). The absence of a period-of-four and presence of a period-of-two behavior at high pH in Fig. 5.3h thus suggests that while the acceptor-side remains functional, the donor-side does not cycle and becomes at least partly inhibited.

This is not necessarily in disagreement with the experimental results of the delayed fluorescence experiments (Zaharieva et al., 2011): Christen et al. (1999) suggested that their

---

[33]Note that in the here shown data, the PSII sample was exposed to the low and high pH values for a long time, unlike in pH-jump protocols. It is thus very much possible, that the PSII units were overall more damaged in the here presented data than in studies employing pH-jump protocols.

observation of alkaline inhibition could arise from structural changes at the donor-side, which lead to an accelerated decay of the S$_2$ and S$_3$ redox states, possibly by electron donation via Y$_D$. Thus, at alkaline pH, ET at the acceptor-side may function at the same (or even faster) rate than at standard pH values around 6.5, leading to the same amount of recombination fluorescence within the time frame of the experiment (10 µs to 60 ms). At the donor-side, however, the S-state progression may become less efficient, due to shortened half-lives of S$_2$ and S$_3$ (Messinger and Renger, 1994), which are reduced by an alternate electron donor.

5.2.4   Initial and Steady-State Spectra in H$_2$O and D$_2$O

The initial spectra following flash-excitation (i.e. the spectra averaged 100–500 ns after the flash) are very similar for all S-state transitions (Fig. 5.7a). The initial spectra resemble a mixture of P680$^+$/P680 (especially >1620 cm^{-1}) and Q$_A^-$/QA spectra (especially the prominent peak at 1478 cm^{-1}), see e.g. work by Nagao et al. (2017b) and Berthomieu et al. (1990). The features of the initial difference spectra do not appear equally around the zero line (transparent lines), but rather seem to exhibit an upshifted baseline (which is especially visible in the effectively featureless region above 1750 cm^{-1}), as recently reported by our group (Dekmak et al., 2023). The reason for this upshifted baseline is the broad P680$^+$ electronic band that overlies the vibrational bands in our entire accessible wavenumber region (1890–1300 cm^{-1}) region (Okubo et al., 2007). As discussed by Dekmak et al. (2023), an approximate background correction can be performed by subtracting the time-resolved P680$^+$ signal (as measured at around 1780 cm^{-1}) from all individual transients (see also Chapter 4.3); in Fig. 5.7a the background corrected data is shown in opaque colors. Note that this approach assumes that the P680$^+$ electronic band has the same magnitude in the entire spectral region of interest—which is an arguably acceptable approximation for the ~1800–1300 cm^{-1} region. For a more detailed look at the initial spectra (in H$_2$O and D$_2$O), see Fig. A3.1 in the Appendix.

Figure 5.7b shows the steady-state spectra of the individual S-state transitions. The features are overall very similar to those reported for spinach membrane fragments (pH 6.5) by Hillier and Babcock (2001); the differences that do appear could be due to differences in measurement conditions (temperature, pH and flash spacing), as well as the fact that they did not deconvolve the spectra (thus larger deviations at higher flash numbers are expected).

The features in the here presented steady-state spectra are also overall similar as reported for *T. vestitus* core complexes (pH 6.0) by Suzuki et al. (2005b), as well as for *Synechocystis* sp. PCC 6803 core complexes (pH 6.0) by Kim and Debus (2019). Some differences are noticeable, but likely relate to sample differences; this will be discussed in detail in Chapter 6.

Figure 5.7b comprises spectra measured in H$_2$O as well as D$_2$O; for the individual S-state transitions the following observations were made:

S$_1$→S$_2$ transition
The bands in the 1700–1600 cm^{-1} region of the 1st flash spectrum are near identical to early reports on spinach PSII membranes (Noguchi et al., 1995a,b; Hillier and Babcock, 2001). Noguchi et al. (1995b) assigned the features to amide I modes arising from different secondary structures: 1678(–)/1668(+) cm^{-1} to turns, 1668(+)/1660(–) to turns or random
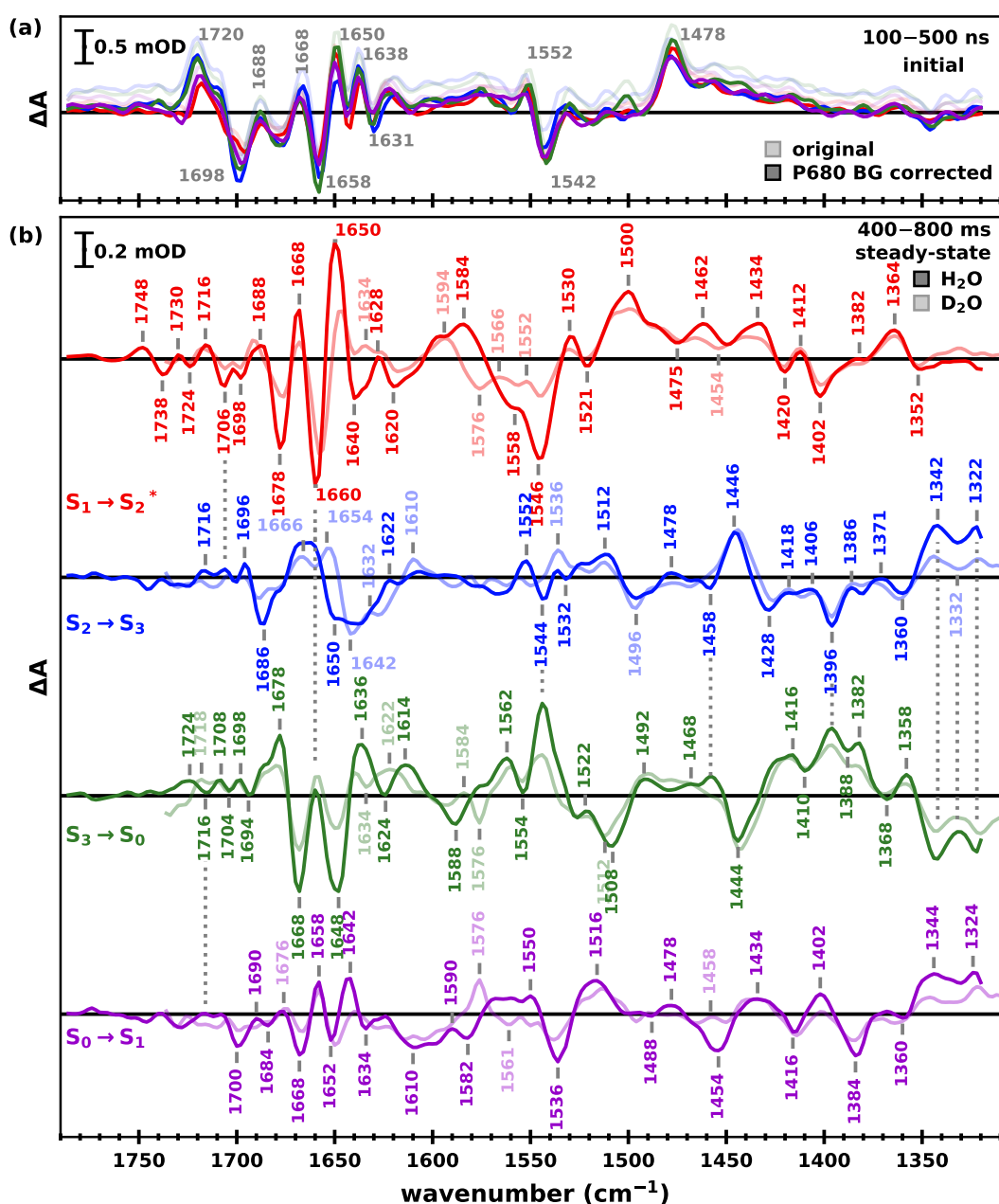
Figure 5.7: Initial and steady-state IR difference spectra of spinach PSII particles. (a) Initial spectra, obtained by averaging the data between 100–500 ns, are shown for the $S_1 \to S_2$ (*red*), $S_2 \to S_3$ (*blue*), $S_3 \to S_0$ (*green*) and $S_0 \to S_1$ (*purple*) transition. Transparent lines show the original initial spectra, while the darker opaque lines show the initial spectra after subtraction of the P680 background (as measured at 1780 cm^{-1}, see Chapter 4.3). For initial spectra in D_2O buffer see Fig. A3.1 in the Appendix. **(b)** Steady-state spectra as determined by averaging the data between 400–800 ms. The darker lines show the spectra in H_2O-based buffer (pH 6.2), while the lighter transparent lines show the spectra in D_2O buffer (pD 6.2). The data in the bottom panel was corrected for its P680 background; the non-corrected spectra however look effectively identical (*not shown*). The spectra were deconvolved assuming a starting population of 74% S_1, 14% S_2 and 12% S_0 and a miss factor of 8% (H_2O) or 12% (D_2O). For the $S_1 \to S_2$ transition, the non-deconvolved first flash data minus 14% S_2 and 12% S_0 is shown (denoted $S_1 \to S_2^*$). The vertical dotted lines indicate identical peak positions to the spectra above. The measurements were done at 10 °C and pL 6.2 in presence of PPBQ.

coils, 1660(–)/1650(+) to α-helices or random coils and 1650(+)/1640(–) cm^{-1} to β-sheets. The band appearing at 1634 cm^{-1} in D$_2$O was also observed in that study and was assigned to a downshifted amide I mode associated with a random coil structure. A similar behavior was observed for *Synechocystis* sp. PCC 6803 core complexes by Service et al. (2014).

The appearance of a band at 1576 cm^{-1} in D$_2$O was interpreted as an upshift of the negative feature at 1558 cm^{-1} by Noguchi et al. (1995b) (in their study both peaks were upshifted by 3 cm^{-1} compared to the here presented results). Experiments with ^{15}N-substitution in the same study showed that amide II contributions are relatively small and are only in part responsible for the absorption difference in that spectral region. They instead attributed the changes upon deuteration to asymmetric COO$^-$ stretch modes and furthermore suggested that the band at 1576 cm^{-1} arises from a carboxylate residue which is strongly H-bonded to the Mn$_4$CaO$_x$-cluster.

The band at 1584(+) upshifts to 1594(+) cm^{-1} upon H/D exchange—similar to features previously observed around 1589–1587 and 1594–1593 cm^{-1} (Service et al., 2010; Noguchi et al., 1995b)–and was also assigned to an H-bonded carboxylate, due to its insensitivity to ^{15}N labeling and its strong down-shift upon ^{13}C labeling (Yamanari et al., 2004; Noguchi and Sugiura, 2003).

Bands around 1552(+)/1546(–)/1530(+)/1521(–), in contrast, were affected by both ^{13}C and ^{15}N isotope labeling (Noguchi and Sugiura, 2003; Yamanari et al., 2004) and are thus (at least in part) assignable to amide II modes, as also discussed by (Service et al., 2010).

The symmetric COO$^-$ region ($\sim$1450–1300 cm^{-1}) does not show a strong perturbation upon deuteration. It was shown in measurements of different free carboxylate compounds that indeed the symmetric COO$^-$ stretch modes undergo only minimal to no upshifts in D$_2$O compared to H$_2$O, while the asymmetric COO$^-$ modes upshifted by 7–20 cm^{-1} (Noguchi et al., 1995b).

$S_2 \rightarrow S_3$ transition

The 1700–1600 cm^{-1} region in Fig. 5.7b (*blue*) shows less distinct, broader features, likely from several overlapping amide I modes. The features in H$_2$O look different than reported for *T. vestitus* (Noguchi and Sugiura, 2002b; Noguchi, 2007), which could be due to sample specific differences (the species as well core particles vs. membrane particles). It has also been shown that the level of hydration has a strong influence on the amide I region (Noguchi and Sugiura, 2002a). The rapid-scan FTIR steady-state spectrum reported in the PhD thesis of Schönborn (2017, p. 196), however, resembles the data shown here, albeit the features are slightly more defined in the FTIR spectrum (which may be due to a higher spectral resolution).

Interestingly, in D$_2$O—unlike in H$_2$O—the 1700–1600 cm^{-1} region does resemble the features reported by Noguchi and Sugiura (2002b). It seems that for a clear interpretation of deuteration-induced shifts in this region a higher spectral resolution may be necessary.

A band at 1552 cm^{-1} possibly downshifts to 1536 cm^{-1}, which is of higher intensity in D$_2$O. The region between 1580 and 1510 cm^{-1} in the D$_2$O spectrum however has a few small features that are hardly above noise level, complicating an interpretation of this region. The features in the symmetric COO$^-$ region once more show only very small ($\sim$2 cm^{-1}) to no shifts upon deuteration.

$S_3 \rightarrow S_0$ transition

Besides some relative intensity changes, the region between 1500–1300 cm^{-1} in Fig. 5.7b

(*green*) again appears hardly perturbed upon H/D exchange. A band at 1508 cm^{-1} seems to upshift to 1512 cm^{-1}. A band at 1588(–) seems to downshift to 1576(–) cm^{-1}. The feature at 1576 cm^{-1}, however, is also present in H_2O as a shoulder, thus an alternative interpretation could that the negative 1576 cm^{-1} feature is merely masked in H_2O by another (positive) feature, which upshifts to 1584 cm^{-1} upon deuteration. Features at 1636(+)/ 1624(–)/1614(+) cm^{-1} appear upshifted in D_2O to 1640(+)/1634(–)/1622(+) cm^{-1}.

Aside from some differences in amplitude ratios, the steady-state spectrum of the here shown $S_3 \rightarrow S_0$ transition in H_2O is near identical to the step-scan FTIR steady-state spectrum of spinach PSII reported by Greife et al. (2023).

$S_0 \rightarrow S_1$ transition
Upon H/D exchange, a negative feature at 1454 cm^{-1} is replaced by a positive feature at 1458 cm^{-1}; furthermore, features at 1590(+) and 1582(–) cm^{-1} disappear, while features at 1576(+) and 1561(–) cm^{-1} appear. The 1576(+) cm^{-1} feature in D_2O was also observed by Noguchi and Sugiura (2002b), who pointed it out as a reversal from the 1576(–) D_2O feature of the $S_1 \rightarrow S_2$ transition. (Unlike in the here shown spectra, they did not observe 1576(–) cm^{-1} feature in the $S_3 \rightarrow S_0$ transition.)

As discussed by Service et al. (2014), the 1750–1710 cm^{-1} region harbors keto and ester C=O modes of chlorophylls and other co-factors, as well carbonyl C=O stretching modes of protonated carboxylates. The assignment to co-factor or amino-acid carboxylates can be attempted by H/D exchange: The carbonyl C=O stretch modes are weakly coupled to C–O–H bending modes in H_2O, but not in D_2O, which causes a downshift by 4–20 cm^{-1} upon deuteration (Service et al., 2014; Barth, 2000; Takei et al., 2008; Noguchi, 2024). However, the features in this region in the steady-state spectra are quite small and partly close to noise-level in the here presented data, with exception of the 1st flash data: the 1748(+)/1738(–)/ 1730(+)/1724(–)/1716(+)/1706(–) features (Fig. 5.7, *red*) are well resolved and agree with previous reports on spinach PSII (Hillier and Babcock, 2001) and core complexes from *T. vestitus* (Suzuki et al., 2009) (although in the latter study the 1716(+) peak is split into two peaks). In contrast, for *Synechocystis* core complexes a strong negative feature has been (reproducibly) observed at 1746 cm^{-1} (e.g. Service et al., 2014). A detailed view of the 1760–1710 cm^{-1} region is shown in Fig. A3.3 in the Appendix; in part this region will be discussed in later parts of this chapter.

For a limited spectral range, initial and steady-state spectra were also measured at pH 4.6, 5.4 and 7.0. The spectra will not be discussed here in detail, but can be found in the Appendix (Fig. A3.4).

5.3   The $S_1 \rightarrow S_2$ Transition

The deconvolution into pure S-state transitions generally works better when omitting the 1st flash data, as a certain contribution to the IR difference signal, e.g. from broken PSII units, may exclusively arise after the 1st flash data. However, if the 1st flash is omitted, then the 5th flash data (which is already very mixed concerning S-state distribution) is the one with the highest $S_1 \rightarrow S_2$ information content and thus there is quite some uncertainty concerning the deconvolved $S_1 \rightarrow S_2$ data. For this reason, analyzing the non-deconvolved 1st flash data may often be the better choice. As the initial dark-adapted population was found to be sub-optimally mixed in the here presented data (74% S_1, 14% S_2 and 12% S_0), the following compromise was undergone: 14% and 12% of the deconvolved $S_2 \rightarrow S_3$ and
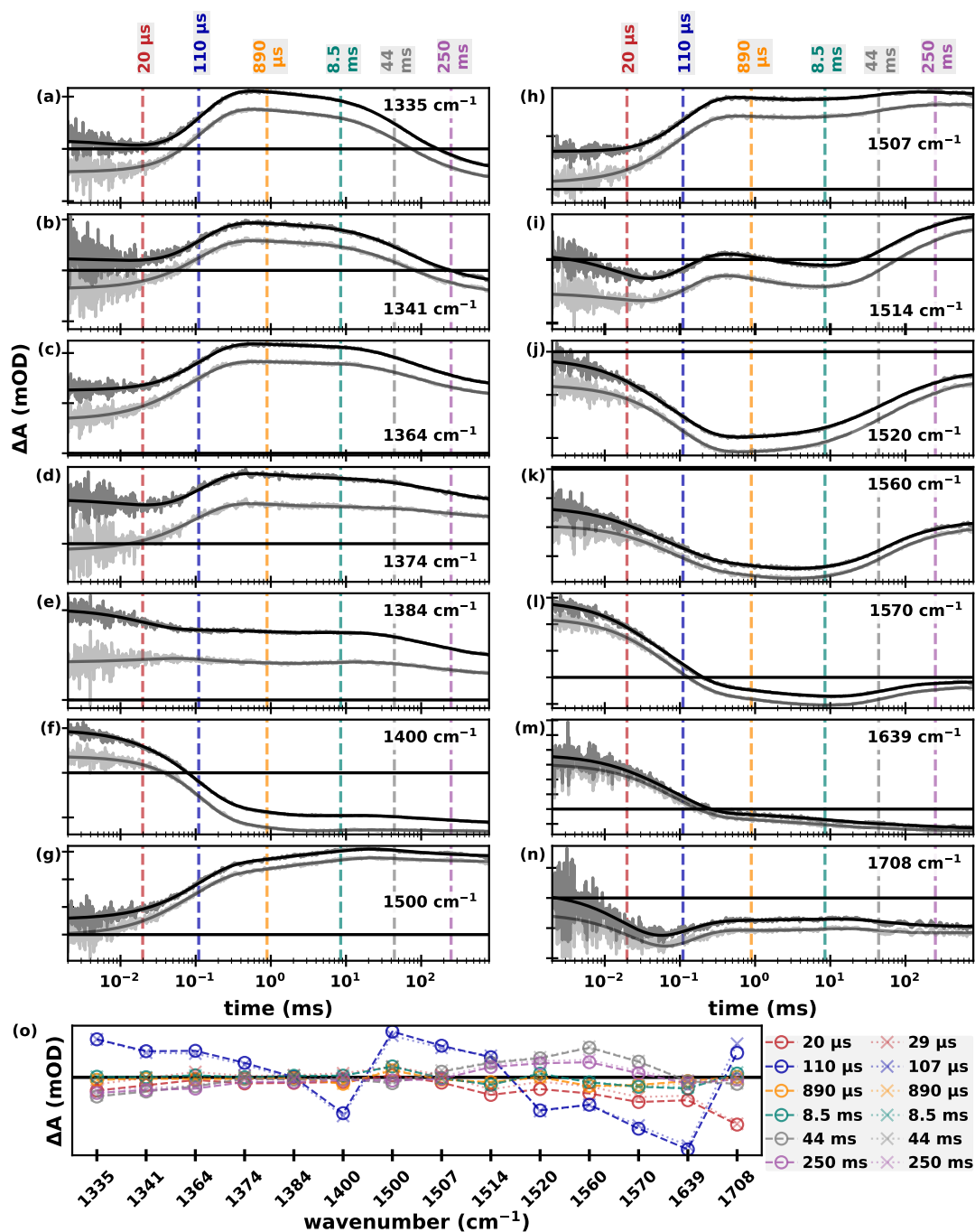
Figure 5.8: Results of globally fitting transient absorption changes of the $S_1 \rightarrow S_2^*$ transition at 14 different wavenumbers to a sum of six exponentials. (a–n) Transients (*dark grey*) and their fit curves (*black*). The (global) time constants are indicated by vertical dashed lines. The transients are additionally shown after a correction for their $P680^+$ background (*light grey*), as measured at 1780 cm^{-1}, see Chapter 4.3. The y-axis ticks indicate 0.1 mOD. **(o)** Wavenumber-dependent amplitudes of the six exponential components for the fits without (*circles*) and with (*crosses*) $P680^+$ background correction. See text for details on the fitting approach. The $S_1 \rightarrow S_2$ transients were obtained by subtracting 14% S_2 and 12% S_0 from the non-deconvolved first flash data. All measurements were done at 10 °C and pH 6.2.

$S_0 \rightarrow S_1$ data, respectively, were subtracted from the 1st flash data (in the following denoted as $S_1 \rightarrow S_2{}^*$).

Fourteen high S/N transients were selected that showed strongly pronounced kinetics around 100 μs (i.e. the expected time constant for the ET event; see Chapter 1.5.1 for an overview of the events of the S-state cycle). These transients were globally fit to a sum of six exponentials in the range from 2 μs–800 ms (Fig. 5.8a–n). The four slowest time constants, which should correspond to acceptor-side processes, were constrained to values pre-determined by fitting the 1st flash kinetics at 1478 cm^{-1} (a wavenumber with negligible donor-side contributions, see Figs. A3.5 and A3.6). The two faster time constants were left free to vary. The wavenumber-dependent amplitudes of the thus determined global time constants are shown in Fig. 5.8o.

As discussed in Chapter 4.3, the mid-IR vibrational difference bands are overlaid by a P680$^+$ electronic band and hence P680$^+$ reduction kinetics contribute to the transients. In addition to the original transients, Figure 5.8a–n also shows the transients after subtraction of the P680$^+$ background (*light grey*). The corrected transients were fit in the same manner as before and the resulting non-constrained time constants are similar to the ones obtained without background correction (20 vs. 29 μs and 110 vs. 107 μs). The amplitudes of most exponential components are near identical with and without P680$^+$ background correction; merely the fastest phase is strongly affected by the correction (its amplitudes mostly move closer to zero), as shown in Fig. 5.8o (crosses and dotted lines). The 110/107 μs component dominates the kinetics at nearly all wavenumbers and is in good agreement with previous values reported for the ET step of the $S_1 \rightarrow S_2$ transition (Dekker et al., 1984; Haumann et al., 1997; Gerencsér and Dau, 2010; Klauss et al., 2012a).

Next, the obtained time constants were fixed in a global fit across the time-resolved spectral data set (see Fig. A3.7a in the Appendix for the temporal evolution of the first flash spectra). Figure 5.9 shows the resulting six decay associated spectra, as well as the initial spectrum (of the fit range) y_0, for fits with (*red*) and without (*black*) P680$^+$ background subtraction. Visual inspection shows that the initial spectrum as well as the DAS of the fast microsecond component are clearly affected by the background correction, while the slower DAS are hardly affected. This is expected, as P680$^+$ reduction should be mostly completed with a time constant of about 30 μs (Renger, 2004, and citations therein); see also Dekmak et al. (2023). In the following, the spectra will be discussed one by one:

(a) The y_0 spectrum at 2 μs shows an overall very strong resemblance to $Q_A{}^-/Q_A$ spectra (Hienerwadel et al., 1996; Suzuki et al., 2005a). Some peaks are also in agreement with P680$^+$/P680 (especially around 1500–1700 cm^{-1}) and $Y_Z{}^{ox}/Y_Z$ spectra (especially the 1558(–)/1551(+)/1543(–)/1531(+) cm^{-1} feature) (Okubo et al., 2007; Nagao et al., 2017b). This is expected, as at 2 μs the Q_A should be mostly present in its semi-quinone form (Nuijs et al., 1986; Robinson and Crofts, 1983; de Wijn and Van Gorkom, 2001), while P680 and Y_Z should be partly in their oxidized and partly in their neutral forms (Renger, 2004).

(b) For most parts (especially >1630 cm^{-1}), the DAS of the 20/29 μs phase strongly resembles FTIR P680$^+$/P680 spectra (e.g. Nagao et al., 2017b; Okubo et al., 2007) recorded on Mn depleted PSII—but reflected along the x-axis—indicating that the DAS corresponds to P680$^+$ reduction. The prominent feature at 1554(–)/1540(+) cm^{-1}, however, could be indicative of some $Y_Z{}^{ox}$ reduction as there is some resemblance to inverted $Y_Z{}^{ox}/Y_Z$ spectra (Nagao et al., 2017b). This at first seems at odds, as we expect P680$^+$ reduction to happen alongside Y_Z oxidation. However, the next phase (110/107 μs) is
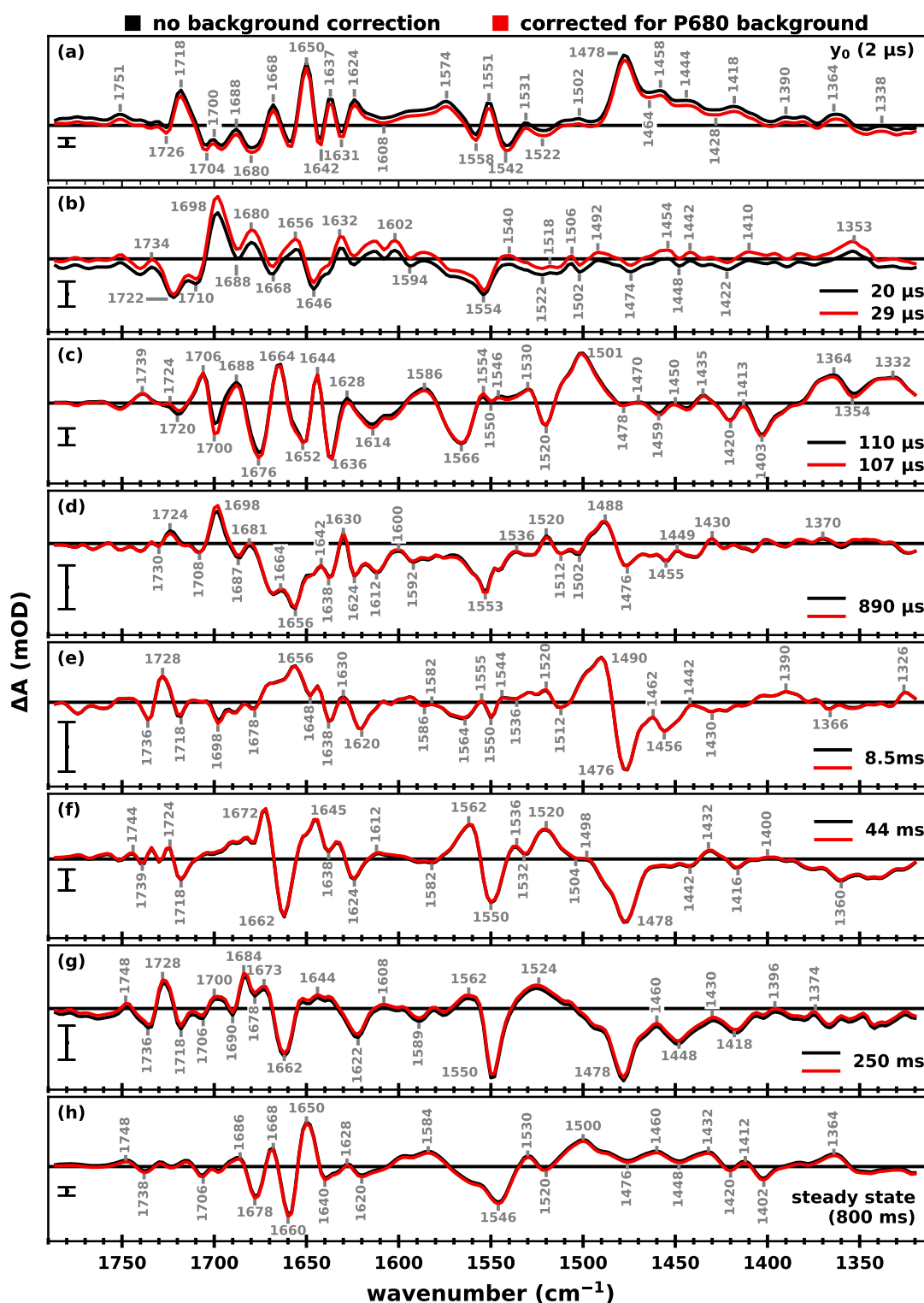
Figure 5.9: Decay associated spectra of the $S_1 \rightarrow S_2^*$ transition. (a) Initial spectrum at 2 µs (y_0). **(b–g)** DAS of the six exponential components. **(h)** Steady-state spectrum (at 800 ms), obtained by addition of all six DAS and the initial spectrum ($y_0 + \sum A_i$). All spectra are shown with (*red*) and without (*black*) P680-background correction. The DAS were obtained by fitting the time-resolved spectral data set with time constants predetermined by the fits shown in Fig. 5.8 (fit range 2 µs–800 ms). The scale bar in each panel corresponds to 0.1 mOD. All measurements were done at 10 °C and pH 6.2. The $S_1 \rightarrow S_2$ data was obtained by subtracting 14% S_2 and 12% S_0 from the non-deconvolved first flash data.

associated with Y_Z^{ox} reduction (*see below*). Events with time constants of about 30 and 110 μs will clearly overlap (as demonstrated in Fig. 5.10) and thus it is not surprising that the two events are not perfectly separated by the DAS analysis. This interpretation suggests that the $P680^+$ reduction contributes significantly more strongly than the simultaneously occurring Y_Z oxidation, which is in line with a similar observation we reported recently (Dekmak et al., 2023). The DAS of the 20/29 μs phase with vs. without $P680^+$ background correction differ mostly by a vertical shift (some relative peak heights are also affected, but the peak positions remain effectively identical).

(c) The DAS of the 110/107 μs component shows a strong similarity (especially >1600 cm^{-1} and in parts around 1560–1520 cm^{-1}) to Y_Z^{ox}/Yz spectra recorded on Mn depleted PSII (Berthomieu et al., 1998; Nagao et al., 2017b)— but reflected along the x-axis—indicating this phase is associated with Y_Z^{ox} reduction, which is in agreement with the above assignment of this phase to the ET step (Mn4→Y_Z^{ox}). Three features stand out when comparing the here presented spectra to previously reported Y_Z^{ox}/Yz spectra: The strongly pronounced and quite broad 1586(+)/1566(–) and 1520 (–)/1501(+) features, as well as the bands at 1403(–)/1364(+)/1354(–)/1332(+) cm^{-1}. Interestingly, all of these features (with exception of 1332(+) cm^{-1}) are also clearly visible in the S_1→S_2 steady-state spectrum (panel h; see also Fig. 5.7b, *red*). This could indicate that these features arise from Mn-oxidation induced changes around the Mn_4CaO_x cluster, as sensed by surrounding carboxylate residues, as has been hypothesized (Debus, 2016; Nakamura and Noguchi, 2016; Greife et al., 2023). Y_D^{ox}/YD spectra reported by Nagao et al. (2017b) show a prominent 1518(–)/1503(+) feature, thus the possibility was considered that the 1520(–)/1501(+) feature in the here presented data could indicate Y_D^{ox} formation upon the first excitation flash. However, the same DAS obtained on S_1→S_2 data that was deconvolved under omission of the first flash data shows a very similar prominent feature (see Fig. A3.10 in the Appendix), thus it seems unlikely that it arises from Y_D^{ox} formation.
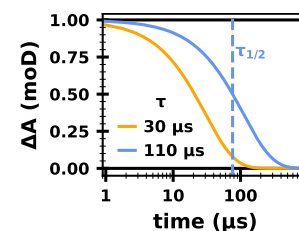

Figure 5.10: Exponential function with a 30 μs vs. a 110 μs time constant.

As the S_1→S_2 transition does not involve a proton release from the Mn_4CaO_x cluster (Schlodder and Witt, 1999) nor a water insertion event, all the slower components observed by time-resolved IR are likely associated with acceptor-side events:

(d) – (e) The DAS of the 890 μs and 8.5 ms components could be related to ET from Q_A^- to Q_B, which is expected to occur in around that time (de Wijn and Van Gorkom, 2001) (the millisecond component was assigned to the case that the Q_B site is empty and a quinone has to bind before ET can take place). An indication for this is also the differential feature at about 1490(+)/1478(–), which could arise because Q_A^- and Q_B^- have similar—but not identical—spectra with strong peaks at 1478 and 1480 cm^{-1}, respectively. Alternatively, the differential feature, which is especially strongly pronounced in the slower component, could indicate an upshift of the Q_A^- band because of structural or electrostatic changes around the acceptor-side.

(f) – (g) The DAS of the 44 and 250 ms components have many features in common with each other, but also some clear differences. They both show a strong negative feature around 1478 cm^{-1}, indicating semiquinones are becoming neutral quinones, either by oxidation or reduction. Q_A^-→Q_A decay by charge recombination likely contributes

in PSII units that fail to advance to the S_2 state. The 1562(+)/1550(−)/1536(+) features also resemble Q_A^- decay (Berthomieu et al., 1990; Suzuki et al., 2005a) (see also Fig. 4.13b), as does the broad negative feature centered around 1360 cm^{-1} in the 44 ms DAS. The 44 ms DAS additionally shows indications of Fe^{2+} reduction (Berthomieu and Hienerwadel, 2001; Takahashi et al., 2010) (see also Fig. 4.13): Compared to the 250 ms DAS, the 1662(−)/1672(+) cm^{-1} and 1562(+)/1550(−) features are more prominent; as these features appear both in Q_A^-/Q_A as well as Fe^{2+}/Fe^{3+} spectra with the same sign, this could indicate that iron oxidation is additionally taking place (furthermore the 1536(+) is missing in the 250 ms DAS). Thus, we are possibly observing $Q_A^- \rightarrow Q_A$ and/or $Q_B^- \rightarrow Q_B$ as well as $Fe^{2+} \rightarrow Fe^{3+}$. As discussed in Chapter 4.2, in presence of artificial electron acceptor PPBQ, it is expected that PPBQ is doubly reduced following odd flashes by accepting an electron from Q_A^- as well as from Fe^{2+}. The 1718(−)/1728–1724(+) cm^{-1} feature in panels (e)–(g) are further hints that Q_A^- oxidation is observed in these steps: a similar feature in Q_A^-/Q_A spectra has been assigned to 13^3-ester C=O stretching vibration of the D1 pheophytin (Berthomieu et al., 1990).

(g) For the discussion of the steady-state spectrum see Fig. 5.7b and accompanying text. Note that the spectrum shown here (in panel g) corresponds to the IR difference absorption recorded at 800 ms, while the spectrum in Fig. 5.7b shows the average between 400–800 ms, thus there may be some subtle differences.

5.3.1 Kinetic and Spectral Changes upon H/D Exchange

When exchanging a PSII sample into a D_2O-based buffer, the majority of the exchangeable protons (H$^+$) should be replaced by deuterons (D$^+$); tightly bound H-atoms, on the other hand, will not exchange through a mere buffer change. Generally speaking, kinetic processes involving water or proton movement are expected to slow down in D_2O. Furthermore, vibrational frequencies of e.g. protonatable amino acid side chains are expected to shift upon H/D exchange (because of altered atom weight and altered bond strength). Thus, H/D exchange can provide valuable information for the assignment of IR bands to specific chemical groups, as well as the assignment of kinetics to specific processes.

Figure 5.11a–j shows ten transients of PSII spinach membranes in D_2O-based buffer associated with the $S_1 \rightarrow S_2$ transition. Analogously to the measurements in H_2O discussed above, the select transients were fit globally to a sum of exponentials; the resulting time constants and their amplitudes are shown in panel k. The transients (and fit results) are additionally shown after subtraction of a P680$^+$ background which results in a negative offset of all entire transients along the y-axis. Similarly to the results in H_2O, the fastest component is most strongly affected by the background correction, as also confirmed by visual inspection of the transients (the amplitude of this phase becomes mostly smaller).

A direct comparison of the transient IR changes at 1364 cm^{-1} in H_2O and D_2O is given in Fig. 5.12. Visual inspection of the normalized transients confirms that the 110 μs kinetic is only marginally slower in D_2O (148 μs), which corresponds to a kinetic isotope effect of 1.3. This is in good agreement with previous spectroscopic observations of 1.2–1.3 (e.g. Gerencsér and Dau, 2010; Klauss et al., 2012a; Sakamoto et al., 2017).

The time constants in D_2O were again fixed in a global fit across a time-resolved spectral data set; the resulting DAS for the two fastest components are shown in Fig. 5.13 alongside their H_2O counterparts. The DAS obtained on P680$^+$ background corrected data look similar (see Fig. A3.9 in the Appendix).
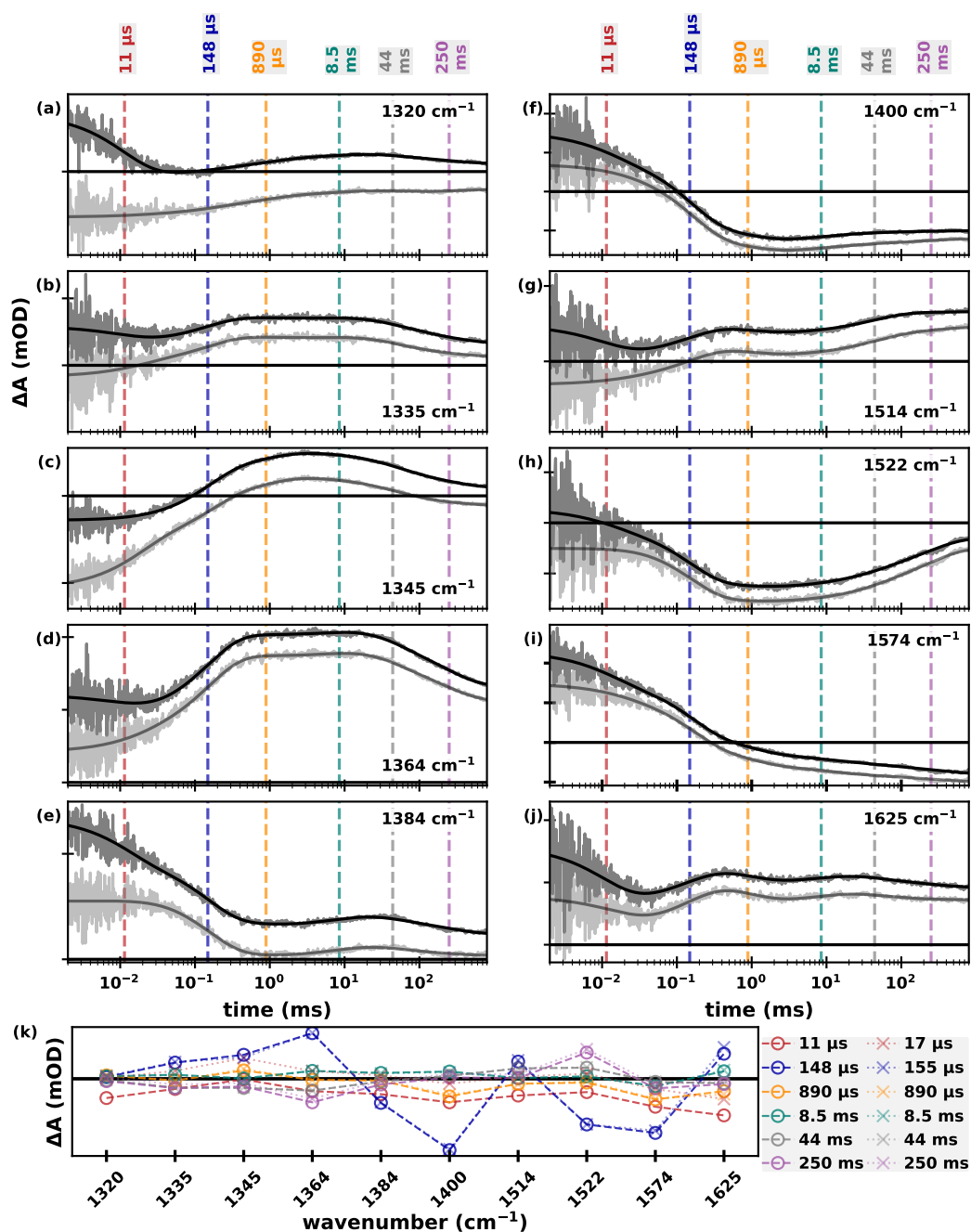
Figure 5.11: Results of globally fitting transient absorption changes of the $S_1 \to S_2^*$ transition in D_2O at 10 different wavenumbers to a sum of six exponentials. (a–j) Transients (*dark grey*) and their fit curves (*black*). The (global) time constants are indicated by vertical dashed lines. The transients are additionally shown after a correction for their $P680^+$ background (*light grey*), as measured at 1790 cm^{-1}, see Chapter 4.3. The y-axis ticks indicate 0.1 mOD. **(k)** Wavenumber-dependent amplitudes of the six exponential components for the fits without (*circles*) and with (*crosses*) $P680^+$ background correction. See text for details on the fitting approach. The $S_1 \to S_2$ transients were obtained by subtracting 14% S_2 and 12% S_0 from the non-deconvolved first flash data. All measurements were done at 10 °C and pD 6.2.
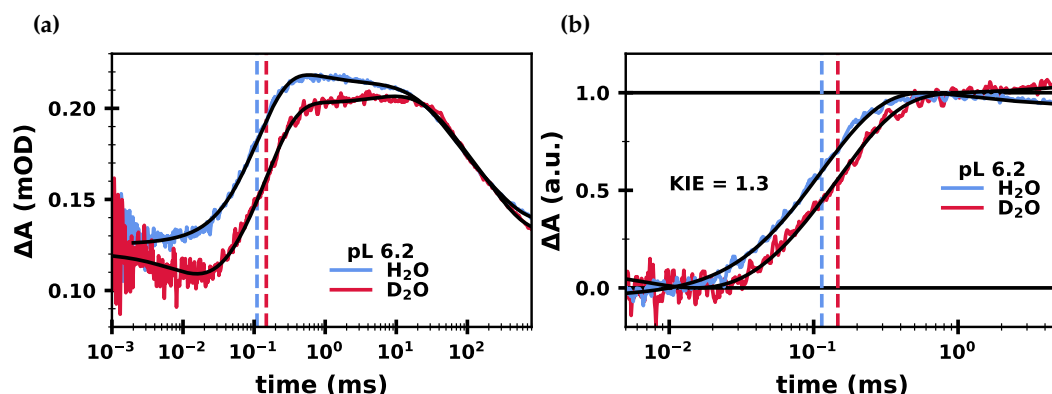
Figure 5.12: Comparison of transient IR absorption changes of the S$_1$→S$_2$* transition at 1364 cm^{-1} in H$_2$O and D$_2$O. The absorption changes are shown **(a)** non-normalized on a logarithmic x-axis (1 μs–800 ms) and **(b)** on a smaller time frame (5 μs–5 ms) shifted and normalized to overlay the transients between 10 μs and 1 ms. The time constants of the 114 μs (H$_2$O) and 147 μs (D$_2$O) phase are indicated with vertical dashed lines. The slow microsecond phase (890 μs) is effectively absent at this wavenumber; the strongly pronounced microsecond rise should thus represent predominantly the ET event. The transients were smoothed with a sliding average algorithm with a window size of 5 data points.
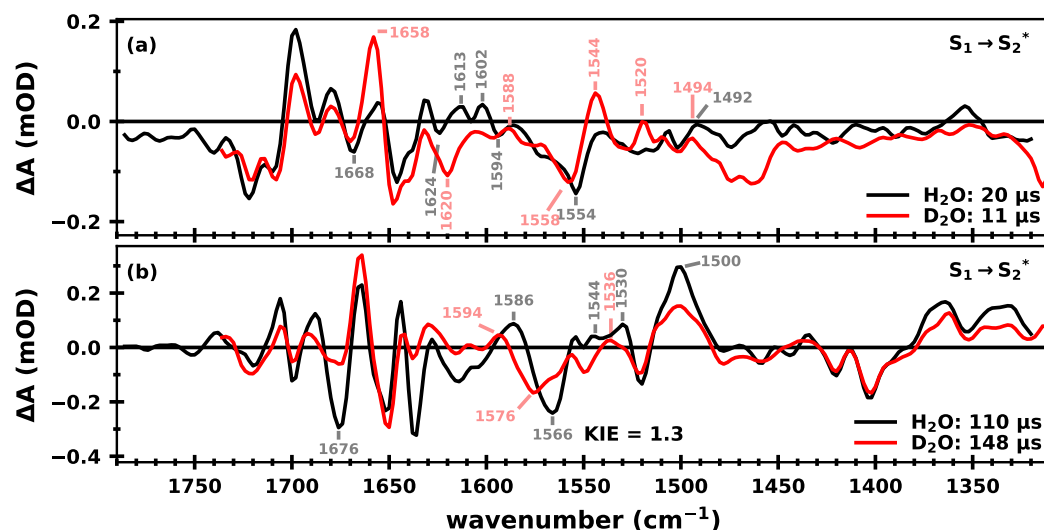

Figure 5.13: Decay associated spectra of the S$_1$→S$_2$* transition in H$_2$O and D$_2$O. (a) DAS of fast microsecond phase in H$_2$O (*black*) and D$_2$O (*red*). **(b)** DAS of slower microsecond phase (likely associated with the ET event expected in that time range) in H$_2$O (*black*) and D$_2$O (*red*). The DAS were obtained by fitting the time-resolved spectral data set with time constants predetermined by the fits shown in Figures 5.8 and 5.11. The DAS of transients corrected for their P680$^+$ background kinetics can be found in Fig. A3.9 in the Appendix. All measurements were done at 10 °C and pL 6.2. The S$_1$→S$_2$ transients were obtained by subtracting 14% S$_2$ and 12% S$_0$ from the non-deconvolved first flash data (denoted S$_1$→S$_2$*).

115

The DAS of the ~10–20 μs phase (Fig. 5.13a) appears overall quite similar in H_2O and D_2O. The strong bands between 1730–1630 cm^{-1} differ only in their relative peak amplitudes, supporting assignment of this phase also in D_2O to $P680^+$ reduction.[34]

If our assignment further above is correct, the DAS of the ~100–150 μs component should mostly correspond to the ET from Mn4 to Y_Z^{ox}. As discussed above, the H_2O DAS has a strong similarity to spectra of Y_Z^{ox} reduction. Y_Z^{ox}/Y_Z spectra are not strongly affected by H/D exchange (Nakamura et al., 2014); thus the majority of absorption changes induced by H/D exchange are thus likely connected to the effect of the Mn4 oxidation on its surrounding amino acid ligands, as well as overall small conformational changes sensed by the amide I and amide II modes.

The 1586(+)/1566(−) feature, which is not present Y_Z^{ox}/Y_Z spectra, upshifts by about 10 cm^{-1} to 1594(+)/1575(−) in D_2O, as is also visible in steady-state spectra (Noguchi et al., 1995b; Noguchi and Sugiura, 2002b); see also (Fig. 5.7). The fact that this spectral feature forms with the time constant of the ET event, supports its previous assignment to carboxylate residues H-bonded to the Mn_4CaO_x cluster (Noguchi et al., 1995b). Candidates for the residues could be D170 and E333, as they are direct ligands to Mn4 (see Fig. 5.43). A $^{12}C/^{13}C$ FTIR study of a D170H mutant, which reverts post-translationally to a glutamate residue, showed that a 1587(+) feature was only marginally affected, while a 1569(−) cm^{-1} peak was strongly diminished (likely downshifted to 1527 cm^{-1}) when ^{13}C-histidine was used (Shimada et al., 2022b). We speculate that this could be an indication that we are observing perturbation of D170 and E333 at mostly 1566 and 1586 cm^{-1}, respectively, upon Mn4 oxidation.

5.3.2 Investigation of the pL Dependency

The pH dependency of the kinetic phase assigned to the $S_1 \rightarrow S_2$ ET step was investigated by measuring transient IR absorption changes at six different pH values and three pD values in H_2O and D_2O, respectively. Figure 5.14 shows all IR transients at 1400 cm^{-1}. While the transients show differences in the relative amplitude of their kinetic components, the phase around 100 μs is similar in all data sets (best seen in the normalized plots, i.e. in panels b and d), indicative of a small pL dependency. At each pL value, at least four transients were globally fit to a sum of exponentials; the resulting time constants of the ET phase are shown in Fig. 5.15.

The values in H_2O fall between about 100–140 μs and seemingly show an optimum around pH 6.0. However, the normalized transients in Fig. 5.14b do not reflect such a clear trend, thus the here observed pH dependency may not be significant. In an alternative analysis of the non-deconvolved 1st flash data, the time constants scattered between 95-130 μs without showing a clear trend (*not shown*). For the three measured pD values, the time constant seemed to become marginally faster at higher pD value (135–150 μs), which is at least partly confirmed by visual inspection of the transients in Fig. 5.14d.

Whether the pL trends in Fig. 5.15 are real or not cannot be definitively concluded at this point. Either way, the results are in agreement with previous observations that the

---

[34]To our knowledge the only published $P680^+/P680$ spectrum in D_2O was solely shown for the entire 2800–1700 region, to demonstrate that the broad electronic band did not change upon deuteration (Noguchi et al., 1998) (thus individual vibrational bands are not discernible). Furthermore, a lack of peak shifts in triplet $^3P680/P680$ spectra upon H/D exchange has been mentioned, but not shown (Noguchi et al., 1993).
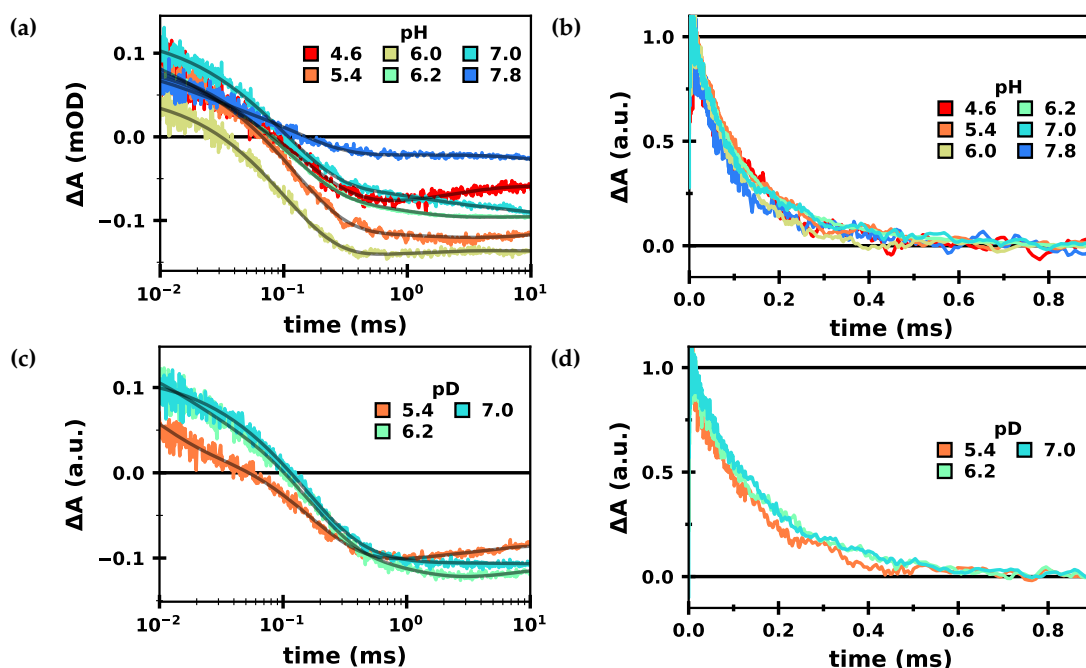
Figure 5.14: Influence of the pL value on the transient absorption changes of the $S_1 \rightarrow S_2^*$ transition at 1400 cm^{-1}. **(a)** The absorption changes (colored lines) at six different pH values on a logarithmic x-axis, along with their fit curves (*grey*). **(b)** Same data as in (a), but on a linear x-axis and shifted and normalized to overlay the transients between 10 μs and 1 ms. **(c)** Transient absorption changes in D_2O at three different pD values (colored lines), along with their fit curves (*black*). **(d)** Same data as in (c), but on a linear x-axis and shifted and normalized to overlay the transients between 10 μs and 1 ms. In (b) and (d) the fit curves are not shown. All $S_1 \rightarrow S_2$ transients were obtained by subtracting 14% S_2 and 12% S_0 from the non-deconvolved first flash data (denoted $S_1 \rightarrow S_2^*$).
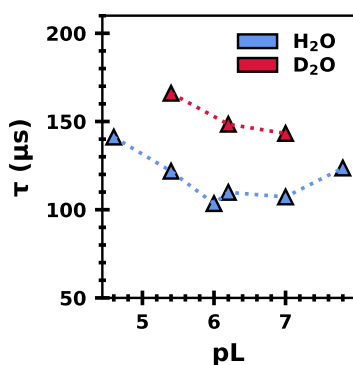

Figure 5.15: Time constant of the ET step in H$_2$O and D$_2$O at different pH and pD values. At each pL value, the time constant was determined by fitting at least four transients globally to a sum of exponentials; only the time constants that are likely associated with the ET step are shown. The values are also given in Tab. A3.1 in the Appendix.

$S_1 \rightarrow S_2$ transition overall does not show a strong pL dependency (Takemoto et al., 2019; Haumann et al., 1997).

5.4 The $S_2 \rightarrow S_3$ Transition

The analysis of the $S_2 \rightarrow S_3$ transition was done on deconvolved data (assuming a dark-adapted population of 74% S_1, 14% S_2 and 12%; see Section 5.1.1 for details). Twenty high S/N transients (pH 6.2) were selected and globally fit to a sum of exponentials. The transients (*dark grey*) along with their fit curves, as well as the determined time constants and
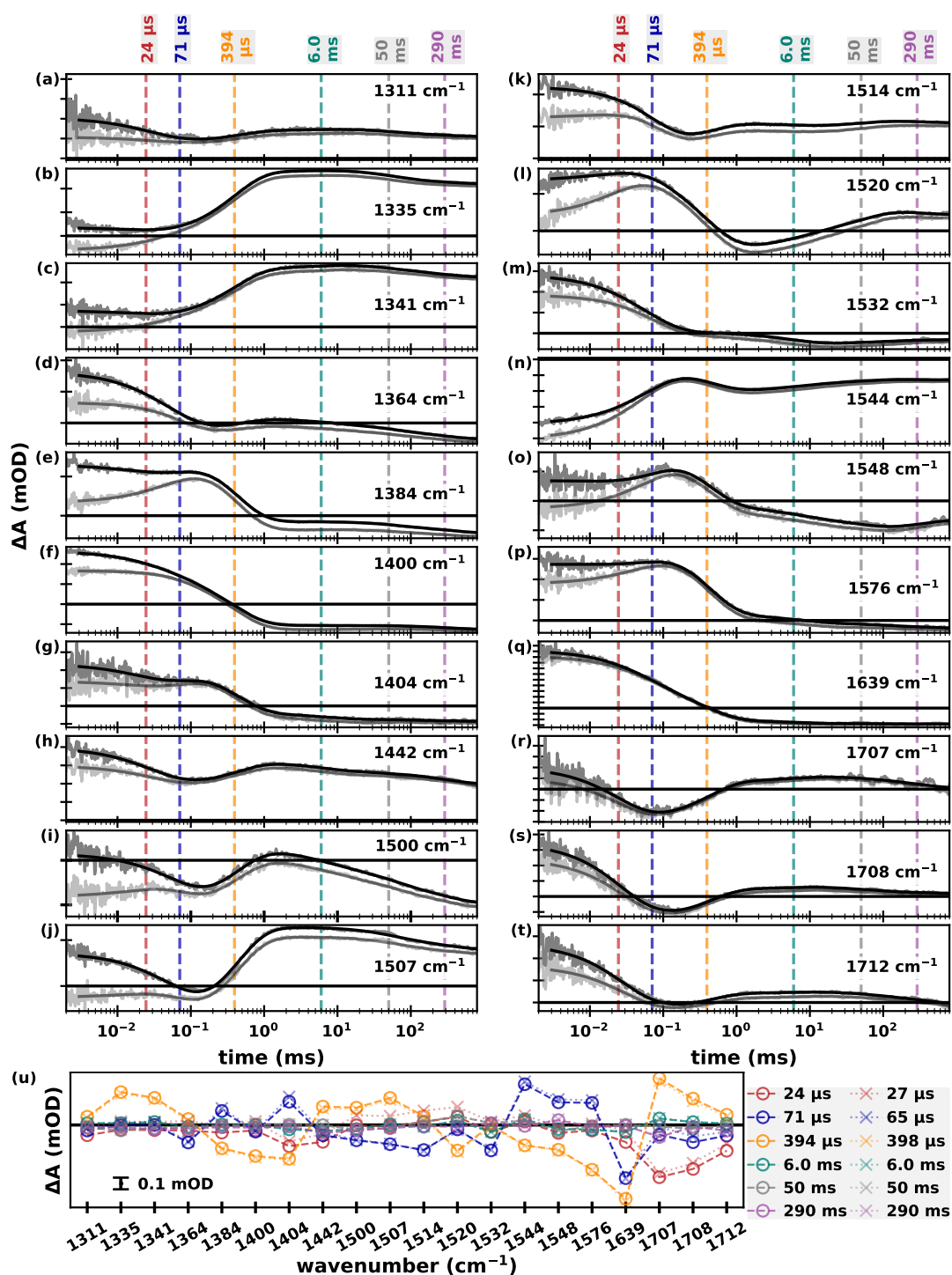
Figure 5.16: Results of globally fitting transient absorption changes of the $S_2 \rightarrow S_3$ transition at 20 different wavenumbers to a sum of six exponentials. (a–t) Transients (*dark grey*) and their fit curves (*black*). The (global) time constants are indicated by vertical dashed lines. The transients are additionally shown after a correction for their $P680^+$ background (*light grey*), as measured at 1780 cm^{-1}, see Chapter 4.3. The y-axis ticks indicate 0.1 mOD. **(u)** Wavenumber-dependent amplitudes of the six exponential components for the fits without (*circles*) and with (*crosses*) $P680^+$ background correction. See text for details on the fitting approach. All transients were deconvolved assuming a starting population of 74% S_1, 14% S_2 and 12% S_0; they were smoothed with a sliding average algorithm with a window size of three data points. All measurements were done at 10 °C and pH 6.2.
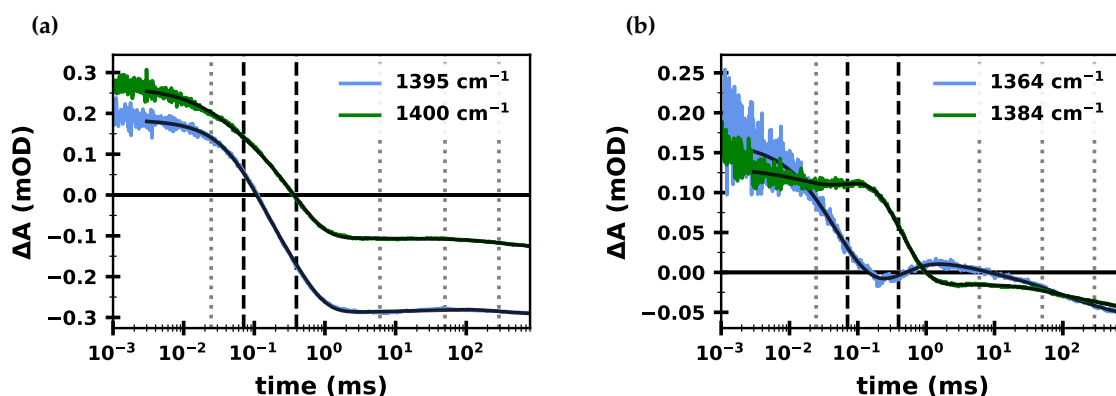
Figure 5.17: Transient absorption changes of the $S_2 \rightarrow S_3$ transition in the symmetric stretching region of carboxylates. (a) IR difference absorption at 1395 (*blue*) and 1400 cm^{-1} (*green*); the time constants determined as described in Fig. 5.16 are indicated with dotted vertical lines. The time constants associated with the PT and ET are highlighted by dashed vertical lines. **(b)** IR difference absorption at 1364 (*blue*) and 1384 cm^{-1} (*green*). The amplitudes of the PT and ET phase have opposite signs and are thus visually easier to distinguish than in the transients shown in (a). All transients were measured at pH 6.2 and 10 °C. They were deconvolved assuming a starting population of 74% S_1, 14% S_2 and 12% S_0.

their wavenumber-dependent amplitudes are shown in Fig. 5.16a–u. The transients are also shown after subtraction of their P680$^+$ background (*light grey*). Fitting the P680$^+$-corrected data gave similar results; merely the amplitude of the fastest phase was strongly affected.

All time constants were unconstrained in the fit of the non-background-corrected data. The thus determined three slowest time constants (6.0, 50 and 290 ms), which are temporally assigned to acceptor-side events, were then fixed in the fit of the P680$^+$-corrected data.

From the six determined time constants, the 71 and 394 µs phases are of most interest: Based on previously reported time constants (Klauss et al., 2012a; Sakamoto et al., 2017) they can be assigned to the PT and ET event of the $S_2 \rightarrow S_3$ transition.

In a previous study, we observed the temperature-dependence of the kinetics of the $S_2 \rightarrow S_3$ transition at 1395 and 1400 cm^{-1} (Mäusle et al., 2020). At those two wavenumbers, however, the ET and PT kinetic have amplitudes of the same sign, making it harder to distinguish the two (see Fig. 5.17a). At 1364 and 1384 cm^{-1}, on the other hand, the two phases have opposite signs and can more easily be distinguished (Fig. 5.17b). In the previous study (Mäusle et al., 2020) we fixed the ET step to literature values (550 µs at 10 °C), which however did not give good fit results for the here presented data. Here, we instead rely on the assumption that globally fitting several wavenumbers with strongly varying amplitudes of the different kinetic phases results in good estimations of the time constants.

As for the $S_1 \rightarrow S_2^*$ data, the determined time constants were again fixed in a global fit across the time-resolved spectral data set, resulting in six distinct DAS (Fig. 5.18). The DAS are near identical for P680$^+$-corrected and non-corrected data sets. The only exceptions are the DAS of the fastest component (panel b), as well as the initial spectrum y_0 (panel a), which have amplitudes of about zero above 1740 cm^{-1} in the background-corrected version, while the non-corrected DAS is vertically shifted to more negative values across the entire spectral region. In the following, the spectra will be discussed one by one:
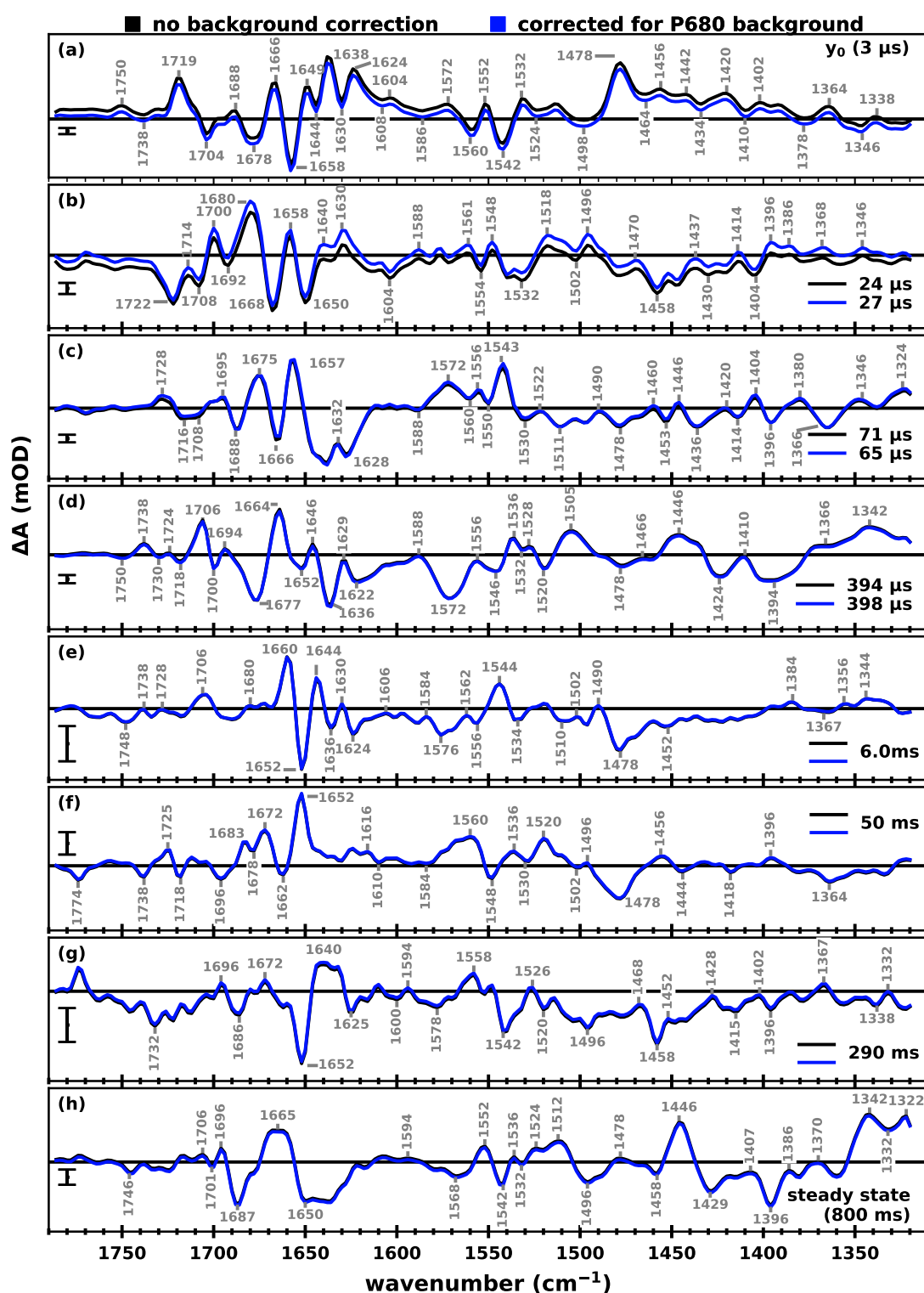
Figure 5.18: Decay associated spectra of the $S_2{\rightarrow}S_3$ transition. (a) Initial spectrum at 3 µs (y_0) and **(b–g)** DAS of the six exponential components. The DAS were obtained by fitting the time-resolved spectral data set with time constants predetermined by the fits shown in Fig. 5.16 (fit range 3 µs–800 ms). **(h)** Steady-state spectrum (at 800 ms), obtained by addition of all six DAS and the initial spectrum ($y_0 + \sum A_i$). All spectra are shown with (*blue*) and without (*black*) P680-background correction. The time-resolved spectral data set (acquired at 10 °C and pH 6.2) was deconvolved assuming a starting population of 74% S_1, 14% S_2 and 12% S_0. The scale bar in each panel corresponds to 0.1 mOD.

(a) Besides some differences in amplitude ratios and small changes (1–2 cm^{-1}) in peak positions, the y_0 spectrum of the S$_2$→S$_3$ data is near identical to that of the S$_1$→S$_2$ transition (see Fig. 5.9a and accompanying text). This indicates that around 2–3 μs a similar population of Q_A^-, P680$^+$ and Y_Z^{ox} is present in both S-state transitions.

(b) The 24/27 μs DAS strongly resembles an inverted P680$^+$/P680 spectrum (Nagao et al., 2017b; Okubo et al., 2007), despite some small differences in peak positions. The relative peak amplitudes also differ a bit; e.g. the peak at 1700(+) is smaller than that at 1680(+), while in the P680$^+$/P680 spectrum reported by Okubo et al. (2007) their 1701 cm^{-1} feature is much more pronounced than the feature at 1682 cm^{-1}. While the 20/29 μs DAS of the S$_1$→S$_2^*$ data also showed some Y_Z^{ox} reduction (as discussed in Section 5.3; Fig. 5.9b), the DAS shown here rather shows some subtle evidence of Y_Z^{ox} formation: The broad negative peak around 1532 cm^{-1} could be caused by the strongly pronounced 1543(−) cm^{-1} feature of Y_Z^{ox}/Y_Z spectra. When comparing the Y_Z^{ox}/Y_Z and P680$^+$/P680 spectra reported in Nagao et al. (2017b), one can find several peaks at very similar positions in both spectra, which should cancel each other out if Y_Z^{ox} is formed concomitantly with P680$^+$ reduction (e.g. peaks at about 1531(+) and 1630(−) cm^{-1}). However, these features show up with opposite sign in the DAS here, indicating either P680$^+$ or Y_Z^{ox} reduction. As Y_Z^{ox} formation (rather than its reduction) is expected, this can be taken as an indication that the P680$^+$ contribution to the IR difference bands is significantly larger than the Y_Z^{ox} contribution.

(c) Small contributions of P680$^+$ and Y_Z^{ox} decay seem likely, but otherwise the 71/65 μs DAS does not show a strong resemblance to (known) spectral signatures of any co-factors.

(d) The DAS of the 394/398 μs phase shows clear indication of Y_Z^{ox} reduction, especially in the 1730–1629 cm^{-1} region (Nagao et al., 2017b; Nakamura et al., 2014; Berthomieu et al., 1998), which agrees well with the assignment of this phase to the ET step of the S$_2$→S$_3$ transition. The prominent 1572(−) cm^{-1} appears to mirror a similar positive feature of the 71/65 cm^{-1} DAS.

(e) The 6 ms DAS shows some similarity to the 8.5 ms DAS of the S$_1$→S$_2$ transition (Fig. 5.9e); the 1478(−)/1490(+) cm^{-1} differential feature could again indicate ET from Q_A^- to Q_B. The strong 1544(+) and 1706(+) cm^{-1} bands are not present in the S$_1$→S$_2$ DAS and the amide I region also shows large differences. It seems that both DAS are associated with similar but not identical acceptor-side processes. An overlay of both DAS, alongside that of the 2.5 ms phase of the S$_3$→S$_0$ transition, is shown in Fig. A3.17c in the Appendix.

(f) The DAS of the 50 ms phase looks similar to that of the 44 ms of the S$_1$→S$_2$ transition shown further above, as well as to that of the 50 ms phase of the S$_3$→S$_0$ transition shown in the next subchapter (an overlay of all three is shown in Fig. A3.17d in the Appendix). The DAS show a strong resemblance to inverted Q_A^-/Q_A spectra (Remy et al., 2004; Berthomieu et al., 1990) (see also Fig. 4.13b), which might indicate Q_A^- recombination, possibly with Y_Z^{ox} in PSII centers that fail to advance to the next S-state.

(g) The DAS of the 290 ms phase has a comparably very small amplitude (as indicated by the scale bar), thus the S/N is also visibly poorer than for the other DAS. This phase likely corresponds to a relaxation process/recombination reaction of some sort, but the poor S/N hinders a clear assignment. It shows some similarity with the 290 ms

DAS found for Mn depleted spinach PSII membrane particles (see Fig. 4.12 in Chapter 4.4).

(h) The steady-state spectrum at 800 ms shown here is near identical to that in Fig. 5.7, which shows the averaged spectra between 400–800 ms; see Section 5.2.4 for the latter's discussion.

In measurements with PPBQ, ET from Q_A^- to Fe^{3+} is expected about 30 µs at RT (Petrouleas and Diner, 1987; Chernev et al., 2011) after even-flashed illumination (possibly a bit later at 10 °C). Clear indications of this are however not present in the 24/27 µs nor in the 71/65 µs DAS (nor in any other spectrum in Fig. 5.18). This in strong contrast to the 44 ms DAS of the $S_1 \rightarrow S_2$ (Fig. 5.9f) and $S_3 \rightarrow S_0$ transition (Fig. 5.27g), which show clear indication of Fe^{2+} oxidation—see also an overlay of both in Fig. A3.17. The reason for this may be simple: Several features of Q_A^- oxidation and Fe^{3+} reduction are similar, but of opposite sign, and thus they likely cancel each other out during the $S_2 \rightarrow S_3$ transition. This would *inter alia* explain the very small amplitude of the 1478 cm^{-1} feature in the 24/27 and 71/65 µs DAS. During the odd-numbered S-state transitions, on the other hand, the similar (same-signed) Q_A^- and Fe^{2+} oxidation features add up and thus become more prominent.

An indication that the Fe^{3+} reduction is indeed happening around 50 µs in even-numbered S-state transitions, while Fe^{2+} oxidation is occurring around 40 ms in odd-numbered transitions, is provided by the analysis of the 1478 cm^{-1} in the Appendix: Fig. A3.6b shows that the amplitudes of the ∼40 ms and ∼50 µs phases both exhibit a strong period-of-two dependency on the flash-number. While the ∼40 ms phase is especially pronounced following an odd number of flashes, the opposite is true for the ∼50 µs.

5.4.1 Kinetic and Spectral Changes upon H/D Exchange

As for the data in H_2O, a selection of transients acquired in D_2O-based buffer was fit to a sum of six exponentials. The transients and the determined time constants and their amplitudes are shown in Fig. 5.19a–r and s, respectively. Analysis after P680$^+$ background subtraction gave similar results (see light grey transients in panels a–r and crosses in panel s); merely the amplitude of the fastest component was again strongly affected.

The time constants in H_2O which were assigned to the PT and ET step at the Mn_4CaO_x cluster (71 and 394 µs) appeared to slow down to 219 and 798 µs in D_2O, which corresponds to KIEs of 3.1 and 2.0 (or 4.4 and 2.1 in the P680$^+$ corrected data). Figure 5.20a and b show transients at 1364 and 1384 cm^{-1}, respectively, demonstrating the slowed-down kinetics in D_2O compared to H_2O.

A KIE of 2.0–2.1 for the ET step is marginally larger than the 1.7–1.9 reported previously (Gerencsér and Dau, 2010; Zaharieva et al., 2016; Sakamoto et al., 2017), but in agreement with earlier reports of 2.1–2.3 by Haumann et al. (1997); Karge et al. (1997). While the KIE of about 3–4 found here for the PT step is smaller than previous reports of 4–6 (Klauss et al., 2012a; Zaharieva et al., 2016), it is clearly larger than the very small KIE of 1.2 observed by Sakamoto et al. (2017) (also in a time-resolved IR study). Unlike the latter study, the data presented here thus supports the assignment of a proton release phase prior to ET step. The ET step itself is nevertheless likely also coupled to a PT event, as suggested previously (Haumann et al., 1997; Klauss et al., 2012a) and also supported by the relatively large KIE of 2.0 found here.

The determined time constants in D_2O were fixed in a global fit across a time-resolved spectral data set, analogously to the values in H_2O. The thus obtained decay associated
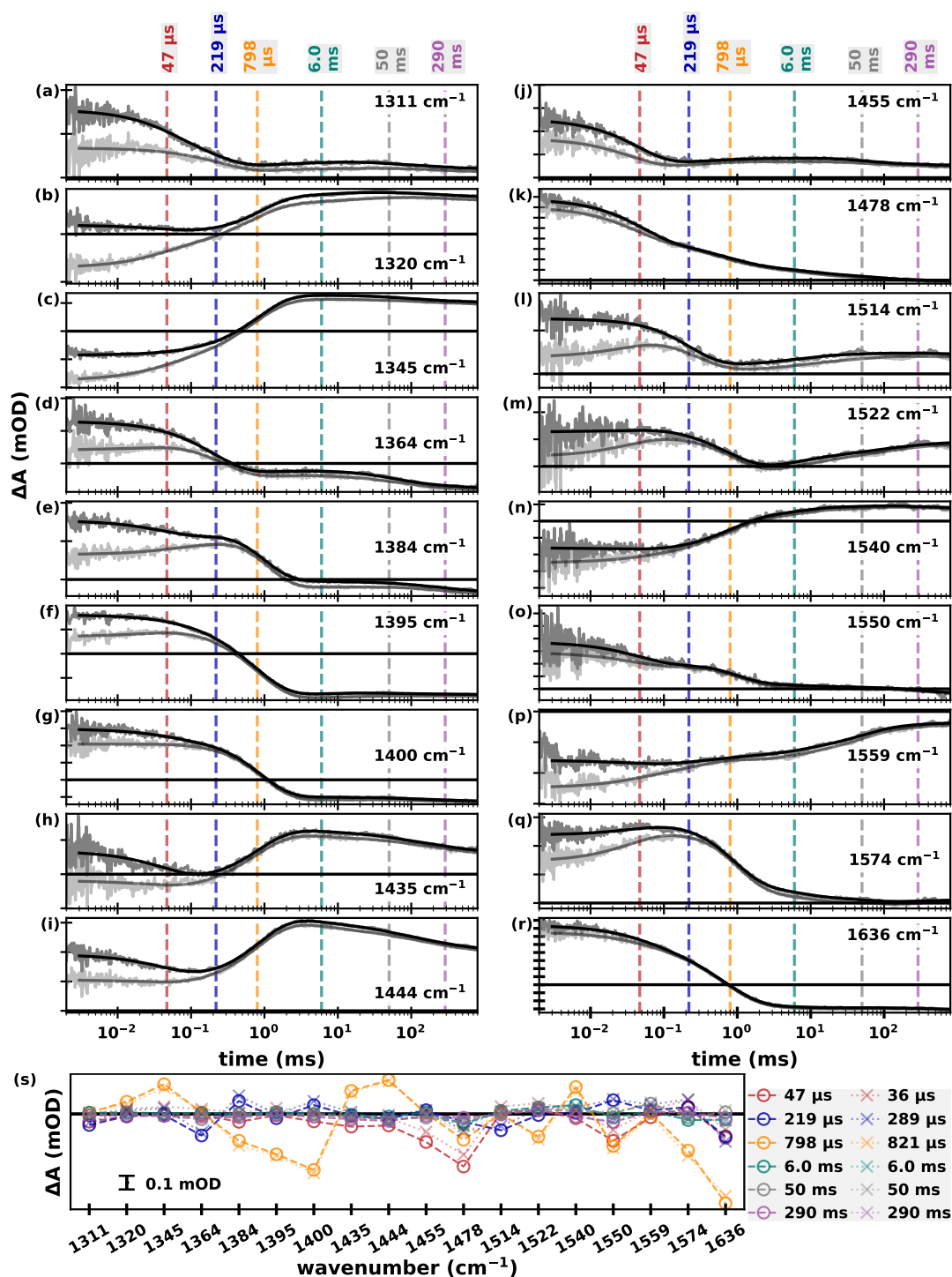
Figure 5.19: Results of globally fitting transient absorption changes of the S$_2$→S$_3$ transition in D$_2$O at 18 different wavenumbers to a sum of six exponentials. (a–r) Transients (*dark grey*) and their fit curves (*black*). The (global) time constants are indicated by vertical dashed lines. The transients are additionally shown after a correction for their P680$^+$ background (*light grey*), as measured at 1790 cm^{-1}, see Chapter 4.3. The y-axis ticks indicate 0.1 mOD. **(s)** Wavenumber-dependent amplitudes of the six exponential components for the fits without (*circles*) and with (*crosses*) P680$^+$ background correction. See text for details on the fitting approach. All transients were deconvolved assuming a starting population of 74% S$_1$, 14% S$_2$ and 12% S$_0$; they were smoothed with a sliding average algorithm with a window size of three data points. All measurements were done at 10 °C and pD 6.2.
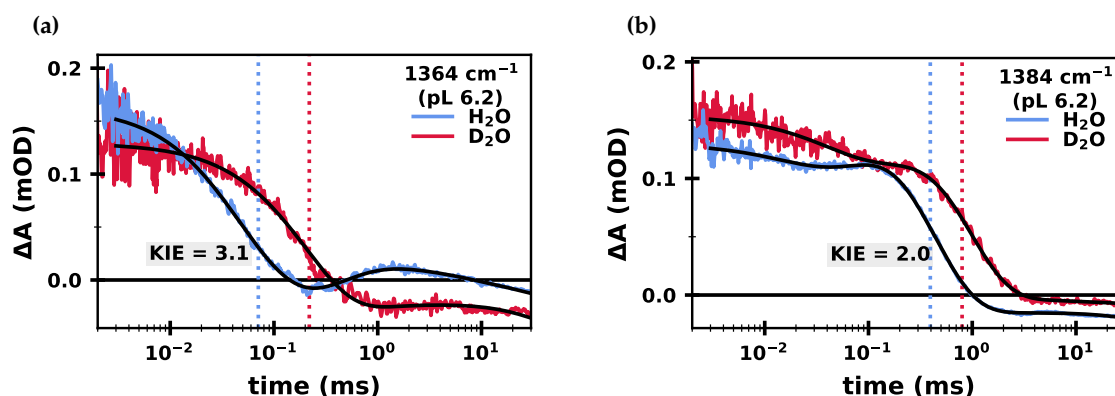
Figure 5.20: Transient absorption changes of the $S_2 \rightarrow S_3$ transition at 1364 and 1384 cm^{-1} in H$_2$O and D$_2$O. (a) IR difference absorption at 1364 cm^{-1} in H$_2$O- and D$_2$O-based buffer (*blue* and *red*, respectively). The PT phase—unlike the ET phase—is strongly pronounced. **(b)** IR difference absorption at 1384 cm^{-1}. Here the ET-phase is strongly present, while the PT phase is only weakly pronounced. All transients were deconvolved assuming a starting population of 74% S$_1$, 14% S$_2$ and 12% S$_0$; they were smoothed with a sliding average algorithm with a window size of three data points.

spectra are shown in Fig. 5.21a and b for the PT and ET step, respectively, alongside their H$_2$O counterparts. The spectra in H$_2$O and D$_2$O are overall similar, supporting the assign-
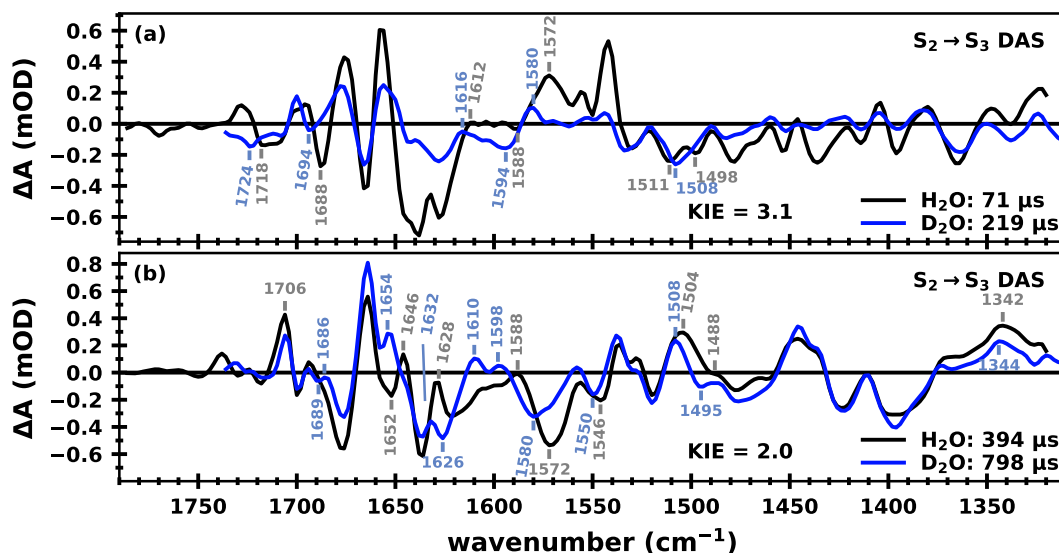

Figure 5.21: Decay associated spectra of the non-P680-background corrected $S_2 \rightarrow S_3$ transition in H$_2$O and D$_2$O. (a) DAS of a 71 μs phase in H$_2$O (*black*), which slows down to 219 μs in D$_2$O (*blue*). These kinetics are likely associated with the PT event. **(b)** DAS of a 394 μs phase in H$_2$O (*black*), which slows down to 798 μs in D$_2$O (*blue*) and is likely associated with the ET event expected in this time range. The DAS were obtained by fitting the time-resolved spectral data set with time constants predetermined by the fits shown in Figures 5.16 and 5.19. The time-resolved spectral data set was deconvolved assuming a starting population of 74% S$_1$, 14% S$_2$ and 12% S$_0$ and a miss factor of 8% (H$_2$O) or 12% (D$_2$O). The equivalent DAS for P680$^+$ corrected data can be found in Fig. A3.11 in the Appendix.

ment to the same processes. The DAS of the PT phase (71/219 µs) show several strongly pronounced changes in amplitude, especially in the amide I region. Several band shifts were also observed, e.g. the features at 1572(+) and 1588(–) cm^{-1} upshift by 6–8 cm^{-1} to 1580(+) and 1594(–) cm^{-1}; very similar shifts were found in the DAS of the ET step (panel b).

A mode of bicarbonate coordinated with Fe^{3+} at 1658 cm^{-1} has previously been reported to upshift to 1686 cm^{-1} in D_2O, while a mode of bicarbonate ligated to Fe^{2+} at 1338 upshifts to 1344 cm^{-1} (Hienerwadel and Berthomieu, 1995). In Fig. 5.21b we indeed see a negative feature at 1652 cm^{-1} become weaker in D_2O and a new negative feature appearing at 1689 cm^{-1}, alongside a small upshift of the 1342(+) cm^{-1} band. Furthermore, a strong negative feature was reported to appear at 1625 cm^{-1} upon deuteration, which indeed also appears in the here shown data, which could indicate that Fe^{3+} reduction is observed in this step. However, ET from Q_A^- to Fe^{3+} has been reported to occur within about 30 µs (Chernev et al., 2011; Diner and Petrouleas, 1987; Petrouleas and Diner, 1987), which is an order of magnitude faster. The here described band shifts may thus not be related to Fe^{3+} reduction and any similarity in band shifts may be coincidental. Further investigation is required for clarity.

5.4.2   Investigation of the pL Dependency

To gain further insight into the nature of the observed kinetics, IR absorption changes of $S_2 \rightarrow S_3$ transition were observed at several different pH and pD values. Visual inspection of the transients at 1395 cm^{-1} reveal a clear pL dependency in H_2O (Fig. 5.22a–b) as well as in D_2O (Fig. 5.22c–d). Note that in panels b and d the data is shown normalized between 1 µs and 10 ms for easier visual comparison. At 1544 cm^{-1}, the transients show a strong, but complicated pH and pD dependency (panels e and f, respectively); the pL is shown to clearly impact more than just a single kinetic component.

The effect of the pL on the kinetics was quantified for each pL value by performing global multi-exponential fits of at least four wavenumbers; the resulting time constants assigned to the PT and ET step are shown in Fig. 5.23. The time constants of both phases show a clear pL dependency. The PT phase becomes faster at higher pH value, with a $\tau_{pH\,5.4}/\tau_{pH\,7.0}$ ratio of 2.5 (although at 7.8 the phase is slightly slower again). While this is a clearly much stronger pH effect than observed by Takemoto et al. (2019) (they reported $\tau_{pH\,5.0}/\tau_{pH\,7.0} = 1.2$), it is similar to the effect observed by Klauss et al. (2015) (they reported $\tau_{pH\,5.5}/\tau_{pH\,7.0} = 2.8$ at 20 °C).

The ET phase also became faster with higher pH—except at pH 7.8, where a time constant similar to that at pH 5.4 was determined. The $\tau_{pH\,5.4}/\tau_{pH\,7.0}$ ratio of 1.3 is still indicative of a non-negligible pH dependency, which is clearly stronger than found by Gerencsér and Dau (2010) ($\tau_{pH\,5.5}/\tau_{pH\,7.0} = 1.15$ at 23 °C), but significantly weaker than found by Takemoto et al. (2019) ($\tau_{pH\,5.0}/\tau_{pH\,7.0} = 2.3$).

The pD dependency was more pronounced than the pH dependency for both phases (with $\tau_{pH\,5.4}/\tau_{pH\,7.0}$ ratios of 2.7 and 3.3 for the PT and ET, respectively).

Overall, the pL dependency observed in the here presented data (together with the KIEs discussed further above) support the assignment of the two investigated kinetic phases to processes involving proton transfer. The fast phase could indeed correspond to a proton removal step. The weaker, but still clearly pronounced pH dependency of the slower phase is in agreement with the assignment of the ET step of the $S_2 \rightarrow S_3$ transition to a PT-coupled ET (Haumann et al., 1997; Klauss et al., 2012a).
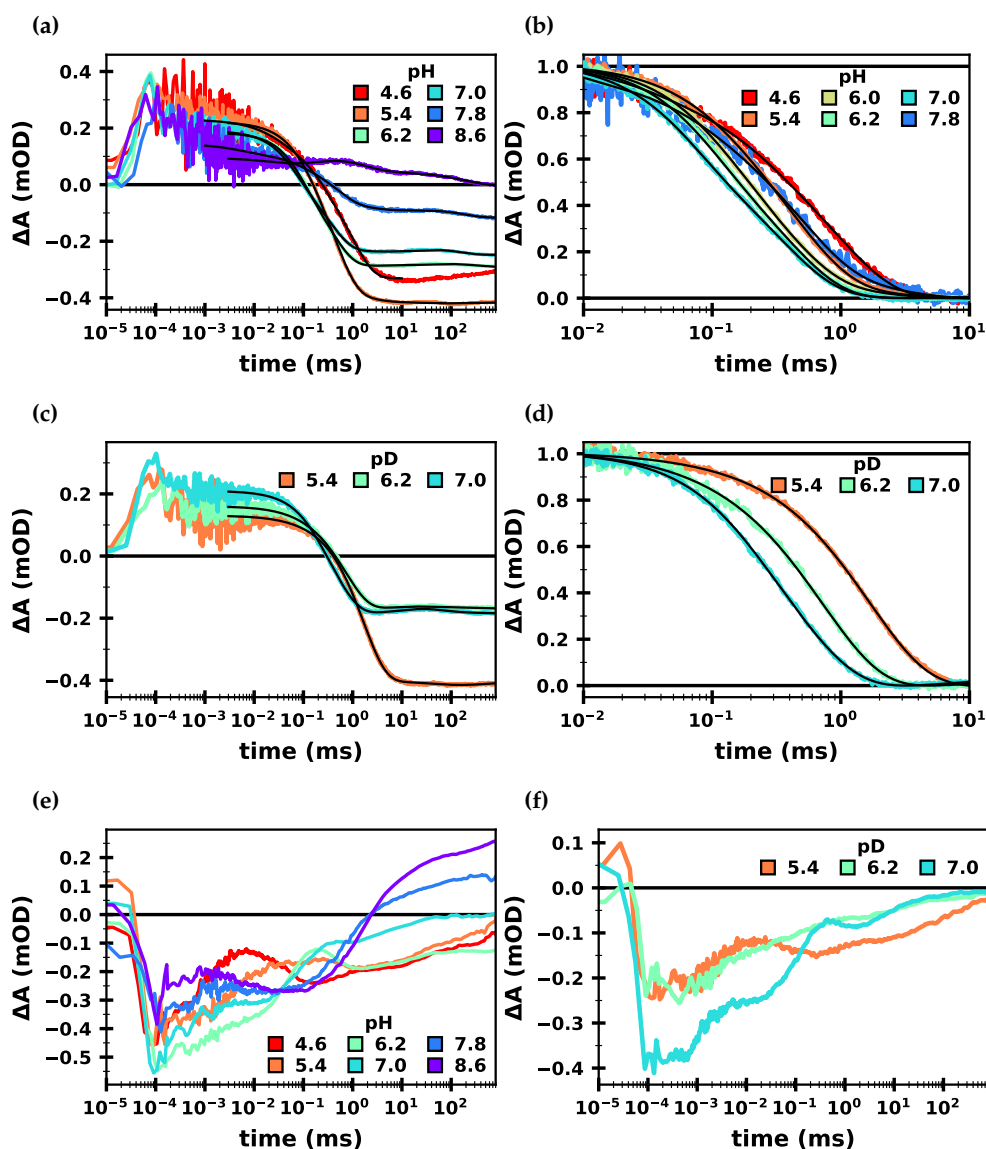
Figure 5.22: Influence of the pH and pD value on the $S_2 \rightarrow S_3$ transition at 1395 and 1544 cm^{-1}. **(a)** Absorption changes at 1395 cm^{-1} (*colored lines*) at six different pH values on a logarithmic x-axis, along with their fit curves (*black*). **(b)** The data as in (a), but shifted and normalized to overlay the decay kinetics. **(c)** Absorption changes at 1395 cm^{-1} in D$_2$O (*colored lines*) at three different pD values, along with their fit curves (*black*). **(d)** The data as in (c), but shifted and normalized to overlay the decay kinetics. **(e)** Absorption changes at 1544 cm^{-1} in H$_2$O (*colored lines*) at six different pH values. **(f)** Absorption changes at 1544 cm^{-1} in D$_2$O (*colored lines*) at three different pD values.

For future experiments, observation of the pH dependency at wavenumbers where the ET and PT phase are easily distinguishable would be helpful, e.g. at 1364 and 1384 cm^{-1}, which seem to be dominated by PT and ET contributions, respectively (see Fig. 5.20). This would help to determine the pH dependency more reliably. In the here presented data it cannot be guaranteed that a separation of the two phases was always entirely possible, especially at the more extreme pH values. As shown in Fig. 5.22e, the transients at 1544 cm^{-1}, e.g., changed so drastically with the pH value that a robust analysis was difficult.
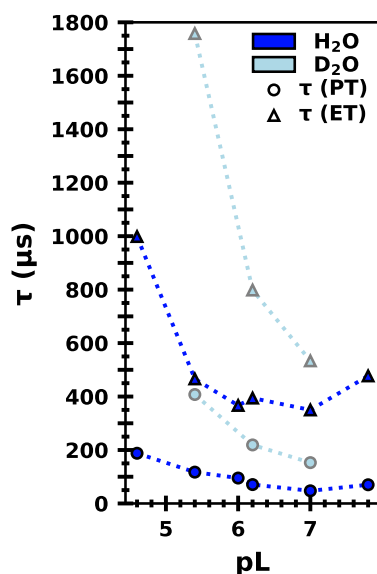
Figure 5.23: Time constants of the PT and ET phases ($S_2 \rightarrow S_3$) in H_2O and D_2O at different pH and pD values. At each pL value, the time constant was determined by fitting at least four transients globally to a sum of exponentials; only the time constants that are likely associated with the PT (*circles*) and ET (*triangles*) steps are shown. Data in H_2O and D_2O is shown in dark and light blue, respectively. The time constants can also be found in Tab. A3.2 in the Appendix.

5.5 The $S_3 \rightarrow S_0$ Transition

As for the $S_2 \rightarrow S_3$ transition, analysis of the $S_3 \rightarrow S_0$ transition was done on deconvolved data sets (assuming a dark-adapted population of 74% S_1, 14% S_2 and 12% S_0). Again, a number of high S/N transients were chosen for global multi-exponential analysis. Fitting the transients without constraint, however, proved to be difficult. Several different fit approaches with varying number of exponential components and with or without additional constraints were attempted. Figure 5.24 shows the results of three different fit approaches (at 1384, 1400 and 1532 cm^{-1}), in which one time constant was always fixed to 2.5 ms, i.e. the expected value for the final ET step (at 10 °C), which occurs concomitantly with oxygen evolution (Haumann et al., 1997; Klauss et al., 2012a; Greife et al., 2023). In panel a and b, the step preceding O_2 evolution was fixed to 340 µs and 890 µs, respectively. In both cases the fit quality was insufficiently good, as judged by the residuals shown above the fit curves. When including both the 340 and 890 µs component (panel c), the fit quality improved drastically. This is also demonstrated in Fig. 5.25, which shows a close-up of the 1532 cm^{-1} transient for the time range in question: While the first two fit curves cannot simulate the observed kinetics, the third approach clearly explains the data well.

Thus, the third approach was chosen, i.e. three time constants were fixed (to 340 µs, 890 µs and 2.5 ms). The reason for requiring two time constants in the hundreds of microseconds time range could be due to two donor-side processes: in a time-resolved IR study by Noguchi et al. (2012), the authors reported time constants of 190 and 550 µs, which they assigned to a proton release and a slower protein relaxation process (the former observed in the strongly H-bonded O-H stretching region at 2500 cm^{-1}; the latter observed via carboxylate vibrations at 1400 cm^{-1}).

A simpler reason for requiring the two time constants could be due to an acceptor-side event occurring with a similar—but not identical—rate. In fact, a mentioned before a time constant of 890 µs was found for the 1st flash data at 1478 cm^{-1} (see Fig. A3.6). As no donor-side processes are expected during the $S_1 \rightarrow S_2$ transition in that time range, this is likely attributable to an acceptor-side event, which is then likely to also occur in the $S_3 \rightarrow S_0$ transition (due to the periodicity of two of the acceptor side)—which is why the value of 890 µs was chosen alongside 340 µs.
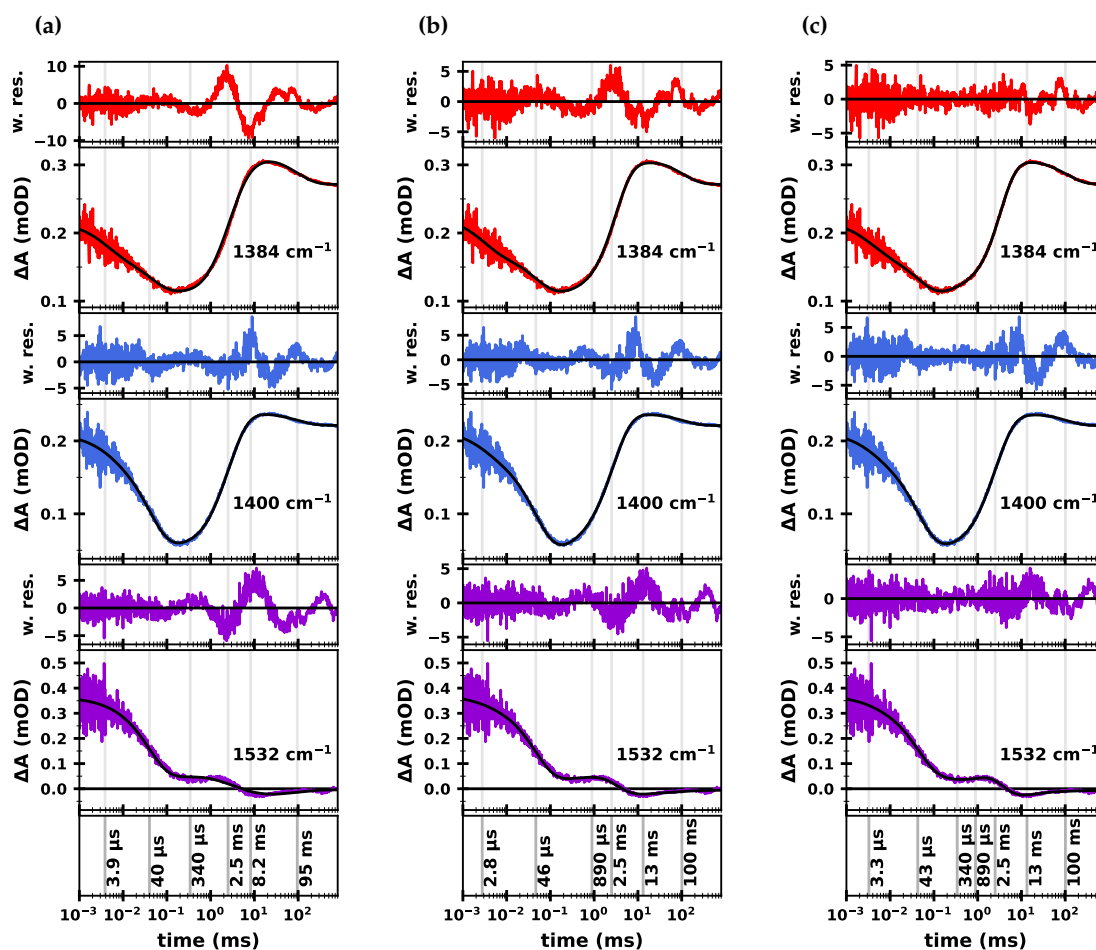
Figure 5.24: Three fit approaches for the $S_3 \rightarrow S_0$ transition. In all approaches, transients at 1384, 1395, 1400, 1442, 1507, 1514, 1520, 1532, 1538, 1548, 1550, 1552, 1576 and 1708 cm^{-1} were fit globally to a sum of exponentials (fit range 1 μs–800 ms); only 1384 (*red*), 1400 (*blue*) and 1532 cm^{-1} (*purple*) are shown here. Each transient in each panel is show together with its fit curve (*black*); the weighted residuals are shown above the transients in matching colors. The time constants are indicated with vertical grey lines. **(a)** Fit with six exponentials, where two time constants were fixed ($\tau_3 = 340$ μs and $\tau_4 = 2.5$ ms). **(b)** Fit with six exponentials, where two time constants were fixed ($\tau_3 = 890$ μs and $\tau_4 = 2.5$ ms). **(c)** Fit with seven exponentials, where three time constants were fixed ($\tau_3 = 340$ μs, $\tau_4 = 890$ μs and $\tau_5 = 2.5$ ms). All transients were deconvolved assuming a starting population of 74% S_1, 14% S_2 and 12% S_0 and a miss factor of 8%. The measurements were done at 10 °C and pH 6.2.
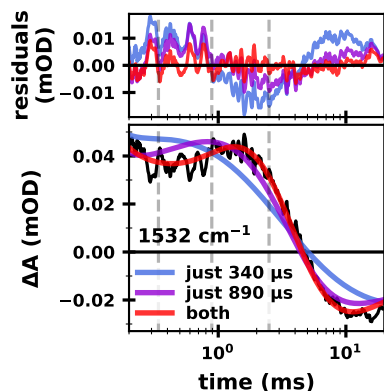
Figure 5.25: Fit quality of three different fit approaches of the $S_3 \rightarrow S_0$ transition at 1532 cm^{-1}. Transient IR absorption changes (*black*) and three different fit curves (*colored lines*) from the fitting procedure detailed in Fig. 5.24. Visual inspection of the (non-weighted) residuals (top panel), as well as the fit curves clearly favor the approach that includes both a 340 and 890 μs phase (*red*), rather than just 340 μs (*blue*) or just 890 μs (*purple*). The data was smoothed with a sliding average algorithm with a window size of 5 data points for easier visual inspection.

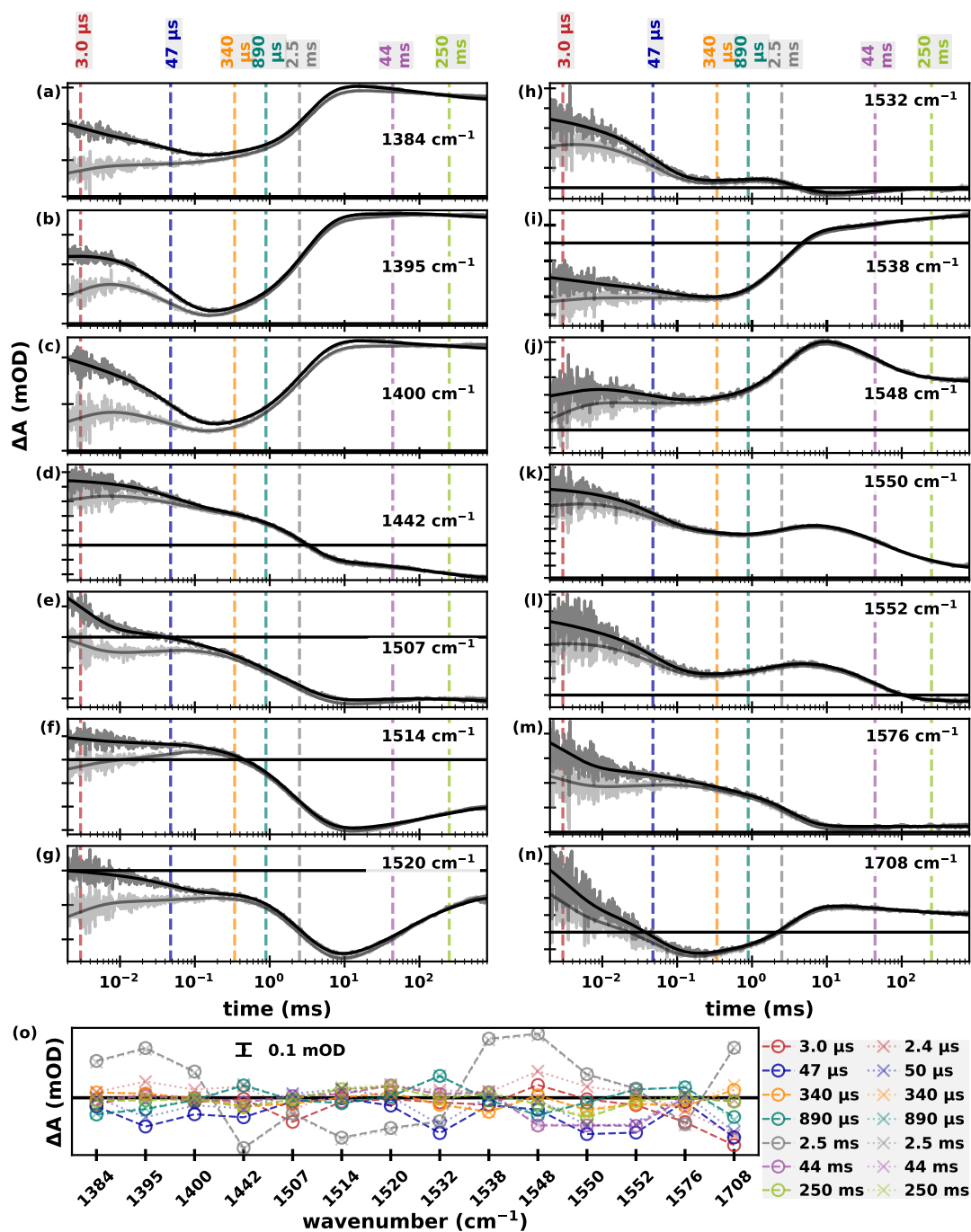**Figure 5.26: Results of globally fitting transient absorption changes of the $S_3 \rightarrow S_0$ transition at 14 different wavenumbers. (a–t)** Transients (*dark grey*) and their fit curves (*black*). The (global) time constants are indicated by vertical dashed lines. The transients are additionally shown after a correction for their P680$^+$ background (*light grey*), as measured at 1780 cm^{-1}, see Chapter 4.3. The y-axis ticks indicate 0.1 mOD. The transients were fit globally to a sum of seven exponentials; five time constants were fixed ($\tau_3 = 340$ µs, $\tau_4 = 890$ µs, $\tau_5 = 2.5$ ms, $\tau_6 = 44$ ms and $\tau_7 = 250$ ms), all other variables were left free to vary (see text for details on the fit approach). The fit range was 1 µs–800ms. **(o)** Wavenumber-dependent amplitudes of the seven exponential components for the fits without (*circles*) and with (*crosses*) P680$^+$ background correction. See text for details on the fitting approach. All transients were deconvolved assuming a starting population of 74% S_1, 14% S_2 and 12% S_0; they were smoothed with a sliding average algorithm with a window size of three data points. All measurements were done at 10 °C and pH 6.2.

For the final data fitting, the two fastest time constants were left unconstrained, but the two slowest were fixed to 44 and 250 ms, as rationalized for the $S_1 \rightarrow S_2$ transition. The 8.5 ms phase, which was included in the fit of $S_1 \rightarrow S_2$ (see Fig. 5.9), was omitted here to avoid over-fitting (because of its close temporal proximity to the 2.5 ms phase). Figure 5.26a–n shows the fit results of all 14 selected transients; panel o shows time constants and their wavenumber-dependent amplitudes. Fitting the transients after subtracting their $P680^+$ background (light grey) gave similar results; merely the amplitude of the fastest phase was again strongly affected (crosses in panel o).

The pre-determined time constants were fixed in a global fit of the time-resolved spectral data set; the resulting decay associated spectra are shown in Fig. 5.27. In the following, the spectra will be discussed one by one:

(a) The y_0 spectrum at 0.5 μs is overall similar to the y_0 spectra of the $S_1 \rightarrow S_2$ and $S_2 \rightarrow S_3$ transitions (Figs. 5.9a and 5.18a), again indicating the presence of Q_A^- and $P680^+$. There are some differences, however, notably including the absence of a 1704(–) cm^{-1} feature and the instead strongly pronounced 1698(–) cm^{-1} peak. As these differences may simply be due to the slightly different fit ranges, they will not be discussed here in detail. Indeed, the spectra averaged around 100-500 ns in Fig. 5.7a, as well as the spectra recently reported by our group (Dekmak et al., 2023) indicate that the S-state dependence of the early spectra is quite low.

(b) – (c) The 3.0/2.4 μs and 47/50 μs DAS are clearly associated with $P680^+$ reduction, *inter alia* recognizable by the nearly featureless, negative signal above 1750 cm^{-1}, which shifts to zero upon $P680^+$ background subtraction. The 3.0/2.4 μs DAS shows signs of Y_Z^{ox} formation, such as the strongly pronounced peaks at 1708(–) and 1664(–) cm^{-1}. The 1556(–)/1546(+) cm^{-1} feature possibly arises from $P680^+$ and Y_Z^{ox} features canceling each other out. The features in the amide I region of the 47/50 μs DAS seem to rather indicate dominating $P680^+$ reduction. The feature at 1551(–)/1543(+)/ 1530(–) cm^{-1} is very similar to features in Y_Z^{ox}/Y_Z spectra (Nagao et al., 2017b) possibly indicating Y_Z^{ox} *reduction*—however, this is much too early for reduction by the Mn_4CaO_x cluster and would thus indicate Y_Z^{ox} recombination with the acceptor side. Alternatively, this feature could be due to $P680^+$ reduction: Most of previously reported $P680^+/P680$ spectra were obtained on Mn depleted samples and it cannot be excluded that its spectral signature differs in intact PSII. In fact, we recently reported a double difference spectrum (10 μs minus 500 ns), which we assigned to be dominated by $P680^+$ reduction and this spectrum showed a similar feature (Dekmak et al., 2023).

(d) – (e) The DAS of the 340 and 890 μs components show many mirrored features with respect to each other, very likely indicating that there is strong cross-talk between the two components (meaning they are mathematically poorly separated from each other and thus the resulting spectra are poorly resolved). This will be discussed in more detail further down.

(f) The strong 1544(+) and 1706(+) cm^{-1} features in the 2.5 ms DAS could indicate Y_Z^{ox} reduction, even though the amide I region does not clearly reflect this. The features in the amide I region (1678(+)/1670(–)/1660(+)/1648(–) cm^{-1}) instead resemble those of the steady-state spectrum (see panel j and Fig. 5.7b, *green*), possibly indicating that the majority of the overall structural changes to the protein occur during this phase (although the 1660(+) cm^{-1} peak is significantly more pronounced in the DAS than in the steady-state spectrum). In fact, this is further supported by the observation that
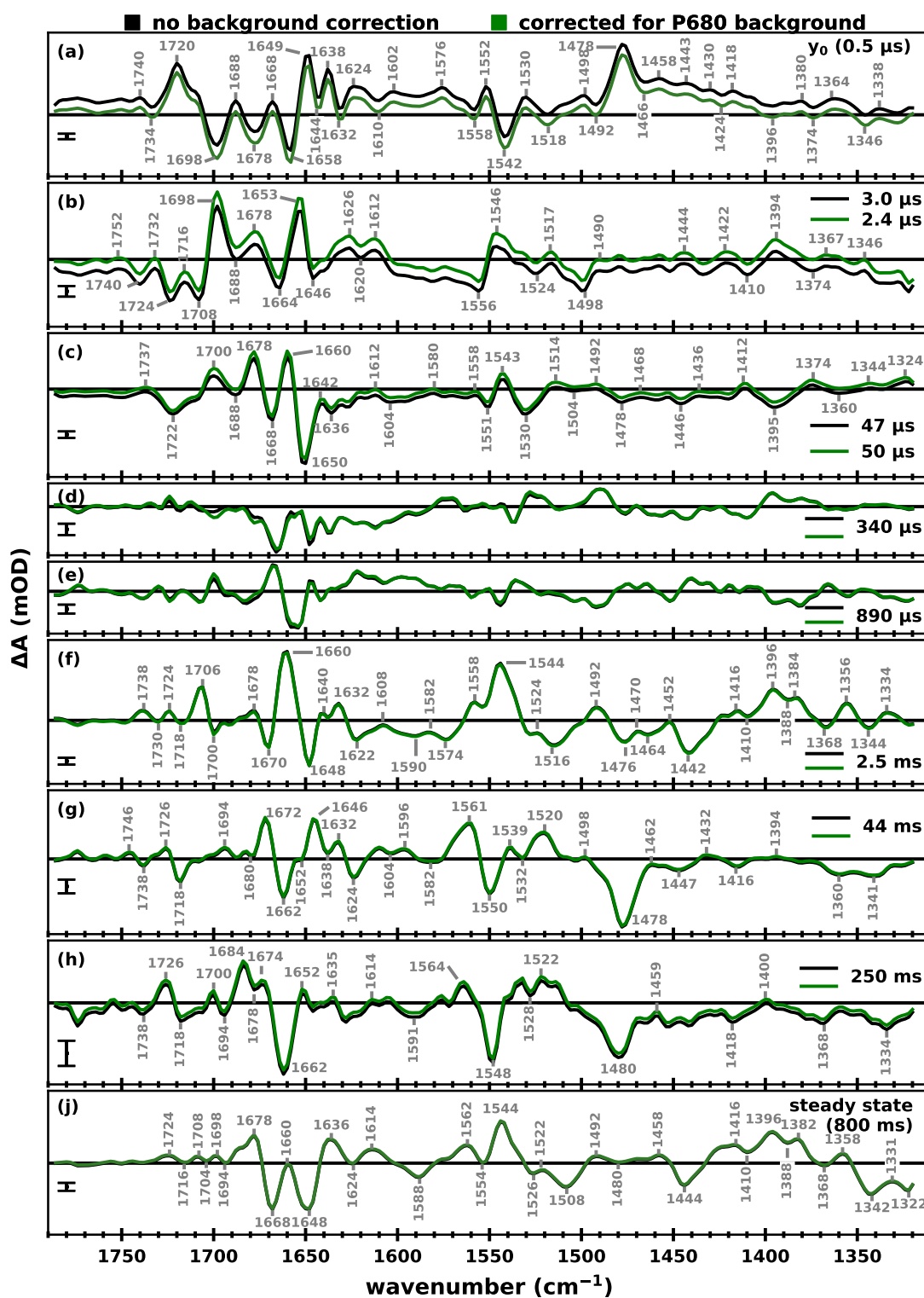
Figure 5.27: Decay associated spectra of the $S_3 \rightarrow S_0$ transition. (a) Initial spectrum at 0.5 μs (y_0) and **(b–h)** DAS of all seven components. The DAS were obtained by fitting the time-resolved spectral data set with time constants predetermined by the fits shown in Fig. 5.26 (fit range 0.5 μs–800 ms). **(j)** Steady-state spectrum (at 800 ms), obtained by addition of all seven DAS and the initial spectrum ($y_0 + \sum A_i$). All spectra are shown with (*green*) and without (*black*) P680-background correction. The time-resolved spectral data set (acquired at 10 °C and pH 6.2) was deconvolved assuming a starting population of 74% S_1, 14% S_2 and 12% S_0. The scale bar in each panel corresponds to 0.1 mOD.

the 1554(–)/1544(+)/1526(–) cm^{-1} features in the amide II region are also present in the steady-state spectrum. The region below 1450 cm^{-1} also shows a strong similarity to the steady-state spectrum, despite the 1342(–) and 1322(–) cm^{-1} features appearing less pronounced.

(g) The DAS of the 44 ms phase is very similar to that of the $S_1{\rightarrow}S_2$ (see Fig. A3.17d for a direct comparison). The strong resemblance to inverted Q_A^-/Q_A spectra (Berthomieu et al., 1990) as well as to inverted Fe^{2+}/Fe^{3+} spectra (Berthomieu and Hienerwadel, 2001; Takahashi et al., 2010) could indicate ET from both Q_A^- and Fe^{2+} to a secondary quinone acceptor (as is expected in experiments with PPBQ; see also Fig. 4.4). Similarly as in the equivalent $S_1{\rightarrow}S_2$ DAS (Fig. 5.9f), the 1672(+)/1662(–) cm^{-1} as well as the 1582(–)/1561(+)/1550(–)/1539(+) cm^{-1} features strongly resemble those reported for Fe^{2+}/Fe^{3+} FTIR spectra (see also Fig. 4.13c).

(h) The DAS of the 250 ms phase is very similar to that of the $S_1{\rightarrow}S_2$ transition (Fig. 5.9g). The direct comparison of both DAS (Fig. A3.17e) reveals that the $S_3{\rightarrow}S_0$ DAS is clearly more noisy, which is likely merely a side-effect of the deconvolution procedure. The prominent peaks at 1480(–), 1548(–) and 1662(–) cm^{-1} are indicative of Q_A^- and/or Q_B^- decay, possibly due to backward ET and recombination with the donor-side. The overall amplitudes of this DAS are significantly smaller than those of the other DAS.

(i) The steady-state spectrum at 800 ms shown here is near identical to that in Fig. 5.7, which shows the averaged spectra between 400–800 ms; see Section 5.2.4 for a discussion of the latter.

As discussed above, two phases in the hundreds of microseconds (340 and 890 µs) were needed for a sufficiently good simulation of the data, likely to account for the PT phase preceding O_2 evolution, as well as acceptor-side kinetics. However, as these time constants are very close to each other, they are very likely not well separated; even more so, since the individual transients of the time-resolved spectral data set are of comparably low S/N. This raises the question of whether either of the two DAS can reliably represent the PT DAS—and if yes, which one.

Recently, Greife et al. (2023) published a step-scan FTIR study on spinach PSII, showing DAS of the ET step, as well as the preceding PT step. This gives the opportunity for a direct comparison here: Fig. 5.28 thus shows the two DAS as well as the steady-state spectrum in a similar style as in the mentioned paper, allowing for easy comparison by visual inspection. The steady-state spectrum and the DAS of the ET phase are indeed overall very similar to the respective FTIR spectra. In Fig. 5.28a the PT DAS is assumed to be represented by the 340 µs time constant. While in parts similar to the results of the step-scan FTIR study, the PT DAS diverges quite strongly in many regions, most notably between 1740–1700 cm^{-1}, 1600–1560 cm^{-1} and 1440–1340 cm^{-1} (hatched with grey lines). When instead assuming the 890 µs phase reflects the PT phase (Fig. 5.28b), there is a wider agreement with the FTIR step-scan data. However, unlike in the FTIR data, a crucial peak around 1570(+) cm^{-1} is not present in the here shown DAS and also the 1400–1390 cm^{-1} region still deviates quite strongly.

As neither of the 340 and 890 µs DAS can be reliably and unambiguously assigned to the PT step, it became clear that an acceptor-side correction would be necessary. As acceptor-side kinetics show a period-of-two behavior, they should be the same in the $S_1{\rightarrow}S_2$ and $S_3{\rightarrow}S_0$ transitions. Furthermore, donor-side kinetics of the $S_1{\rightarrow}S_2$ transition should be completed within ~100 µs and slower components should be attributable exclusively to acceptor-side events. Thus, the 890 µs component reported in Chapter 5.3 should contain
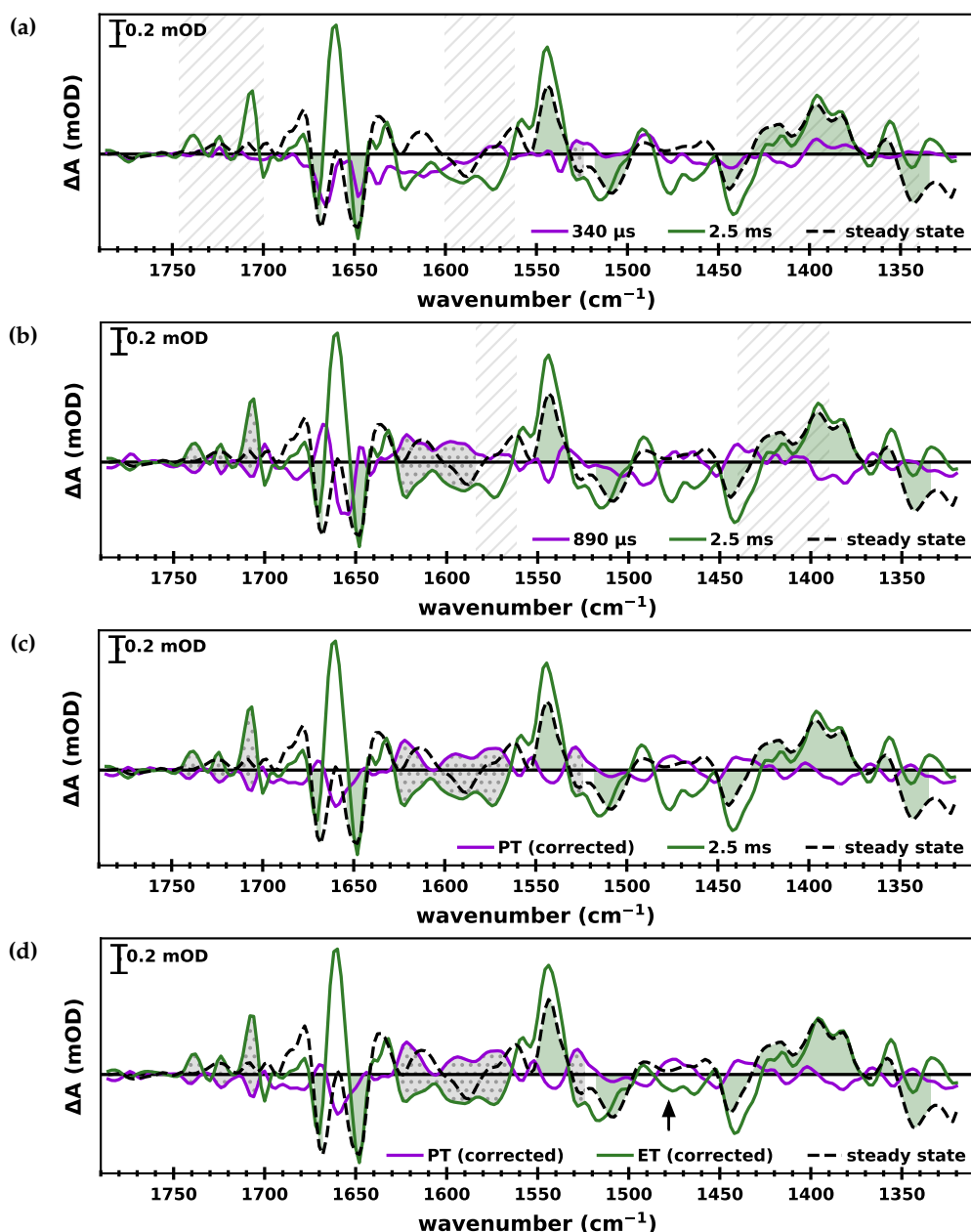
Figure 5.28: Decay associated spectra of the PT and ET step alongside the steady-state spectrum of the S₃→S₀ transition for different approaches. Spectral regions in which the ET phase (*green*) shows a similar behavior as the steady-state spectrum (*dashed black*) are shaded in *green*. Regions where the PT behavior (*purple*) is reversed by the ET step are shaded in *dotted grey*. All DAS are results of a seven-exponential fit, including $\tau_3 = 340$ µs, $\tau_4 = 890$ µs and $\tau_5 = 2.5$ ms. The PT DAS is shown for **(a)** assuming it is described by the 340 µs phase **(b)** assuming it is described by the 890 µs phase and **(c–d)** after performing an acceptor-side correction (as detailed in Fig. 5.29). In panels (a), (b) and (c) the ET phase is represented by the 2.5 ms DAS; in panel (d) it is shown after an acceptor-side correction (i.e. after subtraction of the 8.5 ms DAS of S₁→S₂). In (a) and (b) regions in which the DAS of the PT phase do not agree well with previous FTIR results (Greife et al., 2023) are indicated by grey hatched lines.
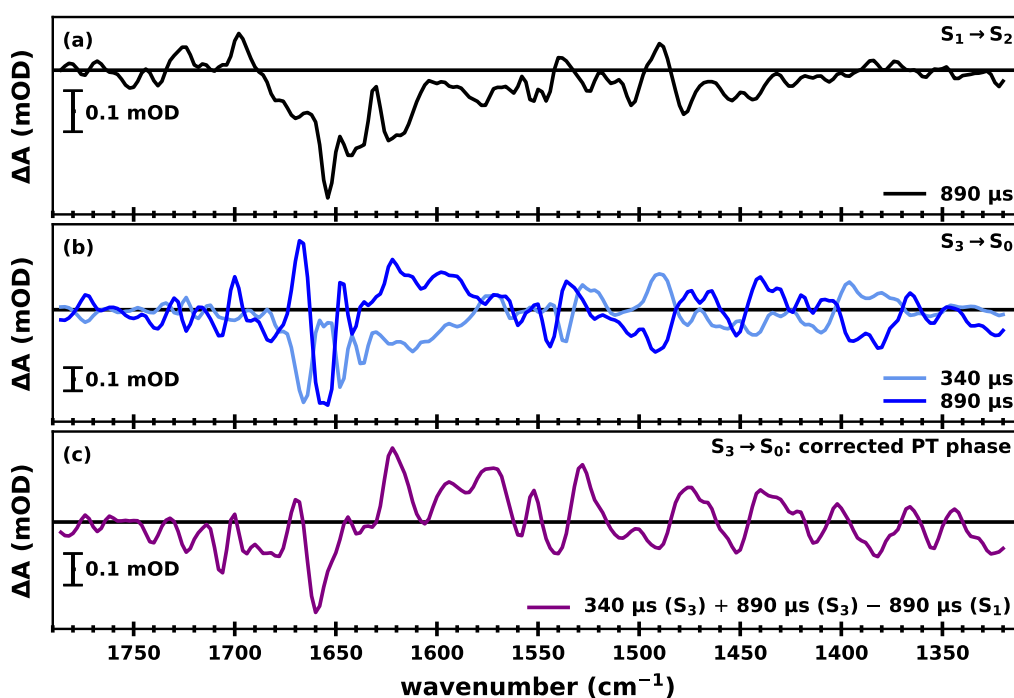
Figure 5.29: Correction of the DAS of the PT phase for acceptor-side contributions. (a) DAS of the 890 μs phase of the $S_1 \rightarrow S_2$ data set. As donor-side reactions are expected to be (to a large extent) completed at this time point, this DAS should reflect mostly acceptor-side contributions. **(b)** DAS of the 340 and 890 μs phases of $S_3 \rightarrow S_0$, corresponding to the fit approach shown in Fig. 5.24c. Both DAS are likely a mixture of donor-side PT event and acceptor-side contributions. **(c)** Sum of the two DAS shown in (b) minus the DAS shown in (a). This should reflect the first $S_3 \rightarrow S_0$ PT event without acceptor-side contributions.

the same acceptor-side information which is also mixed in the 340 and 890 μs components of the $S_3 \rightarrow S_0$ transition (see Fig. 5.29a and b). Addition of the 340 and 890 μs $S_3 \rightarrow S_0$ DAS and subtraction of the $S_1 \rightarrow S_2$ 890 μs DAS results in a corrected PT DAS shown in Fig. 5.29c. This corrected DAS alongside the ET DAS and steady-state spectrum is shown in Fig. 5.28c; it shows overall good agreement with the FTIR DAS (Greife et al., 2023). Presumably the 8.5 ms phase (assigned to acceptor-side events) found for the $S_1 \rightarrow S_2$ data is also present in the $S_3 \rightarrow S_0$ data and thus likely contributes to the 2.5 ms phase. Subtraction of the 8.5 ms $S_1 \rightarrow S_2$ DAS from the $S_3 \rightarrow S_0$ 2.5 ms DAS has—for most parts—only a subtle effect on the ET DAS (Fig. 5.28d). It does however result in a notably diminished 1478(−) cm^{-1} feature.

Plotting the ET DAS alongside the steady-state spectrum (Fig. 5.28c–d) confirms the observation made further above that the two spectra are very similar in the amide I and amide II region, as well as in the symmetric carboxylate stretching region below 1450 cm^{-1}. In other regions, i.e. between 1700 and 1740 cm^{-1} as well as between about 1630 and 1560 cm^{-1} the ET phase appears to revert absorption changes initiated by the PT phase. These observations are overall very similar to those made by Greife et al. (2023).

Figure 5.30 shows the transient absorption changes at 1382, 1568 and 1708 cm^{-1}, allowing for a direct comparison with the equivalent step-scan data shown by Greife et al. (2023). Note that here data at 1568 cm^{-1} is shown, rather than that at 1570 cm^{-1}: In this wavenumber region the visibility of the PT rising phase seems to be very much wavenumber-dependent and appears most pronounced at 1568 cm^{-1}. This will be discussed in more detail in the
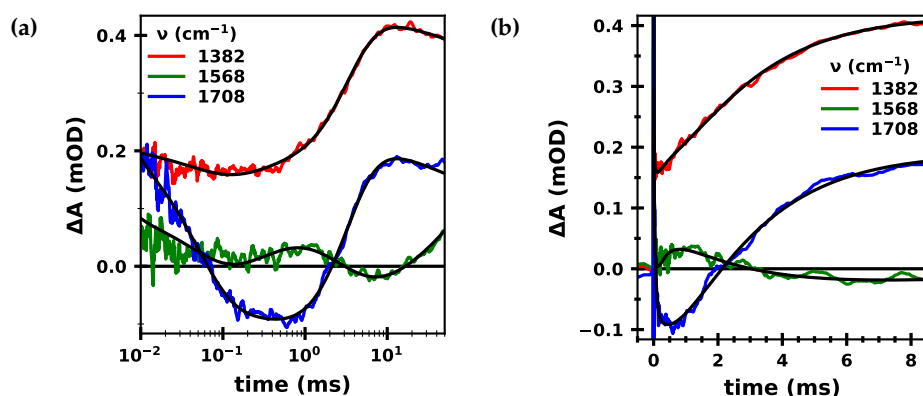
Figure 5.30: Transient abortion changes of $S_3 \rightarrow S_0$ at 1382, 1568 and 1708 cm^{-1}. The data is shown on **(a)** a logarithmic and **(b)** a linear x-axis. All transients were deconvolved assuming a starting population of 74% S_1, 14% S_2 and 12% S_0. The shown data is part of the time-resolved spectral data set; it was however not smoothed along the wavenumber axis. All data was acquired at 10 °C and pH 6.2.

concluding discussion further down (Section 5.6). The transients shown here show some differences to the step-scan FTIR data, which could simply be due to the lower spectral resolution of the FTIR data. Both data sets nevertheless demonstrate a pre-ET "lag phase" behavior at 1382 cm^{-1} and a pre-ET behavior at 1708 and 1568 cm^{-1}, which is (at least partly) reversed by the ET phase.

The mechanistic implications from the DAS results, as well as new insight gained from the here presented results in comparison to the step-scan FTIR results will be discussed further down (Chapter 5.5.3). Note that the DAS obtained on a deconvolved data set assuming an alternative starting population of 75% S_1 and 15% S_0 gave very similar results (*not shown*).

5.5.1 Kinetic and Spectral Changes upon H/D Exchange

Similarly to the situation with the H_2O data, finding a good fit approach for the D_2O data proved difficult. In the end, 14 high S/N transients were fit globally to a sum of exponentials, whereby most of the time constants were fixed (*inter alia* to 400 µs, 890 µs and 3.4 ms). The transients and fit curves, as well as the wavenumber-dependent amplitudes of the exponential components are shown in the Appendix (Fig. A3.12).

Since most of the time constants were fixed, estimating a kinetic isotope effect from them is not meaningful. Figure 5.31 shows transients at 1384 and 1400 cm^{-1} in H_2O and D_2O. To attempt to estimate the effect of H/D exchange, the transients were normalized such that their millisecond rise starts at zero and ends at 1. From the half-lives of these rising phases a KIE of 1.3–1.5 was determined, which is in agreement with previous observations for the ET phase (Klauss et al., 2012a; Zaharieva et al., 2016). The position of the minimum value was found 2.6–3.6 times later in D_2O than in H_2O, which could relate to a slowed PT event; previously KIEs of about 2.5 were reported (Zaharieva et al., 2016; Gerencsér and Dau, 2010).

Global analysis across the entire time-resolved spectral data set was again done with the predetermined time constants. Just as for the H_2O data, the DAS of the PT phase was calculated by adding the DAS of the two slow microsecond phases (400 and 890 µs) and
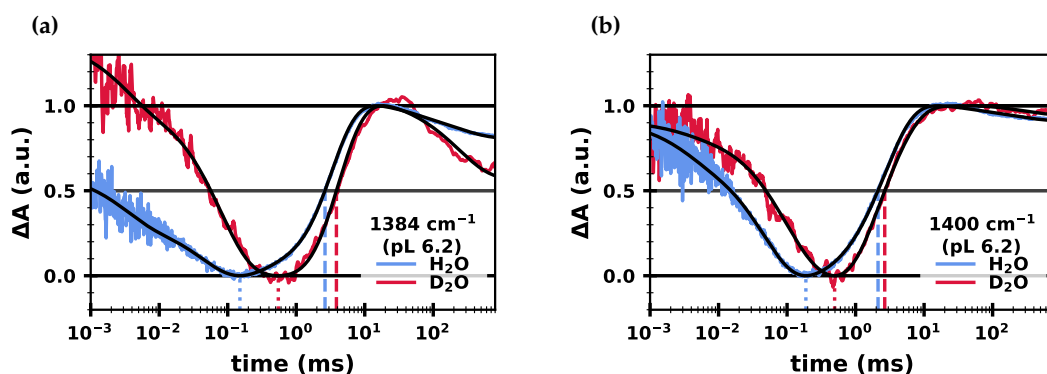
Figure 5.31: Kinetic isotope effect of the $S_3 \to S_0$ transition at 1384 and 1400 cm^{-1}. (a) Difference IR absorption at 1384 cm^{-1} in H_2O (*blue*) and D_2O (*red*) together with their fit curves (*black*). The half-life of the millisecond rise phase increases from $\tau_H = 2.6$ ms to $\tau_D = 3.9$ ms (KIE = 1.5). The minimum shifts from $t_{min,H} = 151$ μs to $t_{min,D} = 547$ μs (KIE = 3.6). **(b)** Difference IR absorption at 1400 cm^{-1} in H_2O (*blue*) and D_2O (*red*) together with their fit curves (*black*). The half-life of the millisecond rise phase increases from $\tau_H = 2.1$ ms to $\tau_D = 2.7$ ms (KIE = 1.3). The minimum shifts from $t_{min,H} = 188$ μs to $t_{min,D} = 494$ μs (KIE = 2.6). In both panels, the half-life of the millisecond rise phase is indicated with dashed lines; the minimal value is indicated with dotted lines.

subtracting the 890 μs DAS of the $S_1 \to S_2$ transition (shown in Fig. A3.13 in the Appendix). The DAS of the ET and the corrected PT phase, as well as the steady-state spectrum, are shown in Fig. 5.32. In the amide I and amide II regions, as well as below 1450 cm^{-1}, the DAS of the ET phase resemble the steady-state spectrum, as observed further above for the data in H_2O. Reversed behavior of ET and PT phase was also observed, although with some changes compared to the H_2O data, as will be discussed in more detail further down.
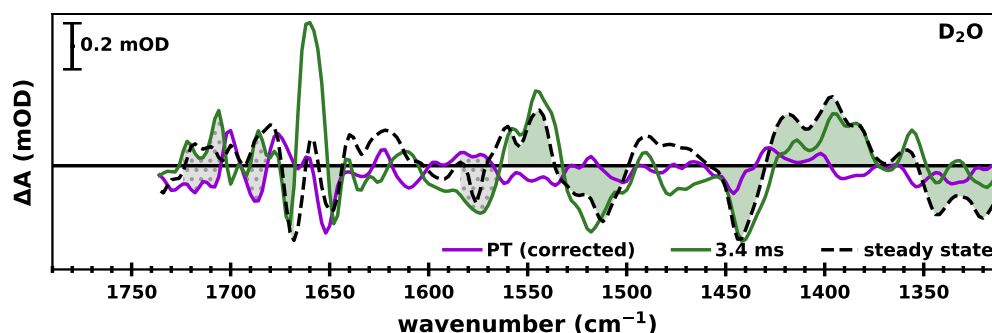
Figure 5.32: Decay associated spectra in D_2O of the ET and (acceptor-side corrected) PT step alongside the steady-state spectrum of the $S_3 \to S_0$ transition. Spectral regions in which the ET phase (*green*) shows a similar behavior as the steady-state spectrum (*dashed black*) is shaded in *green*. Regions where the PT behavior (*purple*) is reversed by the ET step are shaded in *dotted grey*. The DAS were obtained from a seven-component exponential fit (see Fig. A3.12 in the Appendix), where five time constants were fixed, including $\tau_3 = 400$ μs, $\tau_4 = 890$ μs and $\tau_5 = 3.4$ ms. The DAS of the PT phase was corrected for acceptor-side contributions equivalent to the procedure for H_2O (see Fig. A3.13 in the Appendix). The time-resolved spectral data set was deconvolved assuming a starting population of 74% S_1, 14% S_2 and 12% S_0 and a miss factor of 12%.

5.5.2 Investigation of the pH Dependency

Figure 5.33a shows the transients at 1400 cm^{-1} measured at different pH values; transients at 1514 cm^{-1} are additionally shown in Fig. A3.14 in the Appendix. As the relative amplitudes of different kinetic phases evidently change with the pH, it is difficult to visually assess the effect on the kinetics. In Fig. 5.33b the transients are normalized such that the millisecond phase becomes comparable, revealing that the millisecond kinetics become faster with increasing pH value. At pH 7.8, however, the kinetics appear to be similarly slow as at pH 4.6. Figure 5.33c–d show the same plots for data measured in D$_2$O, clearly showing faster kinetics at higher pD values.

To quantify the pL effect, the transients were fit globally (at least four wavenumbers per pL value) to a multi-exponential function. As discussed above, obtaining meaningful fit results for the pre-ET phases was difficult, thus only the results for the millisecond rise phase (assigned to the ET step) will be looked at in detail. Unlike in the results shown further above for the data at pL 6.2, the time constants were not fixed in the analysis here. The resulting time constants are shown in Fig. 5.34.

The pH effect on the ET step is stronger than observed by Gerencsér and Dau (2010), who observed a $\tau_{\mathrm{pH\,5.5}}/\tau_{\mathrm{pH\,7.0}} = 1.03$ at 20 °C, while here we report $\tau_{\mathrm{pH\,5.4}}/\tau_{\mathrm{pH\,7.0}} = 1.15$. This is clearly more in line with the ratio of 1.14 observed by Klauss et al. (2015) (also at
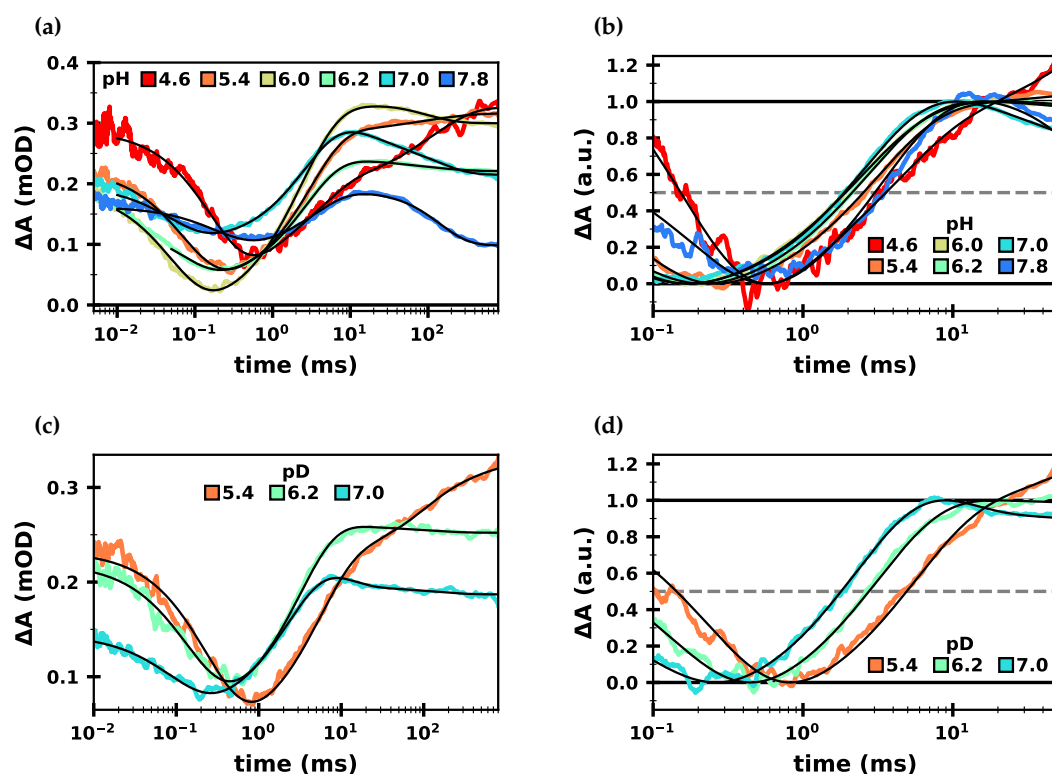
Figure 5.33: Influence of the pH and pD value on the S$_3$→S$_0$ transition at 1400 cm^{-1}. **(a)** Absorption changes at 1400 cm^{-1} (*colored lines*) at six different pH values, along with their fit curves (*black*). **(b)** The same data as in (a), but shifted and normalized. **(c)** Absorption changes at 1400 cm^{-1} in D$_2$O (*colored lines*) at three different pD values, along with their fit curves (*black*). **(d)** The same data as in (c), but shifted and normalized. All transients were deconvolved assuming a starting population of 74% S$_1$, 14% S$_2$ and 12% S$_0$.

Figure 5.34: Time constants of the ET phase ($S_3 \rightarrow S_0$) in H_2O and D_2O at different pH and pD values. At each pL value, the time constant was determined by fitting at least four transients globally to a sum of exponentials; only the time constants that are likely associated with the ET step (*triangles*) are shown. Data in H_2O and D_2O is shown in *dark* and *light green*, respectively. The values are also given in Tab. A3.3 in the Appendix.
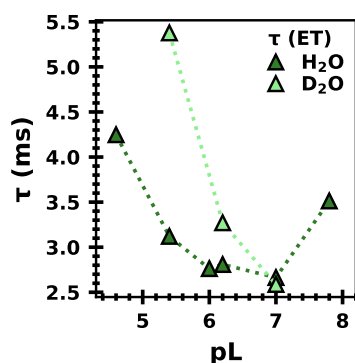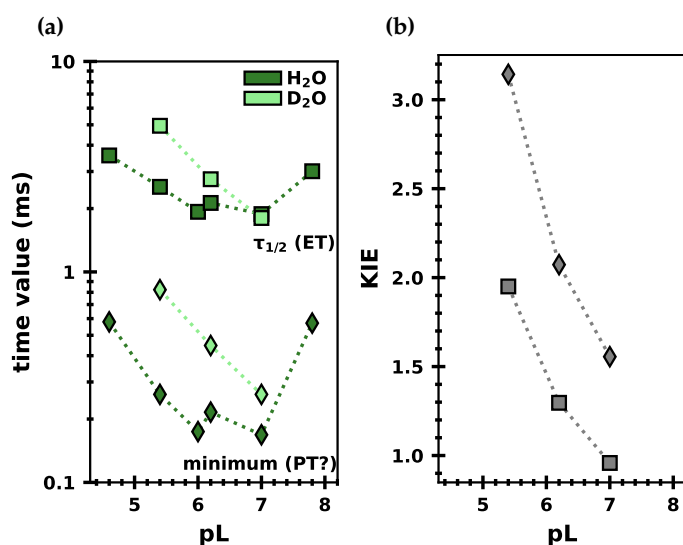

Figure 5.35: Half-times of the ET phase ($S_3 \rightarrow S_0$) in H_2O and D_2O at different pH and pD values, along with the pre-ET minima at 1400 cm⁻¹. **(a)** The half-times (*squares*) of the millisecond rising phase as well as the preceding minima (*diamonds*). The values were determined at various pH (*dark green*) and pD values (*light green*) as demonstrated in Fig. 5.31 for the data sets at pL 6.2. **(b)** The resulting KIEs (τ_D / τ_H). The values are also given in Tab. A3.3.

20 °C). The latter study found that the ET step became faster with increasing pH until pH 6.5; at pH 7.0 they observed a slightly slower rate. This is qualitatively in line with the observation that τ_{ET} is effectively the same at pH 6.2 and 7.0 and slower at both higher and lower pH values. The observation of an optimal pH between 6.2 and 7.0 is also in agreement with other studies (Bernát et al., 2002; Christen et al., 1999; Suzuki et al., 2005b).

In addition to multi-exponential fitting, the data was also subjected to the treatment demonstrated in Fig. 5.31 for the data at pL 6.2: The data was normalized and shifted to overlay the millisecond rising phases and subsequently their half-times as well as the time points of their minima were determined; the resulting values are shown in Fig. 5.35a. The half-times show a similar pL-dependency as the millisecond time constants, confirming the above discussion.

The location of the pre-ET minima also revealed a clear pL dependency. The slow-down of 216 μs to 447 μs in D_2O at pL 6.2 (KIE = 2.1) is similar to previous observations for the pre-ET lag phase (Gerencsér and Dau, 2010; Zaharieva et al., 2016), which reported KIEs of about 2.4–2.5. A very strong pH dependency as reported by Gerencsér and Dau (2010) ($\tau_{pH\ 5.4} / \tau_{pH\ 7.0} > 7$) is, however, not found here ($t_{min}(pH\ 5.4) / t_{min}(pH\ 7.0) = 1.6$). The KIEs of all half-times and minima are shown in Fig. 5.35b.

Interestingly, at pL 7.0, nearly the same values were obtained for τ_{ET} (and $\tau_{1/2}$) in both H_2O and D_2O. Visual inspection of normalized transients at 1395 and 1514 cm⁻¹ (Fig. 5.36) confirm this observation: the millisecond kinetics appear to be near identical in
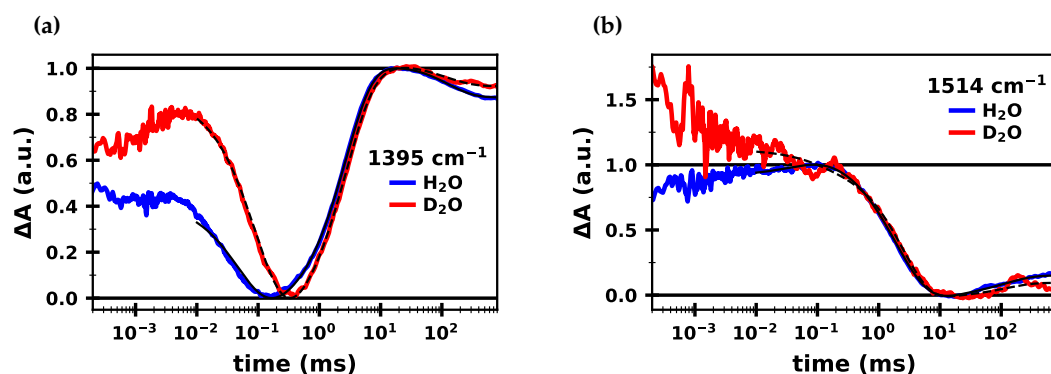
Figure 5.36: Transient absorption changes ($S_3\rightarrow S_0$) at 1395 and 1514 cm^{-1} in H$_2$O and D$_2$O at pL 7.0. IR absorption changes are shown shifted and normalized to facilitate visual comparison of the millisecond kinetics at **(a)** 1395 cm^{-1} and **(b)** 1514 cm^{-1} in H$_2$O (*blue*) and D$_2$O (*blue*). The fit curves (*black*) are shown together with the measured data (*colored lines*).

both conditions. Possibly the proton and/or water movement associated with the electron transfer event in the $S_3\rightarrow S_0$ transition is no longer rate-limiting at pL 7.0.

5.5.3   Mechanistic Implications of the ET and PT Decay Associated Spectra

Suggestions by Previous Studies

The PT and ET DAS, as well as the steady-state spectrum show an overall very similar behavior as in the step-scan FTIR data reported previously; Fig. 5.37 shows a detailed view of three spectral regions, just as shown in the paper by Greife et al. (2023). The areas shaded in grey indicate regions were the ET steps reverses the behavior of the preceding PT step. The two peaks around 1570 and 1595 cm^{-1} in Fig. 5.37b in fact show an even clearer mirrored behavior in the ET and PT DAS than in the step-scan data.

Greife et al. (2023) interpreted the peaks between 1600–1550 cm^{-1} and those between 1750–1700 cm^{-1} to be indicative of carboxylate side chains that are deprotonated and protonated, respectively. The reversible behavior seen in the PT and ET DAS is thus suggested to indicate the deprotonation of a carboxylate during the PT phase and its reprotonation concomitantly with the ET step. They assign these peaks (specifically those at 1707, 1723 and 1744 cm^{-1}) to two glutamic acid side chains: D1-E65 and D2-E312, forming a protonatable dyad (they suggest that likely E312 is protonated and hydrogen bonded to E65, but cannot exclude the opposite case). From this assignment, and further supported by *in silico* calculations, they propose a reaction scheme with the following steps:

(i)   Deprotonation of E312 with a time constant of about 300 μs, releasing a proton to the bulk (the first PT step denoted in the S-state cycle)

(ii)   A concerted movement of one electron from O6 to Y_Z^{ox} and movement of a proton from O6 to D61 ($\sim$2.5 ms)

(iii)   Peroxide formation between O6 and O5 (fast)

(iv)   O$_2$ formation and release, concomitant with H$^+$ release from D61 to the bulk (fast)

(v)   Insertion of a new substrate water into the Mn$_4$CaO$_x$ cluster (fast)

(vi)   Reprotonation of the E312–E65 dyad (fast).

The steps above denoted as "fast" indicate reactions faster than the rate-limiting 2.5 ms, which are thus not experimentally separable from the rate-limiting step.
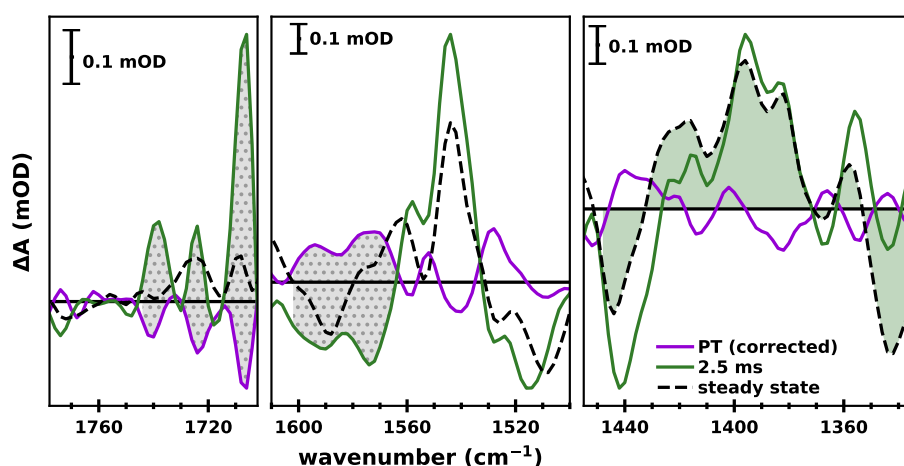
Figure 5.37: Detailed view of the decay associated spectra of the ET and (acceptor-side corrected) PT step alongside the steady-state spectrum of the $S_3 \rightarrow S_0$ transition. Spectral regions in which the ET phase (*green*) shows a similar behavior as the steady-state spectrum (*dashed black*) is shaded in *green*. Regions where the PT behavior (*purple*) is reversed by the ET step are shaded in *dotted grey*. The DAS were obtained from a seven-component exponential fit, where three time constants were fixed ($\tau_3 = 340$ μs, $\tau_4 = 800$ μs and $\tau_5 = 2.5$ ms). The PT phase was corrected for acceptor-side contributions as detailed in Fig. 5.29. The data shown in here is the same as in Fig. 5.28c.

While the E65–E312 pair, which sits at the exit of the proposed Cl1-channel, has been previously suggested to function as a proton relay or gate (Hussein et al., 2021, 2023; Bondar and Dau, 2012), Greife et al. (2023) specifically suggest distinct protonation and deprotonation phases, based on the step-scan FTIR results. The crucial assignment of the peaks at 1707, 1723 and 1744 cm^{-1} to E65/E312, however, was recently challenged because of the absence of their downshift upon H/D exchange (as reported in the Supporting information of Greife et al. (2023)): Using QM/MM calculations, Noguchi (2024) proposed expected IR frequencies for the protonated E65–E312 dyad in H_2O as well as D_2O, demonstrating that strong downshifts are expected for the C=O stretch bands of protonated carboxylates upon deuteration.

In this *in silico* study, four possible conformations of the protonated E65–E312 dyad were identified: two open ("open E312" and "open E65") and two closed conformations ("closed E312" and "closed E65"), which are suggested to allow or prohibit proton egress through the Cl1-channel, respectively. In the closed forms, E312 and E65 are hydrogen bonded to each other via a proton that sits either at E312 (closed E312) or at E65 (closed E65). In the open forms one of the two glutamates is also protonated, but they are not hydrogen bonded to each other. While the calculated frequencies of these four conformations varies between 1776–1696 cm^{-1}, all of them show a strong deuteration induced downshift of 20–37 cm^{-1}. Noguchi (2024) thus concludes that the 1707 cm^{-1} peak of the step-scan FTIR study is not assignable to the E65/E312 nor to any protonated carboxylate. Instead they assign it to Y_Z^{ox} reduction: as shown previously by their group (Nagao et al., 2017b), the 13^1-keto C=O stretching vibration of chlorophyll P_{D1} of P680 is perturbed by Y_Z^{ox} formation, giving rise to the 1707/1699 cm^{-1} signal typically seen in Y_Z^{ox}/Y_Z spectra (Berthomieu et al., 1998; Okubo et al., 2007; Nagao et al., 2017b).

Concerning the functional role of the E65–E312 dyad, Noguchi (2024) suggests a mere proton gate behavior, in which the dyad is mostly in its closed form, only briefly opening up for proton egress by a small conformational change and subsequently closing again, all within a single distinguishable phase. If this were the case, only the closed form would be observable and thus no change in IR absorption would be expected. The author furthermore suggests that a slight rotation of E65 observed by SFX studies (Hussein et al., 2021; Bhowmick et al., 2023) could relate to this gating behavior—however, if the dyad were indeed to open and close too quickly to be observed by time-resolved IR, it should also not be observable by SFX studies. On the other hand, if the dyad were to remain open long enough for observation, this should be visible in time-resolved IR difference spectra via shifting C=O bands between 1776–1696 cm^{-1}.

New Insight from the here Presented Data

Figure 5.38 shows the DAS of the PT and ET phases obtained in H$_2$O (*blue*) and D$_2$O (*red*). As in the step-scan FTIR study, a slight downshift of the 1724 cm^{-1} band by 2–6 cm^{-1} is observed, while a feature around 1707 cm^{-1} is observable in both H$_2$O and D$_2$O. In the here presented data, however, a new feature clearly emerges at 1688 cm^{-1} and at 1686 cm^{-1} in the PT and ET DAS, respectively (Fig. 5.38a and b). These features could arise from downshifts of the 1707 cm^{-1} features by 19–21 cm^{-1}, which would explain the decreased amplitudes of the 1707 cm^{-1} features upon deuteration. The magnitude of such a downshift is in excellent agreement with the QM/MM study discussed above (Noguchi, 2024).

If this assignment is correct, what causes the non-shifting 1707 cm^{-1} feature? As the ET step refers to an electron transfer from the Mn$_4$CaO$_x$ cluster to Y$_Z^{ox}$, a (positive) contri-
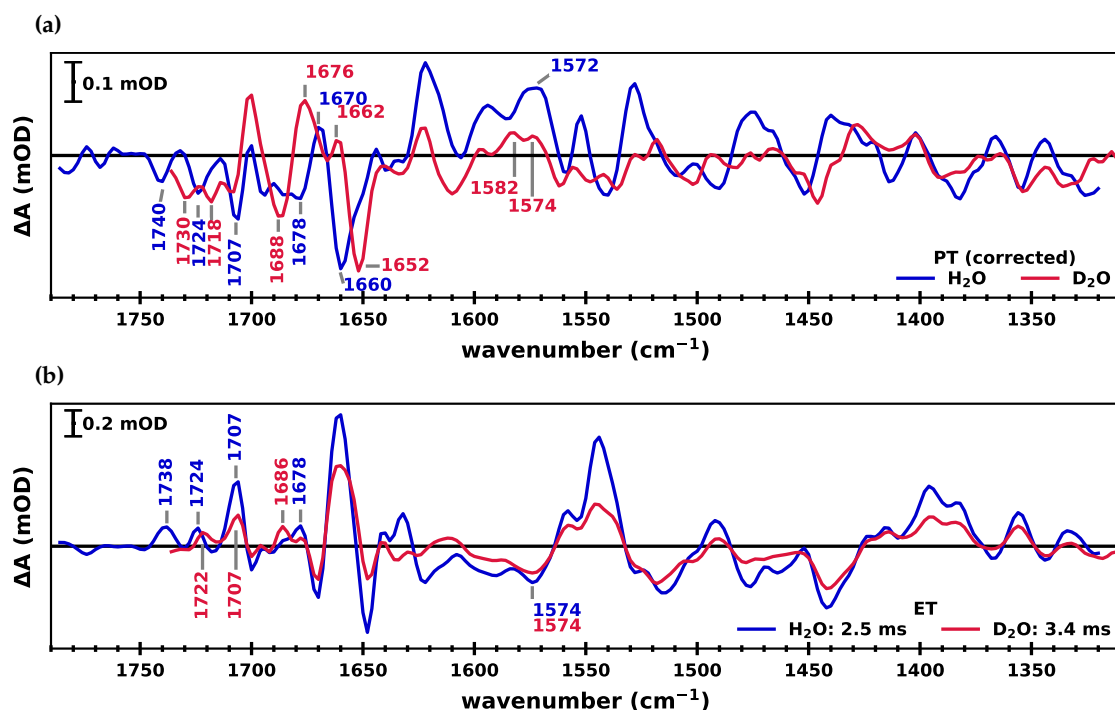

(a)

(b)

Figure 5.38: Direct comparison of the decay associated spectra of the ET and PT phases of S$_3$→S$_0$ in H$_2$O and D$_2$O. (a) Acceptor-side corrected DAS of the PT phase in H$_2$O (*blue*) and D$_2$O (*red*). **(b)** DAS of the ET phase in H$_2$O (*blue*) and D$_2$O (*red*). The data shown here is the same as shown in Figs. 5.32 and 5.28c.
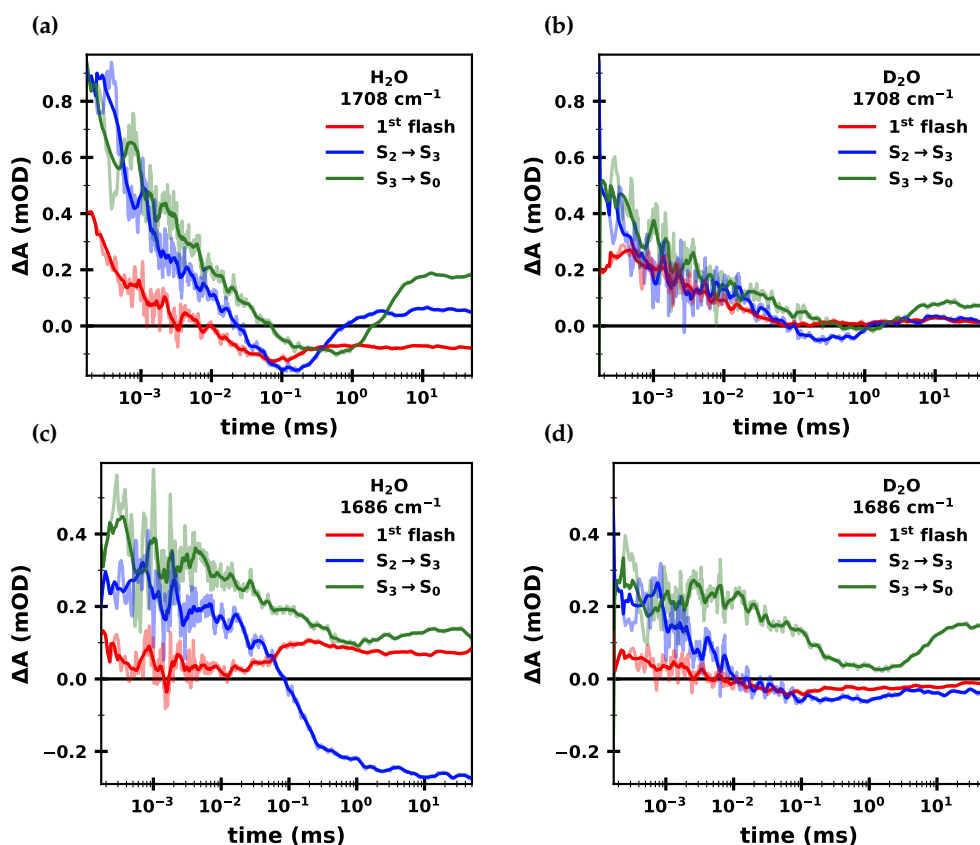
Figure 5.39: Transients at 1708 and 1686 of the first three S-state transitions in H_2O and D_2O. Transient IR absorption changes are shown for the first flash (predominantly $S_1 \rightarrow S_2$) (*red*), the $S_2 \rightarrow S_3$ (*blue*) and $S_3 \rightarrow S_0$ transition (*green*) at **(a)** 1708 cm^{-1} in H_2O, **(b)** 1708 cm^{-1} in D_2O, **(c)** 1686 cm^{-1} in H_2O and **(d)** 1686 cm^{-1} in D_2O. The shown transients were taken from the time-resolved spectral data, but without any smoothing along the wavenumber axis. The transients were smoothed along the time axis with a sliding average window of 10 data points (*transparent*). They were smoothed a second time, with a window of 20 data points (*opaque*) for easier visual inspection. The measurements were done at 10 °C and pL 6.2.

bution of Y_Z^{ox} to the 1707 cm^{-1} feature (which does not shift upon H/D exchange) in the ET DAS is likely and even expected as mentioned in both the FTIR and QM/MM studies (Greife et al., 2023; Noguchi, 2024). If the negative feature at 1707 cm^{-1} in the PT DAS were assignable to Y_Z^{ox}, however, this would indicate Y_Z^{ox} formation in the hundreds of microseconds, which is not expected. Possibly the slight changes in the Y_Z^{ox}–His190 distance observed in that time range by an SFX study (Bhowmick et al., 2023) could enhance the electrochromic effect of Y_Z^{ox} on P680, giving rise to a signal mimicking Y_Z oxidation.

An alternative interpretation of the 1686–1688 cm^{-1} feature in D_2O could be an upshift of the 1678 cm^{-1} feature in H_2O, which cannot be ruled out at the present time. Additional experiments with isotope-labeled nitrogen and carbon could potentially help to distinguish between amide I bands and C=O stretch bands of protonated carboxylates.

Figure 5.39a shows the transients at 1708 cm^{-1} for the first three S-state transitions. All three transients show an initially positive difference absorption, which subsequently decays with multiphasic kinetics. In all three transients a clear rise is observed with the time constant of their respective ET step (about 100 µs, 400 µs and 2.5 ms), supporting
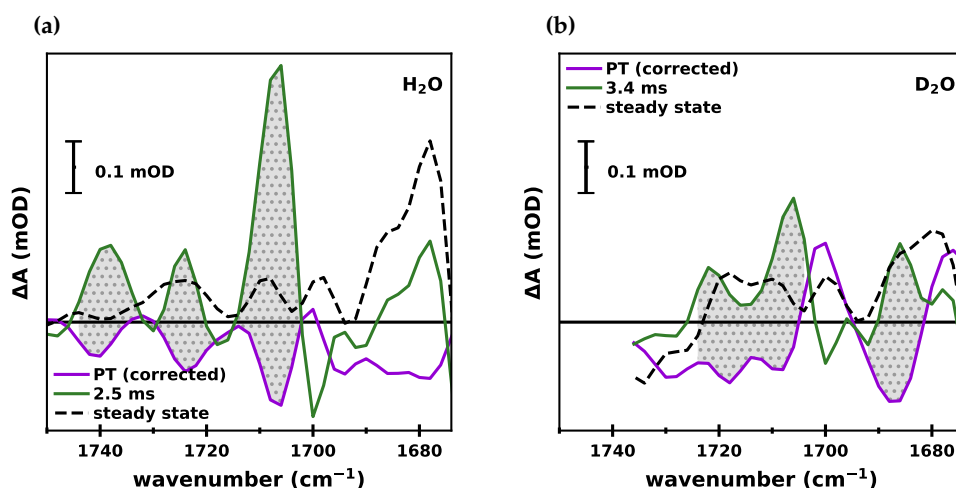
Figure 5.40: Detailed view of the DAS of the ET and (acceptor-side corrected) PT step alongside the steady-state spectrum of the $S_3 \to S_0$ transition in H_2O and D_2O between 1670 and 1750 cm^{-1}. The DAS of the ET and PT steps are shown in *green* and *purple*, respectively, while the steady-state spectra are shown in *black* (*dashed*) in **(a)** H_2O and **(b)** D_2O. Regions were PT and ET behavior reverse each other are shown shaded in *dotted grey*.

the notion that Y_Z^{ox} reduction is visible at this wavenumber. If the absorption changes at this wavenumber were exclusively due to Y_Z oxidation and reduction one might expect the amplitudes to be the same in all S-state transitions. The absorption changes of the $S_1 \to S_2$ transition, however, are significantly smaller than those of the following two S-state transitions (this also holds true when accounting for the $P680^+$ background, as shown in Fig. A3.20 in the Appendix). In D_2O, on the other hand, the absorption changes are of similar amplitude for all three S-state transitions (Fig. 5.39b). This suggests that an additional group, besides Y_Z, contributes to 1708 cm^{-1} in H_2O in both the $S_2 \to S_3$ as well as the $S_3 \to S_0$ transition and that this vibration may shift away in D_2O.

Comparing the absorption changes of the $S_3 \to S_0$ transition at 1686 cm^{-1} in H_2O and D_2O (Fig. 5.39c and d), shows that a clear rising phase (with the time constant of the ET phase) appears upon deuteration. For the other two S-state transitions the 1686 cm^{-1} kinetics are harder to assess, as clearly other events are contributing: In H_2O the $S_2 \to S_3$ transition shows a strong decay, which mostly disappears in D_2O. This could be taken as an indication that a newly appearing rising phase cancels out the decaying phase; this is, however, mere speculation.

An alternative assignment of the 1686 cm^{-1} feature in D_2O could be to the bicarbonate mode of the Fe^{3+} state which shifts from 1658 to 1686 cm^{-1} upon deuteration (Hienerwadel and Berthomieu, 1995). However, if that were the case, the $S_1 \to S_2$ transient should show a rise with the same time constant as in the $S_3 \to S_0$ transition, but this is not observed. Furthermore, while the appearance of the bicarbonate mode during Fe^{2+} to Fe^{3+} oxidation is expected, its disappearance (negative peak) during the PT step cannot be easily explained. In any way, the slow $\sim$44 ms DAS (in H_2O) of the 1st flash as well as the $S_3 \to S_0$ transition show indication of Fe^{2+} oxidation (as discussed in Chapters 5.3 and 5.5), speaking against Fe^{3+} formation already in the 3.4 ms phase in D_2O. Slower Fe^{3+} formation ($\sim$100 ms) is also clearly observed by rapid-scan FTIR (Greife, *in preparation*). The assignment of the

143

1686 cm^{-1} feature in the ET and PT DAS in D$_2$O to a bicarbonate mode thus seems very unlikely.

Overall, the here presented data supports the assignment by Greife et al. (2023) of the 1707 cm^{-1} feature in the S$_3\rightarrow$S$_0$ DAS (in part) to a carboxylate side chain which undergoes deprotonation in the PT step and subsequent reprotonation concomitant with the ET step; this feature appears to downshift by 19-21 cm^{-1} in D$_2$O (highlighted Fig.5.40). Furthermore, the data suggests a similar behavior in the S$_2\rightarrow$S$_3$ transition (as will be discussed further in the next Section).

There are several possible reasons that could explain why the feature at 1686 cm^{-1} was not observed in the step-scan FTIR study. Compared to the QCL data, the step-scan FTIR data has to undergo a much larger amount of data processing steps and corrections. The heat artefact correction, e.g., is much less straight forward for the FTIR data than it is for the QCL data (see thesis by Greife, *in preparation*). Furthermore, the absorption is especially high in the amide I region, thus little signal reaches the detector, resulting in a poorer S/N than in other regions. All in all, it is possible that quality of D$_2$O FTIR data set was simply not high enough to resolve this feature.

5.6 Summary and Concluding Discussion

Kinetic Analysis

In this Chapter, time resolved IR changes were observed for all S-state transitions; the S$_1\rightarrow$S$_2$, S$_2\rightarrow$S$_3$ and S$_3\rightarrow$S$_0$ transitions were analyzed in detail. Time constants for several distinct steps of donor-side as well as acceptor-side kinetics were determined from globally fitting a small number of high S/N transients. While the focus lay on measurements done at pL 6.2 in H$_2$O as well as D$_2$O, data obtained at lower and higher pL values was also presented. The time constants determined for the PT and ET steps of the S-state cycle are summarized in Fig. 5.41a.

For the ET step of the S$_1\rightarrow$S$_2$ transition, only a small kinetic isotope effect of 1.3–1.4 was observed (Fig. 5.41b) and a very small pL dependency, which was barely above noise level. This is overall in agreement with previous spectroscopic results (Sakamoto et al., 2017; Takemoto et al., 2019; Klauss et al., 2012a; Gerencsér and Dau, 2010; Zaharieva et al., 2016).

The proposed PT step of the S$_2\rightarrow$S$_3$ transition showed a strong pL dependency with accelerated kinetics at higher pL values; at pH 7.8, however, the kinetics slowed again. Together with a high H/D KIE of about 3.1 at pL 6.2 (or even 4.4 for the P680$^+$ corrected data), this indeed supports the assignment of this phase to a PT event associated with the removal of a proton from the OEC. From temperature-dependent measurements we previously reported an activation energy of around 500 meV for this PT event (Mäusle et al., 2020)—similar to what was observed by a photothermal beam deflection (PBD) study (Klauss et al., 2012a). Thus, although the high KIE of around 3–4 found here is still smaller than what was found in the PBD study, it seems likely that the PT event of both studies— as well as the here presented PT phase—refer to the same event. This is an important observation, as there is still some disagreement concerning the nature of the pre-ET step of S$_2\rightarrow$S$_3$ transition: The group of Takumi Noguchi reported only a very small KIE for a ~100 µs phase and virtually no pH dependence (Sakamoto et al., 2017; Takemoto et al., 2019), thus assigning this phase not to a proton removal from the Mn$_4$CaO$_x$ cluster, but merely to a proton or water movement near the OEC.
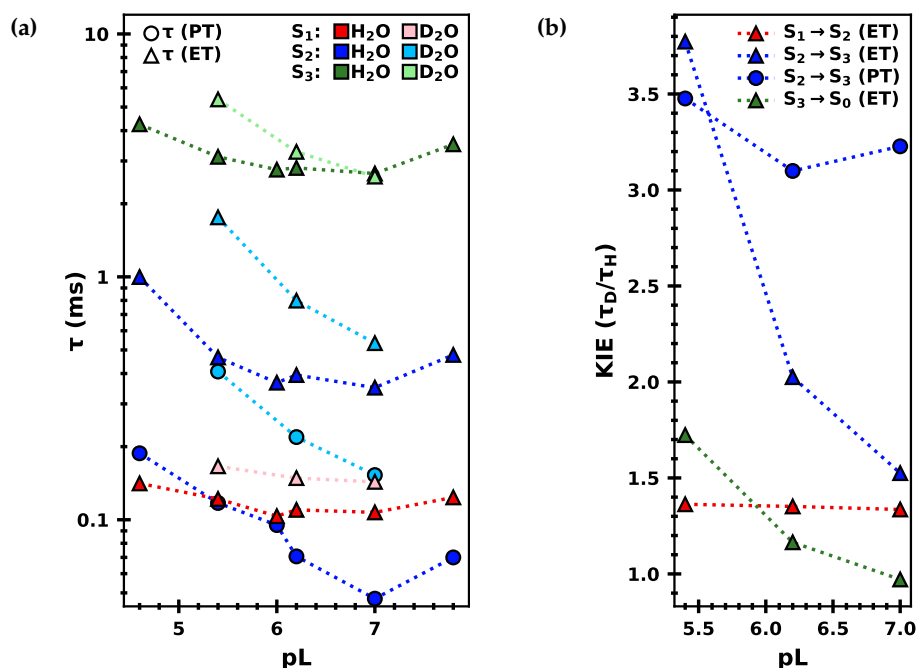
Figure 5.41: Overview of the time constants of the PT and ET phases of in H_2O and D_2O at different pH and pD values, and the resulting KIE. (a) Time constants of the $S_1{\rightarrow}S_2$ (*red*), $S_2{\rightarrow}S_3$ (*blue*) and $S_3{\rightarrow}S_0$ (*green*) transition in H_2O (*darker colors*) and D_2O (*lighter colors*). At each pL value, the time constant was determined by fitting at least four transients globally to a sum of exponentials; only the time constants that are likely associated with the PT (*circles*) and ET (*triangles*) steps are shown. **(b)** The kinetic isotope effect, determined by dividing the time constants measured in D_2O by the time constants in H_2O at three different pL values (5.4, 6.2 and 7.0).

While the pH dependency of the ET step of the $S_2{\rightarrow}S_3$ transition was found to be weaker and the H/D KIE smaller (i.e. at pL 6.2–7.0) than for the PT step, both were found to be relatively high, supporting the notion that the ET step is coupled to a PT (Haumann et al., 1997; Klauss et al., 2012a). The KIE itself was strongly pL-dependent, varying between 1.5 at pL 7.0 and 3.8 at pL 5.4.

The transients of the $S_3{\rightarrow}S_0$ transition proved difficult to fit in a meaningful manner, likely *inter alia* because of strongly overlapping acceptor-side kinetics during the pre-ET events. Thus, pH effect and H/D KIE was analyzed only for the ET step by multi-exponential fitting. The ET phase showed a small, but still sizeable pL dependency, with a seemingly optimal pH value of 7.0. While KIEs of 1.7 and 1.2 were observed at pL 5.4 and 6.2, no deuteration-induced slow-down was observed at pL 7.0 (KIE = 1.0). Analysis of the half-times of the millisecond rising phases at 1400 cm^{-1} gave qualitatively similar results (see Fig. 5.35). The pre-ET minima at 1400 cm^{-1} were identified as a possible proxy for the preceding PT step: The values obtained at pL 6.2 are in agreement with previous reports and resulted in a similar KIE (2.1 vs. 2.4–2.5) (Gerencsér and Dau, 2010; Zaharieva et al., 2016). The pL dependency of these pre-ET minima, however, was much less pronounced that in previous reports for the pre-ET lag phase (Klauss et al., 2015; Gerencsér and Dau, 2010).

For the spectral analysis (see next point) the time constants of the PT and ET phases were fixed to literature values; an additional pre-ET phase was fixed to 800 μs.

Table 5.1: Tentative assignments of the DAS to donor- and acceptor-side events. The time constants are given without/with $P680^+$ background correction where applicable. The DAS can be seen in Figs. 5.9 ($S_1 \rightarrow S_2$), 5.18 ($S_2 \rightarrow S_3$) and 5.27 ($S_3 \rightarrow S_0$).

$S_1 \rightarrow S_2$		$S_2 \rightarrow S_3$		$S_3 \rightarrow S_0$	
				3/2 µs	$P680^+$ reduction; Y_Z oxidation
20/29 µs	$P680^+$ reduction	24/27 µs	$P680^+$ reduction	47/50 µs	$P680^+$ reduction
110/107 µs	ET step; Y_Z^{ox} reduction	71/65 µs	PT step; Fe^{3+} reduction by Q_A^- (?)	340 µs	(PT/acceptor-side)
890 µs	$Q_A^- \rightarrow Q_B$	394/398 µs	ET step; Y_Z^{ox} reduction	890 µs	(PT/acceptor-side)
8.5 ms	$Q_A^- \rightarrow Q_B$	6.0 ms	acceptor-side ($Q_A^- \rightarrow Q_B$?)	2.5 ms	ET step; Y_Z^{ox} reduction; $Q_A^- \rightarrow Q_B$ (?)
44 ms	Q_B reduction by Q_A^- and Fe^{2+}	50 ms	Q_A^-/Q_A recombination (?)	44 ms	Q_B reduction by Q_A^- and Fe^{2+}
250 ms	Q_A^-/Q_A recombination	290 ms	?	250 ms	Q_A^-/Q_A recombination

Spectral Analysis via Decay Associated Spectra

Spectral analysis of the kinetics at pL 6.2 of the three discussed S-state transitions was performed by fixing the above summarized predetermined time constants in a global fit across time-resolved spectral data sets with comparatively low S/N. This resulted in decay associated spectra, which facilitated the assignment of the observed kinetics to specific events (as summarized in Table 5.1).

The DAS of the ET and PT phases of the S-state cycle are shown in Fig. 5.42 for the $S_1 \rightarrow S_2$, $S_2 \rightarrow S_3$ and $S_3 \rightarrow S_0$ transitions, highlighting regions in which steady-state and ET show a similar spectral behavior (colored areas), as well as regions in which ET and PT show reversed behavior (grey areas).

As stated by Greife et al. (2023), the similarity between the steady-state spectrum and the ET DAS in the symmetric carboxylate stretch region ($\sim$1450–1300 cm^{-1}) of the $S_3 \rightarrow S_0$ transition (Fig. 5.42c, *shaded green*) supports the assignment of this region to mostly carboxylate side chains, which are in close proximity to the Mn_4CaO_x cluster and are thus sensitive to (redox) changes of the OEC. In addition, parts of the amide I and amide II regions also show strong similarity between ET DAS and steady-state spectrum, supporting the notion that the final ET step and O_2 evolution event results in significant structural changes. The peak at 1660 cm^{-1}, however, clearly stands out, as the peak is much larger in the ET DAS than in the steady-state spectrum (as also observed by FTIR; see the Supporting Information of Greife et al. (2023)). This is explicable by the strong negative amplitude at this wavenumber of the 44 and 250 ms phases (see Fig. 5.27g and h), which may in part be indicative of Fe^{2+} oxidation (Hienerwadel and Berthomieu, 1995). Interestingly, the $S_1 \rightarrow S_2$ and $S_2 \rightarrow S_3$ DAS do not show such a strong agreement of the ET DAS with the steady-state spectrum in the amide I region.

The symmetric carboxylate stretch region of the ET DAS of the $S_1 \rightarrow S_2$ and $S_2 \rightarrow S_3$ transitions are only in parts similar to their respective steady-state spectra. This could give hints towards assignment of the carboxylate ligands to spectral bands: Only one Mn atom is oxidized in each transition and likely the direct ligands of the respective Mn atom will
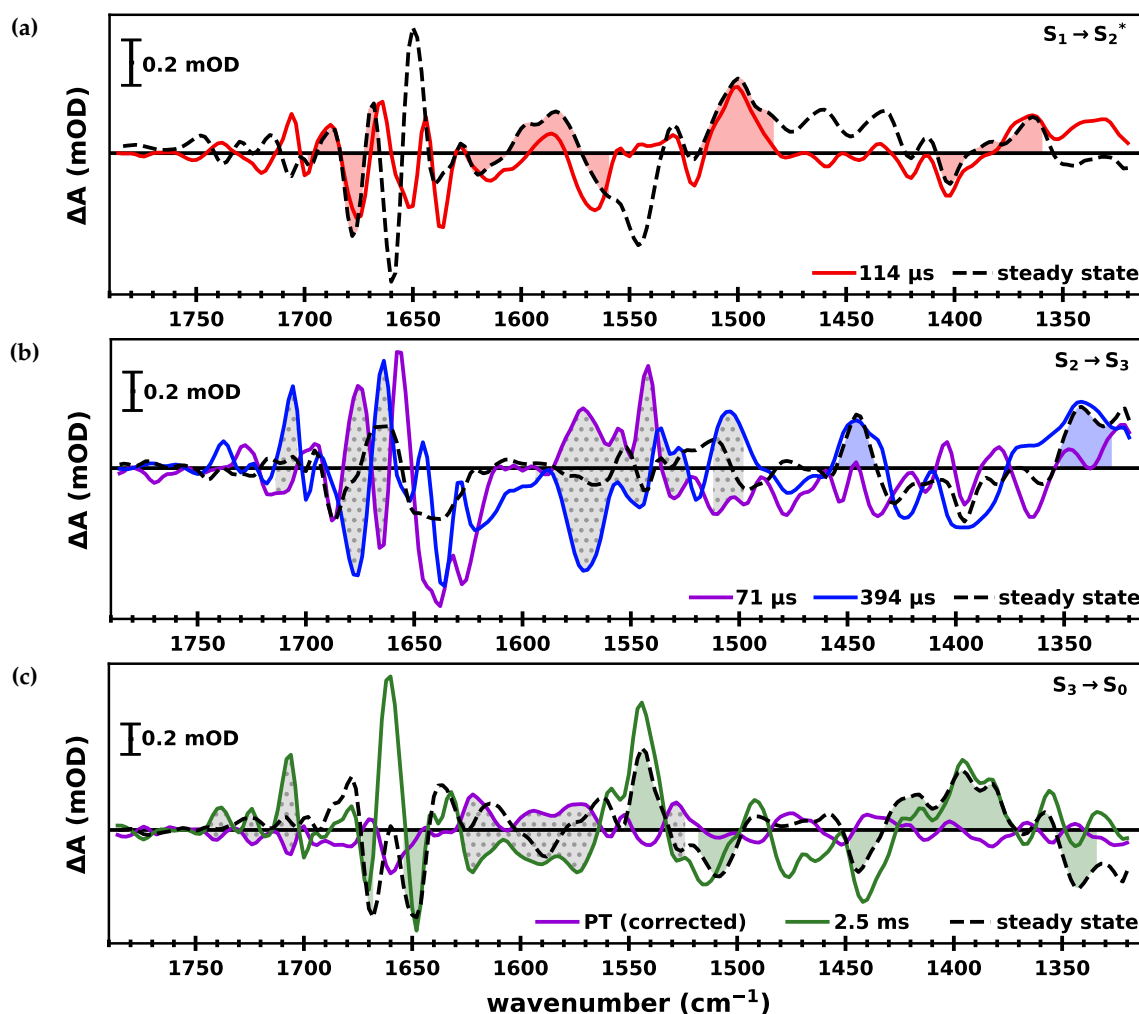
Figure 5.42: Decay associated spectra of the PT and ET steps alongside the steady-state spectra of the first three S-state transitions. Spectra of the **(a)** $S_1 \to S_2$, **(b)** $S_2 \to S_3$ and **(c)** $S_3 \to S_0$ transition. Spectral regions in which the ET phase (*red, blue* or *green*) shows a similar behavior as the steady-state spectrum (*dashed black*) is shaded in the respective color of the ET phase. Regions where the PT behavior (*purple*) is reversed by the ET step are shaded in *dotted grey*. The spectra were deconvolved assuming a starting population of 74% S_1, 14% S_2 and 12% S_0 and a miss factor of 8% (H_2O) or 12% (D_2O). For the $S_1 \to S_2$ transition, the non-deconvolved first flash data minus 14% S_2 and 12% S_0 is shown (denoted $S_1 \to S_2^*$).

be most perturbed, causing shifts of their vibrational frequencies (and thus giving rise to IR difference absorption signals).

In the $S_1 \to S_2$ transition likely candidates causing the difference bands around 1400 and 1360 cm^{-1} (Fig. 5.42a) are D170 and E333 (the direct ligands to Mn4; see Fig. 5.43). Indeed, as summarized by Debus (2016), a QM/MM study simulating IR difference spectra (Nakamura and Noguchi, 2016) found that the prominent negative feature around 1400 cm^{-1} arises mainly from D170 and E333, both shifting to around 1360 cm^{-1} upon Mn4 oxidation and the associated C–O and Mn–O distance changes. It should be noted, however, that the QM/MM study found that all the carboxylate ligands contribute at several different wavenumbers in this region, hence the overall very broad features.
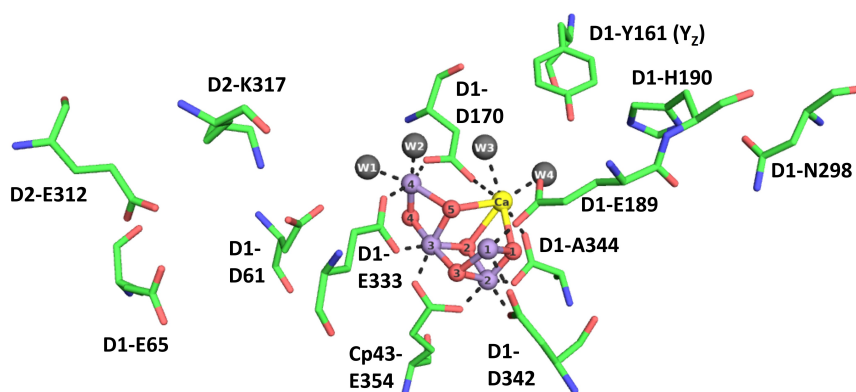
Figure 5.43: The Mn$_4$CaO$_x$ cluster with its carboxylate ligands and other relevant nearby amino acids. Manganese atoms are shown in purple, oxygen in red, calcium in yellow, nitrogen in blue and carbon in green. The four water ligands of the Mn cluster are shown as grey spheres (W1–W4). This image was rendered in PyMOL using the structure by Bhowmick et al. (2023) with PDB ID 8f4H; it shows the SFX structure of PSII from *T. vestitus* 150 µs into the S$_2$→S$_3$ transition.

In the S$_2$→S$_3$ transition Mn1 is oxidized, thus it seems likely that the direct carboxylate ligands of Mn1, i.e. E198 and D342, contribute to the positive bands around 1450 and 1340 cm^{-1} (Fig. 5.42b).

In the S$_3$→S$_0$ transition, three out of four Mn atoms change their oxidation state, likely causing a significant perturbation of the IR absorption of all (or most of) the carboxylate ligands, thus explaining the overall great similarity between ET DAS and steady-state spectrum in the 1450–1300 cm^{-1} region.

Reversible Behavior of PT and ET vs. Lag-Phase Behavior in S$_2$→S$_3$ and S$_3$→S$_0$

Figure 5.44: Transient absorption changes of S$_2$→S$_3$ at select wavenumbers displaying different kinds of kinetic behavior. (a–h) IR difference absorption (pH 6.2, 10 °C) at eight different wavenumbers (*colored lines*) together with their fit curves (*black*). The time constant of the PT (71 µs) and ET event (394 µs) are indicated by a *purple* and *blue* vertical line, respectively. Arrows of the same color indicate the sign of the corresponding amplitudes. All transients were deconvolved assuming a starting population of 74% S$_1$, 14% S$_2$ and 12% S$_0$. They were *not* corrected for their P680 background.
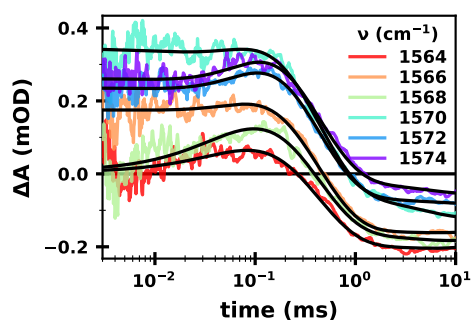
Figure 5.45: $S_2{\to}S_3$ transients around 1570 cm^{-1}. Transients from the time-resolved spectral data (pH 6.2) set are shown for every 2 cm^{-1} between 1564–1574 cm^{-1}. These transients were not smoothed along the wavenumber axis. The fit curves are shown in *black*.

Figure 5.44 shows several transients of the $S_2{\to}S_3$ transition displaying different kinds of behavior: Panels a, b and g show a "lag phase" behavior, in which the PT phase appears to be silently "waiting" for the ET event, panel c shows a biphasic decay and panels d, e, f and h show a reversed behavior of PT and ET. Most of these behaviors are as expected from the DAS further above (Fig. 5.42b). However, at 1570 cm^{-1} the DAS indicate a strong reversed behavior between PT and ET, which is not apparent in Fig. 5.44g. While the fit parameters reveal a sizeable positive amplitude of the PT phase, its presence is obscured by the more strongly pronounced ET decay, as well as a preceding decaying 24 μs phase. Comparing individual transients between 1564–1574 cm^{-1} (Fig. 5.45) reveals that the visibility of the PT rising phase depends strongly on the exact wavenumber: While at 1570 cm^{-1} the rising phase is effectively indiscernible, it is clearly visible at 1568 cm^{-1}.

For the $S_3{\to}S_0$ transition, the reversible behavior is also easily assessed by visual inspection of some transients (see 1532, 1559 and 1740 cm^{-1} in Fig. 5.46). However, it is strongly obscured at others, likely due to an acceptor-side and donor-side PT occurring with similar time constants (as discussed further above). At 1570 cm^{-1} e.g. (panel e), the rising behav-
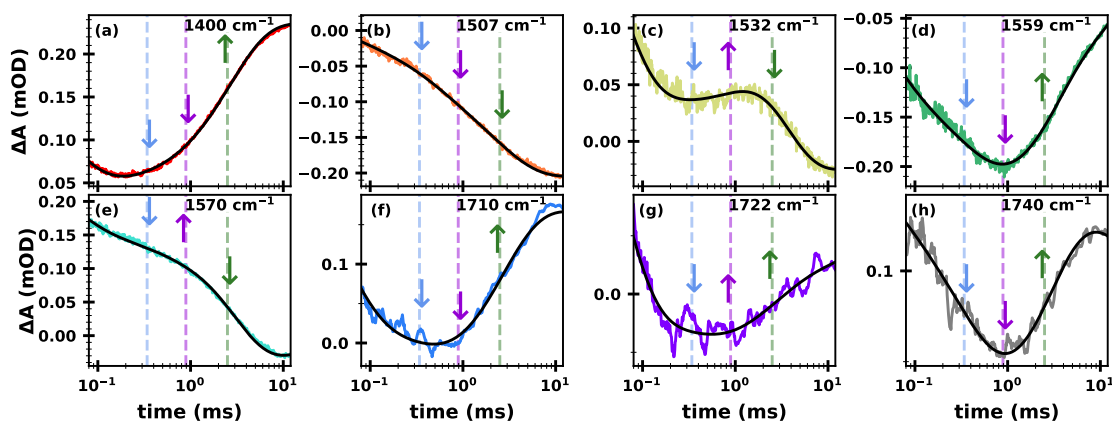
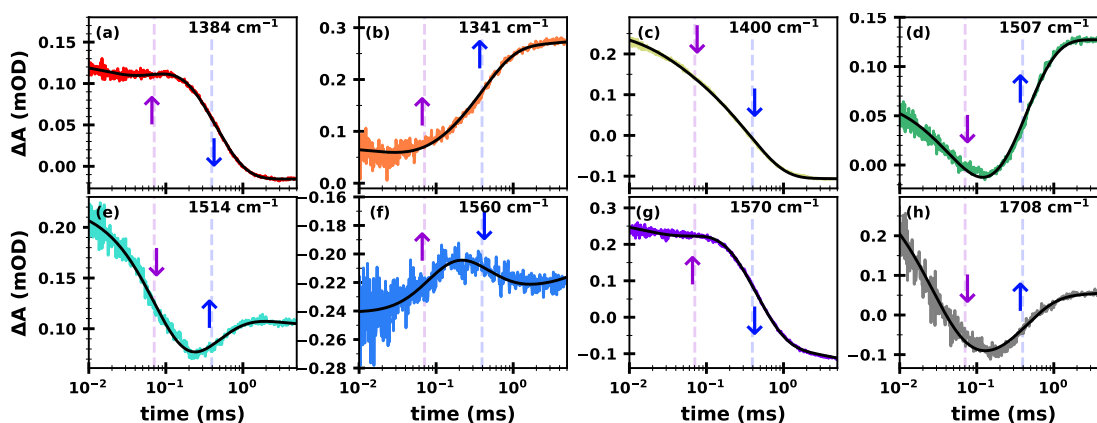**Figure 5.46: Transient absorption changes of $S_3{\to}S_0$ at select wavenumbers displaying different kinds of kinetic behavior. (a–h)** IR difference absorption at eight different wavenumbers (*colored lines*) together with their fit curves (*black*). The time constant of the two pre-ET phases (340 and 890 μs) and that of the ET event (2.5 ms) are indicated by *light blue*, *purple* and *green* vertical lines, respectively. Arrows of the same color indicate the sign of the corresponding amplitudes. All transients were deconvolved assuming a starting population of 74% S_1, 14% S_2 and 12% S_0. They were *not* corrected for their P680$^+$ background nor for acceptor-side contributions. All data was acquired at 10 °C and pH 6.2.

ior of the 800 μs phase is hardly noticeable by eye; a correct estimation of the amplitudes is difficult. Note that the shown transients—unlike the PT DAS in Fig. 5.42c—were not corrected for an acceptor-side contribution (see Fig. A3.16 for an attempt at an acceptor-side correction of the 1570 cm^{-1} transient). Similarly as for the $S_2 \rightarrow S_3$ transition, in the region around 1570 cm^{-1} the visibility of the PT phase is highly wavenumber-dependent (see Fig. A3.15): While at 1570 cm^{-1} the PT rise is nearly indiscernible, it is clearly visible at 1568 cm^{-1} (unfortunately, only low S/N data was obtained at 1568 cm^{-1}).

Mechanistic Implications for $S_2 \rightarrow S_3$ and $S_3 \rightarrow S_0$
The PT and ET DAS of both the $S_2 \rightarrow S_3$ and the $S_3 \rightarrow S_0$ transition show clear reversed behavior at 1707 cm^{-1}, as well as (with opposite signs) around 1570 cm^{-1} (Fig 5.42). In a step-scan FTIR study of the $S_3 \rightarrow S_0$ transition, this was assigned to a the deprotonation (with the PT phase) and reprotonation (with the ET phase) of the carboxylate dyad E312/E65 (Greife et al., 2023). This assignment was recently challenged by Noguchi (2024) on the grounds that the 1707 cm^{-1} feature did not downshift in D_2O as expected for a carboxylate C=O stretch mode.

The here presented data, however, shows new evidence that the assignment of the step-scan FTIR study may be valid after all: The amplitude of the 1707 cm^{-1} peak is significantly smaller in D_2O than in H_2O and appears to downshift by about 20 cm^{-1} to 1686 cm^{-1}. The transients also reflect this behavior: While in H_2O the reversed behavior is strongly pronounced at 1708 cm^{-1} and hardly at 1686 cm^{-1} (Fig. 5.47b, *dark blue* and *black*), in D_2O the 1708 cm^{-1} and 1686 cm^{-1} features become weaker and stronger, respectively (*grey* and *light blue*). This implies that part of the 1707 cm^{-1} feature, which downshifts in D_2O, is assignable to the transient de- and reprotonation of a carboxylate, while the non-shifting part of the feature is likely assignable to Y_Z^{ox}.

A similar behavior is observed for most of the respective transients of the $S_2 \rightarrow S_3$ transition (Fig. 5.47a). At 1868 cm^{-1} in H_2O, however, it seems that another feature contributes in the form of a strong decaying phase, somewhat obscuring the behavior. The 1707 cm^{-1} feature is of similar amplitude in the DAS of both the $S_2 \rightarrow S_3$ and $S_3 \rightarrow S_0$ transition (Fig. 5.42b–c). In contrast, the ET DAS of the $S_1 \rightarrow S_2$ transition also shows this feature, but with only about half the amplitude of the others (Fig. 5.42a). This could imply that the Y_Z^{ox} con-

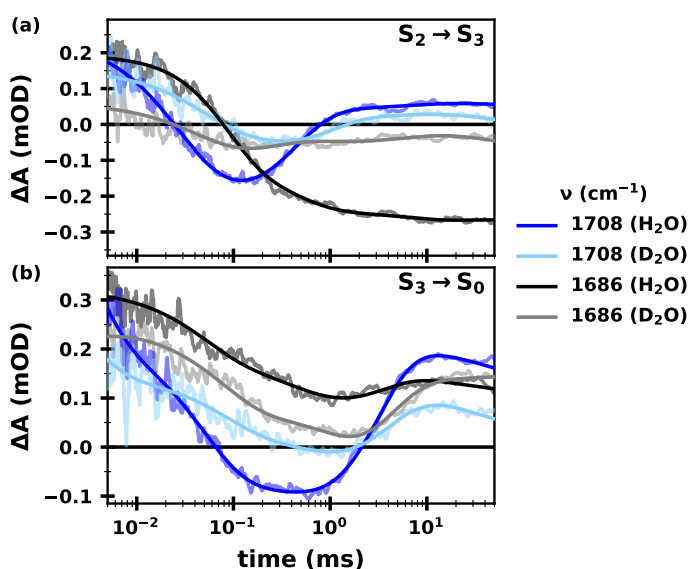**Figure 5.47: IR difference absorption at 1708 and 1686 cm^{-1}.** Transient IR absorption changes are shown at 1708 cm^{-1} in H_2O and in D_2O (*dark blue* and *light blue*, respectively), as well as 1686 cm^{-1} in H_2O and in D_2O (*black* and *grey*, respectively) for **(a)** the $S_2 \rightarrow S_3$ and **(b)** the $S_3 \rightarrow S_0$ transition. All data was acquired at 10 °C and pL 6.2.
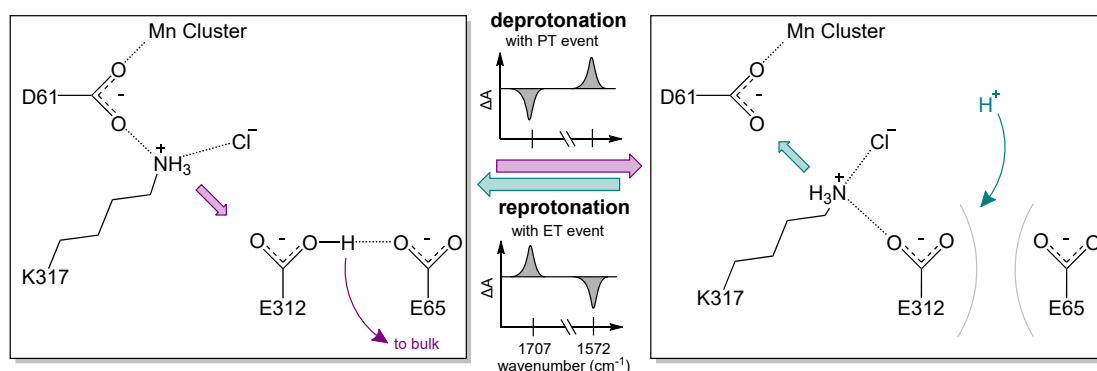
Figure 5.48: Scheme of the proposed de- and reprotonation of the E312/E65 dyad. By shifting closer to the glutamate dyad, the side chain of K317 forms an H-bridge with the carboxylate side chain of E312. This promotes the deprotonation of E312, leading to a proton removal to the bulk (*purple arrows*). A 1707 cm^{-1} band associated with the C=O stretch of a protonated carboxylate disappears (negative difference signal), while a feature associated with the COO$^-$ asymmetric stretch of deprotonated carboxylates appears at 1572 cm^{-1} (positive difference signal). These events occur in the first "PT step" of the $S_2{\to}S_3$ and $S_3{\to}S_0$ transitions. In the ET step, K317 moves back towards D61 and the E312/E65 dyad is protonated (*green arrows*), leading to a positive difference signal at 1707 and a negative difference signal at 1572 cm^{-1}. This figure is based on the mechanism proposed for the $S_3{\to}S_0$ transition by Greife et al. (2023).

tribution to this feature is comparable in all three S-state transitions and that a similar mechanism of de- and reprotonation of the E312/E65 dyad takes place in the $S_2{\to}S_3$ and $S_3{\to}S_0$ transitions. When the protonated carboxylate C=O mode disappears at 1707 cm^{-1}, a deprotonated carboxylate COO$^-$ asymmetric stretch mode should appear further down; and indeed the feature around 1570 cm^{-1} shows the expected behavior in both transitions. The 1572 cm^{-1} feature upshifts to 1580 cm^{-1} ($S_2{\to}S_3$) and a bit less clearly to 1582–1574 cm^{-1} ($S_3{\to}S_0$) in D$_2$O, which is overall consistent with the expected behavior of a carboxylate side chain band (Barth, 2007; Noguchi et al., 1995b).

The features at 1724 and 1740 cm^{-1}, which were also assigned to the E65/E312 carboxylate pair in the step-scan FTIR study, do not show such a clear reversed behavior in PT and ET DAS of the $S_2{\to}S_3$ transition (Fig. 5.42b). In the transients, however, a reversed behavior is discernible (Fig. A3.21c–d in the Appendix). This discrepancy may be caused by the spectral smoothing performed prior to the DAS analysis, especially since strong acceptor-side contributions are found nearby: Previously, acceptor-side bands were identified at 1721 and 1745 cm^{-1} and assigned to electrochromic effects of Q_A^- and Q_B^-, respectively, on adjacent pheophytins (Suzuki et al., 2005a). The transients at 1720 cm^{-1} indeed show a clear period-of-two behavior (Fig. A3.21a–b).

The proposed mechanism of de- and reprotonation of the E312/E65 dyad, as suggested by Greife et al. (2023), is shown as a general scheme in Fig. 5.48. The data presented here suggests that such a mechanism of proton removal from the OEC could be valid for both the $S_3{\to}S_0$ as well as the $S_2{\to}S_3$ transition.

The importance of the two glutamates has also been demonstrated by mutation studies (Kuroda et al., 2021; Service et al., 2010; Shimada et al., 2022a). Alternative scenarios to the de- and reprotonation mechanism, such as proton gating by the E312/E65 dyad (Noguchi, 2024; Hussein et al., 2023), can currently however not be ruled out entirely.

Outlook

Obtaining time-resolved spectral data sets of ^{15}N or ^{13}C labeled PSII could greatly help to move towards definitive assignments of transiently formed IR features. The QCL setup presents the possibility of obtaining such time-resolved spectral data sets within a short amount of measuring time, in stark contrast to the extremely time-costly step-scan FTIR experiments. For obtaining ^{15}N or ^{13}C labeled PSII, however, store-bought spinach cannot be used as a source. Instead, these studies would be best performed on PSII from *T. vestitus* (or other cyanobacteria), grown on medium enriched with the isotope in question (as e.g. done by Noguchi and Sugiura (2003)). While the S/N of IR measurements on PSII cores from *T. vestitus* is somewhat poorer than that of measurements on PSII membrane particles from spinach (see Chapter 6), this would nevertheless be feasible—likely simply requiring more averaging.

The here presented data were found to have a non-ideal initial dark-adapted population—most importantly a non-zero S_2 population. The data was deconvolved taking such a population into account. However, it was assumed, that the starting population was the same for all measurements, which is most likely a strong simplification. Analysis of the here presented data with an alternative deconvolution approach assuming a starting population of 85% S_1 and 15% S_0 gave overall comparable results (*not shown*) and did not change any main conclusions. This is a good indication that the here presented analysis is not too strongly dependent on a precise estimation of the dark population. Nevertheless, repeating these experiments with an improved measurement protocol will be crucial to validate the results and conclusions of this chapter, especially in view of the opposing views in current literature (Greife et al., 2023; Noguchi, 2024).

6 | Comparative Analysis of IR Spectroscopy on PSII from Spinach, *T. vestitus* and *Synechocystis*

S INCE the beginning of research on PSII on a molecular level over fifty years ago, a wide variety of samples have been studied: From entire cells and intact thylakoid membranes to PSII-enriched membrane particles and down to core complexes stripped entirely of their membrane. Furthermore, many different photosynthetic organisms have been used as PSII sources. While some studies aim at addressing organism-specific characteristics of oxygenic photosynthesis, others aim to achieve a general characterization of PSII-related events. In the latter case, the choice of organism is often for practical reasons (e.g. easy and well established PSII preparation protocols, sample stability, etc.).

Crystallographic studies (including SFX studies) of PSII have been performed mostly on cyanobacterial PSII core complexes from *Thermosynechococcus vestitus* BP-1 (e.g. Kern et al., 2018; Bhowmick et al., 2023) and *Thermosynechococcus vulcanus* (e.g. Umena et al., 2011; Li et al., 2024), while many spectroscopic studies have been performed on eukaryotic PSII from spinach (e.g. Bernát et al., 2002; Klauss et al., 2012a) or from pea seedlings (e.g. Haumann et al., 1997). A complete atomistic understanding of the events that eventually lead to oxygen evolution can only be obtained by combining the results of many different studies and thus it is essential to investigate in what ways the nature of PSII samples influences the outcome of experiments.

IR spectroscopic studies have been performed on spinach PSII membrane particles (e.g. Noguchi et al., 1995b; Mäusle et al., 2020; Greife et al., 2023), as well as on core complexes from *T. vestitus* (e.g. Noguchi and Sugiura, 2003; Takemoto et al., 2019) and *Synechocystis* sp. PCC 6803 (e.g. Debus, 2021; Shimada et al., 2022b). While spinach PSII samples are very stable and can be prepared within a day, cyanobacterial PSII core complexes are more fragile and require growing the organisms in bioreactors over several weeks or even months. The study of site-directed mutants as well as isotopically labeled PSII (e.g. ^{13}C and ^{15}N),

however, cannot be done on store-bought spinach; such studies require full control of the organisms' growing conditions and are typically done with cyanobacteria (or algae).

In this chapter, we explore similarities and differences of time-resolved IR data obtained on PSII from spinach, *T. vestitus* and *Synechocystis*. This may facilitate the comparison of IR studies on different PSII samples—also in future studies—and help understand whether observed differences are real (i.e. related to differences in photosynthetic events) or whether they are artefactual (i.e. arise from issues with sample stability, or from differences in the experimental setups, etc.).

6.1   Experimental Details

PSII membrane particles were prepared from fresh spinach leaves as described in Chapter 3.1. PSII core particles from *Thermosynechococcus vestitus* BP-1 (*T. vestitus*) were prepared by Rebeca Perez, Yvonne Zilliges and Janis Hantke as described previously (Mäusle et al., 2020). PSII core particles from *Synechocystis* sp. PCC 6803 (in the following simply referred to as *Synechocystis*) were prepared by Richard J. Debus and Robert L. Burnap and their respective co-workers as described previously (de Lichtenberg et al., 2021; Debus, 2014; Tang and Diner, 1994).

The samples were prepared for IR spectroscopic experiments as detailed in Chapter 3.5. The cyanobacterial samples were concentrated, but (with exception of the measurements in D_2O) not exchanged into a measurement buffer.

The standard flash-protocol of measuring for 6 s without excitation ("dark signal") followed by 10 saturating excitation flashes per sample spot was employed for all measurements. A flash-induced heat artefact was accounted for as described in Chapter 2.4.1.

Unless stated otherwise, data shown in this Chapter was always obtained in H_2O-based buffer at pH 6.2 (spinach PSII) or pH 6.0 (cyanobacterial core complexes) and at a measurement temperature of 10 °C. All measurements were done in the presence of an exogenous electron acceptor: PPBQ for spinach PSII samples and ferricyanide for the cyanobacterial core complexes. Deconvolution of the cyanobacterial data into pure S-state transitions was done assuming a starting population of 85% S_1 and 15% S_0; the 1st flash data was omitted by the deconvolution algorithm. The spinach PSII data was deconvolved as described in the previous chapter, assuming a starting population 74% S_1, 12% S_0 and 14% S_2.

6.2   S-State Cycling Efficiency

Figure 6.1 shows the flash-number dependent steady-state IR absorption at six wavenumbers for spinach PSII (*blue*), PSII from *T. vestitus* (*green*) and PSII from *Synechocystis* (*red*). All samples show a clear period-of-four pattern and at most wavenumbers the patterns are also overall very similar. At 1335 cm^{-1} (panel a) the oscillatory pattern of the spinach sample appears to exhibit an additional period-of-two contribution, which is not visible in the other two samples. This is unsurprising, as the exogenous electron acceptor PPBQ can take up two electrons, leading to a period-of-two acceptor-side behavior in spinach. Ferricyanide, on the other hand, can be reduced only once and has to be exchanged after every flash. Thus, a period-of-two behavior is not expected in the cyanobacterial samples. The different acceptor-side behavior is confirmed by looking at the transient absorption change at 1478 cm^{-1} (Fig. A4.1 in the Appendix), which has previously been assigned to the C$\doteq$O stretching mode of Q_A^- (Berthomieu et al., 1990).
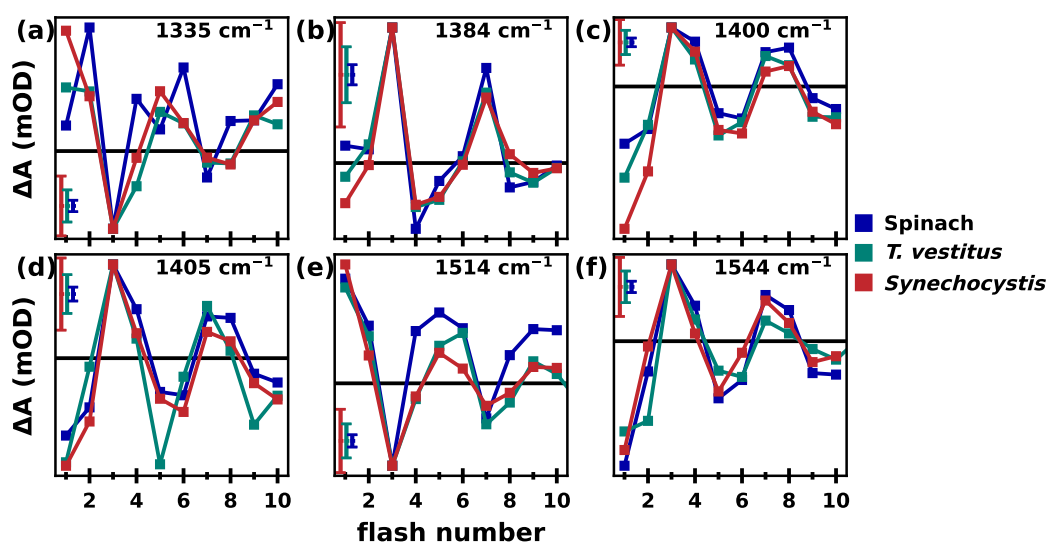
Figure 6.1: Flash-number dependent steady-state IR difference absorption of three different wild-type PSII variants. The steady-state values were obtained by averaging the last 100 ms of each flash-induced transient (700–800 ms after the excitation flash) and is shown as a function of flash-number at **(a)** 1335 cm^{-1}, **(b)** 1384 cm^{-1}, **(c)** 1400 cm^{-1}, **(d)** 1405 cm^{-1}, **(e)** 1514 cm^{-1} and **(f)** 1544 cm^{-1}. Data from PSII membrane particles from spinach is shown in *blue*, PSII core particles from *T. vestitus* in *green* and PSII core particles from *Synechocystis* in *red*. Each panel has a separate size bar for each sample which corresponds to 20 μOD (the scaling was chosen such that the third flash value and the zero line are identical for all samples).

For each sample type, the miss factor was estimated for individual transients at various wavenumbers; the resulting average miss factor for each sample is shown in Fig. 6.2. Note that while the error ranges of the miss factors (as determined by the standard deviations) overlap between the samples, the standard error of the mean is quite small (*not shown*), indicating that the difference between the average miss factors is indeed significant. Spinach PSII showed the overall lowest miss factor (8%), followed by *T. vestitus* (10%) and *Synechocystis* (12%). This is in agreement with Isgandarova et al. (2003), who also found that at 10 °C the miss factor was slightly higher in thylakoids from *T. vestitus* than in those from

Figure 6.2: Miss factors from time-resolved IR data of different PSII sample types. For each IR transient, the miss factor was estimated from a sequence of 10 flash-induced transients, as described in Chapter 2.3.3. Shown here is the average miss factor for PSII membrane particles from spinach (*blue*), PSII core particles from *T. vestitus* (*green*) and PSII core particles from *Synechocystis* (*red*); the error bars represent the standard deviations. The miss factor was estimated for 40, 16 and 23 individual data sets at various wavenumbers for PSII from spinach, *T. vestitus* and *Synechocystis*, respectively. Note that per sample type multiple distinct measurements were performed on several different measurement days.
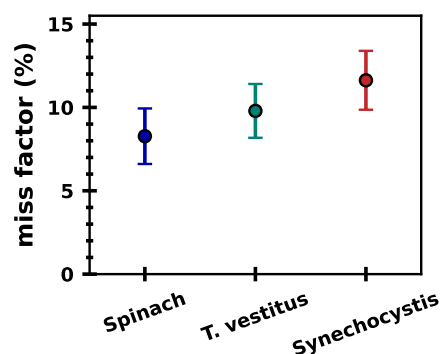
spinach (about 11% and 9%, respectively). They furthermore found that the miss factor was strongly temperature dependent for both organisms, but in different ways: spinach PSII showed the lowest miss factor at the lowest investigated temperature (3 °C), while *T. vestitus* had its miss factor optimum at 25 °C.

For *Synechocystis* thylakoids, values as low as 7% (Dilbeck et al., 2012) and as high as 14% (Dilbeck et al., 2013) have been reported at pH 6.5 (at 20 °C and 30 °C, respectively). Altogether this might indicate a qualitatively similar temperature dependence of the miss factor of *Synechocystis* as for *T. vestitus*, but a systematic study is required to confirm this. Such a study would be of interest, as this could give insight as to whether the different temperature dependencies of spinach and *T. vestitus* are connected to general properties of higher plants vs. cyanobacteria or whether the thermophilic nature of *T. vestitus* plays a role (*Synechocystis* in contrast is mesophilic).

The activation energy of the O_2-formation step has been found to be different between the three species: Liang (2018) reported about 230 meV and 360–380 meV for spinach and *T. vestitus*, respectively, while Bao and Burnap (2015) reported 480 meV for *Synechocystis*. The associated time constants at 10 °C reveal that O_2-evolution occurs fastest in spinach PSII, followed by *T. vestitus* and finally *Synechocystis*. A slower O_2-evolution rate increases the probability of backward ET, leading to charge recombination. This in turn results in miss events, thus likely contributing to the here observed differences in miss factor. As the miss factor of the $S_2 \rightarrow S_3$ transition is thought to be especially large (Han et al., 2012), this however cannot be the sole reason. An investigation of species-dependent activation energies of other steps of the S-state cycle could provide further insight.

6.3 Initial and Steady-State Spectra

Time-resolved spectral data sets were obtained for all three samples, but only across a limited spectral range for the cyanobacterial samples (1324–1644 and 1312–1610 cm^{-1}, for *T. vestitus* and *Synechocystis*, respectively). The initial spectra (averaged between 100–500 ns) of all S-state transitions looked similar; Fig. 6.3 shows the initial spectrum of the 1st flash data. The spectra were normalized such that the prominent band at 1478 cm^{-1} is of the same amplitude in all three sample types; the noise level—as indicated in the bottom by the IR difference signal in absence of excitation—is clearly higher for the cyanobacterial samples than for the spinach sample.

All three sample types show many overall similar features at about 1575(+), 1560–1558(−), 1552–1548(+) and 1362(+) cm^{-1}. A feature at 1542–1540(−) cm^{-1} is also present in all three samples, but with strongly varying amplitude. PSII from spinach and *T. vestitus* furthermore show similar features at about 1637(+) and 1630(−) cm^{-1}, as well as some small peaks below 1460 cm^{-1}. The latter are in part also hinted at in the *Synechocystis* spectrum, but appear poorly resolved.

Many of the prominent features are typical for Q_A^-/Q_A spectra (Berthomieu et al., 1990). As the $P680^+/Q_A^-$ charge separated pair forms within about 300 ps, this is expected and there are very likely also $P680^+/P680$ contributions, as discussed in Chapter 5.2.4 for the spinach spectra ranging up to 1780 cm^{-1}. In the here shown spectral range, however, $P680^+/P680$ features are likely masked by the stronger Q_A^-/QA features.

Figure 6.4 shows the steady-state spectra of the $S_1 \rightarrow S_2$, $S_2 \rightarrow S_3$ and $S_3 \rightarrow S_0$ transitions, as well as a non-excited dark spectrum indicating the noise level. For the $S_1 \rightarrow S_2$ transition the 1st flash data is shown, while the data was deconvolved for the other S-state transitions.
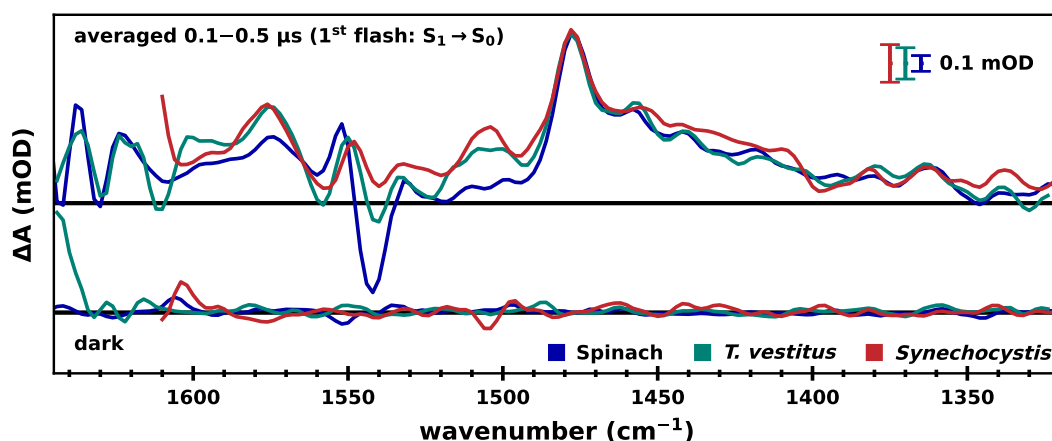
Figure 6.3: Initial spectra of the $S_1 \rightarrow S_2$ transition of PSII from spinach, *T. vestitus* and *Synechocystis*. The spectrum was obtained by averaging the 1st flash data at each wavenumber between 0.1–0.5 µs. Data from PSII membrane particles from spinach is shown in *blue*, PSII core particles from *T. vestitus* in *green* and PSII core particles from *Synechocystis* in *red*. The spectra are scaled differently for each PSII species, as indicated by the colored scale bars, for easier visual comparison. The time-resolved spectral data sets were smoothed linearly along the time-axis with a sliding average algorithm ($n = 10$); Gaussian smoothing ($\sigma = 2.5$) was applied to the wavenumber axis, resulting in a resolution of about 6–8 cm^{-1}.

Note that the deconvolution process introduces additional noise, thus the 1st flash spectrum is better resolved than the following transitions (especially noticeable for the *Synechocystis* spectra). The $S_0 \rightarrow S_1$ transition was overall poorly resolved for both cyanobacterial samples and has thus been omitted here. In the following, the spectra in Fig. 6.4 will be discussed one by one:

$S_1 \rightarrow S_2$ Transition

The 1st flash spectra (Fig. 6.4a) of all three samples show many similar features; however, there are also some clear differences. In the cyanobacterial spectra a peak at 1478–1480 cm^{-1} stands out, which is not present in spinach PSII. This could relate to a non-negligible semiquinone population, indicating that the acceptor-side processes are not yet complete at 400–800 ms. It may also relate to a higher number of non-Q_B units in the core complex samples, leading to long-lived Q_A^- species. In previous FTIR reports on *Synechocystis* and *T. vestitus*, the 1478 cm^{-1} features are much less pronounced or absent (e.g. Suzuki et al., 2006; Debus, 2021), which is easily explained: the FTIR spectra were typically recorded for several seconds after the excitation flash, giving the acceptor-side processes more time to complete—and the semiquinone signals to relax—than in the here shown data.

All three species exhibit features around 1500(+) and 1544(–) cm^{-1}, but the exact peak position differs slightly between the samples. A negative feature at 1522 cm^{-1}, on the other hand is at exactly the same position in all samples. A feature at 1558 cm^{-1} that appears merely as a shoulder in spinach PSII, appears as negative peaks in the cyanobacterial spectra (especially pronounced in *T. vestitus*), which is consistent with previous reports on *Synechocystis* and *T. vestitus* (e.g. Debus, 2021; Suzuki et al., 2006). For spinach PSII, however, sometimes merely a shoulder (Suzuki et al., 2006; Schönborn, 2017) and sometimes a distinct negative peak as for cyanobacterial samples has been reported (Noguchi et al., 1995a; Hillier and Babcock, 2001).
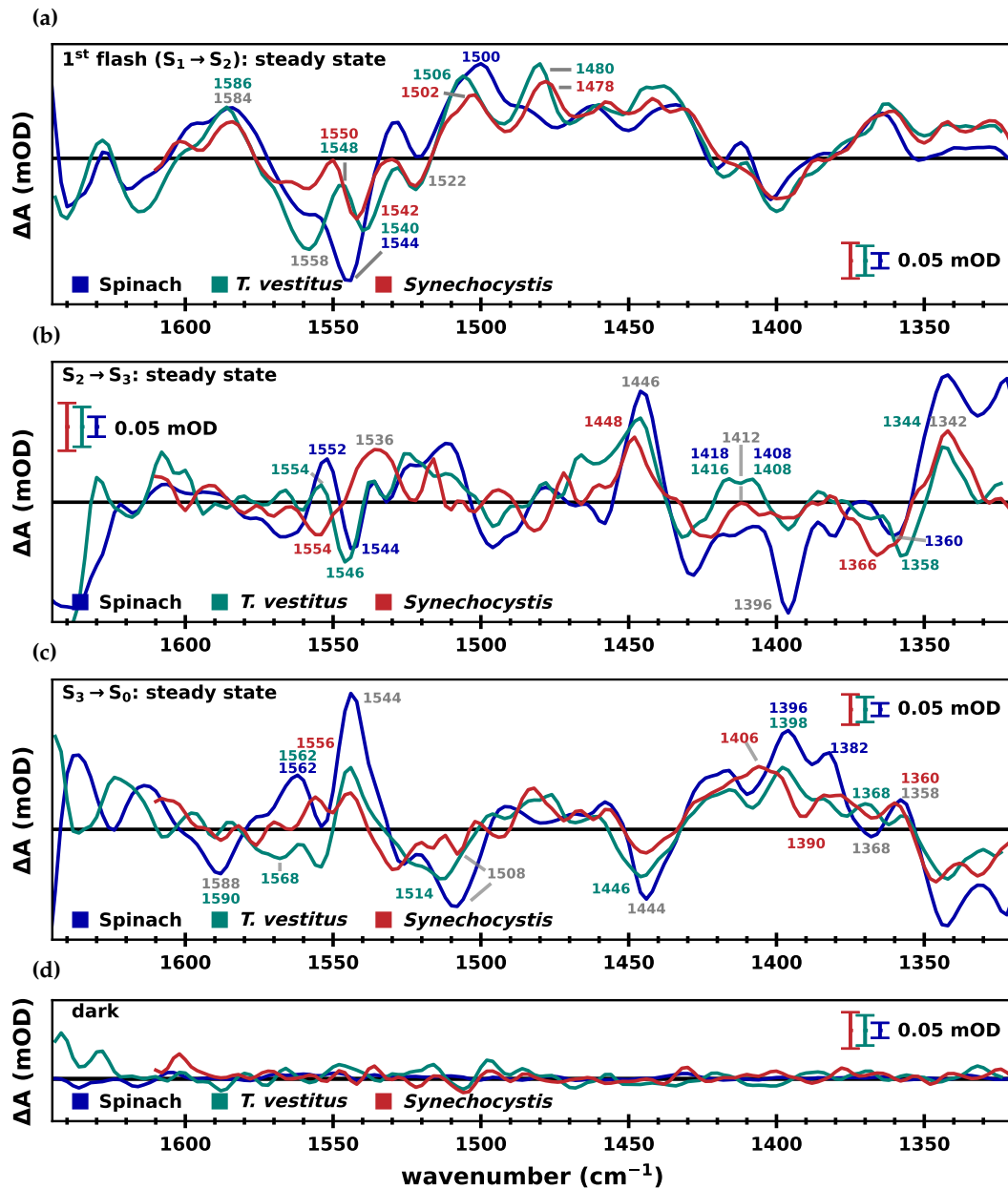
157

Figure 6.4: Steady-state spectra of three S-state transitions of PSII from spinach, *T. vestitus* and *Synechocystis*. Steady-state spectra, obtained by averaging the data at each wavenumber between 400–800 ms of **(a)** the first flash data (predominantly $S_1 \rightarrow S_2$), **(b)** the $S_2 \rightarrow S_3$ transition and **(c)** the $S_3 \rightarrow S_0$ transition. **(d)** Noise-level as indicated by dark spectra of the same time range, obtained without excitation flash. Data from PSII membrane particles from spinach is shown in *blue*, PSII core particles from *T. vestitus* in *green* and PSII core particles from *Synechocystis* in *red*. The spectra are scaled differently for each PSII species, as indicated by the colored scale bars, for easier visual comparison. The time-resolved spectral data sets (acquired in 2 cm^{-1} steps) were smoothed linearly along the time-axis with a sliding average algorithm ($n = 10$); Gaussian smoothing ($\sigma = 2.5$) was applied to the wavenumber axis, resulting in a resolution of about 6–8 cm^{-1}. The spectra were furthermore deconvolved assuming a starting population of 74% S_1, 12% S_0 and 14% S_2 (spinach PSII) or 85% S_1 and 15% S_0 (cyanobacterial PSII) and miss factors of 8% (spinach), 10% (*T. vestitus*) and 12% (*Synechocystis*).

As shown in Chapter 5.3, the feature around 1558 cm^{-1}, as well as a feature around 1584(+) cm^{-1}, appears concomitant with oxidation of a Mn atom in spinach PSII; both have previously been assigned to COO$^-$ residues H-bonded to the Mn$_4$CaO$_x$ cluster (Noguchi et al., 1995b; Noguchi and Sugiura, 2003). The cyanobacterial spectra both feature a positive peak at about 1550 cm^{-1}, which is absent in the spinach spectrum, possibly because it is masked by the very strong negative feature at 1544 cm^{-1}.

S$_2$→S$_3$ Transition

The features in the S$_2$→S$_3$ steady-state spectra (Fig. 6.4b) are overall of smaller amplitude than those of the S$_1$→S$_2$ transition; some of the small peaks, especially in the *Synechocystis* spectrum, are barely resolved and should not be over-interpreted. The most prominent features at around 1342(+) and 1446(+) cm^{-1} are present in all samples as is a negative feature at 1396 cm^{-1}, although the latter is only very weakly present in *Synechocystis*. A feature at 1360–1358(–) cm^{-1} in the spinach and *T. vestitus* spectra appears only as a shoulder in *Synechocystis*, which instead shows a prominent negative peak at 1366 cm^{-1}. All samples exhibit a positive feature at 1536 cm^{-1}, which is much broader in *Synechocystis* than in the other two spectra. The spectra of spinach and *T. vestitus* furthermore have a positive peak around 1554 cm^{-1}, which is negative in *Synechocystis*.

The *T. vestitus* spectrum agrees overall well with previous reports (Suzuki et al., 2006), as does the spinach spectrum (see Chapter 5.2.4). In the *Synechocystis* spectrum, several typically present prominent peaks are absent, e.g. features at about 1568(–) and 1395(–) cm^{-1} reported by Service et al. (2010) and Debus (2021). This is in part likely due to the poor S/N of the here presented data. It is striking, however, that there are also prominent differences between previously published *Synechocystis* FTIR spectra: While e.g. Debus (2021) reports a distinctive 1555(+)/1545(–) feature—similar to that of the here shown spinach data—this feature is absent in a different study of the same group (Service et al., 2010). Possible reasons for this will be discussed further down.

S$_3$→S$_0$ Transition

The S$_3$→S$_0$ steady-state spectra (Fig. 6.4c) of all three samples follow an overall similar shape. Again, some differences nevertheless stand out: In the symmetric carboxylate C=O stretch region, spinach and *T. vestitus* show a prominent peak at around 1396(+) cm^{-1}, which is replaced by a broad feature centered around 1406(+) cm^{-1} in *Synechocystis*. While all spectra show a maximum at about 1382 cm^{-1}, the *Synechocystis* spectrum stands out with a prominent minimum at 1390 cm^{-1}. This is in agreement with previous FTIR studies of *Synechocystis* (Kim et al., 2018) as well as spinach and *T. vestitus* (Suzuki et al., 2006). The *T. vestitus* spectrum exhibits a small peak at 1368(+) cm^{-1}, while spinach does not; the same behavior was observed by Suzuki et al. (2006).

Prominent features at about 1444(–) and 1544(+) cm^{-1} were observed for all samples, also in agreement with the above mentioned literature. The positive features around 1480 cm^{-1} in the cyanobacterial samples appear more strongly pronounced than in previous reports (e.g. Kim et al., 2018; Suzuki et al., 2006), likely due to unfinished acceptor-side processes, as discussed for the S$_1$→S$_2$ transition further above.

The strong negative feature at 1588 cm^{-1} is only very weakly present in the cyanobacterial samples; in previously reported spectra, however, both *Synechocystis* (Kim et al., 2018) as well as *T. vestitus* (Suzuki et al., 2006) also showed prominent negative features at this wavenumber. Thus, this is likely no true difference between the samples but rather an arte-

fact, possibly due to poor S/N (see panel d for an estimate of the noise level; the true noise level should however be even higher due to the deconvolution process).

All in all, the here presented spectra are in good agreement with previous reports. Some apparent differences between the samples shown here are likely artefactual due to insufficient S/N (especially concerning the *Synechocystis* data); several clear differences in prominent peaks, however, are reproducible and thus likely relate to species differences and/or differences in properties resulting from the sample nature (core complexes vs. membrane particles).

6.4   Kinetic Analysis: Transient Absorption Changes at Single Wavenumbers and Decay Associated Spectra

Figure 6.5 shows the transient IR absorption changes corresponding to the four S-state transitions at 1384 and 1544 cm^{-1} for all three samples; transients at 1395, 1405, 1400 and 1514 cm^{-1} are additionally shown in Figs. A4.2 and A4.3 in the Appendix.

Visual comparison of the transients at 1384 cm^{-1} between the PSII variants (Fig. 6.5a, c, e) shows overall strong similarity, despite clear differences in S/N; the same holds true for other wavenumbers in the symmetric carboxylate stretch region shown in the Appendix. Looking at the transients at 1544 cm^{-1} (Fig. 6.5b, d, f) paints a different picture: Besides the prominent millisecond rise in the $S_3 \rightarrow S_0$ transients (*green*) there are hardly any similarities. The most striking difference is the starting ΔA signal: while in spinach the initial IR difference signal is strongly negative, in *T. vestitus* the initial signal is about zero and in *Synechocystis* it is positive.

As 1544 cm^{-1} is—at least in part—an amide II band, the strong sample dependence may in part be due to species-dependent differences in the PSII structure. It has also been shown that the hydration level of the sample strongly influences the steady-state IR spectra in the amide II region (Noguchi and Sugiura, 2002a); possible effects on early spectra are unknown.

The strong differences in the nanosecond to microsecond time range could also be due to differences in the P680$^+$ background. To explore this possibility, the transients of the $S_3 \rightarrow S_0$ transition are shown in Fig. 6.6a with (*pink* and *light blue*) and without (*dark colors*) subtraction of their P680$^+$ background (*T. vestitus* is shown only without P680$^+$ correction, as a P680$^+$ transient was not acquired for this sample). Visual inspection shows that the P680$^+$ background does not explain the differences, even when directly overlaying the millisecond kinetics of the transients (Fig. 6.6b).

Another possible explanation for the strong differences at 1544 cm^{-1} could be varying contributions of broken centers, e.g. by centers that have lost their Mn$_4$CaO$_x$ cluster. Figure 6.6c shows the transients of the $S_3 \rightarrow S_0$ transition of the three PSII variants alongside the transition in Mn depleted spinach. Indeed, the overall shape of the Mn depleted transient, which starts with a positive difference absorption, could possibly explain the strongly differing IR signals in the nanosecond to microsecond region. Figure 6.6d further explores this option: The three PSII variants are again shown normalized to their millisecond rise phase. Addition of the intact and Mn depleted spinach transients and subsequent normalization indeed approximately simulates the shape of the *T. vestitus* transient (*black*). Adding three times the Mn depleted transient to the intact transient and subsequently normalizing instead results in a transient which approximately simulates the *Synechocystis* transient (*grey*). While this is of course no definitive proof, the here shown analysis could suggest that the
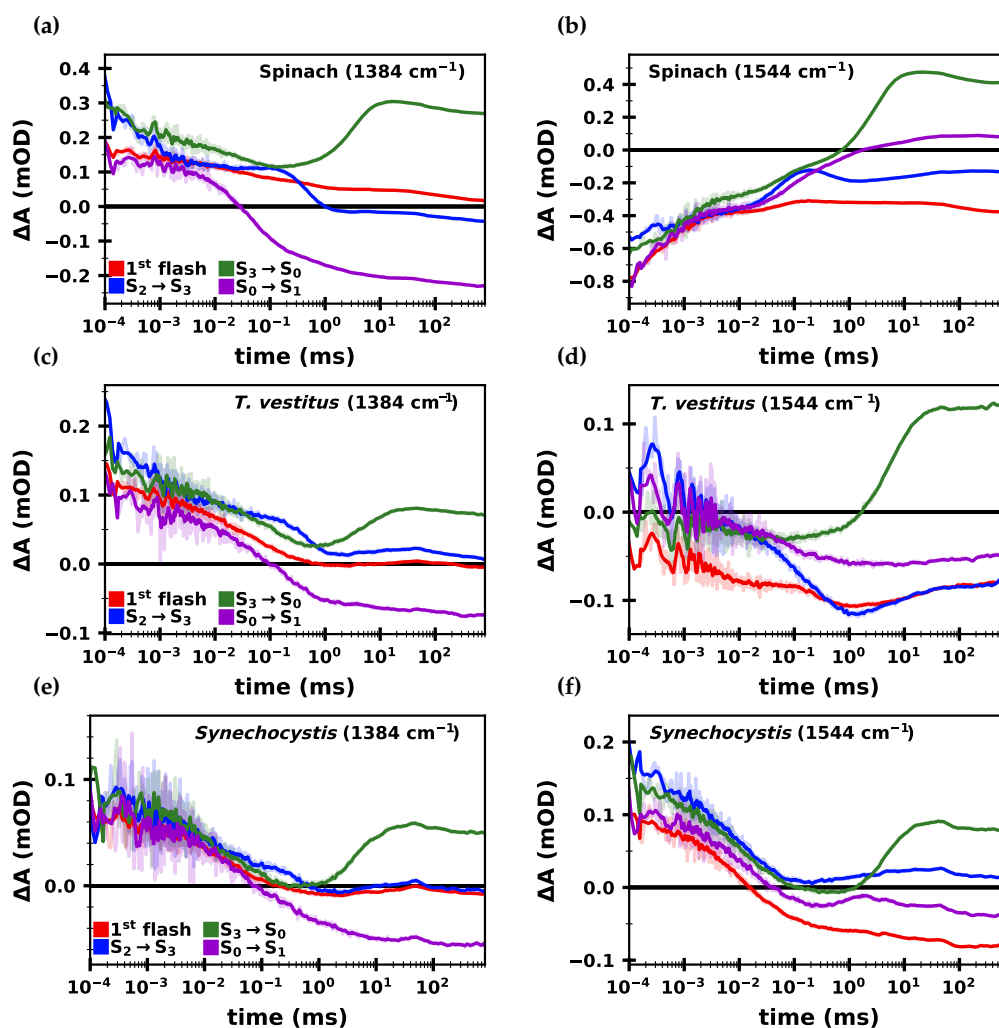
Figure 6.5: IR difference absorption of the S-state transitions of PSII from spinach, *T. vestitus* and *Synechocystis* at 1384 and 1544 cm^{-1}. Each panel shows four transients corresponding to the $S_1 \rightarrow S_2$ (*red*), $S_2 \rightarrow S_3$ (*blue*), $S_3 \rightarrow S_0$ (*green*) and $S_0 \rightarrow S_1$ (*purple*) transition. For the $S_1 \rightarrow S_2$ transition the first flash data is shown; for the other transitions the data was deconvolved assuming a starting population of 85% S_1 and 15% S_0). The first and second column show data at 1384 and 1544 cm^{-1}, respectively. The data was acquired on **(a–b)** spinach PSII membrane particles, **(c–d)** core complexes from *T. vestitus* and **(e–f)** core complexes from *Synechocystis*. All transients were smoothed with a sliding average algorithm with a window size of $n = 10$ (*opaque colors*); non-smoothed transients are shown in transparent colors.

Synechocystis sample exhibits the highest number of broken centers, followed by *T. vestitus* and finally spinach, resulting in strongly differing transients at 1544 cm^{-1}. As shown in Fig. 4.15 in Chapter 4, in some wavenumber regions the intact and Mn depleted spinach spectra differ much more strongly from each other than in others, which could explain why the transients around 1384 cm^{-1} in Fig. 6.5 are not strongly affected by the possibly differing amount of broken centers.

To exclude a significant influence of the heat artefact correction, all transients were corrected with various alternative heat artefact magnitudes (see Fig. A4.4 in the Appendix), but this did not lead to a higher similarity between the transients.
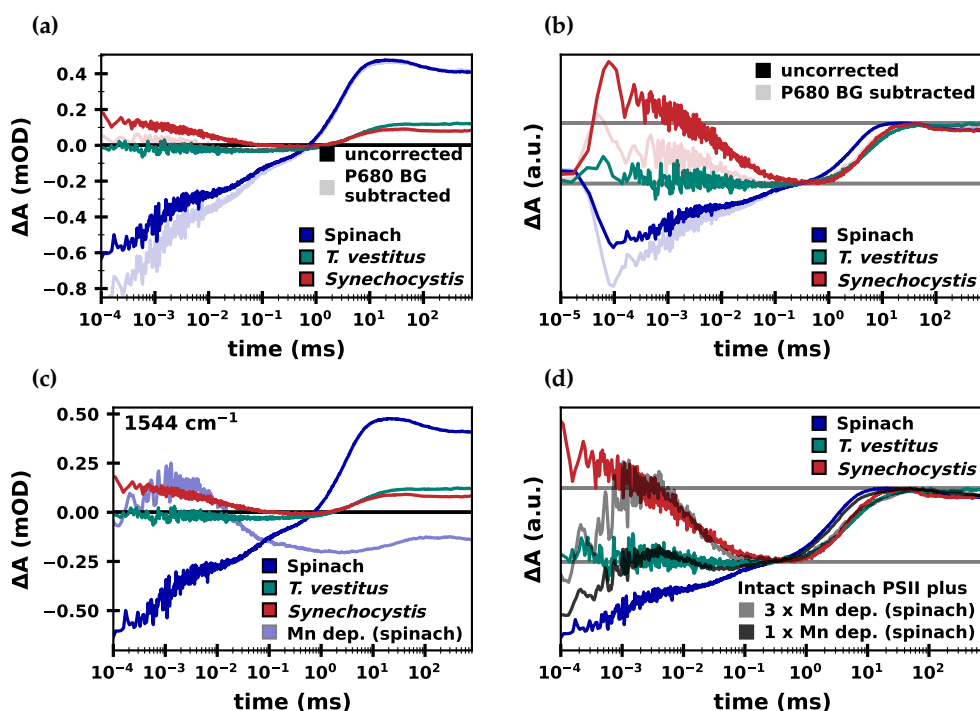
Figure 6.6: Direct comparison of IR absorption changes of the $S_3 \rightarrow S_0$ transition at 1544 cm^{-1} of PSII from spinach, *T. vestitus* and *Synechocystis*. (a) The $S_3 \rightarrow S_0$ transients of spinach (*blue*), *T. vestitus* (*green*) and *Synechocystis* (*red*) are shown in *opaque colors*, alongside with the same transients after subtracting the P680 background (as measured at 1780 cm^{-1}) in *transparent light colors*. (For *T. vestitus* no P680-transient was measured.) **(b)** The same data as in panel (a), but shifted and normalized such that the millisecond rise phase of all transients are overlaid. **(c)** The non-P680-corrected transients as shown in panel (a), together with transient of Mn depleted spinach PSII at 1544 cm^{-1} (*light blue*). **(d)** The non-P680-corrected transients as shown in panel (a), but shifted and normalized such that the millisecond rise phase of all transients are overlaid. Additionally, the sum of n-times the transient from intact spinach PSII and m-times Mn depleted spinach PSII is shown for two different ratios of $n/m = 1/1$ (*dark grey*) and $n/m = 1/3$ (*light grey*). All transients in all panels were deconvolved assuming a starting (dark-adapted) population of 85% S_1 and 15% S_0 (cyanobacterial PSII and Mn depleted spinach PSII) or 74% S_1, 12% S_0 and 14% S_2 (intact spinach PSII).

To further investigate the origin of these species-dependent differences in IR difference absorption, it would be informative to perform time-resolved IR measurements on core particles from spinach as well as Mn depleted *Synechocystis* and/or *T. vestitus* samples.

6.4.1 The $S_2 \rightarrow S_3$ Transition

Transient IR Absorption at Single Wavenumbers

The kinetics of the $S_2 \rightarrow S_3$ transition were further analyzed by globally fitting transients at 1384, 1395, 1514 and 1544 cm^{-1} to a sum of four exponentials between 5 μs and 10 ms for each PSII variant; the resulting fit curves, time constants and wavenumber dependent amplitudes are shown in Fig. 6.7.

For the spinach data similar time constants were obtained as in Chapter 5.4, in which the 71 μs and 394 μs phases (here 76 μs and 372 μs) were assigned to the PT and ET step,
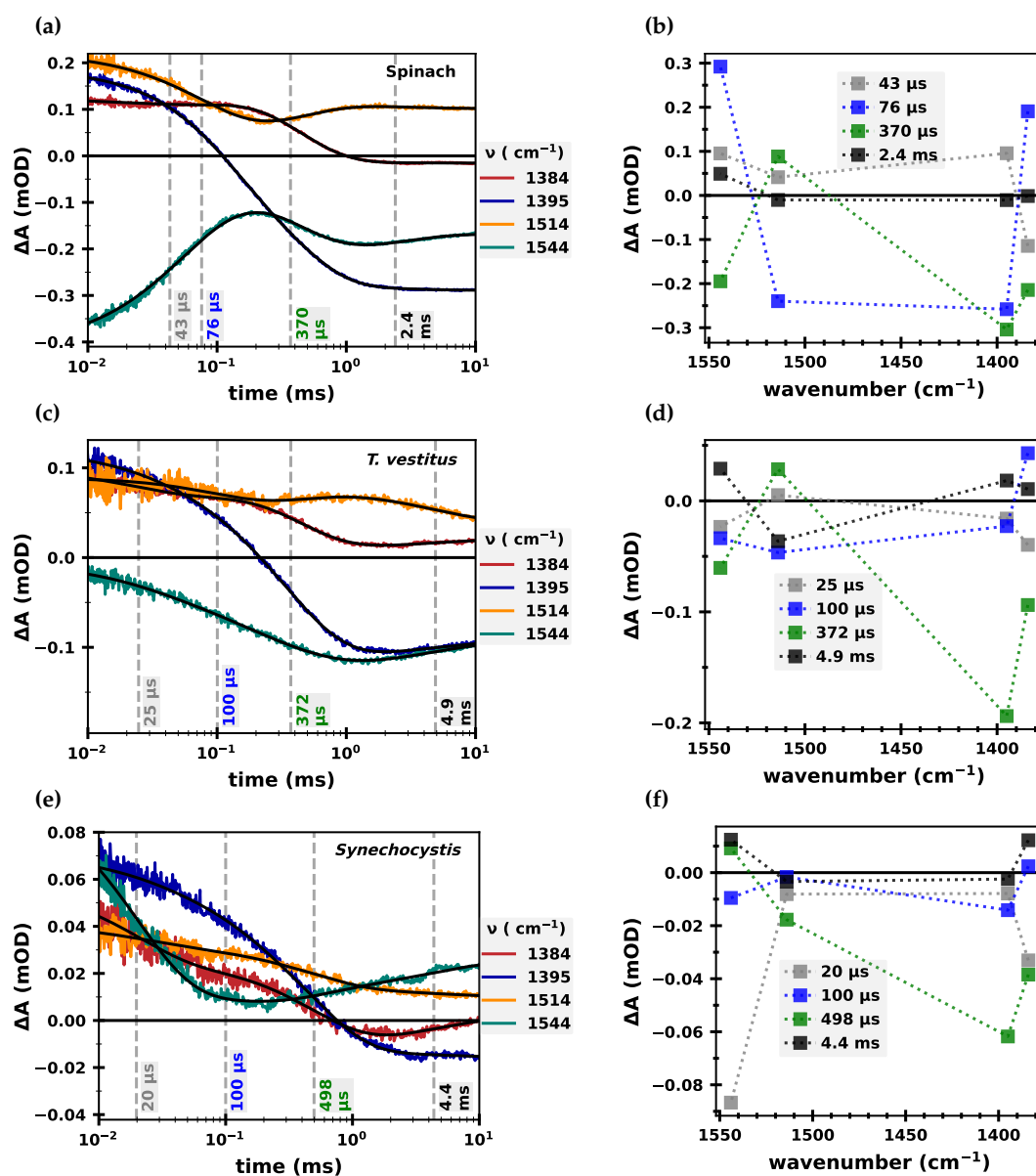
Figure 6.7: Global fit results of the $S_2 \rightarrow S_3$ transition at 1384, 1395, 1514 and 1544 cm^{-1} for PSII from spinach, *T. vestitus* and *Synechocystis*. *Left column:* Transients at 1384 (*red*), 1395 (*blue*), 1514 (*orange*) and 1544 cm^{-1} (*green*) and their fit curves (*black*). The time constants are indicated with vertical lines. *Right column:* Amplitudes of the time constants as a function of wavenumber. Transients and fit results are shown for **(a–b)** spinach PSII membrane particles, **(c–d)** PSII core particles from *T. vestitus* and **(e–f)** PSII core particles from *Synechocystis*. In (e) and (f) the second time constant ($\tau_2 = 100$ µs) was fixed. A non-constrained fit resulted in $\tau_2 = 40$ µs, while the other time constants were hardly affected. A fit with omission of τ_2 also resulted in similar time constants and only marginally poorer residuals (see Fig. A4.5 in the Appendix). All data was deconvolved assuming a starting (dark-adapted) population of 85% S_1 and 15% S_0 (cyanobacterial PSII) or 74% S_1, 12% S_0 and 14% S_2 (spinach PSII).
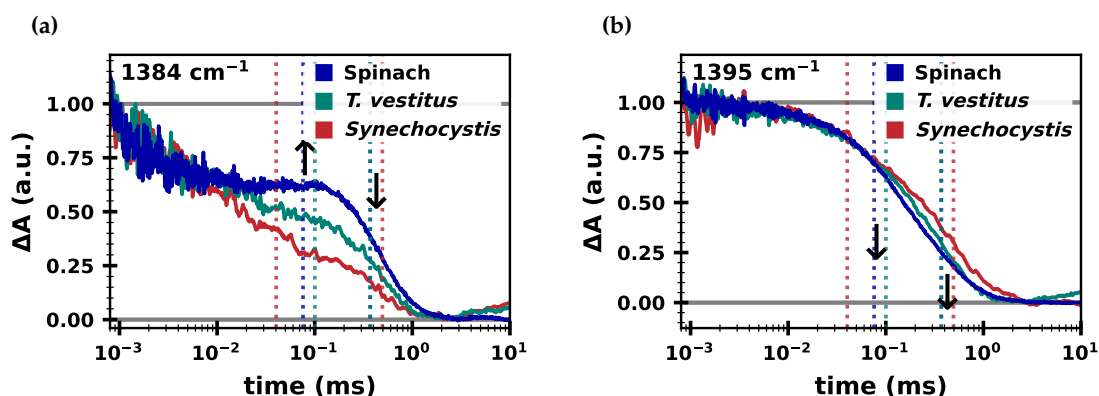
Figure 6.8: Direct comparison of IR absorption changes of the S$_2$→S$_3$ transition at 1384 and 1395 cm^{-1} of three PSII samples. from spinach, *T. vestitus* and *Synechocystis*. Transients of PSII from spinach (*blue*), *T. vestitus* (*green*) and *Synechocystis* (*red*) are at **(a)** 1384 cm^{-1} and **(b)** 1395 cm^{-1}. Two time constants (as determined in Fig.6.7) are show in vertical dotted lines of the same color as the transients they refer to; arrows indicate whether the associated amplitudes are positive or negative. The transients were shifted such that their minimal values are zero and subsequently normalized to their value at 1 μs for easier visual inspection. All data was deconvolved assuming a starting (dark-adapted) population of 85% S$_1$ and 15% S$_0$ (cyanobacterial PSII) or 74% S$_1$, 12% S$_0$ and 14% S$_2$ (spinach PSII).

respectively. The fast microsecond phase is likely assignable to a slow P680$^+$ reduction phase and the millisecond phase should mostly correspond to an acceptor-side process.

Similar time constants were determined for *T. vestitus*. For the *Synechocystis* data, a slightly slower phase of 500 μs (likely corresponding to the ET step) was determined and τ_2 had to be fixed to 100 μs. As shown in Fig. A4.5 in the Appendix, a non-constrained fit resulted in $\tau_2 = 50$ μs and when fitting with only three time exponential components the fit quality was only marginally poorer, although this phase was then omitted entirely. This overall indicates that a kinetic phase around 50–100 μs is very poorly resolved in the here shown *Synechocystis* data.

While in the *T. vestitus* data set the 100 μs phase appears to be reasonably well resolved, its amplitude—relative to the amplitude of the 372 μs phase—is significantly smaller than in the spinach data, especially at 1384 and 1395 cm^{-1} (Figs. 6.7b and d, *blue*). This observation is further explored in Figure 6.8, which shows a direct comparison of normalized S$_2$→S$_3$ transients at both wavenumbers between the three PSII variants: At 1384 cm^{-1} (panel a), PT and ET phase have amplitudes of opposite sign. In the spinach transient, the rising PT phase appears as a plateau because it is preceded and succeeded by a decaying phase. In *T. vestitus* the rising phase is clearly weakened and in *Synechocystis* it is not discernible. At 1395 cm^{-1} (panel b) the ET and PT phases are of the same sign, making it generally harder to distinguish them visually. However, the direct comparison of the three normalized transients clearly shows that in spinach there is a larger contribution to the faster phase than in the other two samples. We previously reported a similar observation for spinach and *T. vestitus* at 1400 cm^{-1} (Mäusle et al., 2020).

These differences in the amplitudes of the pre-ET phases is of significance as it may explain differences in results from our group to that of Takumi Noguchi's group for the S$_2$→S$_3$ transition: In their time-resolved IR experiments on *T. vestitus*, they found only a small H/D kinetic isotope effect and hardly any pH effect on the pre-ET phase (Sakamoto

et al., 2017; Takemoto et al., 2019), which clearly contrasts the results reported in Chapter 5.4.1 as well as other spectroscopic results on spinach PSII (Klauss et al., 2012a; Zaharieva et al., 2016). This will be discussed in more detail further down (Chapter 6.5).

Decay Associated Spectra
The above pre-determined time constants were fixed in global fits across the time-resolved spectral data sets; the resulting decay associated spectra of the PT and ET phases are shown in Fig. 6.9a and b, respectively. The PT phase of *Synechocystis* is likely overall not well resolved, as it was already poorly resolved in the higher S/N single wavenumber transients and will thus not be discussed in detail. For spinach PSII, the DAS obtained in Chapter 5.4 are shown.

The PT DAS of spinach and *T. vestitus* show clear similarities: A broad positive peak at 1572 cm^{-1}, as well as features at 1520(+), 1453(−), 1446(+) and 1404(+) cm^{-1}. All three DAS show similar features at around 1382(+) and 1364(−) cm^{-1}. While the spinach DAS shows a prominent feature at 1542(+) and a smaller one at 1556(+) cm^{-1}, *T. vestitus* instead shows a prominent peak at 1552(+) and small negative one at 1540(−) cm^{-1}.
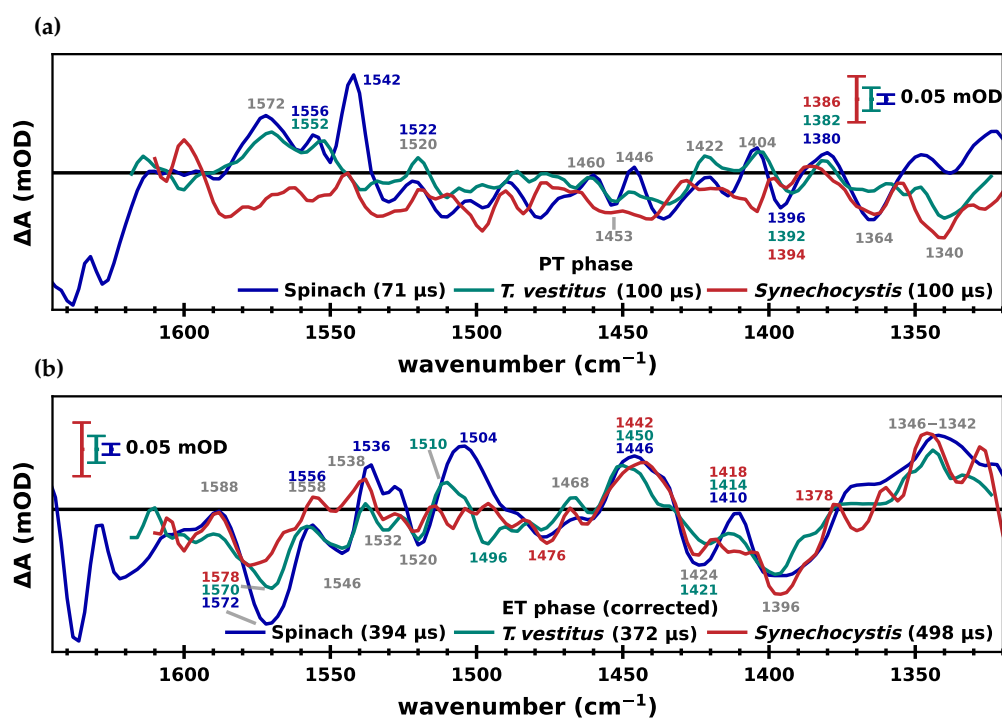

Figure 6.9: Comparison of the decay associated spectra of the PT and ET phase of the S$_2$→S$_3$ transition of three different PSII samples. DAS assigned to **(a)** the PT phase (∼100 µs) and **(b)** the ET phase (∼370–500 µs) is shown for spinach (*blue*), *T. vestitus* (*green*) and *Synechocystis* (*red*). The DAS of spinach PSII are redrawn from those shown in Chapter 5). The DAS of the cyanobacterial samples were obtained by fixing pre-determined time constants across a time-resolved spectral data set; the ET phase was corrected for acceptor-side contributions by subtracting a corresponding DAS of the 1st flash data. The spectra were scaled differently to facilitate visual inspection as indicated by the differently sized colored scale bars (each referring to 50 µOD). All data was deconvolved assuming a starting (dark-adapted) population of 85% S$_1$ and 15% S$_0$ (cyanobacterial PSII) or 74% S$_1$, 12% S$_0$ and 14% S$_2$ (spinach PSII) prior to the fitting procedure.

The ET phase (Fig. 6.9b) appears relatively well resolved for all three PSII variants—although the many very small peaks in the *Synechocystis* spectrum presumably stem from noise in the data and (just as for the PT DAS) should not be over-interpreted. The ET DAS of the cyanobacterial samples were corrected for acceptor-side contributions by fitting the 1st flash spectrum with the same time constants and then subtracting the corresponding DAS from $S_2 \rightarrow S_3$ DAS; see Fig. A4.6 in the Appendix for non-corrected DAS. For the PT step this was not done, as the donor-side ET event of the $S_1 \rightarrow S_2$ transition is expected to occur at around 100 µs. For the spinach DAS a correction of the $S_2 \rightarrow S_3$ transition is not as
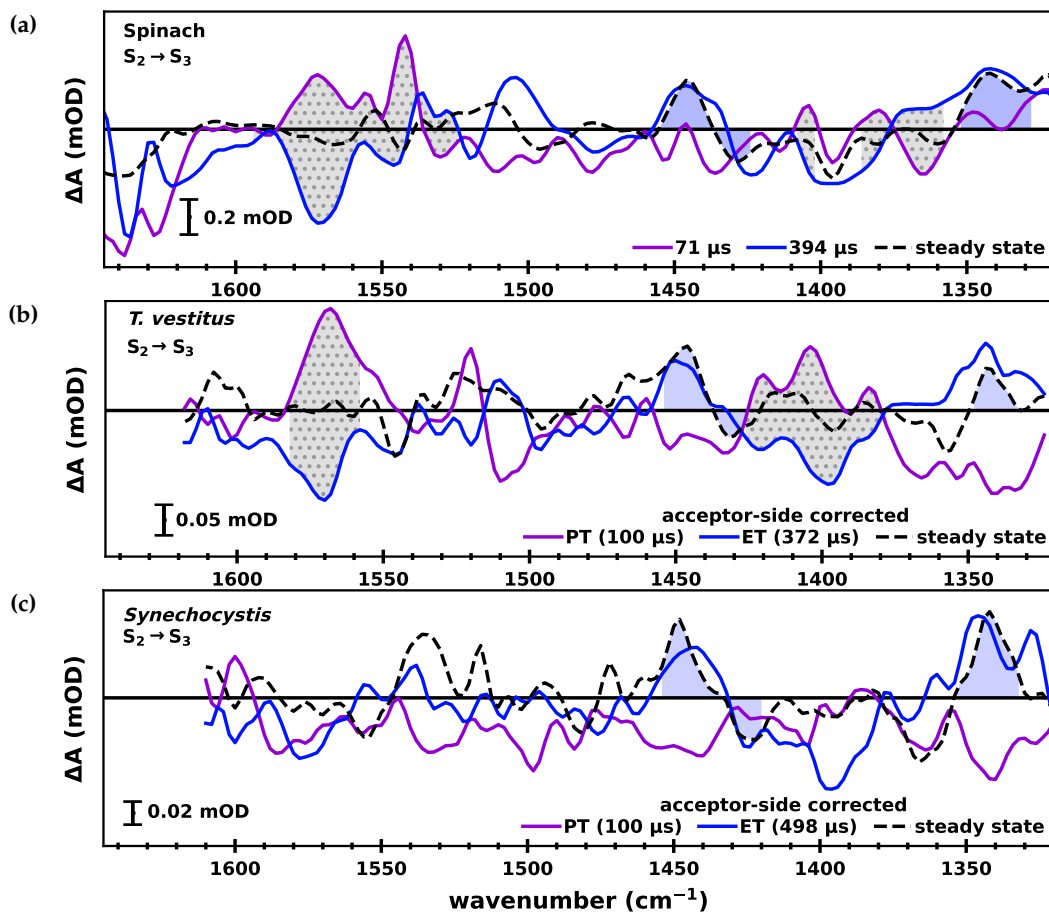

Figure 6.10: Decay associated spectra of the $S_2 \rightarrow S_3$ transition of PSII from *T. vestitus* and *Synechocystis*. The PT phase is shown in *purple*, the ET phase in *blue* and the steady state spectra (average of 400–800 ms) in *dashed black* for **(a)** spinach, **(b)** *T. vestitus* and **(c)** *Synechocystis*. The time constants were first determined by fitting a small number of high S/N transients and then fixed in a global fit across a large time-resolved spectral data set. The spinach DAS is redrawn from Fig. 5.42. The cyanobacterial DAS for both the PT and ET phases were corrected for acceptor-side contributions by fitting the 1st flash data with the same time constants and subtracting the resulting relevant DAS (see main text for more details); DAS without acceptor-side correction are shown in Fig. A4.7 in the Appendix. All data was deconvolved assuming a starting (dark-adapted) population of 85% S_1 and 15% S_0 (cyanobacterial PSII) or 74% S_1, 12% S_0 and 14% S_2 (spinach PSII). Regions of the spectra in which PT and ET show inverted behavior are shaded in *dotted grey*; regions in which the steady-state and ET DAS are similar are shaded in *blue*.

straight-forward (and was hence not performed) because of the period-of-two behavior of PPBQ in contrast to the one-electron chemistry of ferricyanide.

All three samples show pronounced features at around 1572(−)/1588(+) cm^{-1} and 1446(+)/1422(−) cm^{-1}. The negative feature at 1476 cm^{-1} in the *Synechocystis* DAS may hint at an imperfect acceptor-side correction. All three DAS show negative features at 1532 and 1520 cm^{-1}, as well as around 1396 cm^{-1}.

Figures 6.10a, b and c show the ET and PT DAS of the $S_2{\rightarrow}S_3$ transition alongside the steady-state spectrum for spinach, *T. vestitus* and *Synechocystis*, respectively. Similar peaks around 1450 and 1340 cm^{-1} are present in the ET DAS and the steady-state spectrum of all three samples (shaded blue areas). Some similarity of ET phase and steady-state spectra is also visible around 1430(−) cm^{-1}, possibly indicating a band shift from 1430 to 1450 cm^{-1}.

A reversed behavior of PT and ET phase around 1570 cm^{-1} is observed in spinach and *T. vestitus*, as well as around 1405 cm^{-1} and 1385 cm^{-1}. In *Synechocystis* the ET DAS also shows negative signals around those wavenumbers, but the PT DAS does not show positive features, possibly because the latter phase is overall too poorly resolved as discussed further above.

6.4.2   The $S_3{\rightarrow}S_0$ Transition
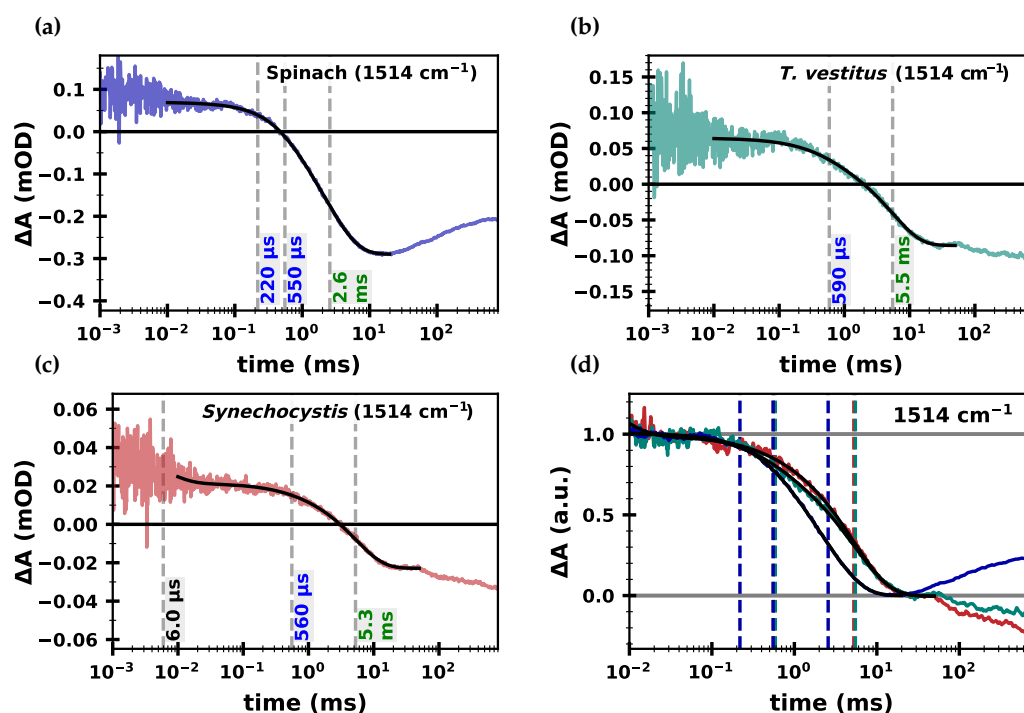
Figure 6.11: Fit results of the $S_3{\rightarrow}S_0$ transition at 1514 cm^{-1} for three different PSII samples. The transients (*colored lines*) together with their fit curves (*black*) are shown for PSII from **(a)** spinach, **(b)** *T. vestitus* and **(c)** *Synechocystis*. The time constants are indicated with vertical dashed lines. In **(d)** all three transients are shown together (shifted and normalized for easier visual inspection); vertical lines of matching colors indicate the time constants. All data was deconvolved assuming a starting (dark-adapted) population of 85% S_1 and 15% S_0 (cyanobacterial PSII) or 74% S_1, 12% S_0 and 14% S_2 (spinach PSII). An alternative global fit of four wavenumbers is shown in Fig. A4.8 in the Appendix.

As discussed in Chapter 5, fitting the $S_3 \rightarrow S_0$ transition in a meaningful manner proved difficult. As this chapter *inter alia* aims at finding possible differences between the different PSII variants, fixing the time constants to literature values was not a well suitable option. Instead, fitting was here performed only at 1514 cm^{-1}, as shown in Fig. 6.11a–c, which for spinach PSII resulted in similar time constants as the ones chosen in Chapter 5.[35] A normalized overlay of the three transients (panel d) visually confirms a similarly fast microsecond phase of around 500 μs in all samples and a millisecond phase that is faster in spinach (2.5 ms) than in the cyanobacterial samples (5.3 and 5.5 ms); the latter is also well visible at 1395/1405 cm^{-1} (Fig. A4.10). This likely relates in part rather to the type of sample (membrane particles vs. core particles) than the organism, as a similar (even slightly stronger) slowdown was observed when comparing pea seedling thylakoids to core particles (Haumann et al., 1997). However, as discussed further above, a species-dependency of the time constant of O_2-evolution of various thylakoid membrane samples has also been reported (Liang, 2018).
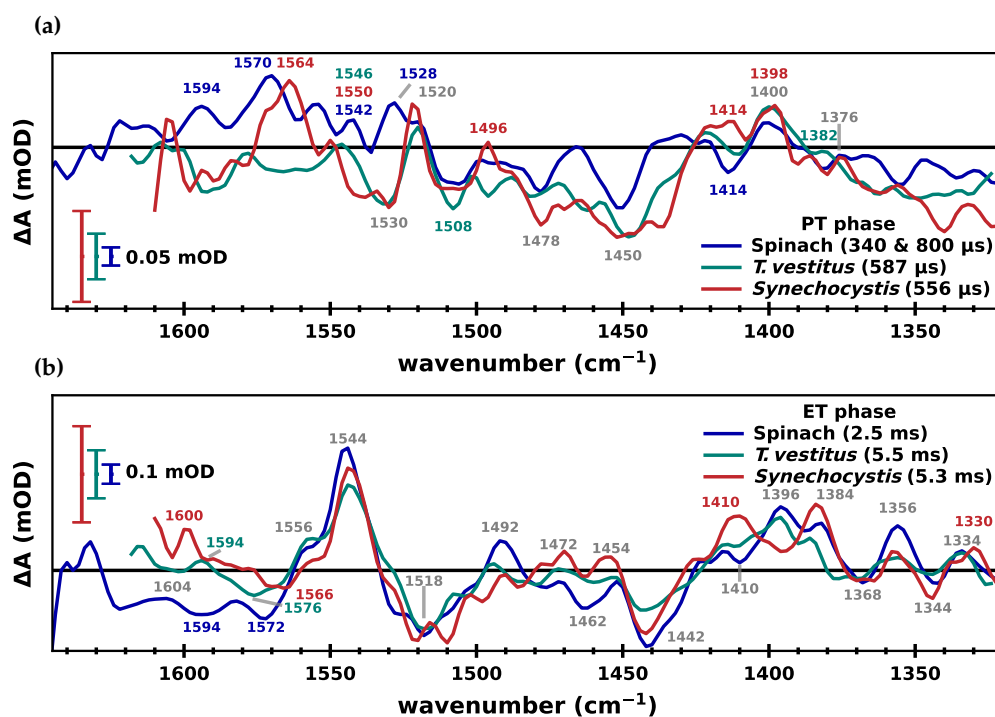

Figure 6.12: Comparison of the decay associated spectra of the PT and ET step of the $S_3 \rightarrow S_0$ transition of three different PSII samples. The DAS corresponding to **(a)** the PT and **(b)** the ET step are shown for spinach PSII (*blue*) (as determined in Chapter 5), *T. vestitus* (*green*) and *Synechocystis* (*red*). The latter two DAS were obtained as shown in Fig. 6.13. The spectra were scaled differently to facilitate visual inspection as indicated by the differently sized colored scale bars. All data was deconvolved assuming a starting (dark-adapted) population of 85% S_1 and 15% S_0 (cyanobacterial PSII) or 74% S_1, 12% S_0 and 14% S_2 (spinach PSII). All PT DAS and the cyanobacterial ET DAS were corrected for acceptor-side contributions by subtracting DAS of the $S_1 \rightarrow S_2$ transition. Non-corrected DAS are shown in Fig. A4.9 in the Appendix.

---

[35]An example of an alternative unconstrained global fit of four transients per PSII variant is shown in Fig. A4.8 in the Appendix.

The obtained time constants were fixed in global fits across time-resolved spectral data sets, resulting in the decay associated spectra shown in Fig. 6.12 (note that these DAS were corrected for acceptor-side contributions; non-corrected DAS are shown in Fig. A4.9 in the Appendix). For spinach PSII, the DAS obtained in Chapter 5.5 are shown.

The DAS of the microsecond phase (Fig. 6.12a), assigned to the pre-ET proton removal phase, shows several clear similarities between the samples, including the features around 1400(+), 1450(−), 1508(−) and 1520(+) cm^{-1}. Spinach and *Synechocystis* show similar strongly
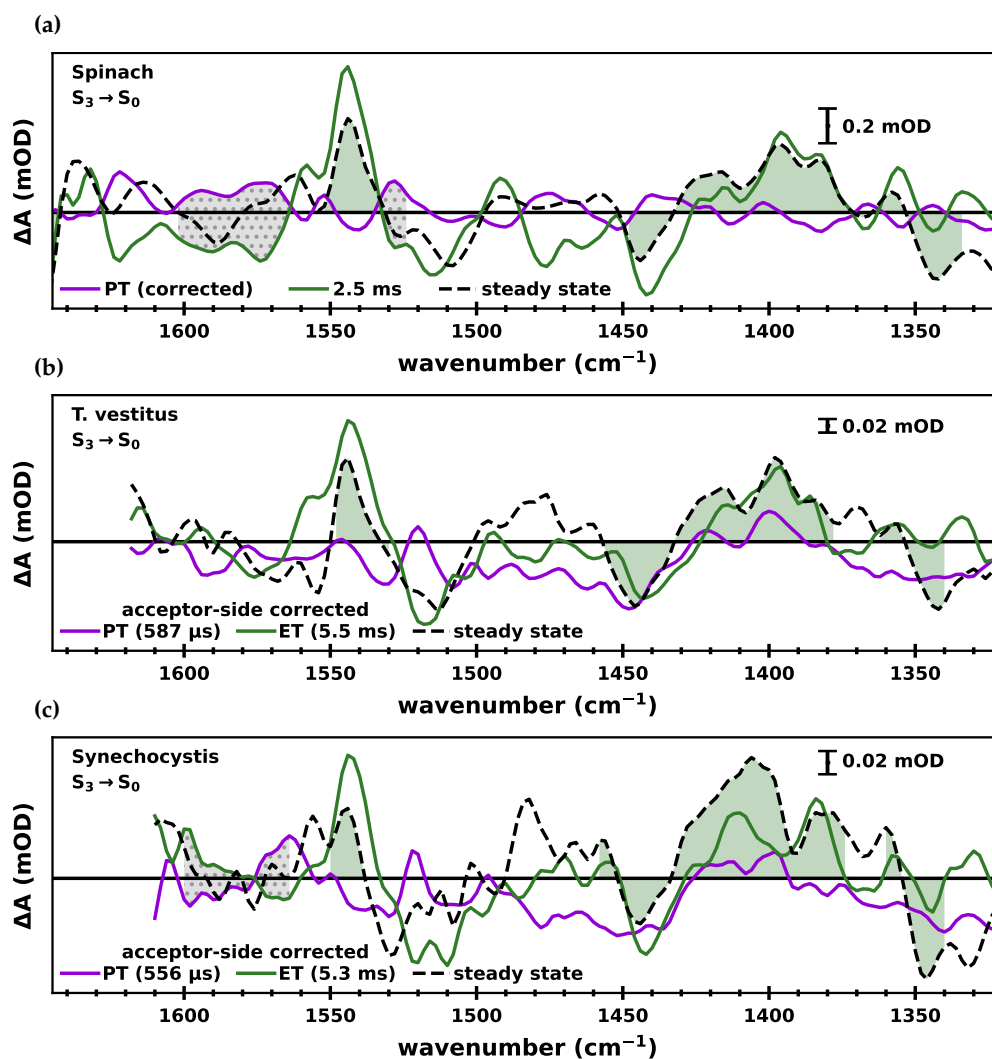

Figure 6.13: Decay associated spectra of the S$_3$→S$_0$ transition of PSII from *T. vestitus* and *Synechocystis*. The PT phase is shown in *purple*, the ET phase in *green* and the steady state spectra (average of 400–800 ms) in *dashed black* lines for **(a)** *T. vestitus* and **(b)** *Synechocystis*. The time constants were first determined by fitting a small number of high S/N transients and then fixed in a global fit across a large time-resolved spectral data set. The DAS for both the PT and ET phases were corrected for acceptor-side contributions by fitting the 1st flash data with the same time constants and subtracting the resulting relevant DAS (see main text for more details). All data was deconvolved assuming a starting (dark-adapted) population of 85% S$_1$ and 15% S$_0$ (cyanobacterial PSII) or 74% S$_1$, 12% S$_0$ and 14% S$_2$ (spinach PSII). Regions of the spectra in which PT and ET show inverted behavior are shaded in *dotted grey*; regions in which the steady-state and ET DAS are similar are shaded in *green*.
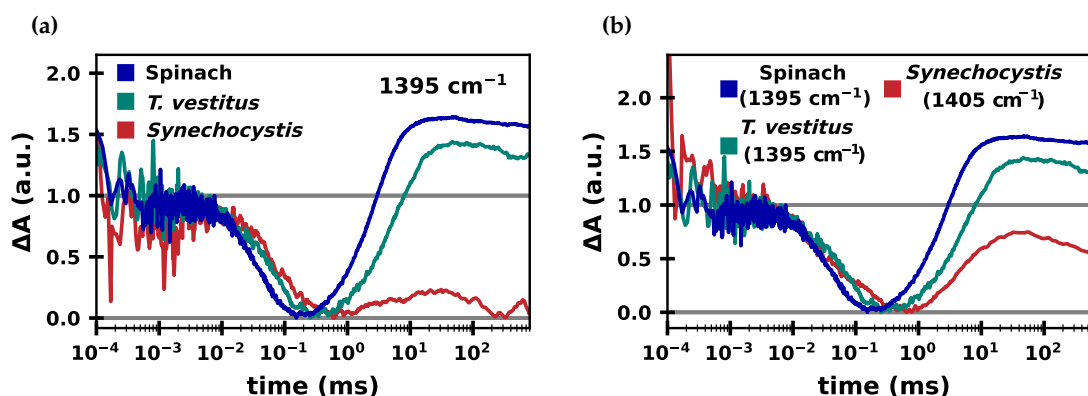
Figure 6.14: Direct comparison of IR absorption changes of the $S_3 \to S_0$ transition at 1395 and 1405 cm^{-1} of PSII from spinach, *T. vestitus* and *Synechocystis*. Data from PSII membrane particles from spinach is shown in *blue*, PSII core particles from *T. vestitus* in *green* and PSII core particles from *Synechocystis* in *red*; the transients were shifted such that their minimal values are at zero and subsequently normalized to their value at 1 µs, enabling a direct visual comparison. **(a)** Comparing the transients at 1395 cm^{-1} shows that a millisecond-rising phase is strongly pronounced in spinach and *T. vestitus*, but is nearly entirely absent in *Synechocystis*. **(b)** Replacing the transient of *Synechocystis* with data acquired at 1405 cm^{-1}, reveals a similar millisecond-rise phase. All transients were deconvolved assuming a starting (dark-adapted) population of 85% S_1 and 15% S_0 (cyanobacterial PSII) or 74% S_1, 12% S_0 and 14% S_2 (spinach PSII).

pronounced positive features around 1564–1570 cm^{-1}; in *T. vestitus*, however, this peak is absent.

The three DAS of the ET phase (Fig. 6.12b) show many similarities and appear overall well resolved. They all show pronounced features at 1544(+), 1442(–), 1368(–), 1356(+) and 1344(–) cm^{-1}, as well as a negative feature around 1570 cm^{-1}. While spinach and *T. vestitus* show a strong positive peak 1396 cm^{-1}, *Synechocystis* rather exhibits a minimum at that wavenumber, with pronounced peaks at either side (1384(+) and 1410(+) cm^{-1}).

Figure 6.13a, b and c shows the ET and PT DAS of the $S_3 \to S_0$ transition alongside the steady-state spectrum for spinach, *T. vestitus* and *Synechocystis*, respectively. For all three samples, the ET DAS and the steady-state spectrum show similar features around 1544(+) as well as between 1450–1340 cm^{-1}. However, between about 1380–1360 cm^{-1} both cyanobacterial steady-state spectra show positive features that are absent in their respective ET DAS. Furthermore, as observed further above, the ET DAS as well as the steady-state spectrum of *Synechocystis* exhibit a clear minimum around 1395 cm^{-1}. Indeed, comparing transients at 1395 cm^{-1} between the three samples, shows that while the other two PSII variants show a strong millisecond rising behavior, this phase is effectively absent in *Synechocystis* (Fig. 6.14a). When, however, comparing the absorption changes of *Synechocystis* at 1405 cm^{-1} to those of the other two samples at 1395 cm^{-1}, a similar rising behavior is observed (Fig. 6.14b).

At around 1560–1570 cm^{-1} (Fig. 6.13, *shaded grey*), both spinach and *Synechocystis* also show a reversed behavior between PT and ET DAS (with a positive PT and negative ET phase), while in *T. vestitus* the PT phase does show a peak at 1580 cm^{-1}, but below zero. Whether this is a true difference between the samples or whether the PT phase is merely too poorly resolved in *T. vestitus*, requires further investigation. At around 1530 cm^{-1}, spinach

PSII also shows a reversed behavior between the PT and ET phases, while the cyanobacterial samples have peaks around 1520 cm^{-1}. Unlike in the spinach DAS, however, the cyanobacterial PT phases are barely above zero here and thus have much smaller amplitudes than the corresponding ET peaks.

6.5 H/D Kinetic Isotope Effect

To further assess possible differences between the different PSII variants, measurements in D_2O were performed on *T. vestitus* and *Synechocystis*; unlike for spinach, however, only a very limited amount of data was acquired. Figure 6.15 shows the normalized transient absorption changes at 1395/1405 cm^{-1} in H_2O and D_2O for all three PSII variants. Visual inspection of the $S_2 \rightarrow S_3$ transition (panel a) reveals a pronounced slowdown of the multiphasic microsecond decay kinetics in D_2O. In the $S_3 \rightarrow S_0$ transition (panel b) the data quality of *Synechocystis* was very poor and is thus not shown; for spinach and *T. vestitus* both the microsecond decay as well as the millisecond rise phase appear slowed in D_2O.[36]

As the $S_3 \rightarrow S_0$ transition is difficult to fit meaningfully, as discussed further above, it will not be analyzed in more detail; more high S/N data is required for closer investigation.

Three transients of the $S_2 \rightarrow S_3$ transition of *T. vestitus* were fit globally to a sum of exponentials to quantify the observed kinetic isotope effect; the resulting fit curves, time constants and wavenumber-dependent amplitudes are shown in Fig. 6.16. For the PT and ET step, time constants of 282 and 905 µs were determined, corresponding to KIEs of 2.8 (PT) and 2.4 (ET). For spinach, similarly strong KIEs were obtained (3.1 and 2.0; see Chapter 5).
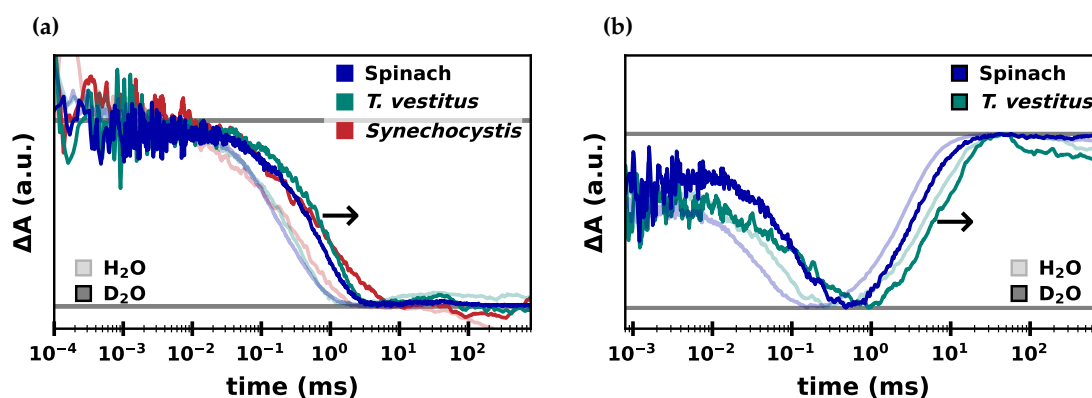

Figure 6.15: Normalized kinetics of the $S_2 \rightarrow S_3$ and $S_3 \rightarrow S_0$ transition in H_2O and D_2O of three different PSII samples. Transient IR absorption changes at 1395 cm^{-1} of spinach PSII (*blue*) and PSII from *T. vestitus* (*green*), as well as absorption changes at 1405 cm^{-1} of PSII from *Synechocystis* (*red*) in H_2O (*transparent colors*) and D_2O (*opaque colors*) of the **(a)** $S_2 \rightarrow S_3$ and **(b)** $S_3 \rightarrow S_0$ transition. Arrows indicate the kinetic slow-down in D_2O. The transients were shifted and normalized relative to each other for easier visual inspection. In (b) the *Synechocystis* data was omitted due to poor S/N, but is instead shown in Fig. A4.11 of the Appendix. All data was deconvolved assuming a starting (dark-adapted) population of 85% S_1 and 15% S_0 (cyanobacterial PSII) or 74% S_1, 12% S_0 and 14% S_2 (spinach PSII).

---

[36] Figure A4.11 in the Appendix shows the $S_3 \rightarrow S_0$ transition of *Synechocystis* in H_2O and D_2O, indicating—despite poor S/N—slowed kinetics of both the pre-ET and ET phases.
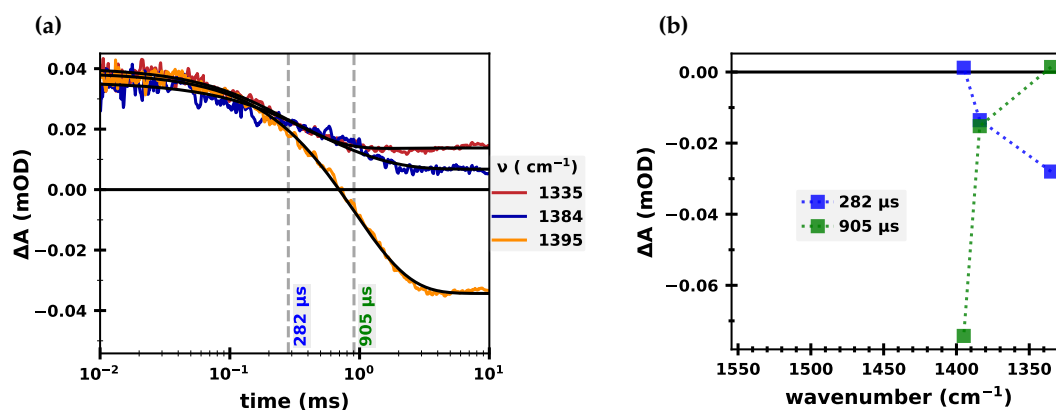
Figure 6.16: Results of globally fitting five IR absorption transients of the $S_2 \rightarrow S_3$ transition of PSII from *T. vestitus* in D_2O. (a) Transient IR changes at 1335 (*red*), 1384 (*blue*) and 1395 (*orange*) and their fit curves (*black*). The time constants are indicated with vertical dashed lines. **(b)** The amplitudes of the determined time constants as a function of wavenumber. An alternative fit approach (using less transients and less exponential components) is shown in Fig. A4.12 in the Appendix. All data was deconvolved assuming a starting (dark-adapted) population of 85% S_1 and 15% S_0.

While this supports the assignment of the PT phase to a proton removal event from the Mn_4CaO_x cluster (Klauss et al., 2012a), it is in disagreement with previous time-resolved IR reports: Sakamoto et al. (2017) found only a very small KIE of 1.2 for the ~100 µs phase. They interpreted this phase as rearrangements in the H-bond network in the general vicinity of Y_Z^{ox}, *inter alia* because they detected this phase at 1514 cm^{-1}. They underline the lack of strong KIE of the 100 µs phase at 1514 cm^{-1}; however in our spinach PSII transients of the same wavenumber this phase is clearly more strongly slowed down in D_2O (see Fig. A4.13 in the Appendix).

One may argue that in Fig. 6.15a it is hard to visually assess whether both or just one of the two decaying components are slowed down—and to what extent—as it is difficult to distinguish two kinetic phases of the same amplitude sign by eye. However, Fig. 6.17 clearly shows a deuteration-induced slow-down of the faster phase at 1335 cm^{-1}.
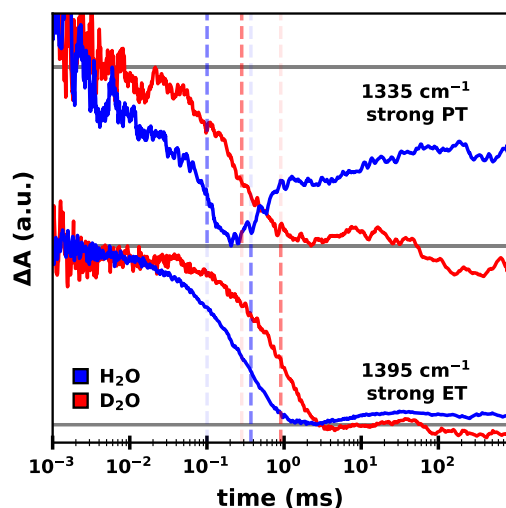
Figure 6.17: H/D kinetic isotope effect of the PT and ET event of the $S_2 \rightarrow S_3$ transition in PSII from *T. vestitus*. Transient IR absorption changes are shown at 1335 cm^{-1} (top) and 1395 cm^{-1} (bottom) in H_2O (*blue*) and D_2O (*red*). The time constants (as determined in Fig. 6.16) associated with the PT and ET event are indicated by vertical lines. The faster kinetic (PT) is strongly visible at 1335 cm^{-1} and slows from 100 µs in H_2O to 282 µs in D_2O (KIE = 2.8). The slower phase (ET) is more pronounced at 1395 cm^{-1} and slows from 372 µs to 905 µs (KIE = 2.4). All transients were shifted and normalized relative to each other for easier visual inspection.

The data shown here thus suggest that *T. vestitus* exhibits a similar pre-ET phase as spinach PSII, indicating that the differences between our results and that of Takumi Noguchi's group are not due to elementary differences between PSII from spinach and *T. vestitus*. The different results may however arise from differences in how strongly the PT phase is reflected in absorption changes at certain wavenumbers. An alternative fit of the *T. vestitus* D_2O data shown in Fig. A4.12 in the Appendix demonstrates that the PT phase is so weakly pronounced at 1384 and 1395 cm^{-1} that in a global fit without 1335 cm^{-1} a mono-exponential fit curve (with $\tau = 900$ µs) simulates the data well (with only a slightly poorer fit quality than a bi-exponential fit).

Further experiments on *T. vestitus*, including pH dependent measurements and higher S/N time-resolved spectral measurements, could help to further clarify the situation. Additional data of *T. vestitus* in D_2O, *inter alia* at 1514 cm^{-1}, will be necessary to unambiguously show whether the nature of the PSII sample influences the kinetics and to assess how the different results between Noguchi's group and ours can be reconciled.

6.6 Summary and Concluding Discussion

In this chapter, time-resolved IR data on spinach PSII membrane particles was compared to that of PSII core particles from two cyanobacteria: thermophilic *T. vestitus* and mesophilic *Synechocystis*. It was shown that at some wavenumbers (such as 1384 cm^{-1}) the flash-induced transient absorption changes are very similar between all three samples, while at other wavenumbers (such as 1544 cm^{-1}) they are very different. The time-dependent $P680^+$ background as well as the heat artefact correction procedure were excluded as major contributors to these wavenumber-dependent differences. Instead, the influence of broken (Mn depleted) PSII centers was pinpointed as a likely candidate.

Indeed, when comparing double difference spectra of intact minus Mn depleted spinach PSII at two time slices with double difference spectra of intact spinach PSII minus *Synechocystis*, the similarities are very pronounced (Fig. 6.18). This strongly suggests, that the relative amount of PSII units which lack a functional donor side is higher in the cyanobacterial core complexes than in spinach PSII membrane particles. As the magnitude of the influence of Mn depleted centers on the IR difference absorption is wavenumber-dependent, some transients will be more strongly affected by a higher number of broken PSII units than others.

This may indeed also explain differences between previously reported FTIR spectra of *Synechocystis*: The strongly pronounced 1545(–) cm^{-1} feature in the $S_2 \rightarrow S_3$ steady-state spectra reported by Debus (2021) might be masked by a positive feature due to broken PSII centers in other studies by the same group (e.g. Service et al., 2010). This hypothesis is supported by comparing the reported steady-state O_2-evolution rates of those studies: while the former reports about 5.8 mmol O_2/(mg Chl)/h, the later reports only 4.9–5.4 O_2/(mg Chl)/h.

It should be noted that the here presented spectra on *Synechocystis* possibly has an especially large fraction of broken centers due the relatively long measurement time required to obtain time-resolved spectral data: Each sample spot was subjected to a total of about 250 flashes per sample spot, which is more than double compared to the study by Debus (2021). As the time-resolved spectral data set was acquired starting at low wavenumbers, it is furthermore possible that the contribution of broken centers steadily increases from 1300 to 1600 cm^{-1} (assuming that each excitation flash leads to further damage to the sample).
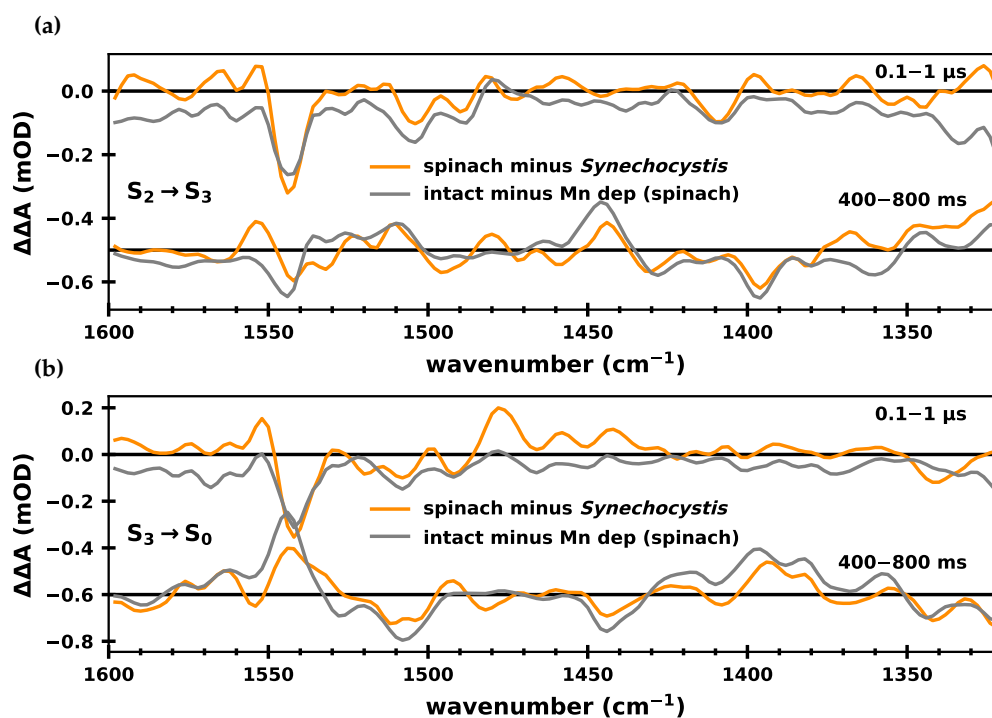
Figure 6.18: Comparison of double difference spectra of intact spinach PSII, Mn depleted spinach PSII and intact PSII from *Synechocystis*. Double difference spectra of intact spinach PSII minus *Synechocystis* (*yellow*) and intact spinach PSII minus Mn depleted spinach PSII (*grey*) of **(a)** the $S_2 \rightarrow S_3$ transition and **(b)** the $S_3 \rightarrow S_0$ transition are shown at two time slices (0.1–1 µs and 400–800 ms). All spectra were deconvolved prior to subtraction, assuming a starting population of 85% S_1 and 15% S_0 (cyanobacterial PSII) or 74% S_1, 12% S_0 and 14% S_2 (spinach PSII).

While Fig. 6.18 indicates that the here presented *Synechocystis* spectra are quite impaired, it seems likely that previous FTIR studies on *Synechocystis* are significantly less affected.

While the influence of broken centers appears to explain *inter alia* the large differences at 1544 cm^{-1}, some differences due to "real" differences in the protein still seem likely: The minimum around 1395 cm^{-1} in the steady-state spectrum and ET DAS of the $S_3 \rightarrow S_0$ transition of *Synechocystis* (Fig. 6.13c) could e.g. indicate a difference in carboxylate side-chain ligation around the Mn_4CaO_x cluster compared to other PSII variants. To investigate this further, an alignment study of the protein sequences of the three PSII variants could be insightful, as well as a comparison of 3D models. (For PSII variants without published crystal structures, homology structures could be calculated.)

It should be noted that the spinach data shown in this chapter was measured at pH 6.2, while the cyanobacterial data was acquired at pH 6.0. In Chapter 5, however, it was shown that spinach data acquired at pH 6.2 and 6.0 gave very similar results and thus this small difference in pH should be negligible here.

The DAS analysis of the $S_2 \rightarrow S_3$ and $S_3 \rightarrow S_0$ transitions overall revealed many similarities between the samples. Some differences are likely due to insufficient S/N of the cyanobacterial data; repeated measurements with more averages per wavenumber could help to pinpoint more real (i.e. not artefactual) differences.

One interesting finding in the $S_2 \rightarrow S_3$ DAS was a reversible behavior between PT and ET DAS at around 1570 cm^{-1} as well as 1405 and 1385 cm^{-1} for spinach PSII and *T. vestitus*: In

the latter region, this behavior is less obvious in the spinach DAS and was thus overlooked in the previous chapter. As discussed in detail in Chapter 5.5.3 and 5.6 and as previously suggested by Greife et al. (2023) for the $S_3 \rightarrow S_0$ transition, the $\sim$1570 cm^{-1} features may relate to the asymmetric stretch mode of a deprotonated carboxylate residue, indicating deprotonation during the PT phase and subsequent reprotonation during the ET phase. In that case, a corresponding symmetric stretch mode with equivalent behavior should appear as well—and this may well be the feature at 1405 or 1385 cm^{-1}. Obtaining time-resolved spectra covering a larger wavenumber region (up to $\sim$1750 cm^{-1}) for the cyanobacterial samples could give more insight as to whether the proposed de- and reprotonation mechanism of the E312/E65 dyad (Greife et al., 2023) (see also Fig. 5.48 and accompanying text) could also be valid for cyanobacterial PSII.

A study of the kinetic isotope effect of *T. vestitus* gave comparable results to that of spinach PSII reported in the previous chapter. For the PT phase of the $S_2 \rightarrow S_3$ transition, a KIE of 3.1 and 2.8 was found for spinach and for *T. vestitus*, respectively, in contrast to a previous time-resolved IR study (Sakamoto et al., 2017), which found only a very small KIE of 1.2. The same group also found that this $\sim$100 µs phase showed hardly any pH effect (Takemoto et al., 2019). Unlike in those studies, the here presented data is in agreement with the assignment of this phase to a proton removal step from the Mn_4CaO_x cluster (Klauss et al., 2012a). Further experiments will be necessary to attempt to reconcile the differing time-resolved IR results concerning the pre-ET phase of the $S_2 \rightarrow S_3$ transition; for all other steps and transitions the results are largely in very good agreement (Noguchi et al., 2012; Sakamoto et al., 2017; Takemoto et al., 2019).

This chapter *inter alia* also served as a proof-of-principle that time-resolved spectral data sets can also be obtained on cyanobacterial core complexes with our QCL setup. In future experiments, working with more highly concentrated core complex samples as well as gathering more data per wavenumber would help to improve the S/N. This would improve the global DAS analysis and help to obtain more robust results, which would then allow for a more confident identification of differences between the PSII variants. The usage of cyanobacterial PSII would in principle also allow for time-resolved spectral investigation of mutants—although relatively well functioning mutants would likely be necessary, otherwise a very high amount of sample would be necessary. [15]N and ^{13}C isotope exchange studies of cyanobacterial core complexes could furthermore help to assign transiently formed IR bands, which could *inter alia* give strong support to (or disprove) suggested band assignments—e.g. those suggested in Chapter 5, as well as those in previous time-resolved IR studies by Greife et al. (2023), Noguchi et al. (2012), Sakamoto et al. (2017) and Dekmak et al. (2023).

7 | Evidence for Decoupling of O_2-Evolution and Mn cluster Reorganization in D1-N298A PSII Variant

ALTERNATING proton and electron removal from the Mn_4CaO_x cluster during the S-state cycle allows for the stepwise accumulation of the four oxidative equivalents which are necessary for water oxidation and O_2 evolution. This requires the participation of not only the Mn_4CaO_x cluster itself, but also the surrounding molecular structures. The Mn_4CaO_x cluster is connected to the thylakoid lumen by several channels, i.e. extensive networks of H-bonded water molecules and amino-acid sidechains (Fig. 7.1). Three major channels (termed Cl1, O4 and O1 channel) have been identified that likely facilitate proton egress and/or water substrate delivery (Umena et al., 2011; Bondar and Dau, 2012; Sakashita et al., 2017; Kern et al., 2018; Suga et al., 2019; Ibrahim et al., 2020; Kaur et al., 2021; Hussein et al., 2021; Sirohiwal and Pantazis, 2022).

The Cl1 channel (sometimes also called *broad channel*; highlighted in orange in Fig. 7.1) starts between Y_Z and the Ca ion of the Mn_4CaO_x cluster, leading past aspartate-61 of the
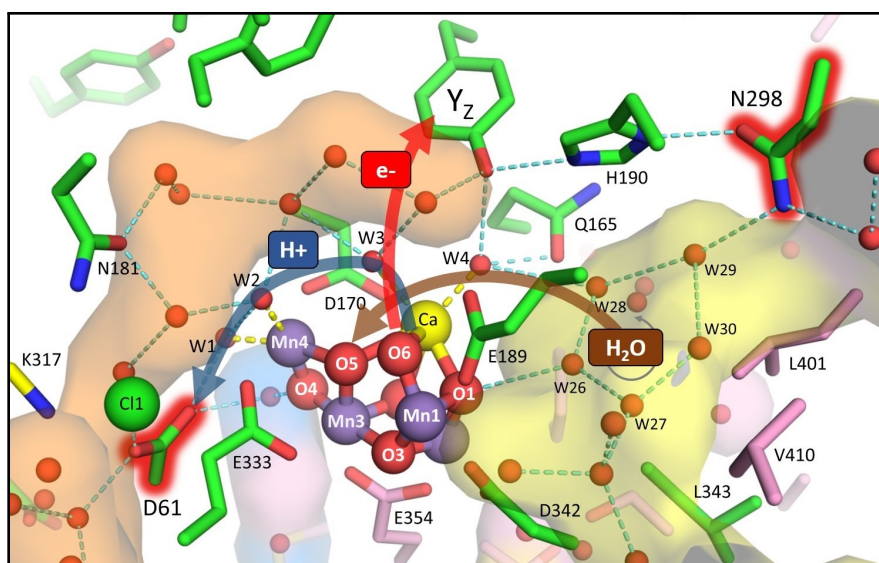
Figure 7.1: Active-site Mn$_4$CaO$_x$ cluster with water molecules and selected residues in its environment. Water molecules and selected residues in the vicinity of the Mn$_4$CaO$_x$ cluster based on the 2.07 Å two-flash (S$_3$-rich) crystallographic model by Kern et al. (2018) (PDB ID: 6DHO, PSII from *T. vestitus*). Residues from the D1, D2, and CP43 subunits are depicted in *green*, *yellow*, and *pink*, respectively; Mn in *purple*, Ca in *yellow*, Cl in *green*. Water molecules and six μ-oxo bridges (O1, O2, . . . , O6) are depicted as *red* or *orange spheres*. The pentagon of H-bonded water molecules, consisting of W26 to W30, has been termed "water wheel" and brought into play as an element of substrate water delivery (Kern et al., 2018; Ibrahim et al., 2020; Hussein et al., 2021; Bhowmick et al., 2023). Approximate boundaries of the Cl1, O4, and O1 channels near the Mn$_4$CaO$_x$ cluster (drawn based on Sakashita et al. (2017)) are depicted in *orange* (Cl1), *blue* (O4), and *yellow* (O1). The proposed directionalities in proton-coupled electron transfer and water insertion in the oxygen-evolving S$_3$→S$_4$→S$_0$ transition are indicated, as are the two key residues investigated here by genetic modification (D1-D61 and D1-N298). This figure is part of a manuscript (*in preparation*) and was made by Richard J. Debus.

D1 subunit (D1-D61), a lysine (D2-K317) and a pair of glutamates (D1-E65 and D2-E312). This pathway has been suggested to facilitate proton egress during the S$_2$→S$_3$ and/or the S$_3$→S$_0$ transition (Service et al., 2010; Rivalta et al., 2011; Pokhrel et al., 2013; Suzuki et al., 2013; Kuroda et al., 2021; Okamoto et al., 2021; Greife et al., 2023; Kaur et al., 2021; Ishikita et al., 2006; Dilbeck et al., 2012; Service et al., 2014; Debus, 2014; Ghosh et al., 2019).

The O1 channel (also called *large channel*; highlighted in yellow in Fig. 7.1) starts around the O1-oxygen and Ca of the Mn$_4$CaO$_x$ cluster and has been identified as the likely substrate water entry pathway (Kern et al., 2018; Suga et al., 2019; Ibrahim et al., 2020; Hussein et al., 2021; Service et al., 2010; Okamoto et al., 2021). It passes by the D1-N298 residue, which is H-bonded to the "water wheel", a cluster of five waters (W26, W27, W28, W29 and W30). This water wheel has been proposed to facilitate substrate access to the Ca-bound W3 and W4 positions (Ibrahim et al., 2020; Hussein et al., 2021).

Mutation studies of the D1-N298 residue revealed decreased steady-state O$_2$-evolution rates (Kuroda et al., 2014; Nagao et al., 2017a) to about 10–12% of the wild-type rate, but the mechanistic origin of the decreased rate could not be identified. Static FTIR experiments showed that the D1-N298A mutation perturbed the H-bond network around the Mn$_4$CaO$_x$ cluster and diminished the efficiencies of the S$_2$→S$_3$ and S$_3$→S$_0$ transitions (Nagao et al.,

2017a). A time-resolved IR study by Okamoto et al. (2021) furthermore showed that the ET rate constants of the $S_1 \rightarrow S_2$ and $S_2 \rightarrow S_3$ transitions were decreased about 3- and 7-fold, respectively, and the $\sim$100 µs pre-ET step of the $S_2 \rightarrow S_3$ transition was slowed by a factor of about 2.5; the $S_3 \rightarrow S_0$ transition was not investigated.

In the here presented study, we combine O_2-polarography, FTIR and time-resolved IR experiments to show that the D1-N298A variant can undergo the $S_3 \rightarrow S_0$ transition with a similar efficiency to that of wild-type. We find that while the O_2-evolution rate under continuous illumination is strongly reduced, the rate constant of flash-induced O_2-formation is comparable to that of wild-type. Time-resolved IR transients reveal a slower phase following O_2 formation, which we assign to a slow-down of the water insertion step. The results on D1-N298A are also compared to those of D1-D61A, which also exhibits a strong decrease in steady-state O_2-formation as well as strongly perturbed time-resolved IR transients. (In the following the two investigated mutants of the D1-subunit will be referred to simply as N298A and D61A.)

This chapter will focus on the results from time-resolved IR, as the other experiments were performed by collaboration partners. The other results will only be presented briefly wherever necessary for a full understanding of the interpretation and discussion of the data.

7.1 Experimental Details

Construction of Wild-Type and Mutant Samples of Synechocystis sp. PCC 6803

The construction and propagation of *Synechocystis* sp. PCC 6803 PSII point mutants, as well as the purification of (wild-type and mutant) core-particles, was done by Richard J. Debus and his co-workers. The D1-N298A mutation was introduced by altering the AAC codon of N298 in the wild-type *psbA*-2 gene to GCC (Chu et al., 1994). The plasmid carrying the mutation was transformed into a *Synechocystis* strain in which all three *psbA* genes have been knocked out and a hexa-histidine (His-tag) has been introduced at the C-terminus of CP47 (Debus et al., 2001). The cell cultures were maintained as described by Debus (2014). The construction and propagation of the D1-D61A mutation was done as described previously (Chu et al., 1995).

Purification of mutant and wild-type thylakoid membranes and PSII core particles was done as described previously (Debus, 2014; Tang and Diner, 1994). Both mutations were verified by DNA sequencing; post-translational reversal of the mutations was excluded by mass spectrometry of the PSII core particles (Mäusle et al., *in preparation*).

Time-Resolved IR Spectroscopy

Time-resolved IR measurements were performed as described in Chapter 3.5.2. The samples were not exchanged into a measurement buffer, but rather kept in their storage buffer and concentrated to about 3 mg Chl/ml. All measurements were performed at 10 °C and at pH 6.0. Five CaF_2 plates were prepared and 39 distinct sample spots were used per plate, resulting in a total of 195 sample spots. The standard flash-protocol of 6 s without excitation, followed by a train of 10 saturating excitation flashes at 1 Hz was applied to each sample spot. About an hour passed before the same sample spot was measured again. Prior to the first measurement, the samples were illuminated with 2 saturating pre-flashes and subsequently given an hour to dark-adapt (see Fig. 2.4 for a scheme of the standard flash protocol). For each wavenumber, data was collected over several hours, and the final

transients were obtained by averaging all individual data sets ($\sim$500–5000 per sample type and wavenumber; see Fig. A5.6).

For analysis of the $S_3{\rightarrow}S_0$ transition of wild-type and N298A, the flash-induced IR data was deconvolved into absorption changes corresponding to the pure S-state transitions, assuming a dark-adapted starting population of 90% S_1 and 10% S_0. As the D61A sample revealed a poor S-state cycling efficiency beyond the S_3-state, a deconvolution was not possible (see below). Thus, the 1st, 2nd and 3rd flash transients of D61A are compared to the deconvolved $S_1{\rightarrow}S_2$, $S_2{\rightarrow}S_3$ and $S_3{\rightarrow}S_0$ transients of the other two samples.

7.2   Results from Time-Resolved Single-Frequency IR Spectroscopy
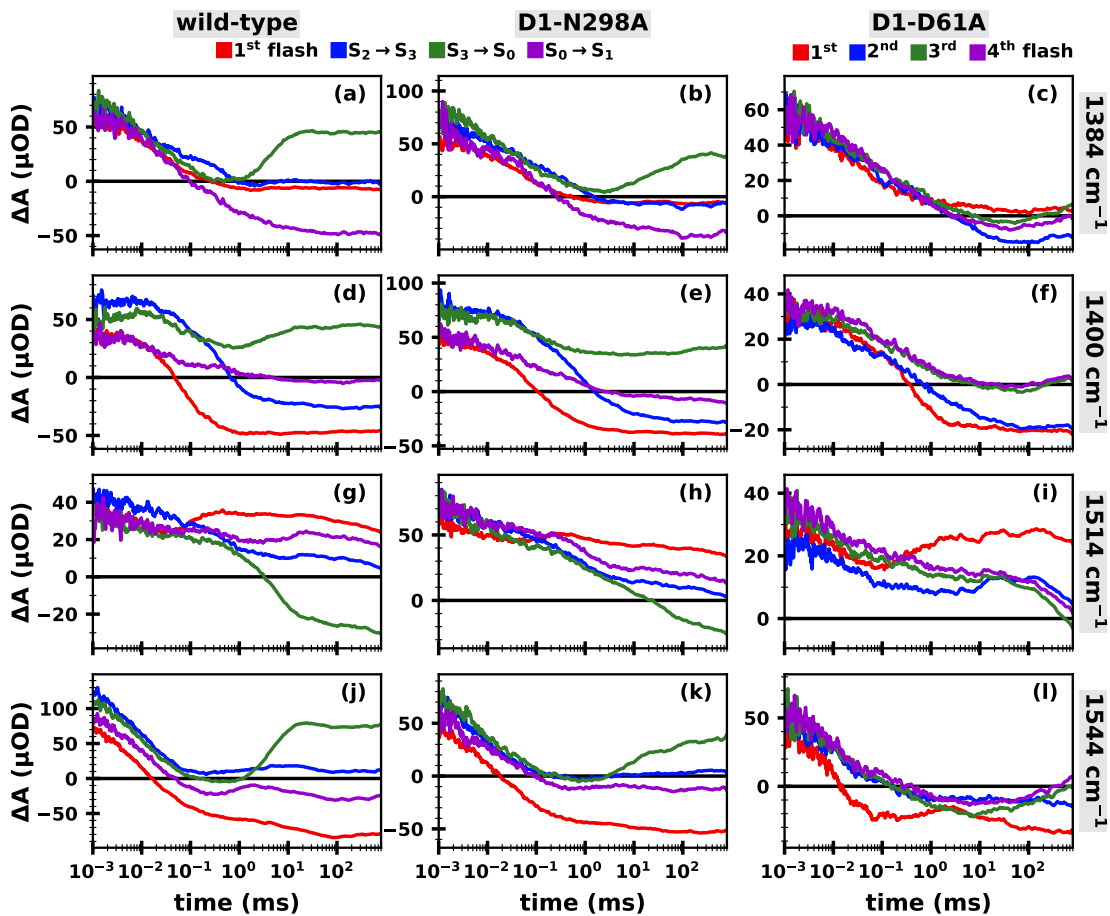
Figure 7.2: Time-resolved IR difference absorption of wild-type and mutant PSII core complexes from *Synechocystis* sp. PCC 6803 during their S-state transitions. The IR absorption changes are shown at **(a–c)** 1384 cm^{-1}, **(d–f)** 1400 cm^{-1}, **(g–i)** 1514 cm^{-1}, **(j–l)** 1544 cm^{-1}. The first column shows the transients corresponding to the $S_1{\rightarrow}S_2$ (*red*), $S_2{\rightarrow}S_3$ (*blue*), $S_3{\rightarrow}S_0$ (*green*) and $S_0{\rightarrow}S_1$ (*purple*) transition of wild-type PSII; the second column shows the same for PSII cores carrying the D1-N298A mutation. For the $S_1{\rightarrow}S_2$ transition, non-deconvolved 1st flash data is shown. The third column shows the non-deconvolved transients following the first four excitation flashes of D1-D61A cores. The wild-type and N298A data was deconvolved assuming a 90% S_1 and 10% S_0 starting population; the non-deconvolved flash-induced transients of wild-type and N298A PSII can be seen in Fig. A5.1 in the Appendix.

179

Transient absorption changes at 1384, 1400, 1514 and 1544 cm^{-1} corresponding to the four S-state transitions are shown in Fig. 7.2 for wild-type PSII (left column) as well as PSII cores carrying the N298A (middle) and D61A mutations (right). Visual inspection reveals an overall strong similarity between wild-type and N298A transients. The D61A transients, however, show a strongly perturbed behavior: while some similarity of the 1st and 2nd flash transients to the wild-type transients is found, the 3rd and 4th flash transients bear hardly any resemblance to their wild-type counterparts. This indicates *inter alia* that the majority of the D61A centers likely do not successfully go through the S$_3 \rightarrow$S$_0$ transition.

The flash-number dependent steady-state values (i.e. the averaged IR absorption difference 700–800 ms after the flash) in Fig. 7.3 confirm the above observations: While the N298A sample shows period-of-four patterns at all four wavenumbers very similar to those of wild-type PSII, the D61A sample exhibits strongly perturbed and dampened patterns. Deconvolution of the flash-induced data into transients corresponding to the four S-state transitions yielded similar estimates of the miss factors for wild-type (13$\pm$2%) and N298A (15$\pm$2%); the D61A data was too strongly perturbed for a reliable deconvolution.
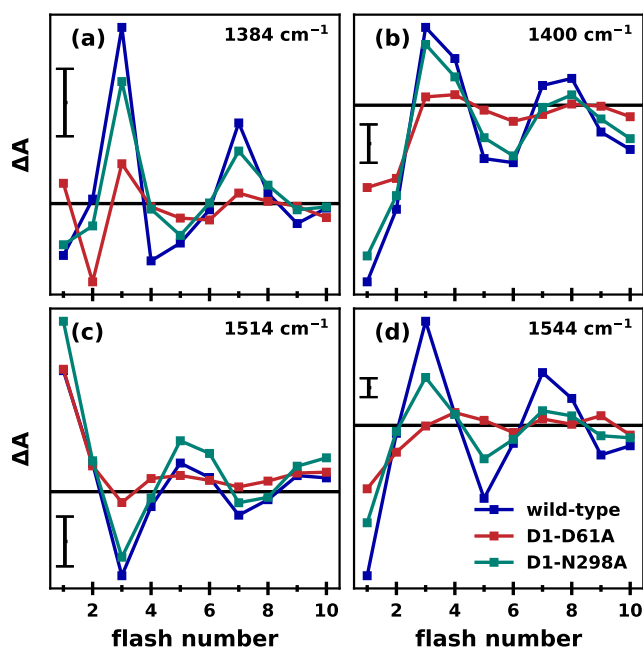
Figure 7.3: Flash-number dependence of the IR difference absorption of PSII core complexes from *Synechocystis* sp. PCC 6803. Data of wild-type PSII (*blue*), as well as PSII with point mutations D61A (*red*) and N298A (*green*) of the D1 protein subunit is shown for **(a)** 1384 cm^{-1}, **(b)** 1400 cm^{-1}, **(c)** 1514 cm^{-1} and **(d)** 1544 cm^{-1}. Each data point was obtained by averaging the IR difference absorption between 700–800 ms following the nth excitation flash (n = 1, ..., 10). The exciting laser flashes were spaced by 1 s. In each panel, the scale bar corresponds to 10 µOD. This figure is part of a manuscript (*in preparation*).

The S$_1 \rightarrow$S$_2$ Transition

For each PSII variant, the first flash transients at the four investigated wavenumbers were globally fit to a sum of exponentials (using Equation 2.7), i.e. the time constants were assumed to be the same for all wavenumbers while the amplitudes were left free to vary. The resulting (normalized) fit curves at 1514 and 1400 cm^{-1}, as well as a subset of the time

Figure 7.4: Time-resolved IR difference data of the 1st flash data of PSII core particles from *Synechocystis* sp. PCC 6803. (a, c) IR difference signal at 1514 cm^{-1} and 1400 cm^{-1}, re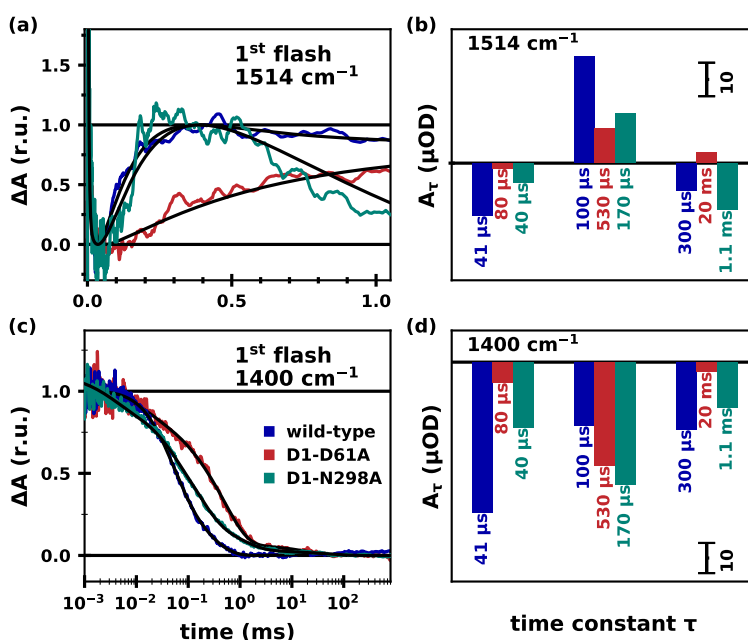spectively, acquired after applying one saturating excitation flash to the sample, which induces predominantly the $S_1 \rightarrow S_2$ transition, of wild-type (*blue*), D61A (*red*) and N298A (*green*). The respective fit curves obtained from globally fitting transients at 1384, 1400, 1514 and 1544 cm^{-1} to a multi-exponential function are shown in black. The transients were normalized and shifted along the y-axis for easier visual inspection. **(b, d)** Time constants obtained from the fit results, along with the amplitudes at 1514 cm^{-1} and 1400 cm^{-1}, respectively. Note that the absolute amplitudes prior to normalization are shown. The fit results at 1384 and 1544 cm^{-1} are not shown (but see Table A5.1). Part of this figure is shown in the Supplementary Information of a manuscript (*in preparation*).

constants and their amplitudes are shown in Fig. 7.4; a full set of fit parameters can be seen in Table A5.1.

The 100 µs phase in wild-type, likely attributable to the ET step of the $S_1 \rightarrow S_2$ transition (e.g. Haumann et al., 1997), is moderately slowed down to 170 µs in the N298A variant. In the D61A variant, this phase appears clearly more strongly slowed down (530 µs). A faster phase of 41 µs in wild-type is effectively unchanged in N298A, except for a lower amplitude of this phase at all wavenumbers (Fig. 7.4 and Table A5.1); in D61A this phase is slowed by a factor of 2.

Okamoto et al. (2021) reported a stronger retardation of the ET step in the N298A mutant at 1400 cm^{-1} (from 95 to 446 µs). One possible explanation for the differing results could be their description of the decay by only two time constants in the relevant time range, while we here describe it with three time constants. While at 1400 cm^{-1} the distinction between the 170 µs and 1.1 ms phase is also not straightforward in the here presented data, it is clear at 1514 cm^{-1}, where the two phases are of opposite sign.

The $S_2 \rightarrow S_3$ Transition

The second flash transients were analyzed analogously to the first flash data, by globally fitting the transients at 1384, 1400, 1514 and 1544 cm^{-1} to a sum of exponentials for each of
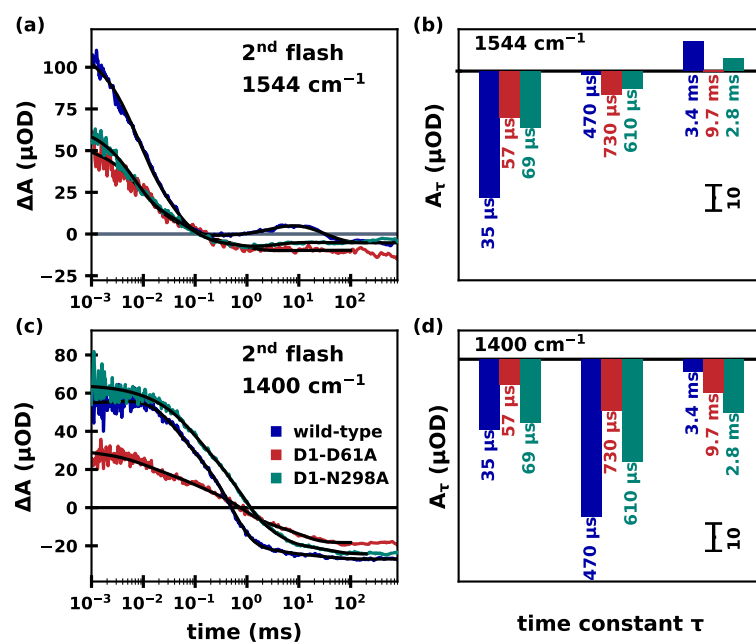
Figure 7.5: Time-resolved IR difference data of the 2nd flash data of PSII core particles from *Synechocystis* sp. PCC 6803. (a, c) IR difference signal at 1544 cm^{-1} and 1400 cm^{-1}, respectively, acquired after applying two saturating excitation flashes to the sample, which induces predominantly the S$_2 \rightarrow$S$_3$ transition, of wild-type (*blue*), D61A (*red*) and N298A (*green*). The respective fit curves obtained from globally fitting transients at 1384, 1400, 1514 and 1544 cm^{-1} to a multi-exponential function are shown in black. **(b, d)** Time constants obtained from the fit results, along with the amplitudes at 1544 cm^{-1} and 1400 cm^{-1}, respectively. Note that the absolute amplitudes prior to normalization are shown. The fit results at 1384 and 1514 cm^{-1} are not shown (but see Table A5.2). Part of this figure is shown in the Supplementary Information of a manuscript (*in preparation*).

the three PSII variants. The transients at 1544 and 1400 cm^{-1}, along with their fit curves, a subset of the time constants and their amplitudes, are reported in Fig. 7.5; a full set of fit parameters can be seen in Table A5.2.

For wild-type PSII, time constants of 35 µs, 470 µs and 3.4 ms were determined. The value 470 µs is within the range of previous reports for the ET step of the S$_2 \rightarrow$S$_3$ transition at 10 °C (Renger and Hanssum, 1992; Haumann et al., 1997; Sakamoto et al., 2017)[37]. A value of 35 µs is faster than expected for the PT step at 10 °C and seems more likely attributable to the slow step of P680$^+$ reduction (Christen et al., 1998). As discussed in the previous Chapter, the PT phase appears to be generally less well resolved in IR transients of cyanobacterial PSII core particles compared to those of spinach PSII. It is likely that the PT phase of about 100 µs contributes to some (unknown) extent to both the 35 and the 470 µs phases. The 35 µs phase slows to 57 and 69 µs in the D61A and N298A mutants, respectively. While it cannot be excluded that the P680$^+$ reduction kinetics are altered in the mutants, this might instead also be due to a slow-down of the poorly resolved PT kinetics, which contribute to this fast phase, leading to an artificial slow-down of the 35 µs phase. Indeed, looking at a normalized linear plot of the microsecond region of the transients at

---

[37]Note that values at 10 °C were not explicitly reported in the first two of these publications, but can be calculated from the given activation energy and related parameters (resulting in time constants of about 550 and 730 µs). Sakamoto et al. (2017) reported 352 µs at 10 °C.
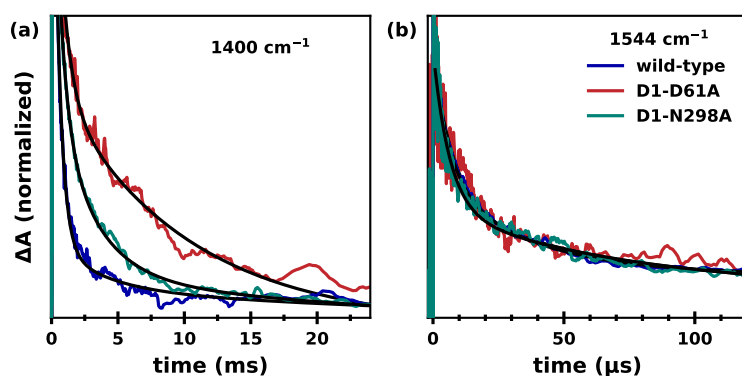
Figure 7.6: Time-resolved IR difference data of the 2nd flash data of PSII core particles from *Synechocystis* sp. PCC 6803. The IR difference signal is shown at **(a)** 1400 cm^{-1} and **(b)** 1544 cm^{-1} on a linear x-axis. The data was normalized and shifted along the y-axis for easier visual comparison. Wild-type data is shown in *blue*, D1-D16A in *red* and D1-N298A in *green*. The same data is shown non-normalized in Fig. 7.5 a and c.

1544 cm^{-1} (which according to Fig. 7.5b seem dominated by the fast microsecond kinetics), the kinetics appear effectively identical in all PSII variants (Fig. 7.6b).

The ET phase of 470 μs appears slightly slowed to 730 and 610 μs in the D61A and N298A variants, respectively. In the D61A variant, the amplitudes at 1400 cm^{-1} of the two microsecond phases are much smaller than in the other two samples and a slower phase of 9.7 ms contributes in a similar amount (Fig. 7.5d). The transient at 1400 cm^{-1} (Fig. 7.5c) thus appears to decay monotonously over several decades from a microsecond down to ~100 ms. In the N298A mutant, a 2.8 ms phase also contributes significantly at 1400 cm^{-1}; in contrast a 3.4 ms phase in wild-type contributes only marginally.

Okamoto et al. (2021) reported wild-type time constants of 114 and 409 μs, which appear slowed to 292 μs and 2.9 ms, respectively, in the N298A PSII variant. While they interpret the ET step to be slowed 7-fold, from our data it rather appears that the monophasic ET step in wild-type possibly becomes biphasic in the N298A mutant: The dominant phase is merely slowed by a factor of 1.3, while the slower phase of 2.8 ms is about 6 times slower than the ET step in wild-type. It seems likely that the 2.8 ms phase found here corresponds to the 2.9 ms phase found by Okamoto et al. (2021). Their 292 μs phase could possibly correspond to a mixture of our 69 and 610 μs phases.

The S$_3$→S$_0$ Transition

For analysis of the S$_3$→S$_0$ transition, the wild-type and N298A data was deconvolved into transients corresponding to the pure S-state transitions; for D61A the non-deconvolved 3rd flash data was used. The S$_3$→S$_0$ transients were fit globally across the four investigated wavenumbers to a multi-exponential function. The transients along with the resulting fit curves, a subset of the time constants and their wavenumber-dependent amplitudes are shown in Fig. 7.7. (Analysis of the non-deconvolved 3rd flash data gave similar results, as shown in Fig. A5.2). The uncertainties of the fit parameters were estimated by fitting various subsets of the four wavenumbers and calculating the standard deviation of all parameters; see Figs. A5.3, A5.4 and A5.5 and the accompanying text in the Appendix for details. A full set of final time constants and amplitudes, along with their standard deviations are given in Table A5.3.
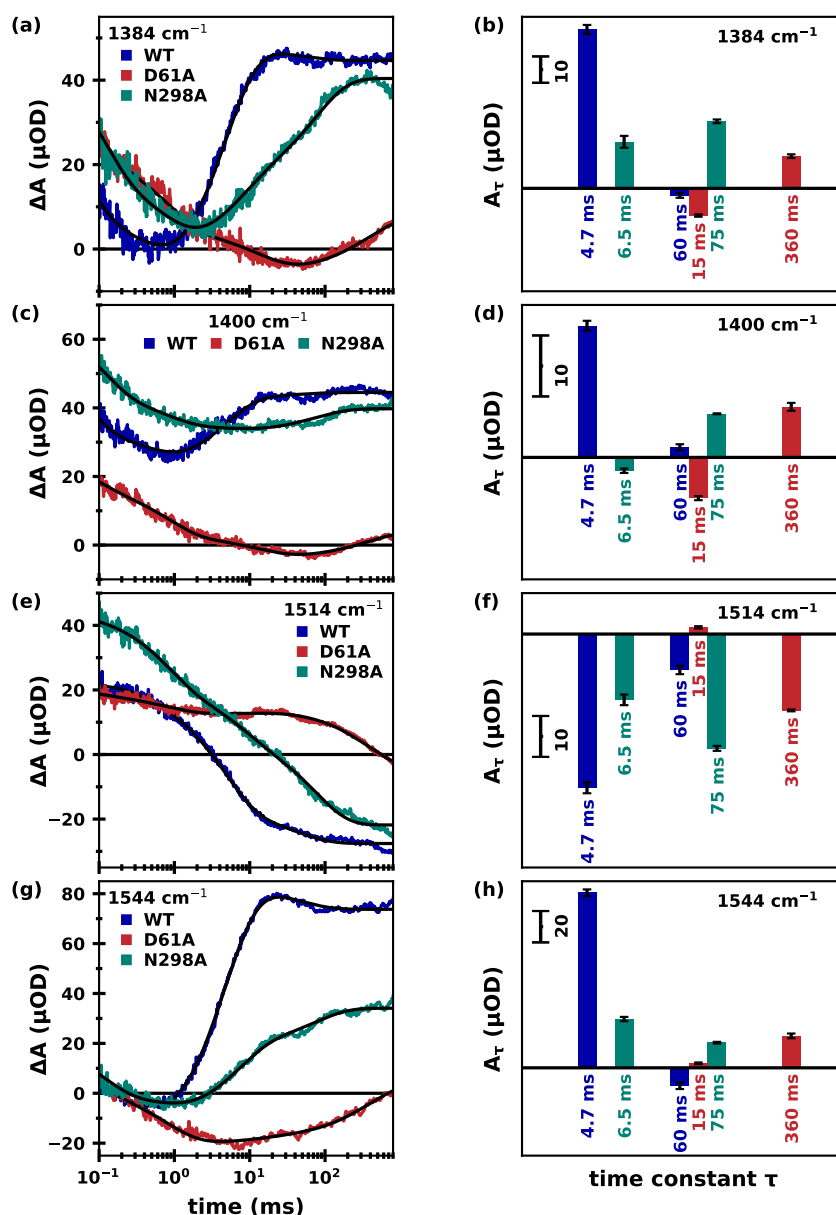
Figure 7.7: Time-resolved IR difference data of the S$_3 \rightarrow$S$_0$ transition of PSII core particles from *Synechocystis* sp. PCC 6803. (a) IR difference signal of the S$_3 \rightarrow$S$_0$ transition obtained from applying a deconvolution algorithm to the wild-type and N298A data obtained from subjecting the samples to 10 consecutive excitation flashes, resulting in four transients corresponding to the pure S-state transitions. The data shown here is similar to the signal obtained after the 3rd saturating excitation flash (Fig. A5.2 in the Appendix). For the D16A variant, the 3rd flash data is shown. The wild-type data is shown in *blue*, D1-D16A in *red* and D1-N298A in *green* at 1384, 1400, 1514 and 1544 cm^{-1} (top to bottom). **(b)** Bar plots of the amplitudes corresponding to the time constants obtained from fitting the data on the left to a sum of exponentials. The time constants were determined globally for all four wavenumbers, while the amplitudes were left free to vary. Here relevant fit results are shown for 1384, 1400, 1514 and 1544 cm^{-1} (top to bottom). For a complete set of fit parameters, see Table A5.3. This figure is part of a manuscript (*in preparation*).

As discussed in Chapters 5 and 6, a robust fitting of the pre-ET phase of the S$_3$→S$_0$ transition was difficult to achieve without fixing the time constants to literature values. Therefore, we will here only consider the millisecond kinetics in detail.

The wild-type data (Fig. 7.7, *blue*) exhibits a predominantly monophasic behavior with a time constant of 4.7 ± 0.3 ms. A slower phase of 60 ± 35 ms contributes to a small extent, especially at 1514 and 1544 cm^{-1}; the large standard deviation of this parameter indicates that this phase is overall not well resolved. The D61A mutant shows several retarded kinetics with a major millisecond phase of 360 ± 60 ms. A slower phase of 15.3 ± 7.3 ms contributes mostly marginally and more clearly at 1400 cm^{-1} (however with a sign opposite of what is expected for the ET step); its large relative standard deviation indicates that this phase is poorly resolved. Visual inspection confirms that the millisecond rise at 1384, 1400 and 1544 and the millisecond decay at 1514 cm^{-1} are clearly severely slowed in the D61A variant compared to the wild-type transients.

The N298A variant shows a more complex behavior: after first only obtaining data at 1400 cm^{-1}, the N298A variant seemed to show severely slowed ET kinetics (Fig. 7.7c). This was at odds with the observation by time-resolved O$_2$ polarography that the flash-induced O$_2$-rate was the same or even slightly *higher* in the mutant compared to wild-type (Assunção, 2022). The additional IR transients at 1384, 1514 and 1544 cm^{-1} (Fig. 7.7a, e, g), however, show a clear biphasic behavior with an additional time constant of 6.5 ± 0.8 ms; at 1544 cm^{-1} this phase is even the dominant one. The slower phase of 75 ± 8 ms contributes at all wavenumbers with the same sign as expected for the ET event (unlike the 60 ms phase in wild-type, possibly indicating that in wild-type the phase is rather attributable to acceptor-side kinetics). These results thus indicate that while O$_2$-formation in the N298A mutant occurs with a similar rate to that in wild-type, a step following O$_2$-release is slowed down.

7.3   Additional Results from FTIR, O$_2$ Polarography and MD Simulations

The above presented IR results are part of a study encompassing results from several different methodologies. As these additional experiments were performed by others, they will not be presented here in detail, but merely summarized briefly.

As mentioned above, time-resolved O$_2$ polarography experiments showed that O$_2$-evolution was slightly faster in N298A than in wild-type, while the steady-state O$_2$-rates are significantly lower in the mutant than in wild-type (Mäusle et al., *in preparation*; Assunção, 2022). Table 7.1 summarizes the time-resolved and steady-state O$_2$-evolution rates measured by O$_2$-polarography, as well as the time constants determined by time-resolved IR, which we assign to the final ET step and associated events.

Temperature-dependent measurements of flash-induced O$_2$-polarography furthermore revealed that while the Gibbs free energy of activation ($\Delta G^{\ddagger}$) of the O$_2$-evolution step is effectively the same for both wild-type and N298A mutant, the activation enthalpy ($\Delta H^{\ddagger}$) of N298A is lower (396 vs. 296 meV) and its activation entropy ($-T_0\Delta S^{\ddagger}$) is higher (187 vs. 280 meV) (Mäusle et al., *in preparation*; Assunção, 2022).

A previous FTIR study comparing wild-type PSII to the N298A mutant showed that while the first two flash-induced spectra showed overall large similarity, despite some reduced relative amplitudes in the N298A variant, the third and fourth flash spectra of N298A were nearly devoid of features (Nagao et al., 2017a). In contrast static FTIR experiments on our samples (Mäusle et al., *in preparation*) revealed a much greater similarity between wild-

Table 7.1: Oxygen-evolution and electron transfer rates for the S$_3$→S$_0$ transition determined by O$_2$-polarography and infrared spectroscopy. The steady-state O$_2$ rates were measured polarographically for illumination with continuous light of saturating intensity. The reaction time constants provide the inverse rate constants of the rate-limiting step in O$_2$-formation. They were determined from time-resolved O$_2$ polarography and infrared spectroscopy using sequences of saturating light flashes for initiating S-state cycle transitions. [‡]Results from Chu et al. (1995). [†]Results (extrapolated) from Bao and Burnap (2015). This table is part of a manuscript (*in preparation*).

	wild-type	D61A	N298A
Steady-state O$_2$ rate (μmol (mg of Chl)$^{-1}$ h^{-1})			
cells (T=25 °C)	665 ± 35	129 ± 41 [‡]	74 ± 7
core complexes (T=25 °C)	5010 ± 50	900 ± 270	670 ± 170
Time-resolved O$_2$ polarography – reaction time constant (ms)			
thylakoids (T=10 °C)	3.0 ± 0.3; 5.5 [†]	99 [†]	1.9 ± 0.3
Time-resolved IR spectroscopy – reaction time constant (ms)			
core complexes (T=10 °C)	4.7 ± 0.3	360 ± 60	6.5 ± 0.8 and 75 ± 9

type and N298A, also in the third and later flashes, in agreement with the time-resolved IR results shown above. Some clear differences in our N298A spectra (as compared to wild-type) are nevertheless discernible, *inter alia* indicating that the protein-water environment near the Mn$_4$CaO$_x$ cluster is perturbed, as suggested previously by Kuroda et al. (2014).

This is further confirmed by MD simulations of the S$_3$Y$_Z^{ox}$ state of wild-type PSII and the N298A variant (Mäusle et al., *in preparation*), which reveal a clear perturbation of the water wheel in the mutant: In the vicinity of the point mutation, the conformational space is less constrained, i.e. the water wheel gains more space. Furthermore, the H-bond between His190–Asn298 is (in parts) replaced by His190–Leu297 in the N298A variant with a broadened H-bond distance distribution. Consequently, the His190 side chain has an increased conformational freedom in the mutant, thus affecting the pK$_a$ of the His-N$_\epsilon$, which donates its proton to Y$_Z$ during the rate limiting S$_3$Y$_Z^{ox}$→S$_4$Y$_Z$ transition. These changes in the mutant may indicate that reaching the required overall conformational state for undergoing the final ET step becomes less probable, thus offering an explanation for the experimental observation of an increased activation entropy in the N298A variant.

7.4 Summary and Concluding Discussion

Extensive H-bond networks in PSII connect the Mn$_4$CaO$_x$ cluster to the thylakoid lumen, allowing for substrate water access and proton egress. Investigating point mutants that disrupt different parts of these H-bond networks can help to gain insight into the function of different channels, as well as the function of specific protein sidechains in the ET and PT steps of the S-state cycle.

We here observed by time-resolved IR spectroscopy that the D16A mutation strongly perturbs the S-state transitions, which is in agreement with previous FTIR findings (Debus, 2014). Furthermore, Chu et al. (1995) found that while D61A cells grew photoautotrophically, they did so more slowly than wild-type and did not grow if Ca^{2+} was omitted from

the growth medium. They also observed that the D61A cells showed only 19% of O_2-evolving activity compared to wild-type cells (the same as in the here presented study).

The here presented IR transients indicate that not only the $S_3 \rightarrow S_0$ transition is strongly perturbed, but also earlier events: The ET step of the $S_1 \rightarrow S_2$ transition seemed slowed by a factor of five. The reason for this may be the relatively close vicinity of the Asp61/Ala61 to Mn4, which is oxidized in the $S_1 \rightarrow S_2$ transition. Mn4 is H-bonded to W1, which in turn is ligated to Mn4 (see Fig. 7.1); the disruption of the Asp61–Mn4 H-bond may make the oxidation of Mn4 less favorable.

Proton egress during the $S_2 \rightarrow S_3$ and $S_3 \rightarrow S_0$ transitions has been suggested to occur via the Cl channel, which passes by Asp61. Thus, the strong perturbation of the IR transients of those transitions is unsurprising. The ET step to Y_Z^{ox} of the $S_3 \rightarrow S_0$ transition has been suggested to be coupled to a Grotthus-type proton transfer from the hydroxide at position O6 to the Asp61 carboxylate side chain (Greife et al., 2023; Siegbahn, 2012; Allgöwer et al., 2022). In light of this, a full inhibition of O_2-evolution in the D61A variant could be expected. The fact that O_2-evolution still takes place, even if strongly retarded, suggests that another residue can substitute for the missing proton acceptor in the mutant.

Visual comparison of the IR transients in Fig. 7.2 shows that the N298A mutant exhibits overall far less perturbed kinetics than the D61A variant. Unlike the Asp61 residue, Asn298 is not a second sphere ligand to the Mn_4CaO_x cluster, but rather a more distant player. Its H-bonds to His190 and to W29 of the water wheel nevertheless suggests importance for the catalytic activity of the OEC, which is clearly proven by the strongly reduced steady-state O_2-production under continuous saturating light (see Table 7.1).

As our time-resolved O_2-polarography measurements revealed that the O_2-evolution is not in fact slowed down, this indicates that it is rather a step following O_2-release which is decelerated in the N298A mutant. In wild-type PSII, O_2-formation is the rate-limiting step of the $S_3 \rightarrow S_0$ transition. Subsequently, in order to reach the S_0-state, a new substrate water still needs to be integrated into the Mn_4CaO_x cluster and a proton needs to released; these steps are shown schematically in Fig. 7.8a–c. We propose that in the N298A variant, O_2-formation takes place at an effectively unchanged rate, but the subsequent water insertion step is severely slowed-down, making it spectroscopically detectable. In the D61A variant, on the other hand, O_2-formation itself is severely slowed-down. In Fig. 7.8 we suggest that the water insertion step in D61A is again invisible, as it is faster than O_2 formation—however, we cannot exclude that the water insertion is also here even more severely slowed down: With a flash frequency of 1 Hz, this could occur outside of our temporal detection window. If this were the case, the poor S-state cycling efficiency of the mutant could be due to insufficient spacing between flashes. The FTIR data, however, were obtained with a 13 s flash spacing and show no obvious indication of an improved cycling efficiency (Debus, 2014).

Our MD simulations show that the water wheel in the N298A variant expands more toward the A298 residue. The water wheel, however, appears less flexible in the mutant, i.e. the individual waters move about less than in wild-type (Mäusle et al., *in preparation*). We hypothesize that the free energy of the initial state of the water insertion step is thus lowered, resulting in a higher activation energy and consequently a major-slow down of this step.

The MD simulations furthermore demonstrated that the His190-Asn298 H-bond is replaced by a His190-Leu297 H-bond in the N298A variant. The H-bond in the mutant, however, shows a broader bond length distribution with a bias towards longer bond lengths, in-
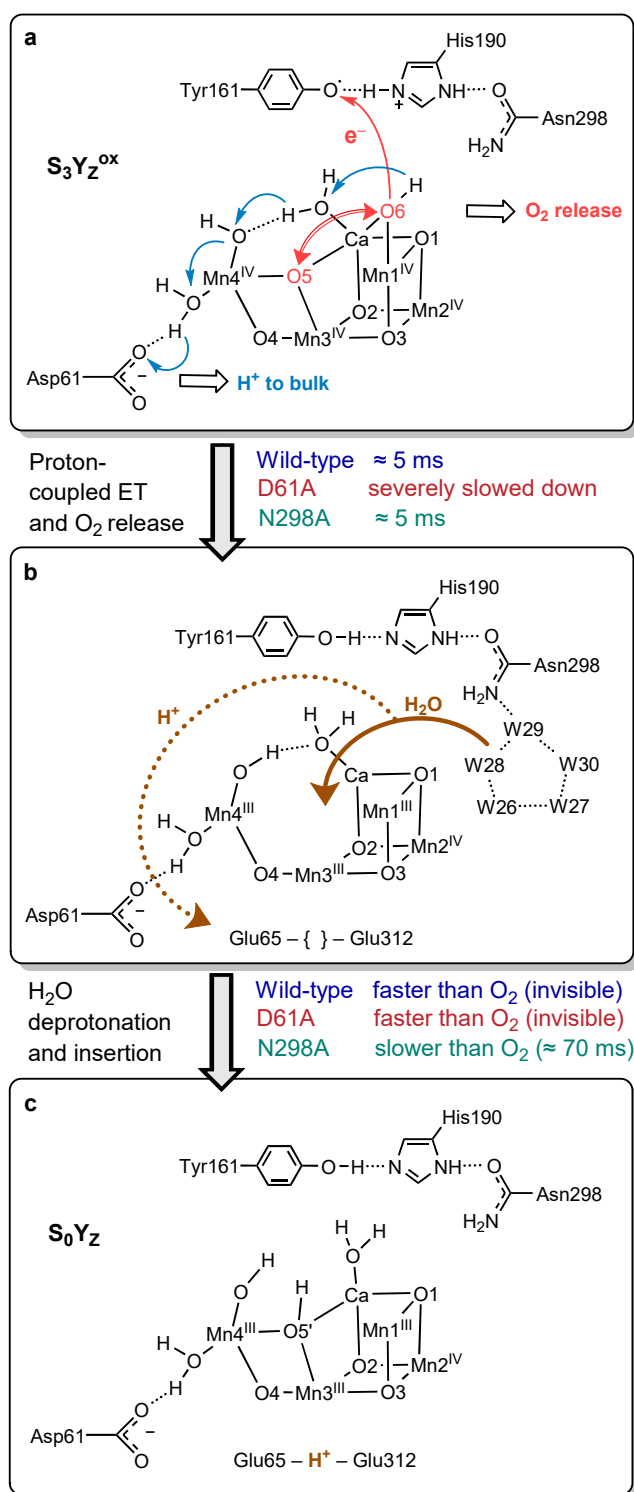
Figure 7.8: Reaction scheme showing the Mn$_4$CaO$_x$ cluster as well as the Asp61 (D61), Tyr191 (Y$_Z$), His190 and Asn298 (N298) residues during the S$_3$→S$_0$ transition. (a) Oxygen atom O6 is oxidized by transferring an electron to Y$_Z$; the proton bound to O6 is concomitantly transferred to D61 in a Grotthus-type mechanism. Subsequently, O6 and O5 form an O=O bond while reducing Mn4, Mn3 and Mn1 from +IV to +III. This step takes place within about 5 ms in wild-type PSII as well as in PSII containing the N298A mutation but is severely slowed down in the D61A mutant. **(b)** A new water molecule is inserted into the Mn$_4$CaO$_x$ cluster, and a proton is simultaneously released to the bulk, leading to **(c)** the formation of the S$_0$ state. This step is slower than O$_2$ release and thus "invisible" in wild-type PSII as well as in PSII containing the D61A mutation. In the N298A mutant, however, this step is slowed down roughly ten-fold, and thus becomes visible for spectroscopic methods. This figure is part of a manuscript (*in preparation*).

dicating an overall weakened H-bond. This may indicate an overall higher conformational flexibility of His190, which may in turn result in a lower probability to reach the transition state conformation needed for the ET from O6 to Y$_Z^{ox}$ and subsequent O$_2$-formation. A lowered probability to reach the transition state conformation is in line with the polarographically observed increase in entropy of activation. The coincident reduction in enthalpy of activation nevertheless results in a similar O$_2$-evolution rate.

We propose that the N298A mutant offers a (so far) unique opportunity to decelerate the events following O_2-formation and thus to investigate them spectroscopically. The here presented results may stimulate new time-resolved experiments on substrate-water insertion, and so contribute to a full understanding of photosynthetic water splitting in PSII.

8 | Tracking Electron Transfer in Photosystem I

ELECTRON transfer in Photosystem I can go down two parallel pathways, termed the A- and B-branch. In Chapter 8.1, nanosecond ET is tracked in PSI from *Thermosynechococcus vestitus* BP-1 with time-resolved IR spectroscopy, revealing biphasic kinetics with time constants of 33 and 364 ns. Moreover, time-resolved spectra measured with the QCL setup are shown to reproduce photoaccumulated $P700^+/P700$ FTIR spectra. Following stable absorption difference up to about a millisecond, the IR transients decay back to zero with multiphasic kinetics.

In Chapter 8.2, ET is tracked in PSI core particles from *Chroococcidiopsis thermalis* PCC 7203, which were grown either under white light (WL) or far-red light (FRL) conditions. Surprisingly, the $P700^+/P700$ spectrum of the FRL form shows more similarity to *T. vestitus* than to WL grown *C. thermalis* sample. The latter exhibits features in its $P700^+/P700$ spectrum that seem to be unique, indicating alterations in or around the primary electron donor. Nanosecond kinetics reveal biphasic behavior in both *C. thermalis* samples, as well as multiphasic millisecond recombination kinetics.

8.1 PSI Core Particles from *T. vestitus*

Following the flash excitation of PSI core particles, charge separation is initiated at P700, generating the charge separated pair $P700^+A_1^-$ within 50 ps. PSI has two highly similar co-

factor branches, the A- and B-branch (see Fig. 1.4 in the Introduction), and electron transfer can proceed down either (Makita and Hastings, 2015; Redding and van der Est, 2006). B-branch kinetics from A_1^- to F_x are about ten times faster than down the A-branch ($\sim$25 vs. 250 ns) (Agalarov and Brettel, 2003; Guergova-Kuras et al., 2001; Joliot and Joliot, 1999; Sétif and Brettel, 1993). The branches merge at F_x and ET to F_a and F_b takes place on the tens to hundreds of nanoseconds time scale. Finally, $F_{a/b}/P700^+$ recombination takes place within about 50–150 ms if no exogenous electron acceptors are added (Golbeck and Bryant, 1991).

As shown in Fig. 1.11 in the Introduction, the ET pathway is altered at low temperatures. Besides some irreversible $F_{a/b}$ formation, flash-excitation at 77 K will lead predominantly to $P700^+/A_{1A}^-$ recombination (with $\tau = 300$ µs), while continuous illumination will lead to photoaccumulation of $P700^+F_x$ (Schlodder et al., 1998; Hastings, 2015; Makita and Hastings, 2015, 2016). B-branch utilization is mostly diminished at low temperatures (Mula et al., 2012; Makita and Hastings, 2015; Agalarov and Brettel, 2003).

In the here presented work, forward ET in PSI from *Thermosynechococcus vestitus* BP-1 is probed with time-resolved IR spectroscopy. To our knowledge, this is the first IR-study reaching nanosecond time resolution at physiological temperatures. Biphasic nanosecond kinetics indicate that ET down the A- and B-branch from A_1^- to F_x is observed throughout the mid-IR regime with time constants of 33 and 364 ns. The $P700^+F_{a/b}$ signal is stable for about a millisecond, after which multiphasic recombination kinetics are observed. The study is complemented by microsecond time-resolved step-scan (TRSS) FTIR experiments at 77 K, yielding $P700^+A_1^-/P700\,A_1$ difference spectra, as well as rapid-scan FTIR experiments for acquiring photoaccumulated $P700^+/P700$ difference spectra, all of which were performed by N. Argawala and V. G. Eichmann.

8.1.1 Experimental Details

The time-resolved single-frequency experiments were performed at 23 °C. The sample was pelleted and prepared for IR measurements as described in Chapter 3.5.3. In contrast to PSII experiments, the measurements were done by repeatedly illuminating the same sample spot. A flash protocol of 2 s without excitation, followed by six saturating excitation flashes was used. The final flash of each flash sequence was of about three times higher energy than the first five flashes. For each wavenumber between 600 and 6000 flash transients were acquired and averaged to reach a good S/N. All transients were corrected for a heat artefact following the procedure laid out in Chapter 2.4.1.

In addition to the high S/N single-frequency transients, a time-resolved spectral data set was acquired in 2 cm^{-1} steps[38] with only 6 transients averaged per wavenumber (300 transients were averaged for wavenumbers below 1500 cm^{-1}), but in return covering the majority of the available spectral region (1772–1312 cm^{-1}). This data set was smoothed with a sliding average algorithm with a window size of ten along the quasi-logarithmic time axis (with the smallest bin size comprising 15 ns). Gaussian smoothing with $\sigma = 2.5$ was applied along the wavenumber axis[39], resulting in a spectral resolution of about 6–8 cm^{-1}.

---

[38]There are two gaps, i.e. missing data points, at 1652 and 1734 cm^{-1}, due to insufficient IR signal reaching the detector.

[39]In the published manuscript, a sliding average algorithm was used for smoothing also along the wavenumber axis; the results remain unchanged.

Multi-exponential fitting of both the spectral as well as the high S/N data set was done using the least squares approach described in Chapter 2.3.4 using Equation 2.8.[40] When fitting the nanosecond kinetics, the exponential function was iteratively convolved with the instrument response function (IRF), which was estimated to have a Gaussian shape with a width of $\sigma = 17$ ns (for details see Chapter 2.3.4).

In addition to the pelleted PSI samples, a liquid low-OD PSI sample was prepared to allow for the comparison of high- and low OD data. This was done by first exchanging the PSI sample into TRIS-buffer (buffer 6 in Tab. 3.4) using spin columns and subsequently concentrating the sample using a 100 kDA cutoff centrifugal filter, following the procedure described for cyanobacterial PSII core complexes in Chapter 3.5.2.

As the FTIR measurements were performed by others, details are not described here, but may instead be found in the article (Mäusle et al., 2024).

8.1.2 Millisecond QCL Spectra Reproduce Photoaccumulated FTIR Spectra

Figure 8.1a shows a photoaccumulated $P700^+/P700$ FTIR difference spectrum, as well as a QCL spectrum obtained by averaging the 0.1–1 ms region of each transient and a decay associated spectrum of a 125 ms phase; the origin of the latter will be discussed later in more detail. While the photoaccumulated FTIR spectrum is commonly referred to as a $P700^+/P700$ spectrum, it is more precisely a $P700^+F_{a/b}^-/P700\,F_{a/b}$ spectrum. It has been shown, however, that the iron sulfur clusters contribute only marginally in the 1800–1200 cm^{-1} region (Breton et al., 1999; Hastings et al., 2001); their vibrations are rather expected to be below 500 cm^{-1} (Chu et al., 2000, 1999). The three spectra look very similar, indicating that we are also seeing signals predominantly related to $P700^+/P700$ in both QCL spectra.

As previously observed (Breton, 2001; Nabedryk et al., 2000), $P700^+$ displays broad, positive electronic absorption bands. Such features are clearly visible in Fig. 8.1c, spanning the 4000–1200 cm^{-1} region of the $P700^+/P700$ FTIR spectrum. This broad electronic absorption difference overlies the vibrational difference bands present in the 1800–1300 cm^{-1} region, causing an upshift of the entire spectrum. This is clearly visible in Fig. 8.1a, when comparing the spectra to the zero line.

In addition to the RT spectra, low temperature FTIR spectra were obtained using two different approaches: (i) continuous illumination, resulting in a photoaccumulated $P700^+/P700$ spectrum, and (ii) averaging the first 54 μs of a flash-induced step-scan FTIR difference spectrum, resulting in a $P700^+A_1^-/P700\,A_1$ spectrum (Fig. 8.1b).

Wavenumbers displaying A_{1A} kinetics at 77 K can be identified by finding peaks that are present in the $P700^+A_1^-/P700\,A_1$, but not in the $P700^+/P700$ spectrum. As the $P700^+/P700$ spectra at 77 K and RT are very similar to each other, one could expect 77 K A_{1A} kinetics to also have a similar spectral fingerprint at RT.

From this approach, eight wavenumbers were selected for acquiring high S/N data QCL transients at RT: Comparison of the low temperature spectra suggested that A_1 bands should be found around 1510, 1494 and 1415 cm^{-1}, while at 1430 and 1482 cm^{-1} little or no A_1 contribution is expected. The bands at 1494 and 1415 cm^{-1} are known to be associated with stretching vibrations of the $C_1{=}O$ and $C_4{=}O$ groups of the A-branch phyl-

---

[40]Note that the equation used here is different from the one used in previous chapters. In this Chapter, a decaying phase has a *positive* amplitude and y_0 describes the offset at t→ ∞.
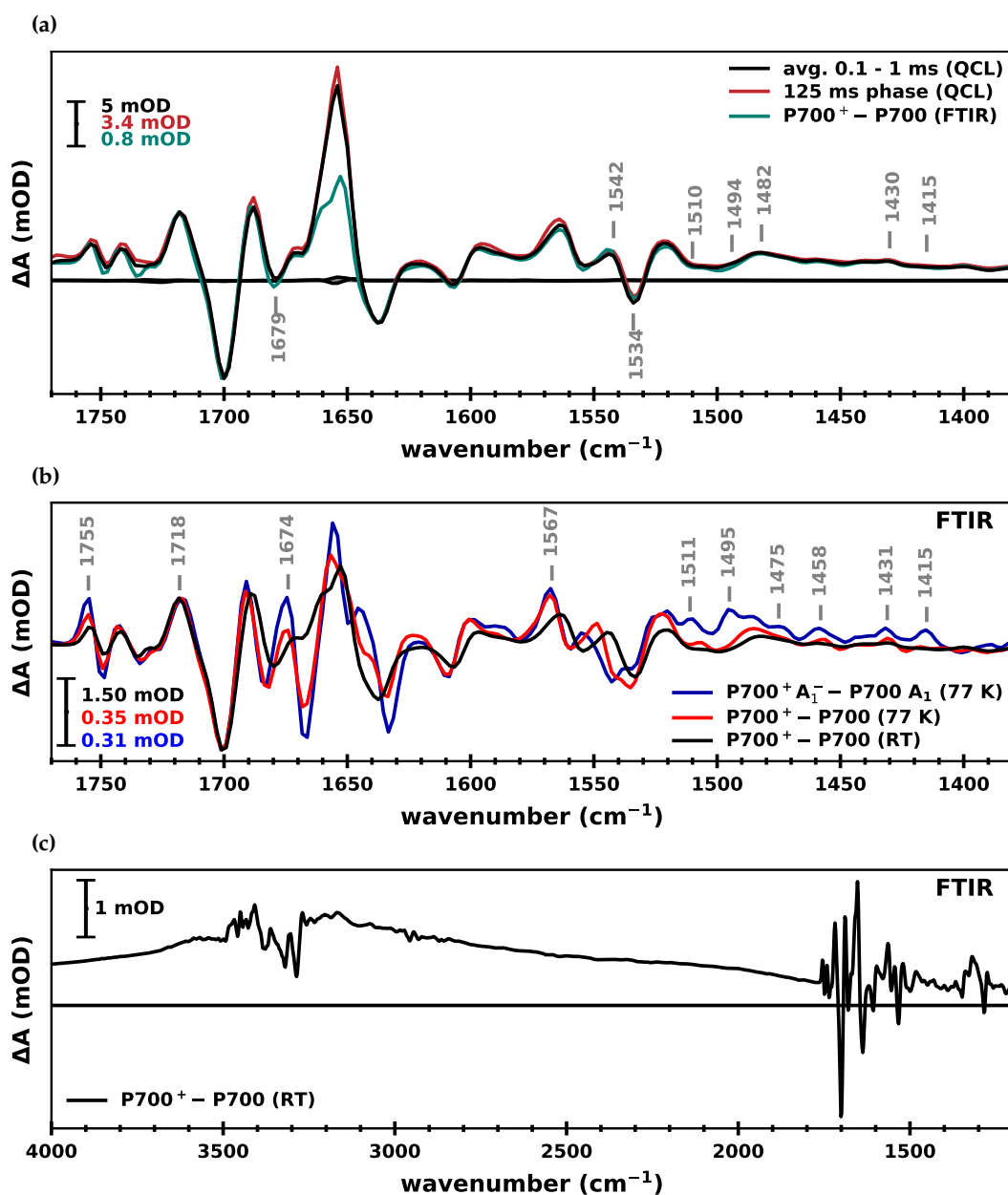
Figure 8.1: Infrared difference spectra of PSI core particles from *T. vestitus*. (a) A QCL spectrum (*black*) obtained by averaging the signal at 0.1–1 ms after the flash of each transient. The black line around zero was obtained in the same way but from transients recorded without an excitation flash, thus indicating the noise level. Additionally shown are a decay associated spectrum (*red*) of the 125 ms phase obtained by globally fitting the millisecond region of the time-resolved spectral QCL data set to a sum of five exponentials, as well as a photoaccumulated $P700^+/P700$ FTIR spectrum (*green*). The transient absorption changes of the labeled wavenumbers are shown in Fig. 8.2. **(b)** Microsecond time-resolved $P700^+A_1^-/P700$ A_1 FTIR difference spectrum at 77 K (*blue*), alongside photoaccumulated $P700^+/P700$ FTIR spectra at 77 K (*red*) and at RT (*black*). **(c)** Extended spectral range of the photoaccumulated $P700^+/P700$ FTIR spectrum at RT. This spectrum is the same as shown in *green* and *black* in panels (a) and (b), respectively. The spectra in (a) and (b) were scaled to the 1718(+)/1700(−) difference band. A modified version of this figure has been published in Mäusle et al. (2024). All FTIR data was acquired by N. Argawala and V. G. Eichmann.

losemiquinone anion (Hastings, 2015; Rohani et al., 2019). 1534, 1542 and 1679 cm^{-1} were additionally selected for their strong P700$^+$/P700 peaks.

8.1.3   Biphasic Nanosecond Kinetics Reflect Forward ET down A- and B-branch

Flash-induced transient absorption changes of select wavenumbers at RT are shown in Fig. 8.2 on a linear time scale up to 2 μs and on a logarithmic time scale between 2 μs and 800 ms. All transients display clear nanosecond kinetics, but show virtually no change in difference absorption on the microsecond scale. They all decay back to zero within hundreds of milliseconds.

The transients were fit globally to a sum of two exponentials and a non-decaying phase (offset y_0) with a fit range from below zero to 5 μs; the resulting fit curves, characterized by time constants of 33 and 364 ns, are shown in solid grey lines. These kinetic rates are in line with previous spectroscopic reports for the ET from $A_{1B}^- \rightarrow F_x$ and $A_{1A}^- \rightarrow F_x$ (Agalarov and Brettel, 2003; Sétif and Brettel, 1993; Schlodder et al., 1998; Li et al., 2006). Figure 8.3 shows the amplitudes of both kinetic phases, as well as the offset y_0 off the eight fitted transients.

In an attempt to further characterize the nanosecond kinetics, a global bi-exponential fit across the entire (low S/N) time-resolved spectral data set was performed, whereby the time constants were fixed to the predetermined values of 33 and 364 ns. The resulting amplitudes were plotted as a function of wavenumber, resulting in decay associated spectra of the two phases. The fit quality of the 33 ns phase was generally very poor, due to very poor S/N of the early data points. The DAS of this phase is thus not reliable and has been omitted here (but may be found in Fig. A6.1 of the Appendix). The DAS of the 364 ns phase, on the other hand, is well resolved and shows very clear spectral features (Fig. 8.4).
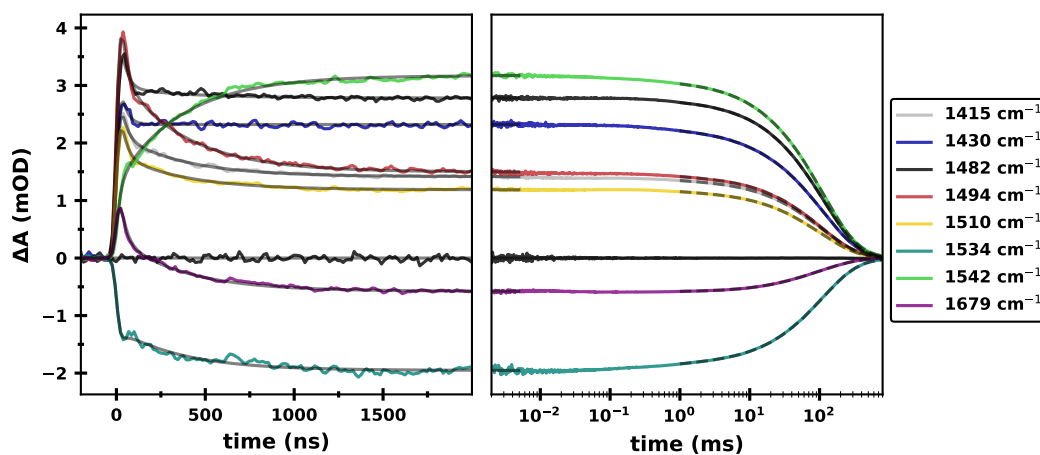

Figure 8.2: Flash-induced transient IR absorption changes at eight wavenumbers. The IR difference signal is shown on a linear scale up to 2 μs (*left*) and on a logarithmic x-axis from 2 μs–800 ms (*right*). Transient absorption changes are shown for 1415 (*grey*), 1430 (*blue*), 1482 (*black*), 1494 (*red*), 1510 (*yellow*), 1534 (*dark green*), 1542 (*light green*) and 1679 cm^{-1} (*purple*). The signal in absence of laser flash excitation is shown oscillating around zero in *black* (measured at 1482 cm^{-1}) and serves as a demonstration of the noise level. The fit curves obtained from globally fitting the transients to a sum of two exponentials in the nanosecond region (up to 5 μs) are shown in *solid grey* lines; the fit curves using five exponentials in the millisecond region (1–800 ms) are shown in *dashed grey* lines. A modified version of this figure has been published in Mäusle et al. (2024).
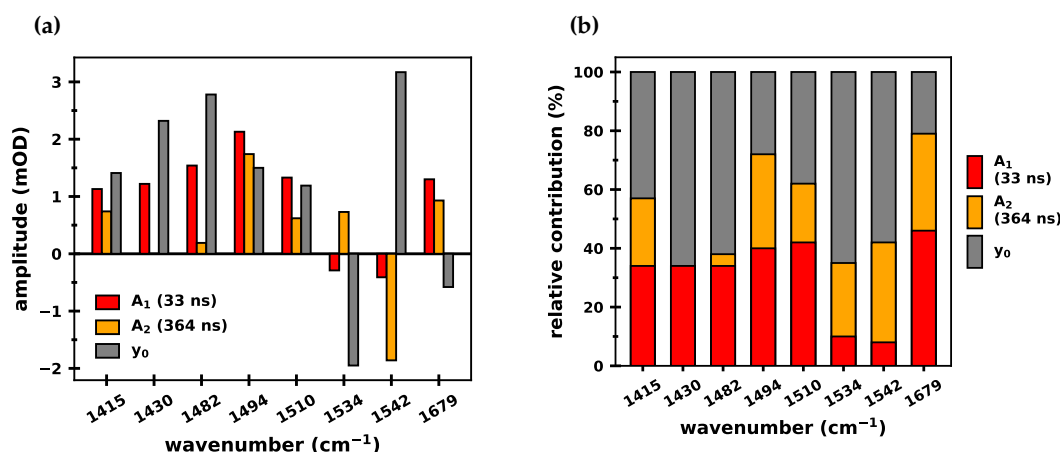
Figure 8.3: Results of the global analysis of the nanosecond region of the data in Fig. 8.2. The parameters were obtained from a global fit to a sum of two exponentials and a non-decaying phase (offset y_0) with a fit range from below zero to 5 μs. **(a)** Absolute amplitudes A_1 and A_2 of the exponential components (τ_1=33 ns and τ_2=364 ns) and offset y_0 for each wavenumber. The offset y_0 effectively corresponds to the value at 5 μs. **(b)** Relative contribution of A_1, A_2 and y_0 at each wavenumber. A_1, A_2 and y_0 correspond to contributions of A_{1B}^-, A_{1A}^- and $P700^+$, respectively. The values shown in this figure are also given in Table A6.1 in the Appendix. A modified version of this figure has been published in Mäusle et al. (2024).
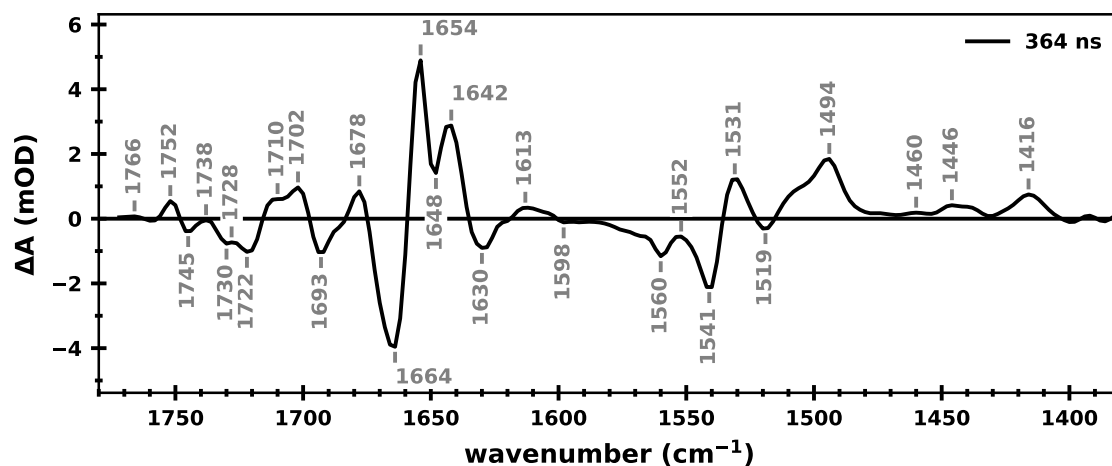

Figure 8.4: Decay associated spectrum of 364 ns phase of PSI core particles from *T. vestitus*. The DAS was obtained by globally fitting the time-resolved spectral data set to a sum of two exponentials and an offset with the two time constants fixed to 33 and 364 ns (the values obtained from fitting the data in Fig. 8.2).

The peak positions are similar to an $A_1^- - A_1$ double difference spectrum reported for PSI core particles from *Synechocystis* sp. PCC 6803 (Hastings, 2015).

8.1.4   Exploring Different Fit Approaches for the Nanosecond Kinetics

It is striking that the amplitude of the 33 ns phase is generally more pronounced than that of the 364 ns phase (Fig. 8.3a), even though ET is thought to happen preferentially down the (slower) A-branch (Makita and Hastings, 2015). This discrepancy may in part be due to
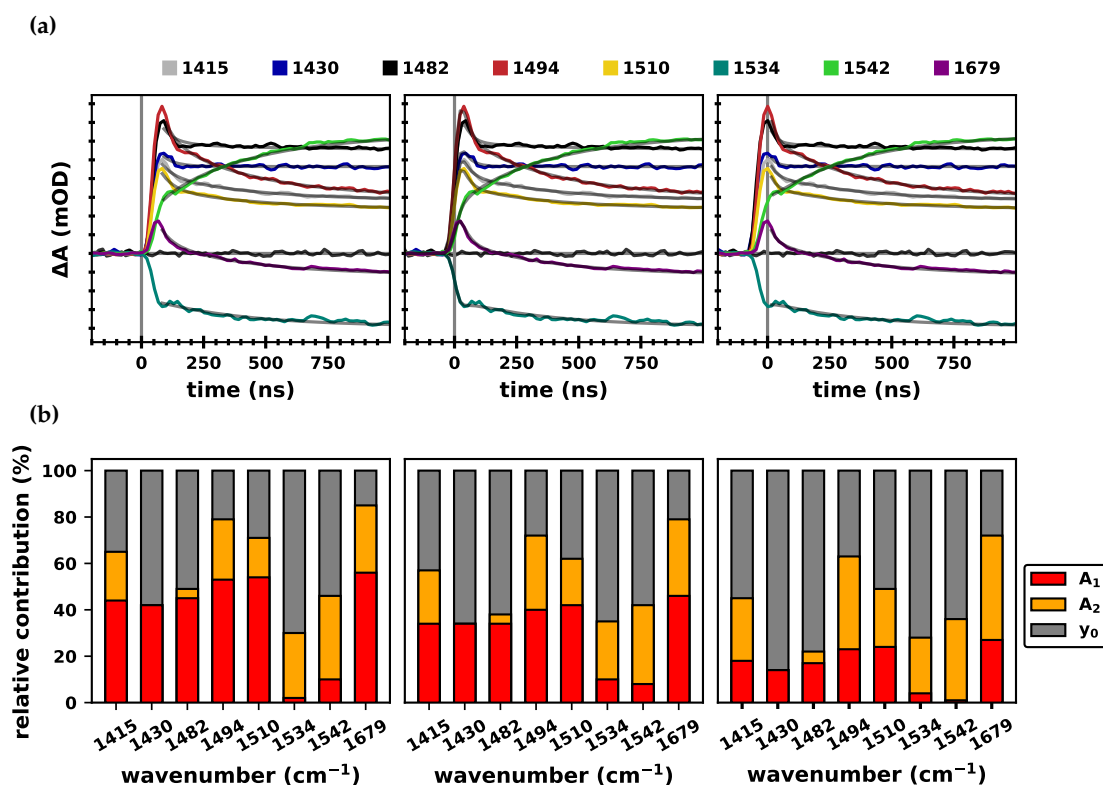
(a)

(b)

Figure 8.5: Comparison of different fit approaches of the nanosecond kinetics of PSI from *T. vestitus*. (a) Flash-induced IR absorption changes at 1415 (*grey*), 1430 (*blue*), 1482 (*black*), 1494 (*red*), 1510 (*yellow*), 1534 (*dark green*), 1542 (*light green*) and 1679 cm^{-1} (*purple*); the fit curves are shown in grey. The data is the same as shown in Fig. 8.2. *Left*: The data is here shown on the original time axis, with t=0 as determined by the photodiode data. The fits were performed between 75 ns and 5 µs to a simple sum of two exponentials and an offset, resulting in $\tau_1 = 49$ ns and $\tau_2 = 367$ ns. *Center*: A fitting procedure was applied in which the sum of exponentials was iteratively convolved with the IRF. This approach required shifting the transients such that their initial half-rise point coincides with $t = 0$. The fit range was -0.5 to 5 µs and resulted in $\tau_1 = 33$ ns and $\tau_2 = 364$ ns. This approach was deemed the most suitable and was used in Figures 8.2 and 8.3. *Right*: The time axis was here shifted such that the initial peaks of the data sets coincided with $t = 0$. The fits were then performed between 0 and 5 µs to a simple sum of two exponentials and an offset, resulting in $\tau_1 = 25$ ns and $\tau_2 = 355$ ns. **(b)** The relative contribution of the amplitudes of the bi-exponential fits obtained from the three different approaches, displayed in the same order as in (a). This figure has been published in parts in the supplementary information of Mäusle et al. (2024).

the relatively high uncertainty of the fast kinetic: The 33 ns phase is very much at the limit of the time resolution of the setup (the smallest data bin size being 15 ns), which is why both the time constant as well as its amplitude very much depend on the fit approach and should only be seen as a rough estimate.

Three different fit approaches were explored (Fig. 8.5) and will be discussed in the following:

(i) In the first approach the data is fitted to a simple sum of two exponentials and an offset, using the original time axis with $t = 0$ as determined by the photodiode data (Fig. 8.5, *left*). The fit range was 75 ns (i.e. starting the initial peak) to 5 µs, resulting

in time constants of 49 and 367 ns. The main issue with this approach is the very large—most likely strongly overestimated—amplitudes of the fast phase.

(ii) A second approach is to account for the instrument response, by iteratively convolving the exponential function with the IRF during the fitting procedure (see also Fig. 2.9). This approach also simulates the initial rise due to instrumentation response, thus the time axis has to be adjusted such that the initial half-rise point coincides with $t = 0$ and the fit range here was chosen to be -0.5 to 5 μs. This approach yielded the time constants of 33 and 364 ns reported in Section 8.1.3.

(iii) The third approach is to shift the data such that their initial peaks coincide with $t = 0$. Justification for this is the simplified assumption that the initial ET steps leading up to reduction of the phylloquinones happen much faster than the time resolution of the instrument, and thus the initial peaks should be reached within $t = 0$ (which is only valid, however, if the instrumentation response is sufficiently fast). In this approach the fit range is 0 to 5 μs and yielded time constants of 25 and 355 ns. This approach produced smaller A_1 amplitudes than the other two approaches.

While the slower time constant τ_2 varied only with a relative standard deviation of 1.4% between the three approaches, the fast time constant τ_1 exhibits a relative standard deviation of 28.0%. The amplitudes A_1 of the fast phase vary similarly strong between the approaches. The approach which accounts for the IRF was deemed most suitable, as it does not require determination of $t = 0$ in such a subjective way as the third approach does. In any way the amplitude of the fast phase should not be over-interpreted in the here presented data; ratios of the two amplitudes cannot be quantified reliably. If the time resolution of the setup were to be improved in the future, repeating these experiments may be very much worthwhile.

8.1.5   Multiphasic Millisecond Recombination Kinetics

Following the initial nanosecond kinetics, the transients in Fig. 8.2 show no big absorption changes up to about 1 ms, before decaying back to zero. These millisecond kinetics were analysed by a global fit of the eight data sets (fit range 1–800 ms), which required five exponential components for a satisfactory fit quality (as judged by the residuals); the determined time constants are 1.2, 10.3, 44.7, 126 and 373 ms. As we previously assigned the plateau-like signal around 0.1–1 ms to $P700^+/F_{A/B}^-$ and as there are no electron acceptors present in the sample that would promote further forward electron transfer, we can safely assume that the millisecond kinetics are dominated by $P700^+/F_{A/B}^- \rightarrow P700/F_{A/B}$ recombination kinetics. Near-IR spectroscopic experiments have also shown complex multiphasic recombination events (Vassiliev et al., 1997).

The time constants determined from fitting the high S/N transients were again fixed in a global fit across the entire time-resolved spectral data set. The resulting five decay associated spectra are shown in Fig. 8.6. The by far most dominant kinetic has a time constant of 126 ms and its spectral features are near identical to the $P700^+/P700$ spectra, as shown in Fig. 8.1. In fact, all of the millisecond DAS have a very similar spectral shape (see Fig. A6.2 in the Appendix for a normalized display of the DAS). Merely the 1.2 ms DAS shows some strongly pronounced deviations, which likely simply arise from the fact that a 1.2 ms time constant is naturally poorly resolved for a fit range starting at 1 ms. Furthermore, the amplitude of the 1.2 ms phase is much smaller than those of all other phases.
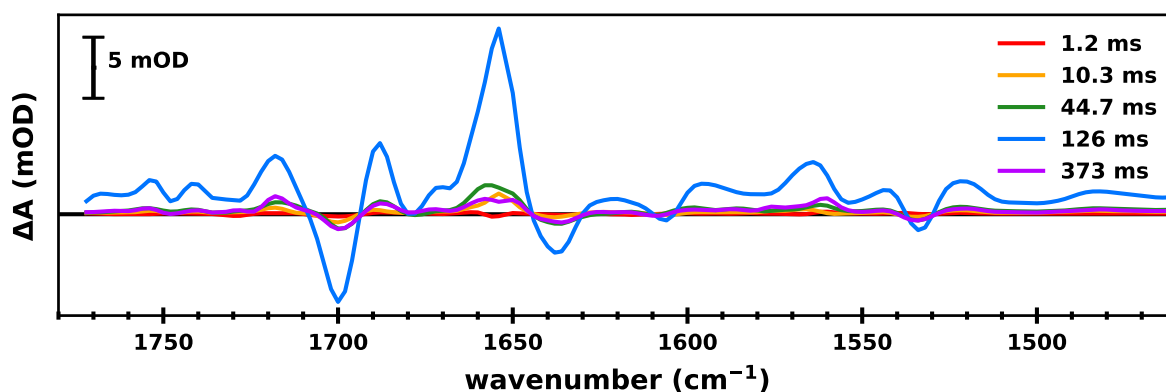
**Figure 8.6: Decay associated spectra of the millisecond kinetics of PSI core particles from
T. vestitus.** The DAS was obtained by globally fitting the time-resolved spectral data set
to a sum of five exponentials and an offset with the time constants fixed to 1.2, 10.3, 44.7,
126 and 373 ms (the values obtained from fitting the data in Fig. 8.2. The dominant 126 ms
phase is near identical to the spectrum obtained from averaging the 0.1–1 ms window of the
transients (see also Fig. 8.1). Fig. A6.2 shows the same DAS as here but normalized to their
peak at 1700 cm^{-1}.

8.1.6   Effect of Flash Spacing on the Transient Absorption Changes

The main set of measurements were done at 1 s flash interval (1 Hz). To investigate whether
the flash frequency influences the absorption changes, a few experiments were also done at
10 s flash interval (0.1 Hz). Comparing transient absorption changes at 1417 cm^{-1} for both
flash spacings (Fig. 8.7) shows that a longer spacing between flashes increases the overall
difference signal slightly. Scaling the 0.1 Hz data down to match amplitude of the 1 Hz
data (by multiplication with a factor of 0.9), reveals that the nanosecond kinetics remain
unchanged between the two data sets (*light blue* and *red* curves in Fig. 8.7), while the mil-
lisecond recombination kinetics are slightly affected: the 1 Hz data has a more pronounced
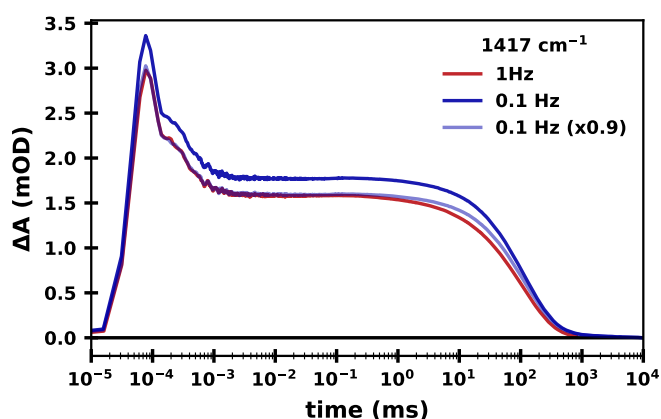
**Figure 8.7: Flash-induced transient absorption changes of PSI core particles from *T. vesti-
tus* at 1417 cm^{-1} measured with two different flash spacings.** The absorption changes at 1
and 0.1 Hz are shown in *red* and *dark blue*, respectively. The 0.1 Hz data is additionally shown
in *light blue* multiplied with a factor of 0.9 for better visual comparison with the 1 Hz data.
Visual inspection shows that the nanosecond kinetics are identical, while the millisecond
recombination kinetics are slightly altered by the choice of flash spacing.

∼20 ms phase, while the 0.1 Hz data has a stronger ∼300 ms phase (*analysis not shown*). A ∼120 ms phase is dominant at both flash frequencies.

The reasons for changes in the recombination kinetics are presently unclear. Further data is required to first assign the multiphasic recombination kinetics to individual reactions before an interpretation of the influence of the flash spacing can be attempted. In this project, however, the nanosecond kinetics are of main interest and these results show that a 1 Hz flash frequency is suitable (i.e. not too fast) for their study.

8.1.7   Comparison of a Dry High-OD Sample and a Liquid Low-OD Sample

The measurements on *T. vestitus* were done on a rather dry sample with a very high optical density. After having done the time-resolved IR measurements, an attempt to measure an FTIR spectrum was undertaken, but the optical density of the sample was too high in the mid-IR region. The absolute FTIR data shown in Fig. 8.8b show that the transmitted signal was so low, that it led to a flat-lined saturated absorption signal.

To determine whether the high optical density and dryness of the sample had an influence on the kinetics, some more experiments were done on a low-OD liquid sample. The strong water/amide I peak around 1800 cm^{-1} together with the absence of a strong amide II peak around 1550 cm^{-1} in the absolute FTIR spectrum (Fig. 8.8b, *light blue*) confirm the liquid condition as well as the low optical density of the sample.

Transient absorption changes were measured for the high- and low OD PSI samples at several wavenumbers. As shown in Fig. 8.8 for 1482, 1494 and 1542 cm^{-1}, the flash-induced absorption changes are about ten times more strongly pronounced in the dry high-OD sample, which is naturally expected due to the higher PSI concentration. After
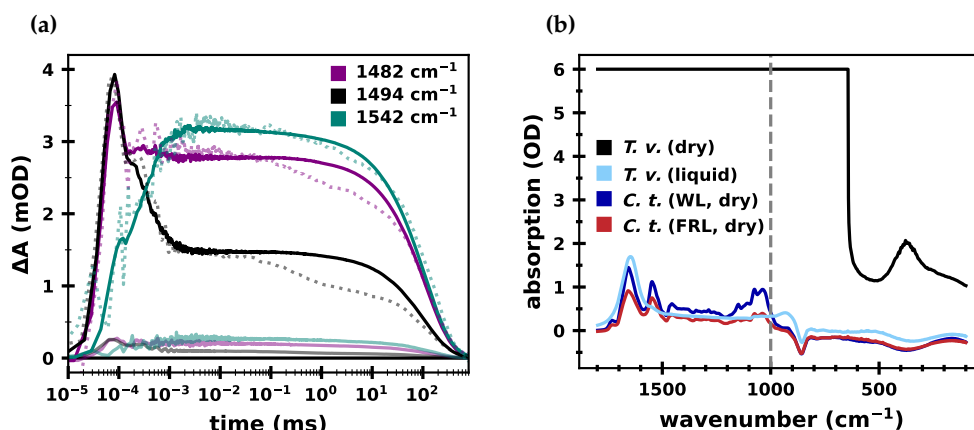

Figure 8.8: Comparison of a high-OD dry *T. vestitus* PSI sample and a low-OD liquid sample. (a) Flash-induced transient absorption changes at 1482 (*red*), 1494 (*black*) and 1542 cm^{-1} (*blue*) are shown for a high-OD sample (*opaque*) and a low-OD sample (*transparent*). The low-OD data has a much lower signal and is thus also shown multiplied by a scaling factor (*dotted lines*) to match the high-OD signal. It is apparent that the nanosecond kinetics are identical between the samples, while the millisecond recombination kinetics differ. **(b)** Absolute FTIR spectra of the high-OD (*black*) and low-OD (*light blue*) *T. vestitus* sample, as well as *C. thermalis* PSI grown under white light (*dark blue*) and far-red light conditions (*red*). The data below 100 cm^{-1} is not meaningful because of a filter installed in the setup and was only included to show more clearly that the *T. vestitus* signal is saturated in the area of interest.

multiplication of the low-OD data with a scaling factor, visual inspection clearly shows that the nanosecond kinetics remain unchanged. The millisecond kinetics, however, are strongly impacted. Reasons for this may be connected to the different states of dryness of the sample, rather than the optical density. Possibly the availability of the added artificial electron donors plays a role—further careful experiments are needed for clarification. When the nanosecond kinetics are of main interest, however, this data confirmed that a high-OD dry sample is suitable.

The S/N of the low-OD data is clearly poorer than the that of the high-OD data, as can be best seen with the normalized data in Fig. 8.8a. For the transient at 1494 cm^{-1} 30.000 data sets were averaged for the low-OD data, but only 600 for the high-OD data, which translates to measurement times of 11 hours vs. 15 minutes. This reveals a big advantage of the single-frequency IR setup: the possibility of measuring on thick samples and thus greatly reducing the data acquisition time.

8.1.8   Discussion

The three spectra in Fig. 8.1 are very similar, despite being collected in very different ways. For the FTIR spectrum P700$^+$F$_{a/b}^-$ is accumulated by continuously illuminating the sample. In the flash-induced QCL transients P700$^+$ is formed within picoseconds and A$_1^-$ within nanoseconds. Within hundreds of nanoseconds ET from A$_1^-$ to F$_x$ and on to F$_{a/b}$ takes place, bringing the system into a P700$^+$F$_{a/b}^-$ state, the same as achieved by continuously illuminating the sample. The decay associated spectrum of the 125 ms is nearly identical to the P700$^+$F$_{a/b}^-$ QCL spectrum, indicating that the millisecond kinetics are directly related to P700$^+$F$_{a/b}^-$→P700 F$_{a/b}$ recombination.

The DAS of the other millisecond phases are also very similar (see Fig. A6.2 in the Appendix), but show some small deviations, which might be an indication that they reflect other recombination processes, such as P700$^+$F$_x^-$→P700 F$_x$ or recombination of P700$^+$ with exogenous electron donors. Further experiments with addition of exogenous electron acceptors and/or on PSI samples that lack F$_{a/b}$ or F$_x$ could allow for a definite assignment of the different recombination phases to specific processes. Calculating double difference spectra of the DAS of the recombination phases could then yield reliable F$_{a/b}^-$/F$_{a/b}$ as well as F$_x^-$/F$_x$ spectra.

The only significant difference between the QCL and the FTIR spectra in Fig. 8.1 is at the peak around 1655 cm^{-1}. It is possible that the higher amide I peak in the QCL data is an artefact due to the fact that the sample was very thick: While the nanosecond kinetics were generally not influenced by the high optical density (Fig. 8.8a), it could be that specifically the amide I region, due to very high absolute absorption values, might have been compromised. Further experiments on a lower-OD sample are needed to clarify this.

It is also possible that the difference of the amide I peak arises from different F$_{a/b}^-$ populations between the two methods: As mentioned above, it has been shown the iron-sulfur clusters only contribute minimally to the P700$^+$F$_{a/b}^-$/P700 F$_{a/b}$ difference spectra in the 1800–1200 cm^{-1} region (Breton et al., 1999; Hastings and Sivakumar, 2001), which is why they are commonly referred to more simply as P700$^+$/P700 spectra. Noguchi et al. (1996) observed mostly negligible contributions of iron-sulfur clusters to the difference spectra of bacterial reaction centers, with exception, however, of the amide I region. If the different

amide I amplitude of the QCL vs. FTIR spectra were due to the iron-sulfur clusters one would however expect further small differences, rendering this explanation unlikely.

Biphasic electron transfer from A_1 to F_x has previously been probed by observing time-resolved absorption changes at 480 ms, yielding time constants of 11 and 340 ns at RT for PSI from *Synechocystis* sp. PCC 6803 (Agalarov and Brettel, 2003). The faster and slower time constants have been shown to be associated with the B- and A-branch, respectively (Guergova-Kuras et al., 2001). In this work we observed biphasic nanosecond kinetics in the IR difference transients across the 1800–1300 cm^{-1} range, with time constants of 33 and 364 ns (Figs. 8.2 and 8.3).

At 1494 cm^{-1}, a band that (at 77 K) has been assigned to the $C_1{=}O$ group of PhQ$^-$ in the A_{1A} binding site (Rohani et al., 2019), exhibits well-resolved biphasic nanosecond kinetics (see Fig. A6.4 in the Appendix for PhQ structure and numbering). Both phases have large amplitudes, together making up 72% of the total observed absorption change (40% associated with the fast phase and 32% associated with the slow phase). The other 28% are due to the (on a microsecond scale) non-decaying absorption change (y_0). The contributions of the amplitudes A_1 and A_2 and the offset y_0 are directly associated with the contributions of A_{1B}^-, A_{1A}^- and P700$^+$. All three co-factors exhibit a positive absorption change at 1494 cm^{-1} upon their reduction, which is in line with the results from the FTIR spectra at 77 K (Fig. 8.1b).

The kinetics at 1415 and 1510 cm^{-1}, which are likely due to the $C{=}C$ stretching mode of the semiquinone rings and the $C_4{=}O$ groups of PhQ$^-$ (Rohani et al., 2019), show a similar behavior as the kinetic at 1494 cm^{-1}, but with less pronounced slow nanosecond phases. This is also reflected in the P700$^+$A$_1^-$/P700 A$_1$ FTIR spectrum, where the 1415 and 1511 cm^{-1} peaks are smaller than the feature at 1495 cm^{-1}.

At 1679 cm^{-1}, the absorption change is initially positive but then decays to negative value within hundreds of nanoseconds; the P700$^+$/P700 FTIR spectrum at RT also exhibits a negative peak. This indicates that the absorption change resulting from the reduction of A_1 is positive, but once A_1^- diminishes the negative absorption change due to P700$^+$ becomes visible. The nanosecond kinetics at this wavenumber are possibly associated with amide I vibrations from amino acids near the A_1 phylloquinones or with keto carbonyl modes of the chlorophylls in the A_0 or A_{-1} binding pockets (Sivakumar et al., 2005; Hastings, 2015). A definite assignment requires further investigation.

At 1430 and 1482 cm^{-1}, a fast 33 ns decay is visible with hardly any further absorption change on the nanosecond and microsecond time scale. The 33 ns phase and the non-decaying P700 contribution account for 35 and 61% of the absorption change at 1482 cm^{-1} and even for 34% and 66% at 1430 cm^{-1} (Fig. 8.3). As pointed out before, the 33 ns phase is very close to the temporal resolution of the setup (>15 ns) and is barely resolved. The amplitudes of this phase are highly uncertain and depend strongly on the fit approach. The fact that the 33 ns phase shows both negative and positive amplitudes and that those amplitudes differ strongly in their intensity nevertheless confirms that this phase is not merely an instrumental artefact.

Fig. 8.9 compares the 33 ns phase at 1679 cm^{-1} to a transient at 1770 cm^{-1}, where we do not expect any phylloquinone contributions (Fig. 8.1b): While the transient at 1770 cm^{-1} indeed shows no nanosecond contribution above noise level, the fast nanosecond phase clearly contributes strongly at 1679 cm^{-1}. This is further confirmed by an alternative fit curve, obtained with only one nanosecond component ($\tau = 276$ ns), which clearly fails to simulate the data well. Fitting the 1770 cm^{-1} transient using the same procedure as for the

other transients, however also produces a non-zero amplitude for the fast phase (*not shown*). In conclusion, the fast nanosecond phase is real, but poorly resolved and its amplitudes are likely overestimated by the fit approach.

Since the kinetics at 1430 and 1482 cm^{-1} show a 33 ns phase, but virtually no 364 ns contribution, it is unlikely that the fast phase at these wavenumbers is directly associated with molecular groups of the B-branch phylloquinone (i.e. if the assumption holds true that A_{1A}^- and A_{1B}^- have absorption bands at similar frequencies), as we might then expect also a contribution of the slower phase. The 33 ns phase could instead here be associated with an amino acid residue between A_{1B} and F_x. We speculate that we have uncovered spectral asymmetry between the two branches, but confirmation of this will require measurements with a better temporal resolution, so that an artefactual 33 ns phase can be entirely ruled out.

Figure 8.9: Comparison of the fast nanosecond phase at 1679 (*purple*) and 1770 cm^{-1} (*blue*) of PSI from *T. vestitus*. The transient at 1679 cm^{-1} is shown together with its fit curve (*black, solid*). The curve from fitting with only one nanosecond component ($\tau = 276$ ns) is shown a dashed black line.

At 1542 cm^{-1} (Fig. 8.2) we potentially also observe a spectral asymmetry between the two branches: the fast phase has a much lower amplitude than the slower phase. However, this might also simply reflect differing utilization-probability between the two branches: It was found that the A/B branching ratio is roughly 60/40 to 80/20 in cyanobacterial PSI core complexes (Makita and Hastings, 2015; Savitsky et al., 2010; Xu et al., 2003). However, with the current temporal resolution of the measurements this is only speculation.

At 1534 cm^{-1} the amplitudes of the slow and fast nanosecond phases are of opposite sign, which could indicate another branch-asymmetry. However, the amplitude of the fast phase is very small and has a large error (see Table A6.1 in the Appendix); visual inspection of Fig. 8.2 confirms that the 33 ns phase is clearly poorly resolved.

While the here presented data overall show a clear biphasic behavior in the nanosecond region, the limited time resolution of the experimental setup does not allow an in-depth analysis of the fast component; both the amplitude as well as the exact value of the fast component are poorly determined. As was shown in Fig. 8.5, the fit approach has a strong impact on the fast time constant, but especially also on its amplitudes.

If, as previously suggested (Rohani et al., 2019), the kinetic at 1494 cm^{-1} is assignable to the $C_1{=}O$ group of the A-side PhQ^- and if the B-side PhQ^- absorbs at this wavenumber in a comparable manner, we would expect the amplitudes of the nanosecond phases to reflect the cyanobacterial B/A branch-utilization ratio of 40/60 to 20/80 in favor of the A-branch. Fit approach 3 in Fig. 8.5, unlike the other two approaches, achieves an amplitude ratio in that range, again underlining that over-interpretation of the data should be avoided.

The decay associated spectrum of the slow nanosecond phase (Fig. 8.4) shows similar spectral features as the $A_1^- {-} A_1$ double difference spectrum reported for PSI core particles from *Synechocystis* sp. PCC 6803 (Hastings, 2015). The relative amplitudes of the peaks, however, differ greatly, which may—at least in part—be due to the differing measurement temperatures (RT vs. 77 K). A striking difference is the small amplitude of the 1678 cm^{-1} peak in DAS vs. the very large peak at 1675 cm^{-1} in the $A_1^- {-} A_1$ of *Synechocystis* PSI; while
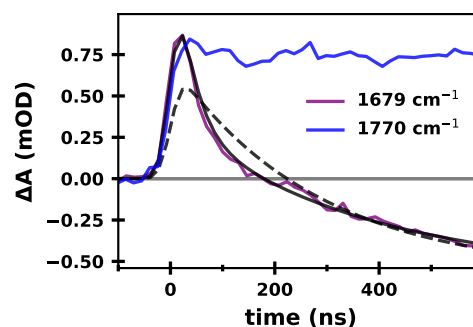
the peak at 1654 cm^{-1} in the DAS is much larger than the peak at 1660 cm^{-1} for *Synechocystis* PSI. These differences may arise from species- and/or temperature-dependent differences in the amide I mode. Visual inspection of figure 8.1b shows strong differences between P700$^+$/P700 spectra at RT and 77 K in the amide I region; possibly the A$_1^-$ $-$A$_1$ spectra are similarly affected by temperature.

8.1.9 Conclusions and Outlook

In this work we observed flash-induced biphasic nanosecond kinetics with time constants of 33 and 364 ns, which we assign to forward electron transfer down the B- and A-branch, respectively. This is in good agreement with visible spectroscopy studies (Agalarov and Brettel, 2003). The instrumental time resolution is currently mostly limited by the IR detector with its integrated 10 MHz pre-amplifier, as well as the sampling rate of the A/D converter, which allows a smallest bin size of about 15 ns. The 33 ns phase is thus only poorly resolved and there is a significant uncertainty regarding its quantification. If the temporal resolution were to be improved in the future, this would open new possibilities for characterizing the A- and B-branch, including the determination of branch-utilization ratios.

One way to circumvent the issue with the time resolution could be to perform experiments on PSI particles with slowed-down forward ET. One possibility would be to incorporate high-potential quinones into the A$_1$ binding site (Hastings, 2015). While the A$_1^-$/A$_1$ spectra would surely be different from that of the native system (Agarwala et al., 2023), it could still help to pinpoint asymmetries between the two branches.

8.2 PSI Core Particles from *C. thermalis* Grown under Far-Red Light and White Light Conditions

Some cyanobacteria, such as *Chroococcidiopsis thermalis* PCC 7203 (*C. thermalis*), are capable of adapting their photosynthetic apparatus to far-red light conditions by a process termed far-red light photoacclimation (FaRLiP); see Elias et al. (2024) for a recent review. This process includes the replacement of several protein subunits in PSI and PSII with paralogues capable of harvesting and employing long-wavelength light between 700–800 nm (while wavelengths above 750 nm are usually not accessible to cyanobacteria). When grown under far-red light (FRL) conditions, 7–8 Chl *a* molecules in PSI from *C. thermalis* are replaced with Chl *f*, which has an absorption spectrum shifted to longer wavelengths (Nürnberg et al., 2018). The location of the Chl *f* molecules within PSI is still a subject of debate, as are their possible effects on the ET kinetics.

In this Chapter, PSI from FRL as well as white-light (WL) grown *C. thermalis* is investigated with time-resolved IR spectroscopy. ET from A$_1^-$ to F$_x$, down the A- and B-branch, is observed. P700$^+$/P700 spectra, as well as A$_{1A}^-$/A$_{1A}$ decay associated spectra of WL-PSI and FRL-PSI are compared to the spectra of *T. vestitus*. Surprisingly, WL-PSI from *C. thermalis* exhibits some unusual characteristics, indicating alterations in or around P700.

8.2.1 Experimental Details

The experiments were mostly performed analogously to the experiments on PSI from *T. vestitus*. Low S/N time-resolved spectral data sets were measured in 1 cm^{-1} increments for both the WL and FRL variant and with only 6 transients per wavenumber throughout

the entire spectral region. The WL data set has gaps, i.e. missing data points due to insufficient IR signal reaching the detector, at 1495, 1653, 1723, 1746, 1759, 1768, 1772 cm^{-1}); the FRL data set has gaps at 1495, 1653, 1734, 1794 cm^{-1}. The time-resolved spectral data set was smoothed with a sliding average algorithm with a window size of ten along the quasi-logarithmic time axis (with the smallest bin size comprising 15 ns). Gaussian smoothing with $\sigma = 2.5$ was applied along the wavenumber axis, resulting in a spectral resolution of about 6 cm^{-1}.

As in Chapter 8.1, Equation 2.8 is used for fitting the transients, meaning that rising and decaying kinetics have negative and positive amplitudes, respectively (in contrast to the results on PSII shown in previous chapters).

T. vestitus data from Chapter 8.1 will be shown in some of the following figures for direct comparison. All FTIR data was acquired and analyzed by N. Argawala and V. G. Eichmann.

8.2.2 Spectral Differences Between the PSI Variants

Figure 8.10a shows spectra of PSI from WL and FRL grown *C. thermalis* as well as PSI from *T. vestitus* at 0.1–1 ms after the flash. All three spectra are very similar to RT photoaccumulated P700$^+$/P700 FTIR spectra of the same sample type, although the *C. thermalis* samples show some more differences in relative amplitudes than the *T. vestitus* spectra (see Fig. A6.3 in the Appendix for a comparison of QCL and FTIR spectra; for *T. vestitus* see Fig. 8.1a). The QCL spectrum of *T. vestitus* in Fig. 8.10a shows clearly stronger difference absorption bands than the *C. thermalis* spectra. This is unsurprising as the *C. thermalis* samples had a far lower optical density, as confirmed by their absolute FTIR spectra (Fig. 8.8b).

While PSI from FRL grown *C. thermalis* shows a similar positive spectral offset as PSI from *T. vestitus*, the same is not the case for WL grown *C. thermalis*. This becomes even more clear when considering an extended spectral range of the P700$^+$/P700 FTIR spectra (Fig. 8.10d): The very broad difference band spanning the entire 4000–1300 cm^{-1} region—which has been shown to be a P700$^+$ electronic absorption band (Breton, 2001)—is clearly far less pronounced in PSI from WL grown *C. thermalis* (the samples used for the FTIR experiments were all of similar optical density, *not shown*).

For easier visual comparison, the two *C. thermalis* spectra are shown in Fig. 8.10b normalized to their 1700/1718 cm^{-1} difference signal, revealing a number of band shifts and changes in band intensity. Surprisingly, when instead comparing PSI from FRL grown *C. thermalis* to PSI from *T. vestitus* (Fig. 8.10c), the differences between the spectra are much more subtle and indeed similar to what was found for PSI from WL and FRL grown *Fischerella thermalis* PCC 7521 (*F. thermalis*) (Hastings et al., 2019).

8.2.3 Nanosecond Kinetics of Forward ET and their Spectral Signature

Flash induced absorption changes were monitored at seven wavenumbers for PSI from FRL and WL grown *C. thermalis*, as shown in Fig. 8.11a and b, respectively. On first glance the FRL grown *C. thermalis* transients overall resemble those of *T. vestitus* in Fig. 8.2, while the WL grown *C. thermalis* transients appear very different. Upon closer inspection it becomes clear that the two *C. thermalis* samples actually show similar nanosecond kinetics, but differ greatly in their offset due to the P700$^+$ signal. As observed in the P700$^+$/P700 spectra in Fig. 8.10a and d, PSI from WL *C. thermalis*, unlike the other two samples, does not show a strong positive upshift. As a result, the WL *C. thermalis* transients show difference signals
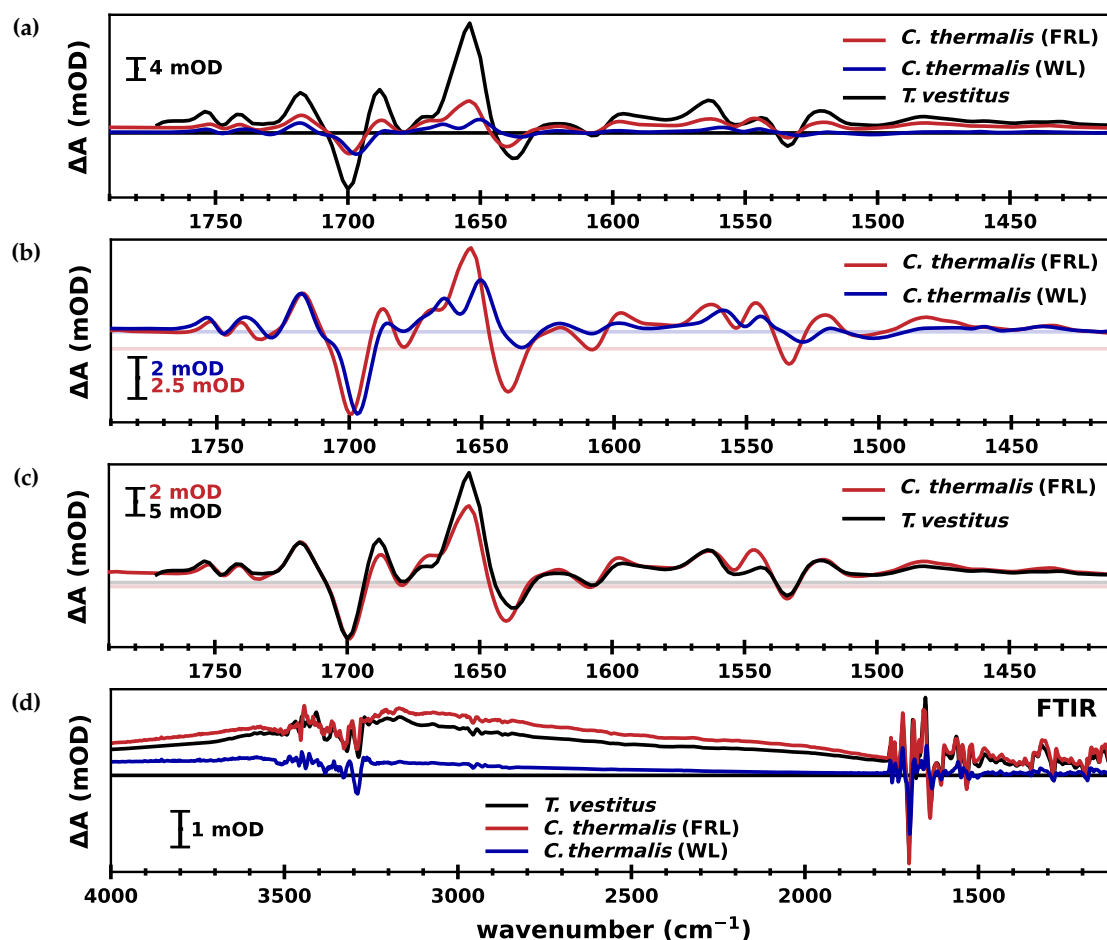
Figure 8.10: Infrared difference spectra of PSI core particles from *C. thermalis* and *T. vestitus*. **(a)** Non-normalized QCL spectra of *C. thermalis* grown under far-red light (*red*) and white-light conditions (*blue*), as well as a spectrum of *T. vestitus* (*black*), obtained by averaging the signal between 0.1–1 ms at each wavenumber. All three spectra are very similar to photoaccumulated (P700$^+$−P700) FTIR spectra (*not shown*). **(b)** WL and FRL *C. thermalis* spectra from (a), scaled to their 1718(+)/1700(–) difference band for easier visual comparison. **(c)** Spectra of *T. vestitus* and FRL grown *C. thermalis*, scaled to their 1718(+)/1700(–) difference band for easier visual comparison. **(d)** Photoaccumulated (P700$^+$−P700) FTIR difference spectra of all three samples at RT in an extended wavenumber range of 4000–1100 cm. The FTIR spectra were measured by N. Argawala and V. G. Eichmann. The *T. vestitus* data shown in this figure is also shown in Fig. 8.1.

much closer to zero. This also has an effect on the S/N: the WL *C. thermalis* transients are significantly noisier than those of the other two samples. Additionally, the WL *C. thermalis* transients show kinetics on the tens to hundreds of microseconds time scale which are not apparent in the other samples' transients.

To characterize the nanosecond kinetics, both sets of transients of the *C. thermalis* samples were fit globally to a sum of two exponentials and an offset, analogously to the main fit approach used for *T. vestitus*, which accounts for the IRF (see Section 8.1). For the FRL grown samples time constants of 37 and 585 ns were determined; the WL grown sample revealed slower kinetics of 41 and 959 ns. The amplitudes of the two components showed an overall similar behavior between the two samples, although the values were generally
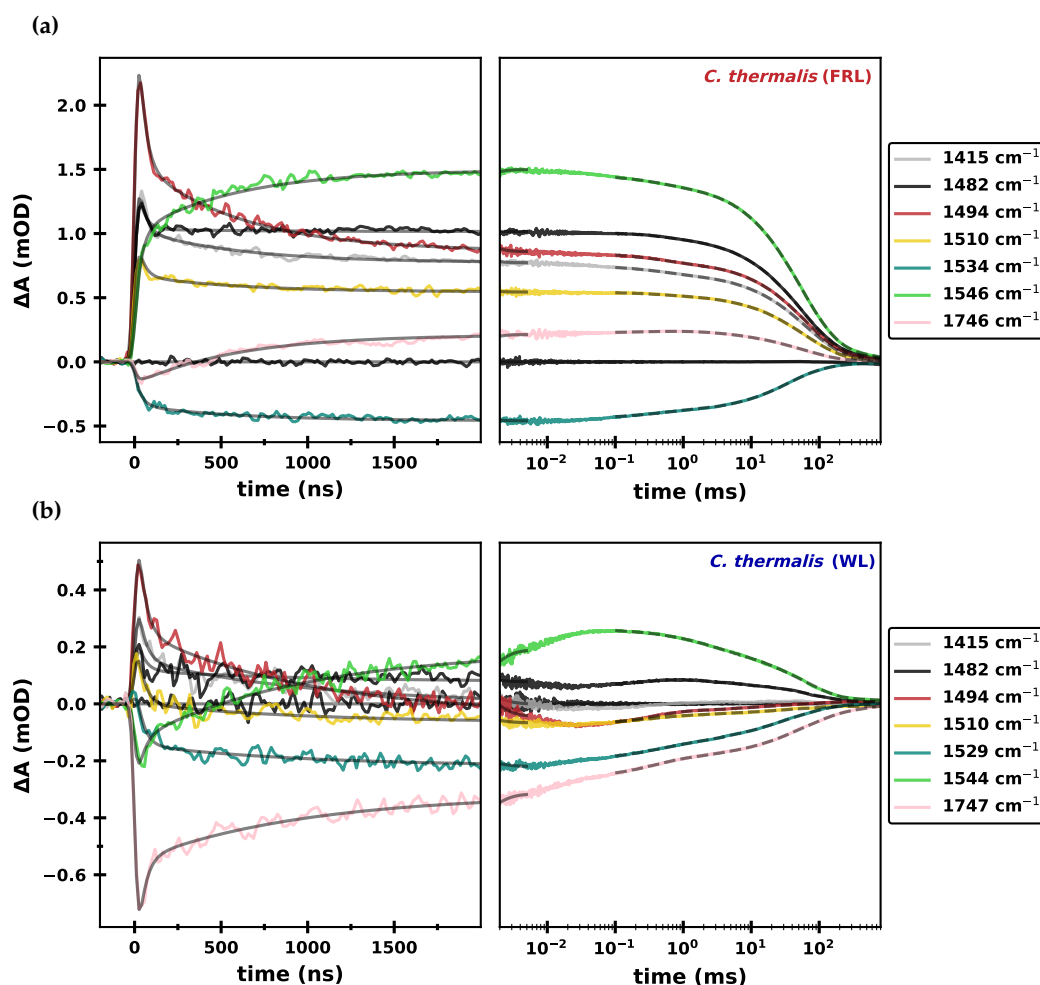
Figure 8.11: Flash-induced transient IR absorption changes of PSI from *C. thermalis* at seven wavenumbers. The IR difference signal is shown on a linear scale up to 2 ms (*left*) and on a logarithmic x-axis from 2–800 ms (*right*). **(a)** Transient absorption changes for FRL grown *C. thermalis* at 1415 (*grey*), 1482 (*black*), 1494 (*red*), 1510 (*yellow*), 1534 (*dark green*), 1542 (*light green*) and 1746 cm^{-1} (*pink*). **(b)** Transient absorption changes for WL grown *C. thermalis* at 1415 (*grey*), 1482 (*black*), 1494 (*red*), 1510 (*yellow*), 1529 (*dark green*), 1544 (*light green*) and 1747 cm^{-1} (*pink*). In both (a) and (b) the fit curves obtained from globally fitting the transients to a sum of two exponentials in the nanosecond region (up to 5 μs) are shown in *solid grey* lines; the fit curves using five exponentials in the millisecond region (0.1–800 ms) are shown in *dashed grey* lines. The signal in absence of laser flash excitation is shown oscillating around zero in *black* (measured at 1482 cm^{-1}) and serves as a demonstration of the noise level.

larger in the FRL grown sample (Fig. 8.12a). When looking at the amplitude plots, the most striking difference between the samples is again the difference in their offset: The contribution of y_0 is much smaller in the WL *C. thermalis* at all wavenumbers, even reaching nearly zero at 1415 and 1494 cm^{-1} (Fig. 8.12).

Some major differences in the amplitude ratios were detected: At 1544 cm^{-1} the amplitude of the slower phase is more pronounced than that of the faster phase in the WL sample, but *vice versa* in the FRL sample; at 1746 cm the WL sample shows a strong negative contribution of the fast phase, which is basically absent in the FRL sample.
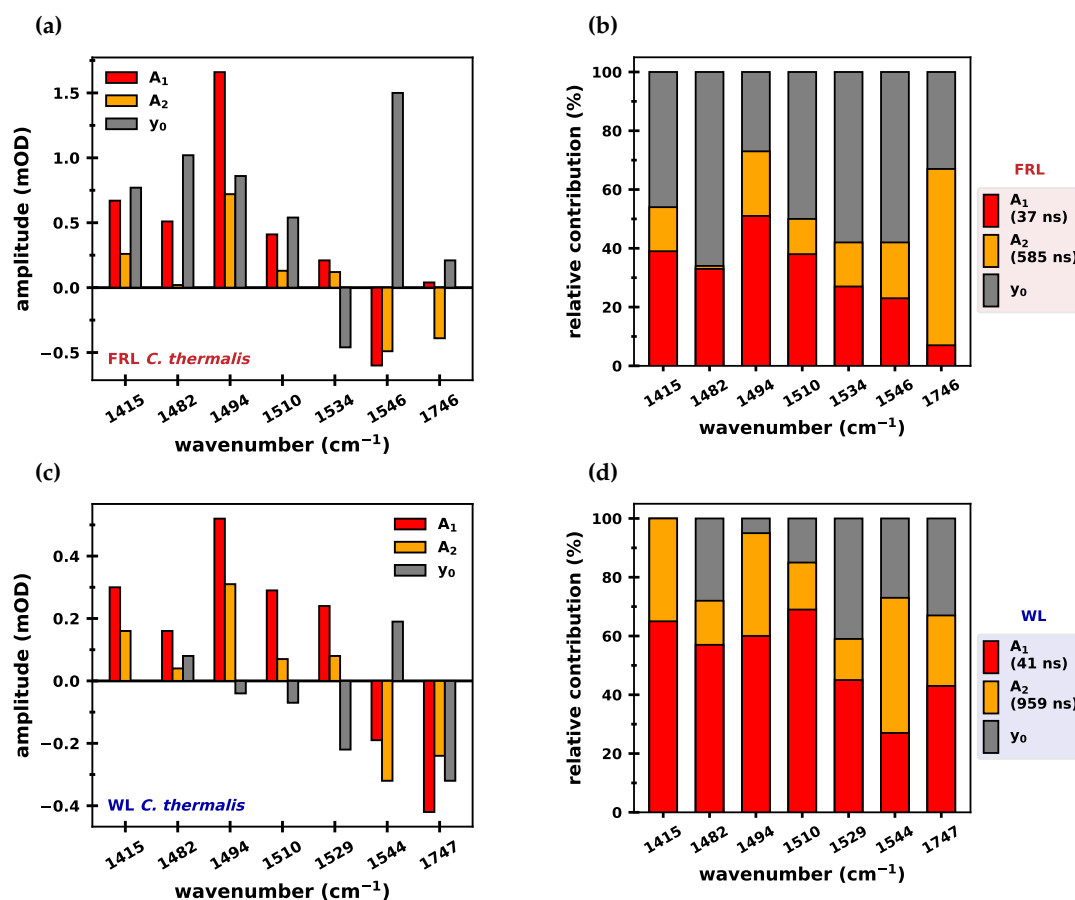
Figure 8.12: Results of the global analysis of the nanosecond region of the data in Fig. 8.11. The parameters were obtained from bi-exponential fits of the data up to 5 µs after the flash. **(a)** Absolute amplitudes A_1 and A_2 of the exponential components ($\tau_1 = 37$ ns and $\tau_2 = 585$ ns) and offset y_0 of FRL grown *C. thermalis* PSI (Fig. 8.11a), and **(b)** relative contributions of A_1, A_2 and y_0. **(c)** Absolute amplitudes A_1 and A_2 of the exponential components ($\tau_1 = 41$ ns and $\tau_2 = 959$ ns) and offset y_0 of WL grown *C. thermalis* PSI (Fig. 8.11b), and **(d)** relative contributions of A_1, A_2 and y_0. A_1, A_2 and y_0 correspond to contributions of A_{1B}^-, A_{1A}^- and $P700^+$, respectively.

To facilitate visual comparison of the kinetics between the three PSI samples, the nanosecond region of the transients at 1494 cm^{-1} are displayed normalized to their value at 100 ns (the point at which the influence of the fast phase is negligible) and vertically offset to their value at 3 µs in Fig. 8.13a. It is clearly visible that the slow nanosecond phase is the fastest in *T. vestitus* and the slowest in WL grown *C. thermalis*. The fast nanosecond phase looks the same in all three samples; whether or not there are significant differences cannot be determined with the current temporal resolution of the setup.

To further characterize the nanosecond kinetics, the obtained time constants were fixed in a global fit of the time-resolved spectral data sets of the *C. thermalis* PSI samples. The resulting decay associated spectra of the fast phases were very noisy—even more so than for the *T. vestitus* data—and are thus not shown here. The DAS of the slower phase, on the other hand, show clear spectral features (Fig. 8.14). Comparing the DAS of the three samples reveals many similarities, which supports the assumption that the slow nanosecond phase
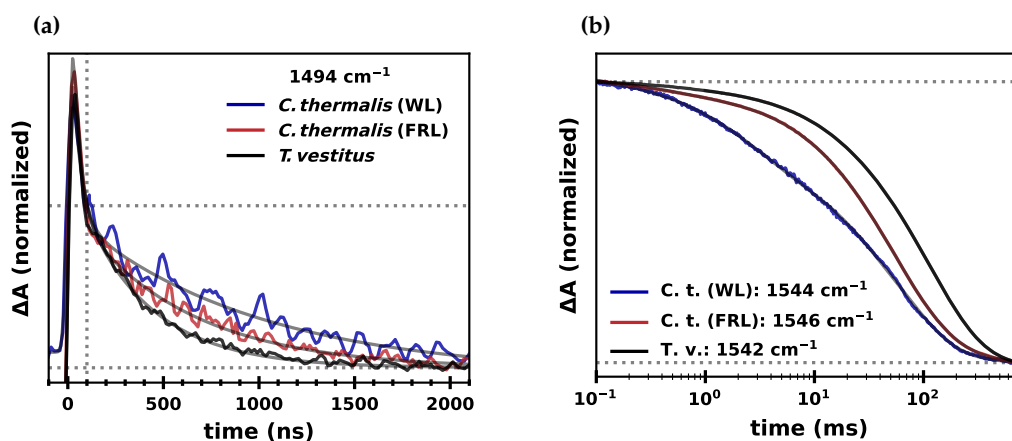
Figure 8.13: Direct comparison of transient IR absorption changes of PSI from FRL and WL *C. thermalis* as well as PSI from *T. vestitus*. **(a)** Nanosecond absorption changes at 1494 cm^{-1}, offset to their value at 3 µs and normalized to their value at 100 ns. The WL *C. thermalis* transient was smoothed with a sliding average algorithm with a window size of 3. **(b)** Millisecond absorption changes at 1544 cm^{-1} (WL grown *C. thermalis*), 1546 cm^{-1} (FRL grown *C. thermalis*) and 1542 cm^{-1} (*T. vestitus*). The transients are offset to their value at 800 ms and normalized to their value at 0.1 ms.

is sufficiently well resolved in the low S/N spectral data sets. In contrast, the DAS of the fast nanosecond phase looks very different for each sample, another indication that the fast phase is insufficiently resolved in the low S/N spectral data sets (*not shown*).
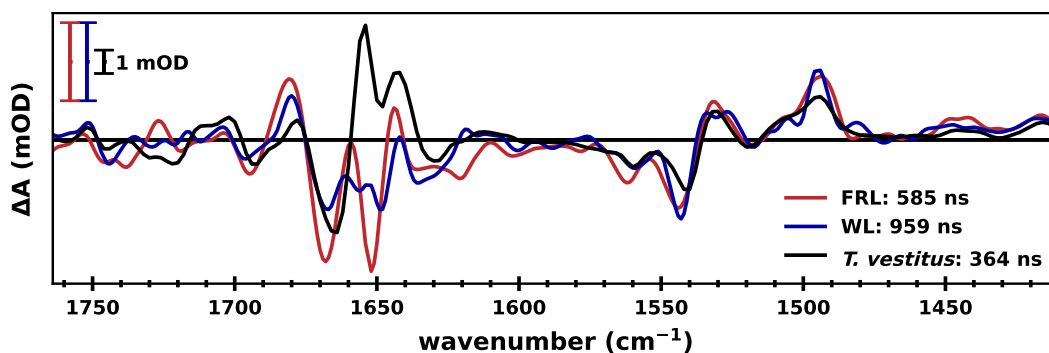

Figure 8.14: Decay associated spectra of the slow nanosecond phases of three PSI variants. The DAS of the 364 ns phase of *T. vestitus* PSI is shown in *black*, the DAS of the 595 ns phase of FRL grown *C. thermalis* is shown in *red* and the DAS of the 962 ns phase of WL grown *C. thermalis* is shown in *blue*. The DAS were obtained by globally fitting the low S/N time-resolved spectral data sets to a sum of two exponentials with the two time constants fixed to the values obtained from fitting the data in Fig. 8.2 and Fig. 8.11. The DAS were smoothed by applying a sliding average algorithm with a window-size of 2 data points.

8.2.4 Recombination Kinetics

The millisecond kinetics of the seven transients of each *C. thermalis* PSI variant were analyzed by globally fitting them to a sum of five exponentials in the range of 0.1–800 ms; the resulting fit curves are shown in dashed grey lines in Fig. 8.11. The obtained time constants
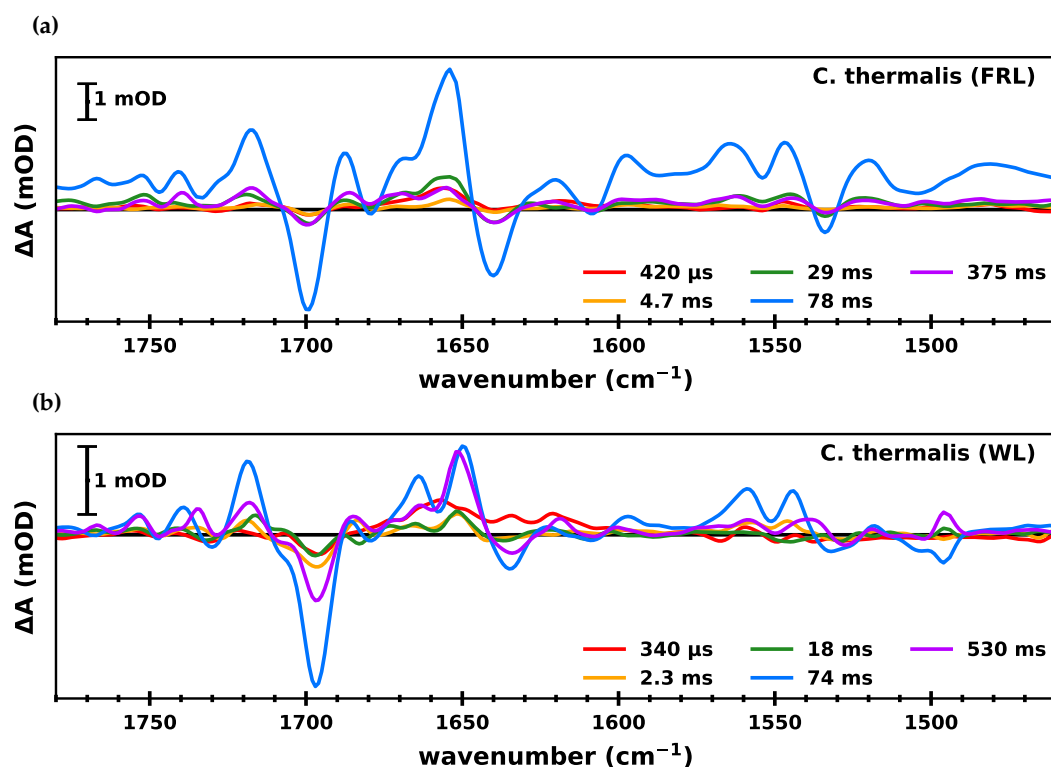
Figure 8.15: Decay associated spectra of the millisecond kinetics of PSI core particles from C. thermalis. The DAS were obtained by globally fitting the time-resolved spectral data sets to a sum of five exponentials and an offset. **(a)** DAS of FRL grown *C. thermalis*, with the time constants fixed to 0.42, 4.7, 29, 78 and 375 ms. The time constants were obtained from fitting the data in Fig. 8.11a. **(b)** DAS of WL grown *C. thermalis*, with the time constants fixed to 0.34, 2.3, 18, 74 and 530 ms. The time constants were determined by fitting the data in Fig. 8.11b.

were similar for both variants, but—with exception of the slowest phase—overall slightly slower for FRL grown *C. thermalis* (0.42, 4.7, 29, 78 and 375 ms) than for the WL grown form (0.34, 2.3, 18, 74 and 530 ms).

In Fig. 8.13b the kinetics of all three PSI variants at around 1544 cm^{-1} are normalized to their value at 0.1 ms, enabling a direct visual comparison. WL grown *C. thermalis* shows non-negligible fast decay components, which are far less pronounced in the other two samples. The reasons for this are not clear and require further investigation. As shown in Fig. 8.8 for *T. vestitus*, the dryness of the sample seems to have an influence. However, this might also have rather been an effect of the electron donor concentration; further experiments are needed for clarification.

As for *T. vestitus*, the determined millisecond time constants were fixed in a global fit across the time-resolved spectral data sets of each *C. thermalis* samples. The resulting decay associated spectra are shown in Fig. 8.15. The DAS of the FRL grown variant show that the recombination kinetics are dominated by the 78 ms component.

For the WL grown variant, it is a similar phase (74 ms) that is most dominant, but unlike for the other two PSI variants, the other four millisecond components also contribute in non-negligible amounts.

8.2.5   Discussion

WL-PSI from C. thermalis exhibits an unusual P700$^+$/P700 spectrum

The QCL spectra of the 0.1–1 ms region of PSI from WL and FRL grown *C. thermalis* (Fig. 8.10) are highly similar to their photoaccumulated P700$^+$ F$_{a/b}^-$/P700/F$_{a/b}$ FTIR counterparts. The dominant phase of the millisecond recombination kinetics (Fig. 8.15) also has a very similar spectral fingerprint in both samples, indicating that the ∼75 ms DAS is likely directly associated with P700$^+$/F$_{a/b}^-$→P700/F$_{a/b}$ recombination in both variants.

When grown under far-red light conditions, gene expression in organisms that can undergo FaRLiP, such as *C. thermalis*, is altered to produce several paralogous proteins that replace some of the core subunits (including PsaA and PsaB) of the photosystems (Zhao et al., 2015). The FRL-PSI form of *C. thermalis* contains several Chl *f* molecules (Nürnberg et al., 2018), allowing the cells to photosynthesize using light that WL-PSI forms cannot harvest. *T. vestitus* cannot undergo FaRLiP and thus produces a WL-PSI form.

Going into the experiments on *C. thermalis*, the expectation was that their P700$^+$/ P700 spectra would show some subtle differences, similar to what was observed for *F. thermalis* (Hastings et al., 2019). However, as is blatant in Fig. 8.10, the WL-PSI form of *C. thermalis* displays a P700$^+$/P700 spectrum that differs strongly from the FRL-PSI form, as well as from *T. vestitus*.

First of all, it is striking that the mid-IR broad electronic absorption band (Fig. 8.10d) is much less pronounced in PSI from WL *C. thermalis* than in the other two samples shown here. As a result, its difference spectrum in the 1800–1300 cm^{-1} region is hardly affected by a positive upshift along the y-axis, but instead the difference bands are more evenly distributed around zero.

In early reports of P700$^+$/P700 spectra, a broad electronic band was not always observed (Nabedryk et al., 1996) and P700 was initially interpreted to be monomeric. Advancements in the detection sensitivity of FTIR experiments later led to a revision of this interpretation, as broad bands were observed after all (Breton, 2001). The intensity of the mid-IR broad band was argued to be dependent on several factors, including (i) the asymmetry of P700$^+$: if the charge is predominantly localized on one chlorophyll, this will lead to a lower intensity of the band, (ii) the strength of the resonance interaction, which allows the electron to move between the two chlorophylls: weak resonance interaction leads to a lower band intensity and (iii) the pigment species: different chlorophylls might inherently give rise to broad mid-IR bands of different magnitude (Breton et al., 1992; Noguchi et al., 1998).

The weakly pronounced broad mid-IR band of WL-PSI from *C. thermalis* (Fig. 8.10d) could thus indicate that the charge is more localized on one of the P700 pigments and/or the resonance interaction between the two pigments is disfavored, e.g. by changes in the orientation and/or overlap of the pigments, or by changes in their molecular environment. It could also be an indication that one or both of the P700 pigments is of a different nature than in other PSI variants.

Careful inspection of the IR difference bands in the 1760–1480 cm^{-1} region reveals several differences to previously reported P700$^+$/P700 spectra (as well as to the spectrum of *T. vestitus* shown in this work): In the review by Breton (2001) spectra of four different PSI species are shown, which all have negative features at 1533 and 1735 cm^{-1} and positive features at 1742 and 1652–1654 cm^{-1}. These features are all down-shifted by 2–6 cm^{-1} (to 1529, 1729, 1739 and 1650 cm^{-1}, respectively) in WL-PSI from *C. thermalis* (Fig. 8.16). Fur-
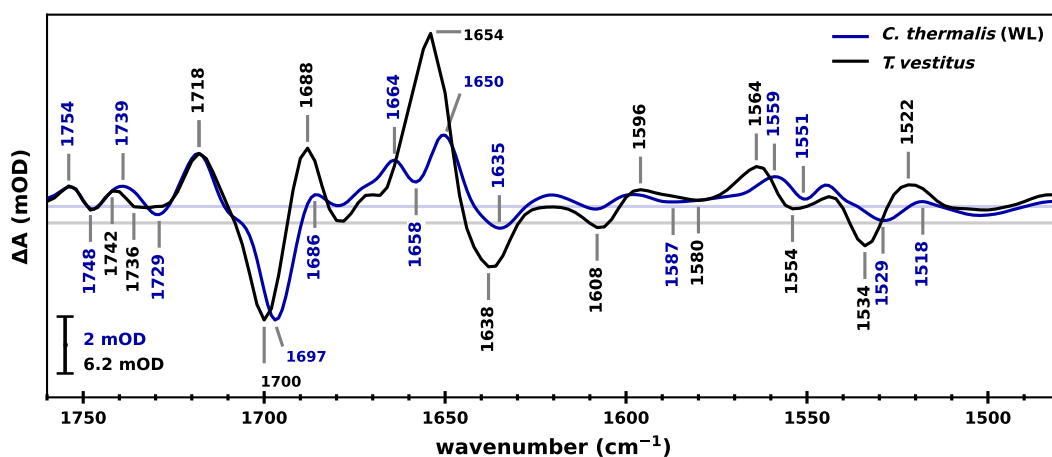
Figure 8.16: Infrared difference spectra of PSI core particles from WL grown *C. thermalis* and *T. vestitus*. QCL spectra of *C. thermalis* grown under white-light conditions (*blue*), as well as a spectrum of *T. vestitus* (*black*), obtained by averaging the signal between 0.1–1 ms at each wavenumber. The spectra are shown scaled to their difference band at about 1718(+)/1700(−) for easier visual comparison. Note that the exact position of the negative peak labeled as 1736 cm⁻¹ (*black*) was determined from the FTIR spectrum shown in Fig. 8.1a. The *T. vestitus* QCL spectral data set has a gap 1734 cm⁻¹ and thus has a higher imprecision around that wavenumber.

thermore, the prominent peak at 1664 cm⁻¹, which is clearly separate from the 1650 cm⁻¹ peak, has not been observed for other cyanobacterial PSI. A similar feature was however observed in PSI from *Chlamydomonas reinhardtii* (*C. reinhardtii*) (Hastings et al., 2001; Breton, 2001).

Difference bands around 1749(−)/1754(+) cm⁻¹ and 1733–1735(−)/1742(+) cm⁻¹ have previously been assigned to the 13³-methyl ester C=O group of the P_B and P_A pigments of P700⁺/ P700 (Breton, 2001, 2006). (For numbering of the chlorophyll atoms see Fig. 1.12 in the Introduction.) Figure 8.16 shows clearly, that the P_B band is the same in WL-PSI from *C. thermalis* and *T. vestitus*, while the P_A band is downshifted in *C. thermalis*.

Difference bands at around 1697–1700(−)/1718(+) cm⁻¹ and 1637(−)/1656(+) have been assigned to 13¹-keto C=O group of P_B and P_A, respectively (Breton, 2001, 2006). The P_B bands of WL-PSI from *C. thermalis* and *T. vestitus* are both within the range of previously reported positions; the P_A band of *C. thermalis*, however, appears strongly perturbed upon P700⁺ formation: the broad peak around 1654 cm⁻¹ appears to be split in two (1650 and 1664 cm⁻¹). Around 1650 cm⁻¹, a contribution of amide I modes is expected (Barth, 2007; Hamacher et al., 1996), so the 1656(+) peak could generally be a mixture of amide I and 13¹-keto C=O vibrations. If the P_A 13¹-keto C=O mode were to upshift to 1664 cm⁻¹ in *C. thermalis* WL-PSI, this could explain the two distinct peaks (with the one at 1650 cm⁻¹ then associated with amide I vibrations). If the P_A 13¹-keto C=O group is indeed upshifted in *C. thermalis*, this could indicate weakened H-bonding of P_A compared to other PSI variants (Breton et al., 1999).

A band at 1534–1536(−) cm⁻¹ has been suggested to be associated with the chlorophyll macrocycle, but the authors could not exclude an attribution to an amide II mode (Hamacher et al., 1996). Either way, the downshift of this band in WL-PSI from *C. thermalis* could imply an altered protein environment of P700.

Comparison of WL-PSI and FRL-PSI

The fact that WL-PSI exhibits a usual $P700^+/P700$ spectrum, as discussed above, makes a direct comparison to FRL-PSI more difficult. The $P700^+/P700$ spectra of (WL-PSI) *T. vestitus* and FRL grown *C. thermalis* are quite similar (Fig. 8.10c), with only some subtle differences that on first glance appear similar to differences reported for PSI from WL vs. FRL grown *F. thermalis* (Hastings et al., 2019). However, it cannot be excluded that *T. vestitus* and *C. thermalis* exhibit some species related differences, which may negatively affect the identification of spectral changes due to FaRLiP. As a compromise, FRL-PSI will be compared to both WL-PSI from *C. thermalis* and to PSI from *T. vestitus* in the following. As discussed above, the unusual features of *C. thermalis* WL-PSI seem to be associated mostly with P_A, thus a comparison of P_B features between FRL and WL-PSI from *C. thermalis* may still be reasonable.

Figure 8.17 shows the three $P700^+/P700$ spectra with labeled peaks, as well as double difference spectra (DDS) of the WL forms minus FRL-PSI. The P_B 13^3-methyl ester C=O $1754(+)/1748(-)$ difference band is downshifted by 1–2 cm^{-1} in FRL-PSI compared to both WL-PSI forms. The $1718(+)$ peak of the P_B 13^1-keto C=O remains unchanged in all PSI variants, but its associated negative peak varies between 1700–1697 cm^{-1}. The FRL-PSI peak (1699 cm^{-1}) shows an upshift of 2 cm^{-1} when compared to WL-PSI from *C. thermalis*.[41] This down- and up-shift of the P_B C=O features is in perfect agreement with what was observed for *F. thermalis* (Hastings et al., 2019).

The P_A 13^1-keto C=O difference band at $1654(+)/1638(-)$ in *T. vestitus* seems hardly upshifted in FRL-PSI ($1654(+)/1640(-)$ cm^{-1}). However, in the FTIR spectrum with 2 cm^{-1} resolution (Fig. A6.3 in the Appendix), FRL-PSI shows a splitting of the 1654 cm^{-1} peak to 1654 and 1659 cm^{-1}, which could indicate a 5 cm^{-1} upshift of the keto C=O mode. This is again similar to the upshift of 6 cm^{-1} observed in *F. thermalis*. In contrast, the P_A methyl ester C=O mode downshifts slightly by 1–3 cm^{-1} in FRL-PSI from $1742(+)/1736(-)$ in *T. vestitus* to $1741(+)/1733(-)$ cm^{-1}.

DFT calculations by Hastings et al. (2019) on chlorophylls in THF suggest that the neutral Chl *f* keto C=O bands should be 11 cm^{-1} upshifted compared Chl *a*, while the additional 2^1-formyl C=O group unique to Chl *f* is expected to give a feature around 31 cm^{-1} downshifted from its keto C=O mode. Upon cation formation, the formyl C=O mode should upshift around 21 cm^{-1}.

We do not see a large upshift of either of the C=O keto modes, neither do we see large features assignable to a formyl C=O mode, which suggests that neither P_A nor P_B of P700 are Chl *f* in FRL PSI from *C. thermalis*. The shifts in the FRL spectrum are likely rather electrochromic effects of other nearby molecules on P700. In line with what was reported for *F. thermalis* (Hastings et al., 2019), the $1692(-)/1702(+)$ cm^{-1} feature in the DDS (Fig. 8.17c) could arise from a keto C=O mode of a Chl *a* in WL-PSI, which is replaced with Chl *f* in FRL-PSI. This upshift of 10 cm^{-1} matches the above-mentioned calculated value. Because the magnitude of the feature suggests a strong electrochromic effect and thus a close vicinity to P700, Hastings et al. (2019) assign it to Chl *a*/Chl *f* in a A_{-1} site. The features at 1754–$1756(+)/1750(-)$ cm^{-1} in both DDS of Fig. 8.17 are also in line with this assignment, as they suggest a shift in the corresponding methyl ester C=O mode of the chlorophyll in question.

---

[41]However, the FRL-PSI peak (1699 cm^{-1}) appears slightly downshifted when comparing to *T. vestitus* (1700 cm^{-1}), thus, because of the unusual *C. thermalis* WL-PSI spectrum, some uncertainty remains.
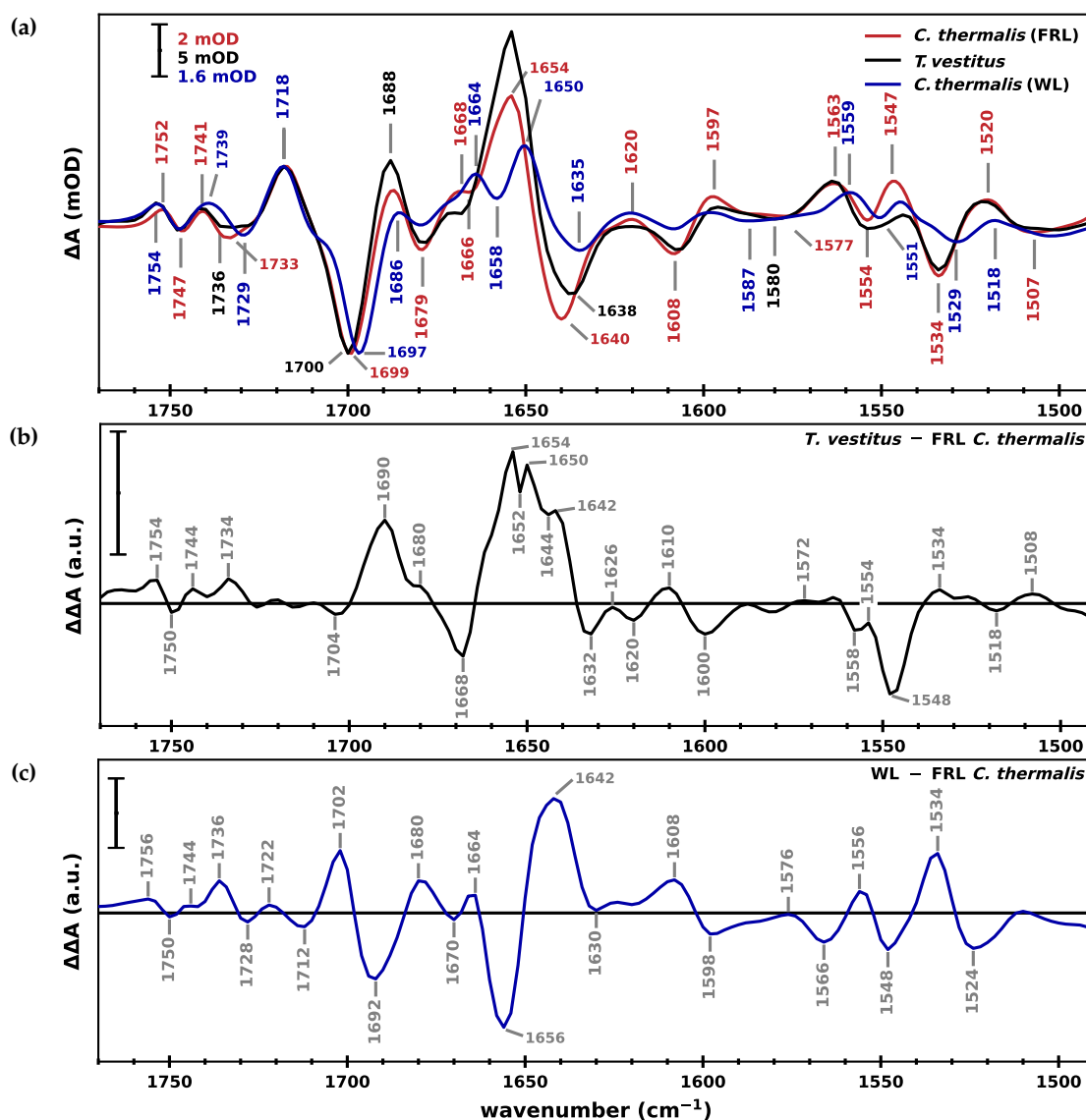
Figure 8.17: Infrared difference and double difference spectra of PSI core particles from _T. vestitus_ and WL and FRL grown _C. thermalis_. (a) QCL spectra of _C. thermalis_ grown under white (_blue_) and far-red light conditions (_red_), as well as a spectrum of _T. vestitus_ (_black_), obtained by averaging the signal between 0.1–1 ms at each wavenumber. The spectra are shown scaled to their difference band at about 1718(+)/1700(−) for easier visual comparison. **(b)** Double difference spectrum of the _T. vestitus_ and FRL grown _C. thermalis_ spectra shown in (a). **(c)** Double difference spectrum of the WL grown and FRL grown _C. thermalis_ spectra shown in (a). The scale bar in (b) and (c) is of the same size as in (a).

Features at 1630–1632(−)/1608–1610(+)/1598–1600(−) cm^{-1} are visible in both DDS of Fig. 8.17, but it is not clear what they are caused by. The features in the amide II region (around 1548 cm^{-1}) are an indication that all three PSI variants in this work exhibit some differences in the protein environment of P700.

While the assignment of a Chl f in an A$_{-1}$ site is aligned with other spectroscopic results (Nürnberg et al., 2018; Kaucikas et al., 2017; Zamzam et al., 2019) (but see also Cherepanov et al. (2020)), it is at odds with structural studies, which have given no evidence for Chl f units in the electron transport chain (ETC)(Gisriel et al., 2022, 2020; Kato et al., 2020). A

recent study by Gisriel et al. (2023), however, softened their previous statements (which claimed no change in the ETC): they found that the chlorophyll in the A_{0B} binding site is slightly rotated in all available FRL-PSI structures compared to WL-PSI. Whether such a mere slight rotation could explain the changes in the $P700^+/P700$ spectra of FRL-PSI is questionable. More experiments will be needed for a definitive answer to the question of whether Chl *f* is present in the ETC or not.

Nanosecond kinetics of C. thermalis WL-PSI and FRL-PSI

Biexponential global fits of transients at seven different wavenumbers (Fig. 8.11) yielded time constants of 41 and 959 ns (WL-PSI) and 37 and 585 ns (FRL-PSI). We assign the fast component to $A_{1B}^- \rightarrow F_x$ and the slow component to $A_{1A}^- \rightarrow F_x$, analogously to the results on *T. vestitus*. As discussed in detail in Chapter 8.1 for *T. vestitus*, there is a high uncertainty regarding both exact value as well as amplitude of the fast nanosecond component, as it is at the limit of the setup's temporal resolution. This is also evident in Fig. 8.13, which shows the normalized transients at 1494 cm^{-1} of all three PSI variants: while the differences in slow nanosecond kinetics are discernible by visual inspection, the fast nanosecond kinetics look the same. Whether or not there is a significant difference in the magnitude of the fast nanosecond kinetic between the three PSI variants cannot be concluded from this data.

The slow nanosecond component, on the other hand, is well resolved and implies that the A-branch kinetics from phylloquinone A_1^- to F_x are slower in FRL-PSI from *C. thermalis* than in *T. vestitus*, and even slower in WL-PSI from *C. thermalis*. Figure 8.18 shows decay associated spectra of this kinetic—with labeled peaks for easier comparison—for the three PSI variants. (In the following we assume that F_x does not contribute significantly (Breton et al., 1999; Hastings and Sivakumar, 2001); for numbering of a phylloquinone molecule see Fig. A6.4 in the Appendix.) The three DAS show the following similarities:

(i) clear peaks at 1494(+) and 1418–1416(+) cm^{-1}, which have been previously assigned to semiquinone (A_1^-) $C_1{=}O$ and $C_4{=}O$ modes, respectively (Rohani et al., 2019);

(ii) 1752–1753(+)/1744–1746(–) cm^{-1} difference peaks (although in FRL-PSI they are barely above noise-level and seem to be overlaid by another feature), which have been suggested to arise from the 13^3 ester C=O mode of A_0, due to electrochromic effects (Sivakumar et al., 2005);

(iii) peaks at 1693–1696(–)/1678–1681(+) cm^{-1}, previously assigned to the 13^1 keto C=O of A_0 (Sivakumar et al., 2005; Hastings, 2015);

(iv) features at 1678–1681(+)/1664–1668(–) cm^{-1}, assigned to amide I modes (Sivakumar et al., 2005);

(v) features at 1559–1562(–)/1551–1554(+)/1531–1534(+)/1517–1519(–) cm^{-1}, which are in part assignable to amide II modes (Sivakumar et al., 2005).

The observation of these features in the here presented DAS support the assignment of the slow nanosecond kinetic to ET from A_1^- to F_x. Some features, however, appear uniquely in the DAS of FRL-PSI:

(i) a small, but clearly discernible pair of bands at 1738(–)/1727(+)/1719(–) cm^{-1} is not observed for the two WL-PSI forms. It is present, even though weakly pronounced, in $A_1^- - A_1$ 77 K FTIR double difference spectra of *Synechocystis* sp. PCC 6803 (Hastings, 2015);

(ii) the negative feature at 1630 cm^{-1} (*T. vestitus*) or 1636 cm^{-1} (*C. thermalis* WL-PSI) appears to be split in two in FRL-PSI: 1636(–)/1630(+)/1621(–) cm^{-1}. The 1630 cm^{-1} feature, however, is possibly present in the broad shoulder of 1636(–) cm^{-1} in WL-PSI.
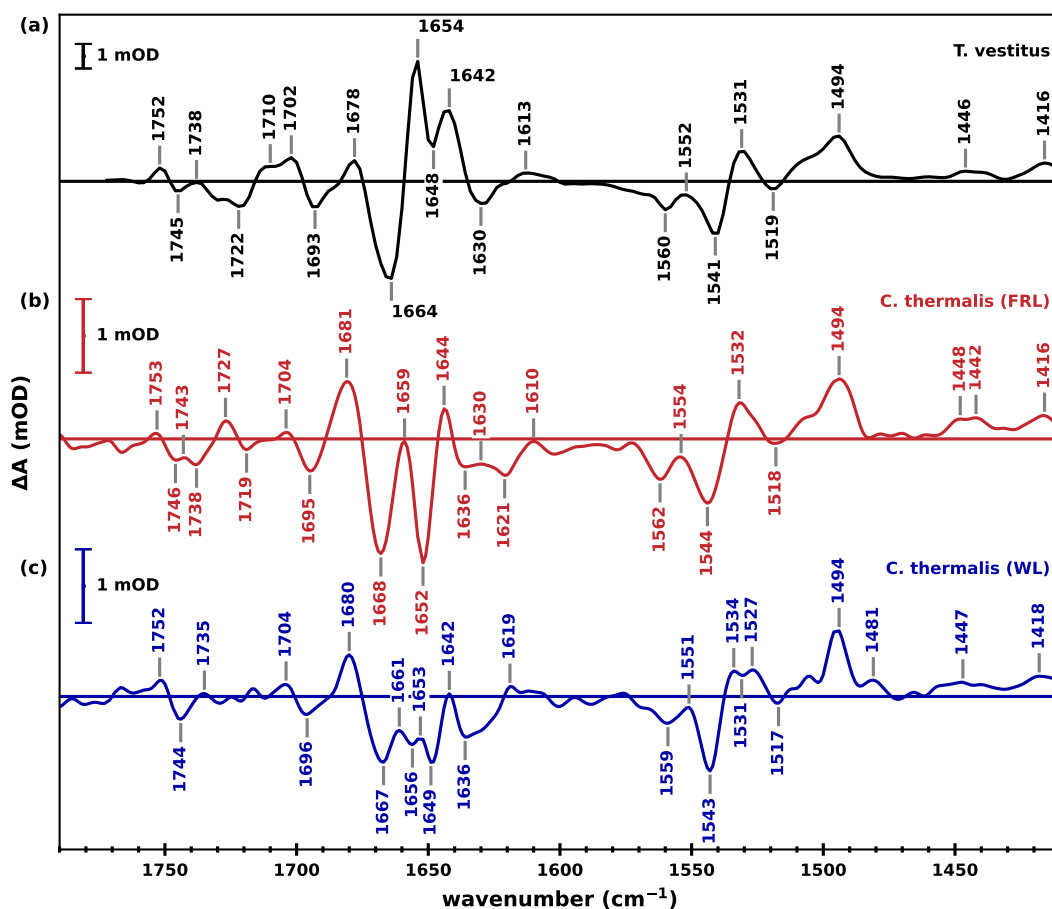
Figure 8.18: Detailed look at the decay associated spectra of the slow nanosecond phases (A_{1A}^{-}/A_{1A}) of three PSI variants. The DAS of the 364 ns phase of *T. vestitus* PSI is shown in *black*, the DAS of the 585 ns phase of FRL grown *C. thermalis* is shown in *red* and the DAS of the 959 ns phase of WL grown *C. thermalis* is shown in *blue*. The DAS were obtained by globally fitting the low S/N time-resolved spectral data sets to a sum of two exponentials with the two time constants fixed to the values obtained from fitting the data in Fig. 8.2 and Fig. 8.11. The DAS were smoothed by applying a sliding average algorithm with a window-size of 2 data points. The data shown here is identical to the data shown in Fig. 8.14.

One first glance, the features between 1640 and 1680 cm^{-1} look vastly different between the three PSI variants. Besides some small wavenumber shifts, they however only differ (albeit strongly) in their relative amplitudes. The FRL-PSI DAS looks very similar to the $A_1^{-} - A_1$ FTIR spectra on *Synechocystis* sp. PCC 6803 (Hastings, 2015) in this spectral region. In WL-PSI from *C. thermalis*, the peak around 1654 cm^{-1} (*T. vestitus*) or 1659 cm^{-1} (FRL-PSI) appears to be split into 1661(+)/1656(−)/1649(+) cm^{-1}. Possibly this is connected to the unusual 1664(+)/1658(−)/1650(+) feature in the P700^{+}/P700 difference spectrum (Fig. 8.17a). If the latter is due to P700^{+}/P700 itself, which appears to be the case due to the magnitude of this feature, this would imply a quite long-range electrochromic effect.

An interpretation of the differences in the $A_1^{-} - A_1$ spectra is difficult, also since some bands have not been assigned yet, and will likely require further experiments.

8.2.6   Conclusions and Outlook

$P700^+/P700$ difference spectra were obtained for PSI from WL- and FRL-grown *C. thermalis*. FRL-PSI showed similarity to spectra of FRL-PSI from *F. thermalis* (Hastings, 2015), supporting their conclusion that both P700 pigments remain Chl *a* and that an A_{-1} site could be occupied by Chl *f*. The latter assignment cannot, however, be proven nor disproven by the here presented data. Comparison of FRL-PSI to WL-PSI was complicated by the fact that WL *C. thermalis* exhibits an unusual $P700^+/P700$ spectrum, with clear differences to previously reported spectra of other PSI variants (Breton, 2001; Hastings et al., 2019). The here presented data suggests alterations of pigment P_A of P700 and/or its environment.

Biphasic nanosecond kinetics were observed in PSI from WL- and FRL-grown *C. thermalis*, assigned to ET from A_1^- to F_x down the A-and B-branch. FRL-PSI exhibited faster A-side kinetics than the WL form (585 ns vs. 959 ns), but slower kinetics than *T. vestitus* (364 ns). Due to seemingly unusual properties of WL PSI from *C. thermalis*, it is difficult to conclude from this whether (and how) forward ET is affected by FaRLiP. The fast nanosecond phases exhibited the same trend, i.e. WL-PSI from *C. thermalis* showed the slowest kinetics (41 ns), followed by FRL-PSI (37 ns) and PSI from *T. vestitus* (33 ns), but due to the limited temporal resolution of the setup, this observation must be evaluated as uncertain.

Decay associated spectra of the slow nanosecond phases exhibited features that support the assignment to $A_1^- - A_1$. Some clear differences between the DAS of the three PSI variants were pinpointed, but more experiments will be necessary for a comprehensive interpretation.

8.3   Summary and Key Results

Flash-induced biphasic nanosecond kinetics were observed at various wavenumbers in three different PSI variants (PSI from *T. vestitus*, as well as PSI from WL- and FRL-grown *C. thermalis*), which were assigned to forward ET from A_1^- to F_x down the A- and B-branch. Multiphasic decay back to zero occurred within hundreds of milliseconds. A summary of the time constants is shown in Table 8.1.

From spectral time-resolved data sets, $P700^+/P700$ difference spectra were obtained, in agreement with FTIR photoaccumulated spectra. Global analysis furthermore resulted in DAS of the slow nanosecond phase, which showed similarity to low temperature FTIR A_1^-/A_1 double difference spectra of *Synechocystis* sp. PCC 6803 (Hastings, 2015). The

Table 8.1: Time constants of forward and backward electron transfer in three PSI variants. The time constants were determined by global fits across seven or eight transients (see Figs. 8.2 and 8.11). The nanosecond and millisecond time constants were determined separately from different fits. The dominant millisecond phase is printed in bold.

assignment	τ_1 (ns) $A_{1B}^- \to F_x$	τ_2 (ns) $A_{1A}^- \to F_x$	τ_3 (ms)	τ_4 (ms)	τ_5 (ms)	τ_6 (ms)	τ_7 (ms)
				$P700^+$ recombination			
T. vestitus	33	364	1.2	10.3	44.7	**126**	373
C. thermalis (WL)	41	959	0.34	2.3	18	**74**	530
C. thermalis (FRL)	37	585	0.42	4.7	29	**78**	375

P700$^+$/P700 spectrum of FRL-PSI from *C. thermalis* resembles that of FRL-PSI from *F. thermalis* (Hastings et al., 2019). WL-PSI from *C. thermalis*, however, exhibits an unusual P700$^+$/P700 spectrum, indicating alterations of the pigment P$_A$ of P700 and/or its direct (unusually conserved) environment.

9 | Summary and Outlook

In the here presented work, time-resolved single-frequency IR spectroscopy was applied to PSII and PSI, to gain new insight into the molecular mechanism of light-induced ET and PT processes. A schematic outline of the thesis is shown in Figure 9.1. In the following, the key results of the thesis will be summarized.
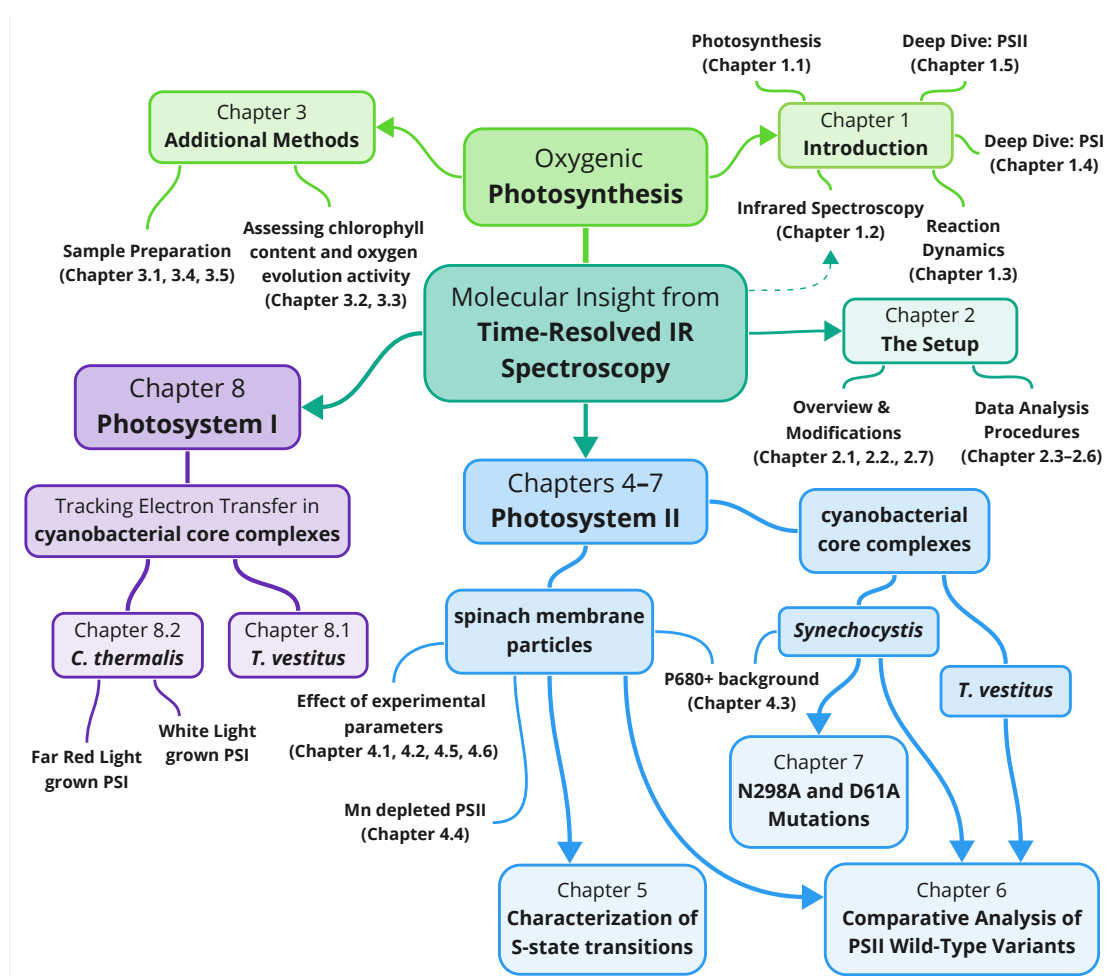

Figure 9.1: Schematic overview of this thesis.

9.1 Key Results

Experimental Advances (Chapter 2)

The quantum cascade laser (QCL)-based time-resolved single-frequency IR setup was first built by Philipp Simon (2019). While it was functional, it was relatively complicated to handle, both on software and hardware level. Modifications to the setup and its software were necessary (i) to improve the experimental efficiency (*inter alia* to allow for short-term projects on the setup, e.g. by master students) and (ii) to improve the overall reliability, especially concerning data quality. The following is a summary of the most important improvements:

▶ A systematic error in the setup—which led to imprecise measurements of the excitation flash intensity and thus to an imprecise heat artefact correction (see Chapter 2.7)—was discovered and resolved. A motorized attenuator was added to the excitation beam path, which allows for remote regulation of the excitation flash intensities without changing the Q-switch delay. Besides resolving the aforementioned error, this has the advantage of allowing pulse properties, such as the pulse width, to remain largely unchanged between excitation flashes (which further improves the accuracy of the heat artefact correction). Small (but significant) changes to the setup software greatly reduced issues during data acquisition. Furthermore, a way to easily acquire time-resolved spectral data sets with the setup was implemented in the data acquisition software (in C++). This allowed for the first-ever acquisition of QCL-based time-resolved spectral IR data sets on both photosystems (PSII and PSI).

▶ A data processing script was implemented in Python to automatically pre-process the data, including the following steps: (i) the time-resolved absorption changes are calculated from the raw channel data, whereby the reference channel is used to correct the signal from QCL-internal fluctuations, (ii) the data is filtered, removing e.g. data sets with over-saturated signals, as well as data sets with random drifts or other severe noise, (iii) all remaining data sets are averaged and subjected to a heat artefact correction, and (iv) the final processed data is saved as excel files, which can easily be loaded into Python at a later time for data analysis—but can also be examined without requiring Python knowledge. Automated data pre-processing is especially crucial for handling time-resolved spectral data, as otherwise data acquired at hundreds of individual wavenumbers need to be processed manually to obtain a single spectral data set. The data processing script automatically generates several figures, which inform the user on the various steps, allowing them to manually adjust any step if required. Furthermore, various fitting functions were implemented, including functions for decay associated spectra (DAS) analysis as well as a fitting procedure for the analysis of sub-microsecond data, which accounts for the instrument response function. Many of these scripts and functions have since also been used by others working with the setup.

Photosystem II: Key Results

▶ PSII depleted of its catalytic Mn_4CaO_x cluster (Chapter 4.4): While many FTIR studies have been published on Mn depleted PSII, this thesis presents the first-ever time-resolved IR data on the system. The measurements revealed a still functional acceptor-side, reflected in a typical period-of-two behavior. Global analysis of a time-resolved

spectral data set resulted in DAS strongly resembling $P680^+/P680$ and Q_A^-/Q_A FTIR spectra (Okubo et al., 2007; Berthomieu et al., 1990), while the steady-state spectra strongly resembled Fe^{3+}/Fe^{2+} or Fe^{2+}/Fe^{3+} FTIR spectra following an odd or even number of excitation flashes, respectively (Berthomieu and Hienerwadel, 2001; Takahashi et al., 2010). Double difference spectra of intact minus Mn depleted PSII revealed that the spectral differences are especially pronounced at some wavenumbers (e.g. in the amide I and II regions), indicating that in those spectral regions the influence of broken PSII centers (i.e. PSII units that have lost their Mn_4CaO_x cluster) on IR measurements may be especially strong.

▶ S-state transitions of spinach PSII (Chapter 5): High-quality transients were obtained at select wavenumbers; in addition a time-resolved spectral data set covering the region of 1780 to 1310 cm^{-1} was acquired at a lower signal-to-noise ratio (S/N). Global fitting of the high S/N transients reproduced many time constants of the ET and PT events of the S-state cycle, as well as the slowest $P680^+$ reduction step and several acceptor-side related kinetics. By comparing data analysis with and without accounting for the $P680^+$ background kinetics—arising from a broad $P680^+$ electronic band overlaying the vibrational bands (e.g. Noguchi et al., 1998)—it was shown that kinetics slower than about 30 μs are mostly unaffected by the background kinetics. Global analysis of the time-resolved spectral data sets resulted in DAS which facilitated the assignment of the kinetics to different events. Additional measurements in D_2O allowed for the quantification of kinetic isotope effects (KIE) as well as the observation of deuteration-induced band shifts.

Measurements at several pH values between 4.6–7.8 revealed a relatively strong pH dependency of the time constants of both the PT and ET step of the $S_2{\to}S_3$ transition. Together with a KIE of 3.1–4.4 found for the PT step, this supports the previous assignment of this kinetic phase to a proton removal from the Mn_4CaO_x cluster (Klauss et al., 2012a), rather than merely to the rearrangement of a hydrogen-bond network as suggested by others (Sakamoto et al., 2017). The pH dependency of the ET step of the $S_3{\to}S_0$ transition was weaker, but still sizable, while any pH dependency observed for the $S_1{\to}S_2$ transition was barely above noise level.

DAS analysis of the $S_1{\to}S_2$ transition showed that peaks at about 1360(+), 1400(−) and 1585(+) cm^{-1} in the steady-state spectrum are formed concomitant with the ET step. These difference bands likely arise from symmetric (1360 and 1400 cm^{-1}) and asymmetric (1585 cm^{-1}) C=O stretch modes of carboxylate residues ligated to the Mn_4CaO_x cluster (Noguchi and Sugiura, 2003; Nakamura and Noguchi, 2016), which are perturbed upon oxidation of a Mn atom. In the $S_2{\to}S_3$ transition, the same is true for peaks at 1340(+) and 1450(+) cm^{-1}, while in other spectral regions, including around 1580–1540 cm^{-1} and 1707 cm^{-1}, the behavior of the PT step is reversed by that of the ET step, similar as discussed for the $S_3{\to}S_0$ transition below.

DAS analysis of the $S_3{\to}S_0$ transition resulted in mostly very similar spectra for the PT and ET steps as recently reported by step-scan FTIR (Greife et al., 2023). Reversible behavior of PT and ET DAS is observed between 1700–1740 cm^{-1} and 1600–1560 cm^{-1}, while the peaks between 1450–1350 cm^{-1} seem to be formed mostly concomitant with the ET step. The PT and ET DAS obtained from data in D_2O show a peak at around 1688–1686 cm^{-1} (not resolved in the step-scan FTIR data), which could arise from a deuteration-induced down-shift of part of the 1707 cm^{-1} band. This in turn would sup-

port the assignment by Greife et al. (2023) of the 1707 cm^{-1} peak to the carboxylate side chain of a glutamate (D1-E65 or D2-E312), which was interpreted to deprotonate and re-protonate concomitantly with the PT and ET event, respectively—an assignment which was recently challenged by Noguchi (2024) precisely because of the lack of down-shift of the 1707 cm^{-1} band upon deuteration in the FTIR study.

If the proposed mechanism of transient de- and reprotonation of D1-E65 or D2-E312 is correct, the $S_2{\rightarrow}S_3$ DAS suggest that a very similar process may take place in the $S_2{\rightarrow}S_3$ transition.

▶ Comparison of PSII wild-type variants (Chapter 6): The comparative analysis of spinach PSII membrane particles and PSII core particles from *T. vestitus* and *Synechocystis* revealed some clear differences: (i) the ET rate of the $S_3{\rightarrow}S_0$ transition is slower in the cyanobacterial samples, which likely relates at least in part to the sample type (core particles) rather than species-specific differences; (ii) the PT step of the $S_2{\rightarrow}S_3$ transition appears to be strongly reflected in IR absorption changes (e.g. around 1395 cm^{-1}) in spinach PSII, less so in *T. vestitus* and the least in *Synechocystis*, which may explain differences in the results of the group of Takumi Noguchi as compared to ours; (iii) some spectral differences are observable, *inter alia* a minimum at 1395 cm^{-1} in the $S_3{\rightarrow}S_0$ steady-state spectrum and the ET DAS of *Synechocystis*, which is absent in the other two samples. It was furthermore found that at some wavenumbers (e.g. 1384 cm^{-1}) the transients of all three variants resemble each other relatively strongly, while at others (e.g. 1544 cm^{-1}) they differ drastically. Differing levels of intactness of the samples were identified as a probable source for this observation: It was shown that double difference spectra of spinach PSII minus *Synechocystis* are very similar to double difference spectra of intact minus Mn depleted spinach PSII, indicating that a larger fraction of broken centers (i.e. PSII units lacking their Mn_4CaO_x cluster) in the cyanobacterial core complexes could be responsible for the altered transient absorption changes.

For *T. vestitus*, additional measurements were performed in D_2O, revealing similarly high H/D kinetic isotope effects in the $S_2{\rightarrow}S_3$ transition as for spinach PSII. While this is at odds with a time-resolved IR study by Sakamoto et al. (2017) which found a much smaller KIE for the pre-ET phase, it is in qualitative agreement with the results from a photothermal beam deflection study by Klauss et al. (2012a).

▶ D1-D61A and D1-N298A mutants (Chapter 7): The S-state transitions of two PSII point mutants (D1-D61A and D1-N298A) were compared to those of wild-type PSII core complexes from *Synechocystis*. Time-resolved IR measurements showed that while the D1-D61A mutant exhibited overall very strongly perturbed kinetics and a poor S-state cycling efficiency, the D1-N298A mutant was found to exhibit a similar miss factor as wild-type PSII. Time-resolved O_2-polarography furthermore showed that the O_2-rate of D1-N298A was similar to that of the wild-type; O_2-measurements under continuous illumination, however, revealed a severely decreased O_2 production. IR difference transients of the $S_3{\rightarrow}S_0$ transition of D1-N298A offer an explanation: While wild-type PSII showed predominantly monophasic millisecond kinetics (τ = 4.7 ms), D1-N298A exhibited a biphasic behavior with time constants of 6.5 ms and 75 ms. We propose that while O_2-evolution occurs at an effectively unaltered rate, the water insertion step (which needs to occur to reach the S_0-state) is severely slowed down. If this assignment is correct, it means that this crucial step—which is spectroscopically invisible in wild-type PSII be-

cause it is faster than the rate-limiting event—has become detectable in the D1-N298A mutant.

Photosystem I: Key Results

▶ *T. vestitus* (Chapter 8.1): Forward ET down the A- and B-branches was tracked in PSI core complexes from *T. vestitus*, constituting the first published time-resolved IR study of PSI which reached nanosecond time resolution at room temperature (Mäusle et al., 2024). ET from A_{1A} and A_{1B} to F_x was found to occur with time constants of 363 and 33 ns, respectively. $P700^+/F_{a/b}^-$ was formed within about 1 µs and was found to be stable for about 1 ms. $P700^+/P700$ recombination kinetics were observed to occur with multiphasic decay kinetics on the millisecond to hundreds of milliseconds time scale.

▶ *C. thermalis* (Chapter 8.2): When grown under far-red light (FRL) conditions, *C. thermalis* is capable of producing a chlorophyll *f*-containing PSI variant, which allows the cyanobacterium to utilize lower-wavelength light (Gan et al., 2014). Forward ET down the A- and B-branches was observed in PSI from *C. thermalis* grown under (i) white light (WL) or (ii) FRL conditions. $P700^+/P700$ spectra of FRL grown *C. thermalis* showed similarity to those previously reported for FRL grown *F. thermalis* (Hastings et al., 2019). $P700^+/P700$ spectra of WL grown PSI from *C. thermalis* exhibited unusual features, possibly indicating an unusual P_A pigment or alterations in its (usually conserved) protein environment.

▶ Decay associated spectra of the A-branch kinetics were obtained for all three PSI variants, which showed similarity to low temperature FTIR A_1^-/A_1 double difference spectra of *Synechocystis* (Hastings, 2015), thus demonstrating a new way to spectrally characterize the phylloquinones.

9.2 Outlook

Time-resolved IR spectroscopy is a powerful tool for observing light-induced protein reactions. Its sensitivity to protonation states of individual amino acid side chains renders it invaluable for PSII research, as proton movement steps are an essential part of the S-state cycle.

While many static FTIR studies have been performed on PSII, only one (extremely time-costly) time-resolved step-scan study has been published to date (Greife et al., 2023). Our custom built QCL setup offers the unique opportunity to acquire time-resolved spectral data sets of PSII samples within short measurement times: as demonstrated in this thesis, the step-scan FTIR results were reproduced with data obtained from only a week's worth measuring time.

Acquiring more such time-resolved spectral data sets in various different conditions (pH, temperature, buffer ingredients, water analogues, isotope exchanges) and combining the results with the information from time-resolved crystal structures (e.g. Bhowmick et al., 2023) could pave the way to a deeper understanding of the details of oxygenic O_2 production within PSII.

We showed that the D1-N298A mutant likely shows a severely slowed water insertion step in the $S_3 \rightarrow S_0$ transition. This offers new possibilities for experimental investigation

of this crucial water insertion/Mn_4CaO_x cluster reorganization step—with further time-resolved IR experiments, but also with other methods.

As for PSII, many rapid scan FTIR experiments have been performed on PSI. In addition, various step-scan FTIR experiments have also been published on PSI—but always at low temperatures. The QCL setup, in contrast, has enabled us to observe forward (and backward) electron transfer in PSI at room temperature, *inter alia* allowing for the spectral characterization of phylloquinones. Further future experiments, e.g. on PSI with incorporated non-native phylloquinones, could offer new insights into A- and B-branch kinetics. If the time resolution of the setup were to be improved slightly, further time-resolved IR experiments could also contribute towards a definitive answer as to where chlorophyll *f* molecules are positioned in PSI from FRL grown *C. thermalis*.

With each experiment on photosystems, we move closer towards a full understanding of oxygenic photosynthesis, one of nature's most essential processes. This knowledge may enable us to learn from natural photosynthetic reactions and processes, ultimately allowing us to design new artificial methods for harvesting clean energy.

10 | References

Abzaliyeva, A. (2020). *Activation Energies in the Photosynthetic Water-Oxidation Cycle Determined with Time-Resolved Single-Frequency IR Spectroscopy*. Master's thesis, Freie Universität Berlin.

Agalarov, R. and Brettel, K. (2003). Temperature dependence of biphasic forward electron transfer from the phylloquinone(s) A_1 in photosystem I: Only the slower phase is activated. *Biochim. Biophys. Acta*, 1604(1):7–12.

Agarwala, N., Makita, H., and Hastings, G. (2023). Time-resolved FTIR difference spectroscopy for the study of photosystem I with high potential naphthoquinones incorporated into the A_1 binding site. *Biochim. Biophys. Acta*, 1864(1):148918.

Ahlbrink, R., Haumann, M., Cherepanov, D., Bögershausen, O., Mulkidjanian, A., and Junge, W. (1998). Function of tyrosine Z in water oxidation by photosystem II: Electrostatical promotor instead of hydrogen abstractor. *Biochemistry*, 37(4):1131–1142.

Allakhverdiev, S. I. (1994). Reconstitution of the water-oxidizing complex in manganese-depleted photosystem II complexes by using synthetic binuclear manganese complexes. *Biochemistry*, 33(40):12139–12148.

Allgöwer, F., Gamiz-Hernandez, A. P., Rutherford, A. W., and Kaila, V. R. (2022). Molecular Principles of Redox-Coupled Protonation Dynamics in Photosystem II. *J. Am. Chem. Soc.*, 144(16):7171–7180.

Assunção, R. (2022). *Dynamics and kinetics of the O_2-evolution step in Photosystem II: a time-resolved polarography and X-ray spectroscopy study*. PhD thesis, Freie Universität Berlin.

Atkins, P., de Paula, J., and Keeler, J. (2018). *Physical Chemistry*. Oxford University Press, 11th edition.

Bandaranayake, K. M., Wang, R., Johnson, T. W., and Hastings, G. (2006). Time-resolved FTIR difference spectroscopy for the study of photosystem I particles with plastoquinone-9 occupying the A_1 binding site. *Biochemistry*, 45(42):12733–12740.

Bao, H. and Burnap, R. L. (2015). Structural rearrangements preceding dioxygen formation by the water oxidation complex of photosystem II. *Proc. Natl. Acad. Sci. U.S.A*, 112(45):E6139–E6147.

Barth, A. (2000). The infrared absorption of amino acid side chains. *Prog. Biophys. Mol. Biol.*, 74(3-5):141–173.

Barth, A. (2007). Infrared spectroscopy of proteins. *Biochim. Biophys. Acta*, 1767(9):1073–1101.

Barth, A. and Zscherp, C. (2002). What vibrations tell us about proteins. *Q. Rev. Biol.*, 35(4):369–430.

Bearden, A. J. and Malkin, R. (1972). The bound ferredoxin of chloroplasts: A role as the primary electron acceptor of photosystem I. *Biochem. Biophys. Res. Commun.*, 46(3):1299–1305.

Bernát, G., Morvaridi, F., Feyziyev, Y., and Styring, S. (2002). pH dependence of the four individual transitions in the catalytic S-cycle during photosynthetic oxygen evolution. *Biochemistry*, 41(18):5830–5843.

Berthold, D. A., Babcock, G. T., and Yocum, C. F. (1981). A highly resolved, oxygen-evolving photosystem II preparation from spinach thylakoid membranes. *FEBS Lett.*, 134(2):231–234.

Berthomieu, C. and Hienerwadel, R. (2001). Iron coordination in photosystem II: Interaction between bicarbonate and the Q_B pocket studied by fourier transform infrared spectroscopy. *Biochemistry*, 40(13):4044–4052.

Berthomieu, C. and Hienerwadel, R. (2005). Vibrational spectroscopy to study the properties of redox-active tyrosines in photosystem II and other proteins. *Biochim. Biophys. Acta*, 1707:51–66.

Berthomieu, C., Hienerwadel, R., Boussac, A., Breton, J., and Diner, B. A. (1998). Hydrogen bonding of redox-active tyrosine Z of photosystem II probed by FTIR difference spectroscopy. *Biochemistry*, 37(30):10547–10554.

Berthomieu, C., Nabedryk, E., Mäntele, W., and Breton, J. (1990). Characterization by FTIR spectroscopy of the photoreduction of the primary quinone acceptor Q_A in photosystem II. *FEBS Lett.*, 269(2):363–367.

Bhowmick, A., Hussein, R., Bogacz, I., Simon, P. S., Ibrahim, M., Chatterjee, R., Doyle, M. D., Cheah, M. H., Fransson, T., Chernev, P., Kim, I. S., Makita, H., Dasgupta, M., Kaminsky, C. J., Zhang, M., Gätcke, J., Haupt, S., Nangca, I. I., Keable, S. M., Aydin, A. O., Tono, K., Owada, S., Gee, L. B., Fuller, F. D., Batyuk, A., Alonso-Mori, R., Holton, J. M., Paley, D. W., Moriarty, N. W., Mamedov, F., Adams, P. D., Brewster, A. S., Dobbek, H., Sauter, N. K., Bergmann, U., Zouni, A., Messinger, J., Kern, J., Yano, J., and Yachandra, V. K. (2023). Structural evidence for intermediates during O_2 formation in photosystem II. *Nature*, 617(7961):629–636.

Blankenship, R. E. (2021). *Molecular mechanisms of photosynthesis*. John Wiley & Sons.

Boardman, N. K. and Anderson, J. M. (1964). Isolation from spinach chloroplasts of particles containing different proportions of chlorophyll *a* and chlorophyll *b* and their possible role in the light reactions of photosynthesis. *Nature*, 203(4941):166–167.

Bondar, A. N. and Dau, H. (2012). Extended protein/water H-bond networks in photosynthetic water oxidation. *Biochim. Biophys. Acta*, 1817(8):1177–1190.

Breton, J. (2001). Fourier transform infrared spectroscopy of primary electron donors in type I photosynthetic reaction centers. *Biochim. Biophys. Acta*, 1507(1-3):180–193.

Breton, J. (2006). FTIR studies of the primary electron donor, P700. In Golbeck, J. H., editor, *Photosystem I: The Plastocyanin: Ferredoxin Oxidoreductase in Photosynthesis*, pages 271–289. Springer.

Breton, J., Hienerwadel, R., and Nabedryk, E. (1997). FTIR difference spectrum of the photooxidation of the primary electron donor of photosystem II. In Carmona, P., Navarro, R., and Hernanz, A., editors, *Spectroscopy of Biological Molecules: Modern Trends*, pages 101–102. Springer.

Breton, J., Nabedryk, E., and Leibl, W. (1999). FTIR study of the primary electron donor of photosystem I (P700) revealing delocalization of the charge in P700$^+$ and localization of the triplet character in ^{3}P700. *Biochemistry*, 38(36):11585–11592.

Breton, J., Nabedryk, E., and Parson, W. W. (1992). A New Infrared Electronic Transition of the Oxidized Primary Electron Donor in Bacterial Reaction Centers: A Way To Assess Resonance Interactions between the Bacteriochlorophylls. *Biochemistry*, 31(33):7503–7510.

Breton, J., Xu, W., Diner, B. A., and Chitnis, P. R. (2002). The two histidine axial ligands of the primary electron donor chlorophylls (P700) in photosystem I are similarly perturbed upon P700$^+$ formation. *Biochemistry*, 41(37):11200–11210.

Brettel, K., Schlodder, E., and Witt, H. T. (1984). Nanosecond reduction kinetics of photooxidized chlorophyll-a_{II} (P-680) in single flashes as a probe for the electron pathway, H$^+$-release and charge accumulation in the O_2-evolving complex. *Biochim. Biophys. Acta*, 766(2):403–415.

Buchta, J., Grabolle, M., and Dau, H. (2007). Photosynthetic dioxygen formation studied by time-resolved delayed fluorescence measurements — Method, rationale, and results on the activation energy of dioxygen formation. *Biochim. Biophys. Acta*, 1767(6):565–574.

Byrdin, M., Santabarbara, S., Gu, F., Fairclough, W. V., Heathcote, P., Redding, K., and Rappaport, F. (2006). Assignment of a kinetic component to electron transfer between iron-sulfur clusters F_X and $F_{A/B}$ of Photosystem I. *Biochim. Biophys. Acta*, 1757(11):1529–1538.

Casey, J. L. and Sauer, K. (1984). EPR detection of a cryogenically photogenerated intermediate in photosynthetic oxygen evolution. *Biochim. Biophys. Acta*, 767:21–28.

Chen, M., Schliep, M., Willows, R. D., Cai, Z.-L., Neilan, B. A., and Scheer, H. (2010). A Red-Shifted Chlorophyll. *Science*, 329:1318–1319.

Cherepanov, D. A., Semenov, A. Y., Mamedov, M. D., Aybush, A. V., Gostev, F. E., Shelaev, I. V., Shuvalov, V. A., and Nadtochenko, V. A. (2022). Current state of the primary charge separation mechanism in photosystem I of cyanobacteria. *Biophys. Rev.*, 14(4):805–820.

Cherepanov, D. A., Shelaev, I. V., Gostev, F. E., Aybush, A. V., Mamedov, M. D., Shen, G., Nadtochenko, V. A., Bryant, D. A., Semenov, A. Y., and Golbeck, J. H. (2020). Evidence that chlorophyll *f* functions solely as an antenna pigment in far-red-light photosystem I from *Fischerella thermalis* PCC 7521. *Biochim. Biophys. Acta*, 1861(5-6):148184.

Chernev, P., Fischer, S., Hoffmann, J., Oliver, N., Assunção, R., Yu, B., Burnap, R. L., Zaharieva, I., Nürnberg, D. J., Haumann, M., and Dau, H. (2020). Light-driven formation of manganese oxide by today's photosystem II supports evolutionarily ancient manganese-oxidizing photosynthesis. *Nat. Commun.*, 11(1).

Chernev, P., Zaharieva, I., Dau, H., and Haumann, M. (2011). Carboxylate shifts steer interquinone electron transfer in photosynthesis. *J. Biol. Chem.*, 286(7):5368–5374.

Christen, G., Reifarth, F., and Renger, G. (1998). On the origin of the '35-μs kinetics' of $P680^{+\bullet}$ reduction in photosystem II with an intact water oxidising complex. *FEBS Lett.*, 429(1):49–52.

Christen, G. and Renger, G. (1999). The role of hydrogen bonds for the multiphasic $P680^{+\bullet}$ reduction by Y_Z in photosystem II with intact oxyen evolution capacity. Analysis of kinetic H/D isotope exchange effects. *Biochemistry*, 38(7):2068–2077.

Christen, G., Seeliger, A., and Renger, G. (1999). $P680^{+\bullet}$ reduction kinetics and redox transition probability of the water oxidizing complex as a function of pH and H/D isotope exchange in spinach thylakoids. *Biochemistry*, 38(19):6082–6092.

Chu, H. A., Gardner, M. T., Hillier, W., and Babcock, G. T. (2000). Low-frequency fourier transform infrared spectroscopy of the oxygen-evolving complex in Photosystem II. *Photosynth. Res.*, 66(1-2):57–63.

Chu, H. A., Gardner, M. T., O'Brien, J., and Babcock, G. T. (1999). Low-Frequency Fourier Transform Infrared Spectroscopy of the Oxygen-Evolving and Quinone Acceptor Complexes in Photosystem II. *Photosynth. Res.*, 38(14):4533–4541.

Chu, H.-A., Hillier, W., and Debus, R. J. (2004). Evidence that the C-Terminus of the D1 Polypeptide of Photosystem II is Ligated to the Manganese Ion that Undergoes Oxidation During the S_1 to S_2 Transition: An Isotope-Edited FTIR Study. *Biochemistry*, 43:3152–3166.

Chu, H. A., Nguyen, A. P., and Debus, R. J. (1994). Site-Directed Photosystem II Mutants with Perturbed Oxygen-Evolving Properties. 1. Instability or Inefficient Assembly of the Manganese Cluster *in Vivo*. *Biochemistry*, 33(20):6137–6149.

Chu, H. A., Nguyen, A. P., and Debus, R. J. (1995). Amino Acid Residues That Influence the Binding of Manganese or Calcium to Photosystem II. 1. The Lumenal Interhelical Domains of the D1 Polypeptide. *Biochemistry*, 34(17):5839–5858.

Çoruh, O., Frank, A., Tanaka, H., Kawamoto, A., El-Mohsnawy, E., Kato, T., Namba, K., Gerle, C., Nowaczyk, M. M., and Kurisu, G. (2021). Cryo-EM structure of a functional monomeric

Photosystem I from *Thermosynechococcus elongatus* reveals red chlorophyll cluster. *Commun. Biol.*, 4(1):304.

Cox, N., Pantazis, D. A., and Lubitz, W. (2020). Current Understanding of the Mechanism of Water Oxidation in Photosystem II and Its Relation to XFEL Data. *Annu. Rev. Biochem.*, 89:795–820.

Şener, M., Strümpfer, J., Hsin, J., Chandler, D., Scheuring, S., Hunter, C. N., and Schulten, K. (2011). Förster energy transfer theory as reflected in the structures of photosynthetic light-harvesting systems. *ChemPhysChem*, 12(3):518–531.

Dau, H. and Greife, P. (2023). Applicability of Transition State Theory to the (Proton-Coupled) Electron Transfer in Photosynthetic Water Oxidation with Emphasis on the Entropy of Activation. *Inorganics*, 11(10):389.

Dau, H., Kurz, P., and Weitze, M.-D. (2019). *Künstliche Photosynthese*. Springer.

de Lichtenberg, C., Avramov, A. P., Zhang, M., Mamedov, F., Burnap, R. L., and Messinger, J. (2021). The D1-V185N mutation alters substrate water exchange by stabilizing alternative structures of the Mn_4Ca-cluster in photosystem II. *Biochim. Biophys. Acta*, 1862:148319.

de Wijn, R. and Van Gorkom, H. J. (2001). Kinetics of electron transfer from Q_A to Q_B in photosystem II. *Biochemistry*, 40(39):11912–11922.

Debus, R. J. (2014). Evidence from FTIR difference spectroscopy that D1-Asp61 influences the water reactions of the oxygen-evolving Mn_4CaO_5 cluster of photosystem II. *Biochemistry*, 53(18):2941–2955.

Debus, R. J. (2015). FTIR studies of metal ligands, networks of hydrogen bonds, and water molecules near the active site Mn_4CaO_5 cluster in Photosystem II. *Biochim. Biophys. Acta*, 1847(1):19–34.

Debus, R. J. (2016). Identifying carboxylate ligand vibrational modes in photosystem II with QM/MM methods. *Proc. Natl. Acad. Sci. U.S.A*, 113(45):12613–12615.

Debus, R. J. (2021). Alteration of the O_2-Producing Mn_4Ca Cluster in Photosystem II by the Mutation of a Metal Ligand. *Biochemistry*, 60(51):3841–3855.

Debus, R. J., Campbell, K. A., Gregor, W., Li, Z.-L., Burnap, R. L., and Britt, R. D. (2001). Does Histidine 332 of the D1 Polypeptide Ligate the Manganese Cluster in Photosystem II? An Electron Spin Echo Envelope Modulation Study. *Biochemistry*, 40:3690–3699.

Dekker, J. P., Plijter, J. J., Ouwehand, L., and Van Gorkom, H. J. (1984). Kinetics of manganese redox transitions in the oxygen-evolving apparatus of photosynthesis. *Biochim. Biophys. Acta*, 767(1):176–179.

Dekmak, M. Y., Mäusle, S. M., Janosch, B., Simon, P. S., and Dau, H. (2023). Tracking the first electron transfer step at the donor side of oxygen-evolving photosystem II by time-resolved infrared spectroscopy. *Photosynth. Res.*

Diem, M. (2015). *Modern Vibrational Spectroscopy and Micro-Spectroscopy: Theory, Instrumentation and Biomedical Applications*. John Wiley & Sons, Ltd.

Dilbeck, P. L., Bao, H., Neveu, C. L., and Burnap, R. L. (2013). Perturbing the water cavity surrounding the manganese cluster by mutating the residue D1-Valine 185 has a strong effect on the water oxidation mechanism of photosystem II. *Biochemistry*, 52(39):6824–6833.

Dilbeck, P. L., Hwang, H. J., Zaharieva, I., Gerencser, L., Dau, H., and Burnap, R. L. (2012). The D1-D61N mutation in Synechocystis sp. PCC 6803 allows the observation of pH-sensitive intermediates in the formation and release of O_2 from photosystem II. *Biochemistry*, 51(6):1079–1091.

Diner, B. A. and Petrouleas, V. (1987). Q_{400}, the non-heme iron of the photosystem II iron-quinone complex. A spectroscopic probe of quinone and inhibitor binding to the reaction center. *Biochim. Biophys. Acta*, 895(2):107–125.

Dismukes, G. C. and Siderer, Y. (1981). Intermediates of a polynuclear manganese center involved in photosynthetic oxidation of water. *Proc. Natl. Acad. Sci. U.S.A.*, 78(1):274–278.

Eckert, H. J. and Renger, G. (1988). Temperature dependence of P680$^+$ reduction in O$_2$-evolving PS II membrane fragments at different redox states S$_i$ of the water oxidizing system. *FEBS Lett.*, 236(2):425–431.

Elias, E., Oliver, T. J., and Croce, R. (2024). Oxygenic Photosynthesis in Far-Red Light: Strategies and Mechanisms. *Annu. Rev. Phys. Chem.*, pages 231–256.

Enami, I., Okumura, A., Nagao, R., Suzuki, T., Iwai, M., and Shen, J. R. (2008). Structures and functions of the extrinsic proteins of photosystem II from different species. *Photosynth. Res.*, 98(1-3):349–363.

Evans, M. G. and Polanyi, M. (1935). Some applications of the transition state method to the calculation of reaction velocities, especially in solution. *T. Faraday. Soc.*, 31:875–894.

Eyring, H. (1935). The activated complex in chemical reactions. *J. Chem. Phys.*, 3(2):107–115.

Gan, F., Zhang, S., Rockwell, N. C., Martin, S. S., Lagarias, J. C., and Bryant, D. A. (2014). Extensive remodeling of a cyanobacterial photosynthetic apparatus in far-red light. *Science*, 345(6202):1312–1317.

Gerencsér, L. and Dau, H. (2010). Water oxidation by photosystem II: H$_2$O-D$_2$O exchange and the influence of pH support formation of an intermediate by removal of a proton before dioxygen creation. *Biochemistry*, 49(47):10098–10106.

Ghosh, I., Khan, S., Banerjee, G., Dziarski, A., Vinyard, D. J., Debus, R. J., and Brudvig, G. W. (2019). Insights into Proton-Transfer Pathways during Water Oxidation in Photosystem II. *J. Phys. Chem. B*, 123(39):8195–8202.

Gisriel, C., Shen, G., Kurashov, V., Ho, M. Y., Zhang, S., Williams, D., Golbeck, J. H., Fromme, P., and Bryant, D. A. (2020). The structure of Photosystem I acclimated to far-red light illuminates an ecologically important acclimation process in photosynthesis. *Sci. Adv.*, 6:eaay6415.

Gisriel, C. J., Bryant, D. A., Brudvig, G. W., and Cardona, T. (2023). Molecular diversity and evolution of far-red light-acclimated photosystem I. *Front. Plant Sci.*, 14:1289199.

Gisriel, C. J., Flesher, D. A., Shen, G., Wang, J., Ho, M. Y., Brudvig, G. W., and Bryant, D. A. (2022). Structure of a photosystem I-ferredoxin complex from a marine cyanobacterium provides insights into far-red light photoacclimation. *J. Biol. Chem.*, 298(1):101408.

Gläser, M., Wolff, C., and Renger, G. (1976). Indirect Evidence for a Very Fast Recovery Kinetics of Chlorophyll-a$_{II}$ in Spinach Chloroplasts. *Z. Naturforsch. C*, 31(11-12):712–721.

Glasoe, P. K. and Long, F. A. (1960). Use of glass electrodes to measure acidities in deuterium oxide. *J. Phys. Chem.*, 64(1):188–190.

Golbeck, J. H. (2006). *Photosystem I. The Light-Driven Plastocyanin: Ferredoxin Oxidoreductase*. Springer.

Golbeck, J. H. and Bryant, D. A. (1991). Photosystem I. *Current topics in bioenergetics*, 16:83–177.

Görlin, M. (2012). *Light-induced and time-resolved FTIR difference spectroscopy of Photosystem II*. Master's thesis, Freie Universität Berlin.

Govindjee, Shevela, D., and Björn, L. O. (2017). Evolution of the Z-scheme of photosynthesis: a perspective. *Photosynth. Res.*, 133(1-3):5–15.

Greife, P., Schönborn, M., Capone, M., Assunção, R., Narzi, D., Guidoni, L., and Dau, H. (2023). The electron-proton bottleneck of photosynthetic oxygen evolution. *Nature*, 617(7961):623–628.

Greife, P. F. (*in preparation*). *Elucidating Oxygen Evolution Mechanisms at the Manganese Cluster of Photosystem II: Insights from Hydrogen Bonding Networks and Water Analogue Substitution through Time Resolved Infrared Spectroscopy*. PhD thesis, Freie Universität Berlin.

Guergova-Kuras, M., Boudreaux, B., Joliot, A., Joliot, P., and Redding, K. (2001). Evidence for two active branches for electron transfer in photosystem I. *Proc. Natl. Acad. Sci. U.S.A*, 98(8):4437–4442.

Hamacher, E., Kruip, J., Rögner, M., and Mäntele, W. (1996). Characterization of the primary electron donor of photosystem I, P700, by electrochemistry and Fourier transform infrared (FTIR) difference spectroscopy. *Spectrochim. Acta A*, 52:107–121.

Han, G., Chernev, P., Styring, S., Messinger, J., and Mamedov, F. (2022). Molecular basis for turnover inefficiencies (misses) during water oxidation in photosystem II. *Chem. Sci.*, 13(29):8667–8678.

Han, G., Mamedov, F., and Styring, S. (2012). Misses during water oxidation in photosystem II are S state-dependent. *J. Biol. Chem.*, 287(16):13422–13429.

Hastings, G. (2006). Fourier transform infrared studies of the secondary electron acceptor, A1. In Golbeck, J. H., editor, *Photosystem I: The Light-Driven Plastocyanin: Ferredoxin Oxidoreductase*, pages 301–318. Springer.

Hastings, G. (2015). Vibrational spectroscopy of photosystem I. *Biochim. Biophys. Acta*, 1847(1):55–68.

Hastings, G., Makita, H., Agarwala, N., Rohani, L., Shen, G., and Bryant, D. A. (2019). Fourier transform visible and infrared difference spectroscopy for the study of P700 in photosystem I from *Fischerella thermalis* PCC 7521 cells grown under white light and far-red light: Evidence that the A_{-1} cofactor is chlorophyll f. *Biochim. Biophys. Acta*, 1860(6):452–460.

Hastings, G., Ramesh, V. M., Wang, R., Sivakumar, V., and Webber, A. (2001). Primary Donor Photo-Oxidation in Photosystem I: A Re-Evaluation of ($P700^+ - P700$) Fourier Transform Infrared Difference Spectra. *Biochemistry*, 40(43):12943–12949.

Hastings, G. and Sivakumar, V. (2001). A Fourier transform infrared absorption difference spectrum associated with the reduction of A_1 in photosystem I: Are both phylloquinones involved in electron transfer? *Biochemistry*, 40(12):3681–3689.

Haumann, M., Bögershausen, O., Cherepanov, D., Ahlbrink, R., and Junge, W. (1997). Photosynthetic oxygen evolution: H/D isotope effects and the coupling between electron and proton transfer during the redox reactions at the oxidizing side of photosystem II. *Photosynth. Res.*, 51(3):193–208.

Haumann, M., Liebisch, P., Müller, C., Barra, M., Grabolle, M., and Dau, H. (2005). Biochemistry: Photosynthetic O_2 formation tracked by time-resolved X-ray experiments. *Science*, 310(5750):1019–1021.

Hays, A.-M. M. A., Vassiliev, I. R., Golbeck, J. H., and Debus, R. J. (1999). Role of D1-His190 in the Proton-Coupled Oxidation of Tyrosine Y_Z in Manganese-Depleted Photosystem II. *Biochemistry*, 38(37):11851–11865.

Hienerwadel, R. and Berthomieu, C. (1995). Bicarbonate Binding to the Non-Heme Iron of Photosystem II Investigated by Fourier Transform Infrared Difference Spectroscopy and ^{13}C-Labeled Bicarbonate. *Biochemistry*, 34(50):16288–16297.

Hienerwadel, R., Boussac, A., Breton, J., and Berthomieu, C. (1996). Fourier transform infrared difference study of tyrosine$_D$ oxidation and plastoquinone Q_A reduction in photosystem II. *Biochemistry*, 35(48):15447–15460.

Hienerwadel, R., Boussac, A., Breton, J., Diner, B. A., and Berthomieu, C. (1997). Fourier transform infrared difference spectroscopy of photosystem II tyrosine D using site-directed mutagenesis and specific isotope labeling. *Biochemistry*, 36(48):14712–14723.

Hillier, W. and Babcock, G. T. (2001). S-state dependent fourier transform infrared difference spectra for the photosystem II oxygen evolving complex. *Biochemistry*, 40(6):1503–1509.

Hiyama, T. and Ke, B. (1971). A new photosynthetic pigment, "P430": its possible role as the priary electron acceptor of photosystem I. *Proc. Natl. Acad. Sci. U.S.A*, 68(5):1010–1013.

Hohmann-Marriott, M. F. and Blankenship, R. E. (2011). Evolution of photosynthesis. *Annu. Rev. Plant Biol.*, 62:515–548.

Hussein, R., Ibrahim, M., Bhowmick, A., Simon, P. S., Bogacz, I., Doyle, M. D., Dobbek, H., Zouni, A., Messinger, J., Yachandra, V. K., Kern, J. F., and Yano, J. (2023). Evolutionary diversity of proton

and water channels on the oxidizing side of photosystem II and their relevance to function. *Photosynth. Res.*, 158(2):91–107.

Hussein, R., Ibrahim, M., Bhowmick, A., Simon, P. S., Chatterjee, R., Lassalle, L., Doyle, M., Bogacz, I., Kim, I. S., Cheah, M. H., Gul, S., de Lichtenberg, C., Chernev, P., Pham, C. C., Young, I. D., Carbajo, S., Fuller, F. D., Alonso-Mori, R., Batyuk, A., Sutherlin, K. D., Brewster, A. S., Bolotovsky, R., Mendez, D., Holton, J. M., Moriarty, N. W., Adams, P. D., Bergmann, U., Sauter, N. K., Dobbek, H., Messinger, J., Zouni, A., Kern, J., Yachandra, V. K., and Yano, J. (2021). Structural dynamics in the water and proton channels of photosystem II during the S$_2$ to S$_3$ transition. *Nat. Commun.*, 12(1):6531.

Ibrahim, M., Fransson, T., Chatterjee, R., Cheah, M. H., Hussein, R., Lassalle, L., Sutherlin, K. D., Young, I. D., Fuller, F. D., Gul, S., Kim, I. S., Simon, P. S., de Lichtenberg, C., Chernev, P., Bogacz, I., Pham, C. C., Orville, A. M., Saichek, N., Northen, T., Batyuk, A., Carbajo, S., Alonso-Mori, R., Tono, K., Owada, S., Bhowmick, A., Bolotovsky, R., Mendez, D., Moriarty, N. W., Holton, J. M., Dobbek, H., Brewster, A. S., Adams, P. D., Sauter, N. K., Bergmann, U., Zouni, A., Messinger, J., Kern, J., Yachandra, V. K., and Yano, J. (2020). Untangling the sequence of events during the S$_2 \rightarrow$ S$_3$ transition in photosystem II and implications for the water oxidation mechanism. *Proc. Natl. Acad. Sci. U.S.A*, 117(23):12624–12635.

Isgandarova, S., Renger, G., and Messinger, J. (2003). Functional differences of photosystem II from *Synechococcus elongatus* and spinach characterized by flash induced oxygen evolution patterns. *Biochemistry*, 42(30):8929–8938.

Ishikita, H., Saenger, W., Loll, B., Biesiadka, J., and Knapp, E. W. (2006). Energetics of a possible proton exit pathway for water oxidation in photosystem II. *Biochemistry*, 45(7):2063–2071.

Jeans, C., Schilstra, M. J., and Klug, D. R. (2002). The temperature dependence of P680$^+$ reduction in oxygen-evolving photosystem II. *Biochemistry*, 41(15):5015–5023.

Joliot, P., Barbier, G., and Chabaud, R. (1969). Un Nouveau Modele Des Centres. *Photochem. Photobiol.*, 10(16):309–329.

Joliot, P. and Joliot, A. (1999). In vivo analysis of the electron transfer within photosystem I: Are the two phylloquinones involved. *Biochemistry*, 38(34):11130–11136.

Jordan, P., Fromme, P., Klukas, O., Witt, H. T., Saenger, W., and Krauß, N. (2001). X-Ray crystallographic structure analysis of cyanobacterial photosystem I at 2.5 Å resolution. *Nature*, 411(June):909–917.

Junge, W. (2019). Oxygenic photosynthesis: History, status and perspective. *Q. Rev. Biol.*, 52.

Junge, W. and Nelson, N. (2015). ATP synthase. *Annu. Rev. Biochem.*, 84:631–657.

Karge, M., Irrgang, K. D., and Renger, G. (1997). Analysis of the reaction coordinate of photosynthetic water oxidation by kinetic measurements of 355 nm absorption changes at different temperatures in photosystem II preparations suspended in either H$_2$O or D$_2$O. *Biochemistry*, 36(29):8904–8913.

Kato, K., Shinoda, T., Nagao, R., Akimoto, S., Suzuki, T., Dohmae, N., Chen, M., Allakhverdiev, S. I., Shen, J. R., Akita, F., Miyazaki, N., and Tomo, T. (2020). Structural basis for the adaptation and function of chlorophyll *f* in photosystem I. *Nat. Commun.*, 11(1):238.

Kato, Y. and Noguchi, T. (2022). Redox properties and regulatory mechanism of the iron-quinone electron acceptor in photosystem II as revealed by FTIR spectroelectrochemistry. *Photosynth. Res.*, 152(2):135–151.

Kaucikas, M., Nürnberg, D., Dorlhiac, G., Rutherford, A. W., and van Thor, J. J. (2017). Femtosecond Visible Transient Absorption Spectroscopy of Chlorophyll *f*-Containing Photosystem I. *Biophys. J.*, 112:234–249.

Kaur, D., Zhang, Y., Reiss, K. M., Mandal, M., Brudvig, G. W., Batista, V. S., and Gunner, M. R. (2021). Proton exit pathways surrounding the oxygen evolving complex of photosystem II. *Biochim. Biophys. Acta*, 1862(8):148446.

Ke, B., Hansen, R. E., and Beinert, H. (1973). Oxidation reduction potentials of bound iron sulfur proteins of photosystem I. *Proc. Natl. Acad. Sci. U.S.A*, 70(10):2941–2945.

Kern, J., Chatterjee, R., Young, I. D., Fuller, F. D., Lassalle, L., Ibrahim, M., Gul, S., Fransson, T., Brewster, A. S., Alonso-Mori, R., Hussein, R., Zhang, M., Douthit, L., de Lichtenberg, C., Cheah, M. H., Shevela, D., Wersig, J., Seuffert, I., Sokaras, D., Pastor, E., Weninger, C., Kroll, T., Sierra, R. G., Aller, P., Butryn, A., Orville, A. M., Liang, M., Batyuk, A., Koglin, J. E., Carbajo, S., Boutet, S., Moriarty, N. W., Holton, J. M., Dobbek, H., Adams, P. D., Bergmann, U., Sauter, N. K., Zouni, A., Messinger, J., Yano, J., and Yachandra, V. K. (2018). Structures of the intermediates of Kok's photosynthetic water oxidation clock. *Nature*, 563(7731):421–425.

Kim, C. J., Bao, H., Burnap, R. L., and Debus, R. J. (2018). Impact of D1-V185 on the Water Molecules That Facilitate O_2 Formation by the Catalytic Mn_4CaO_5 Cluster in Photosystem II. *Biochemistry*, 57(29):4299–4311.

Kim, C. J. and Debus, R. J. (2019). One of the Substrate Waters for O_2 Formation in Photosystem II Is Provided by the Water-Splitting Mn_4CaO_5 Cluster's Ca^{2+} Ion. *Biochemistry*, 58(29):3185–3192.

Klauss, A., Haumann, M., and Dau, H. (2012a). Alternating electron and proton transfer steps in photosynthetic water oxidation. *Proc. Natl. Acad. Sci. U.S.A*, 109(40):16035–16040.

Klauss, A., Haumann, M., and Dau, H. (2015). Seven steps of alternating electron and proton transfer in photosystem II water oxidation traced by time-resolved photothermal beam deflection at improved sensitivity. *J. Phys. Chem. B*, 119(6):2677–2689.

Klauss, A., Sikora, T., Süss, B., and Dau, H. (2012b). Fast structural changes (200–900 ns) may prepare the photosynthetic manganese complex for oxidation by the adjacent tyrosine radical. *Biochim. Biophys. Acta*, 1817(8):1196–1207.

Kok, B., Forbush, B., and McGloin, M. (1970). Cooperation of Charges in Photosynthetic O_2 Evolution – I. A linear Four Step Mechanism. *Photochem. Photobiol.*, 11:457–475.

Krieger, A., Rutherford, A. W., and Johnson, G. N. (1995). On the determination of redox midpoint potential of the primary quinone electron acceptor, Q_A, in Photosystem II. *Biochim. Biophys. Acta*, 1229(2):193–201.

Kühn, P., Eckert, H.-J., Eichlerb, H. J., and Renger, G. (2004). Analysis of the $P680^{+\bullet}$ reduction pattern and its temperature dependence in oxygen-evolving PS II core complexes from thermophilic cyanobacteria and higher plants. *Phys. Chem. Chem. Phys.*, 6(2):4838–4843.

Kuroda, H., Kawashima, K., Ueda, K., Ikeda, T., Saito, K., Ninomiya, R., Hida, C., Takahashi, Y., and Ishikita, H. (2021). Proton transfer pathway from the oxygen-evolving complex in photosystem II substantiated by extensive mutagenesis. *Biochim. Biophys. Acta*, 1862(1):148329.

Kuroda, H., Kodama, N., Sun, X. Y., Ozawa, S. I., and Takahashi, Y. (2014). Requirement for Asn298 on D1 protein for oxygen evolution: Analyses by exhaustive amino acid substitution in the green alga Chlamydomonas reinhardtii. *Plant Cell Physiol.*, 55(7):1266–1275.

Larkin, P. J. (2018). *Infrared and Raman Spectroscopy: Principles and Spectral Interpretation*. Elsevier, second edition.

Lavorel, J. (1976). Matrix analysis of the oxygen evolving system of photosynthesis. *J. Theor. Biol.*, 57(1):171–185.

Lawlor, D. (2001). *Photosynthesis: Third Edition.* Bios Scientific Publishers Ltd.

Li, H., Nakajima, Y., Nango, E., Owada, S., Yamada, D., Hashimoto, K., Luo, F., Tanaka, R., Akita, F., Kato, K., Kang, J., Saitoh, Y., Kishi, S., Yu, H., Matsubara, N., Fujii, H., Sugahara, M., Suzuki, M., Masuda, T., Kimura, T., Thao, T. N., Yonekura, S., Yu, L.-j., Tosha, T., Tono, K., Joti, Y., Hatsui,

T., Yabashi, M., Kubo, M., Iwata, S., Isobe, H., Yamaguchi, K., Suga, M., and Shen, J.-R. (2024). Oxygen-evolving photosystem II structures during S_1–S_2–S_3 transitions. *Nature*, 626:670–677.

Li, M., Calteau, A., Semchonok, D. A., Witt, T. A., Nguyen, J. T., Sassoon, N., Boekema, E. J., Whitelegge, J., Gugger, M., and Bruce, B. D. (2019). Physiological and evolutionary implications of tetrameric photosystem I in cyanobacteria. *Nat. Plants*, 5(12):1309–1319.

Li, Y., Est, A. V. D., Lucas, M. G., Ramesh, V. M., Gu, F., Petrenko, A., Lin, S., Webber, A. N., Rappaport, F., and Redding, K. (2006). Directing electron transfer within Photosystem I by breaking H-bonds in the cofactor branches. *Proc. Natl. Acad. Sci. U.S.A.*, 103(7):2144–2149.

Liang, Z. (2018). *Photosynthetic Water Oxidation in Plants and Cyanobacteria - Activation Energy of the O-O Bond Formation Step and Substrate Analogue NH3*. PhD thesis, Freie Universität Berlin.

Long, S. P., Marshall-Colon, A., and Zhu, X. G. (2015). Meeting the global food demand of the future by engineering crop photosynthesis and yield potential. *Cell*, 161(1):56–66.

Lorenz-Fonfria, V. A. (2020). Infrared Difference Spectroscopy of Proteins: From Bands to Bonds. *Chem. Rev.*, 120(7):3466–3576.

Loughlin, P., Lin, Y., and Chen, M. (2013). Chlorophyll *d* and *Acaryochloris marina*: Current status. *Photosynth. Res.*, 116:277–293.

Lubitz, W., Chrysina, M., and Cox, N. (2019). Water oxidation in photosystem II. *Photosynth. Res.*, 142(1):105–125.

Lubitz, W., Pantazis, D. A., and Cox, N. (2023). Water oxidation in oxygenic photosynthesis studied by magnetic resonance techniques. *FEBS Lett.*, 597(1):6–29.

Lukins, P. B., Post, A., Walker, P. J., and Larkum, A. W. (1996). P680$^+$ reduction in oxygen-evolving Photosystem II core complexes. *Photosynth. Res.*, 49(3):209–221.

Makita, H. and Hastings, G. (2015). Directionality of electron transfer in cyanobacterial photosystem I at 298 and 77 K. *FEBS Lett.*, 589(13):1412–1417.

Makita, H. and Hastings, G. (2016). Modeling electron transfer in photosystem I. *Biochim. Biophys. Acta*, 1857(6):723–733.

Malkin, R. and Bearden, A. J. (1971). Primary reactions of photosynthesis: photoreduction of a bound chloroplast ferredoxin at low temperature as detected by EPR spectroscopy. *Proc. Natl. Acad. Sci. U.S.A*, 68(1):16–19.

Mäntele, W., Nabedryk, E., Tavitian, B. A., Kreutz, W., and Breton, J. (1985). Light-induced Fourier transform infrared (FTIR) spectroscopic investigations of the primary donor oxidation in bacterial photosynthesis. *FEBS Lett.*, 187(2):227–232.

Mäusle, S. M., Abzaliyeva, A., Greife, P., Simon, P. S., Perez, R., Zilliges, Y., and Dau, H. (2020). Activation energies for two steps in the $S_2 \rightarrow S_3$ transition of photosynthetic water oxidation from time-resolved single-frequency infrared spectroscopy. *J. Chem. Phys.*, 153(21):215101.

Mäusle, S. M., Agarwala, N., Eichmann, V. G., Dau, H., Nürnberg, D. J., and Hastings, G. (2024). Nanosecond time-resolved infrared spectroscopy for the study of electron transfer in photosystem I. *Photosynth. Res.*, 159(2-3):229–239.

Mclntosh, A. R., Chu, M., and Bolton, J. R. (1975). Flash photolysis electron spin resonance studies of the electron acceptor species at low temperatures in Photosystem I of spinach subchloroplast particles. *Biochim. Biophys. Acta*, 376(120):308–314.

Messinger, J. and Renger, G. (1994). Analyses of pH-Induced Modifications of the Period Four Oscillation of Flash-Induced Oxygen Evolution Reveal Distinct Structural Changes of the Photosystem II Donor Side at Characteristic pH Values. *Biochemistry*, 33(36):10896–10905.

Meyer, B., Schlodder, E., Dekker, J. P., and Witt, H. T. (1989). O$_2$ evolution and Chl a_{II}^+ (P-680$^+$) nanosecond reduction kinetics in single flashes as a function of pH. *Biochim. Biophys. Acta*, 974(1):36–43.

Mezzetti, A., Leibl, W., Breton, J., and Nabedryk, E. (2003). Photoreduction of the quinone pool in the bacterial photosynthetic membrane : identification of infrared marker bands for quinol formation. *FEBS Lett.*, 537:161–165.

Mezzetti, A., Paul, J. F., and Leibl, W. (2023). Identification of a Ubiquinone–Ubiquinol Quinhydrone Complex in Bacterial Photosynthetic Membranes and Isolated Reaction Centers by Time-Resolved Infrared Spectroscopy. *Int. J. Mol. Sci.*, 24(6):5233.

Mezzetti, A., Schnee, J., Lapini, A., and Di Donato, M. (2022). Time-resolved infrared absorption spectroscopy applied to photoinduced reactions: how and why. *Photochem. Photobiol. Sci.*, 21(4):557–584.

Mortimer, R. G. and Eyring, H. (1980). Elementary transition state theory of the Soret and Dufour effects. *Proc. Natl. Acad. Sci. U.S.A*, 77(4):1728–1731.

Müh, F., Glöckner, C., Hellmich, J., and Zouni, A. (2012). Light-induced quinone reduction in photosystem II. *Biochim. Biophys. Acta*, 1817(1):44–65.

Müh, F. and Zouni, A. (2020). Structural basis of light-harvesting in the photosystem II core complex. *Protein Sci.*, 29(5):1090–1119.

Mula, S., Savitsky, A., Möbius, K., Lubitz, W., Golbeck, J. H., Mamedov, M. D., Semenov, A. Y., and Der Est, A. V. (2012). Incorporation of a high potential quinone reveals that electron transfer in Photosystem I becomes highly asymmetric at low temperature. *Photochem. Photobiol. Sci.*, 11(6):946–956.

Nabedryk, E., Leibl, W., and Breton, J. (1996). FTIR spectroscopy of primary donor photooxidation in Photosystem I, *Heliobacillus mobilis*, and *Chlorobium limicola*. Comparison with purple bacteria. *Photosynth. Res.*, 48:301–308.

Nabedryk, E., Schulz, C., Müh, F., Lubitz, W., and Breton, J. (2000). Heterodimeric Versus Homodimeric Structure of the Primary Electron Donor in *Rhodobacter sphaeroides* Reaction Centers Genetically Modified at Position M202. *Photochem. Photobiol.*, 71(5):582.

Nagao, R., Ueoka-Nakanishi, H., and Noguchi, T. (2017a). D1-Asn-298 in photosystem II is involved in a hydrogen-bond network near the redox-active tyrosine Y_Z for proton exit during water oxidation. *J. Biol. Chem.*, 292(49):20046–20057.

Nagao, R., Yamaguchi, M., Nakamura, S., Ueoka-Nakanishi, H., and Noguchi, T. (2017b). Genetically introduced hydrogen bond interactions reveal an asymmetric charge distribution on the radical cation of the special-pair chlorophyll P680. *J. Biol. Chem.*, 292(18):7474–7486.

Nakamura, S., Nagao, R., Takahashi, R., and Noguchi, T. (2014). Fourier transform infrared detection of a polarizable proton trapped between photooxidized tyrosine Y_Z and a coupled histidine in photosystem II: Relevance to the proton transfer mechanism of water oxidation. *Biochemistry*, 53(19):3131–3144.

Nakamura, S. and Noguchi, T. (2015). Infrared Detection of a Proton Released from Tyrosine Y_D to the Bulk upon Its Photo-oxidation in Photosystem II. *Biochemistry*, 54(32):5045–5053.

Nakamura, S. and Noguchi, T. (2016). Quantum mechanics/molecular mechanics simulation of the ligand vibrations of the water-oxidizing Mn_4CaO_5 cluster in photosystem II. *Proc. Natl. Acad. Sci. U.S.A*, 113(45):12727–12732.

Nelson, N. and Ben-Shem, A. (2004). The complex architecture of oxygenic photosynthesis. *Nat. Rev. Mol. Cell Biol.*, 5(12):971–982.

Nelson, N. and Junge, W. (2015). Structure and Energy Transfer in Photosystems of Oxygenic Photosynthesis. *Annu. Rev. Biochem.*, 84:659–683.

Noguchi, T. (2007). Light-induced FTIR difference spectroscopy as a powerful tool toward understanding the molecular mechanism of photosynthetic oxygen evolution. *Photosynth. Res.*, 91(1):59–69.

Noguchi, T. (2024). Mechanism of Proton Transfer through the D1-E65/D2-E312 Gate during Photosynthetic Water Oxidation. *J. Phys. Chem. B*.

Noguchi, T., aki Ono, T., and Inoue, Y. (1995a). Direct detection of a carboxylate bridge between Mn and Ca^{2+} in the photosynthetic oxygen-evolving center by means of Fourier transform infrared spectroscopy. *Biochim. Biophys. Acta*, 1228(2-3):189–200.

Noguchi, T. and Berthomieu, C. (2005). Molecular analysis by vibrational spectroscopy. In Wydrzynski, T. J. and Satoh, K., editors, *Photosystem II: The Light-Driven Water: Plastoquinone Oxidoreductase*, pages 367–387. Springer.

Noguchi, T., Inoue, Y., and Satoh, K. (1993). FT-IR Studies on the Triplet State of P680 in the Photosystem II Reaction Center: Triplet Equilibrium within a Chlorophyll Dimer. *Biochemistry*, 32(28):7186–7195.

Noguchi, T., Inoue, Y., and Tang, X. S. (1999). Hydrogen bonding interaction between the primary quinone acceptor Q_A and a histidine side chain in photosystem II as revealed by Fourier transform infrared spectroscopy. *Biochemistry*, 38(1):399–403.

Noguchi, T., Kusumoto, N., Inoue, Y., and Sakurai, H. (1996). Electronic and vibrational structure of the radical cation of P_{840} in the putative homodimeric reaction center from *Chlorobium tepidum* as studied by FTIR spectroscopy. *Biochemistry*, 35(48):15428–15435.

Noguchi, T., Ono, T.-a., and Inoue, Y. (1995b). A carboxylate ligand interacting with water in the oxygen-evolving center of Photosystem II as revealed by Fourier transform infrared spectroscopy. *Biochim. Biophys. Acta*, 1232:59–66.

Noguchi, T. and Sugiura, M. (2002a). Flash-induced FTIR difference spectra of the water oxidizing complex in moderately hydrated photosystem II core films: Effect of hydration extent on S-state transitions. *Biochemistry*, 41(7):2322–2330.

Noguchi, T. and Sugiura, M. (2002b). FTIR detection of water reactions during the flash-induced S-state cycle of the photosynthetic water-oxidizing complex. *Biochemistry*, 41(52):15706–15712.

Noguchi, T. and Sugiura, M. (2003). Analysis of flash-induced FTIR difference spectra of the S-state cycle in the photosynthetic water-oxidizing complex by uniform ^{15}N and ^{13}C isotope labeling. *Biochemistry*, 42(20):6035–6042.

Noguchi, T., Suzuki, H., Tsuno, M., Sugiura, M., and Kato, C. (2012). Time-resolved infrared detection of the proton and protein dynamics during photosynthetic oxygen evolution. *Biochemistry*, 51(15):3205–3214.

Noguchi, T., Tomo, T., and Inoue, Y. (1998). Fourier transform infrared study of the cation radical of P680 in the photosystem II reaction center: Evidence for charge delocalization on the chlorophyll dimer. *Biochemistry*, 37(39):13614–13625.

Nuijs, A. M., van Gorkom, H. J., Plijter, J. J., and Duysens, L. N. (1986). Primary-charge separation and excitation of chlorophyll *a* in photosystem II particles from spinach as studied by picosecond absorbance-difference spectroscopy. *Biochim. Biophys. Acta*, 848(2):167–175.

Nürnberg, D. J., Morton, J., Santabarbara, S., Telfer, A., Joliot, P., Antonaru, L. A., Ruban, A. V., Cardona, T., Krausz, E., Boussac, A., Fantuzzi, A., and William Rutherford, A. (2018). Photochemistry beyond the red limit in chlorophyll f–containing photosystems. *Science*, 360(6394):1210–1213.

Okamoto, Y., Shimada, Y., Nagao, R., and Noguchi, T. (2021). Proton and Water Transfer Pathways in the $S_2 \rightarrow S_3$ Transition of the Water-Oxidizing Complex in Photosystem II: Time-Resolved Infrared Analysis of the Effects of D1-N298A Mutation and NO_3^- Substitution. *J. Phys. Chem. B*, 125(25):6864–6873.

Okubo, T., Tomo, T., Sugiura, M., and Noguchi, T. (2007). Perturbation of the structure of P680 and the charge distribution on its radical cation in isolated reaction center complexes of photosystem II as revealed by Fourier transform infrared spectroscopy. *Biochemistry*, 46(14):4390–4397.

Pantazis, D. A. (2018). Missing Pieces in the Puzzle of Biological Water Oxidation. *ACS Catal.*, 8(10):9477–9507.

Petrouleas, V. and Diner, B. A. (1987). Light-induced oxidation of the acceptor-side Fe(II) of Photosystem II by exogenous quinones acting through the Q_B binding site. I. Quinones, kinetics and pH-dependence. *Biochim. Biophys. Acta*, 893:126–137.

Pham, L. V. and Messinger, J. (2016). Probing S-state advancements and recombination pathways in photosystem II with a global fit program for flash-induced oxygen evolution pattern. *Biochim. Biophys. Acta*, 1857(6):848–859.

Pokhrel, R., Service, R. J., Debus, R. J., and Brudvig, G. W. (2013). Mutation of lysine 317 in the D2 subunit of photosystem II alters chloride binding and proton transport. *Biochemistry*, 52(28):4758–4773.

Porra, R., Thompson, W., and Kriedemann, P. (1989). Determination of accurate extinction coefficients and simultaneous equations for assaying chlorophylls *a* and *b* extracted with four different solvents: verification of the concentration of chlorophyll standards by atomic absorption spectr. *Biochim. Biophys. Acta*, 975(3):384–394.

Purton, S., Stevens, D. R., Muhiuddin, I. P., Evans, M. C., Carter, S., Rigby, S. E., and Heathcote, P. (2001). Site-directed mutagenesis of PsaA residue W693 affects phylloquinone binding and function in the photosystem I reaction center of *Chlamydomonas reinhardtii*. *Biochemistry*, 40(7):2167–2175.

Rappaport, F., Ishida, N., Sugiura, M., and Boussac, A. (2011). Ca^{2+} determines the entropy changes associated with the formation of transition states during water oxidation by Photosystem II. *Energy Environ. Sci.*, 4(7):2520–2524.

Redding, K. and van der Est, A. (2006). The directionality of electron transport in photosystem I. In Golbeck, J. H., editor, *Photosystem I: The Plastocyanin: Ferredoxin Oxidoreductase in Photosynthesis*, pages 413–437. Springer.

Remy, A., Niklas, J., Kuhl, H., Kellers, P., Schott, T., Rögner, M., and Gerwert, K. (2004). FTIR spectroscopy shows structural similarities between photosystems II from cyanobacteria and spinach. *Eur. J. Biochem.*, 271(3):563–567.

Renger, G. (2004). Coupling of electron and proton transfer in oxidative water cleavage in photosynthesis. *Biochim. Biophys. Acta*, 1655:195–204.

Renger, G. and Hanssum, B. (1992). Studies on the reaction coordinates of the water oxidase in PS II membrane fragments from spinach. *FEBS Lett.*, 299(1):28–32.

Rivalta, I., Amin, M., Luber, S., Vassiliev, S., Pokhrel, R., Umena, Y., Kawakami, K., Shen, J.-R., Kamiya, N., Bruce, D., Brudvig, G. W., Gunner, M. R., and Batista, V. S. (2011). Structural–Functional Role of Chloride in Photosystem II. *Biochemistry*, 50:6312–6315.

Robinson, H. H. and Crofts, A. R. (1983). Kinetics of the oxidation-reduction reactions of the photosystem II quinone acceptor complex, and the pathway for deactivation. *FEBS Lett.*, 153(1):221–226.

Robinson, H. H. and Yocum, C. F. (1980). Cyclic photophosphorylation reactions catalyzed by ferredoxin, methyl viologen and anthraquinone sulfonate. Use of photochemical reactions to optimize redox poising. *Biochim. Biophys. Acta*, 590(1):97–106.

Rohani, L., Makita, H., Levitz, A., Henary, M., and Hastings, G. (2019). Calculated vibrational properties of semiquinones in the A_1 binding site in photosystem I. *Biochim. Biophys. Acta*, 1860(9):699–707.

Rutherford, A. W., Boussac, A., and Faller, P. (2004). The stable tyrosyl radical in Photosystem II: Why D? *Biochim. Biophys. Acta*, 1655(1-3):222–230.

Saito, K., William Rutherford, A., and Ishikita, H. (2015). Energetics of proton release on the first oxidation step in the water-oxidizing enzyme. *Nat. Commun.*, 6:8488.

Sakamoto, H., Shimizu, T., Nagao, R., and Noguchi, T. (2017). Monitoring the reaction process during the $S_2 \rightarrow S_3$ transition in photosynthetic water oxidation using time-resolved infrared spectroscopy. *J. Am. Chem. Soc.*, 139(5):2022–2029.

Sakashita, N., Watanabe, H. C., Ikeda, T., Saito, K., and Ishikita, H. (2017). Origins of Water Molecules in the Photosystem II Crystal Structure. *Biochemistry*, 56(24):3049–3057.

Santabarbara, S., Kuprov, I., Poluektov, O., Casal, A., Russell, C. A., Purton, S., and Evans, M. C. (2010). Directionality of electron-transfer reactions in photosystem I of prokaryotes: Universality of the bidirectional electron-transfer model. *J. Phys. Chem. B*, 114(46):15158–15171.

Sauer, K., Mathis, P., Acker, S., and Van Best, J. A. (1978). Electron acceptors associated with P-700 in Triton solubilized photosystem I particles from spinach chloroplasts. *Biochim. Biophys. Acta*, 503:120–134.

Savitsky, A., Gopta, O., Mamedov, M., Golbeck, J. H., Tikhonov, A., Möbius, K., and Semenov, A. (2010). Alteration of the axial met ligand to electron acceptor A_0 in photosystem I: Effect on the generation of $P_{700}^{\bullet+}$ $A_1^{\bullet-}$ radical pairs as studied by W-band transient EPR. *Appl. Magn. Reson.*, 37:85–102.

Scheiner, S. (2000). Calculation of isotope effects from first principles. *Biochim. Biophys. Acta*, 1458(1):28–42.

Schiller, H. and Dau, H. (2000). Preparation protocols for high-activity Photosystem II membrane particles of green algae and higher plants, pH dependence of oxygen evolution and comparison of the S_2-state multiline signal by X-band EPR spectroscopy. *J. Photochem. Photobiol. B*, 55(2-3):138–144.

Schilstra, M. J., Rappaport, F., Nugent, J. H., Barnett, C. J., and Klug, D. R. (1998). Proton/hydrogen transfer affects the S-state-dependent microsecond phases of $P680^+$ reduction during water splitting. *Biochemistry*, 37(11):3974–3981.

Schlodder, E., Brettel, K., and Witt, H. T. (1985). Relation between microsecond reduction kinetics of photooxidized chlorophyll a_{II} (P-680) and photosynthetic water oxidation. *Biochim. Biophys. Acta*, 808(1):123–131.

Schlodder, E., Falkenberg, K., Gergeleit, M., and Brettel, K. (1998). Temperature dependence of forward and reverse electron transfer from A_1^-, the reduced secondary electron acceptor in photosystem I. *Biochemistry*, 37(26):9466–9476.

Schlodder, E. and Witt, H. T. (1999). Stoichiometry of proton release from the catalytic center in photosynthetic water oxidation. Reexamination by a glass electrode study at pH 5.5–7.2. *J. Biol. Chem.*, 274(43):30387–30392.

Schönborn, M. B. (2017). *Time-resolved step-scan FTIR spectroscopy on photosystem II*. PhD thesis, Freie Universität Berlin.

Schubert, W. D., Klukas, O., Krauß, N., Saenger, W., Fromme, P., and Witt, H. T. (1997). Photosystem I of *Synechococcus elongatus* at 4 Å resolution: Comprehensive structure analysis. *J Mol Biol*, 272(5):741–769.

Schultz, B. J., Mohrmann, H., Lorenz-Fonfria, V. A., and Heberle, J. (2018). Protein dynamics observed by tunable mid-IR quantum cascade lasers across the time range from 10 ns to 1 s. *Spectrochim. Acta A*, 188:666–674.

Service, R. J., Hillier, W., and Debus, R. J. (2010). Evidence from FTIR difference spectroscopy of an extensive network of hydrogen bonds near the oxygen-evolving Mn_4Ca cluster of photosystem II Involving D1-Glu65, D2-Glu312, and D1-Glu329. *Biochemistry*, 49(31):6655–6669.

Service, R. J., Hillier, W., and Debus, R. J. (2014). Network of hydrogen bonds near the oxygen-evolving Mn_4CaO_5 cluster of Photosystem II probed with FTIR difference spectroscopy. *Biochemistry*, 53(6):1001–1017.

Sétif, P. and Brettel, K. (1993). Forward Electron Transfer from Phylloquinone A_1 to Iron-Sulfur Centers in Spinach Photosystem I. *Biochemistry*, 32(31):7846–7854.

Shen, J.-R. (2015). The structure of photosystem II and the mechanism of water oxidation in photosynthesis. *Annu. Rev. Plant Biol.*, 66:23–48.

Shevela, D., Kern, J. F., Govindjee, G., and Messinger, J. (2023). Solar energy conversion by photosystem II: principles and structures. *Photosynth. Res.*, 156(3):279–307.

Shevela, D., Kern, J. F., Govindjee, G., Whitmarsh, J., and Messinger, J. (2021). Photosystem II. *eLS*, 2(7):1–20.

Shevela, D. and Messinger, J. (2012). Probing the turnover efficiency of photosystem II membrane fragments with different electron acceptors. *Biochim. Biophys. Acta*, 1817(8):1208–1212.

Shimada, Y., Kitajima-Ihara, T., Nagao, R., and Noguchi, T. (2020). Role of the O4 Channel in Photosynthetic Water Oxidation as Revealed by Fourier Transform Infrared Difference and Time-Resolved Infrared Analysis of the D1-S169A Mutant. *J. Phys. Chem. B*, 124(8):1470–1480.

Shimada, Y., Sugiyama, A., Nagao, R., and Noguchi, T. (2022a). Role of D1-Glu65 in Proton Transfer during Photosynthetic Water Oxidation in Photosystem II. *J. Phys. Chem. B*, 126(41):8202–8213.

Shimada, Y., Suzuki, T., Matsubara, T., Kitajima-Ihara, T., Nagao, R., Dohmae, N., and Noguchi, T. (2022b). Post-translational amino acid conversion in photosystem II as a possible origin of photosynthetic oxygen evolution. *Nat. Commun.*, 13(1):4211.

Shimizu, T., Sugiura, M., and Noguchi, T. (2018). Mechanism of Proton-Coupled Electron Transfer in the S_0-to-S_1 Transition of Photosynthetic Water Oxidation As Revealed by Time-Resolved Infrared Spectroscopy. *J. Phys. Chem. B*, 122(41):9460–9470.

Shuvalov, V. A., Ke, B., and Dolan, E. (1979). Kinetic and spectral properties of the intermediary electron acceptor A_1 in photosystem I. *FEBS Lett.*, 100(1):1–4.

Siegbahn, P. E. (2006). O-O bond formation in the S_4 state of the oxygen-evolving complex in photosystem II. *Chem. Eur. J.*, 12(36):9217–9227.

Siegbahn, P. E. (2009). Structures and energetics for O_2 formation in photosystem II. *Acc. Chem. Res.*, 42(12):1871–1880.

Siegbahn, P. E. (2012). Mechanisms for proton release during water oxidation in the S_2 to S_3 and S_3 to S_4 transitions in photosystem II. *Phys. Chem. Chem. Phys.*, 14(14):4849–4856.

Siegbahn, P. E. (2013). Water oxidation mechanism in photosystem II, including oxidations, proton release pathways, O–O bond formation and O_2 release. *Biochim. Biophys. Acta*, 1827(8-9):1003–1019.

Simon, P. S. (2019). *Time-Resolved Single Frequency Infrared Absorption Spectroscopy on Photosystem II*. PhD thesis, Freie Universität Berlin.

Sirohiwal, A. and Pantazis, D. A. (2022). Functional Water Networks in Fully Hydrated Photosystem II. *J. Am. Chem. Soc.*, 144(48):22035–22050.

Sivakumar, V., Wang, R., and Hastings, G. (2005). A_1 reduction in intact cyanobacterial photosystem I particles studied by time-resolved step-scan Fourier transform infrared difference spectroscopy and isotope labeling. *Biochemistry*, 44(6):1880–1893.

Snyder, S. W., Rustandi, R. R., Biggins, J., Norris, J. R., and Thurnauer, M. C. (1991). Direct assignment of vitamin K_1 as the secondary acceptor A_1 in photosystem I. *Proc. Natl. Acad. Sci. U.S.A*, 88(21):9895–9896.

Srinivasan, N. and Golbeck, J. H. (2009). Protein-cofactor interactions in bioenergetic complexes: The role of the A_{1A} and A_{1B} phylloquinones in Photosystem I. *Biochim. Biophys. Acta*, 1787(9):1057–1088.

Stirbet, A., Lazár, D., Guo, Y., and Govindjee, G. (2020). Photosynthesis: Basics, history and modelling. *Ann. Bot.*, 126(4):511–537.

Styring, S. and Rutherford, A. W. (1987). In the Oxygen-Evolving Complex of Photosystem II the S_0 State Is Oxidized to the S_1 State by D^+ (Signal II$_{slow}$). *Biochemistry*, 26(9):2401–2405.

Styring, S., Sjöholm, J., and Mamedov, F. (2012). Two tyrosines that changed the world: Interfacing the oxidizing power of photochemistry to water splitting in photosystem II. *Biochim. Biophys. Acta*, 1817(1):76–87.

Suga, M., Akita, F., Yamashita, K., Nakajima, Y., Ueno, G., Li, H., Yamane, T., Hirata, K., Umena, Y., Yonekura, S., Yu, L. J., Murakami, H., Nomura, T., Kimura, T., Kubo, M., Baba, S., Kumasaka, T., Tono, K., Yabashi, M., Isobe, H., Yamaguchi, K., Yamamoto, M., Ago, H., and Shen, J. R. (2019). An oxyl/oxo mechanism for oxygen-oxygen coupling in PSII revealed by an x-ray free-electron laser. *Science*, 366(6463):334–338.

Suzuki, H., Nagasaka, M. A., Sugiura, M., and Noguchi, T. (2005a). Fourier transform infrared spectrum of the secondary quinone electron acceptor Q_B in photosystem II. *Biochemistry*, 44(34):11323–11328.

Suzuki, H., Sugiura, M., and Noguchi, T. (2005b). pH dependence of the flash-induced S-state transitions in the oxygen-evolving center of photosystem II from *Thermosynechoccocus elongatus* as revealed by Fourier transform infrared spectroscopy. *Biochemistry*, 44(5):1708–1718.

Suzuki, H., Sugiura, M., and Noguchi, T. (2009). Monitoring proton release during photosynthetic water oxidation in photosystem II by means of isotope-edited infrared spectroscopy. *J. Am. Chem. Soc.*, 131(22):7849–7857.

Suzuki, H., Taguchi, Y., Sugiura, M., Boussac, A., and Noguchi, T. (2006). Structural Perturbation of the Carboxylate Ligands to the Manganese Cluster upon Ca^{2+} / Sr^{2+} Exchange in the S-State Cycle of Photosynthetic Oxygen Evolution As Studied by Flash-Induced FTIR Difference Spectroscopy. *Biochemistry*, 45(45):13454–13464.

Suzuki, H., Yu, J., Kobayashi, T., Nakanishi, H., Nixon, P. J., and Noguchi, T. (2013). Functional roles of D2-Lys317 and the interacting chloride ion in the water oxidation reaction of photosystem II as revealed by Fourier transform infrared analysis. *Biochemistry*, 52(28):4748–4757.

Takahashi, R., Hasegawa, K., and Noguchi, T. (2008). Effect of charge distribution over a chlorophyll dimer on the redox potential of P680 in photosystem II as studied by density functional theory calculations. *Biochemistry*, 47(24):6289–6291.

Takahashi, R., Hasegawa, K., Takano, A., and Noguchi, T. (2010). Structures and Binding Sites of Phenolic Herbicides in the Q_B Pocket of Photosystem II. *Biochemistry*, 49:5445–5454.

Takei, K.-i., Takahashi, R., and Noguchi, T. (2008). Correlation between the hydrogen-bond structures and the C=O stretching frequencies of carboxylic acids as studied by density functional theory calculations: Theoretical basis for interpretation of infrared bands of carboxylic groups in proteins. *J. Phys. Chem. B*, 112(21):6725–6731.

Takemoto, H., Sugiura, M., and Noguchi, T. (2019). Proton Release process during the S_2-to-S_3 transition of photosynthetic water oxidation as revealed by the pH dependence of kinetics monitored by time-resolved infrared spectroscopy. *Biochemistry*, 58(42):4276–4283.

Tang, X. S. and Diner, B. A. (1994). Biochemical and Spectroscopic Characterization of a New Oxygen-Evolving Photosystem II Core Complex from the Cyanobacterium *Synechocystis* PCC 6803. *Biochemistry*, 33(15):4594–4603.

Tang, X. S. and Satoh, K. (1985). The oxygen-evolving photosystem II core complex. *FEBS Lett.*, 179(1):60–64.

Tavitian, B. A., Nabedryk, E., Mäntele, W., and Breton, J. (1986). Light-induced Fourier transform infrared (FTIR) spectroscopic investigations of primary reactions in photosystem I and photosystem II. *FEBS Lett.*, 201(1):151–157.

Ugur, I., Rutherford, A. W., and Kaila, V. R. (2016). Redox-coupled substrate water reorganization in the active site of Photosystem II - The role of calcium in substrate water delivery. *Biochim. Biophys. Acta*, 1857(6):740–748.

Umena, Y., Kawakami, K., Shen, J. R., and Kamiya, N. (2011). Crystal structure of oxygen-evolving photosystem II at a resolution of 1.9Å. *Nature*, 473(7345):55–60.

Vass, I. and Styring, S. (1991). pH-Dependent Charge Equilibria between Tyrosine-D and the S States in Photosystem II. Estimation of Relative Midpoint Redox Potentials. *Biochemistry*, 30:830–839.

Vassiliev, I. R., Jung, Y. S., Mamedov, M. D., Semenov, A. Y., and Golbeck, J. H. (1997). Near-IR absorbance changes and electrogenic reactions in the microsecond-to-second time domain in photosystem I. *Biophys. J.*, 72(1):301–315.

Vinyard, D. J. and Brudvig, G. W. (2017). Progress Toward a Molecular Mechanism of Water Oxidation in Photosystem II. *Annu. Rev. Phys. Chem.*, 68:101–116.

Wang, R., Sivakumar, V., Li, Y., Redding, K., and Hastings, G. (2003). Mutation induced modulation of hydrogen bonding to P700 studied using FTIR difference spectroscopy. *Biochemistry*, 42(33):9889–9897.

Witt, H., Schlodder, E., Teutloff, C., Niklas, J., Bordignon, E., Carbonera, D., Kohler, S., Labahn, A., and Lubitz, W. (2002). Hydrogen bonding to P700: Site-directed mutagenesis of threonine A739 of photosystem I in *Chlamydomonas reinhardtii*. *Biochemistry*, 41(27):8557–8569.

Wynn, R. M. and Malkin, R. (1988). Characterization of an isolated chloroplast membrane FeS protein and its identification as the photosystem I $Fe-S_A/Fe-S_B$ binding protein. *FEBS Lett.*, 229(2):293–297.

Xu, W., Chitnis, P. R., Valieva, A., Van der Est, A., Brettel, K., Guergova-Kuras, M., Pushkar, Y. N., Zech, S. G., Stehlik, D., Shen, G., Zybailov, B., and Golbeck, J. H. (2003). Electron transfer in cyanobacterial Photosystem I: II. Determination of forward electron transfer rates of site-directed mutants in a putative electron transfer pathway from A_0 through A_1 to F_X. *J. Biol. Chem.*, 278(30):27876–27887.

Yamanari, T., Kimura, Y., Mizusawa, N., Ishii, A., and Ono, T. A. (2004). Mid- to low-frequency fourier transform infrared spectra of S-state cycle for photosynthetic water oxidation in *Synechocystis* sp. PCC 6803. *Biochemistry*, 43(23):7479–7490.

Yamori, W. and Shikanai, T. (2016). Physiological Functions of Cyclic Electron Transport Around Photosystem I in Sustaining Photosynthesis and Plant Growth. *Annu. Rev. Plant Biol.*, 67:81–106.

Yano, J., Kern, J., Irrgang, K. D., Latimer, M. J., Bergmann, U., Glatzel, P., Pushkar, Y., Biesiadka, J., Loll, B., Sauer, K., Messinger, J., Zouni, A., and Yachandra, V. K. (2005). X-ray damage to the Mn_4Ca complex in single crystals of photosystem II: A case study for metalloprotein crystallography. *Proc. Natl. Acad. Sci. U.S.A*, 102(34):12047–12052.

Zaharieva, I., Dau, H., and Haumann, M. (2016). Sequential and Coupled Proton and Electron Transfer Events in the $S_2 \rightarrow S_3$ Transition of Photosynthetic Water Oxidation Revealed by Time-Resolved X-ray Absorption Spectroscopy. *Biochemistry*, 55(50):6996–7004.

Zaharieva, I., Wichmann, J. M., and Dau, H. (2011). Thermodynamic limitations of photosynthetic water oxidation at high proton concentrations. *J. Biol. Chem.*, 286(20):18222–18228.

Zaharieva, I., Grabolle, M., Chernev, P., Dau, H. (2013). Water Oxidation in Photosystem II: Energetics and Kinetics of Intermediates Formation in the $S_2 \rightarrow S_3$ and $S_3 \rightarrow S_0$ Transitions Monitored by Delayed Chlorophyll Fluorescence. In *Photosynthesis research for food, fuel and the future: 15th international conference on photosynthesis*, pages 234—-238. Springer Berlin Heidelberg.

Zamzam, N., Kaucikas, M., Nürnberg, D. J., Rutherford, A. W., and Van Thor, J. J. (2019). Femtosecond infrared spectroscopy of chlorophyll *f*-containing photosystem I. *Phys. Chem. Chem. Phys.*, 21:1224–1234.

Zhang, H., Razeghifard, M. R., Fischer, G., and Wydrzynski, T. (1997). A time-resolved FTIR difference study of the plastoquinone Q_A and redox-active tyrosine Y_Z interactions in photosystem II. *Biochemistry*, 36(39):11762–11768.

Zhao, C., Gan, F., Shen, G., and Bryant, D. A. (2015). RfpA, RfpB, and RfpC are the master control elements of far-red light photoacclimation (FaRLiP). *Front. Microbiol.*, 6:1303.

Zimmermann, J.-L. and Rutherford, A. (1986). Photoreductant-induced oxidation of Fe^{2+} in the electron-acceptor complex of Photosystem II. *Biochim. Biophys. Acta*, 851:416–423.

Zybailov, B., Van Der Est, A., Zech, S. G., Teutloff, C., Johnson, T. W., Shen, G., Bittl, R., Stehlik, D., Chitnis, P. R., and Golbeck, J. H. (2000). Recruitment of a foreign quinone into the A_1 site of photosystem I. II. Structural and functional characterization of phylloquinone biosynthetic pathway mutants by electron paramagnetic resonance and electron-nuclear double resonance spectroscopy. *J. Biol. Chem.*, 275(12):8531–8539.

A | Appendix

A1 QCL Setup: Additional Information

Appendix A1 closely relates to Chapter 2 on *Time-Resolved Single-Frequency Infrared Spectroscopy*. Table A1.1 lists the pulse generator settings used for the measurements in this thesis. Figure A1.1 shows examples of some of the auto-generated plots that are created by the Python data processing script described in Chapter 2.3: Panels a–b show plots of the processed and heat artefact corrected data, panel c shows the calculated heat artefact transient and panel d shows a visualization of the implemented data filters. In the latter, the horizontal lines indicate the filter threshold that can be adjusted by the user. A description of the individual filters is given in Subchapter 2.3.2.

Table A1.1: Pulse generator settings. Channels A, B and C are set to enabled; all other channels should be disabled. When running a measurement, the overall gate/trigger mode needs to be set to *triggered*, which means the pulse generator itself will wait for a trigger. If the mode is set to *disabled*, activating the pulse generator will directly trigger the laser (as well as the data acquisition). The mode is set to *continuous* for calibration purposes and to *burst* for measurements. *This number determines the number of "dark flashes" preceding the first excitation flash. †This number may seem oddly specific. It has been optimized such that time zero coincides with the timing of the laser as recorded by the photo diode.

	Ch A	Ch B	Ch C
triggers	flash lamp	Q-switch	data acquisition
gate	disabled	disabled	disabled
wait	0 pulses	6 pulses*	0 pulses
sync source	T_0	Ch A	Ch B
width	$20\,\mu s$	$20\,\mu s$	$20\,\mu s$
delay	$+0.1\,s$	$+160\,\mu s$	$-1.99996\,ms$†
pol	active high	active high	active high
out	TTL/CMOS	TTL/CMOS	TTL/CMOS
mode	normal	normal	normal
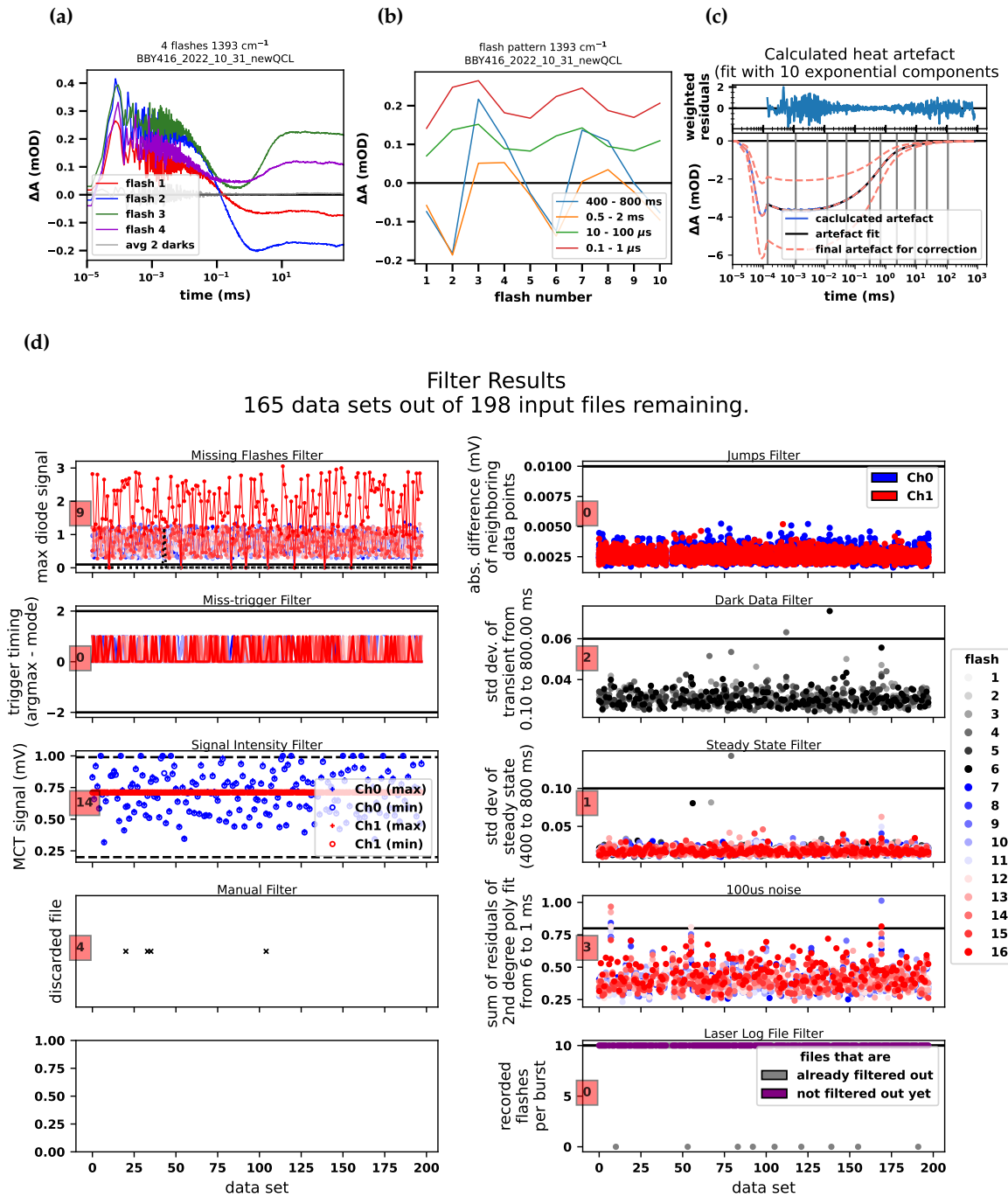
Figure A1.1: Examples for automatically generated figures upon running data processing script. (a) Figure of the first four flash transients (after heat artefact correction). A transient acquired without excitation flash is shown in *grey*. **(b)** A figure of the flash-number dependent IR difference values at four different time points. **(c)** The calculated heat artefact transient (*blue*) and its multi-exponential fit (*dashed line*). Weighted residuals are shown to assess the fit quality. **(d)** Figure showing the results of the individual filters. The number in the little red square indicates the number of data sets discarded by the respective filter.

Figure A1.2 shows the saturation curve data for PSI core particles at 1635 cm^{-1}. Very similar plots for spinach PSII membrane particles are shown in Fig. 2.13 and discussed in Chapter 2.4.2.
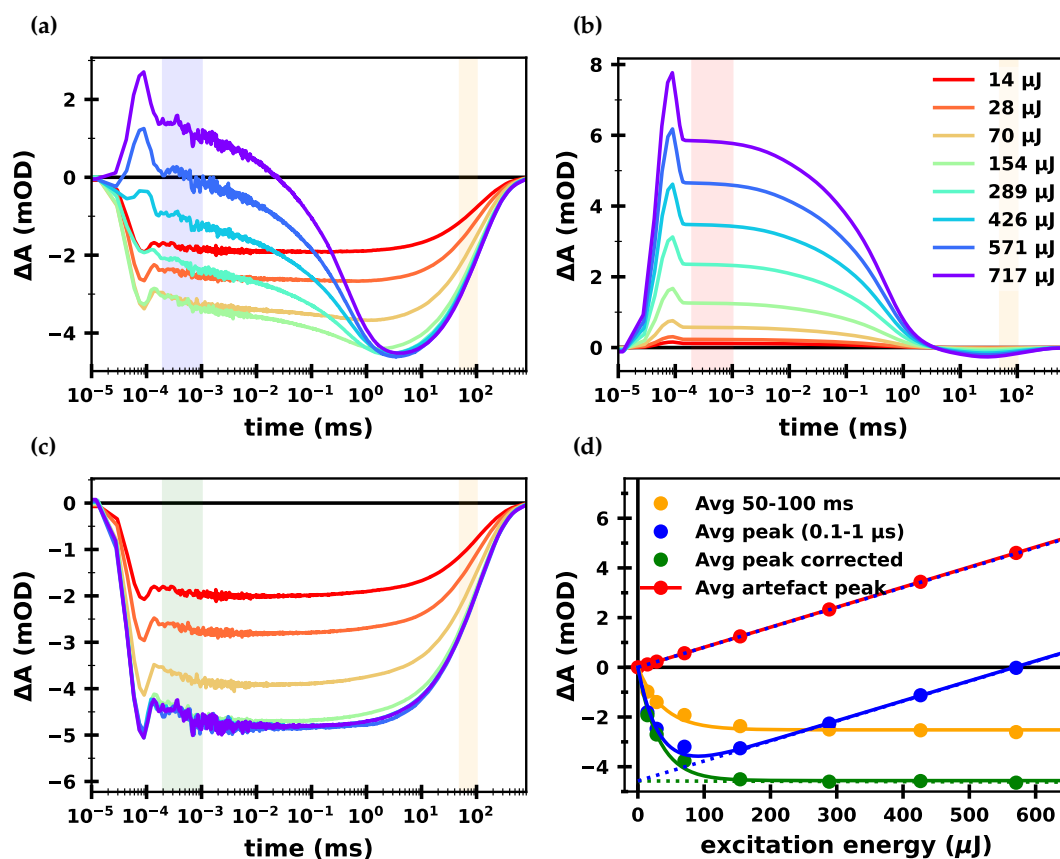
Figure A1.2: Saturation curve of PSI core particles at 1635 cm^{-1}. **(a)** Ten transients averaged over the first five excitation flashes at increasing excitation energy before heat artefact correction. **(b)** A fit of the heat artefact contribution of each transient. The heat artefact transient was calculated from a data set measured at E_{low} = 300 μJ and E_{high} = 700 μJ and fit to a sum of exponentials. The magnitude of the artefact fit was scaled according to the average excitation energy of each data set. **(c)** The ten transients after heat artefact correction. **(d)** Saturation curve obtained from the transients. The yellow dots show the averaged absorption of each transient between 50 and 100 ms (unaffected by the heat artefact); the yellow curve was obtained by fitting the data with one exponential. The blue data shows the averaged peak of each transient (average of 100 ns–1 μs); the curve was obtained by fitting the data with one exponential plus a linear regression. The dotted line is the result of a linear regression of the last four points. The green data shows the averaged peak of each corrected transient, fitted with one exponential. The dotted green line is a linear regression of the last four points. The red dots show the averaged peak of the calculated artefact for each transient. The vertical colored strips in the first three plots show the areas of the transients that were averaged to obtain the data of the same color shown in (d).

A2   Supporting Data and Foundational Results: Additional Figures

Appendix A2 supplements Chapter 4 with additional data and figures. Figure A2.1 shows data of a long-term IR experiment on spinach PSII membrane particles. The measurement was performed on the QCL setup prior to implementing the motorized attenuator and the data set was relatively noisy. Nevertheless, the analysis shows that the time constants determined for the $S_3 \rightarrow S_0$ transition effectively remain the same throughout the ~45 h of measurement. Only the amplitudes of the 2.3 ms phase show a clear trend, i.e. they become
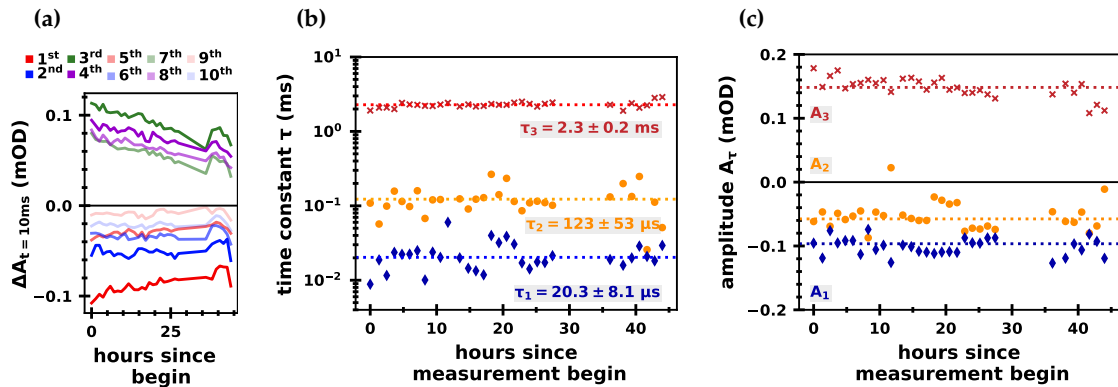
Figure A2.1: Results of a second long-term IR measurement on spinach PSII (preparation 386). (a) The IR difference absorption averaged between 9.5 and 10.5 ms for all 10 flashes as a function of measurement time. **(b)** Time constants and **(c)** their respective amplitudes obtained from fitting the $S_3 \rightarrow S_0$ transient to a sum of exponentials. The average values over all data batches are shown as dotted lines. The measurements were performed at 10°C and pH 6.2; the data was analyzed in batches of 212 data sets (one round of targeting all sample spots).
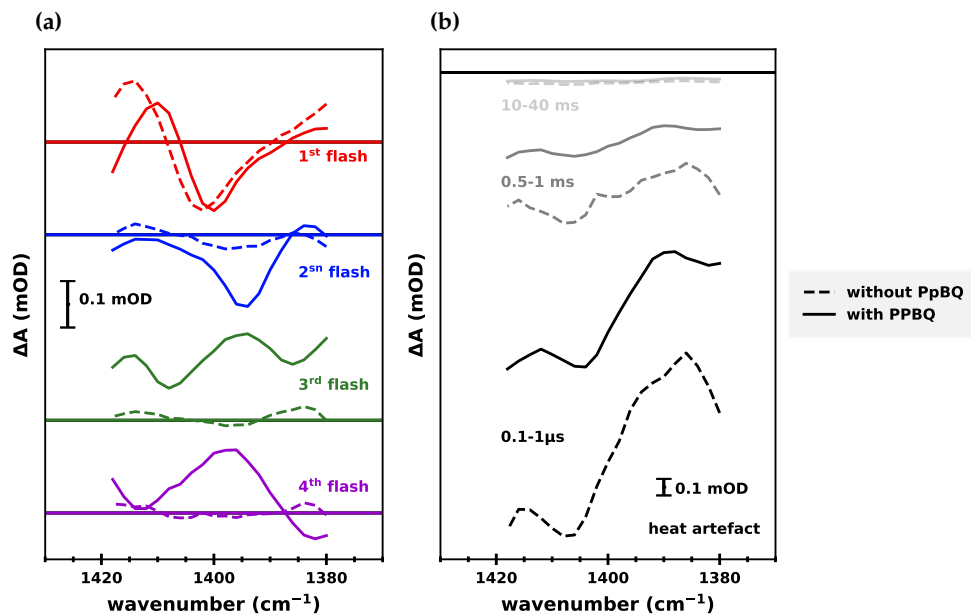
Figure A2.2: Spectra of spinach PSII membrane particles measured with vs. without addition of exogenous electron acceptor PPBQ. (a) Steady-state spectra following the first four excitation flashes, obtained by averaging individual transients between 400–800 ms after the flash. Data with and without the addition of PPBQ is shown in *solid* and *dashed* lines, respectively. **(b)** The heat artefact spectrum of both data sets averaged around three different time points (0.1–1 μs, 0.5–1 ms and 10–40 ms).

smaller at longer measurement times. This further supports to results shown in Fig. 4.2 of a similar (but less noisy) long-term IR measurement.

Figure A2.2 shows spectra between 1420–1380 cm^{-1} of spinach PSII membranes with and without added PPBQ. The shown data obtained *without* PPBQ was acquired after

several rounds of measurements had already been performed; thus a 1 Hz flash sequence was too fast for the acceptor side to recover. This is likely the reason that in Fig. A2.2a the steady-state spectrum following the first flash (dashed red lines) still appears comparable to data obtained in the presence of PPBQ (solid red lines), while the following flashes obtained without PPBQ show very little difference absorption. The heat artefact of the sample without addition of PPBQ has a larger amplitude at all time slices, while the shape of artefact is similar for both samples (Fig. A2.2b). This can be explained by the formation of P680 triplet states in samples without exogenous electron acceptor, leading to a larger laser-induced heating of the sample (Noguchi et al., 1998).

Figure A2.3 shows transients of Mn depleted spinach PSII extracted from the time-resolved spectral data shown *inter alia* in Fig. 4.11. Global analysis of the entire time-resolved spectral data set resulted eight DAS for each S-state transition, as shown in Fig. A2.4; the lowest panel additionally shows the steady-state spectra. This figure supplements Fig. 4.12 by showing not just two but all four S-state transitions. The fit quality is demonstrated by showing the 2D residuals of the $S_3 \rightarrow S_0$ transition (Fig. A2.5a). Panel b
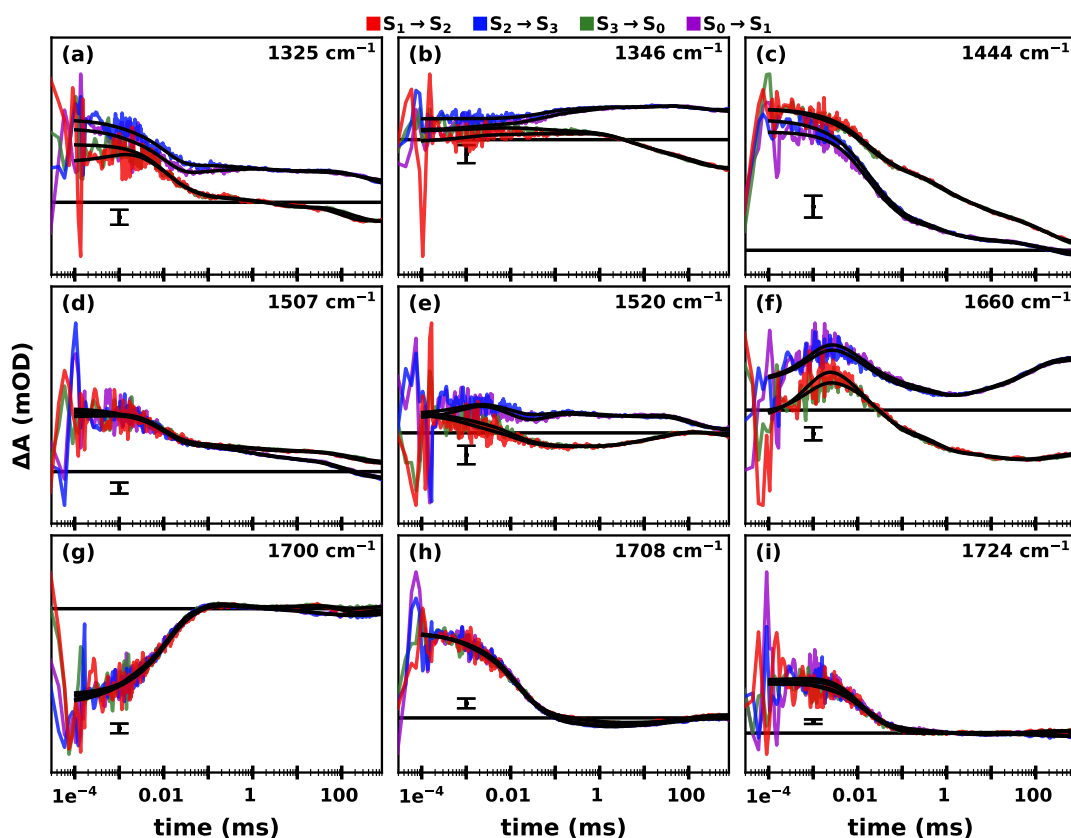
Figure A2.3: Select transients of the Mn depleted PSII spectral data set. For each wavenumber (1325, 1346, 1444, 1507, 1520, 1660, 1700, 1708 and 1724 cm^{-1}) a transient of the $S_1 \rightarrow S_2$ (*red*), $S_2 \rightarrow S_3$ (*blue*), $S_3 \rightarrow S_0$ (*green*) and the $S_0 \rightarrow S_1$ transition (*purple*) is shown together with its fit curve (*black*). Gaussian smoothing ($\sigma = 2.5$) was applied along the wavenumber axis and linear smoothing ($n = 10$) along the time axis. The flash-data was deconvolved assuming a starting population of 85% S_1 and 15% S_0 and a miss factor of 12%. The scale bar corresponds to 0.1 mOD.
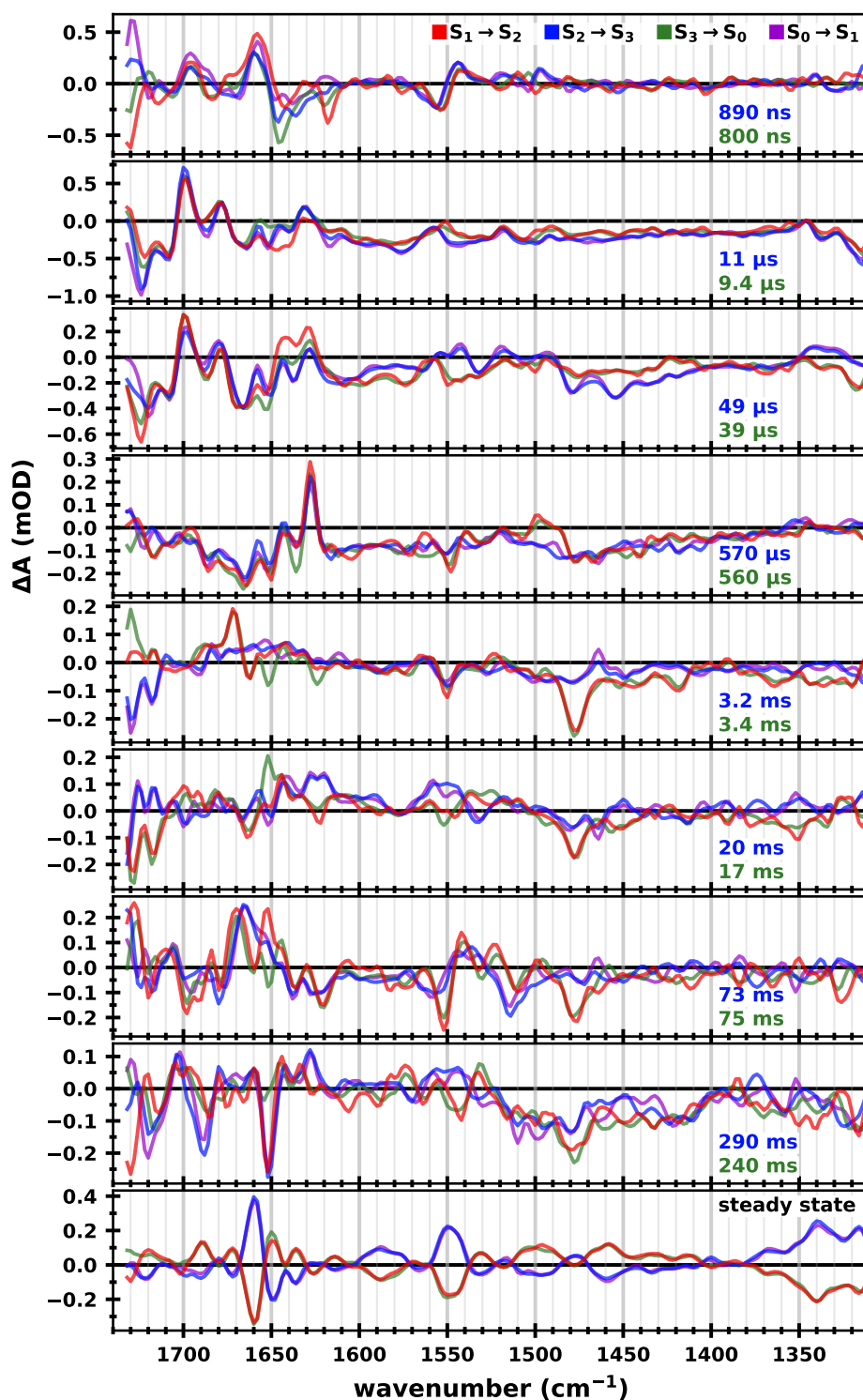
Figure A2.4: Decay associated spectra of Mn depleted spinach PSII. The DAS of the $S_1 \rightarrow S_2$ (*red*), $S_2 \rightarrow S_3$ (*blue*), $S_3 \rightarrow S_0$ (*green*) and $S_0 \rightarrow S_1$ (*purple*) transition were obtained by fitting the spectral data to a sum of 8 exponentials and an offset (Eq. 2.7) between 100 ns and 800 ms. The lowest panel shows the steady state spectra, obtained by averaging the IR signal between 400–800 ms. The time constants were pre-determined by globally fitting a small set of transients (1385, 1395, 1400, 1478, 1514 and 1544 cm^{-1}) with high S/N. The time constants given in *blue* and *green* were used for even- and odd-numbered S-state transitions, respectively.
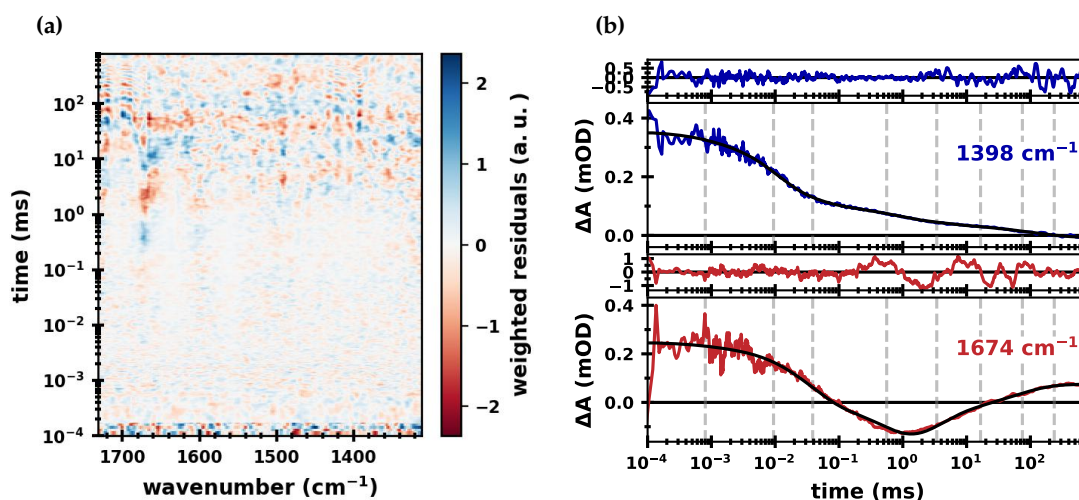
Figure A2.5: Fit quality of the global fit of the spectral data set of Mn depleted PSII.
(a) Weighted residuals corresponding to the DAS resulting from globally fitting the $S_3 \rightarrow S_0$ transition shown in Fig. A2.4. In the amide I region, especially around 1670 cm^{-1}, some transients are not perfectly well defined by the fits around 100 μs to 10 ms. Equivalent 2D residual plots of the other S-state transitions (*not shown*) look very similar to the one shown here. **(b)** Transients at 1398 cm^{-1} (*blue*) and 1674 cm^{-1} (*red*), with their fit curves (*black*) and their weighted residuals (*blue* and *red*, small panels).
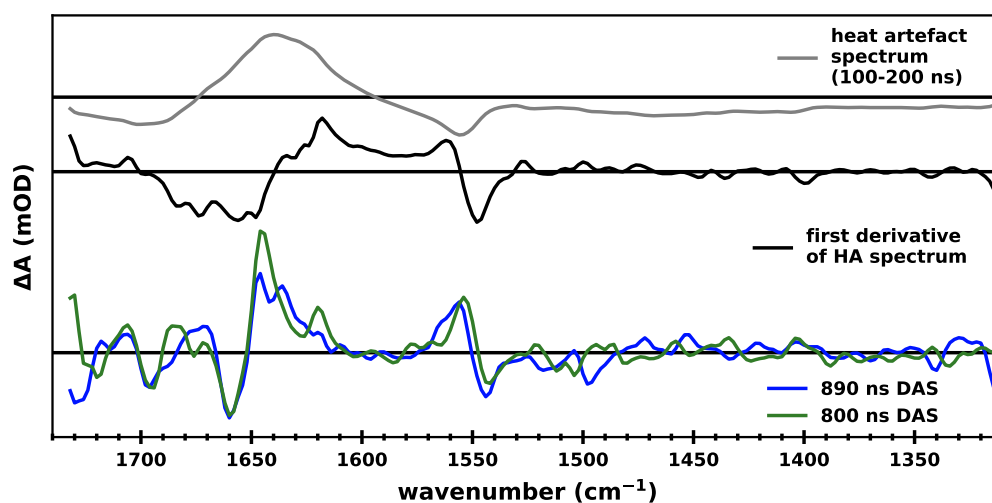
Figure A2.6: Comparison of the first derivative of the heat artefact spectrum with the 800/890 ns DAS of Mn depleted spinach PSII. The heat artefact spectrum of Mn depleted PSII averaged between 100–200 ns (*black*) and its first derivative (*grey*). The derivative resembles the shape of the inverted 890/800 ns DAS of the $S_2 \rightarrow S_3$ (*blue*) and $S_3 \rightarrow S_0$ (*green*) transition of Mn depleted PSII. For more information on the DAS, see Fig. 4.12 and/or Fig. A2.4.

shows two example transients along with their fit curves and residuals, demonstrating that while the fit quality is good around 1398 cm^{-1}, it is somewhat poorer in the amide I region.

The early DAS of 800–890 ns shown in Figs. 4.12 and A2.4 proved difficult to assign, as they have an unusual shape. It was noticed that they show some similarity to the first derivative of the heat artefact spectrum (Fig. A2.6). While this may be coincidental, it may

also indicate that this early kinetic phase is an artefact associated with an imperfect heat artefact correction. Further investigation is required for definitive conclusion.

A3   Spinach PSII: Additional Data, Figures and Tables

Appendix A3 supplements Chapter 5 (*Characterizing the S-State Transitions of Spinach PSII*) with additional data, figures and tables. Figure A3.1 shows the initial spectra (100–500 ns) of four S-state transitions of spinach PSII in H_2O and D_2O before (top panel) and after $P680^+$ background subtraction (bottom panel).
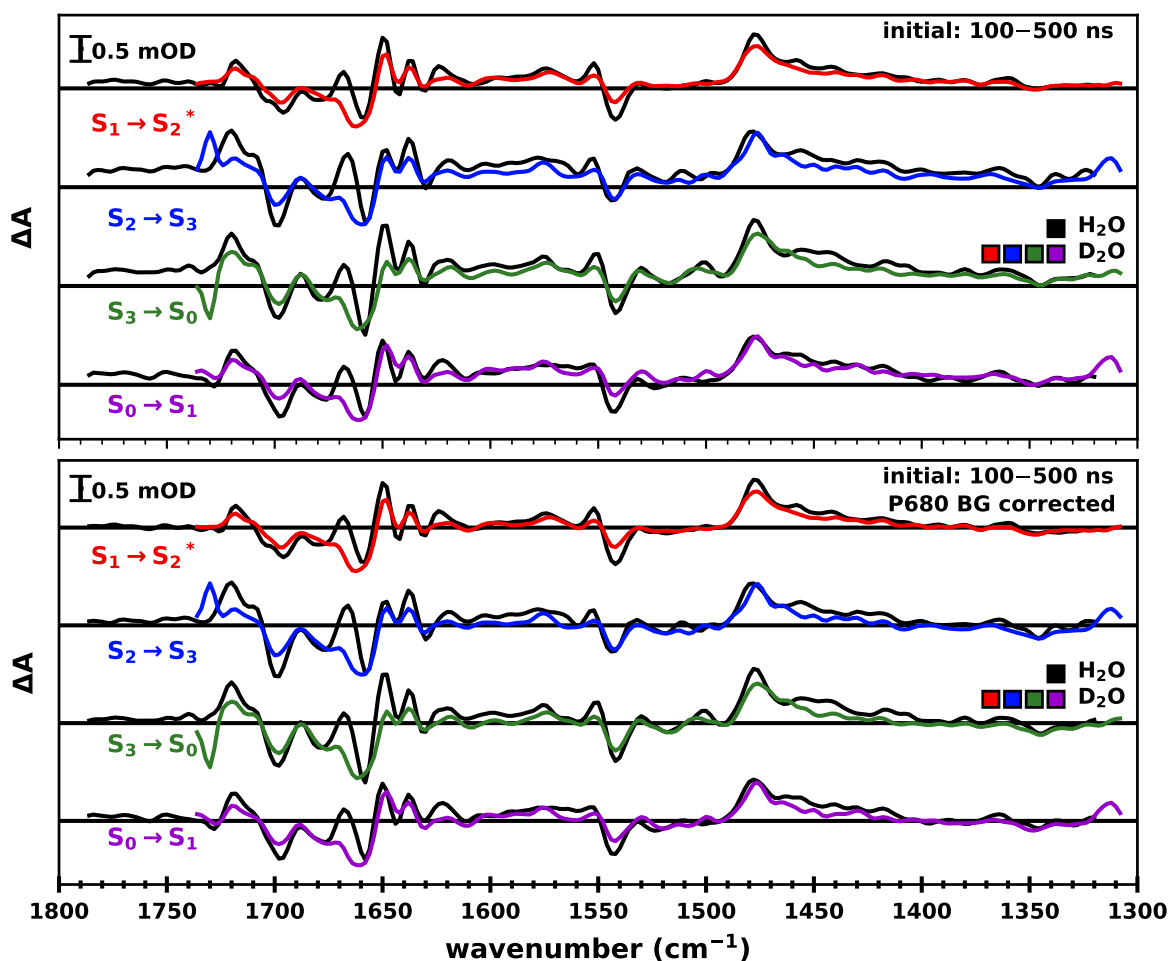
Figure A3.1: Initial IR difference spectra of spinach PSII membrane particles in H_2O and D_2O. *Top:* Initial spectra, obtained by averaging the data between 100—500 ns. Spectra in D_2O (pD 6.2) are shown in color ($S_1 \rightarrow S_2$: *red* $S_2 \rightarrow S_3$: *blue*, $S_3 \rightarrow S_0$: *green* and $S_0 \rightarrow S_1$: *purple*); the spectra in H_2O (pH 6.2) are shown in *black*. *Bottom:* Initial spectra after P680 background subtraction (as measured around 1780 cm^{-1}, see Chapter 4.3). All spectra were deconvolved assuming a starting population of 74% S_1, 14% S_2 and 12% S_0 and a miss factor of 8% (H_2O) or 12% (D_2O). For the $S_1 \rightarrow S_2$ transition, the non-deconvolved first flash data minus 14% S_2 and 12% S_0 is shown (denoted $S_1 \rightarrow S_2^*$).
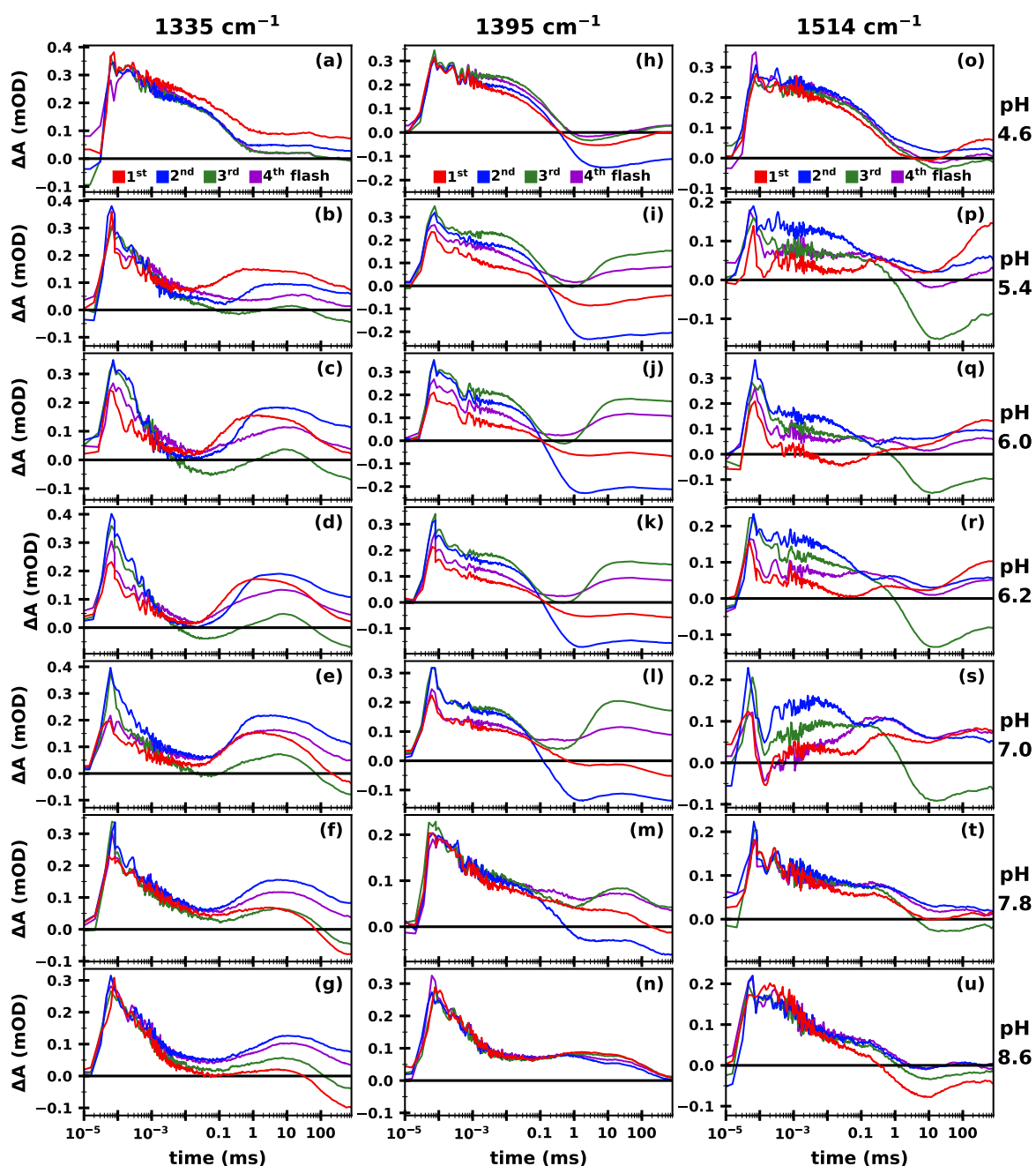
Figure A3.2: IR-difference absorption of four sequential flash-induced transients of spinach PSII at 1384, 1478 and 1544 cm⁻¹ in H₂O buffer at various pH values. Transient absorption changes at **(a–g)** 1355 cm⁻¹, **(h–n)** 1395 cm⁻¹ and **(o–u)** 1514 cm⁻¹ following the 1st (*red*), 2nd (*blue*), 3rd (*green*) and 4th (*purple*) excitation flash are shown from top to bottom at increasing pH values (4.6, 5.4, 6.0, 6.2, 7.0 and 8.6).

Figure A3.2 shows the IR difference transients of spinach PSII in various pH values at 1335, 1395 and 1514 cm⁻¹ following the first four excitation flashes.

Figure A3.3 shows a close-up of the carbonyl C=O stretch region of the steady-state spectra of spinach PSII (the full spectra are shown in Fig. 5.7). This spectral region shows an overall strong similarity to spectra of *T. vestitus* published by Suzuki et al. (2009): *inter*
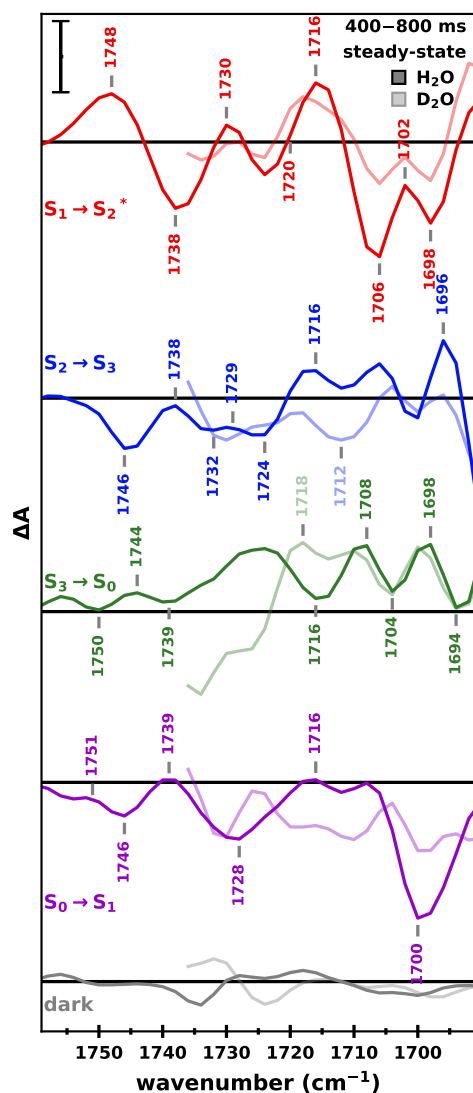
Figure A3.3: Steady-state IR difference spectra of the carbonyl C=O stretch region of spinach PSII membrane particles. Steady-state spectra as determined by averaging the data between 400-800 ms. The darker lines show the spectra in H_2O-based buffer (pH 6.2), while the lighter transparent lines show the spectra in D_2O buffer (pD 6.2). The data was corrected for its P680 background; the non-corrected spectra however look effectively identical (*not shown*). The spectra were deconvolved assuming a starting population of 74% S_1, 14% S_2 and 12% S_0 and a miss factor of 8% (H_2O) or 12% (D_2O). For the $S_1 \rightarrow S_2$ transition, the non-deconvolved first flash data minus 14% S_2 and 12% S_0 is shown (denoted $S_1 \rightarrow S_2^*$). The scale bar corresponds to 0.1 mOD.

alia the long spacing between the peaks at 1744(+) and 1724(+) cm^{-1} in the $S_3 \rightarrow S_0$ transition is also observed in that study.

A comparison of initial (100–500 ns) and steady-state spectra (400–800 ms) at different pH values are shown in Fig. A3.4.

The transient absorption changes at 1478 cm^{-1} following the first four excitation flashes are shown in Fig. A3.5 for measurements in H_2O and D_2O. Each of the four H_2O data sets was fit to a sum of five exponentials and an offset. The resulting time constants were fixed in fits of the D_2O data; visual inspection shows that the fits overall explain the data well. Fits of the D_2O data without constrained time constants gave similar results, as shown in Fig. A3.6a (here the results for all ten flash-induced transients are shown). Figure A3.6b and c additionally show the flash-number dependent amplitudes of the exponential components for the data in H_2O and D_2O, respectively. While the time constants are similar in both buffers, the amplitudes show some notable differences: The ~40 and ~200 ms phases appear less pronounced in D_2O, while the ~800 µs phase shows a larger amplitude—visual inspection of the transients in Fig. A3.5 confirm this observation.

Figures A3.7 and A3.8 show the temporal evolution of the IR difference spectra of the individual S-state transitions in H_2O and D_2O, respectively.
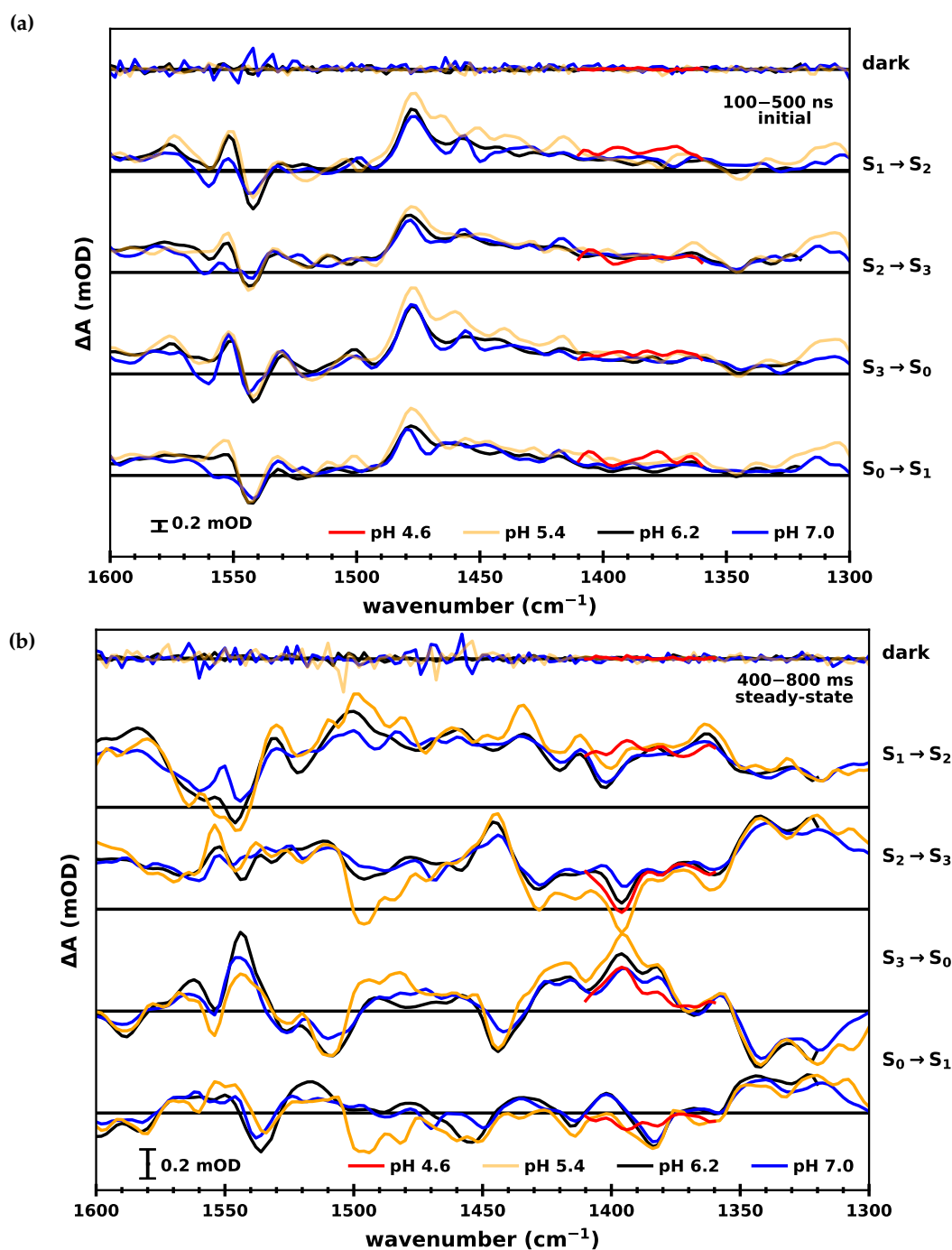
Figure A3.4: Influence of the pH-value on the initial and steady-state IR difference spectra of spinach PSII membrane particles. (a) Initial spectra, obtained by averaging the data between 100–500 ns, are shown for the $S_1 \rightarrow S_2$, $S_2 \rightarrow S_3$, $S_3 \rightarrow S_0$ and $S_0 \rightarrow S_1$ transition, measured at pH 4.6 (*red*), 5.4 (*yellow*), 6.2 (*black*) and 7.0 (*blue*). **(b)** Steady-state spectra of the S-state transitions obtained by averaging the data between 400–800 ms. Both panels additionally show dark data (obtained without applying an excitation flash), indicating the noise level of the spectra. All spectra were deconvolved assuming a starting population of 74% S_1, 14% S_2 and 12% S_0 and a miss factor of 20% (pH 4.6), 12% (pH 5.4), 8% (pH 6.2) and 7% (pH 7.0).

251
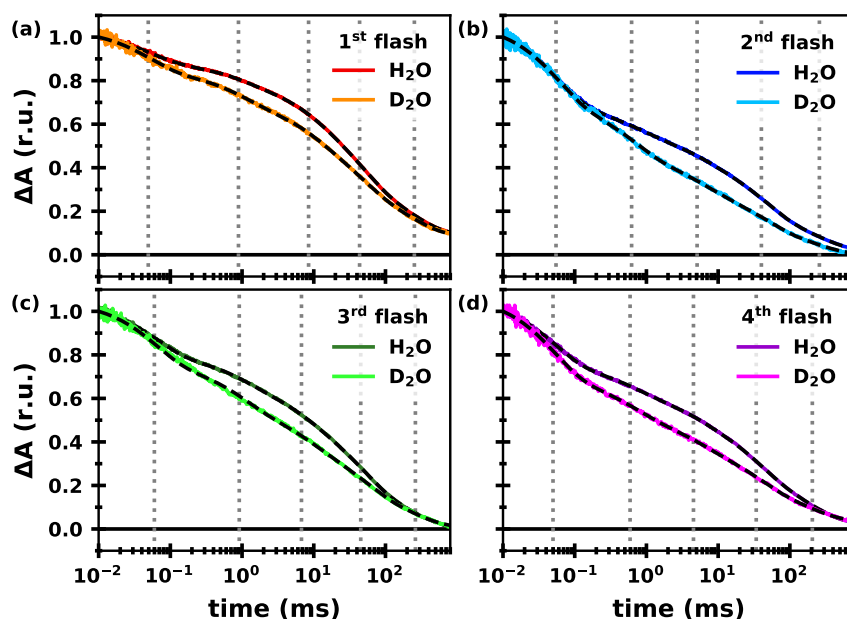
Figure A3.5: Transients absorption changes at 1478 cm^{-1} in H$_2$O and D$_2$O at pL 6.2. Normalized IR absorption changes are shown following the **(a)** first (mostly S$_1\rightarrow$S$_2$), **(b)** second (mostly S$_2\rightarrow$S$_3$), **(c)** third (mostly S$_3\rightarrow$S$_0$) and **(d)** fourth (mostly S$_0\rightarrow$S$_1$) saturating excitation flash. The data in H$_2$O is shown in *darker colors*. Each flash-transient in H$_2$O was fit to a sum of five exponentials and an offset; the resulting time constants (indicated by vertical dotted lines) were fixed in fits of the D$_2$O transients. All fit curves are shown as *dashed black* lines.
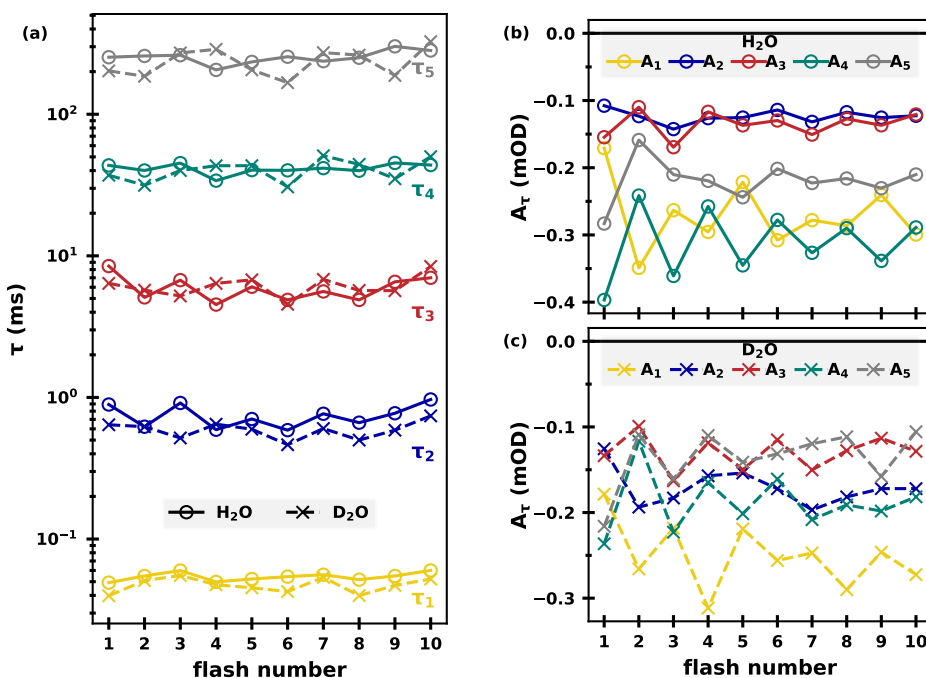
Figure A3.6: Fit parameters of multi-exponential fits of the flash-data at 1478 cm^{-1}. **(a)** Flash-number dependent time constants determined for each of the ten flash-induced transients in H$_2$O (*circles*) and D$_2$O (*crosses*). The corresponding amplitudes **(b)** in H$_2$O and **(c)** in D$_2$O. Unlike the fits shown in Fig. A3.5, the D$_2$O time constants were not constrained here.
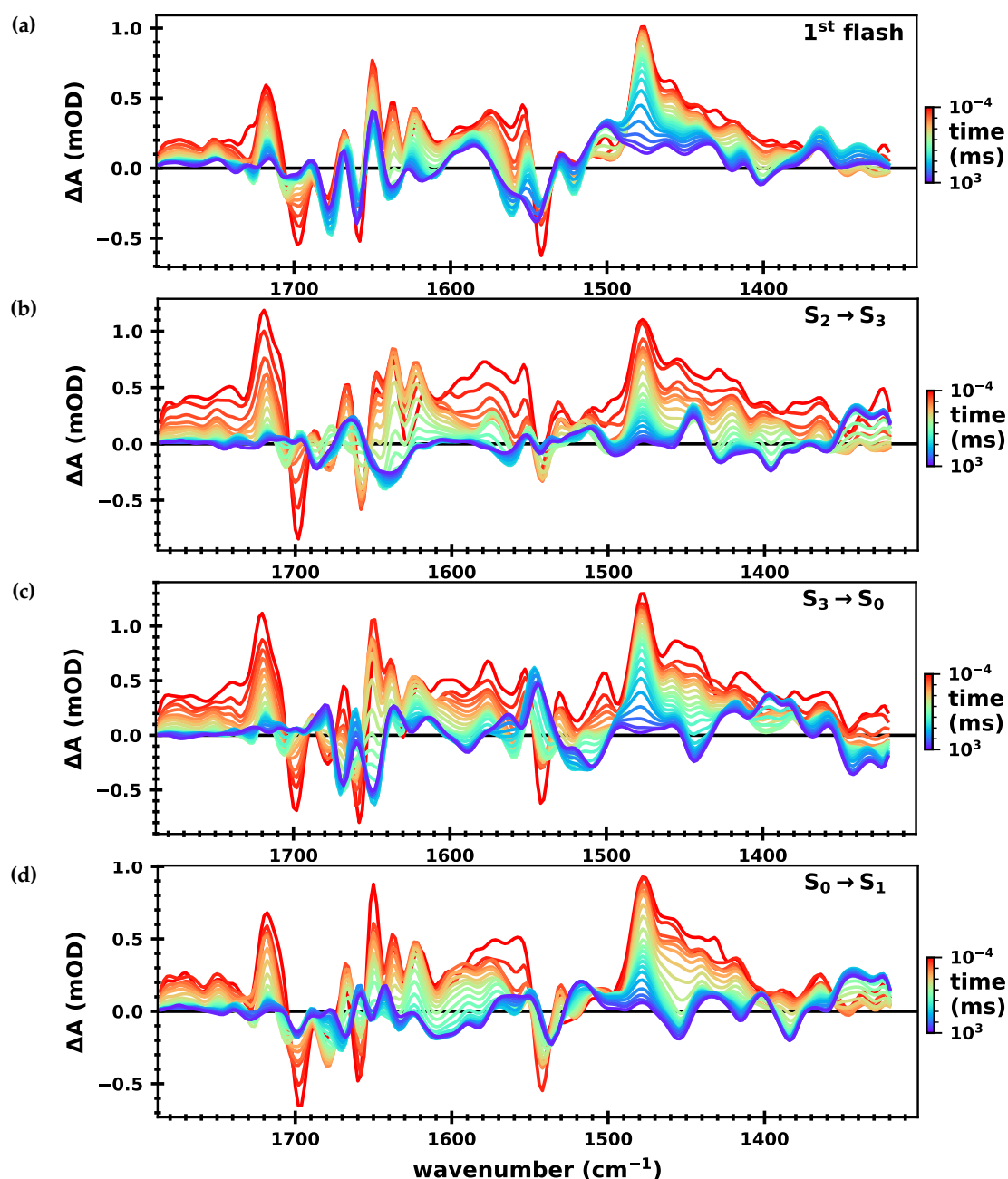
Figure A3.7: Temporal evolution of IR difference absorption spectra of the S-state transitions of spinach PSII in H₂O. The earliest spectra (*red*) show the IR difference absorption averaged between 100 to 215 ns after induction of the **(a)** $S_1 \to S_2$, **(b)** $S_2 \to S_3$, **(c)** $S_3 \to S_0$ and **(d)** $S_0 \to S_1$ transition; the latest spectra (*purple*) where averaged from 464 to 800 ms. Each decade, 10^n, is represented by three logarithmically spaced intervals of $[1 \cdot 10^n, 2.15 \cdot 10^n]$, $[2.15 \cdot 10^n, 4.64 \cdot 10^n]$ and $[4.64 \cdot 10^n, 10 \cdot 10^n]$. The spectra corresponding to the pure S-state transitions were deconvolved from 10 flash-induced spectra, assuming a starting population of 74% S_1, 14% S_2 and 12% S_0 and a miss factor of 8%. For the $S_1 \to S_2$ transition, the (non-deconvolved) first flash data is shown. Gaussian smoothing ($\sigma = 2.5$) was applied along the wavenumber axis and linear smoothing ($n = 10$) along the time axis. The measurements were done at 10 °C and pH 6.2.

Figure A3.8: Temporal evolution of IR difference absorption spectra of the S-state transitions of spinach PSII in D_2O. The earliest spectra (*red*) show the IR difference absorption averaged between 100 to 215 ns after induction of the **(a)** $S_1{\rightarrow}S_2$, **(b)** $S_2{\rightarrow}S_3$, **(c)** $S_3{\rightarrow}S_0$ and **(d)** $S_0{\rightarrow}S_1$ transition; the latest spectra (*purple*) where averaged from 464 to 800 ms. Each decade, 10^n, is represented by three logarithmically spaced intervals of $[1{\cdot}10^n, 2.15{\cdot}10^n]$, $[2.15{\cdot}10^n, 4.64{\cdot}10^n]$ and $[4.64{\cdot}10^n, 10{\cdot}10^n]$. The spectra corresponding to the pure S-state transitions were deconvolved from 10 flash-induced spectra, assuming a starting population of 74% S_1, 14% S_2 and 12% S_0 and a miss factor of 8%. For the $S_1{\rightarrow}S_2$ transition, the (non-deconvolved) first flash data is shown. Gaussian smoothing ($\sigma = 2.5$) was applied along the wavenumber axis and linear smoothing ($n = 10$) along the time axis. The measurements were done at 10 °C and pD 6.2.

A3.1 $S_1 \rightarrow S_2$ Transition

Time constants for the ET step of the $S_1 \rightarrow S_2$ transition were determined at several pH and pD values by globally fitting several high S/N 1st flash transients as discussed in Chapter 5.3; those time constants (shown also in Fig. 5.15) are summarized in Table A3.1.

<table>
<tr><td rowspan="3">Table A3.1: Time constants of the ET phase ($S_1\rightarrow S_2$) in H_2O and D_2O at different pH and pD values. The values correspond to those shown in Fig. 5.15 and were determined by globally fitting the $S_1\rightarrow S_2^*$ transients, i.e. the non-deconvolved first flash data minus 14% S_2 and 12% S_0.</td><td colspan="3" align="center">time constant τ (μs)</td></tr>
<tr><td colspan="3" align="center">ET</td></tr>
<tr><td>pL</td><td>H_2O</td><td>D_2O</td></tr>
<tr><td></td><td>4.6</td><td>141</td><td>—</td></tr>
<tr><td></td><td>5.4</td><td>122</td><td>166</td></tr>
<tr><td></td><td>6.0</td><td>103</td><td>—</td></tr>
<tr><td></td><td>6.2</td><td>110</td><td>148</td></tr>
<tr><td></td><td>7.0</td><td>107</td><td>143</td></tr>
<tr><td></td><td>7.8</td><td>124</td><td>—</td></tr>
</table>

In Chapter 5.3, the DAS in Fig. 5.13 show the results obtained when globally fitting the time-resolved spectral data sets in H_2O and D_2O without $P680^+$ background correction. The results instead obtained when subtracting the $P680^+$ background prior to fitting are shown in Fig. A3.9. The main analysis of the $S_1 \rightarrow S_2$ transition was done on 1st flash transients, from which 14% S_2 and 12% S_0 was subtracted. Alternative results for the H_2O data obtained on the deconvolved $S_1 \rightarrow S_2$ data is shown in Fig. A3.10; these were used for the acceptor-side correction of the $S_3 \rightarrow S_0$ data.
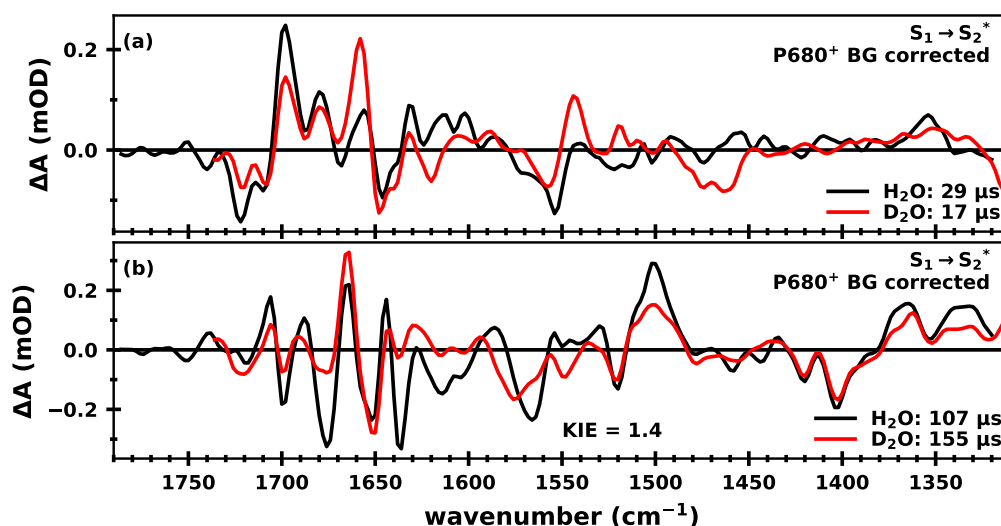
Figure A3.9: Decay associated spectra of the $S_1\rightarrow S_2^*$ spectral data ($P680^+$ background corrected) in H_2O and D_2O. (a) DAS of fast microsecond phase in H_2O (*black*) and D_2O (*red*). **(b)** DAS of slower microsecond phase (likely associated with the ET event expected in that time range) in H_2O (*black*) and D_2O (*red*). The DAS were obtained by fitting the time-resolved spectral data set with time constants pre-determined by the fits shown in Figs. 5.8 and 5.11. The $S_1\rightarrow S_2$ spectra were obtained by subtracting 14% S_2 and 12% S_0 from the non-deconvolved first flash data (denoted $S_1\rightarrow S_2^*$).
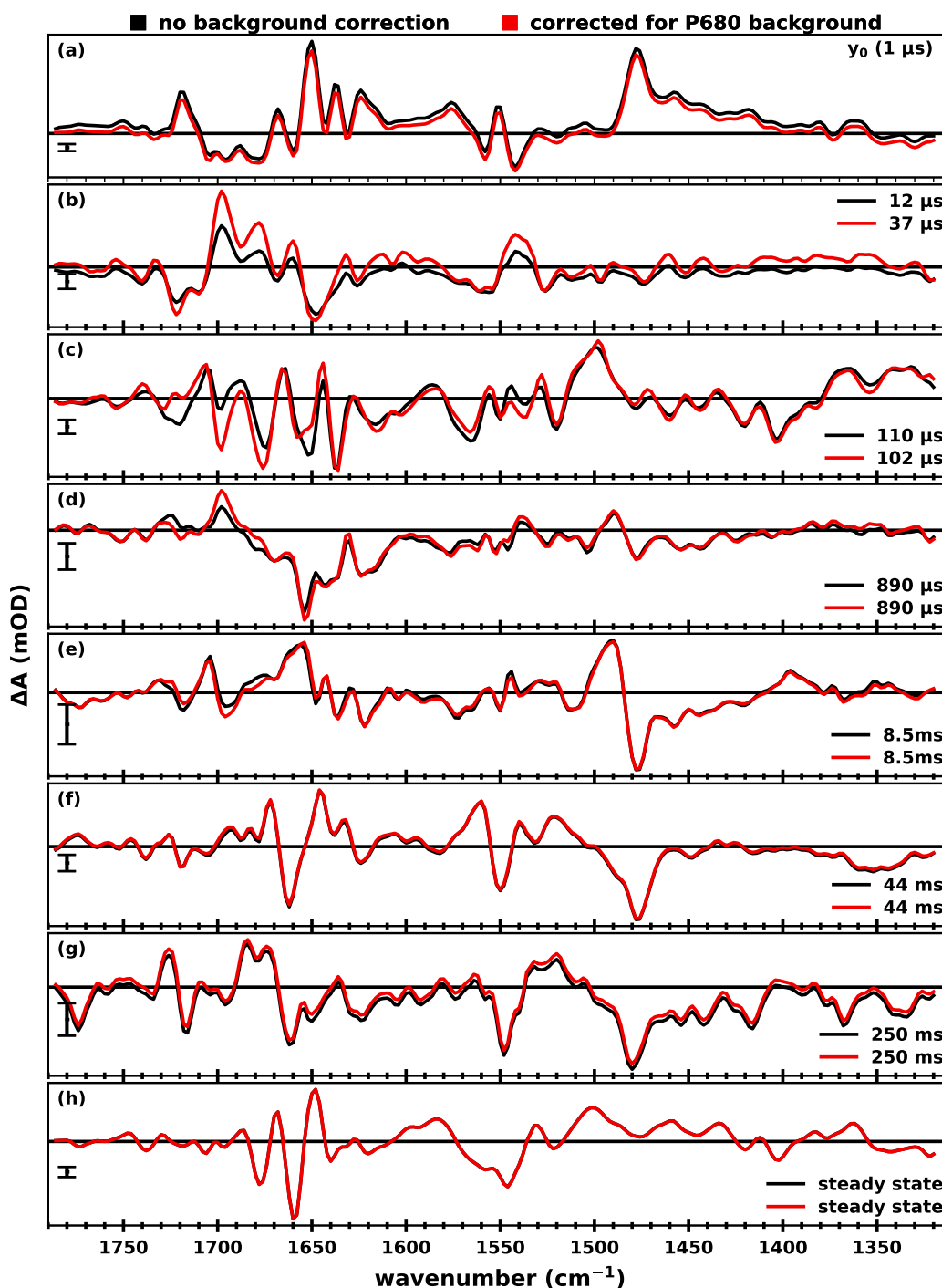
Figure A3.10: Decay associated spectra of the deconvolved $S_1 \rightarrow S_2$ transition. (a) Initial spectrum at 1 μs (y_0). **(b–g)** DAS of the six exponential components. **(h)** Steady-state spectrum (at 800 ms), obtained by addition of all six DAS and the initial spectrum ($y_0 + \sum A_i$). All spectra are shown with (*red*) and without (*black*) P680-background correction. The DAS were obtained by fitting the time-resolved spectral data set with time constants predetermined by the fits shown in Fig. 5.8 (fit range 1 μs–800 ms). The scale bar in each panel corresponds to 0.1 mOD. All measurements were done at 10 °C and pH 6.2. The data was deconvolved assuming a starting population of 74% S_1, 14% S_2 and 12% S_0 and a miss factor of 8% under omission of the 1st flash data.

A3.2 $S_2 \rightarrow S_3$ Transition

Time constants for the ET step of the $S_2 \rightarrow S_3$ transition were determined at several pH and pD values by globally fitting several high S/N transients of the deconvolved $S_2 \rightarrow S_3$ transition, as discussed in Chapter 5.4; those time constants (shown also in Fig. 5.23) are summarized in Table A3.2.

Table A3.2: Time constants of the PT and ET phases ($S_2 \rightarrow S_3$) in H_2O and D_2O at different pH and pD values. The values correspond to those shown in Fig. 5.23.

| | time constant τ (μs) | | | |
| | PT | | ET | |
pL	H_2O	D_2O	H_2O	D_2O
4.6	188	—	999	—
5.4	117	408	466	1758
6.0	95	—	367	—
6.2	71	219	394	798
7.0	47	153	350	534
7.8	70	—	477	—

In Chapter 5.4, the DAS in Fig. 5.21 show the results obtained when globally fitting the time-resolved spectral data sets in H_2O and D_2O without $P680^+$ background correction. The results instead obtained when subtracting the $P680^+$ background prior to fitting are shown in Fig. A3.11.
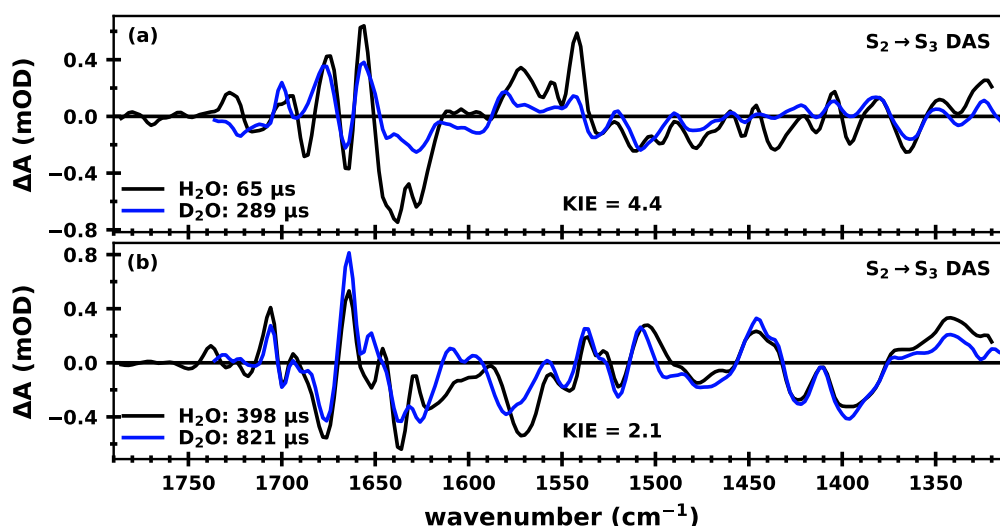
Figure A3.11: Decay associated spectra of the P680-background corrected $S_2 \rightarrow S_3$ transition in H_2O and D_2O. (a) DAS of a 65 μs phase in H_2O (*black*), which slows down to 289 μs in D_2O (*blue*). These kinetics are likely associated with the PT event. **(b)** DAS of a 398 μs phase in H_2O (*black*), which slows down to 821 μs in D_2O (*blue*) and is likely associated with the ET event expected in this time range. The DAS were obtained by fitting the time-resolved spectral data set with time constants pre-determined by the fits shown in Figs. 5.16 and 5.19. The time-resolved spectral data set was deconvolved assuming a starting population of 74% S_1, 14% S_2 and 12% S_0 and a miss factor of 8% (H_2O) or 12% (D_2O).

A3.3 $S_3 \rightarrow S_0$ Transition

Time constants for the ET step of the $S_3 \rightarrow S_0$ transition were determined at several pH and pL values by globally fitting several high S/N transients, as discussed in Chapter 5.5; those time constants (shown also in Fig. 5.34) are summarized in Table A3.3.

Table A3.3: Time constants of the ET phase ($S_3 \rightarrow S_0$) in H_2O and D_2O at different pH and pD values. The values correspond to those shown in Fig. 5.34.

| | time constant τ (ms) | | half-life τ (ms) | | pre-ET minimum (μs) | |
| | ET | | ET | | PT? | |
pL	H_2O	D_2O	H_2O	D_2O	H_2O	D_2O
4.6	4.2	—	3.6	—	579	—
5.4	3.1	5.4	2.5	4.9	262	823
6.0	2.8	—	1.9	—	174	—
6.2	2.8	3.3	2.1	2.8	216	447
7.0	2.7	2.6	1.9	1.8	168	262
7.8	3.5	—	3.0	—	571	—

High S/N transients of the $S_3 \rightarrow S_0$ transition measured in D_2O were fit globally to a sum of exponentials; Figure A3.12a–n shows the transients with (*light grey*) and without (*dark grey*) P680$^+$ background correction. Panel o shows the wavenumber-dependent amplitudes of the resulting exponential components.

Analogously to the H_2O data, the DAS resulting from the global analysis of a time-resolved spectral data set in D_2O again required an acceptor-side correction for the PT phase; the correction procedure is shown in Fig. A3.13.

Figure A3.14 shows non-normalized as well as normalized transients of the $S_3 \rightarrow S_0$ transition at 1514 cm^{-1} in H_2O and D_2O at various pL values. With exception of the transient at pH 4.6, the sub-millisecond kinetics exhibit only a low pL-dependency.

Figure A3.15 shows the transient absorption changes at various wavenumbers between 1566–1598 cm^{-1}. While the pre-ET rising phase is clearly visible at 1566, 1568, 1572 and 1598 cm^{-1}, it is hardly discernible at the other wavenumbers. One possible explanation for this, is the close proximity of several time constants; the exponential components thus partly diminish each other (if they appear with opposite signs).

As discussed at length in Chapter 5.5, an acceptor-side contribution is expected in the relevant time range at most wavenumbers. This may significantly contribute to obscuring the PT phase in the transients around 1570 cm^{-1}. Figure A3.16 shows the 1570 cm^{-1} transient of the $S_1 \rightarrow S_2$ (*red*) and $S_3 \rightarrow S_0$ transition (*light green*), along with their fit curves. Additionally, a S_1 fit curve, which takes only the time constants ≥ 890 μs into account, is shown (*bold black*). This curve should represent only acceptor-side kinetics, as the $S_1 \rightarrow S_2$ donor-side events are completely within about 100 μs. Subtracting this curve from the $S_3 \rightarrow S_0$ transient should thus be equivalent to an acceptor-side correction; the amplitudes of the PT rise and ET decay indeed become visibly more similar (*dark green*).
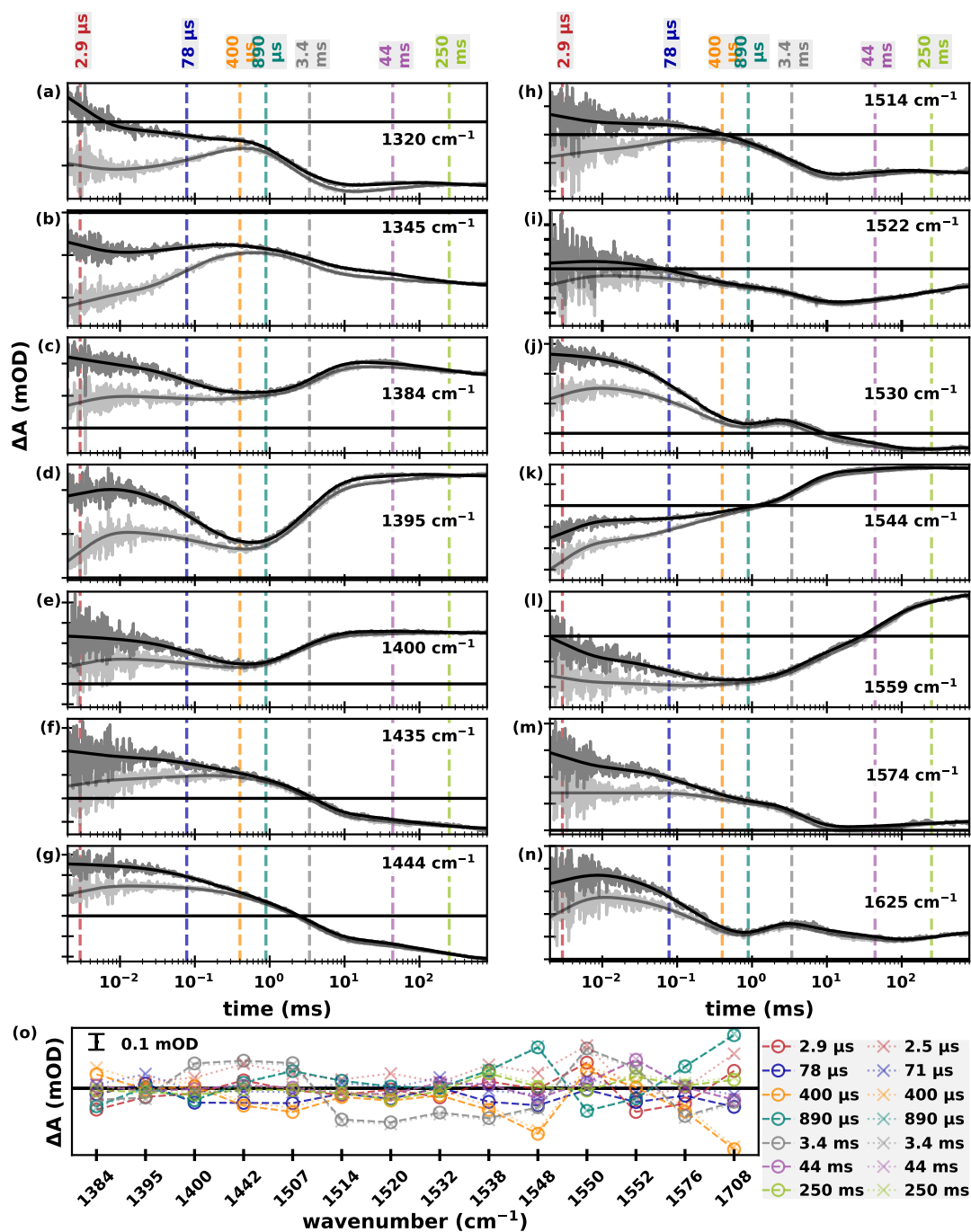
Figure A3.12: Results of globally fitting transient absorption changes of the $S_3 \rightarrow S_0$ transition in D_2O at 14 different wavenumbers. (a–n) Transients (*dark grey*) and their fit curves (*black*). The (global) time constants are indicated by vertical dashed lines. The transients are additionally shown after a correction for their $P680^+$ background (*light grey*), as measured at 1780 cm^{-1}, see Chapter 4.3. The y-axis ticks indicate 0.1 mOD. The transients were fit globally to sums of exponentials; five time constants were fixed ($\tau_3 = 400$ µs, $\tau_4 = 890$ µs, $\tau_5 = 3.4$ ms, $\tau_6 = 44$ ms and $\tau_7 = 250$ ms), all other variables were left free to vary (see text for details on the fit approach). The fit range was 0.5 µs–800ms. **(o)** Wavenumber-dependent amplitudes of the six exponential components for the fits without (*circles*) and with (*crosses*) $P680^+$ background correction. See text for details on the fitting approach. All transients were deconvolved assuming a starting population of 74% S_1, 14% S_2 and 12% S_0; they were smoothed with a sliding average algorithm with a window size of three data points. All measurements were done at 10 °C and pD 6.2.

259

Figure A3.13: Correction of the DAS of the PT phase in D$_2$O for acceptor-side contributions. (a) DAS of the 890 μs phase of the S$_1$→S$_2$ data. As donor-side reactions are expected to be (to a large extent) completed at this time point, this DAS should reflect mostly acceptor-side contributions. **(b)** DAS of the 400 and 890 μs phases of S$_3$→S$_0$, corresponding to the fit approach shown in Fig. A3.12a–b. Both DAS are likely a mixture of donor-side PT event and acceptor-side contributions. **(c)** Sum of the two DAS shown in (b) minus the DAS shown in (a). This should reflect the first S$_3$→S$_0$ PT event without acceptor-side contributions.
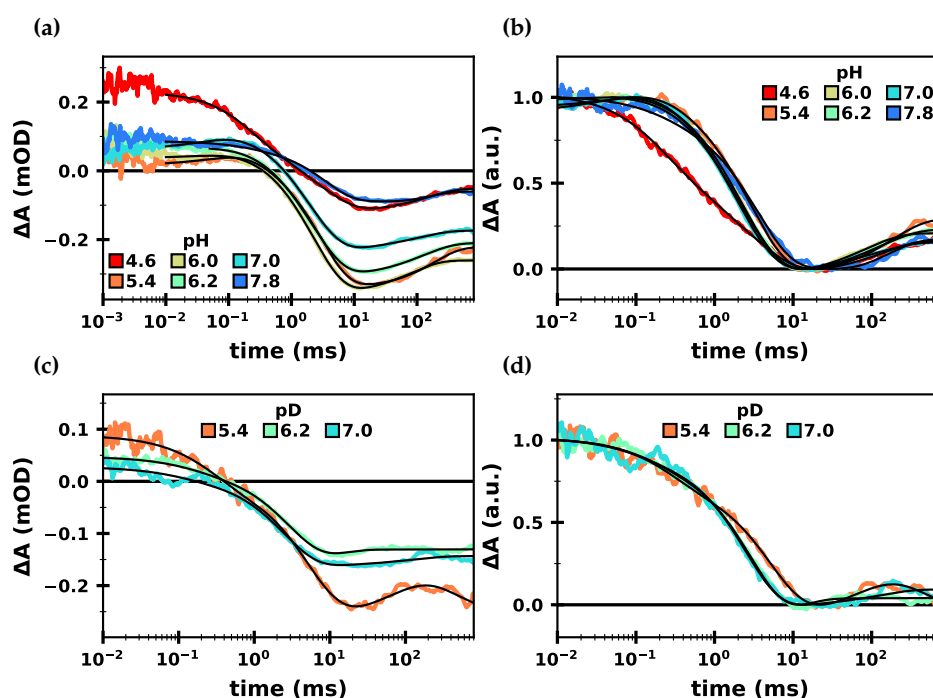
Figure A3.14: Influence of the pH and pD value on the S$_3$→S$_0$ transition at 1514 cm^{-1}. (a) Absorption changes at 1514 cm^{-1} (*colored lines*) at six different pH values, along with their fit curves (*black*). **(b)** The data as in (a), but shifted and normalized. **(c)** Absorption changes at 1514 cm^{-1} in D$_2$O (*colored lines*) at three different pD values, along with their fit curves (*black*). **(d)** The data as in (c), but shifted and normalized. All transients were deconvolved assuming a starting population of 74% S$_1$, 14% S$_2$ and 12% S$_0$.
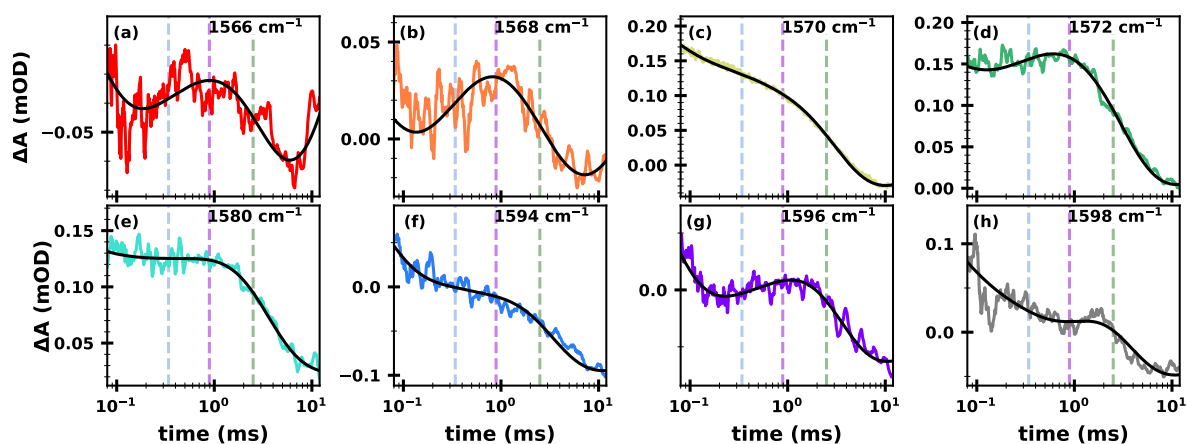
Figure A3.15: Transient absorption changes displaying a pre-ET lag behavior or reversed behavior in their PT and ET phases in $S_3 \rightarrow S_0$. (a–h) IR difference absorption at eight different wavenumbers (*colored lines*) together with their fit curves (*black*). The time constant of the two pre-ET phases (340 and 890 μs) and that of the ET event (2.5 ms) are indicated by light blue, purple and green vertical lines, respectively. Arrows of the same color indicate the sign of the corresponding amplitudes. All transients were deconvolved assuming a starting population of 74% S_1, 14% S_2 and 12% S_0. They were *not* corrected for their P680 background. All data was acquired at 10 °C and pH 6.2.
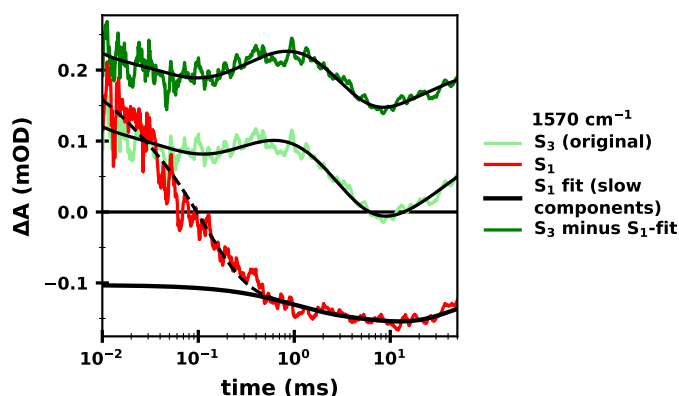
Figure A3.16: Acceptor-side correction of the $S_3 \rightarrow S_0$ transient absorption changes at 1570 cm^{-1}. A 1570 cm^{-1} transient of the $S_1 \rightarrow S_2$ transition (*red*) is shown together with its fit curve (*dashed black line*), as well as a fit curve of only its slow kinetics (*solid black line*). The transient of $S_3 \rightarrow S_0$ (*dark green*) is shown together with its fit curve (*black*). Subtracting the slow-component S_1 fit curve from the S_3 data results in the *light green* data. The transients were deconvolved assuming a starting population of 74% S_1, 14% S_2 and 12% S_0. The shown transients are part of the low S/N time-resolved spectral data set; they were not smoothed along the wavenumber axis. All data was acquired at 10 °C and pH 6.2.

A3.4   Comparison between S-State Transitions

Figure A3.17 shows overlaid DAS of the $S_1 \rightarrow S_2$, $S_2 \rightarrow S_3$ and $S_3 \rightarrow S_0$ transitions to enable easier visual comparison. In a previous analysis approach, in which a starting population of 85% S_1 and 15% S_0 was assumed, the DAS of around 3 ms of the $S_2 \rightarrow S_3$ and $S_3 \rightarrow S_0$ transition looked highly similar (see Fig. A3.18). This was at odds with the assignment of the
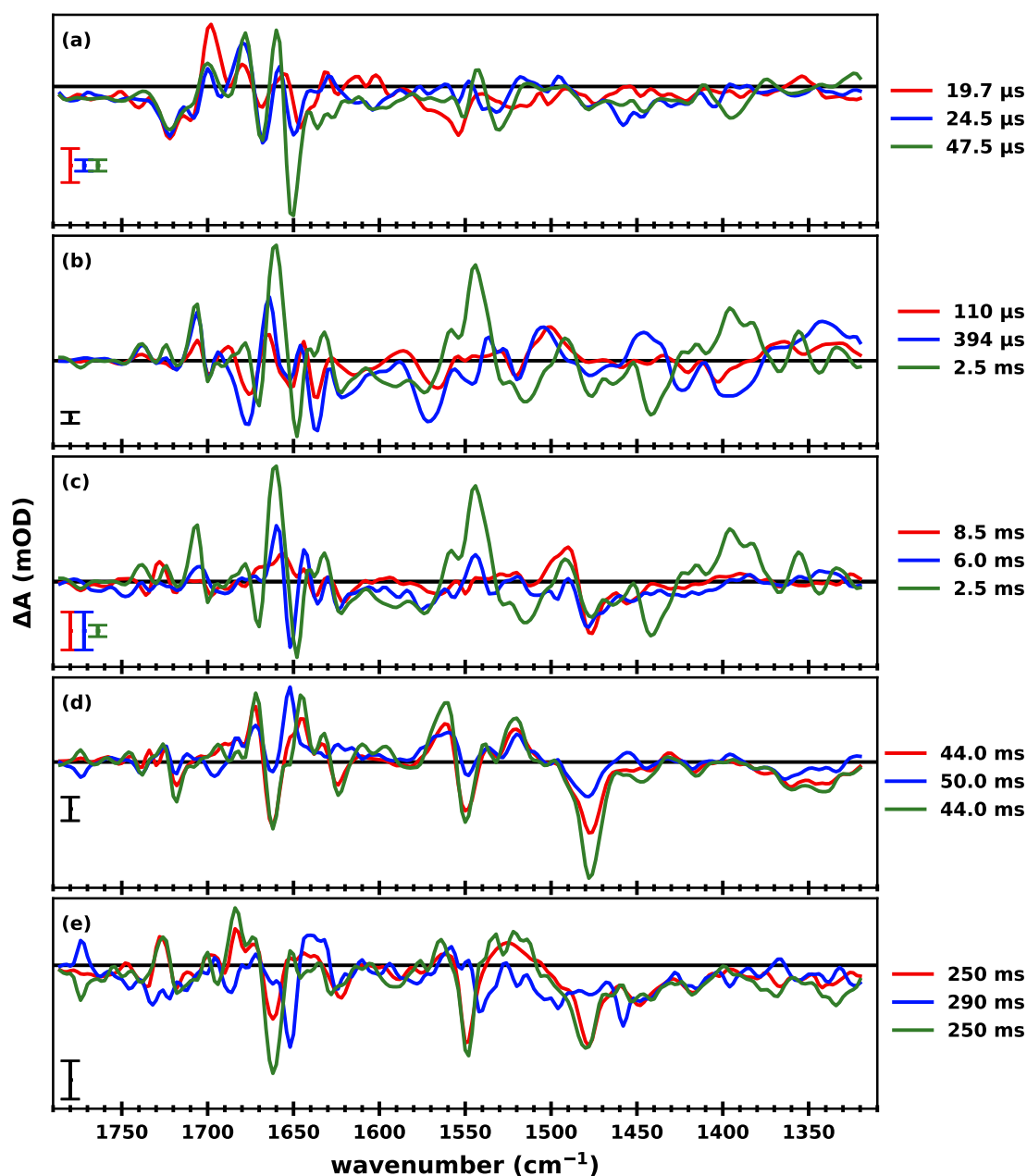
Figure A3.17: Comparison of DAS of the $S_1{\to}S_2$, $S_2{\to}S_3$ and $S_3{\to}S_0$ transitions. (a) ${\sim}20$–50 µs DAS, assigned to mostly $P680^+$ reduction. **(b)** DAS of the components assigned to the ET step of the respective S-state transition. **(c)** DAS of the 2.5–8.5 ms component. The $S_3{\to}S_0$ transition was multiplied by a factor of 0.3, as indicated by the scale bars. **(d)** DAS of the 44–50 ms components. **(e)** DAS of the slowest components. The spectral data was deconvolved assuming a starting population of 74% S_1, 14% S_2 and 12% S_0 and a miss factor of 8%. For the $S_1{\to}S_2$ transition (*red*), the non-deconvolved first flash data minus 14% S_2 and 12% S_0 is shown. The $S_2{\to}S_3$ transition is shown in *blue*; the $S_3{\to}S_0$ transition in *green*. All scale bars correspond to 0.1 mOD. The DAS shown here were *not* corrected for a $P680^+$ background.

2.5 ms phase of $S_3{\to}S_0$ to the ET step leading to O_2-evolution. To investigate the possibility that the deconvolved $S_2{\to}S_3$ data contained a non-negligible $S_3{\to}S_0$ contribution, the de-
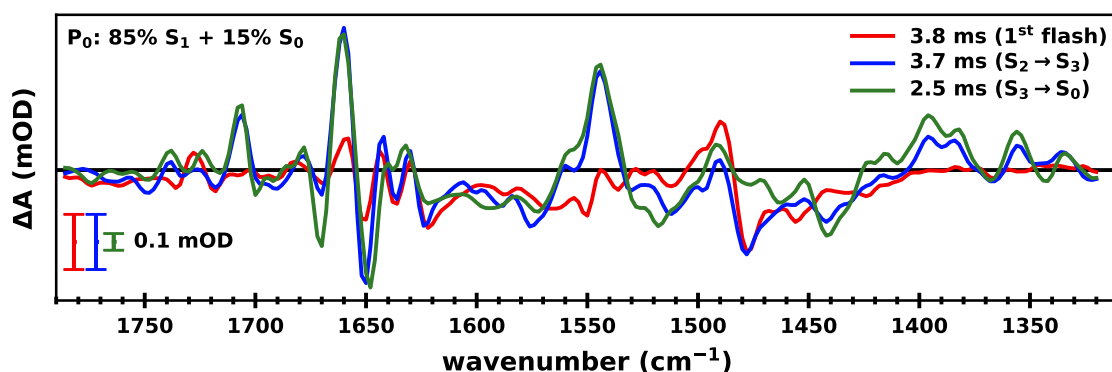
Figure A3.18: DAS of the ∼3 ms phase of the $S_1{\to}S_2$, $S_2{\to}S_3$ and $S_3{\to}S_0$ transitions for a previous deconvolution approach. The time-resolved spectral data set was deconvolved assuming a dark-adapted starting population of 85% S_1 and 15% S_0 and a miss factor of 8%. For the $S_1{\to}S_2$ transition the non-deconvolved 1st flash data is shown. The 3.7 ms DAS of the $S_2{\to}S_3$ data (*blue*) and 2.5 ms DAS of $S_3{\to}S_0$ data (*green*) clearly show strong similarities.

convolution procedure was repeated with five different starting populations (P_0). For each deconvolved data set, the $S_2{\to}S_3$ data was fit with time constants fixed to those obtained with 85% S_1 and 15% S_0. The resulting DAS of the 3.7 ms phase are shown in Fig. A3.19. With an increasing S_2 starting population the amplitudes of many bands in the 3.7 ms become smaller. When assuming a 20% S_2 starting population, the DAS no longer resembles that of the 2.5 ms phase of the $S_3{\to}S_0$ transition and likely instead represents a relatively pure acceptor-side phase. These observations led to a revision of the entire chapter, based on a deconvolution approach which accounted for an S_2 starting population.
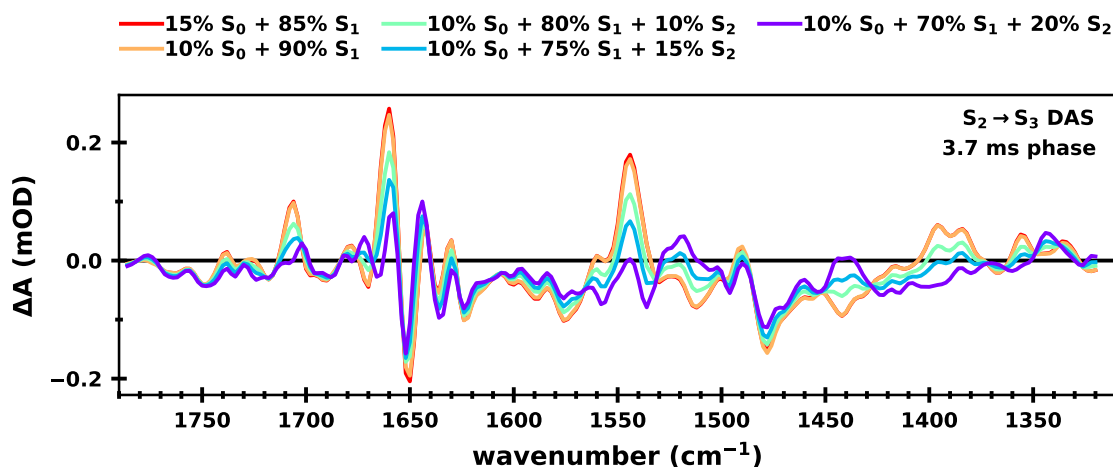
Figure A3.19: DAS of the 3.7 ms phase of the $S_2{\to}S_3$ transition for various deconvolution approaches. The time-resolved spectral data set was deconvolved assuming a miss factor of 8% and different starting populations, as indicated in the figure legend.
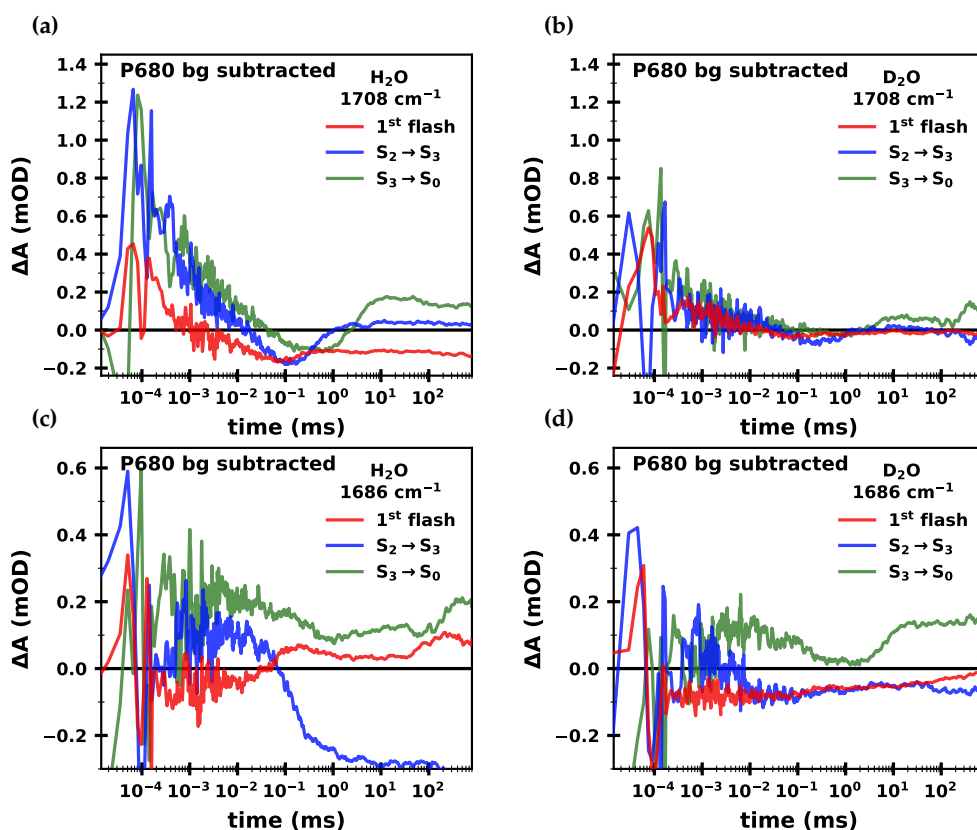
Figure A3.20: Transients at 1708 and 1686 of the first three S-state transitions in H_2O and D_2O after P680 background subtraction. Transient IR absorption changes are shown for the first flash (predominantly $S_1 \rightarrow S_2$) (*red*), the $S_2 \rightarrow S_3$ (*blue*) and $S_3 \rightarrow S_0$ transition (*green*) at **(a)** 1708 cm^{-1} in H_2O, **(b)** 1708 cm^{-1} in D_2O, **(c)** 1686 cm^{-1} in H_2O and **(d)** 1686 cm^{-1} in D_2O. The P680 background, as measured around 1780 cm^{-1}, was subtracted from all transients.

Figure A3.20 shows the S-state transients at 1708 and 1686 cm^{-1} in H_2O and D_2O after P680$^+$ background subtraction (Fig. 5.39 shows the same transients without background correction.)

Figure A3.21 shows transients at 1720, 1724 and 1740 cm^{-1} in H_2O; 1720 cm^{-1} is also shown in D_2O. The kinetics at 1720 cm^{-1} show a clear period-of-two behavior in both cases, which is in agreement with the assignment of a band at 1721 cm^{-1} to an electrochromic effect of Q_A^- on Pheo$_{D1}$ (Suzuki et al., 2005a).
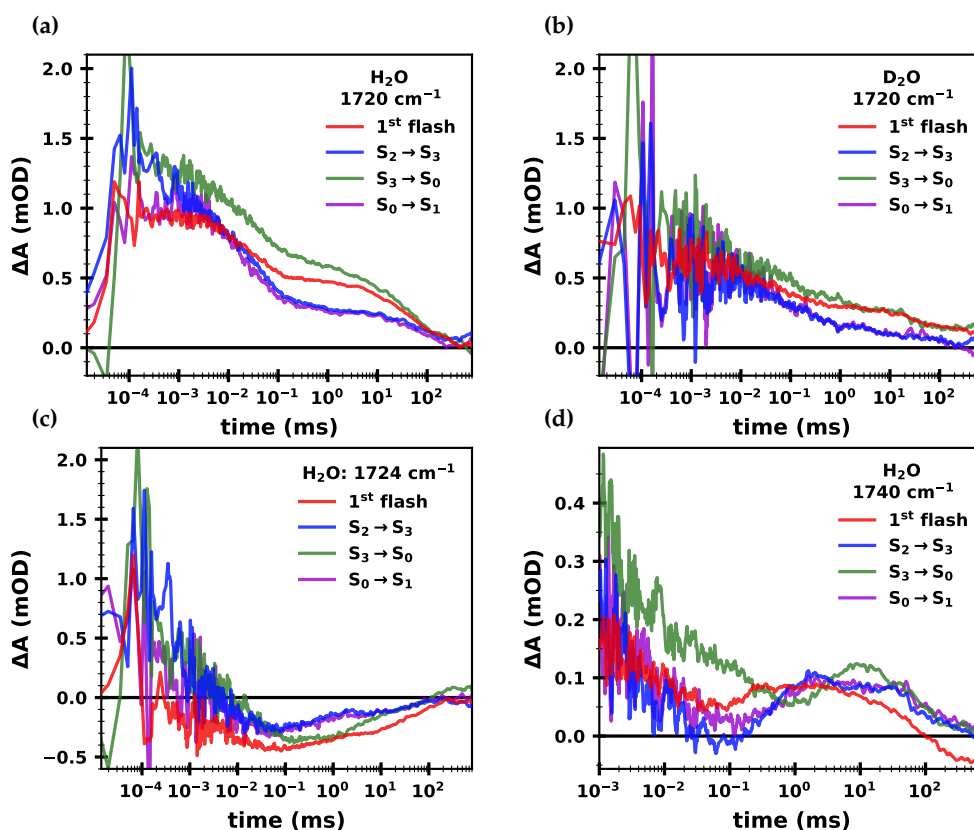
Figure A3.21: Transient IR absorption changes at 1720, 1724 and 1740 cm^{-1}. Flash-induced IR absorption changes at pL 6.2 are shown for the $S_1{\to}S_2$ (*red*), $S_2{\to}S_3$ (*blue*), $S_3{\to}S_0$ (*green*) and $S_0{\to}S_1$ transition (*purple*) at **(a)** 1720 cm^{-1} in H_2O, **(b)** 1720 cm^{-1} in D_2O, **(c)** 1724 cm^{-1} (H_2O) and **(d)** 1740 cm^{-1} (H_2O). The transients were deconvolved assuming a starting population of 74% S_1, 14% S_2 and 12% S_0; for the $S_1{\to}S_2$ transition the non-deconvolved 1st flash data is shown.

A4   Comparison of Spinach and Cyanobacterial PSII: Additional Data
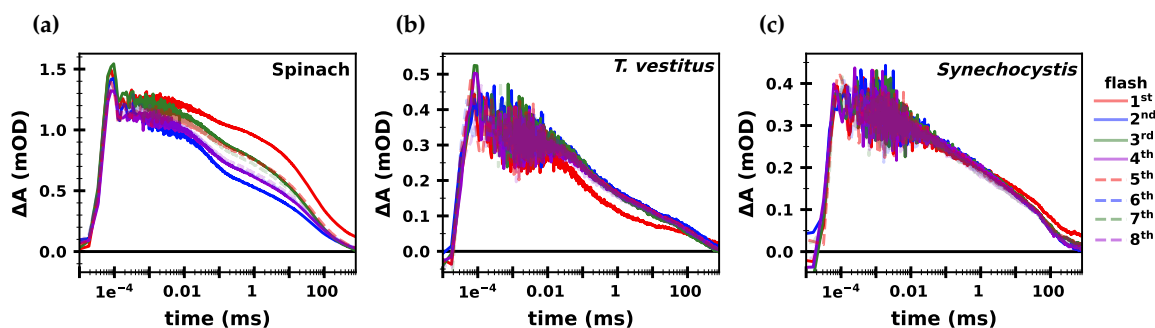
Figure A4.1: Transient absorption changes of three PSII variants at 1478 cm^{-1}. IR difference absorption following eight consecutive excitation flashes is shown for **(a)** spinach PSII membrane particles, **(b)** PSII core complexes from *T. vestitus* and **(c)** PSII core complexes from *Synechocystis*.

Appendix A4 supplements Chapter 6 with additional figures and tables. Figure A4.1 show the transients at 1478 cm^{-1} induced by the first eight excitation flashes for PSII from spinach, *T. vestitus* and *Synechocystis*. While spinach PSII shows a clear period-of-two behavior, the cyanobacterial samples the same behavior after every flash (with exception of the 1st flash). These differences arise from the different exogenous electron acceptor used for the
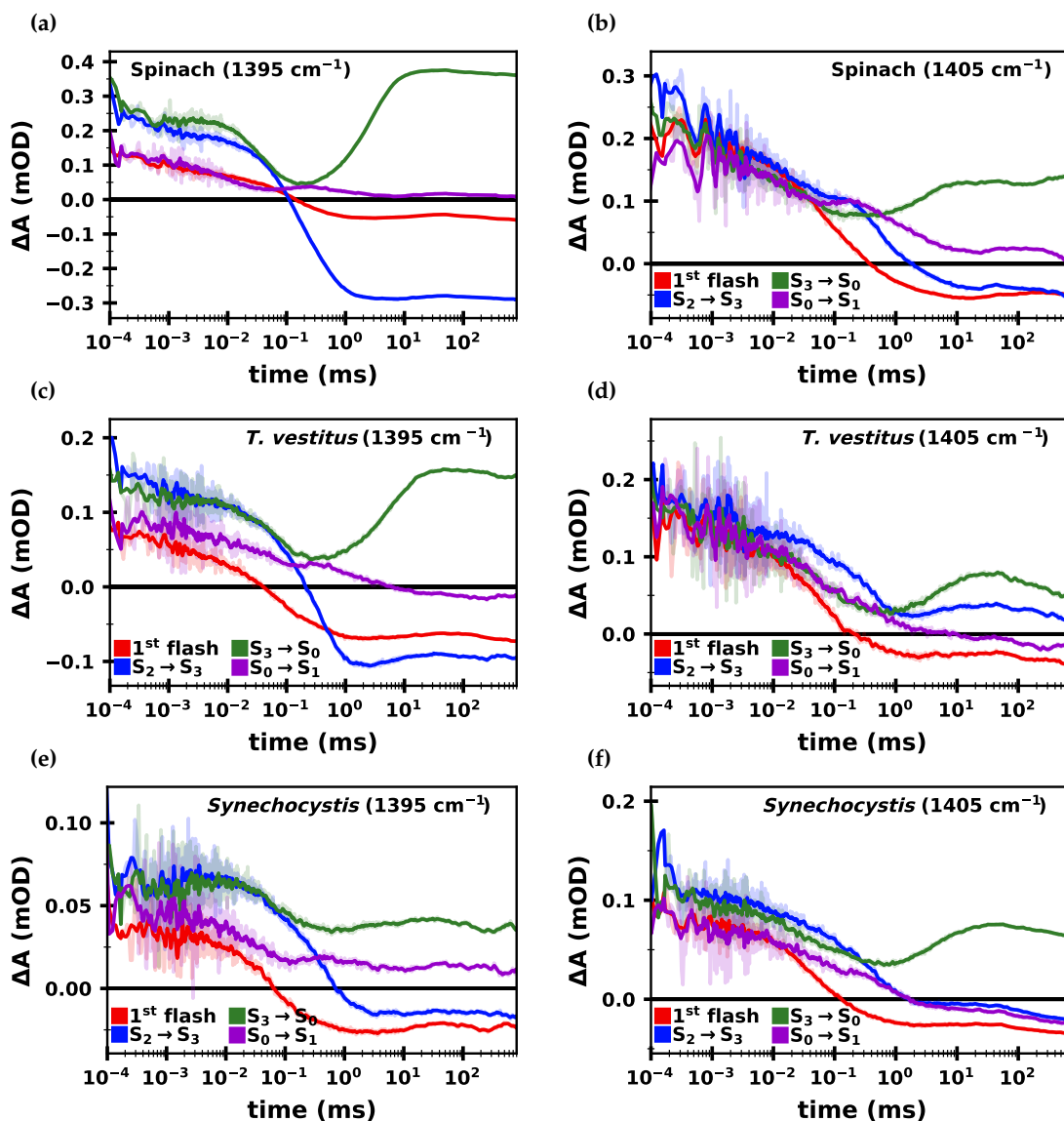
Figure A4.2: IR difference absorption of the S-state transitions of PSII from spinach, *T. vestitus* and *Synechocystis* at 1395 and 1405 cm^{-1}. Each panel shows four transients corresponding to the $S_1{\rightarrow}S_2$ (*red*), $S_2{\rightarrow}S_3$ (*blue*), $S_3{\rightarrow}S_0$ (*green*) and $S_0{\rightarrow}S_1$ (*purple*) transition. For the $S_1{\rightarrow}S_2$ transition the first flash data is shown; for the other transitions the data was deconvolved assuming a starting population of 85% S_1 and 15% S_0 (cyanobacterial PSII) or 74% S_1, 12% S_0 and 14% S_2 (spinach PSII). The first and second column show data at 1395 and 1405 cm^{-1}, respectively. The data was acquired on **(a–b)** spinach PSII membrane particles, **(c–d)** core complexes from *T. vestitus* and **(e–f)** core complexes from *Synechocystis*. All transients were smoothed with a sliding average algorithm with a window size of $n = 10$ (*opaque colors*); non-smoothed transients are shown in *transparent colors*.

spinach membrane particles (PPBQ) and the cyanobacterial core complexes (ferricyanide). While PPBQ is more similar to natural plastoquinones, also accepting two electrons and two protons, ferricyanide can only be reduced once before it needs to be exchanged for an oxidized molecule.
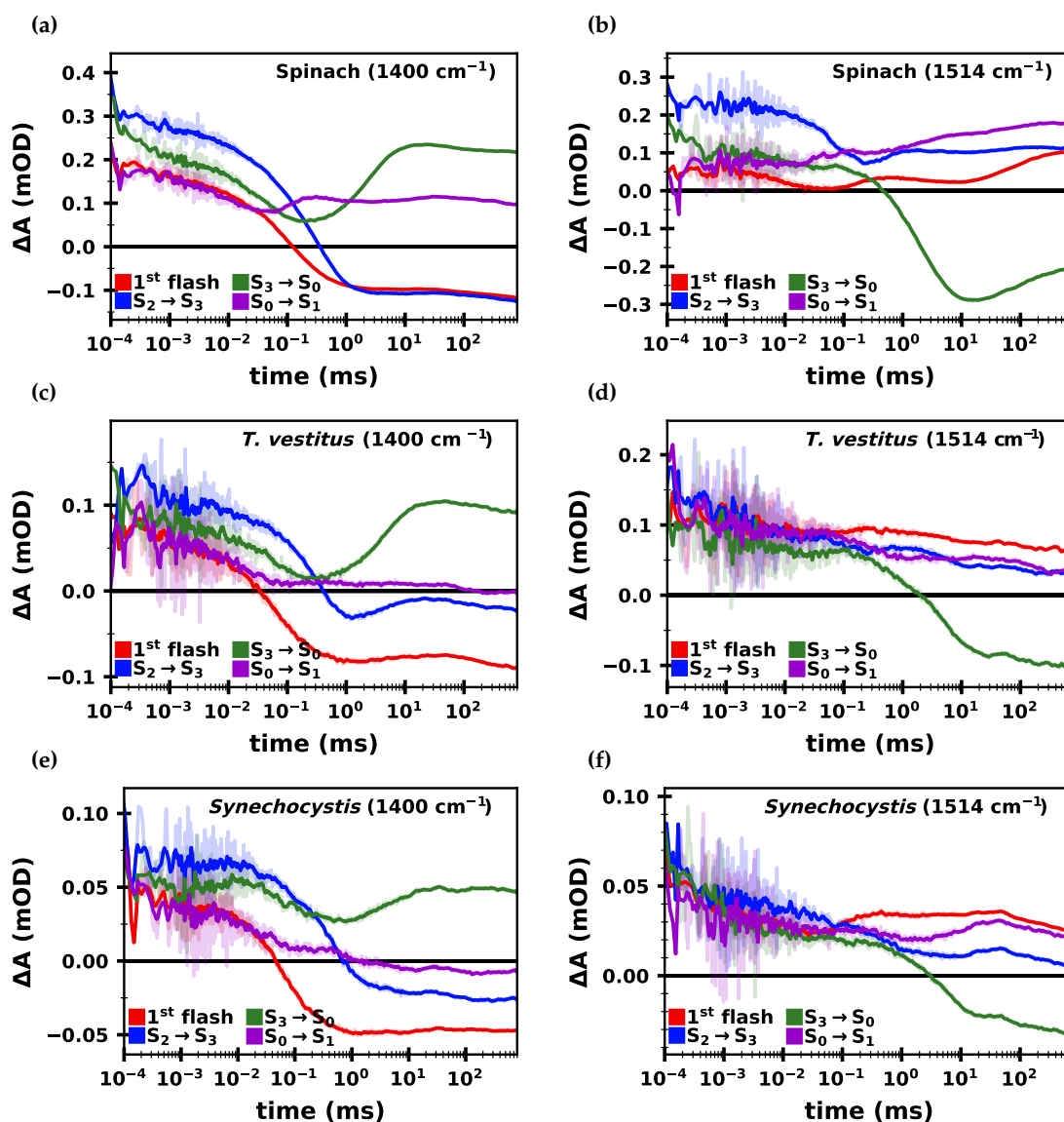
Figure A4.3: IR difference absorption of the S-state transitions of PSII from spinach, *T. vestitus* and *Synechocystis* at 1400 and 1514 cm^{-1}. Each panel shows four transients corresponding to the $S_1 \to S_2$ (*red*), $S_2 \to S_3$ (*blue*), $S_3 \to S_0$ (*green*) and $S_0 \to S_1$ (*purple*) transition. For the $S_1 \to S_2$ transition the first flash data is shown; for the other transitions the data was deconvolved assuming a starting population of 85% S_1 and 15% S_0 (cyanobacterial PSII) or 74% S_1, 12% S_0 and 14% S_2 (spinach PSII). The first and second column show data at 1400 and 1514 cm^{-1}, respectively. The data was acquired on **(a–b)** spinach PSII membrane particles, **(c–d)** core complexes from *T. vestitus* and **(e–f)** core complexes from *Synechocystis*. All transients were smoothed with a sliding average algorithm with a window size of $n = 10$ (*opaque colors*); non-smoothed transients are shown in *transparent colors*.

Figures A4.2 and A4.3 show the S-state transients of spinach, *T. vestitus* and *Synechocystis* at 1395, 1405, 1400 and 1514 cm^{-1}. At all wavenumbers all three PSII variants show a clear S-state dependent behavior.

As described in Chapter 2.7, the energy of the excitation flashes was measured incorrectly for a long time. This led to an incorrect heat artefact correction, or more precisely, the amplitude of the heat artefact was assessed incorrectly. To assess whether such an effect could explain the differences observed between the transients of PSII from spinach, *T. vestitus* and *Synechocystis*, Fig. A4.4 shows the 3rd flash transients at 1544 cm^{-1} of the three samples corrected with various heat artefact amplitudes. Visual inspection shows that the heat artefact *does not* explain the differences.
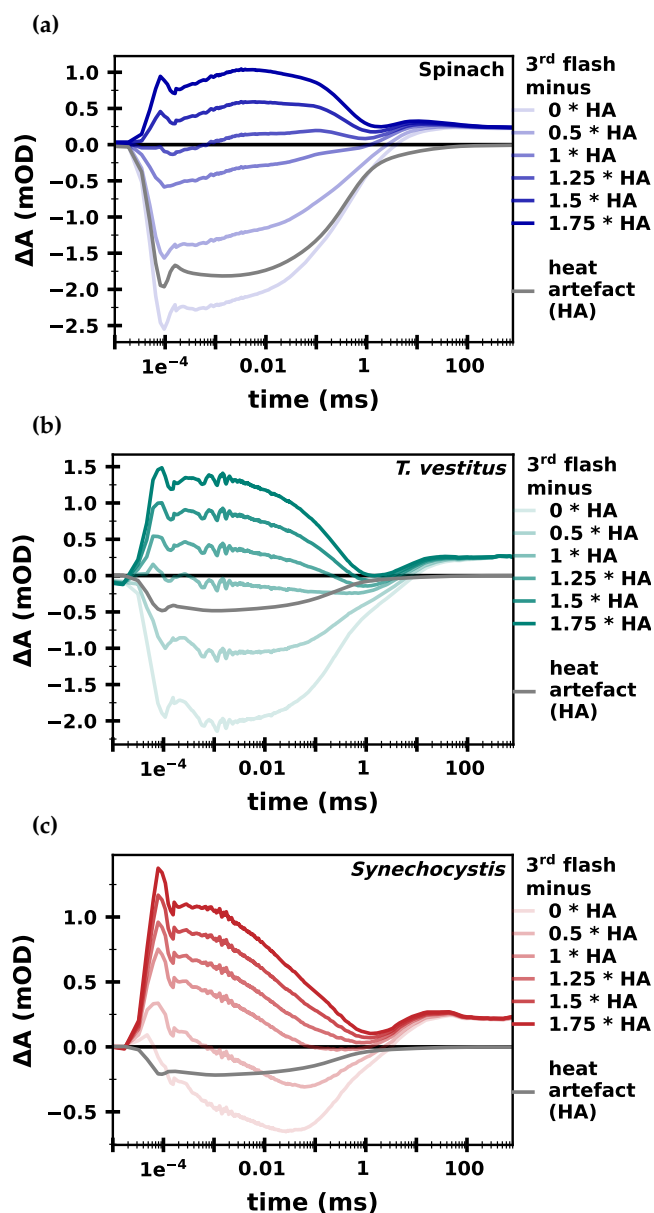
Figure A4.4: Effect of altering the heat artefact correction on 3rd flash transients at 1544 cm^{-1} of three different PSII samples. The heat artefact (*grey*) and heat artefact corrected transients (*colored lines*) are shown for **(a)** PSII spinach membrane particles, **(b)** PSII core particles from *T. vestitus*, **(c)** PSII core particles from *Synechocystis*. From lightest to darkest colors, the transients are shown corrected for n times the heat artefact, with $n = 0$, 0.5, 1, 1.25, 1.5, 1.75 (the lightest transient is thus non-heat artefact corrected). All transients were smoothed with a sliding average algorithm with a window size of $n = 10$.

A4.1   S$_2$→S$_3$ Transition

Figure A4.5 shows two alternative fit approaches of the S$_2$→S$_3$ transition of *Synechocystis*. In the main fit approach (Fig. 6.7) the second phase was fixed to 100 μs, while here all four time constants were left unconstrained (panel a), resulting in $\tau_2 = 50$ μs. A fit with only three exponential components resulted in a complete omission of the 50/100 μs phase, while the fit quality was only marginally poorer. This demonstrates that a phase of 50–100 μs is hardly resolved in these transients.

Figures A4.6 and A4.7 show alternative DAS, which were not corrected for acceptor-side contributions—unlike their counterparts in Figs. 6.9b and 6.10b and c.
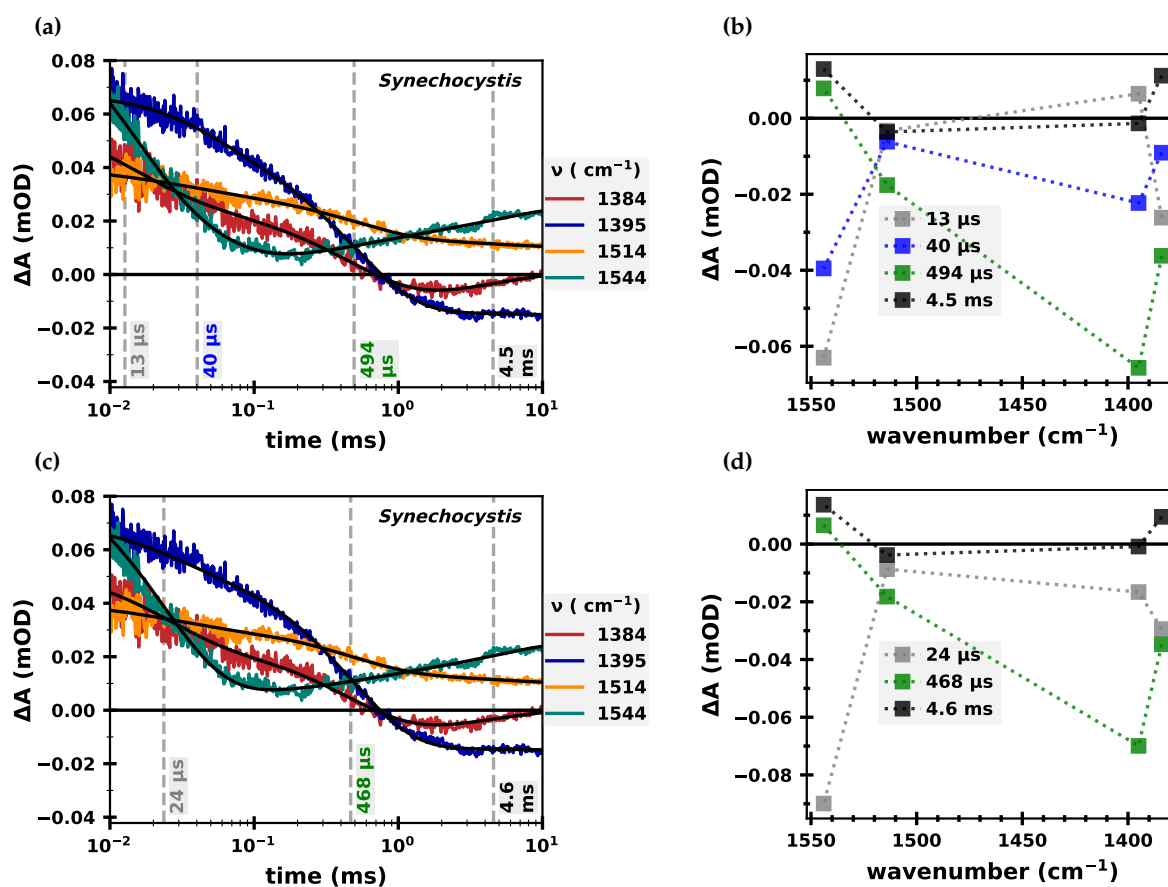
Figure A4.5: Alternative global fit results of the S$_2$→S$_3$ transition at 1384, 1395, 1514 and 1544 cm^{-1} for PSII core particles of *Synechocystis*. *Left column:* Transients at 1384 (*red*), 1395 (*blue*), 1514 (*orange*) and 1544 cm^{-1} (*green*) and their fit curves (*black*). The time constants are indicated with vertical lines. *Right column:* Amplitudes of the time constants as function of wavenumber. Unlike the results shown in Fig. 6.7e–f, the time constants here were unconstrained, with **(a–b)** four and **(c–d)** three time constants.
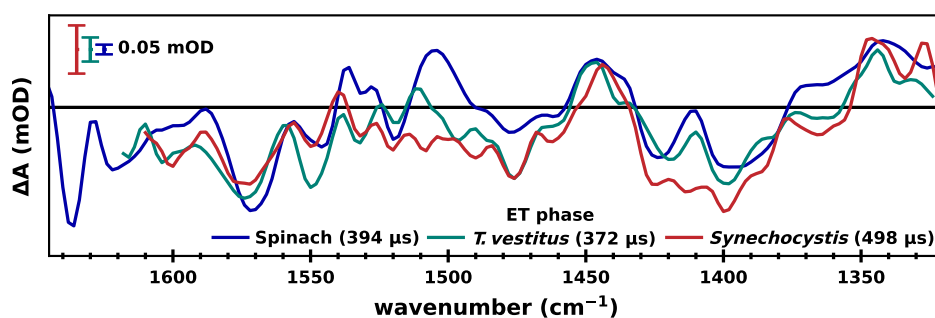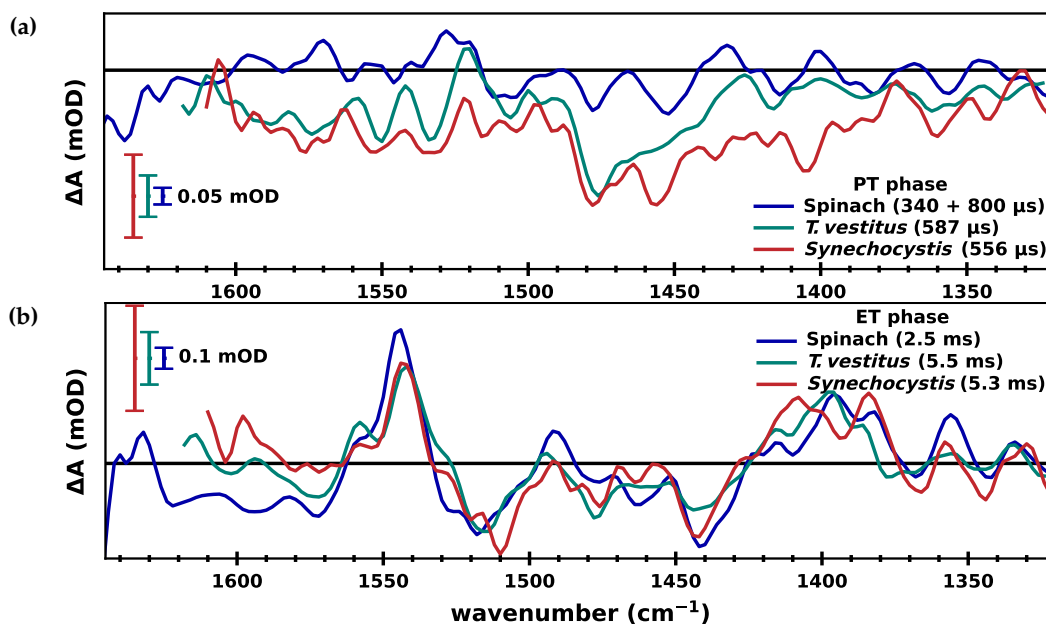
Figure A4.6: Comparison of the decay associated spectra of the non-corrected ET phase of the $S_2 \rightarrow S_3$ transition of three different PSII samples. The DAS assigned to the ET phase (~370–500 μs) are shown for spinach (*blue*), *T. vestitus* (*green*) and *Synechocystis* (*red*). The DAS of spinach PSII are redrawn from that shown in Chapter 5). All DAS were obtained by fixing pre-determined time constants across a time-resolved spectral data set. The spectra were scaled differently to facilitate visual inspection as indicated by the differently sized colored scale bars (each referring to 50 μOD). All data was deconvolved assuming a starting (dark-adapted) population of 85% S_1 and 15% S_0 (cyanobacterial PSII) or 74% S_1, 12% S_0 and 14% S_2 (spinach PSII) prior to the fitting procedure.
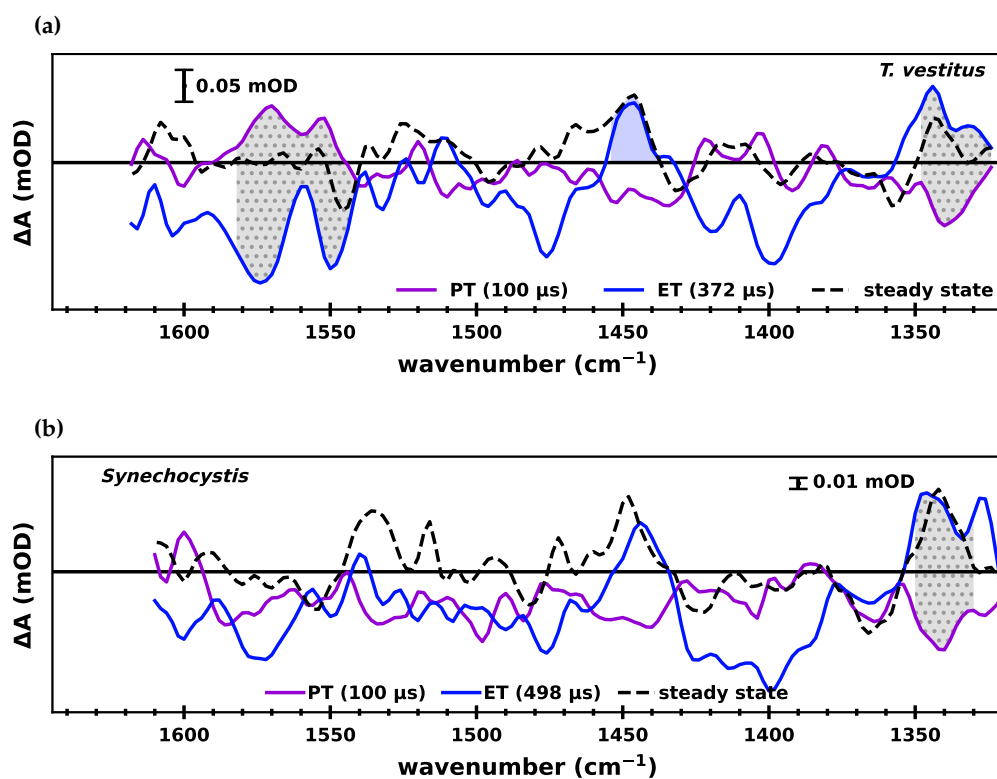

Figure A4.7: Alternative decay associated spectra of the $S_2 \rightarrow S_3$ transition of PSII from *T. vestitus* and *Synechocystis*. The PT phase is shown in *blue*, the ET phase in *green* and the steady state spectra (average of 400–800 ms) in *dashed black* lines for **(a)** *T. vestitus* and **(b)** *Synechocystis*. The time constants were first determined by fitting a small number of high S/N transients and then fixed in a global fit across a large time-resolved spectral data set. Unlike the data shown in Fig. 6.10, the DAS shown here were not corrected for acceptor-side contributions. All data was deconvolved assuming a starting (dark-adapted) population of 85% S_1 and 15% S_0. Regions of the spectra in which PT and ET show inverted behavior are shaded in *dotted grey*.

A4.2 $S_3 \rightarrow S_0$ Transition
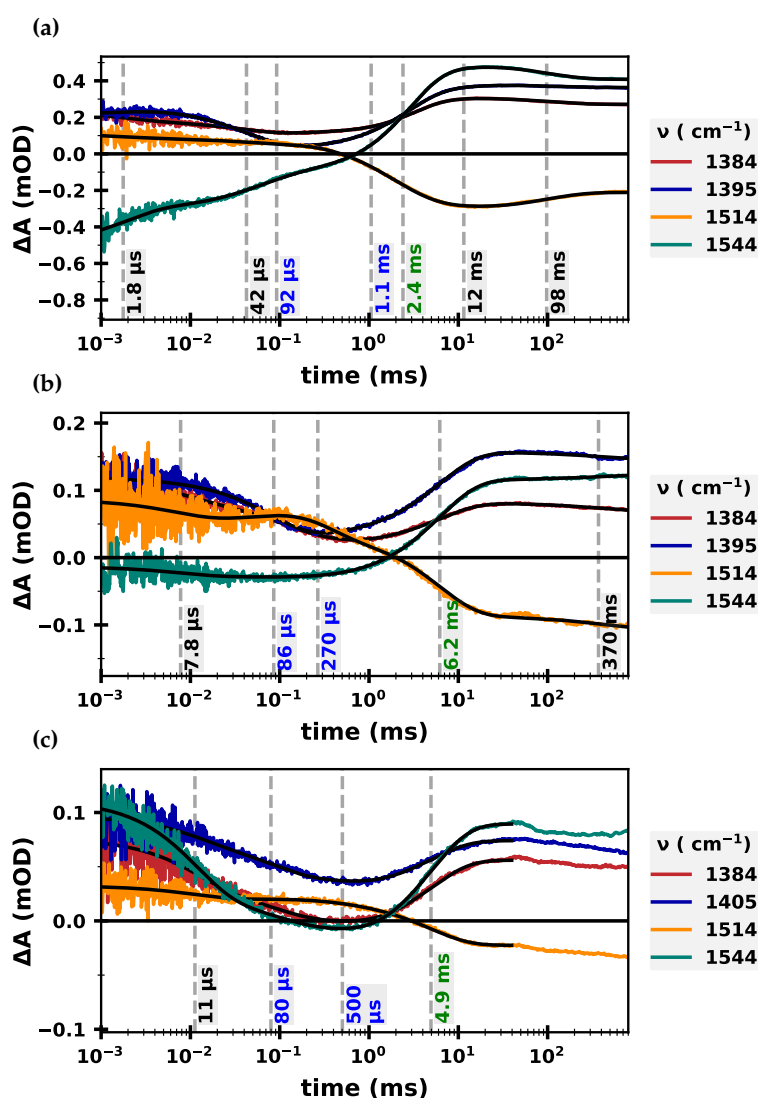
Figure A4.8: Results of a four-wavenumber global fit of the $S_3 \rightarrow S_0$ transition for PSII from spinach, *T. vestitus* and *Synechocystis*. Transients at 1384 (*red*), 1395 (*blue*), 1514 (*orange*) and 1544 cm^{-1} (*green*) and their fit curves (*black*) are shown for **(a)** spinach PSII membrane particles, **(b)** PSII core particles from *T. vestitus* and **(c)** PSII core particles from *Synechocystis*. The time constants are indicated with vertical lines. All data was deconvolved assuming a starting (dark-adapted) population of 85% S_1 and 15% S_0 (cyanobacterial PSII) or 74% S_1, 12% S_0 and 14% S_2 (spinach PSII).

Figure A4.8 shows the results of unconstrained global fits at 1384, 1395, 1514 and 1544 cm^{-1} for PSII from spinach, *T. vestitus* and *Synechocystis* (as opposed to the local fits at 1514 cm^{-1} shown in Fig. 6.11).

Figure A4.9 shows DAS of the PT and ET steps without an acceptor-side correction; the acceptor-side corrected versions are shown in Fig. 6.12.

Figure A4.10 shows the $S_3 \rightarrow S_0$ kinetics of PSII from spinach, *T. vestitus* and *Synechocystis* at 1395 or 1405 cm^{-1}, normalized and shifted to allow for a direct comparison of the

milliseconds kinetics. Visual inspection clearly reveals that the cyanobacterial kinetics are slower than that of spinach.

(a)

(b)

Figure A4.9: Comparison of the decay associated spectra of the non-acceptor-side-corrected PT and ET steps of the $S_3 \rightarrow S_0$ transition of three different PSII samples. The DAS corresponding to **(a)** the PT and **(b)** the ET step are shown for spinach PSII (*blue*), *T. vestitus* (*green*) and *Synechocystis* (*red*). The latter two DAS were obtained as shown in Fig. 6.13. The spectra were scaled differently to facilitate visual inspection as indicated by the differently sized colored scale bars. All data was deconvolved assuming a starting (dark-adapted) population of 85% S_1 and 15% S_0 (cyanobacterial PSII) or 74% S_1, 12% S_0 and 14% S_2 (spinach PSII).
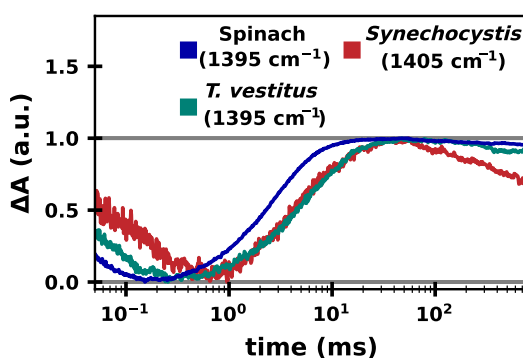
Figure A4.10: Direct comparison of the millisecond IR absorption changes of the $S_3 \rightarrow S_0$ transition at 1395 and 1405 cm^{-1} of PSII from spinach, *T. vestitus* and *Synechocystis*. Data from PSII membrane particles from spinach is shown in *blue*, PSII core particles from *T. vestitus* in *green* and PSII core particles from *Synechocystis* in *red*; the transients were shifted and normalized to overlay their millisecond kinetics. All transients were deconvolved assuming a starting (dark-adapted) population of 85% S_1 and 15% S_0 (cyanobacterial PSII) or 74% S_1, 12% S_0 and 14% S_2 (spinach PSII).

A4.3 H/D Isotope Effect

Figure 6.15b in Chapter 6 shows the $S_3{\rightarrow}S_0$ transients of PSII from spinach and *T. vestitus* in H_2O and D_2O normalized such that a visual comparison of the ET kinetics are facilitated. The data of *Synechocystis* (at 1405 cm^{-1}) were however too noisy and were thus omitted there; instead, they are shown here in Fig. A4.11. In panel a, the data is normalized to emphasise the pre-ET kinetics, while panel b allows for a direct comparison of the ET kinetics in H_2O and D_2O.

Figure A4.12 shows the results of a global mono-exponential fit of *T. vestitus* PSII $S_2{\rightarrow}S_3$ data in D_2O at 1384 and 1395 cm^{-1}. The obtained time constant of 906 μs is similar to
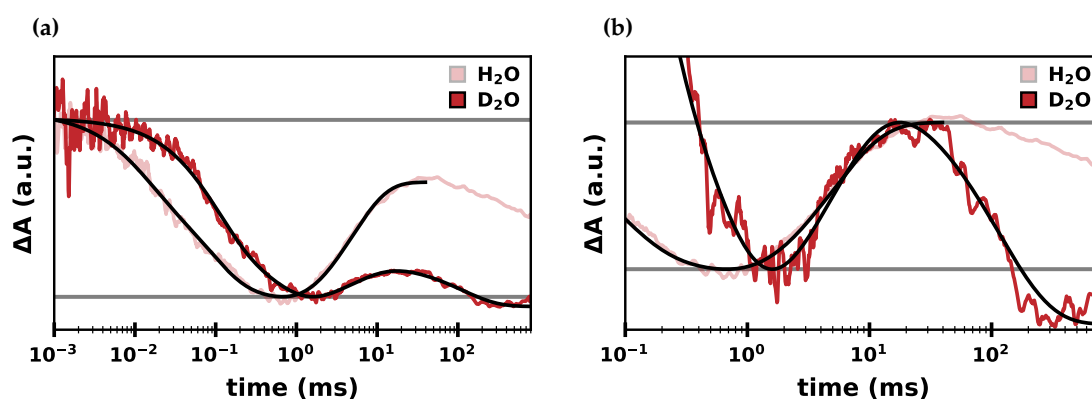
Figure A4.11: Kinetics of the $S_3{\rightarrow}S_0$ transition in H_2O and D_2O of PSII from *Synechocystis*. Transient IR absorption changes are shown at 1405 cm^{-1} in H_2O (*pink*) and D_2O (*red*). In **(a)** the transients were shifted and normalized such that the early decay kinetics can be easily compared, while in **(b)** the millisecond rise kinetics are emphasized. All data was deconvolved assuming a starting (dark-adapted) population of 85% S_1 and 15% S_0.
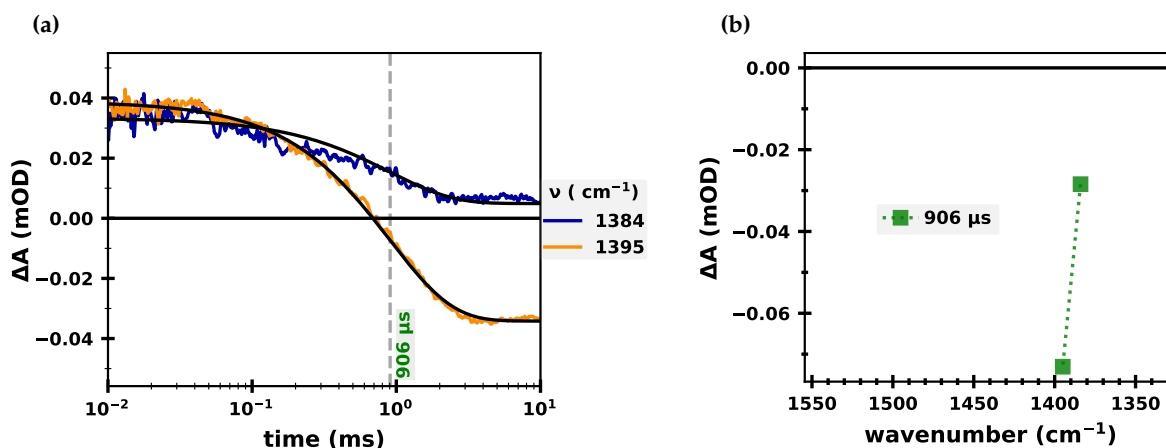
Figure A4.12: Results of an alternative global fit of the $S_2{\rightarrow}S_3$ transition of PSII from *T. vestitus* in D_2O. (a) Transient IR changes at 1384 (*blue*) and 1395 cm^{-1} (*orange*) and their fit curves (*black*) from a mono-exponential fit. **(b)** The amplitudes of the fits shown in (a) as a function of wavenumber. In (a) the time constant is indicated with a vertical dashed line. All data was deconvolved assuming a starting (dark-adapted) population of 85% S_1 and 15% S_0.

that obtained in a bi-exponential fit which also included 1335 cm^{-1} (Fig. 6.16) with only a marginally poorer fit quality. This demonstrates that the pre-ET phase—while clearly present at 1335cm^{-1}—is very poorly resolved at 1384 and 1395 cm^{-1}.

Figure A4.13 shows transients of spinach PSII in H_2O and D_2O at 1514, 1520 and 1532 cm^{-1}. In contrast to a study by Sakamoto et al. (2017) (on PSII from *T. vestitus*), a clear deuteration-induced slow-down is discernible at 1514 cm^{-1}.
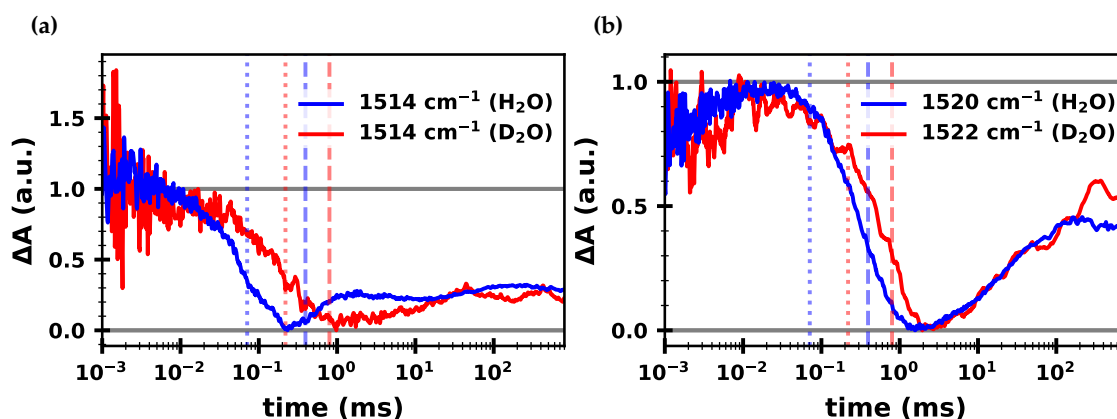
Figure A4.13: Transients of the $S_2{\rightarrow}S_3$ transition around 1514–1520 cm^{-1} of spinach PSII in H_2O and D_2O. Transient absorption changes at **(a)** 1514 cm^{-1} and **(b)** 1522–1520 cm^{-1} H_2O-(*blue*) and D_2O-buffer (*red*) at pL 6.2. The time constants of the PT and ET step as determined by multi-exponential fitting detailed in Chapter 5 are indicated by vertical dotted and dashed lines, respectively (H_2O: 71 and 394 μs; D_2O: 219 and 798 μs). The data was deconvolved assuming a starting (dark-adapted) population of 74% S_1, 12% S_0 and 14% S_2.

A5 D1-N298A and D1-D61A: Additional Data

Appendix A5 supplements Chapter 7 with additional figures and tables.

A5.1 Additional Figures

Figure A5.1 shows the non-deconvolved transients following the first four excitation flashes of wild-type PSII as well the N298A and D61A variants at 1384, 1400, 1514 and 1544 cm^{-1}; their deconvolved counterparts are shown in Fig. 7.2.

The main analysis of the $S_3{\rightarrow}S_0$ transition in Chapter 7 was done on deconvolved data (Fig. 7.7). The same analysis instead performed on the non-deconvolved third flash data gives similar results (Fig. A5.2).
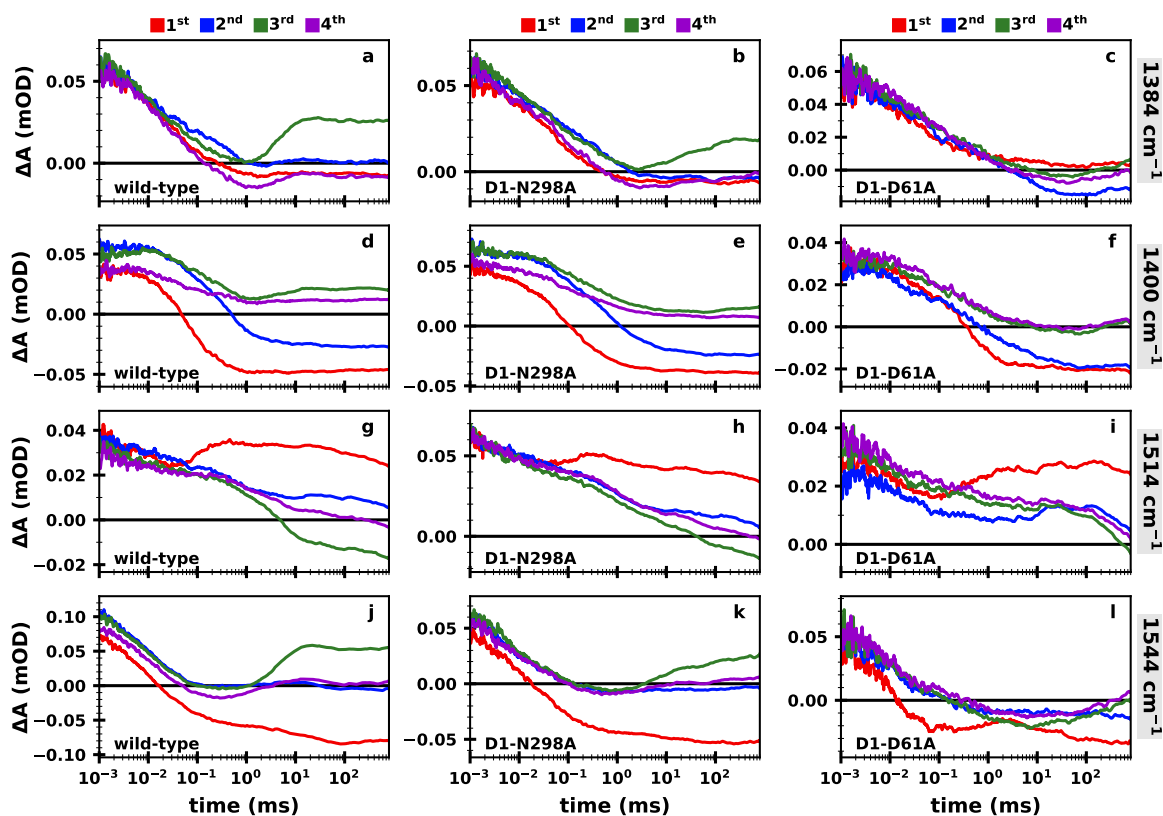
Figure A5.1: Time-resolved IR difference absorption of wild-type and mutant PSII core complexes from *Synechocystis* sp. PCC 6803 following the first four saturating excitation flashes. The IR changes are shown at **(a–c)** 1384 cm^{-1}, **(d–f)** 1400 cm^{-1}, **(g–i)** 1514 cm^{-1}, **(j–l)** 1544 cm^{-1}. The first, second and third column shows the transients of wild-type PSII, N298A and D61A, respectively, following the first (*red*), second (*blue*), third (*green*) and fourth (*purple*) excitation flash.

Error Estimation for the Time Constants and Amplitudes of the $S_3 \rightarrow S_0$ Transition

The error estimations directly obtained from curve fitting algorithms are often standard deviations calculated from a co-variance matrix of the parameters. Those errors may be helpful to during the fitting procedure to e.g. point out strongly co-dependent parameters. However, for relatively well-defined fits, those errors tend to be very small—clearly smaller than the standard deviation one would obtain from repeated measurements on the same sample.

An attempt to calculate more meaningful errors for the $S_3 \rightarrow S_0$ fits of the three PSII variants will be described in the following. Instead of merely using the results of global fits of the transients at 1384, 1400, 1514 and 1544 cm^{-1}, multiple fits were performed with the omission of one or more transients. As we are using four transients, there are $2^4 = 16$ possible combinations of which transients to include in the fit (i.e. 15 that include at least one transient). Thus, for each PSII variant, 15 fits were performed. For all parameters the mean value and the standard deviation were calculated; for both N298A and D61A 5 outliers were omitted. All time constants and amplitudes of the individual fits are shown in Figs. A5.3, A5.4 and A5.5 for wild-type PSII, N298A and D61A, respectively. The average parameters plus/minus the standard deviation are also given in Table A5.3.
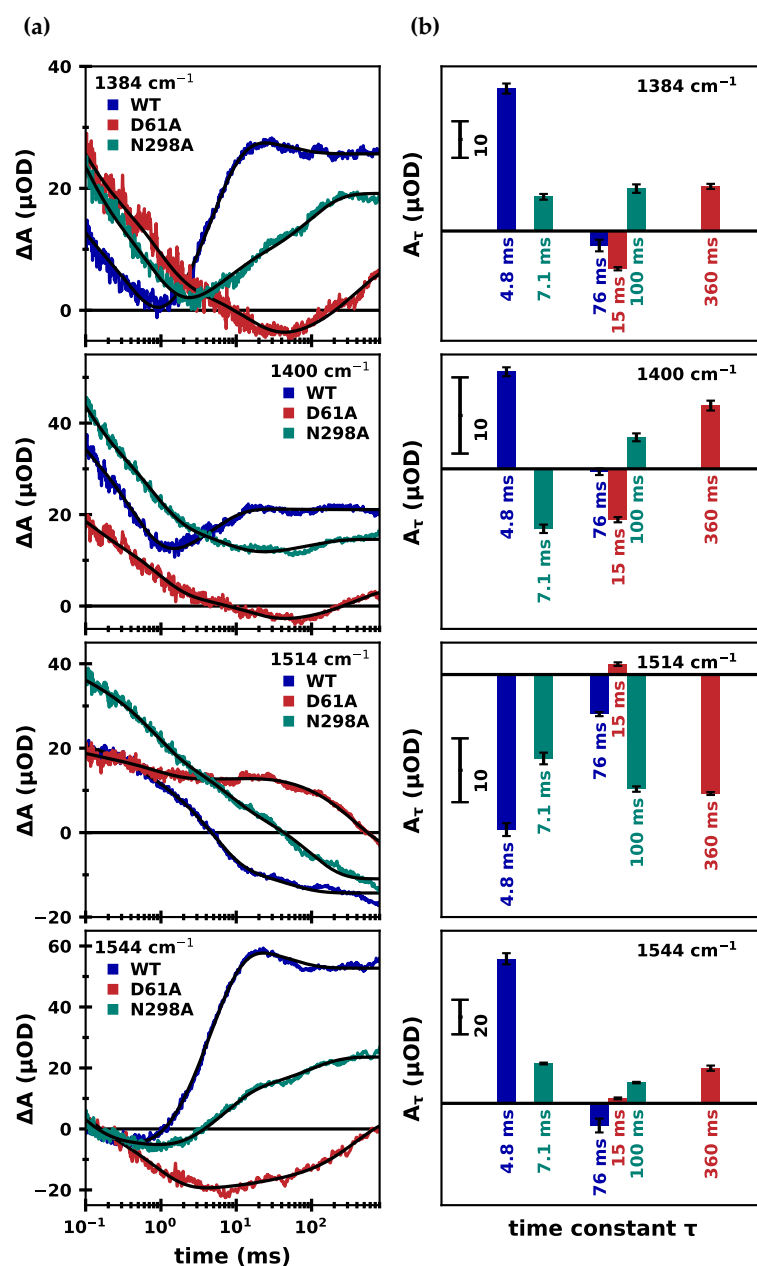
Figure A5.2: Time-resolved IR difference data of the 3rd flash data of PSII core particles from *Synechocystis* sp. PCC 6803. (a) IR difference signal acquired after applying a third saturating excitation flash to the sample. The wild-type data is shown in *blue*, D1-D16A in *red* and D1-N298A in *green* at 1384, 1400, 1514 and 1544 cm^{-1} (top to bottom). **(b)** Bar plots of the amplitudes corresponding to the time constants obtained from fitting the data on the left to a sum of exponentials. The time constants were determined globally for all four wavenumbers, while the amplitudes were left free to vary. Here relevant fit results are shown for 1384, 1400, 1514 and 1544 cm^{-1} (top to bottom). This figure is part of the Supporting Information of manuscript (*in preparation*).
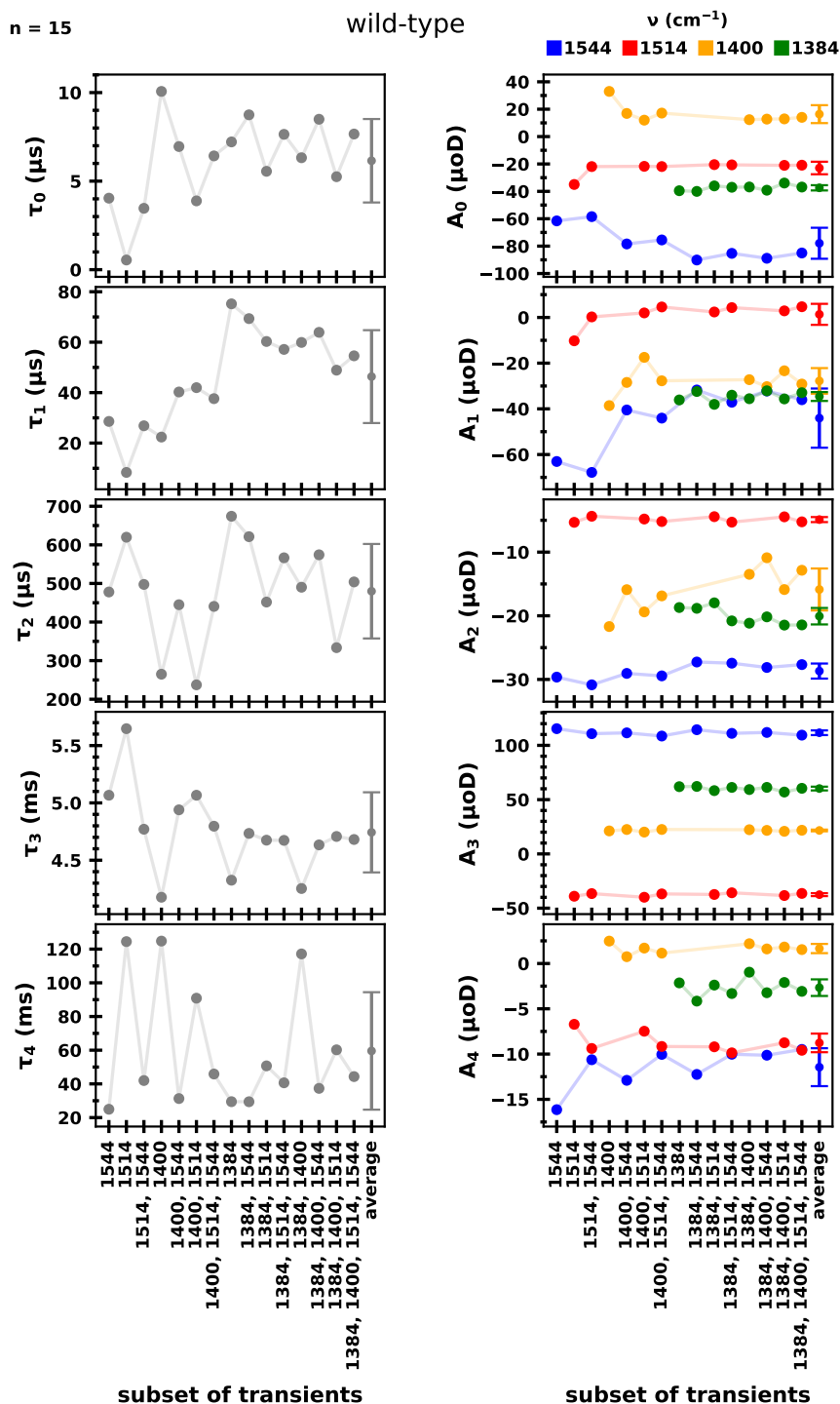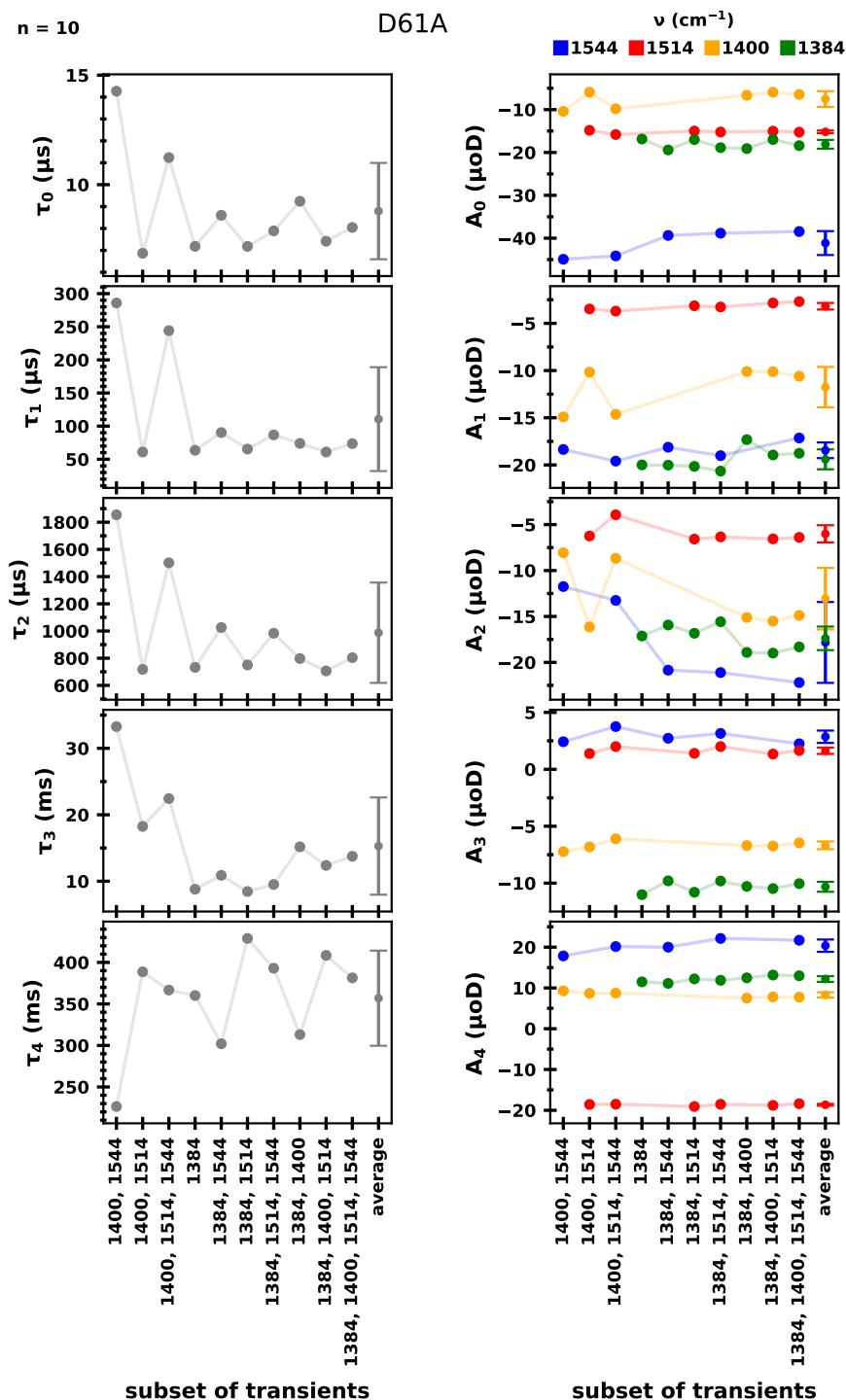
Figure A5.3: Error estimation for the parameters of the $S_3 \rightarrow S_0$ global fit of wild-type PSII. *Left:* Time constants of five exponential components as a function of transients included in the fit. *Right:* Wavenumber-dependent amplitudes of five exponential components as a function of transients included in the fit. The amplitudes at 1544, 1514, 1400 and 1384 cm^{-1} are shown in *blue*, *red*, *yellow* and *green*, respectively. The average and standard deviation of each parameter is shown on the right-hand side in each panel. For more information on the fitting procedure, see text further above.
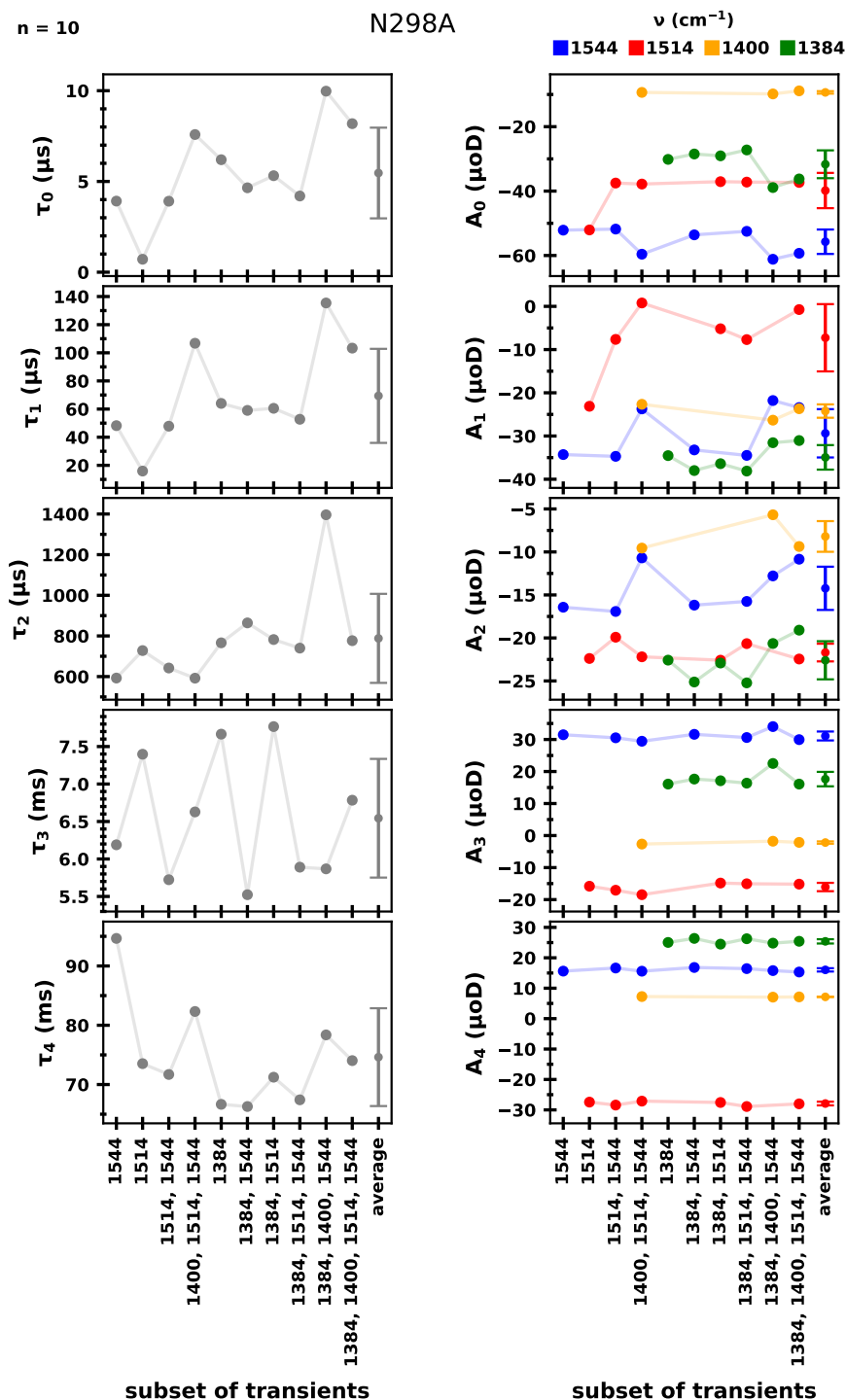
Figure A5.4: Error estimation for the parameters of the S$_3$→S$_0$ global fit of N298A. *Left:* Time constants of five exponential components as a function of transients included in the fit. *Right:* Wavenumber-dependent amplitudes of five exponential components as a function of transients included in the fit. The amplitudes at 1544, 1514, 1400 and 1384 cm^{-1} are shown in *blue*, *red*, *yellow* and *green*, respectively. The average and standard deviation of each parameter is shown on the right-hand side in each panel. For more information on the fitting procedure, see text further above.

Figure A5.5: Error estimation for the parameters of the $S_3 \rightarrow S_0$ global fit of D61A. *Left:* Time constants of five exponential components as a function of transients included in the fit. *Right:* Wavenumber-dependent amplitudes of five exponential components as a function of transients included in the fit. The amplitudes at 1544, 1514, 1400 and 1384 cm^{-1} are shown in *blue*, *red*, *yellow* and *green*, respectively. The average and standard deviation of each parameter is shown on the right-hand side in each panel. For more information on the fitting procedure, see text further above.
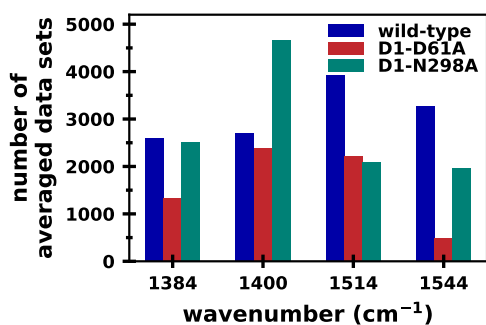
Figure A5.6: Number of averaged data sets per wavenumber. For each of the four investigated wavenumbers, $\sim$500–5000 data sets were averaged to obtain the final analyzed transients, as indicated in *blue*, *red* and *green* for wild-type PSII, D1-D61A and N298A, respectively.

Figure A5.6 indicates the number of averaged data sets at the four investigated wavenumbers for wild-type, *T. vestitus* and *Synechocystis*.

A5.2 Additional Tables

In the following, tables containing the fit results of the $S_1{\to}S_2$, $S_2{\to}S_3$ and $S_3{\to}S_0$ transition of wild-type PSII as well as the D1-N298A and D1-D61A variants are given.

Table A5.1: Time constants and amplitudes of a multi-exponential fit of the 1st flash data ($S_1{\to}S_2$ transition). The given errors are the standard deviations estimated from the covariance matrix calculated during the least-squares minimization (likely underestimating the true uncertainties). The amplitudes were calculated by a matrix inversion rather than fitting them as parameters and thus no error was estimated.

	τ_0	τ_1 (µs)	τ_2 (µs)	τ_3	τ_4	τ_5 (ms)
wild-type		7.4 ± 0.1	40.7 ± 0.2	104.4 ± 1.9 µs	297.3 ± 5.2 µs	7.9 ± 0.1
D61A	220.9 ± 0.1 ns	13.5 ± 0.1	80.3 ± 0.6	529.3 ± 6.0 µs	19.8 ± 0.1 ms	258.8 ± 0.7
N298A	3.0 ± 0.1 µs	40.1 ± 0.2	169.7 ± 1.3	1.1 ± 0.1 ms	15.0 ± 0.1 ms	55.4 ± 1.0

ν (cm^{-1})		A_1 (µOD)	A_2 (µOD)	A_3 (µOD)	A_4 (µOD)	A_5 (µOD)
			wild-type			
1384		-20.6	-32.4	5.4	-19.6	2.4
1400		8.7	-50.1	-21.1	-22.4	0.6
1514		-12.6	-15.7	31.9	-8.3	-0.7
1544		-72.4	-36.9	-16.6	-8.6	-19.1
			D61A			
1384	-53.5	-19.0	-18.3	-7.5	-5.7	2.9
1400	-9.0	-7.7	-6.8	-34.4	-3.2	-0.1
1514	-47.2	-13.8	-1.5	10.2	3.2	-3.0
1544	-64.9	-63.0	-7.0	10.6	-13.6	-4.9
			N298A			
1384	-19.6	-23.1	-18.4	-8.2	2.7	-2.5
1400	-15.6	-21.8	-40.6	-15.0	-0.8	-2.0
1514	-24.1	-5.8	14.9	-14.0	3.7	-8.5
1544	-45.1	-43.3	-15.5	-4.0	-6.9	-1.5

Table A5.2: Time constants and amplitudes of a multi-exponential fit of the 2nd flash data ($S_2 \rightarrow S_3$ transition). The given errors are the standard deviations estimated from the covariance matrix calculated during the least-squares minimization (likely underestimating the true uncertainties). The amplitudes were calculated by a matrix inversion rather than fitting them as parameters and thus no error was estimated.

	τ_1	τ_2 (µs)	τ_3 (µs)	τ_4 (ms)	τ_5 (ms)
wild-type	6.3 ± 0.1 µs	35.4 ± 0.2	472.8 ± 0.7	3.4 ± 0.1	32.5 ± 0.1
D61A	204.7 ± 0.1 ns	8.1 ± 0.1	57.2 ± 0.8	0.7 ± 0.4	9.7 ± 0.1
N298A	6.3 ± 0.1 µs	69.0 ± 0.2	608.0 ± 1.6	2.8 ± 0.1	33.4 ± 0.1

ν (cm^{-1})	A_1 (µOD)	A_2 (µOD)	A_3 (µOD)	A_4 (µOD)	A_5 (µOD)
			wild-type		
1384	-25.8	-14.2	-28.0	7.2	-1.8
1400	9.5	-25.6	-57.5	-4.5	-3.3
1514	-5.1	-4.7	-12.0	-2.9	-2.1
1544	-63.7	-49.8	-1.5	11.7	-14.6
			D61A		
1384	-24.3	-15.4	-19.4	-16.5	-19.7
1400	-24.1	-7.4	-9.4	-18.8	-12.4
1514	-40.4	-8.3	-6.9	-3.7	5.7
1544	-41.5	-36.0	-18.3	-9.2	0.4
			N298A		
1384	-21.3	-16.3	-24.6	-3.9	-1.3
1400	-2.5	-23.1	-37.5	-19.5	-6.0
1514	-15.4	-5.3	-17.2	-8.7	-4.4
1544	-46.1	-22.2	-7.1	5.1	-0.3

Table A5.3: Time constants and amplitudes of a multi-exponential fit of the $S_3 \rightarrow S_0$ transition. The given parameters are the average plus/minus their standard deviation, obtained from fitting several subsets of the four investigated transients (see text further above for details).

	τ_1 (µs)	τ_2 (µs)	τ_3 (µs)	τ_4 (ms)	τ_5 (ms)
wild-type	6.2 ± 2.4	46.4 ± 18.4	479.9 ± 122.4	4.7 ± 0.3	59.6 ± 34.9
D61A	8.8 ± 2.2	110.5 ± 78.4	987.4 ± 368.9	15.3 ± 7.3	356.9 ± 57.3
N298A	5.5 ± 2.5	69.4 ± 33.4	788.1 ± 219.1	6.5 ± 0.8	74.6 ± 8.2

ν (cm^{-1})	A_1 (µOD)	A_2 (µOD)	A_3 (µOD)	A_4 (µOD)	A_5 (µOD)
			wild-type		
1384	-37.4 ± 1.9	-34.6 ± 1.9	-20.1 ± 1.3	60.2 ± 1.7	-2.7 ± 0.9
1400	16.4 ± 6.5	-27.8 ± 5.6	-15.9 ± 3.3	21.6 ± 0.8	1.7 ± 0.5
1514	-22.9 ± 4.6	1.4 ± 4.6	-4.9 ± 0.4	-37.5 ± 1.3	-8.8 ± 1.0
1544	-77.9 ± 11.3	-44.1 ± 13.0	-28.7 ± 1.2	111.6 ± 2.2	-11.4 ± 2.1
			D61A		
1384	-18.1 ± 1.0	-19.4 ± 1.1	-17.4 ± 1.3	-10.3 ± 0.4	12.2 ± 0.7
1400	-7.5 ± 1.8	-11.8 ± 2.1	-13.1 ± 3.3	-6.7 ± 0.3	8.3 ± 0.6
1514	-15.2 ± 0.3	-3.2 ± 0.3	-6.0 ± 0.9	1.6 ± 0.3	-18.6 ± 0.2
1544	-41.1 ± 2.8	-18.4 ± 0.8	-17.8 ± 4.4	2.9 ± 0.5	20.4 ± 1.5
			N298A		
1384	-31.7 ± 4.3	-34.9 ± 2.8	-22.6 ± 2.2	17.6 ± 2.3	25.4 ± 0.7
1400	-9.4 ± 0.4	-24.2 ± 1.5	-8.2 ± 1.8	-2.2 ± 0.4	7.2 ± 0.1
1514	-39.8 ± 5.5	-7.3 ± 7.8	-21.7 ± 1.0	-16.1 ± 1.3	-27.9 ± 0.6
1544	-55.7 ± 3.8	-29.4 ± 5.6	-14.2 ± 2.5	31.1 ± 1.4	16.0 ± 0.5

A6   Photosystem I: Additional Data

Appendix A6 supplements Chapter 8 with additional figures and tables.

Figure A6.1b and c shows examples of the S/N of the time-resolved spectral data set below (average of 300 transients) vs. above 1550 cm^{-1} (average of 6 transients). Above 1550 cm^{-1} the S/N is clearly insufficient to reliably resolve the fast nanosecond phase. The 33 ns DAS in Fig. A6.1a (*red*) is thus not reliable.
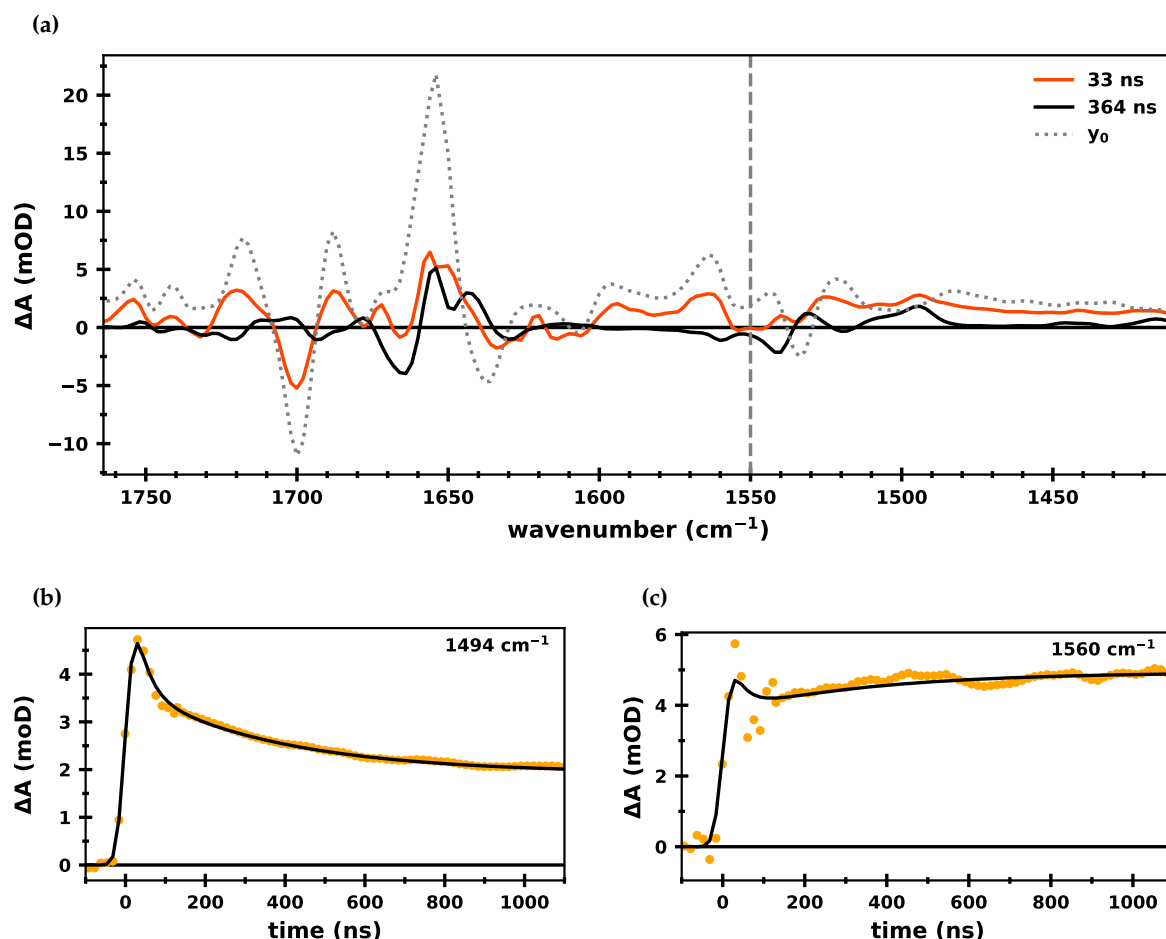

Figure A6.1: Decay associated spectra of the nanosecond phases of PSI core particles from *T. vestitus*. (a) DAS, obtained by globally fitting the time-resolved spectral data set to a sum of two exponentials and an offset with the two time constants fixed to 33 and 364 ns (the values obtained from fitting the data in Fig. 8.2, using the IRF fitting approach. The offset y_0 is shown in grey. **(b)** Time-resolved absorption changes at 1494 cm^{-1} (*yellow*) and fit curve (*black*). Both nanosecond phases are well-resolved. **(c)** Time-resolved absorption changes at 1560 cm^{-1} (*yellow*) and fit curve (*black*). The 33 ns phase is clearly very poorly resolved.

Figure A6.2 shows normalized the millisecond DAS of *T. vestitus*. The data is the same as shown in (the non-normalized) Fig. 8.6, but due to the very large amplitude of the 126 ms phase the shape of the other DAS is hardly discernible without normalization.

The fit results of the global analysis of the nanosecond kinetics of *T. vestitus* at eight high S/N transients are given in Table A6.1; the values are the same as shown graphically in Fig. 8.3.
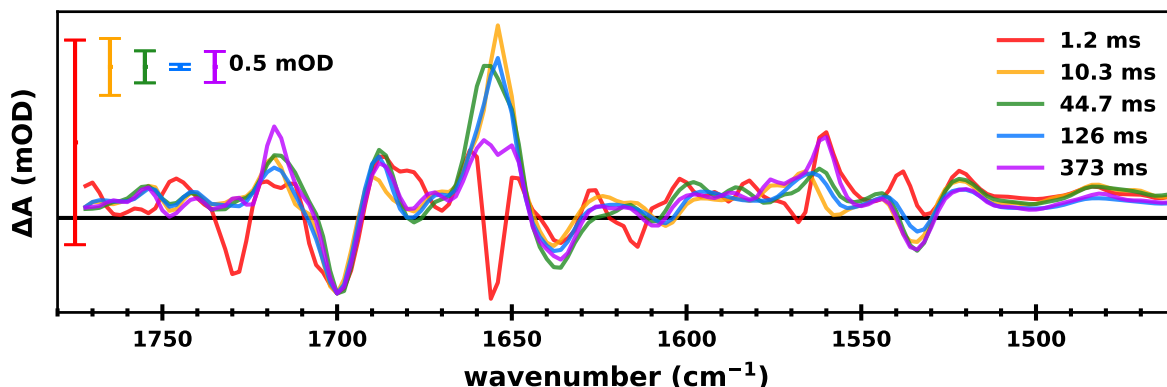
Figure A6.2: Normalized decay associated spectra of the millisecond kinetics of PSI core particles from *T. vestitus*. The DAS was obtained by globally fitting the time-resolved spectral data set to a sum of five exponentials and an offset with the time constants fixed to 1.2, 10.3, 44.7, 126 and 373 ms (the values obtained from fitting the data in Fig. 8.2. The data shown was normalized to the peak at 1700 cm^{-1}, but is otherwise identical to that shown in Fig. 8.6.

Table A6.1: Results from globally fitting the time-resolved IR data in Fig. 8.2 to a sum of two exponentials and an offset. The fit range was -0.5 to 5 μs; the data was iteratively convolved with a Gaussian IRF during the least-squares minimization procedure. The relative contribution of the amplitudes and the offset to the total absorption change from $t = 0$ is given parenthesis. The given error ranges are the parameter uncertainty ranges calculated from the covariance matrix provided by the least squares optimization process (scipy.optimize.least_squares, Python 3.7). This table can also be found in the Supporting Information of the published manuscript (Mäusle et al., 2024).

ν(cm^{-1})	A_1 (mOD) $\tau_1 = 33 \pm 2$ ns	A_2 (mOD) $\tau_1 = 364 \pm 5$ ns	y_0 (mOD)
1415	1.13 ± 0.06 (34%)	0.74 ± 0.02 (23%)	1.41 ± 0.01 (43%)
1430	1.2 ± 0.12 (34%)	0.0 ± 0.04 (0%)	2.32 ± 0.02 (66%)
1482	1.56 ± 0.11 (35%)	0.19 ± 0.03 (4%)	2.78 ± 0.01 (61%)
1494	2.13 ± 0.11 (40%)	1.74 ± 0.04 (32%)	1.5 ± 0.01 (28%)
1510	1.32 ± 0.06 (42%)	0.62 ± 0.02 (20%)	1.19 ± 0.01 (38%)
1534	-0.28 ± 0.12 (10%)	0.73 ± 0.04 (24%)	-1.95 ± 0.02 (66%)
1542	-0.41 ± 0.07 (8%)	-1.86 ± 0.03 (34%)	3.17 ± 0.01 (58%)
1679	1.3 ± 0.07 (46%)	0.93 ± 0.03 (33%)	-0.58 ± 0.01 (21%)

Figure A6.3 shows a direct comparison of FTIR and QCL spectra of PSI from WL and FRL grown *C. thermalis* (the same QCL spectra are also shown in Fig. 8.10).

Figure A6.4 shows the chemical structure of a phylloquinone and relevant numbering of atoms.

(a)

(b)
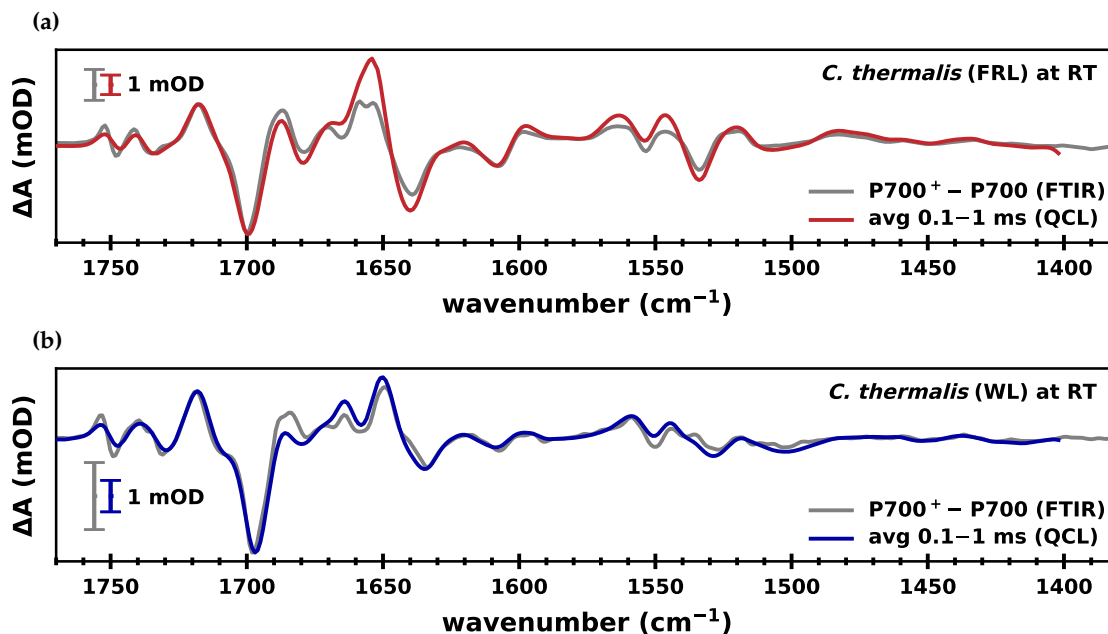
Figure A6.3: QCL and FTIR spectra at RT of PSI from WL and FRL grown *C. thermalis*. **(a)** Photoaccumulated (P700$^+$/P700) FTIR spectra (*grey*) and QCL spectra averaged between 0.1–1 ms (*red or blue*) of PSI from **(a)** FRL gown and **(b)** WL grown *C. thermalis*. The spectra were scaled to their 1718(+)/1700(−) cm^{-1} difference band for easier visual comparison. An extended range of the FTIR data is shown in Fig. 8.10d. The FTIR spectra were measured by N. Argawala and V. G. Eichmann.
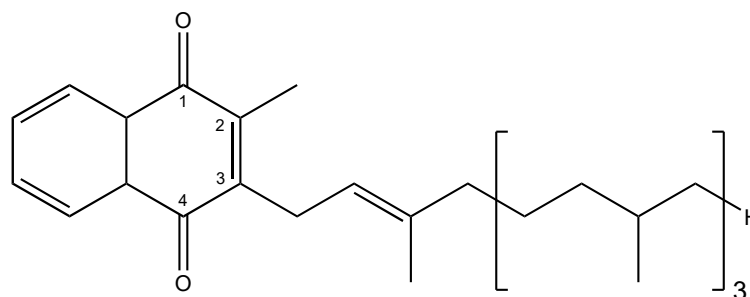
Figure A6.4: Chemical structure of 2-methyl-3-phytyl-1,4-naphtoquinone (phylloquinone). The structure was drawn with ChemDraw; the numbering is as shown in Hastings (2015).

∗ | Acknowledgements